R-08-57

Rock mechanics Laxemar

Site descriptive modelling SDM-Site Laxemar

Eva Hakami, Itasca Geomekanik AB

Anders Fredriksson, Golder Associates AB

Flavio Lanaro, Berg Bygg Konsult AB

John Wrafter, GeoInnova AB

December 2008

Svensk Kärnbränslehantering AB
Swedish Nuclear Fuel
and Waste Management Co

Box 250, SE-101 24 Stockholm
Phone +46 8 459 84 00

SKB

ISSN 1402-3091
SKB Rapport R-08-57

Rock mechanics Laxemar

Site descriptive modelling
SDM-Site Laxemar

Eva Hakami, Itasca Geomekanik AB

Anders Fredriksson, Golder Associates AB

Flavio Lanaro, Berg Bygg Konsult AB

John Wrafter, GeoInnova AB

December 2008

Preface

The report describes the results of the rock mechanics site modelling for Laxemar as part of model version SDM-Site Laxemar. The overall aim of the report is to provide the Repository Design and the Safety Assessment working groups with rock mechanics properties that are typical for the Laxemar local model volume.

In addition to the listed authors, the following people have contributed to the rock mechanics modelling work for SDM-Site Laxemar:

Thushan Ekneligoda, Itasca Geomekanik – *Analysis of borehole stability and porosity effects.*
Malin Johansson, Itasca Geomekanik – *Compilation of stress primary data, Report editing.*
Pär Kinnbom, PKM-Innovation – *WellCad plots in Appendix 1 and 5.*
Caroline van Mourik, BBK – *Compilation of primary data of intact rock.*
Johan Öhman, Golder – *Compilation of primary data of fractures*.

Abstract

As a part of the multidisciplinary site descriptive model for the Laxemar site, the rock mechanics model for version SDM-Site Laxemar is presented in this report. Rock mechanics modelling aims at a comprehensive description of the rock strength, the deformation properties and the in situ state of stress within the Laxemar local model area.

The starting point for the modelling is the geological descriptive model, which divides the local model volume into rock types (and rock domains), fracture domains and deformation zones.

The mechanical description for the intact rock is based on laboratory tests – uniaxial and triaxial compression tests and indirect tensile tests. The model for each rock type includes seven parameters (UCS, σ_{ci}, E, ν, σ_t, c, ϕ), all described as truncated normal distributions. In addition the spatial variation of UCS is analysed and visualised.

The mechanical properties of single fractures are also modelled based on laboratory tests. Tilt tests and direct shear tests have been performed on open, as well as a few sealed, fracture samples taken from drill cores. The description for single fractures includes normal stiffness, shear stiffness, friction, cohesion and dilatancy.

Rock mass properties outside deformation zones are modelled using two different approaches. The empirical approach makes use of drill core mapping data and rock mass classifications indices Q and RMR, and empirical relationships coupling mechanical properties to these indices. The theoretical approach employs numerical simulation of compression of fractured rock blocks, where the fracturing is based on the geological fracture network model (DFN). The two approaches are compared and a final harmonised model attributes mechanical parameter values to the rock mass of the fracture domains of the modelled rock volume. The mechanical properties of deformation zones, at different scales, are modelled in a similar way based on the information obtained from borehole intersects.

The in situ state of stress is estimated through the evaluation of direct measurement data, resulting from overcoring and hydraulic fracturing methods. Indirect stress information is obtained from the observations of occurrence and distribution of borehole breakouts, which is used to further constrain the modelled stress situation. Additional indirect information comes from the few observations of core disking and very limited microcracking in the drill core samples. The possible influence on the stress field, from major deformation zones and from single fractures, is studied using numerical discontinuum models, on two different scales.

Based on the adequate number of laboratory tests and a fair spatial coverage of the samples, the overall confidence in the description of the three dominant intact rock types is judged high. Furthermore, this judgement applies to rock mass properties outside deformation zones and the stress field orientation, while the confidence in models for mechanical properties of single fractures and deformation zones, as well as stress magnitude, is judged to be moderately high.

Sammanfattning

Som en del av den multidisciplinära platsbeskrivningen för Laxemarområdet presenteras den bergmekaniska modellen i denna rapport. Bergmekanisk modellering syftar till en tillfredsställande beskrivning av bergets hållfasthet, dess deformationsegenskaper och bergspänningsförhållandena inom studerat område i Laxemar.

Modelleringen utgår ifrån den geologiska beskrivningen och dess indelning av området i bergarter (och bergdomäner), sprickdomäner och deformationszoner.

Den mekaniska beskrivningen av det intakta berget är baserad på resultaten från laboratorieprovning – enaxiella och triaxiella tryckhållfasthetsförsök och indirekta draghållfasthetsförsök. Beskrivningen för varje bergart innehåller sju parametrar (UCS, σ_{ci}, E, ν, σ_t, c, ϕ) vilka alla beskrivs som trunkerande normalfördelningar. Dessutom analyseras och visualiseras den spatiella variationen hos den enaxiella tryckhållfastheten.

De mekaniska egenskaperna hos sprickor modelleras också baserat på laboratorieprovning. Tilt-försök och direkta skjuv-försök, har utförts på öppna, och ett antal läkta, sprickprov tagna från borrkärnor. Beskrivningen av enskilda sprickor inkluderar normalstyvhet, skjuvstyvhet, friktion, kohesion och dilatation.

Bergmassans egenskaper utanför deformationszoner modelleras med hjälp av två olika angreppssätt. Det empiriska använder resultat från kärnkartering och klassificering med indexen Q och RMR, samt empiriska samband mellan dessa och mekaniska egenskaper. Det teoretiska angreppssättet innebär numerisk simulering av belastning till brott av ett uppsprucket bergblock, där sprickigheten baseras på spricknätverksmodellen i geologiska beskrivningen (DFN). Resultaten från de två angreppssätten jämförs och i en slutlig harmoniserad modell tillskrivs mekaniska parametrar till bergmassan i områdets olika sprickdomäner. De mekaniska egenskaperna hos deformationszoner, av olika storlek, är modellerade på motsvarande sätt baserade på information från borrhål.

Bergspänningsförhållandena i området uppskattas genom analys av mätdata från överborrningsmetod och hydraulisk spräckning. Indirekt spänningsinformation fås från observationer av omfattning och fördelning av bergutfall i borrhål, vilket används för att ytterligare analysera den övre gränsen för förväntad spänning på aktuellt djup. Därutöver fås indirekt spänningsinformation från den begränsade förekomsten av spjälkning av borrkärnor och den mycket låga mikrosprickbildningen i borrkärnan. Den variation i spänningsfältet som man kan förvänta sig, dels på grund av de stora deformationszonerna och dels de mindre sprickorna, har studerats med numeriska diskontinuum-modeller i två olika skalor.

Givet att antalet laboratorietester är relativt stort och den geografiska spridningen av provtagningspunkterna är hygglig, bedöms tilltron till beskrivningen för intakt berg i de tre dominerande bergarterna vara hög. Denna bedömning gäller även för bergmassans egenskaper utanför deformationszonerna och spänningsfältets orientering, medan tilltron i modellerna för enskilda sprickors och deformationszoners mekaniska egenskaper, liksom spänningens magnitud, bedöms vara medelhög.

Contents

1 Introduction

1.1 Background

The Swedish Nuclear Fuel and Waste Management Company (SKB) is undertaking site characterisation at two different locations, the Forsmark and Laxemar-Simpevarp areas, with the objective of siting a geological repository for spent nuclear fuel. The investigations were conducted in a series of campaigns defining data freezes which constitute the basis for versions of site descriptive models. After the last data freeze, 2.3, all the site data were analysed and site descriptive modelling work is carried out. This final site descriptive model (SDM-Site) is an integrated model for the disciplines geology, rock mechanics, thermal properties, hydrogeology, hydrogeochemistry along with a description of the surface system.

Figure 1-1 shows the different SDM-Site report at different levels. This report concerns only the rock mechanics properties only. An important reference for this report is the corresponding reports from the Forsmark site, /Glamheden et al. 2007/, /Glamheden et al. 2008/, /Olofsson et al. 2007/ (background reports) and /SKB 2008/ (main report). The thermo-mechanical properties of the rocks at Laxemar is included in the thermal modelling report /Sundberg et al. 2008/.

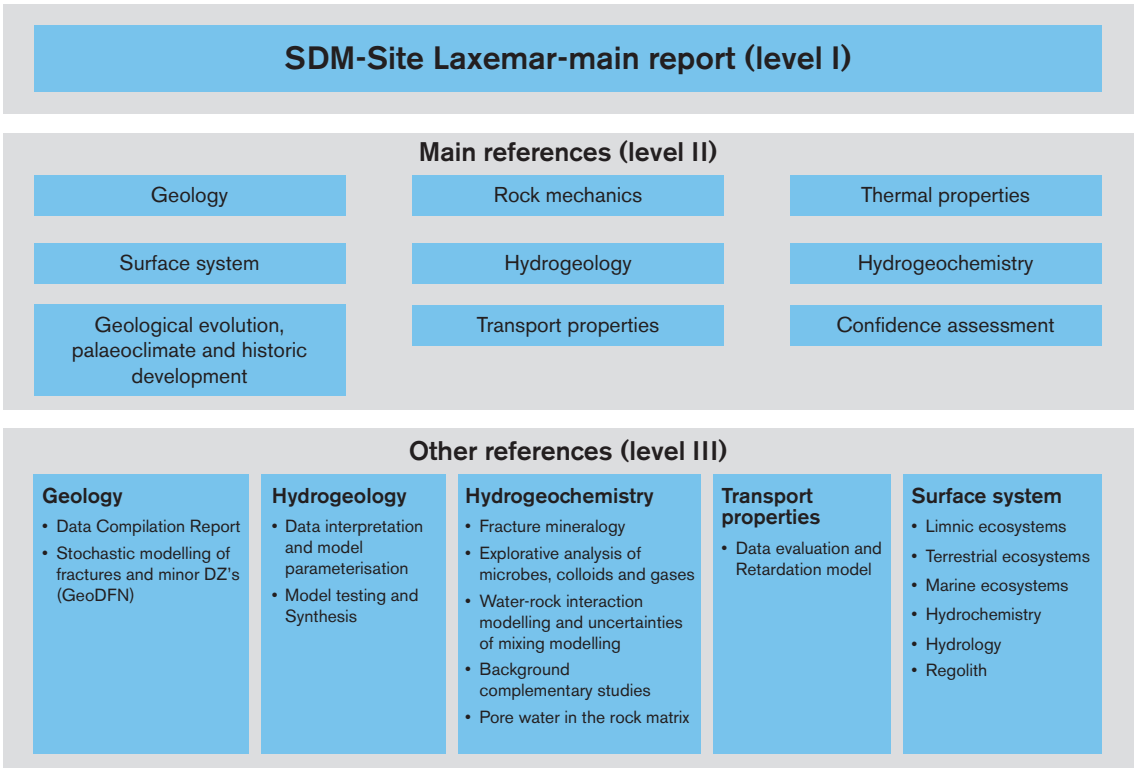

Figure 1-1. *Report structure for the final site description model of the Laxemar site – SDM-Site Laxemar. This report constitutes Rock mechanics, level II.*

1.2 Objective and scope

This report provides a description of the mechanical properties of the rock mass at the Laxemar site in support of SDM-Site Laxemar. The overall aim is to provide the necessary data for design and assessment of long-term safety of a deep repository /Andersson et al. 2000/ and /SKB 2006c/. The specific objectives of the rock mechanics modelling are to:

- Present the current understanding of the mechanical properties of intact rock, single fractures and rock mass in domains presented and described in the corresponding geology modelling /Wahlgren et al. 2008/, as well as assessing the confidence in the presented rock mechanics parameters,
- Present the current understanding of the state of stress, its variability (magnitude and orientation) and its dependence on geological heterogeneities, as well as a quantitative estimate of the uncertainty,
- Incorporate feedback from SR-Can /SKB 2006a/ that is of relevance to the rock mechanics modelling work, thereby further reducing the uncertainties in stress and rock mechanics properties.

Hence, the objective of the current report is not to investigate the stability of tunnels and deposition holes or to indicate where and at what depth a repository may be placed. These analyses will be performed elsewhere in the repository design and safety assessment programme.

1.3 Rock mechanics parameters to be determined

The rock mechanics model shall describe the distribution of the rock mechanics properties and the in situ stresses of the investigated focused area. The model shall also describe the rock quality with regard to constructability /SKB 2000/ and /SKB 2001/. For example, rock mechanics data are used in the repository design to estimate the risk for stability problems and assessment of rock support needs.

Safety assessment requires that the mechanical and thermo-mechanical response of the repository host rock to construction, thermal loading and seismic events can be forecasted with relevant accuracy. Input data to site-specific numerical rock mechanics models must be sufficient that the modelling results allow for reliable conclusions regarding for instance, the scope and extent of mechanically induced disturbances of the hydrological conditions in the far-field and the near-field, and the risk of stress-induced damage around the repository openings /Hökmark et al. 2006/. In the case of reasonably probable and large seismic events, i.e. slip along large zones that are in a state of potential instability towards the end of a glacial cycle, the induced effects on fractures intersecting deposition holes will be calculated using fracture property data derived from the site models /Fälth and Hökmark 2006/.

A compilation of the parameters that are required by different end users and which are included in the rock mechanics site descriptive model are presented in Table 1-1. The thermal expansion of the rock is not included in the table since this parameter is reported in the thermal site descriptive model. Neither is the information from geology, needed as a premise to prepare the rock mechanics description, listed in the table.

Table 1-1. Compilation of rock mechanical parameters included in the site descriptive model with specified end user. Modified after /SKB 2001/.

Parameter group	Parameter	End user
Intact rock	Elastic properties (E ν)	SA
	Crack initiation stress (σ_{ci})	D, SA
	Compressive strength (UCS c ϕ)	D, SA
	Tensile strength (σ_t)	SA
	Micro crack volume	SA (HgC, TP)
Fractures	Deformation properties (K_N K_S)	SA
	Shear strength ($c_{p,r}$ $\phi_{p,r}$ $\psi_{0.5,5,20}$)	D, SA
Rock mass	Elastic properties (E ν)	D, SA
	Compressive strength (c ϕ)	D, SA
	Tensile strength	D
In situ stresses	Orientation	D, SA
	Magnitude	D, SA

D – Repository Design
SA – Safety Assessment
HgC – Hydrogeochemistry
TP – Bedrock transport properties.

1.4 Laxemar setting

The Laxemar-Simpevarp area is located along the coastline of the Baltic Sea in Småland within the municipality of Oskarshamn, about 230 km south of Stockholm (Figure 1-2). The area is characterised by a relatively flat topography in a fissure valley landscape. The investigation area is situated in the western part of one of the planet's ancient continental nuclei, referred to as the Fennoscandian Shield. The part of the shield where the Laxemar-Simpevarp area is situated is dominated by a geological unit referred to as the Transscandinavian Igneous Belt. The bedrock in the latter is dominated by igneous rocks that formed in the time interval 1.86–1.65 Ga /Wahlgren et al. 2008/.

1.5 Locations of the boreholes

Figure 1-3 presents the local model area for model version SDM-Site Laxemar with the locations of drill sites and all boreholes available as of data freeze Laxemar 2.3. Boreholes with prefix "KLX" refer to cored boreholes and those with prefix "HLX" refer to percussion drilled boreholes. A list of all the 21 cored boreholes longer than 400 m located in Laxemar-Simpevarp area is provided in Table 1-2. (Additional holes were cored with a shorter length, but no rock mechanics sampling or characterisation was made in these holes or the percussion drilled holes. The boreholes used in geological modelling, indirectly used also for rock mechanics modelling are not marked in the table.) More detailed listing on available data; the tests performed and sampling locations are found in the corresponding chapters of this report.

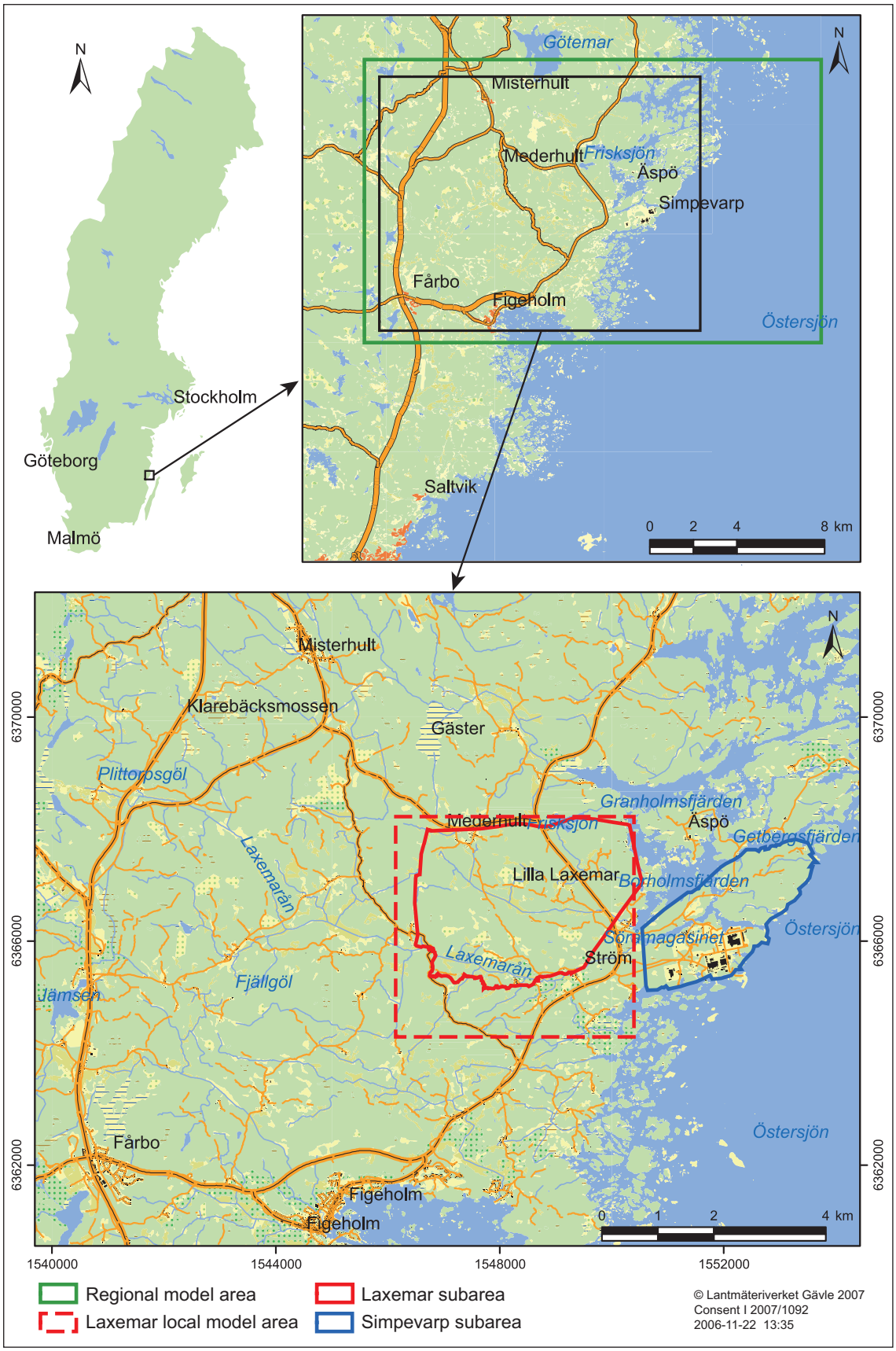

Figure 1-2. *Laxemar settings. The black rectangle shows the spatial extension of the enlarged map. Local model area shown in hatched red.*

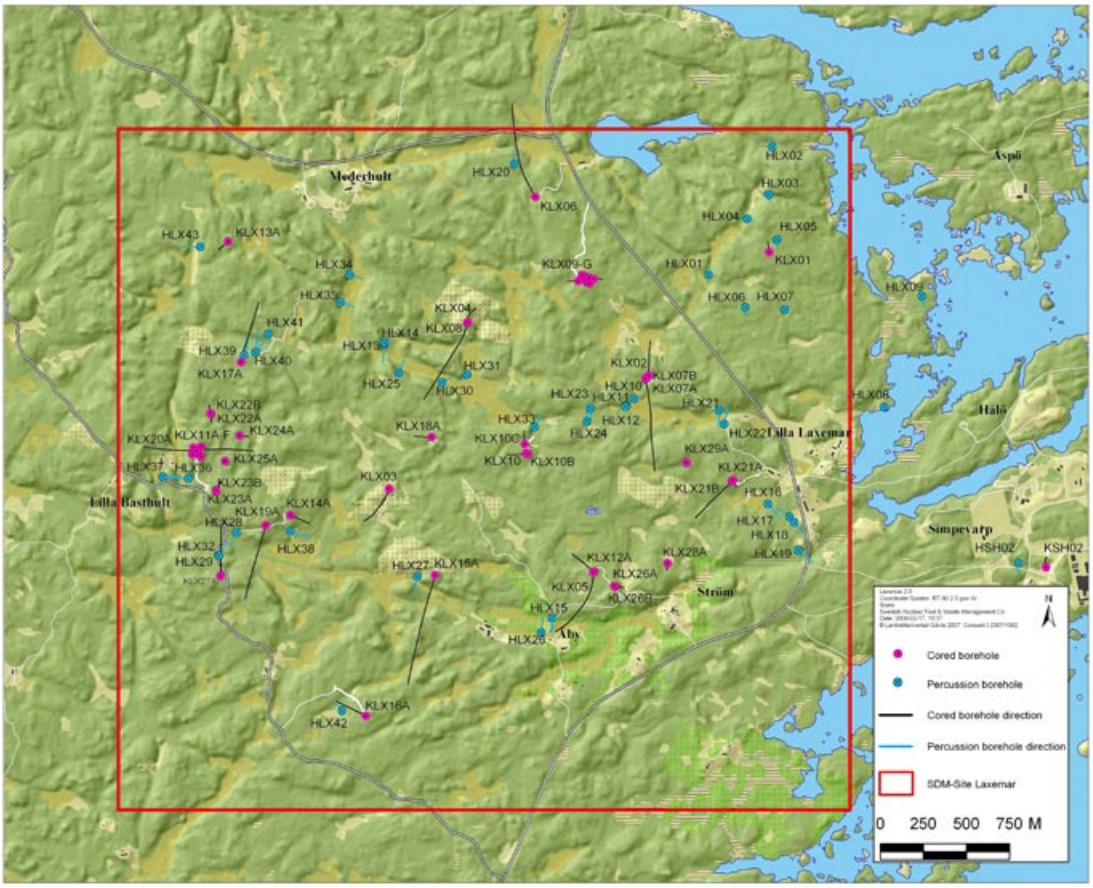

Figure 1-3. *The local model area for SDM-Site Laxemar and the locations for all cored and percussion boreholes.*

1.6 Overview of previous model versions

At the previous model version, Laxemar 1.2 /SKB 2006b/, a rock mechanics model was provided describing the mechanical properties and characteristics of intact rock, fractures, rock mass and rock stresses, as is also done in this current version. The main differences in the description relates to an increased number of laboratory tests, now including all rock types expected to have any significant occurrence and also including characterisation of oxidised rock. In the previous version a large spread in the properties of Ävrö granite was encountered, which is now avoided by a division into two separate rock types used in the description. A further improvement in the description of intact rock is the simulation and visualisation of spatial variation of UCS for different rock domains.

The rock mass properties are currently estimated using roughly the same approach as in model version Laxemar 1.2. However, the characterisation for the rock (mass) in the deformation zones is now more developed, compared to the previous version. Primarily, with the increased amount of geological information of deformation zones, and boreholes now intersections several of them, has enabled a more elaborate rock mechanics description.

The stress model of version Laxemar 1.2 provided predictions for two different stress domains, domain I and domain II, with a fairly large uncertainty in the stress magnitudes of the two. In this current version, following a similar approach, a stress model is provided only for the fracture domains in the focused area. In this area additional stress measurement data have become available from one borehole, KLX12A, which constitutes the main database for the updated stress model.

Table 1-2. List of the core drilled boreholes longer than 400 m within the site investigation program in the Laxemar-Simpevarp area. Each borehole where a certain type of data is available for the rock mechanics modelling is indicated with (x) and where no data is available this is indicated with (–). Available data which were not considered is marked with (o).

	Laboratory testing of intact rock (uniaxial, triaxial or tensile)	Laboratory testing on single fractures (tilt tests or direct shear tests)	Rock mass charaterisation with RMR and Q rating indices	Direct stress measurement (OC or HF/ HTPF)	Occurrence of Borehole breakout checked	Occurrence of Core disking checked
Laxemar						
KLX01*	–	–	o	–	–	X
KLX02*	X	X	X	X	X	X
KLX03*	X	X	X	–	X	X
KLX04*	X	X	X	X	X	X
KLX05*	X	–	X	–	X	X
KLX06*	X	X	–	–	X	X
KLX07A	–	X	–	–	X	X
KLX08	X	–	–	–	X	X
KLX09	–	–	–	–	X	X
KLX10	X	X	X	–	X	X
KLX11A	X	–	X	–	X	X
KLX12A	X	X	–	X	X	X
KLX13A	X	X	–	–	X	X
KLX15A	–	–	X	–	X	X
KLX16A	X	–	–	–	X	X
KLX17A	X	–	–	–	X	X
KLX18A	X	–	–	–	X	X
KLX19A	–	–	X	–	X	X
KLX20A	–	–	–	–	X	X
KLX21B	X	–	–	–	X	X
KLX27A	–	–	–	–	–	X
Simpevarp						
KSH01A*	X	X	o	X	X	X
KSH02*	X	X	o	X	X	X
KSH03A*	–	–	–	–	o	X
KAV01*	–	X	o	–	o	X
KAV04A*	–	–	o	X	X	X

* Included in previous model version Laxemar 1.2.

In total, 12 deep cored boreholes (with a length >500 m) are added, to the previous six, in the focussed volume of Laxemar since model version Laxemar 1.2, which significantly has improved the possibilities for indirect stress modelling, i.e. the study of boreholes breakout and core disking occurrences. The added boreholes also enabled an improved rock mass quality characterisation.

1.7 Nomenclature

The following nomenclature is used within the scope of SDM-Site Laxemar.

Rock type and Rock code

The rock type is the description unit with the smallest scale in the project. For each rock type a specific short *name* is assigned and a certain rock *code* (see Section 1.8.2). The rock types and rock codes are used frequently in rock mechanics modelling and in this report. The longer more descriptive names and the actual description of the rock types are found in /Wahlgren et al. 2008/. Rock types may have clearly different degrees of alteration and still keep the same rock type name and rock code.

Rock unit

A rock unit is defined primarily on the basis of the composition, grain size and inferred relative age of the dominant rock type. Other geological features including the degree of bedrock homogeneity, the degree and style of ductile deformation, the occurrence of alteration and fracture frequency also help define rock units. Both dominant rock type and subordinate rock types are defined for the rock units in the single hole interpretation. Rock units are referred to as RUxx in each single borehole. Thus, there is no unique name for all the rock units at the site.

Rock domain

A rock domain refers to a rock volume in which rock units that show specifically similar rock type composition, grain size, texture, degree of bedrock homogeneity, and degree and style of ductile deformation have been combined and distinguished from each other. A rock domain includes several rock types but is dominated by one main rock type. Different rock domains at Laxemar are referred to as RSMx.

Deformation zone (DZ)

Used as a general notation of a structure along which there is a concentration of brittle, ductile or combined brittle and ductile deformation. In the single-hole interpretation work, deformation zones are referred to as DZxx where the name is coupled to a single borehole. Those deformation zones which are possible to correlate between a surface lineament with a length >1,000 m or have an interpreted true thickness of >10 m in boreholes, are modelled deterministically, and are thus explicitly accounted for in the 3D deterministic deformation zone model. The deterministically modelled deformation zones are given unique names ZSMx zone (intersecting ground surface) or KLXx-DZx (not intersecting ground surface, i.e. only found in boreholes).

Minor deformation zone (MDZ)

All deformation zones that have been identified in a single borehole (i.e. through ESHI) and have an estimated thickness ≤10 m shall be termed minor deformation zones (MDZ). Minor deformation zones are *not* modelled deterministically in RVS, but are handled statistically in the GeoDFN modelling. The MDZ do not have individual names /Hermanson et al. 2008/.

Fracture Domain (FSM)

A fracture domain refers to a rock volume outside deformation zones in which rock units show similar fracture intensity characteristics. Fracture domains at Laxemar are defined on the basis of the single-hole interpretation and its modifications and extensions including identification of minor local deformation zones (MDZ), as presented in /La Pointe et al. 2008/.

The fracture data associated with deformation zones; a) those modelled deterministically in RVS, and b) minor local deformation zones (MDZ), the latter which have been identified in the single-hole interpretation but have not been modelled deterministically, are excluded from the fracture domains for the purpose of initial assessment of fracture domain characteristics (e.g. relative fracture intensity). In the ensuing geological DFN analysis the minor local deformation zones are reintroduced, but are represented by a single fracture.

The term fracture domain is used in the first instance as a basis for the discrete fracture network modelling work (geological DFN). In the rock mechanics model the fracture domains are used in the description of the rock mass properties. Note that in the rock mechanics description the properties of MDZ in the fracture domains are described separately. The different fracture domains at Laxemar are referred to as FSM_x.

Discrete fracture network (DFN)

A discrete fracture network model or DFN involves a description of the fracturing in the bedrock on the basis of a statistical model, which provides geometries, directions and spatial distributions for the fractures within defined fracture domains (including MDZs). The DFN modelling is presented in /La Pointe et al. 2008/ and is summarised by /Wahlgren et al. 2008/.

1.8 Abbreviations and symbols

1.8.1 Abbreviations

The most important abbreviations in use, apart from what was given in the previous nomenclature section, and rock mechanics symbols utilised in the report are also listed, are listed below:

ESHI Extended Single Hole Interpretation /Wahlgren et al. 2008/.

HF Hydraulic fracturing. An in situ stress measurement method.

HTPF Hydraulic Testing on Pre-existing Fractures. An in situ stress measurement method.

OC Overcoring. An in situ stress measurement method.

P_{10} A measure of linear fracture intensity, expressed in this report as the number of fractures per meter (m^{-1}).

P_{21} A measure of areal fracture density, expressed in this report as the fracture trace length per unit of mapped area (m/m^2).

P_{32} A measure of volumetric fracture intensity, expressed in this report as fracture surface area per unit of rock volume (m^2/m^3).

PFL Posiva Flow Log

PFL-f Feature in borehole (single fracture or crush section) with higher conductivity identified with the Posiva Flow Log.

Q Rock Mass Quality index /Barton 2002/

RMR Rock Mass Rating /Bienawski 1989/

RQD Rock Quality Designation /Deere 1964/

RVS Rock Visualisation System

SDM Site Descriptive Model.

1.8.2 SKB rock codes for mechanically tested rock types

Each rock type within the investigated area has been assigned a certain rock code and name that is used for documentation in databases and for model presentations. In the rock mechanics modelling the intact rock properties are described for the most frequently occurring rock types separately. The list of rock codes and names for these rock types are given in Table 1-3. A detailed geological description of each rock type, including mineralogical composition and photographs, is found in /Wahlgren et al. 2008/.

Table 1-3. SKB rock codes and names for rock types in this report.

Rock code	Rock type name
501044 [1)]	*Ävrö granite*
501046	Ävrö quartz monzodiorite
501056	Ävrö granodiorite
501036	Quartz monzodiorite
501030	Fine-grained dioritoid
501033	Diorite/gabbro
511058	Fine-grained granite

1) This rock code is the sum of the two varieties 501046 and 501056.
The rock mechanics properties are modelled for each variety separately.

1.8.3 Symbols

Rock mechanics symbols utilised in the report are listed below.

Roman letters

c	Intact rock cohesion, (MPa)
c_p	Fracture peak cohesion
c_r	Fracture residual cohesion
c_p^{MC}	Fracture peak cohesion related to Mohr-Coulomb model
c_r^{MC}	Fracture residual cohesion related to Mohr-Coulomb model
E	Intact rock Young's modulus
JCS	Joint Compressive Strength, (MPa)
JCS_{100}	Joint Compressive Strength of a 100 mm fracture length
JRC	Joint Roughness Coefficient
JRC_{100}	Joint Roughness Coefficient of a 100 mm fracture length
K_N	Secant normal stiffness, (MPa/mm)
K_{NF}	True normal stiffness
K_{NM}	Measured normal stiffness
K_{NT}	Holder and grout normal stiffness
K_S	Secant shear stiffness, (MPa/mm)
$K_{S0.5,5,20}$	Secant shear stiffness at 0.5, 5 and 20 MPa normal stress, (MPa/mm)
m_i	Hoek-Brown constant for intact rock
UCS	Intact rock uniaxial compressive strength (from uniaxial tests), (MPa)
UCS_T	Intact rock uniaxial compressive strength (from triaxial and uniaxial tests), (MPa).

Greek letters

δ_F	Fracture normal deformation, (mm)
δ_T	Holder and grout normal deformation
ϕ	Intact rock friction angle, (°)
ϕ_b	Fracture basic friction angle
ϕ_p	Fracture peak friction angle
ϕ_r	Fracture residual friction angle
ϕ_b^{BB}	Fracture basic friction angle related to Barton-Bandis model
ϕ_p^{MC}	Fracture peak friction angle related to Mohr-Coulomb model
ϕ_r^{MC}	Fracture residual friction angle related to Mohr-Coulomb model
ν	Intact rock Poisson's ratio
$\sigma_{1,2,3}$	Major, intermediate and minor principal stress
$\sigma_{H,h,v}$	Major horizontal, minor horizontal and vertical stress components
σ_c	Intact rock uniaxial compressive strength
σ_{ci}	Crack initiation stress, (MPa)
σ_n	Fracture normal stress, (MPa)
σ_t	Indirect tensile strength of intact rock
τ	Fracture shear strength, (MPa)
ψ	Dilation angle, (°)
$\psi_{0.5,5,20}$	Fracture dilation angle at 0.5, 5 and 20 MPa normal stress, (°)

1.9 Structure of this report

The rock mechanics modelling work reported here is divided into several parts. Chapter 2 presents a short overview of the geological model with focus on parts of importance for the rock mechanics model. The primary data on intact rock and fractures are presented and models for the mechanical property parameters are developed in Chapter 3 and Chapter 4, respectively.

Chapter 5 provides the estimated rock mass strength and deformation modulus based on empirical and theoretical modelling, and finally presents the final harmonised rock mass property model. A model for the in situ state of stress, based on in situ stress observations and stress modelling attempts is described in Chapter 6. Chapter 7 summarises the rock mechanics model and finally conclusions are drawn in Chapter 8 of the report.

The report is completed by a number of appendices (1–8) that are linked to various parts of the bulk text. Appendix 1 presents WellCad plots including the locations for intact rock sampling and fracture sampling together with geological information for each cored borehole. Appendix 2 presents complementary information on mechanical properties of fractures. Appendices 3 and 4 include additional results from the empirical and theoretical modelling of the rock mass, respectively. WellCad plots of the borehole observations of interest for the stress modelling are presented in Appendix 5. Additional presentation of results from stress measurements are presented in Appendix 6 and from the numerical modelling of stresses in Appendix 7. The simulation of spatial variation of uniaxial compressive strength is reported in Appendix 8.

2 Input from other disciplines

The starting point for the rock mechanics modelling is by necessity the results of the geological modelling. In the analysis of test data the division of intact rock samples is based on the rock types defined in the geological model. The rock domain concept is used in the modelling of the rock mass to determine the dominating rock types in different regions and the division into fracture domains is the basis for the use of DFN in the modelling of rock mass mechanical properties. The deformation zone model is used to define the boundaries for deformation zone sections in boreholes and as major starting point for analysis of stress variation.

2.1 Geological model overview

The SDM-Site Laxemar geological model is described in /Wahlgren et al. 2008/. A brief description of the geological model with its rock types, rock domains, fracture domains and deformation zones is provided here, with emphasis on the factors that have played a direct role in the rock mechanics modelling.

2.1.1 Rock types in the Laxemar area

Three rock types are dominant in the Laxemar local model area; Ävrö granodiorite (501056), Ävrö quartz monzodiorite (501046) (two variants of the Ävrö granite, 501044) and Quartz monzodiorite (501036). The division into the different rock types was based on studies of mineralogical and textural differences between rock samples. The results of the modal and geochemical analyses of all surface and drill core samples from the Laxemar local model volume are presented in Figure 2-1. It may be noted that there is a fairly large spread in composition also among samples that are classified to belong to the same rock type.

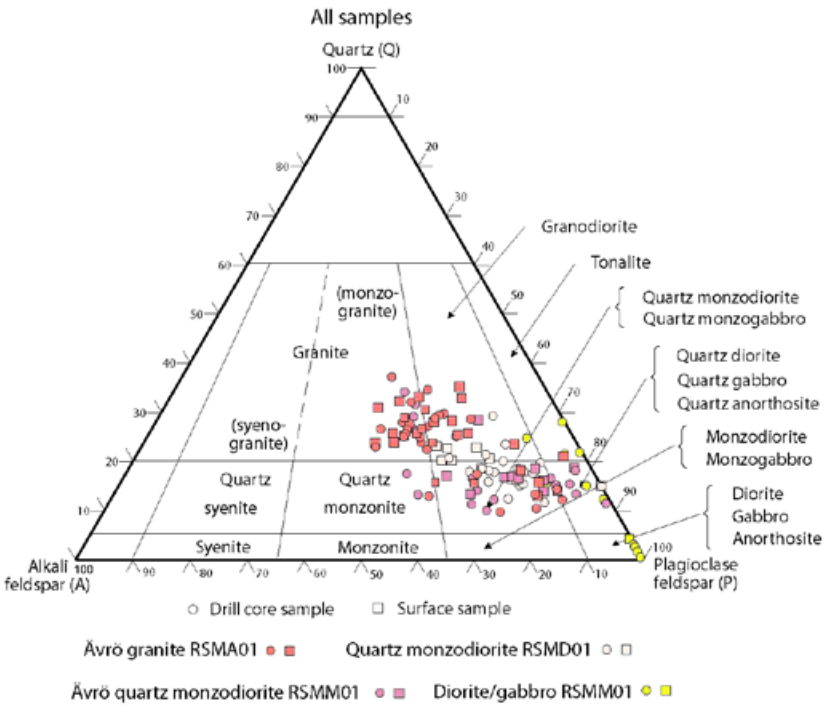

Figure 2-1. *QAP modal composition of the dominant rock types in the Laxemar local model volume /Wahlgren et al. 2008/.*

2.1.2 Rock domain model

Three-dimensional rock volumes, rock domains, in which the lithological characteristics are interpreted as being fairly homogeneous have been devised /Wahlgren et al. 2008/. Each rock domain contains almost all different rock types to some minor extent, but is dominated by one of them. The SDM-Site Laxemar distribution of the rock domains at the surface in the regional scale model is shown in Figure 2-2, the local scale model is shown in Figure 2-3 and Figure 2-4, and a three-dimensional view of the rock domain model inside the local scale model volume is presented in Figure 2-5.

The domain RSMA01 is the largest and is located in the northern part and also south of the local model volume. Domain RSMA01 has a boundary to the domain RSMM01 which is curved and gently dipping towards the north. Inside domain RSMM01 (M as in "mixed") there is a fairly large mix of rock types but the main rock types are the Ävrö quartz monzodiorite and Diorite to Gabbro. The southern boundary of RSMM01, towards domain RSMD01, is also curved and gently dipping towards north, such that the extent of domain RSMD01 is slightly larger at repository depth compared to at ground surface.

The complex domains, RSMP (shown in grey), are not representing a different rock type but the geological description of these domains is quite different since these domains are including several major ductile deformation zones, which significantly has influenced the rocks in the domains.

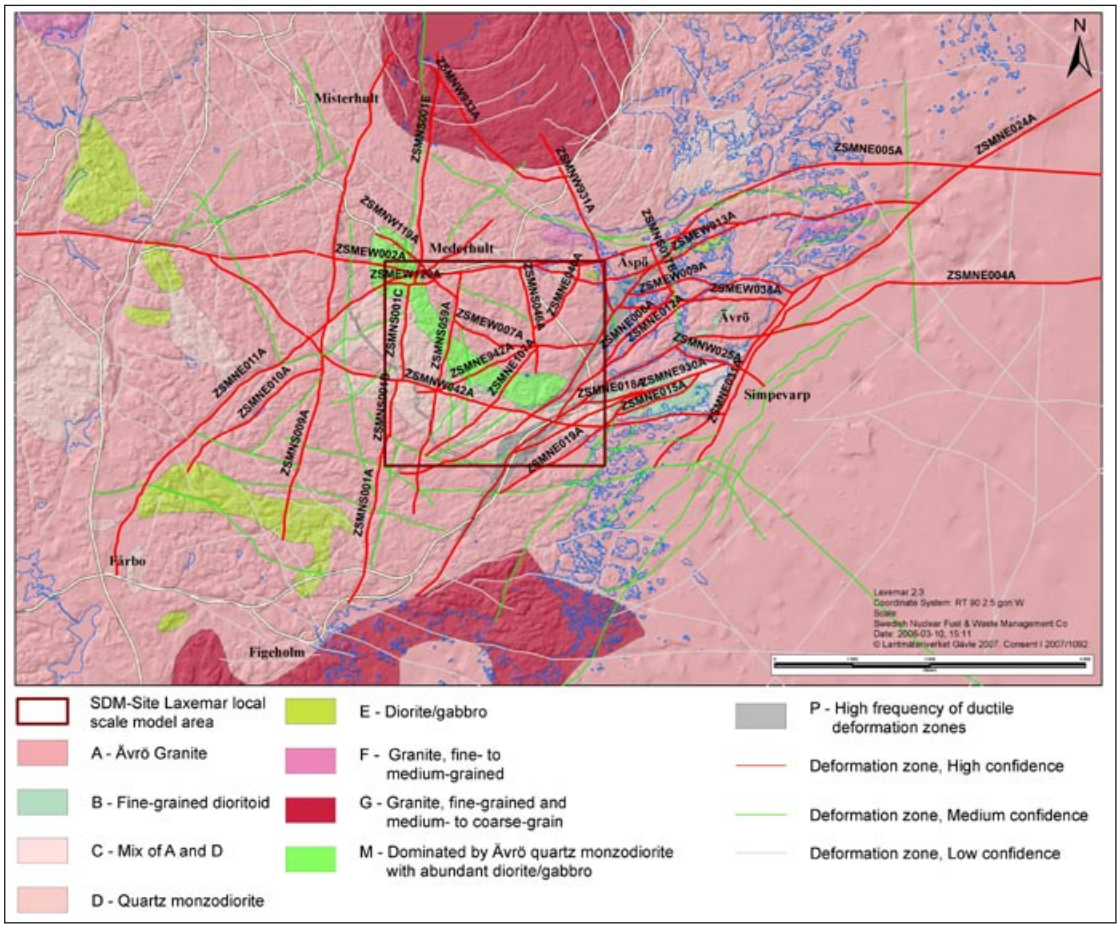

Figure 2-2. *Bedrock geological map of the Laxemar-Simpevarp regional model area including regional deformation zones in the Laxemar and Simpevarp local model areas. For a close up bedrock geological map see Figure 2-3 /Wahlgren et al. 2008/.*

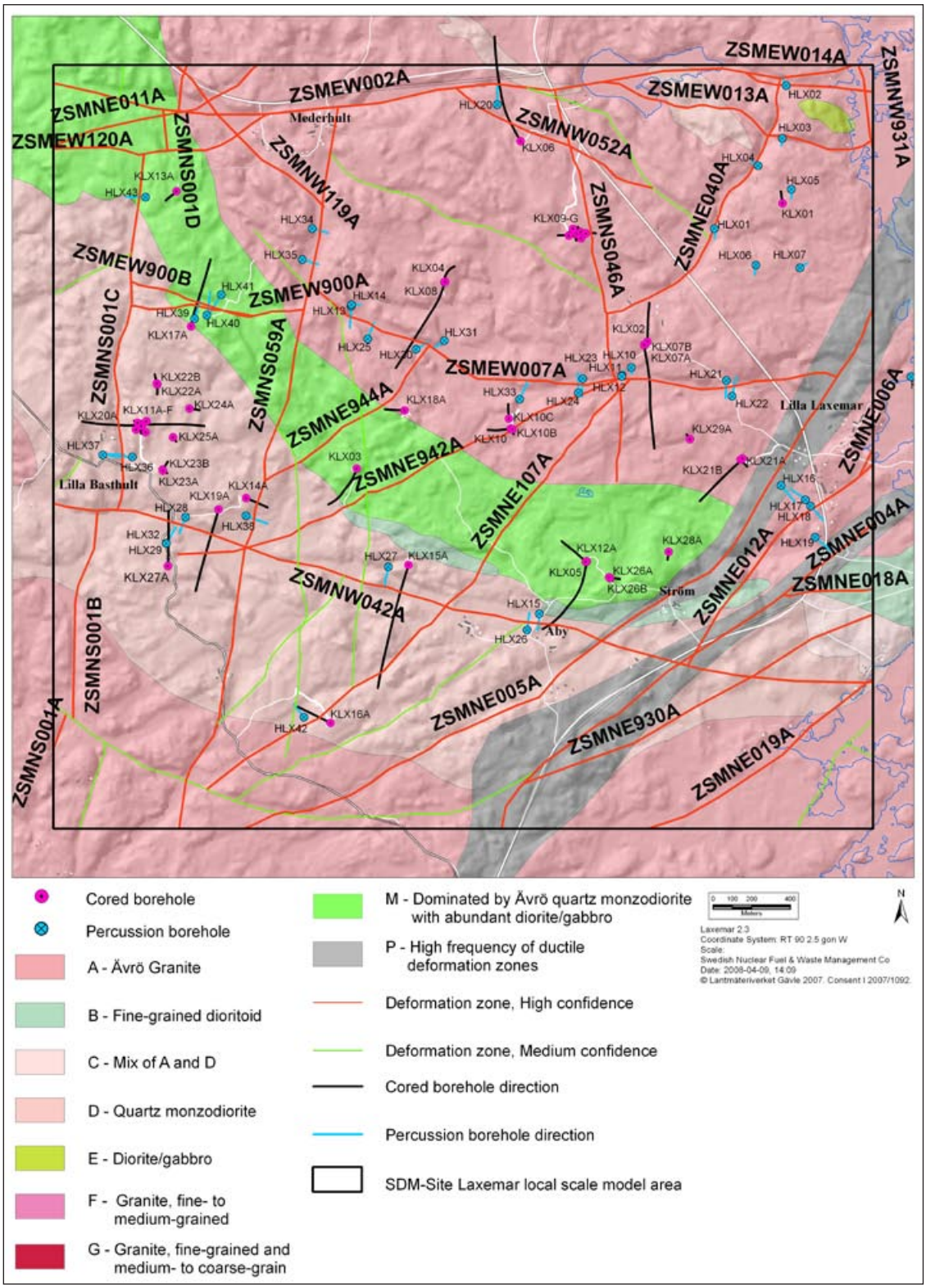

Figure 2-3. *Bedrock geological map of the Laxemar local model area including regional deformation zones; the locations of all the cored boreholes inside the local model volume are also shown /Wahlgren et al. 2008/.*

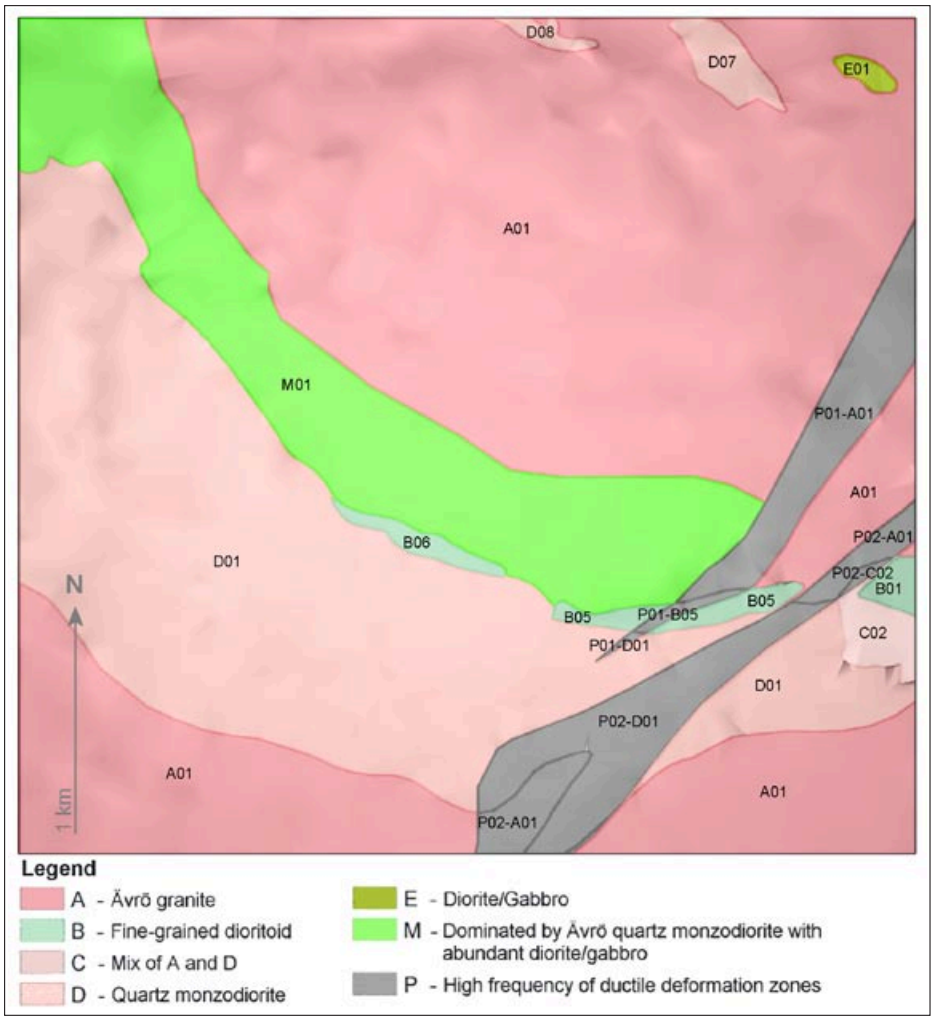

Figure 2-4. *Plan view of the three-dimensional SDM-Site Laxemar rock domain model of the local model volume, plan view at ground surface /Wahlgren et al. 2008/.*

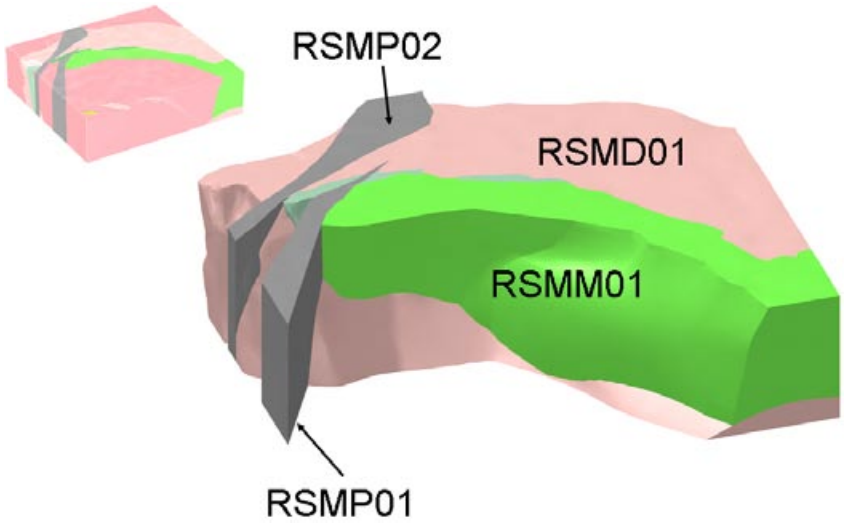

Figure 2-5. *Three dimensional model (birds eye view from north) of rock domains (see plan view in Figure 2-4). Rock domain RSMA01 is made fully transparent in this figure /Wahlgren et al. 2008/. Note that the boundary between rock domains is dipping towards north, such that the proportion of rock domain RSMD01 gets larger with depth.*

The proportions of different rock types in rock domains are shown in Table 2-1 (values are taken on from Figure 4-8, Figure 4-10, Figure 4-13 and Appendix 4 in /Wahlgren et al. 2008/ and the values are rounded off). For Ävrö granite (501044), the division into Ävrö granodiorite (501056) and Ävrö quartz monzodiorite (501046) is made based on /Sundberg et al. 2008/. Similarly the separation of oxidised and non-oxidised portions of the quartz monzodiorite (501036) was taken from Table 5-2 to Table 5-4 in /Sundberg et al. 2008/. Note that all rock types may show some small amount of alteration, while in the table only the amount of the oxidised quartz monzodiorite is separated from the non-oxidised part. Quantitative estimates of proportions of different rock types in rock domain RSMA01 are based only on information from KLX02, KLX04, KLX07A/B, KLX08, KLX10, KLX18A and KLX21B, boreholes being considered more representatives for the bedrock in the central and southern part of the RSMA01 domain.

2.1.3 Model of deterministic deformation zones

The deterministic modelling of deformation zones addresses zones that vary in length from 1,000 m and upwards. The prime difference between the model version SDM-Site Laxemar and previous models concerns the increased number of boreholes with information.

A conceptual geometric model for a brittle deformation zone at Laxemar is presented in Figure 2-6. The deformation zones are subdivided into a transition zone and a core. The transition zone, which ranges from a few metres up to a few hundred metres at Laxemar, exhibits a fracture frequency and commonly also an alteration that are anomalous with respect to that observed in the host rock. If the deformation zone includes a core, the core thickness may vary from a few centimetres up to a few metres. The core is normally composed of a high frequency of fractures and some crushed sections in combination with rock alteration.

Deformation zones were modelled deterministically inside the local model volume /Wahlgren et al. 2008/. Vertical and steeply dipping deformation zones dominate the picture and comprise 48 zones whereas an additional 12 zones are gently dipping. All deformation zones that were modelled deterministically within the local model volume are presented in horizontal and vertical sections in Figure 2-7 and Figure 2-8. Five sets of deformation zones can be distinguished at Laxemar;

- Northeast-southwest
- North-south
- East-west to northwest-southeast, dip to the south
- East-west, dip to the north
- Gently dipping
- Deformation zones without surface connection

Table 2-1. Proportions of rock type occurrence in the three largest rock domains in Laxemar.

Occurrence of Rock type (rock code)	Rock Domain		
	RSMA01 [%]	RSMD01 [%]	RSMM01 [%]
Ävrö granodiorite (501056)	62	0.5	24
Ävrö quartz monzodiorite (501046)	22	0.6	43
Oxidised Ävrö quartz monzodiorite (501046)	4	–	7
Quartz monzodiorite (501036)	3	80	0.4
Oxidised quartz monzodiorite (501036)	–	8	–
Diorite-gabbro (501033)	0.2	0.1	16
Fine-grained granite (511058)	3	5	5
Fine-grained dioritoid (501030)	3	0.3	0.4
Fine-grained diorite-gabbro (505102) [1)]	2	2	2
Granite (501058) [1)]	1	0.4	2
Pegmatite (501061) [1)]	0.3	1	0.5
Dolerite (501027) [1)]	–	2	–

1) Not included in rock mechanics description.

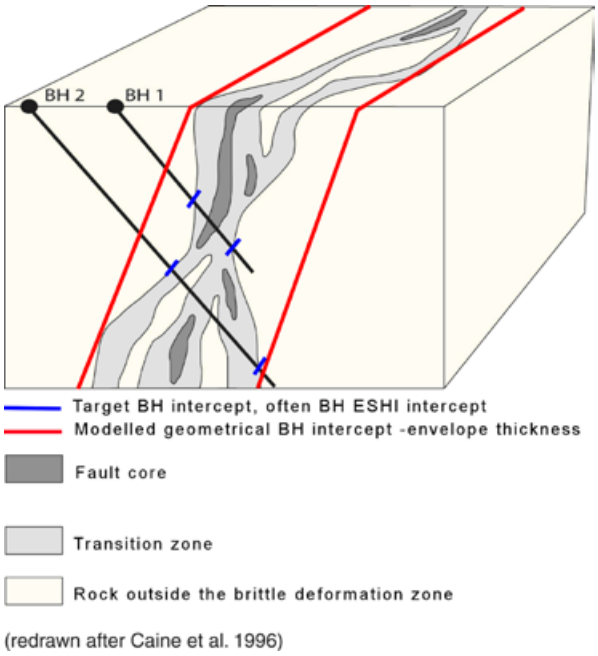

Figure 2-6. *Three-dimensional cartoon illustrating a conceptual geometric model for a brittle deformation zone at Laxemar from /Wahlgren et al. 2008/.*

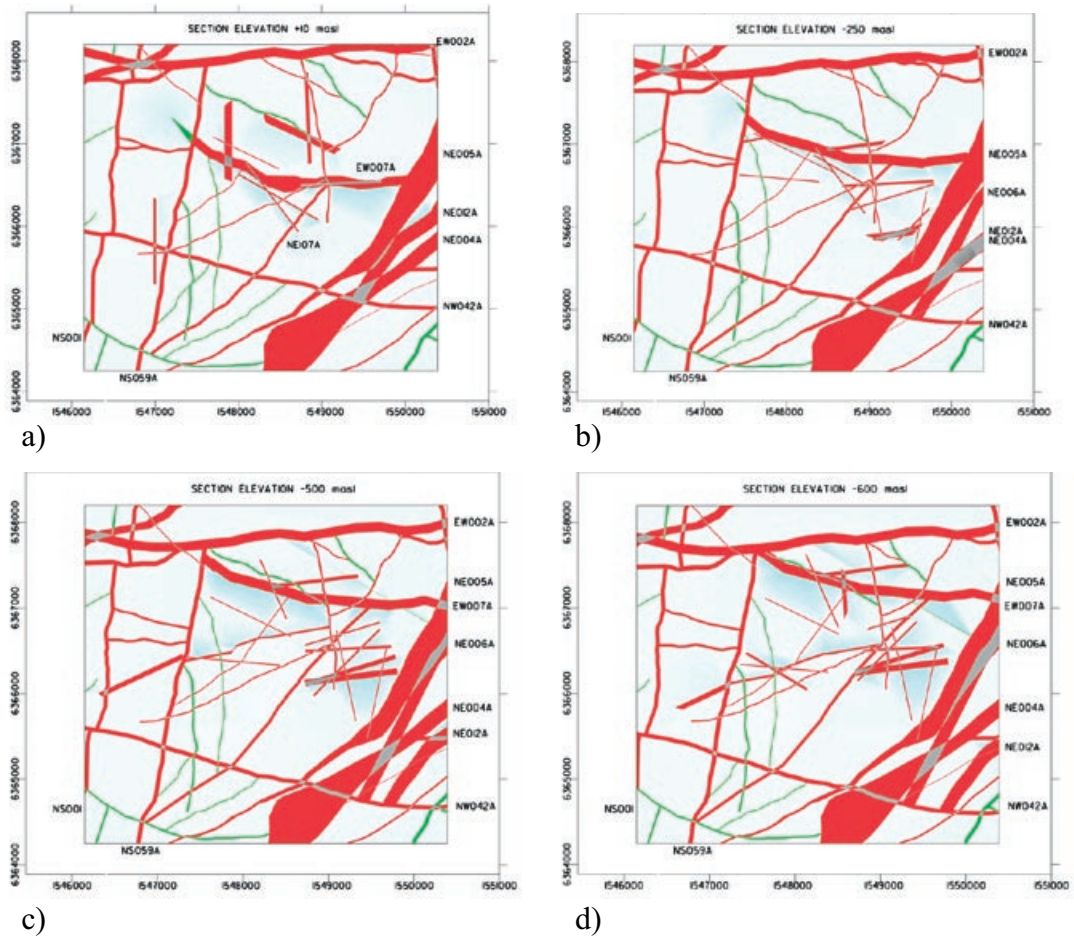

Figure 2-7*. All deformation zones in a horizontal section at four different depths within the local model; Plan views at a) +10 masl, b) –250 masl, c) –500 masl and d) –600 masl, from /Wahlgren et al. 2008/.*

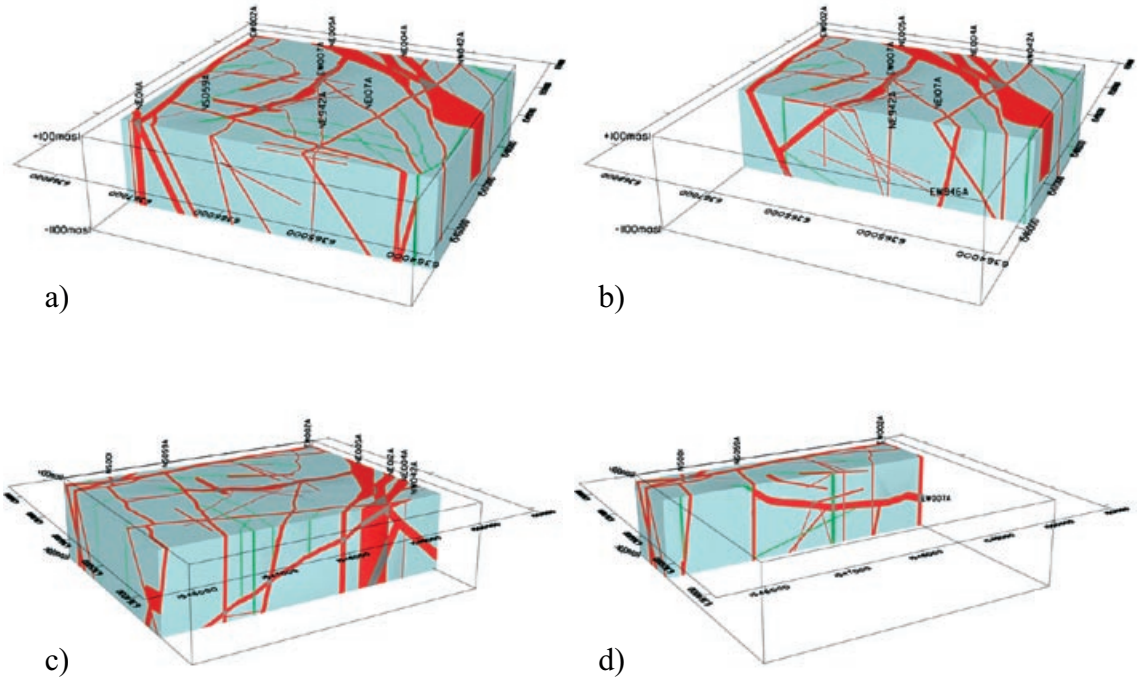

Figure 2-8. *All deformation zones in local model volume, cut at four different vertical sections: a) and b) shows two different N-S sections and c) and d) shows two E-W sections. The model is viewed to the north-east, from /Wahlgren et al. 2008/.*

At the scale of local major and regional deformation zones there are no zones which are solely ductile. Many zones have a ductile origin but all show clear signs of subsequent brittle reactivation. A single zone, ZSMEW007A, which has been investigated by a number of boreholes, is the only zone that is interpreted as being solely brittle with no evidence of an earlier ductile phase.

The character and kinematics of the deformation zones have been studied in detail by /Viola and Venvik Ganerod 2007/. A more extensive overall study of all the available kinematic data across Laxemar and Simpevarp is currently underway. All the evidence to date shows that the brittle history of Laxemar is complex, involving a series of reactivation events.

The division between local minor deformation zones and local major deformation zones is set at an associated surface lineament trace length of 1,000 m. A Laxemar-specific, thickness-length relationship, based on interpreted deterministic deformation zones, suggests that a zone with a true thickness >10 m in boreholes has a length >1,000 m. All deformation zones that have been identified in a single borehole (i.e. through ESHI) and have an estimated thickness ≤10 m are termed minor deformation zones (MDZ). Minor deformation zones are not modelled deterministically in RVS, but are handled statistically in the GeoDFN modelling.

Red staining (oxidation) caused by a fine-grained dissemination of hematite can be found associated with a majority of the deformation zones. Crushed zones are mapped separately during the drill core mapping and often represent sections characterised by increased hydraulic conductivity.

A description of the geological properties (such as length, thickness, fracture frequency, core thickness and alteration) of each of the deterministically modelled deformation zones, including information on the supporting observations and data, can be found in Appendix 14 of the main geology report /Wahlgren et al. 2008/.

The most common fracture minerals in the Laxemar subarea are calcite and chlorite which occur in several different varieties and are present in most of the open fractures. Other common minerals are epidote, quartz, clay minerals, pyrite, prehnite, adularia (K-feldspar), hematite, zeolites (e.g. laumontite and harmotome), gypsum and fluorite /Wahlgren et al. 2008/. The fracture mineralogy is summarised in Figure 2-9.

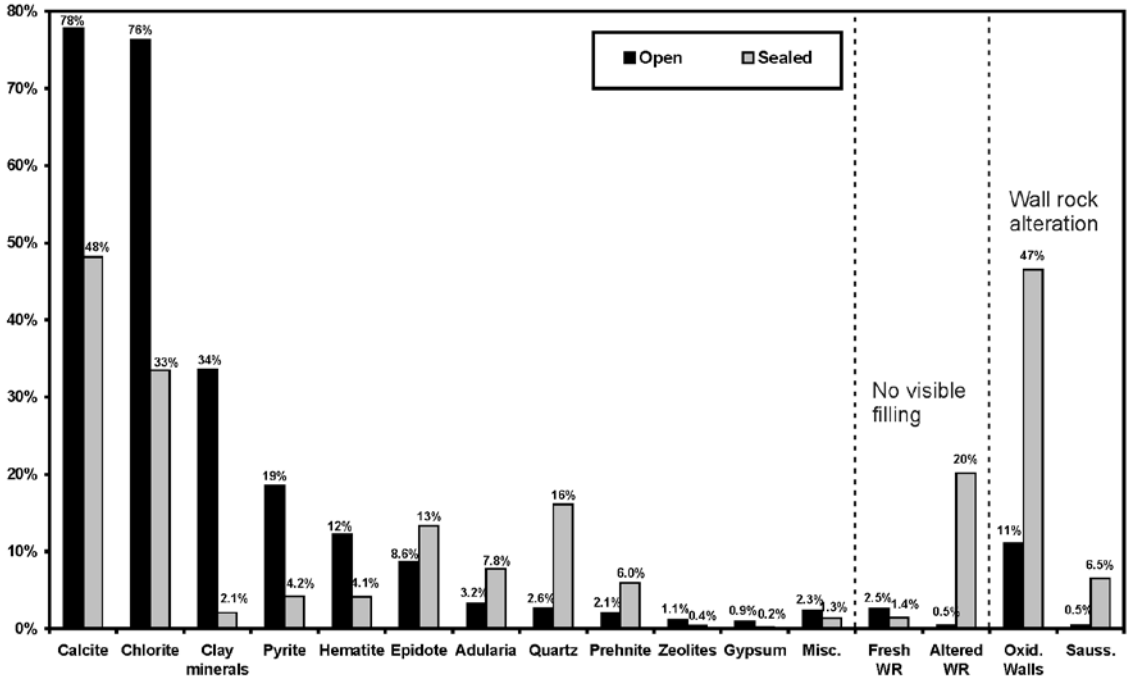

Figure 2-9. *Frequency of fractures (open as well as sealed) filled or coated with specific minerals (several minerals are usually found in the same fracture). Data is from the Boremap mapping from KLX02–KLX29A (also including minerals listed as additional minerals in the Boremap comment files). The number of sealed fractures is 69,229 and the number of open fractures is 33,499. "Adularia" includes "red feldspar" and "white feldspar". Zeolites include minerals mapped as "laumontite" and "zeolites". "Misc." includes fluorite, muscovite, sericite, talc, chalcopyrite, sphalerite, sulfides, amphibole, goethite, apophyllite, barite and biotite. "No visible filling – Fresh WR" are mapped as "Broken fractures with a fresh appearance and no mineral fill" in the Boremap mapping. "No visible filling – Altered WR" are mapped as "oxidised walls", "fractures with epidotized/saussuritized walls" or "bleached fracture walls" without any visible fracture minerals. Wall rock alteration "Oxid. Walls"and "Sauss" show frequency of fractures with oxidised (red-stained) and saussuritized wall rock, respectively; from /Wahlgren et al. 2008/.*

2.1.4 Fracture domain model

A fracture domain refers to a rock volume outside deformation zones in which rock units show similar fracture frequency characteristics. Fracture domains in Laxemar are defined on the basis of the single-hole interpretation work, and the results of the statistical treatment of fractures /La Pointe et al. 2008/. The fracture domain model captures both open and sealed fractures and ultimately forms the basis for development of the geological discrete feature network (DFN) model.

The analysis in /La Pointe et al. 2008/ concluded that six separate fracture domains were possible to distinguish within the local model volume, namely FSM_C (central), FSM_W (west), FSM_N (north), FSM_S (south), FSM_EW007 (proximity of deformation zone ZSMEW007) and FSM_NE005 (proximity of ZSMNE005). Figure 2-10 shows the fracture domain model with the deterministic deformations zones in the local model area.

Fracture domain FSM_C is located in the central part of the volume being focus for the planned repository. The bedrock in this domain can be described as medium fractured rock including a mixture of crystalline rocks. In the northern part the main portion is Ävrö quartz monzodiorite and in the south of this fracture domain the dominating rock type is quartz monzodiorite.

Fracture domain FSM_W and FSM_NE005 show similar fracture intensity as compared to FSM_C, but the proportion of the intensity for different fracture sets vary slightly, such that the N-S set is more frequent in FSM_W, due to influence of the NS oriented deformation zones in the western part of the local model volume.

Fracture domain FSM_EW007 is situated in close proximity of deformation EW007A and a higher frequency of fractures sub-parallel to this deformation zone is observed in this fracture domain. Also the fracture intensity in general is slightly higher in this domain. The main rock type in FSM_EW007 is Ävrö granodiorite, but there is a mixture with the other rock types to some minor extent.

In the northern fracture domain, FSM_N, the fracture intensity is slightly larger than in FSM_C, in the same order as for FSM_EW007 but with a slightly different distribution for the fracture sets.

2.1.5 Discrete fracture network model – DFN

For each fracture domain, the fracture network is described with a fracture network model (DFN) by giving statistical parameters for the expected distribution of fracture size, fracture intensity (location) and fracture orientation /La Pointe et al. 2008/.

The intensity values for the geological DFN model have been derived from outcrops and borehole data. Fractures identified as belonging to deformation zones (as defined by the ESHI) were removed from the data used in the derivation. The summarised fracture intensity (P_{32}) as a function of elevation, in fracture domain FSM_C, is given as an example in Figure 2-11 (see Section 1.8 for definitions of P_{32}). It may be noted that roughly half of the total fracturing consists of sealed fractures in this domain. Further is may be noted that there is no clear depth trend in the fracture intensity.

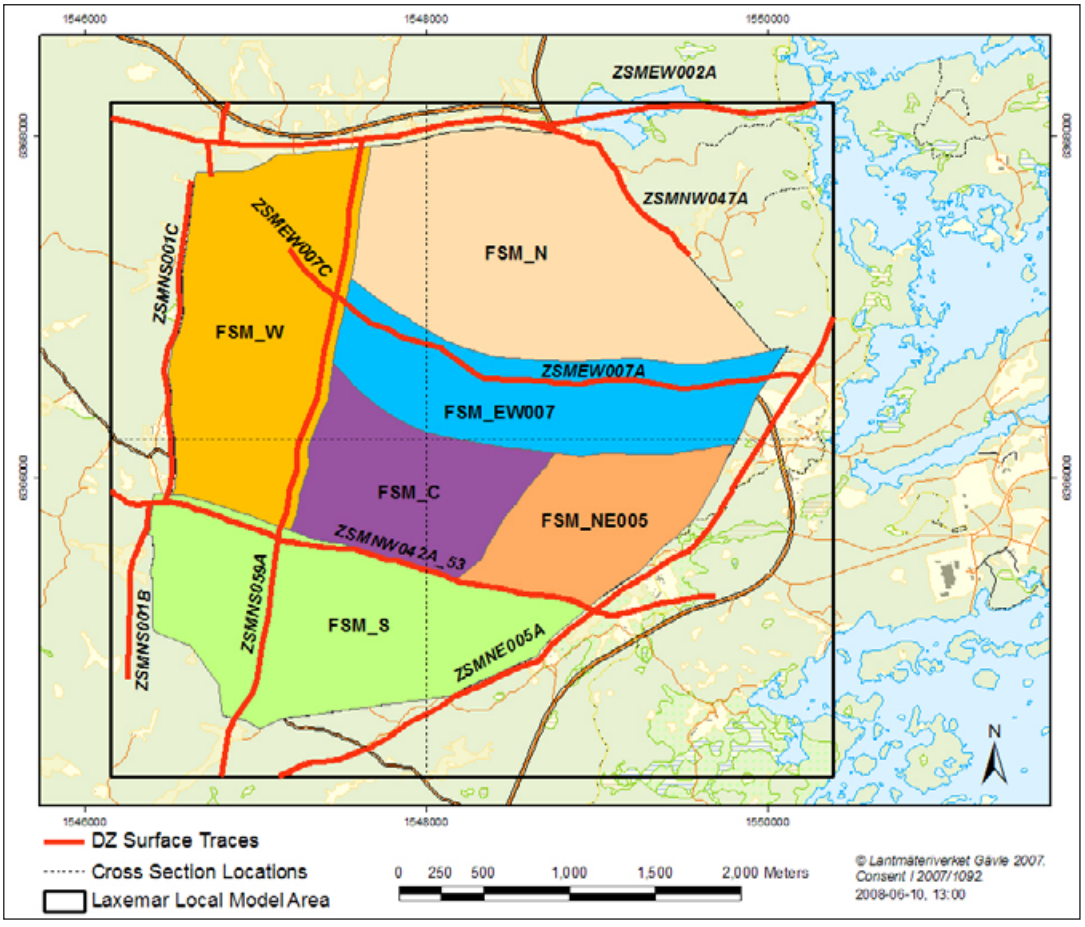

Figure 2-10. *Fracture domains (FSM_x) together with some of the major deterministic deformations zones (ZSMxx) that are encountered in the local model volume at ground level /Wahlgren et al. 2008/. The fracture domains are used to describe volumes with similar properties in terms of fracture intensity and orientation. The same domains are used in the rock mechanics description for rock mass properties.*

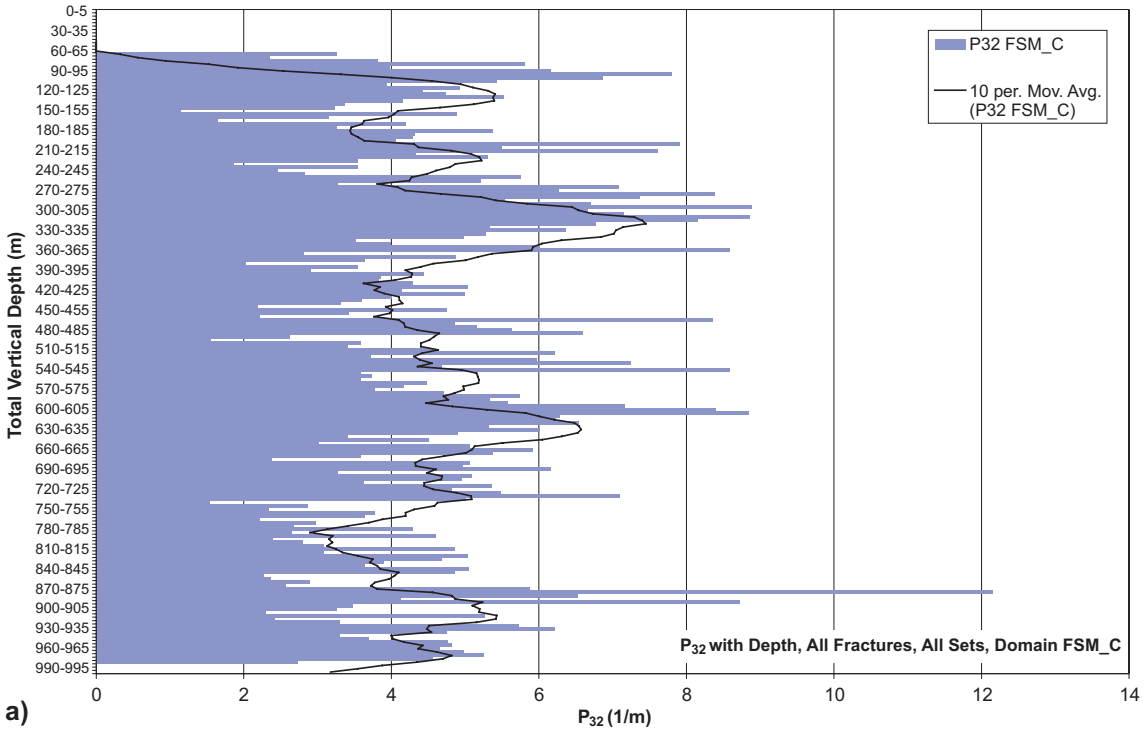

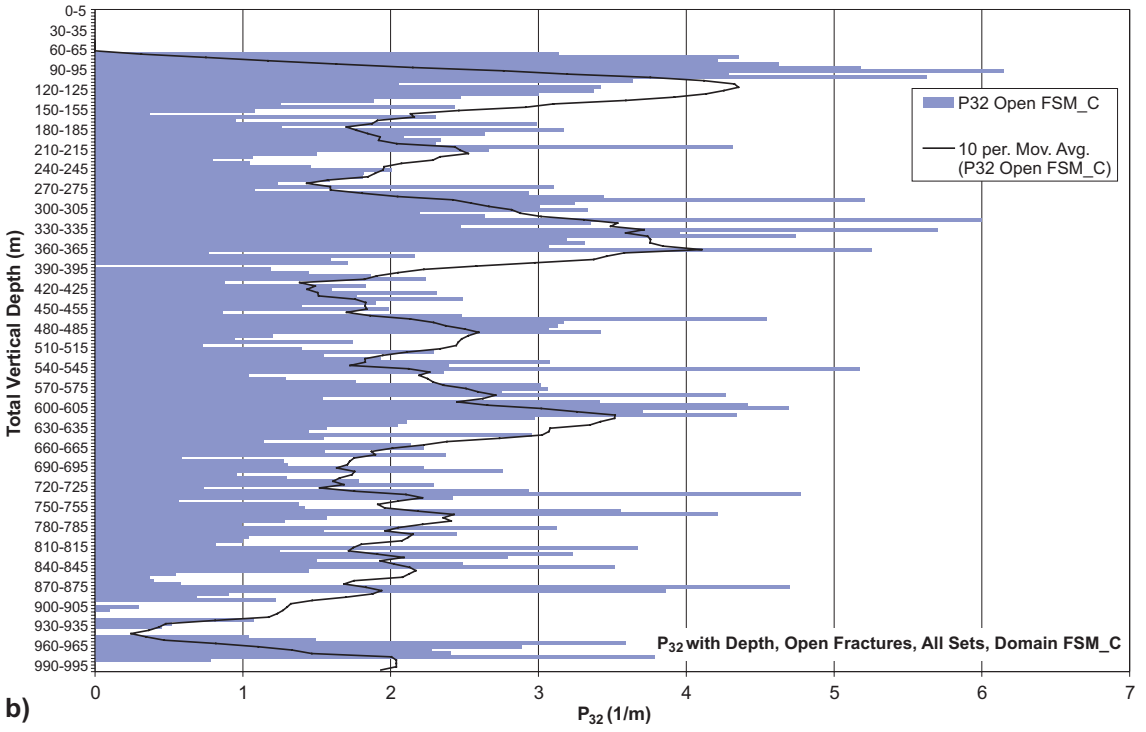

Figure 2-11. *Fracture intensity (P_{32}), in domain FSM_C, as a function of vertical depth for a) all fractures (open and sealed) and b) open fractures only /La Pointe et al. 2008/.*

The orientation of fractures hae also been studied and modelled for each of the fracture domains. In Figure 2-12 the polar stereoplot contours are given for all fractures (open and sealed) and for the open fractures only, in fracture domain FSM_C. Clear fracture set may be identified.

The DFN model comprises alternative models on size and intensity scaling. Adjustment factors for spatial variations in facture intensity based on lithology or depth are also included.

The rock mechanics modelling uses the DFN-model for theoretical modelling of the rock mass properties, see Section 5.1. Further details concerning the DFN model are found in /La Pointe et al. 2008/.

2.1.6 Minor local deformation zones – MDZ

A minor deformation zone (MDZ) is a deformation zones that have been identified in a single borehole (i.e. through ESHI) and have an estimated thickness ≤10 m. MDZ are *not* modelled deterministically in the site description, but are handled statistically in the GeoDFN modelling, i.e. MDZ are treated as large size fractures of the DFN model /La Pointe et al. 2008/.

MDZ in the cored borehole array in Laxemar were identified during the extended single-hole interpretation (ESHI) analysis, the volumetric fracture intensity (P_{32}) for MDZ features was calculated from borehole P_{10} using the Wang approximation (see Section 3.5.1 of /La Pointe et al. 2008/). MDZ P_{32} is presented below in Table 2-2 as a function of fracture set orientation and fracture domain. P_{32} is a measure of the total fracture area within a finite unit volume; it is not an estimate of the number of fractures. For example, fracture domain FSM_C possesses a P_{32} intensity of 0.01 m^2/m^3 for MDZ belonging to the subhorizontal fracture set. This means that, within a cubic rock volume 100 m on a side, a total fracture surface area of 10,000 m^2 can be expected.

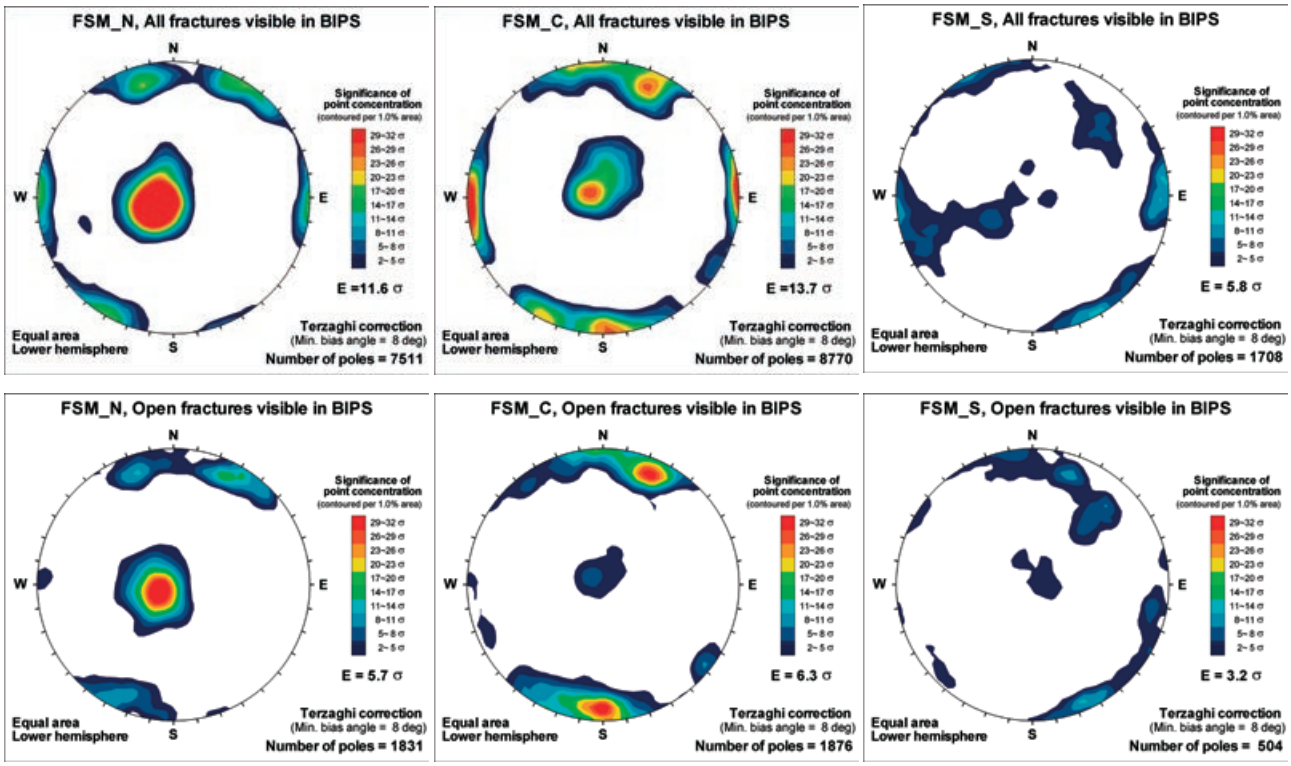

Figure 2-12. *Kamb-contoured polar stereoplots illustrating fracture set orientations from cored boreholes in fracture domains FSM_N, FSM_C, and FSM_S /La Pointe et al. 2008/.*

Table 2-2. Intensity of minor deformation zones (MDZ) of different orientations observed in boreholes from different fracture domains. For a descrition of how the DFN models including MDZ have been verified refer to /La Pointe et al. 2008/ (Definition of P_{32} given in Section 1.7).

Fracture set	MDZ volume intensity P_{32} from the borehole intersection (m^2/m^3)				
	FSM_C	FSM_EW007	FSM_NE005	FSM_W	FSM_N
ENE	0.0031	0.0053	0.0168	0.0056	0.0000
NS	0.0040	0.0154	0.0189	0.0118	0.0037
WNW	0.0048	0.0019	0.0069	0.0038	0.0078
SH	0.0096	0.0240	0.0129	0.0219	0.0234

3 Mechanical properties of the intact rock

3.1 Overview of the primary data

In this chapter the mechanical properties of the Laxemar rock as established from laboratory tests on intact rock samples (i.e. drill core samples) are presented and discussed.

The laboratory tests on intact rock listed in Table 3-1 were performed at SP (the Swedish National Testing and Research Institute). The methodology, standards and performance followed by the testing are described in the following SKB Method Descriptions:

- Uniaxial Compression Tests: SKB MD 190.001e, ver. 3.0 (SKB controlling document)
- Triaxial Compression Tests: SKB MD 190.003e, ver. 2.0 (SKB controlling document)
- Indirect Tensile Tests: SKB MD 190.004e, ver. 2.0 (SKB controlling document)

Samples from drill cores at Laxemar were chosen in the following rock types: fine-grained dioritoid (501030), diorite/gabbro (501033), quartz monzodiorite (501036), Ävrö granodorite (501056), Ävrö quartz monzodiorite (501046) and fine-grained granite (511058). These are the rock types that are expected to constitute more than 3% of the rock volume in the different rock domains (Table 2-1). A larger number of samples were selected from the most frequently occurring rock types.

Figure 3-1a and Figure 3-2a show plots of the uniaxial compressive strength and indirect tensile strength versus the wet density determined in laboratory. The density is expected to reflect some of the differences in the mineral composition (since the mineral themselves have different density, in particular quartz has low density).

For Ävrö granite (501044), the variation in the uniaxial compressive strength with respect to the wet density (determined before UCS testing) showed that the test results can roughly be divided into two groups. The division was based on whether the wet density was larger or smaller than 2,710 kg/m^3 (Figure 3-1b and Figure 3-2b). Also, geological investigations /Wahlgren et al. 2008/ and thermal property modelling /Sundberg et al. 2008/ showed that Ävrö granite may be divided in two different rock type varieties, quartz poor Ävrö quartz monzodiorite and quartz rich Ävrö granodiorite. Accordingly, the data from Sicada on Ävrö granite (501044) were sorted based on the wet density into Ävrö quartz monzodiorite (501046) and Ävrö granodiorite (501056). Such division is assumed in the following sections.

Most of the intact rock samples consisted of unaltered rock. However, several different tested rock types were observed to exhibit alteration in the form of oxidation (mainly faint, weak and medium) and saussuritisation. While the process of oxidization implies chemical reactions that increase the valency of the electropositive part of a compound often in association with an increase of oxygen content, saussuritisation is a metamorphic process that implies replacement of plagioclase with fine-grained aggregates of epidote, albite, calcite etc. /U.S. Bureau of Mines 1996/. The analysis of the available laboratory results on intact rock strength indicates that, in general, oxidisation leads to lower strength than for the unaltered rock, whereas, saussuritisation leads to higher strength than for the unaltered rock. Among the collected samples, saussuritisation was observed only for quartz monzonite to monzodiorite (501036). For this reason, attention is paid to the differences between the laboratory results obtained for:

- Fine-grained dioritoid (501030): all samples
- Diorite/gabbro (501033): all samples
- Quartz monzodiorite (501036): unaltered and saussuritised samples
- Quartz monzodiorite (501036): oxidised samples

- Ävrö quartz monzodiorite (501046): unaltered samples
- Ävrö quartz monzodiorite (501046): oxidised samples
- Ävrö granodiorite (501056): all samples
- Fine-grained granite (511058): all samples.

Figure 3-3 through Figure 3-8 show the variation with depth, and between boreholes, of the uniaxial compressive strength, crack initiation stress, tensile strength, Young's modulus and Poisson's ratio for the rock types at Laxemar where rock mechanics testing results are available. There seems to possibly be a slight reduction of the strength of the Ävrö granite samples with increasing depth of sampling. If so, this could be explained by sample damage due to drilling at higher in situ stress conditions. However, the spatial variation in strength properties is also clear from the data and makes the conclusion about pure depth dependence uncertain.

Table 3-1. Number of tests for each rock mechanics testing method performed for the SDM-Site Laxemar modelling, and the corresponding P-report.

Borehole	Uniaxial compressive tests		Triaxial compressive tests		Indirect tensile tests	
	No of tests [1]	SKB report [7]	No of tests [1]	SKB report [7]	No of tests [1]	SKB report [7]
KSH01A	16 (20) [2,4,6]	P-04-207	9 (13) [3,6]	P-04-208	32 (40) [6]	P-04-62
KSH02	4 (5) [2,4]	P-04-209	3 (5)	P-04-210	10 (12)	P-04-63
KLX02	15	P-04-255	–		30	P-04-256
KLX03	14 (15)	P-05-90	12	P-05-96	20	P-05-91
KLX04	15	P-04-261	14	P-04-262	30	P-04-263
KLX05	16	P-06-300	–		10	P-06-299
KLX06	–		3 (6)	P-05-128	–	
KLX08	6	P-06-32	–		–	
KLX10	10	P-06-37	6	P-06-40	10	P-06-38
KLX11A	4	P-06-270	4	P-06-272	10	P-06-271
KLX12A	11 [5]	P-06-73	4	P-06-76	10	P-06-74
KLX13A	1	P-06-300	–		10	P-06-276
KLX16A	12	P-07-143	–		20	P-07-142
KLX17A	5 (6)	P-07-217	–		–	
KLX18A	3 (4)	P-07-217	–		–	
KLX21B	5	P-07-217	–		–	
Total	137 (145)		55 (64)		192 (202)	

1) The numbers within parenthesis include samples with sealed fractures.
2) One sample missing data for Young's modulus and Poisson's ratio.
3) One sample missing data for Young's modulus and Poisson's ratio.
4) No samples with data for σ_{ci}.
5) One additional sample with Young's modulus and Poisson's ratio.
6) HUT tests /Eloranta 2004a/, /Eloranta 2004b/ and /Eloranta 2004c/ are not included.
7) Report list at the end of the reference chapter (Section 9.1).

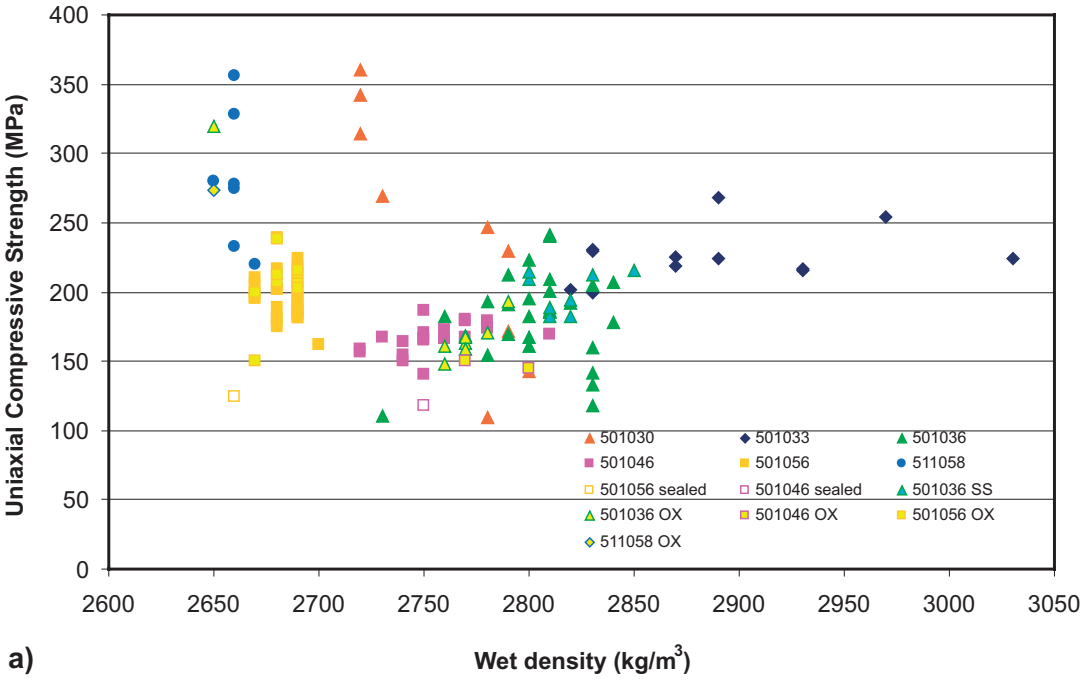

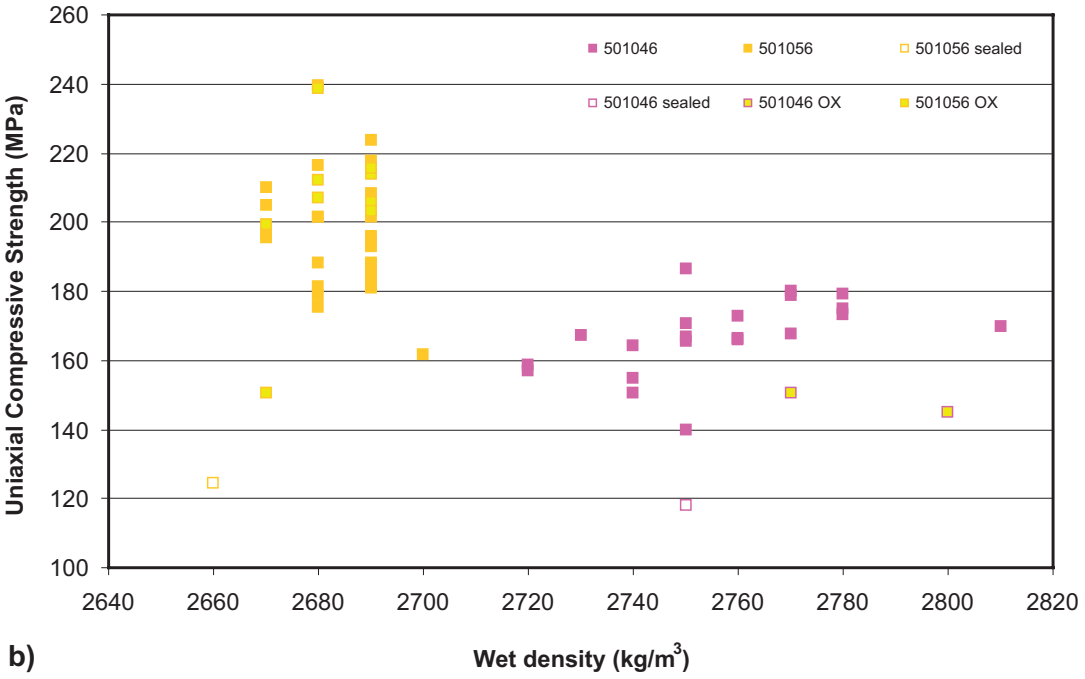

Figure 3-1. *Uniaxial compressive strength versus wet density for the SDM-Site Laxemar modelling: a) for the main rock types; b) for Ävrö quartz monzodiorite (501046) and Ävrö granodiorite (501056). The rock type names for corresponding rock codes in the legends are found in Table 1-3. (OX = oxidised, SS = Saussuritised).*

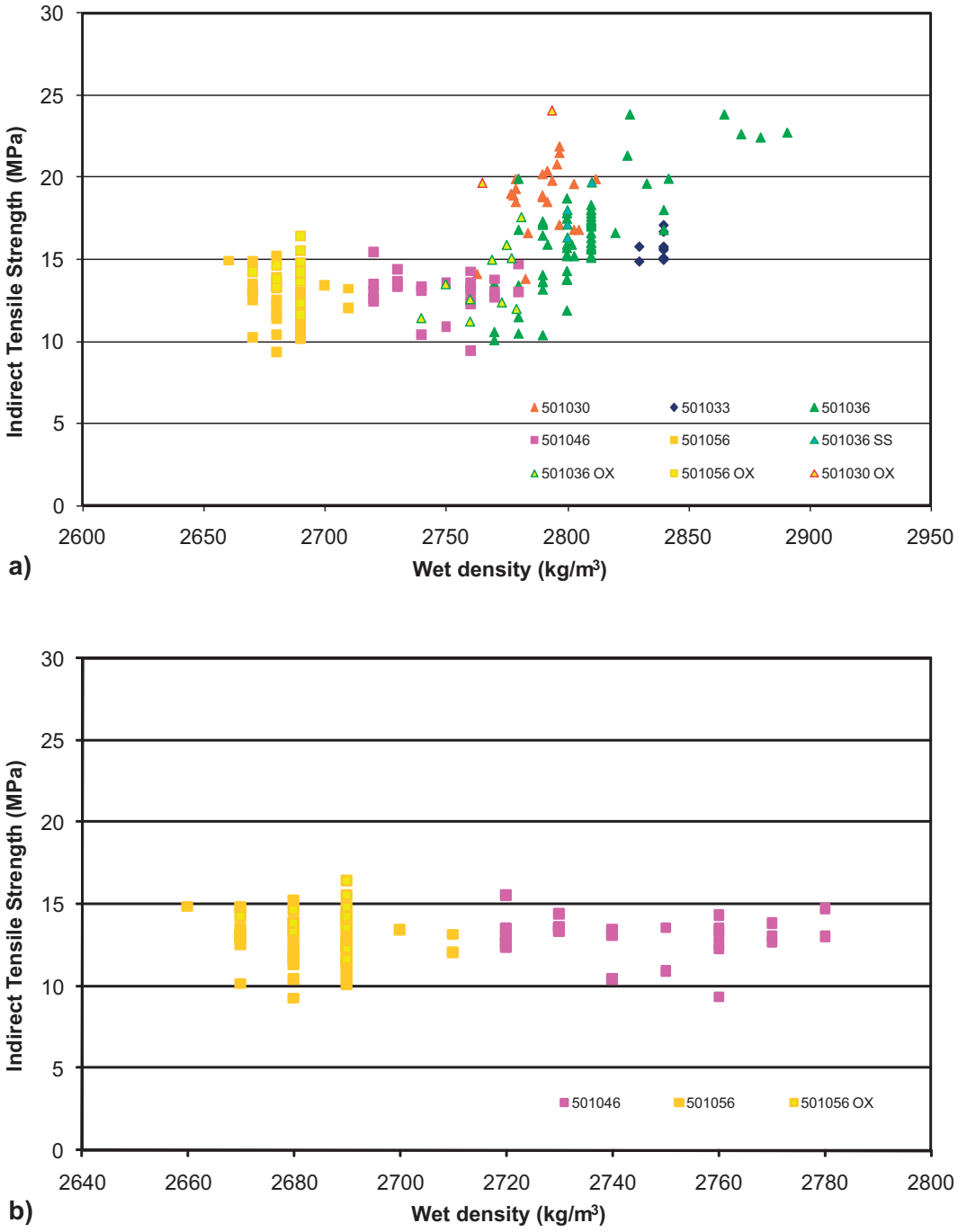

Figure 3-2. *Indirect tensile strength versus wet density for the SDM-Site Laxemar modelling: a) for the main rock types; b) for Ävrö quartz monzodiorite (501046) and Ävrö granodiorite (501056). The rock type names for corresponding rock codes in the legends are found in Table 1-3. (OX = oxidised, SS = Saussuritised).*

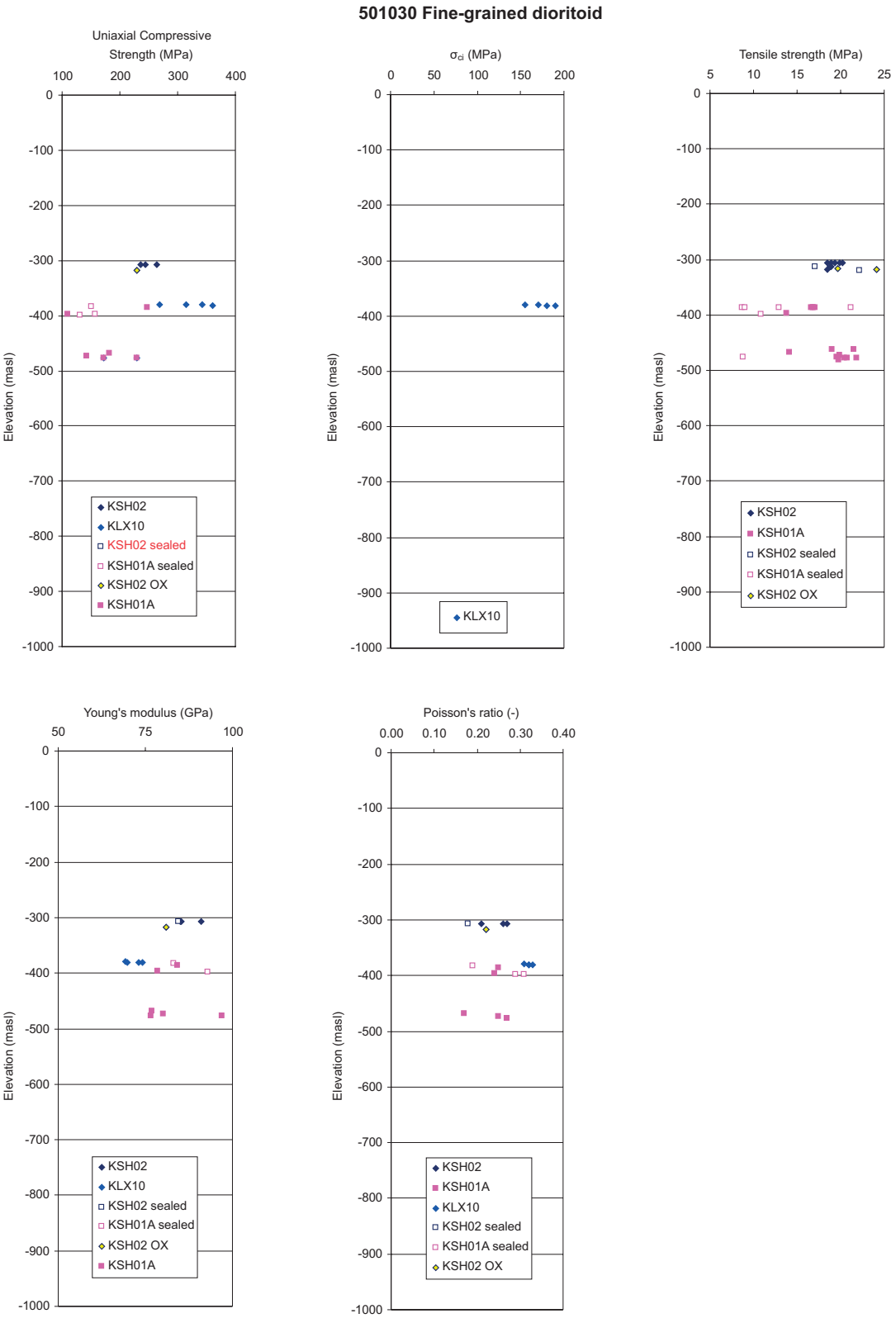

Figure 3-3. *Strength and deformability versus elevation for fine-grained dioritoid (501030).*

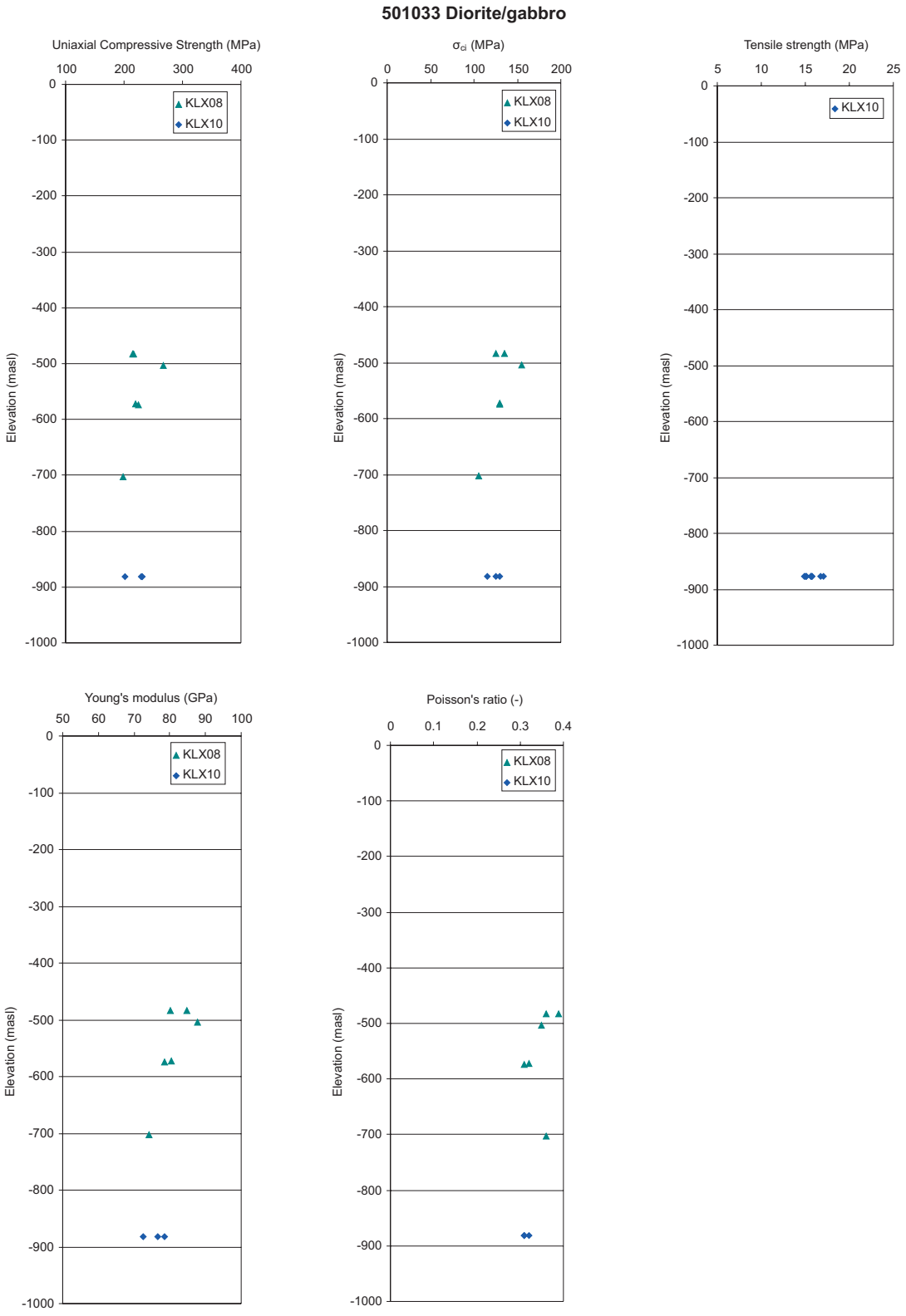

Figure 3-4. *Strength and deformability versus elevation for diorite/gabbro (501033).*

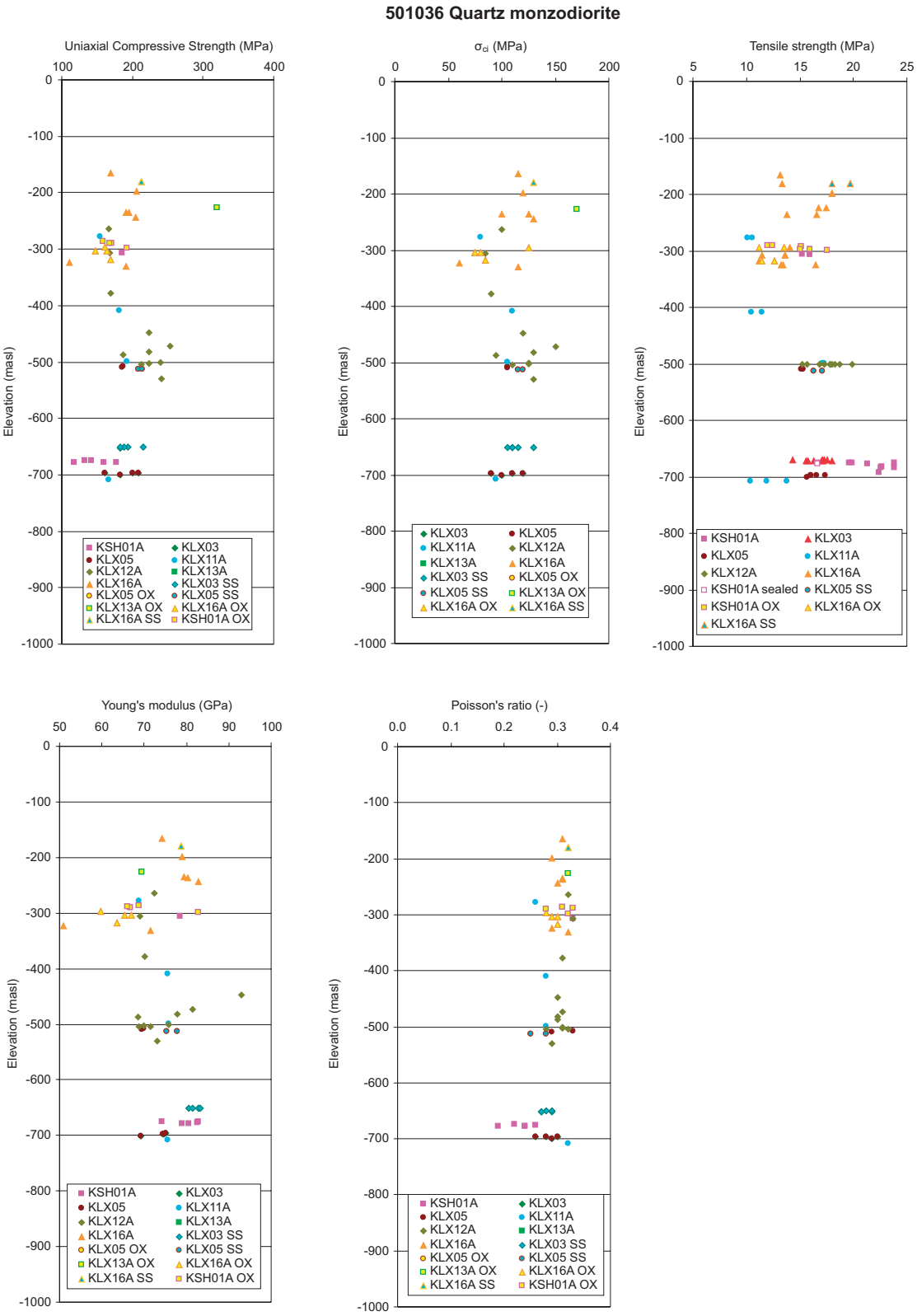

Figure 3-5. *Strength and deformability versus elevation for quartz monzodiorite (501036).*

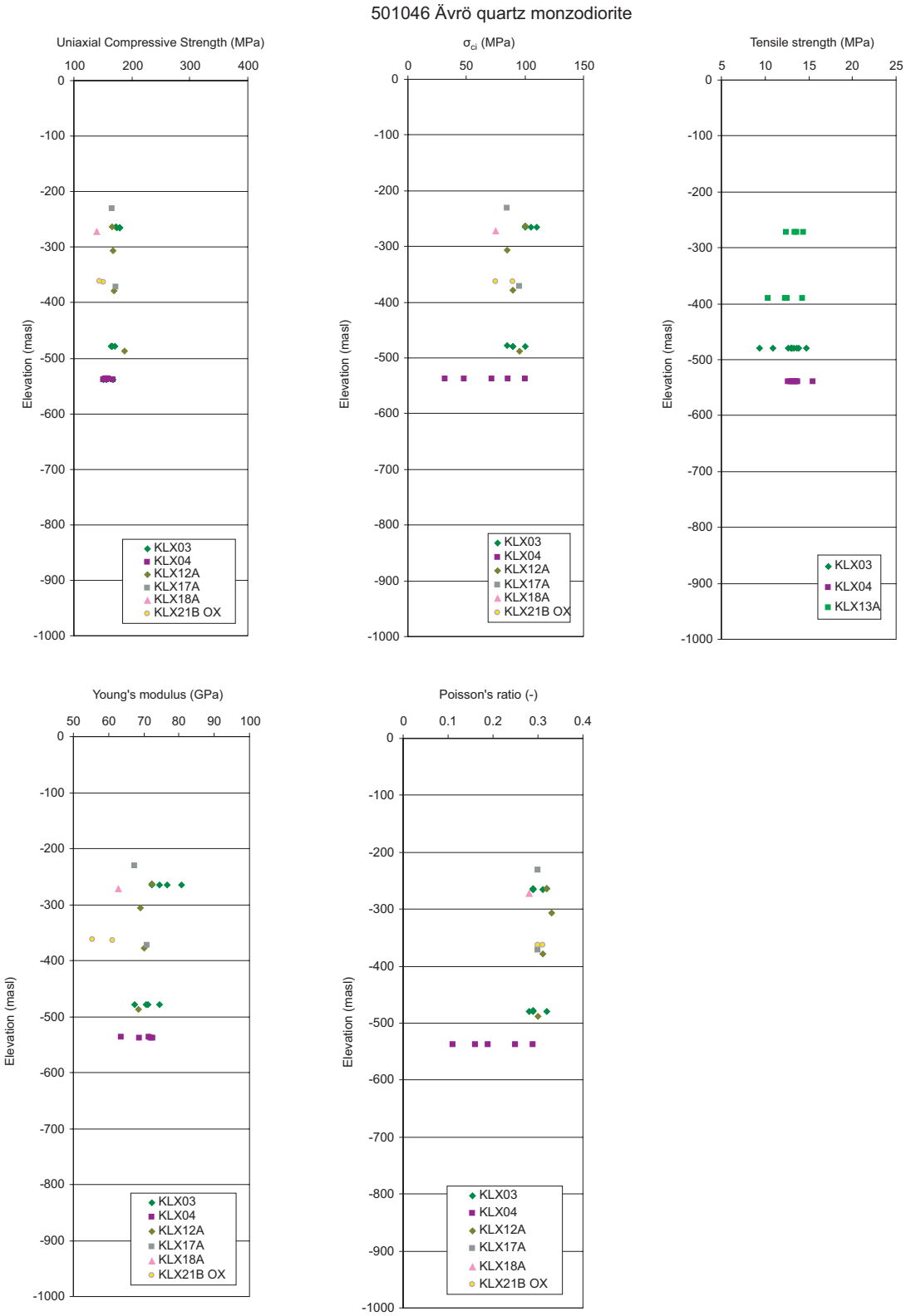

Figure 3-6. *Strength and deformability versus elevation for Ävrö quartz monzodiorite (501046).*

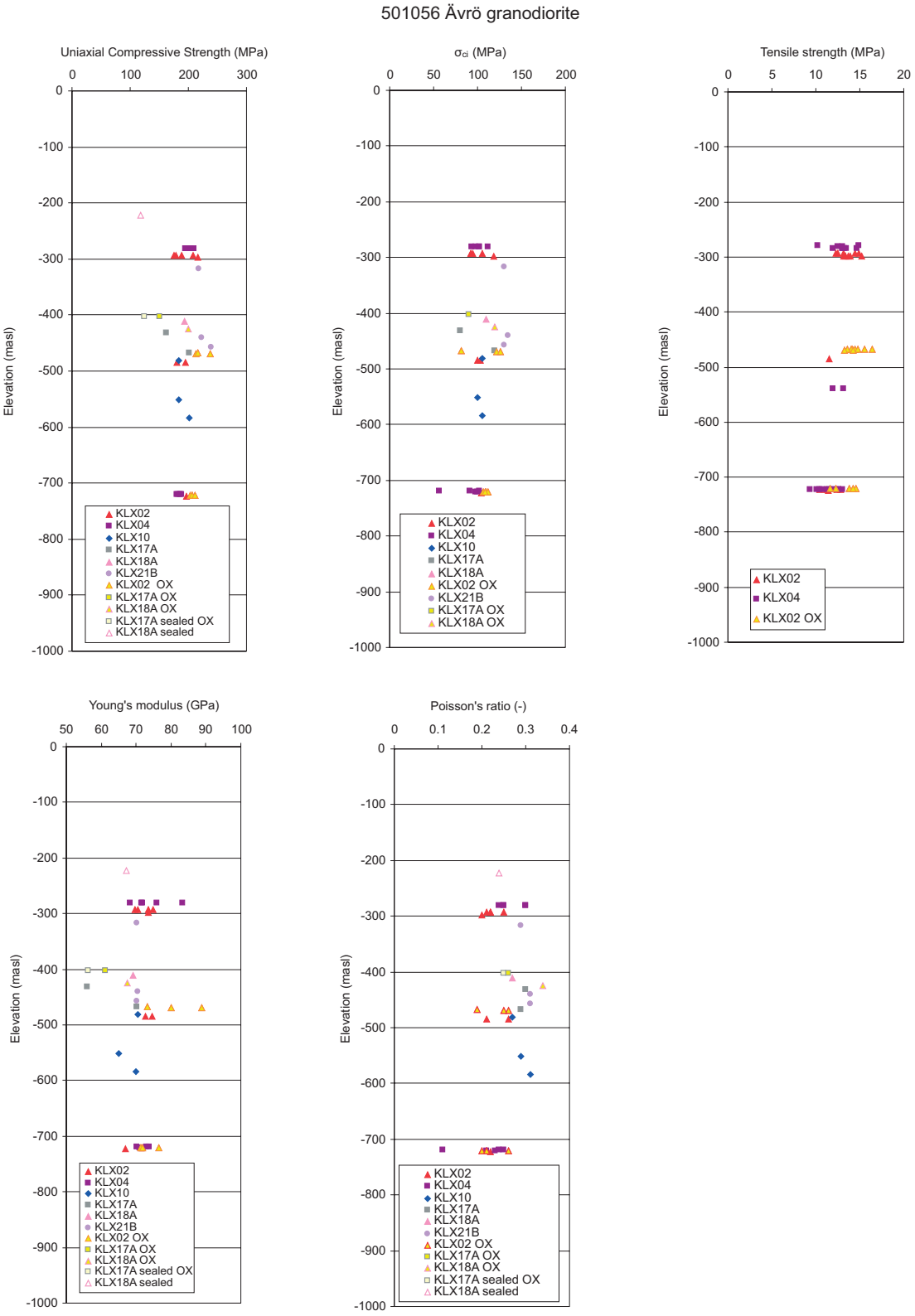

Figure 3-7. *Strength and deformability versus elevation for Ävrö granodiorite (501056).*

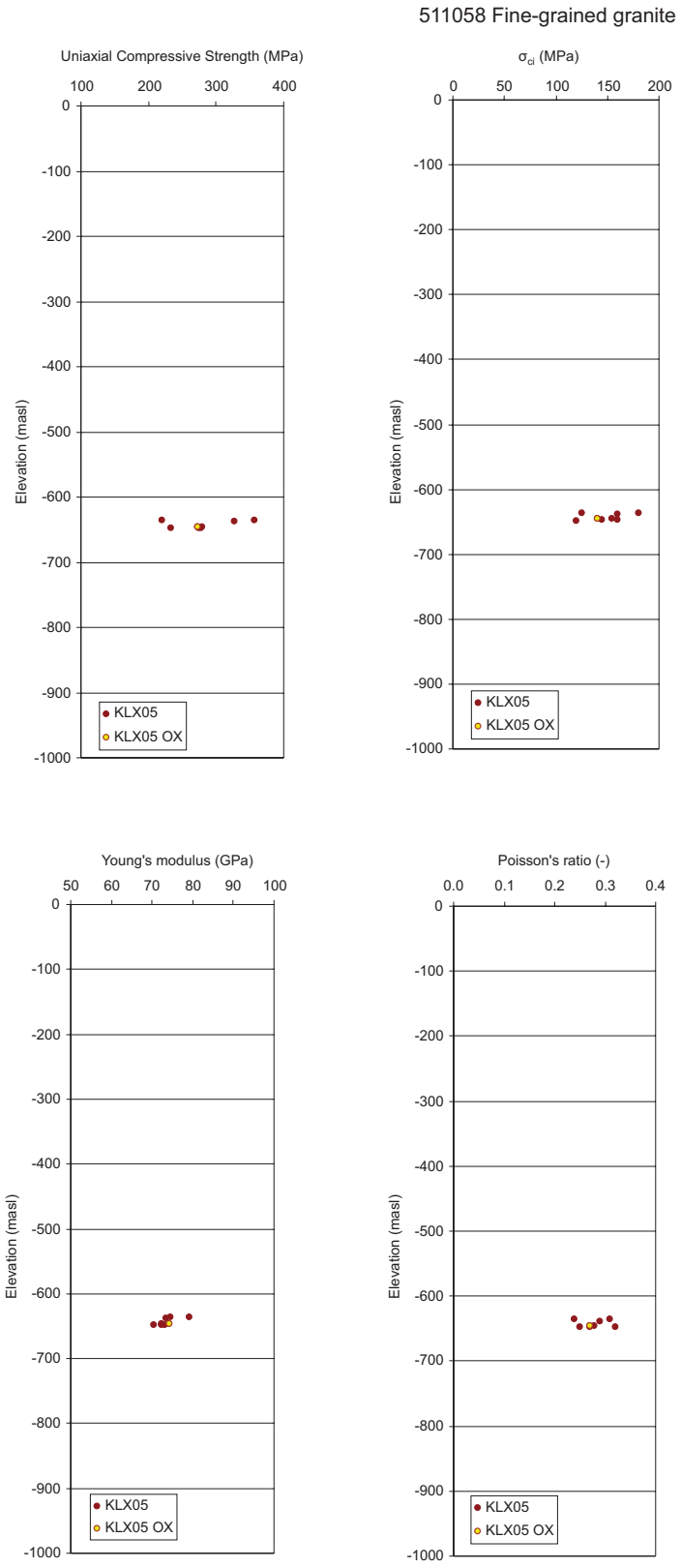

No tensile test results available

Figure 3-8. *Strength and deformability versus elevation for fine grained granite (511058).*

3.2 Strength properties of intact rock

3.2.1 Uniaxial compressive strength

Figure 3-9 shows the histograms of the uniaxial compressive strength values and their statistics is given in Table 3-2.

In general, the average uniaxial compressive strength of the common rock types at Laxemar have values either about 170–190 MPa or about 225–280 MPa, probably depending on the quartz contents of the rock. Moreover, for quartz monzodiorite (501036) and Ävrö quartz monzodiorite (501046), an evident difference can be seen between the strength of the oxidised and unaltered samples. For this reason, in Table 3-2, two sets of uniaxial strength are reported. It must be observed that only two samples of oxidised Ävrö quartz monzodiorite are available.

3.2.2 Crack initiation stress

The crack initiation stress has been evaluated from the uniaxial compressive strength tests according to the procedure presented by /Martin et al. 2001/. The value is a measure of the stress required to initiate tensile cracking in laboratory samples. As for the uniaxial compressive strength, the rock types seem to exhibit average values either around 80–110 MPa or 130–170 MPa. A difference can be observed between oxidised and unaltered samples. The statistics obtained from the laboratory results are summarised in Table 3-3.

In Figure 3-10 cross plots of crack initiation stress and uniaxial compressive strength is shown for the main and subordinate rock types for the SDM-Site Laxemar modelling. Note that there are only two available samples for oxidised Ävrö quartz monzodiorite, therefore they are not plotted. A clear correlation can be observed between the crack initiation stress and the maximum compressive tests, for all rock types. Therefore these parameters should not be considered independent from each other. The shapes of the best fit linear correlation function are in the span 0.52–0.57 (see Figure 3-10).

Table 3-2. Uniaxial compressive strength of the samples used for the SDM-Site Laxemar modelling.

Rock Type	No. of samples	Minimum UCS (MPa)	Mean UCS (MPa)	Median UCS (MPa)	Maximum UCS (MPa)	UCS Std. dev. (MPa)
501030 Fine-grained dioritoid	14	109.3	238.6	239.9	360.7	71.8
501033 Diorite/gabbro	12	199.0	225.5	224.2	268.0	19.4
501036 Quartz monzodiorite unaltered and saussuritised	35	110.2	186.4	188.3	240.9	30.1
501036 Quartz monzodiorite oxidised	9	147.5	183.3	167.7	320.1	52.7
501046 Ävrö quartz monzodiorite unaltered	21	140.0	167.1	167.2	186.6	10.8
501046 Ävrö quartz monzodiorite oxidised	2	145.0	147.7	–	150.3	–
501056 Ävrö granodiorite	36	150.3	197.8	198.1	239.4	18.7
511058 Fine-grained granite	8	219.9	280.4	276.2	356.4	44.7
All samples having sealed fractures	8	44.2	114.3	121.3	158.0	36.8

Table 3-3. Crack initiation stress of the samples for the SDM-Site Laxemar modelling.

Rock Type	No. of samples	Minimum σ_{ci} (MPa)	Mean σ_{ci} (MPa)	Median σ_{ci} (MPa)	Maximum σ_{ci} (MPa)	Std. dev. σ_{ci} (MPa)
501030 Fine-grained dioritoid	9	48	121.6	110	190	53.3
501033 Diorite/gabbro	12	105	129.2	130	155	13.6
501036 Quartz monzodiorite unaltered and saussuritised	35	52	104.0	110	130	21.8
501036 Quartz monzodiorite oxidised	9	65	94.6	80	170	32.9
501046 Ävrö quartz monzodiorite unaltered	21	32	87.8	90	110	18.6
501046 Ävrö quartz monzodiorite oxidised	2	75	82.5	–	90	–
501056 Ävrö granodiorite	36	56	104.4	104	135	15.5
511058 Fine-grained granite	8	120	148.1	150	180	19.8

3.2.3 Tensile strength

Indirect tensile test results, performed by means of the Brazilian test method, are summarised in Table 3-4 and plotted in Figure 3-11 as histograms.

Table 3-4. Indirect tensile strength of the samples for the SDM-Site Laxemar modelling.

Rock Type	No. of samples	Minimum σ_t (MPa)	Mean σ_t (MPa)	Median σ_t (MPa)	Maximum σ_t (MPa)	Std. dev. σ_t (MPa)
501030 Fine-grained dioritoid [1)]	24	13.8	19.0	19.2	24.1	2.3
501033 Diorite/gabbro [2)]	10	14.9	15.7	15.7	17.1	0.7
501036 Quartz monzodiorite unaltered and saussuritised	68	10.1	16.4	16.5	23.8	3.0
501036 Quartz monzodiorite oxidised	10	11.2	13.7	13.1	17.6	2.1
501046 Ävrö quartz monzodiorite unaltered [2)]	28	9.4	13.0	13.2	15.5	1.2
501046 Ävrö quartz monzodiorite oxidised	–	–	–	–	–	–
501056 Ävrö granodiorite [1)]	52	9.3	12.9	13.0	16.4	1.5
511058 Fine-grained granite	–	–	–	–	–	–
All sealed fractures	10	8.7	14.4	14.8	22.2	5.1

1) Statistics includes some oxidised samples.

2) No oxidised samples tested.

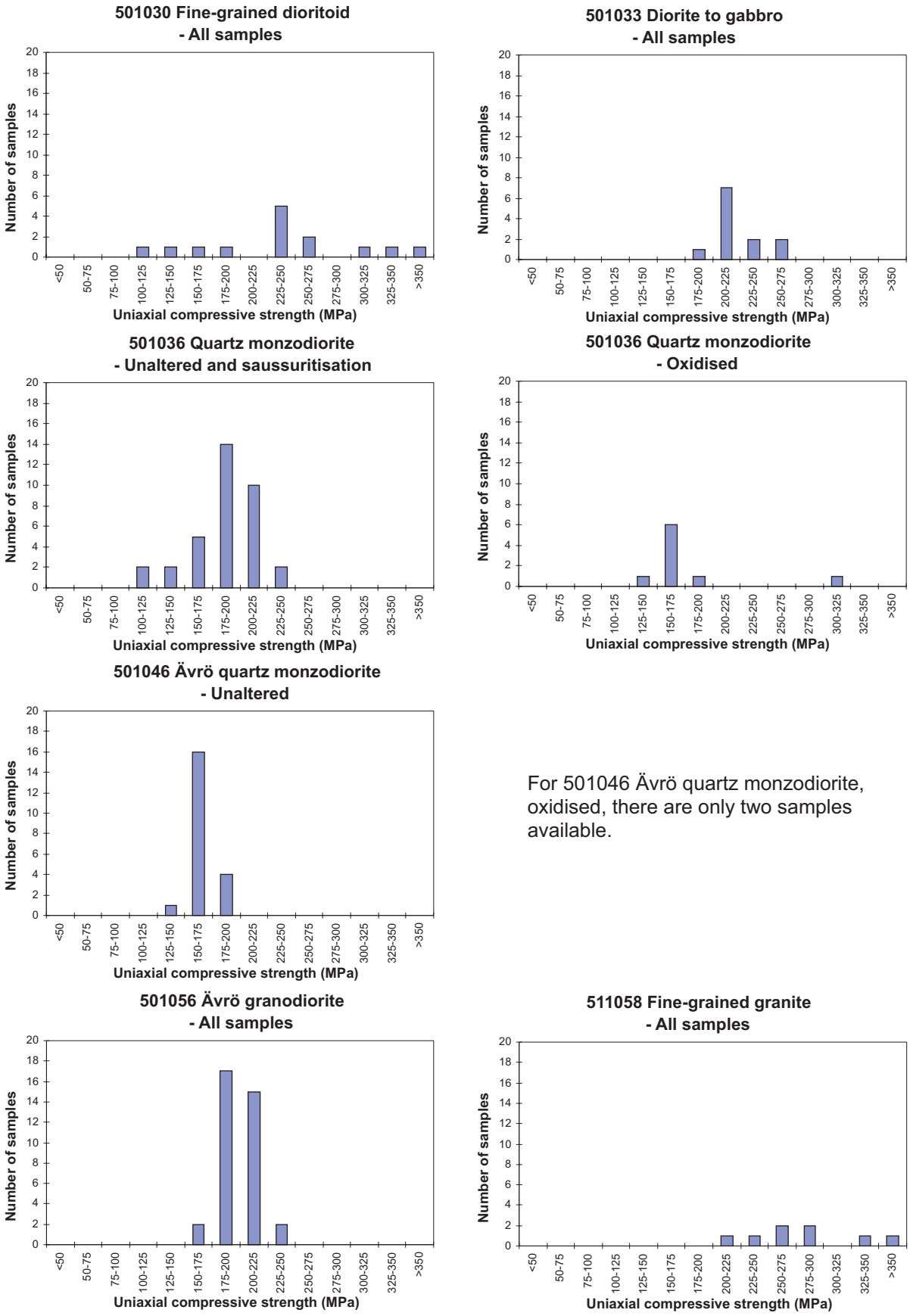

Figure 3-9. *Histograms of the uniaxial compressive strength of the main and subordinate rock types for the SDM-Site Laxemar modelling.*

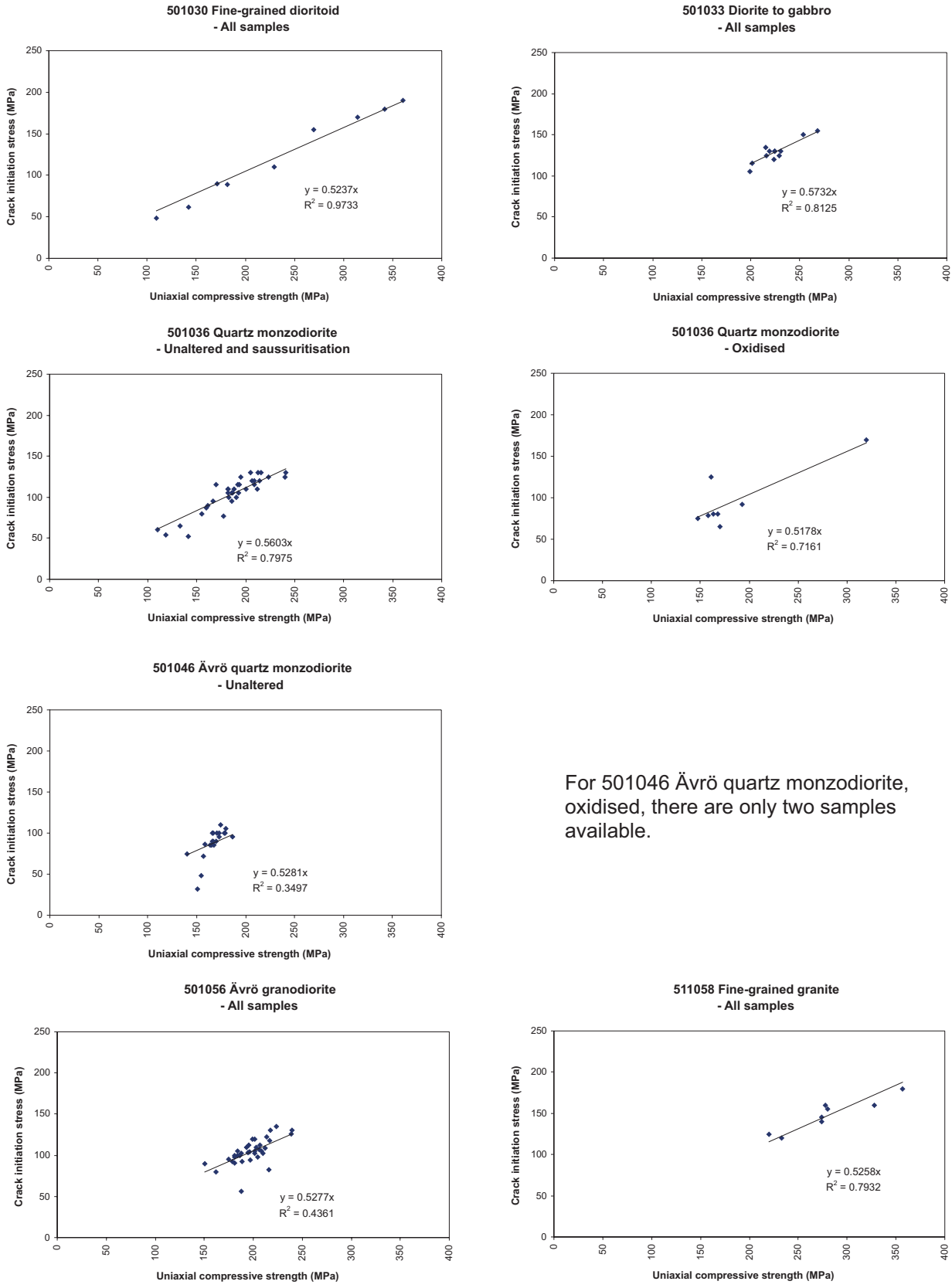

Figure 3-10. *Cross-plots of the crack initiation stress and the uniaxial compressive strength of the main and subordinate rock types for the SDM-Site Laxemar modelling (cf. Table 3-2 and Table 3-3). The best fit linear functions crossing origo, and the error coefficient for these functions, are shown in the diagrams.*

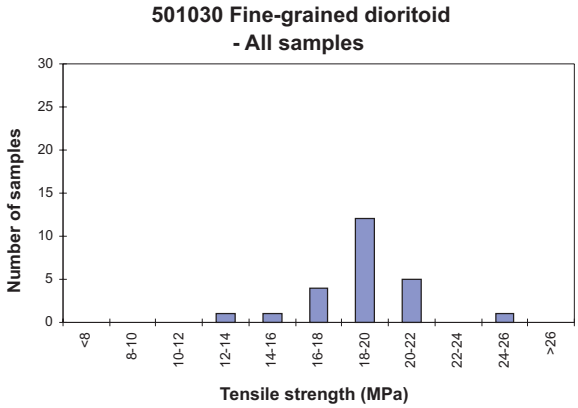

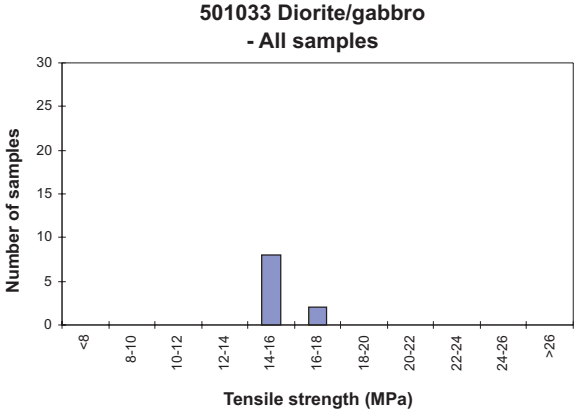

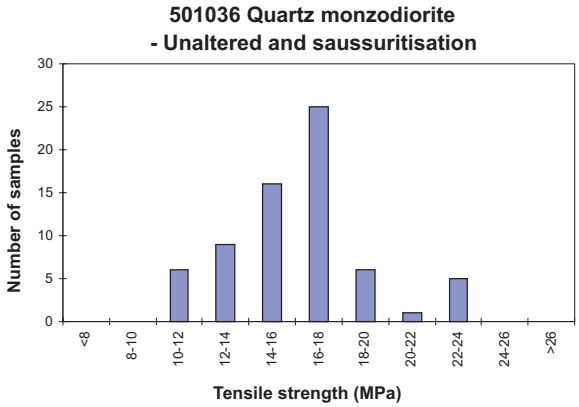

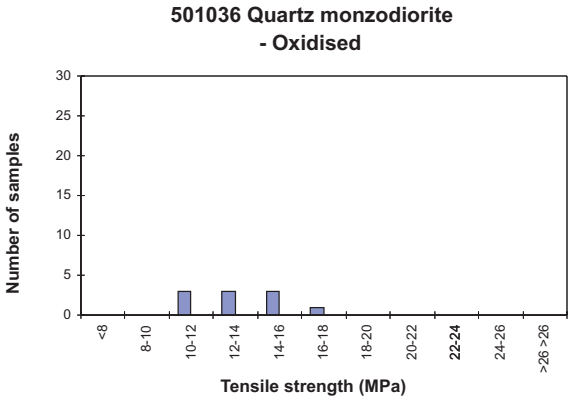

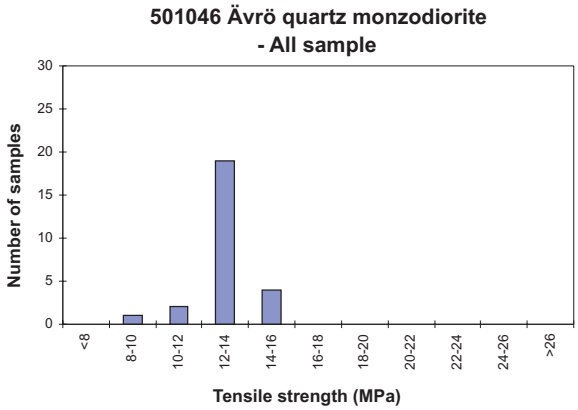

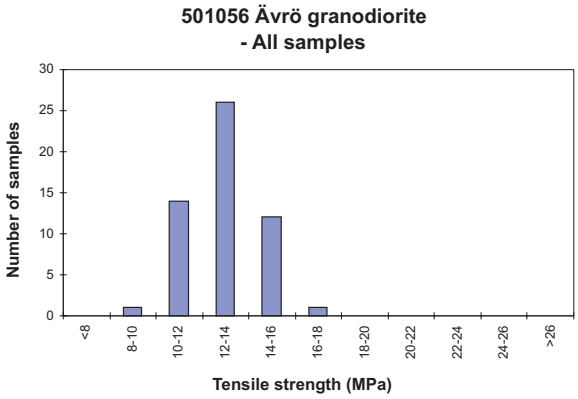

Figure 3-11. *Histograms of the tensile strength of the main and subordinate rock types for the SDM-Site Laxemar modelling.*

3.2.4 Triaxial compressive strength

Laboratory tests of triaxial compressive strength were carried out at the SP Laboratory (Swedish National Testing and Research Institute) on samples from borehole in Table 3-1. In the following analyses, the results of triaxial testing are considered together with the results of uniaxial testing.

For each main rock type (fine-grained dioritoid, quartz monzodiorite, Ävrö granodiorite and Ävrö quartz monzodiorite), the triaxial results were analysed together with the corresponding results of the uniaxial compressive tests. The laboratory results on intact rock samples were interpolated with the Hoek-Brown's Failure Criterion /Hoek et al. 2002/.

$$\sigma'_1 = \sigma'_3 + UCS_T \left(m_i \frac{\sigma'_3}{UCS_T} + 1 \right)^{0.5} \qquad \textit{Equation 3-1}$$

where σ'_1 and σ'_3 are the maximum and minimum principal stress and m_i is a strength parameter typical for each rock type. UCS_T is obtained by matching the uniaxial and triaxial test results and thus slightly differs from uniaxial compressive test results.

When analysing the laboratory results, the intact rock parameters in Table 3-5 are obtained (Figure 3-12 through Figure 3-15). Although obtained in a slightly different way, the results of the UCS_T are in rather good agreement with the values obtained only from uniaxial tests in Table 3-2. For the fine-grained dioritoid (501030), a few additional uniaxial compressive tests were performed in stage Laxemar 2.3, but no additional triaxial tests were performed from the same boreholes. This gave the result that the curve fitting, and the model fit to measured tensile strength, are much better for Laxemar 1.2 data (Figure 3-12a) than for all available data (Figure 3-12b). For this reason, although the average unixial compressive strength increases compared to the earlier modeling stages, it was decided to adopt the triaxial parameters for the Hoek-Brown's and Coulomb's Criterion by ignoring the new uniaxial test results. This will increase the uncertainty on friction angel and cohesion for the fine-grained dioritoid, which however is not among the most dominant rock types at Laxemar.

Table 3-5. Parameters for the Hoek-Brown's Criterion based on the results of uniaxial (u) and triaxial (t) tests performed on intact rock samples from Laxemar.

Rock type	Number of samples		Lower envelope 95% probability		Average		Upper envelope 95% probability	
	u	t	UCS_T (MPa)	m_i	UCS_T (MPa)	m_i	UCS_T (MPa)	m_i
501030 Fine-grained dioritoid [1)]	13	6	119	15	207	14	296	13
501056 Ävrö granodiorite	28	14	160	31	196	29	231	28
501046 Ävrö quartz monzodiorite	18	16	146	20	168	19	189	19
501036 Quartz monzodiorite	31	17	132	22	184	20	235	19
Only samples with sealed fractures	7	9	45	28	120	20	196	18

1) This fitting is obtained from the sub-set of the data for Laxemar 1.2.

The Coulomb's linear approximations of the Hoek-Brown's Criterion were also calculated for a certain stress interval (0 to 15 MPa, Table 3-6). These linear approximations are shown in Figure 3-12 through Figure 3-15. The Hoek-Brown's Criterion also provides an estimation of the tensile strength of the intact rock that can be compared with the laboratory results in Section 3.2.3. The statistics for the samples containing sealed fractures are also reported.

Five samples of quartz monzodiorite were also tested at triaxial compression conditions at the HUT Laboratory /Eloranta 2004b/ employing confining pressures of 2, 7 and 10 MPa, respectively. These results are found to be in good agreement with the SP Laboratory results.

Table 3-6. Parameters for the Coulomb's Criterion based on the results of uniaxial (u) and triaxial (t) tests performed on intact rock sampled for the SDM-Site Laxemar modelling.

Rock type	Number of samples		Lower envelope 95% probability		Average		Upper envelope 95% probability	
	u	t	c (MPa)	ϕ (°)	c (MPa)	ϕ (°)	c (MPa)	ϕ (°)
501030 Fine-grained dioritoid [1)]	13	6	19	51	33	53	47	54
501056 Ävrö granodiorite	28	14	20	59	24	60	28	60
501046 Ävrö quartz monzodiorite	18	16	21	55	24	55	27	56
501036 Quartz monzodiorite	31	17	19	56	26	56	33	57
Only samples with sealed fractures	7	9	9	51	18	54	28	56

1) This fitting is obtained from the sub-set of the data for Laxemar 1.2.

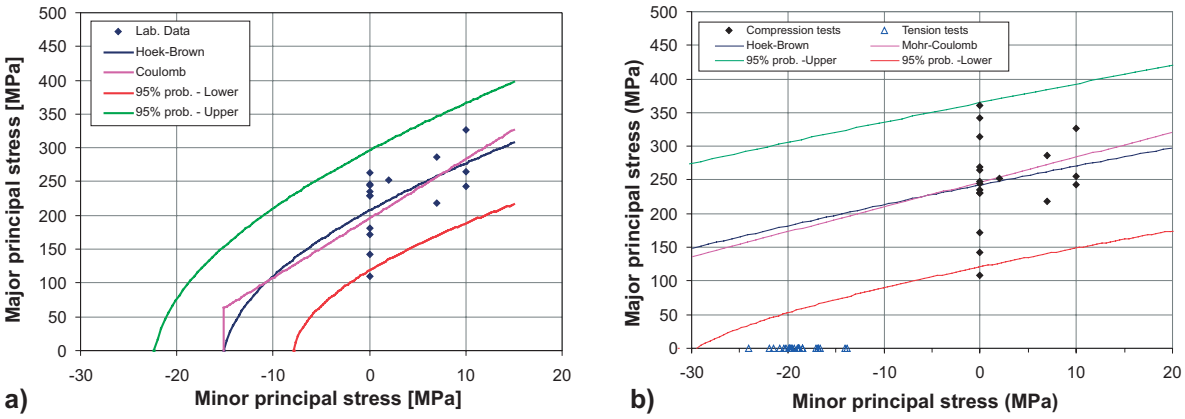

Figure 3-12. *Hoek-Brown's and Coulomb's failure envelopes from uniaxial and triaxial tests for intact samples of Fine-grained dioritoid (501030); a) Datafreeze Simpevarp 1.2 /Lanaro and Fredriksson 2005a/ (see text) and b) All available data (see text). On the x-axis, the indirect tensile strength results are also shown, N.B. not used for the curve fitting.*

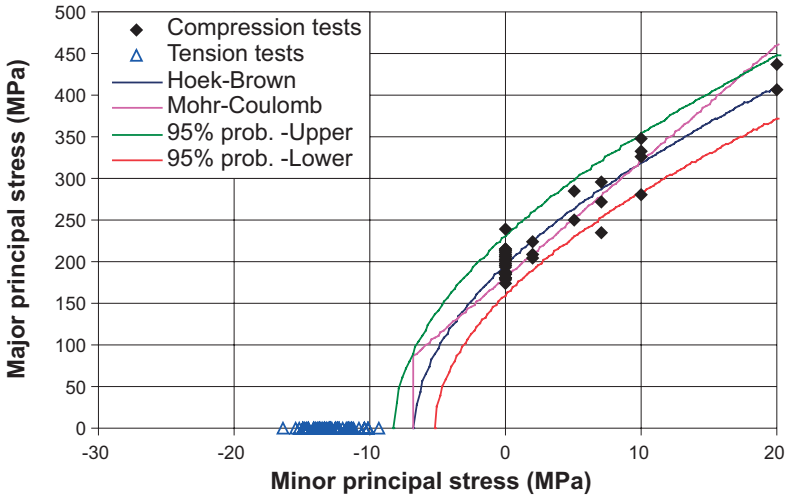

Figure 3-13. *Hoek-Brown's and Coulomb's failure envelopes from uniaxial and triaxial tests for intact samples of Ävrö granodiorite (501056). On the x-axis, the indirect tensile strength results are also shown, N.B. not used for the curve fitting.*

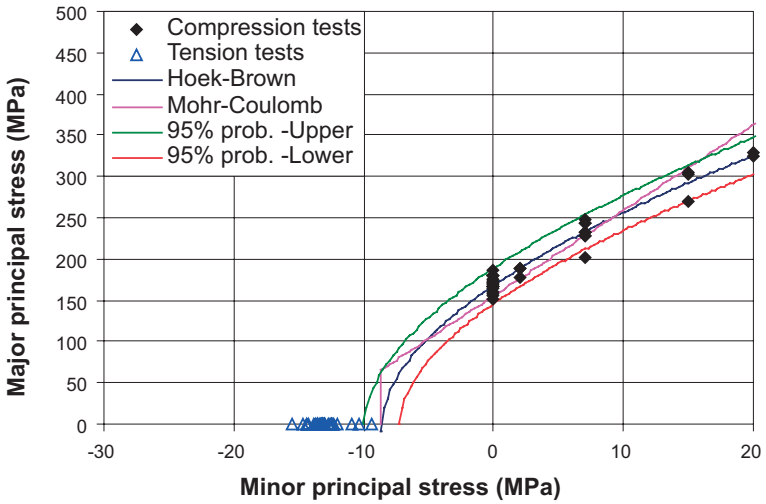

Figure 3-14. *Hoek-Brown's and Coulomb's failure envelopes from uniaxial and triaxial tests for intact samples of Ävrö quartz monzodiorite (501046). On the x-axis, the indirect tensile strength results are also shown, N.B. not used for the curve fitting.*

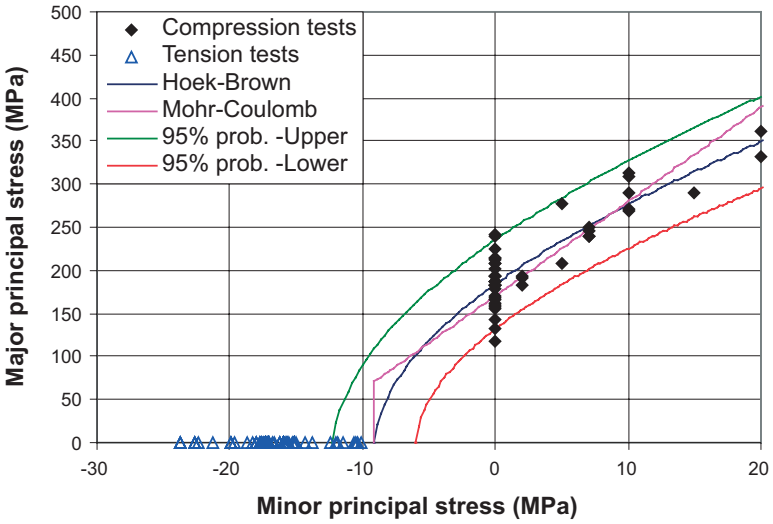

Figure 3-15. *Hoek-Brown's and Coulomb's failure envelopes from uniaxial and triaxial tests for intact samples of Quartz monzodiorite (501036). On the x-axis, the indirect tensile strength results are also shown, N.B. not used for the curve fitting.*

3.3 Deformational properties of the intact rock

3.3.1 Young's modulus

The Young's modulus is evaluated from uniaxial tests. The results are presented in Table 3-7 and in Figure 3-16 as histograms.

In Figure 3-17 cross plots between Young's modulus and uniaxial compressive strength are presented for the main and subordinate rock types for the SDM-Site Laxemar modelling. Note that there are only two samples available for oxidised Ävrö quartz monzodiorite and therefore not plotted.

Table 3-7. Young's modulus of the samples from uniaxial compressive tests for the the SDM-Site Laxemar modelling.

Rock Type	No. of samples	Minimum E (GPa)	Mean E (GPa)	Median E (GPa)	Maximum E (GPa)	Std. dev. E (GPa)
501030 Fine-grained dioritoid	14	69.4	80.2	79.4	97.0	7.9
501033 Diorite/gabbro	12	72.5	80.5	79.4	93.1	5.7
501036 Quartz monzodiorite unaltered and saussuritised	36	51.0	75.8	75.7	83.3	6.3
501036 Quartz monzodiorite oxidised	9	59.8	67.7	66.7	82.9	6.4
501046 Ävrö quartz monzodiorite unaltered	21	62.8	70.9	71.1	80.6	4.0
501046 Ävrö quartz monzodiorite oxidised	2	55.5	58.4		61.3	
501056 Ävrö granodiorite	36	55.9	71.7	71.3	88.7	5.5
511058 Fine-grained granite	8	70.6	73.8	73.4	79.1	2.5
All sealed fractures	7	56.2	78.0	83.1	104.2	18.1

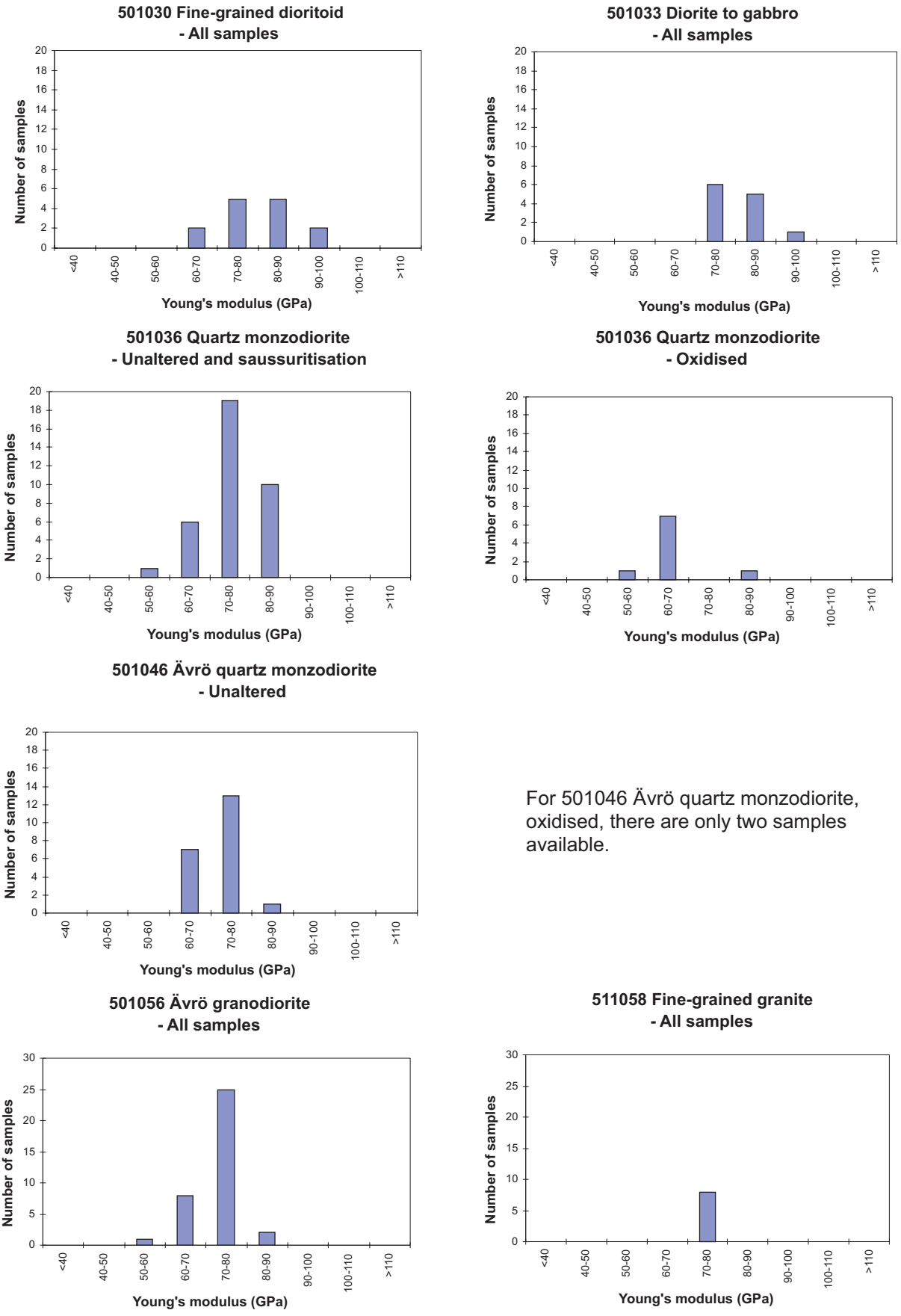

Figure 3-16. *Histograms of the Young's modulus of the main and subordinate rock types for the SDM-Site Laxemar modelling.*

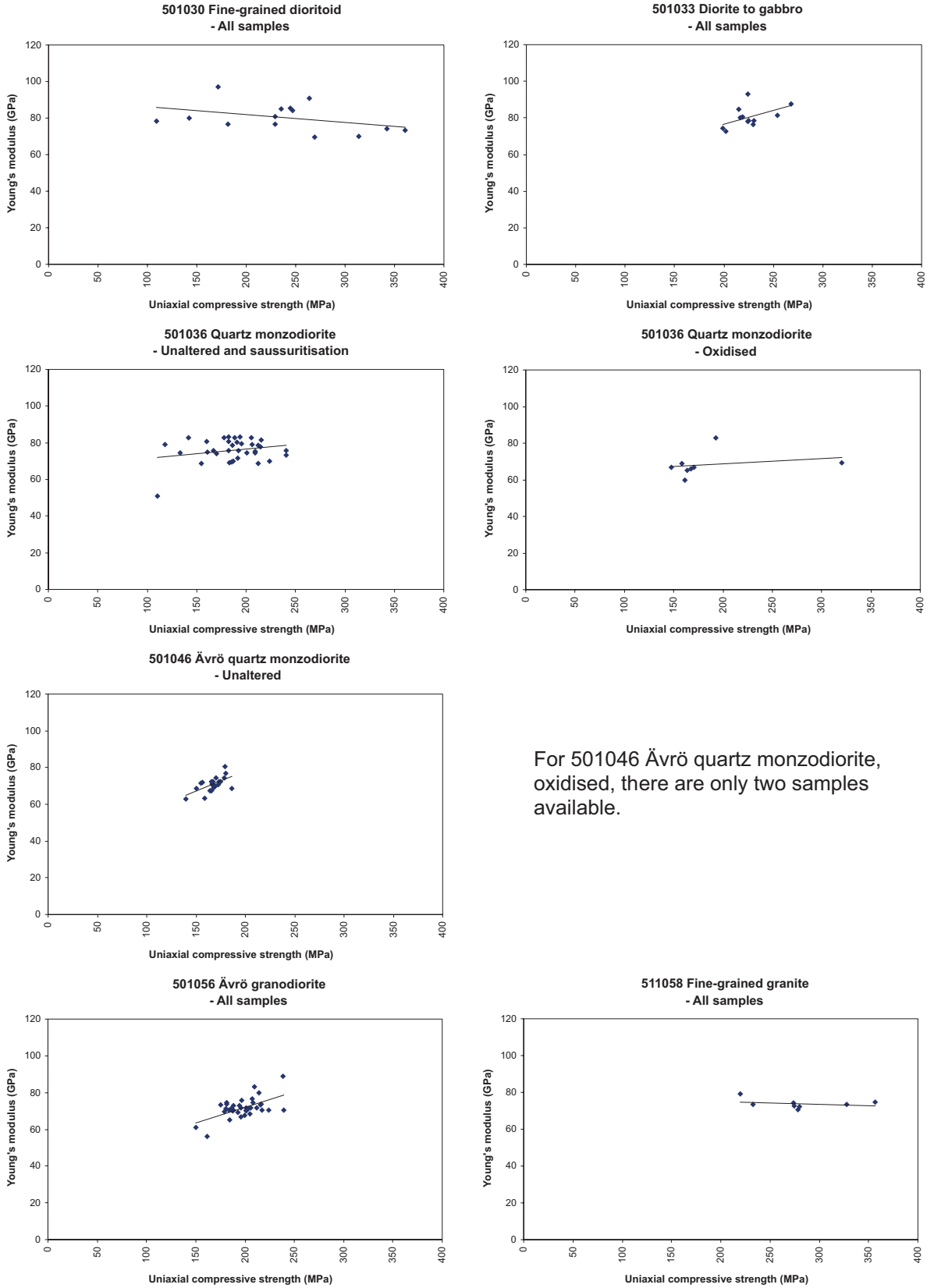

Figure 3-17. *Cross plots of Young's modulus and uniaxial compressive strength for the main and subordinate rock types for the SDM-Site Laxemar modelling (cf. Table 3-2 and Table 3-7.)*

Table 3-8. Poisson's ratio of the samples from uniaxial compressive tests for the SDM-Site Laxemar modelling.

Rock Type	No. of samples	Minimum ν (–)	Mean ν (–)	Median ν (–)	Maximum ν (–)	Std. dev. ν (–)
501030 Fine-grained dioritoid	14	0.17	0.26	0.27	0.33	0.05
501033 Diorite/gabbro	12	0.30	0.33	0.32	0.39	0.03
501036 Quartz monzodiorite unaltered and saussuritised	36	0.19	0.29	0.29	0.33	0.03
501036 Quartz monzodiorite oxidised	9	0.28	0.30	0.30	0.33	0.02
501046 Ävrö quartz monzodiorite unaltered	21	0.11	0.28	0.29	0.33	0.06
501046 Ävrö quartz monzodiorite oxidised	2	0.30	0.31		0.31	
501056 Ävrö granodiorite	36	0.11	0.25	0.25	0.34	0.05
511058 Fine-grained granite	8	0.24	0.28	0.28	0.32	0.03
All sealed fractures	7	0.11	0.22	0.24	0.31	0.07

3.3.2 Poisson's ratio

The Poisson's ratio was evaluated from the uniaxial compressive strength tests. The summary of the statistics for each rock type can be found in Table 3-8.

3.4 Microcracks and pores

Most crystalline rocks naturally contain both crack like pores (called microcracks) and pores with other (less elongated) shapes. Though the microcrack volume percentage is very low, they may have a strong influence on mechanical and transport properties of rocks /e.g. Jaeger et al. 2007/. If a drill core sample has been exposed to strong loads during the drilling, the sample, used for laboratory testing, may have clearly more microcracks than the undisturbed rock in situ. Therefore, an increased amount of microcracks may be a valuable sign of damage in core samples, and is important to take into account in the interpretation of laboratory results.

In case of high in situ rock stresses the stress conditions during drilling becomes such that the micro cracking increases, and the amount of microcracking in samples is therefore also indirect information of value for the stress estimation (Section 6.2.5).

In the following two sections the microcrack laboratory measurements is first presented followed by an estimation of the influence of the natural porosity on the intact rock deformability.

3.4.1 Microcrack volume measurements

To estimate the amount of microcracking in rock samples from the site, triaxial compression test were performed where the volumetric strain was recorded from the beginning of the isotropic compression. The "microcracks" are assumed to all be (almost) closed during the first *non-linear* stage of compression, and this amount of volumetric strain is here taken as the definition of the term maicrocrack volume (see Figure 3-18). This methodology to estimation of the microcracking in samples is further explained in /Jacobsson 2007a/.

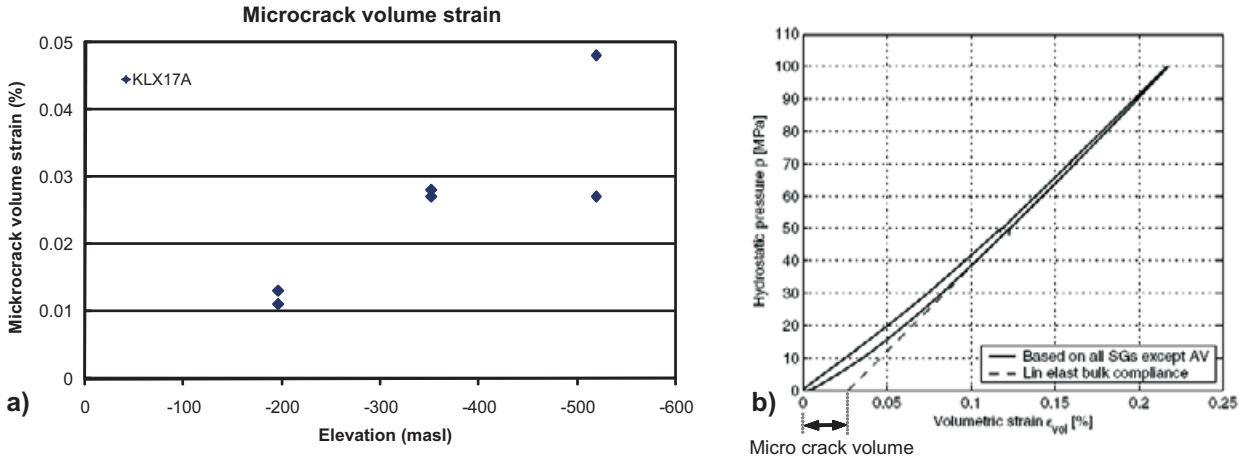

Figure 3-18. *a) Measured microcrack volume versus depth for samples from borehole KLX17A. The two upper samples are Ävrö quartz monzodiorite and the other four samples are Ävrö granodiorite. b) An example of a test curve from borehole KLX17A and the definition of microcrack volume; modified by /Jacobsson 2007a/.*

Twelve samples from boreholes KLX17A were tested in within the Laxemar site investigations and the results are presented in /Jacobsson 2007a/. The samples are of rock type Ävrö granite (501044). The results indicate a fairly linear increase of microcrack volume with depth, from about 0.01% (percentage of the total rock volume) in samples from 200 m depth up to roughly 0.04% in samples from 500 m depth. The total porosity (i.e. the volume percentage for the microcrack together with all other pores) of the samples is about 0.3–0.4%. This means that a very little part of the porosity is closed even under high compression.

However, one important circumstance in the interpretation of these results is the fact that the density of the six samples varies, such that the two samples from about 200 m depth are heavier. This means that according to the subdivision of Ävrö granite (see Section 3.1) the two upper samples are in Ävrö quartz monzodiorite and the other four samples are Ävrö granodiorite. These two varieties do not have exactly the same expected mineral composition and also slightly different expected mechanical properties. Therefore the limited number of triaxial test with measurements of micro crack volume makes it impossible to draw strong conclusion about depth trends. Nevertheless, the generally small microcrack volumes measured at all depths, in relation to the total porosity, indicate that the stresses at these sampling levels are not high enough to cause major damage to the drill core.

This conclusion is in correspondence with the observation from the results of P-wave measurements on the drill core and in the borehole, respectively (shown in Appendix 1). If there where microcracking in the cores a clear difference would be seen between core and borehole and this difference would be increasing with depth. However, no major difference is seen between the core and the rock in the borehole and no particular depth trend. One exception to this is at the bottom of KSH01A at Simpevarp where the core velocities are lower than the borehole velocities. Since this is at elevation 900–1,000 the stresses may be actually high enough here to give microcracking in the core. Also at some points where there are dykes of fine-grained granite there is a difference in P-wave. This rock type seems to be in general more proun to get cracked, also noticed from the few core disking and borehole breakouts. There is a variation in velocity but this is caused by rock type variation.

3.4.2 Effect of pores on elastic properties (in linear stage)

In the elastic stage of the deformation of rock, deformation is in part caused by compression of matrix minerals and in part by the deformation of pores. In crystalline rock, most of the pores are expected to be located in grain boundaries, see Figure 3-19.

Figure 3-19. *Thin section from Ävrö granite where the pores are impregnated with blue colour. The pattern of very thin light blue lines thus indicated the location of microcracks and pores in the rocks. Note the very low porosity and the location of pores along grain boundaries /Drake and Tullborg 2006/. Base of microphotograph corresponds to 30 mm.*

The effects of the pores are studied here to understand their contribution to the elastic properties in the linear stage. To be able to do this analytically the actual shape of all pores is approximated as being spheroidal, with low aspect ratio.

For an ideal case, the pore compressibility (C_{pc}), i.e the derivative of the pore strain with respect to the confining pressure (with pore pressure held constant) is noted

$$C_{pc} = (dV_p/dP_c\ V_p)_{Pp} \qquad \textit{Equation 3-2}$$

where V_p is pore volume, P_c is confining pressure and P_p is pore pressure For a three dimensional thin crack the compressibility should follow

$$C_{pc} = 2(1\text{-}\nu_r)\ /\pi\ G_r\alpha \qquad \textit{Equation 3-3}$$

where ν_r and G_r are poisson ratio and shear modulus of crack free rock. α is aspect ratio of the shape /Zimmerman 1991/. Considering a collection of non interacting pores, after rearrangement the equivalent aspect ratio is $\alpha = 2(1\text{-}\nu)/\pi G_r C_{pc}$, where C_{pc} is the volume-weighted average of the actual pores. Pore strain can be determined with Equation 3-2 and Equation 3-3 with the assumption that the pore pressure is held constant throughout the testing period is used. Pore compressibility is calculated for the pores with aspect ratio (α) of 0.33 together with ν_r = 0.22 and G_r = 30.33 GPa.

This yields $C_{pc} = 4.69\times10^{-5}$ MPa^{-1}. Now consider a rock sample with unit volume with porosity 0.36%. We here considered the close of 10% micro cracks. Thus the available porosity for linear part of elastic strain and stress curve will be 0.4×0.9%. According to Equation 3-2 if the confining pressure is varied from 20 MPa to 70 MPa keeping pore pressure constant, the volumetric strain of pores is about 8.5×10^{-6} which means that strain due to pores is negligible.

In order to study the effect of pores on elastic modulus, the porosity (ϕ) of n spheroids (per unit volume), each of radius r, can be exactly derived

$$\phi = (4/3)\pi\ nr^3\alpha \qquad \textit{Equation 3-4}$$

This gives crack (Γ) density of $\Gamma = 3\phi\ /\ 4\pi\ \alpha$. (Crack density parameter is defined as $\Gamma = N\ r^3\ /V_b$ where N is the number of crack, V_b is volume and r is the radius.)

/Salganik 1973/, /Bruner 1976/ and /Zimmerman 1991/ showed that Poisson ratio and elastic modules vary with porosity according to Equation 3-5 and Equation 3-6 using differential methods in effective moduli theories.

$$v = v_r\, e^{-8\Gamma/5} \qquad \textit{Equation 3-5}$$

$$E = E_r\, e^{-16\Gamma/5} \qquad \textit{Equation 3-6}$$

where E_r and v_r are elastic properties of crack free rock.

According to the previous section (Section 3.4.1) about 90% of the total porosity in Ävro granite is made up of pores (not microcrack closing in non linear stage) and we here assume that the aspect ratio is 0.33 for crack like pores. Thus, the crack density parameter (Γ) yields, 0.0026.

Substituting this value in Equation 3-5 and Equation 3-6, quantifies the effect of porosity for E and v. In Equation 3-7 and Equation 3-8 we express the effect of available porosity.

$$v = 0.995\, v_r \qquad \textit{Equation 3-7}$$

$$E = 0.99\, E_r \qquad \textit{Equation 3-8}$$

The small difference between rock deformability and mineral deformability in the case shown above means that the effect of pore deformability is negligible.

Several research works have been carried out to study the effect of porosity on uniaxial compressive strength. /Dearman 1974/, /Dearman et al. 1978/ and /Lucas-Girot et al. 2002/ have shown exponential relationships between uniaxial compressive strength and porosity. The typical behaviour of uniaxial compressive strength with porosity can be expressed as,

$$UCS = UCS_r\, e^{-c\phi} \qquad \textit{Equation 3-9}$$

where UCS_r is the compressive strength of crack free rock, ϕ is the porosity and c is a constant generally close to three. However further study is necessary to give an exact value of c for crystalline rock. Nevertheless, it can be concluded from Equation 3-9 that for very low porosity values, the compressive strength of rock is close to the matrix mineral compressive strength

3.5 Model for mechanical properties of intact rock and associated uncertainties

Based on the results on rock strength in Table 3-2 to Table 3-4 and on the deformability parameters in Table 3-7 and Table 3-8, the mechanical properties of the predominant rock types can be summarised as in Table 3-9. Based on the number of tests available for each test, the 95% confidence interval of the mean is also calculated.

For quartz monzonite (501036) and Ävrö quartz monzodiorite (501046), the mechanical and deformational properties of the oxidised samples were determined separately. It can be observed in Table 3-10 that all the properties of oxidised samples are lower than for unaltered samples except for the Poisson's ratio. For the oxidised samples of these two rock types, the mean properties in Table 3-9 should be affected by the suggested reduction factors given in the footnotes, based on what was reported in Table 3-10.

Figure 3-20 to Figure 3-22 shows modelled frequency distribution curves for the main and subordinate rock types for the SDM-Site Laxemar modelling of Uniaxial compressive strength, Tensile strength and Young's modulus respectively. A great spread in the distribution of fine-grained dioritoid can be noted. The explanation to this is probably that there is a spatial variation in rock type characteristics (such as grain size), see Figure 3-3. There are only 14 samples behind the model, and the uncertainty in the mean is also therefore set higher (Table 3-9). However, since the expected volumetric occurrence is very low (Table 2-1) and the mean strength is fairly high (Table 3-9) it was considered that the description of this rock type was acceptable.

Table 3-9. Quantified parameters for models of strength and deformation properties for the different rock types for SDM-Site Laxemar.

Parameter	501030 Fine-grained dioritoid	501033 Diorite/ gabbro	501036 Quartz monzodiorite – Unaltered	501046 Ävrö quartz monzodiorite – Unaltered	501056 Ävrö granodiorite	511058 Fine-grained granite
	Mean/stdev Min–Max *Uncertainty*	Mean/stdev Min–Max *Uncertainty*	Mean/stdev Min–Max *Uncertainty*	Mean/stdev Min–Max *Uncertainty*	Mean/stdev Min–Max *Uncertainty*	Mean/stdev Min–Max *Uncertainty*
Uniaxial compressive strength, UCS (MPa)	239/72 100–360 ±*16%*	225/20 200–270 ±*5%*	186 [1]/30 110–240 ±*5%*	167 [1]/11 140–190 ±*3%*	198/19 150–240 ±*3%*	280/45 210–350 ±*11%*
Crack initiation stress, σ_{ci} (MPa)	122/53 48–190 ±*28%*	130/14 105–155 ±*6%*	104 [2]/22 52–130 ±*7%*	88 [2]/19 50–110 ±*9%*	104/16 70–135 ±*5%*	148/20 110–180 ±*9%*
σ_{ci}/UCS [3] (%)	52.4	57.3	56.0	52.8	52.8	52.6
Indirect tensile strength (MPa)	19/2.5 14–24 ±*5%*	16/1 15–17 ±*4%*	16.5 [4]/3.0 10–23 ±*4%*	13 [4]/1.2 10–16 ±*4%*	13/1.5 10–16 ±*3%*	–
Young's modulus (GPa)	80/8 70–97 ±*5%*	80/6 70–92 ±*4%*	76 [5]/6.5 63–83 ±*3%*	71 [5]/4 63–80 ±*3%*	72/5.5 60–83 ±*3%*	74/2.5 70–79 ±*3%*
Poisson's ratio (–)	0.26/0.05 0.17–0.33 ±*3%*	0.33/0.03 0.30–0.39 ±*5%*	0.29 [6]/0.03 0.20–0.33 ±*4%*	0.28 [6]/0.06 0.16–0.33 ±*9%*	0.25/0.05 0.15–0.34 ±*7%*	0.28/0.03 0.22–0.32 ±*8%*
Cohesion (MPa)	33/7 19–47 ±*10%*	*30* [7]	26 [1]/3.5 19–33 ±*4%*	24 [1]/1.5 21–27 ±*2.5%*	24/2 20–28 ±*2.5%*	–
Friction angle (°)	53/0.8 51–54 ±*1%*	*60* [7]	56 [8]/0.3 56–57 ±*0.2%*	55 [8]/0.3 55–56 ±*0.2%*	60/0.3 59–60 ±*0.2%*	–

1) For oxidised rock: mean uniaxial compressive strength and cohesion reduced by 7%.
2) For oxidised rock: mean crack initiation stress reduced by 8%.
3) From Best fit linear correlation curve shown in Figure 3-10. Crack initiation and UCS are correlated.
4) For oxidised rock: mean tensile strength reduced by 20%.
5) For oxidised rock: mean Young's modulus reduced by 14%.
6) For oxidised rock: mean Poisson's ration increased by 8%.
7) Purely estimated valued used by the theoretical modelling.
8) For oxidised rock: no reduction of the friction angle applies.

Table 3-10. Reduction factors for mean strength and deformation properties for oxidised quartzmonzonite to monzodiorite (501036) and Ävrö quartz monzodiorite (501046) for SDM-Site Laxemar.

Parameter	Compressive strength (MPa)	Crack initiation stress (MPa)	Indirect tensile strength (MPa)	Young's modulus (GPa)	Poisson's ratio (–)
501036 Quartz monzodiorite – 9 oxidised samples	–2%	–9%	–20%	–10%	+4%
501046 Ävrö quartz monzodiorite – 2 oxidised samples	–11%	–6%	No data available	–18%	+11%
Suggested reduction factor	–7%	–8%	–20%	–14%	+8%

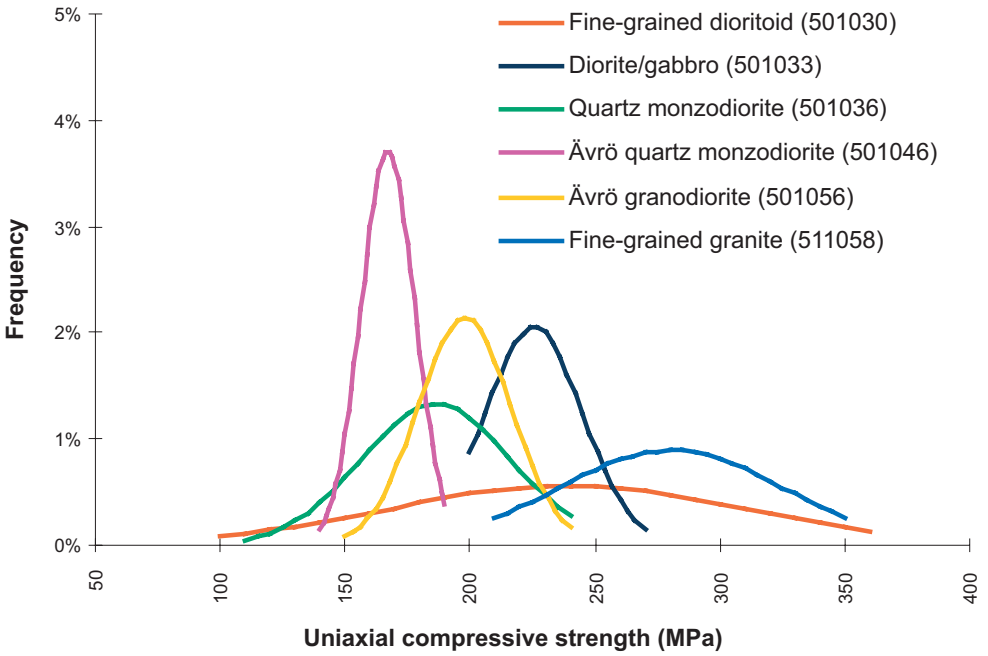

Figure 3-20. *Models for frequency distributions of the different rock codes for uniaxial compressive strength test samples; see Table 3-9, which gives the rock type name and corresponding mean standard deviation and truncation values.*

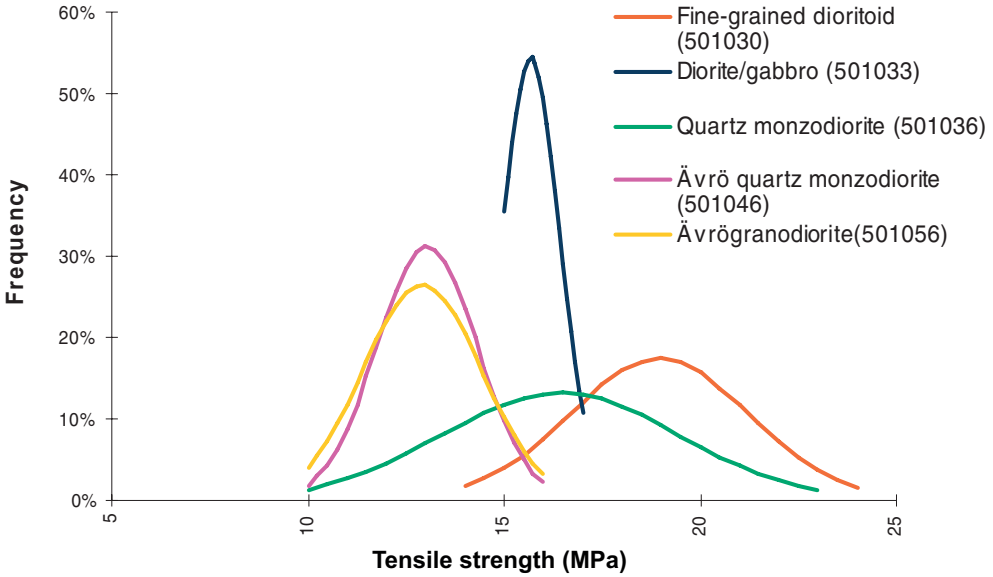

Figure 3-21. *Models for frequency distributions of the different rock codes for indirect tensile strength test samples; see Table 3-9, which gives the rock type name and corresponding mean standard deviation and truncation values.*

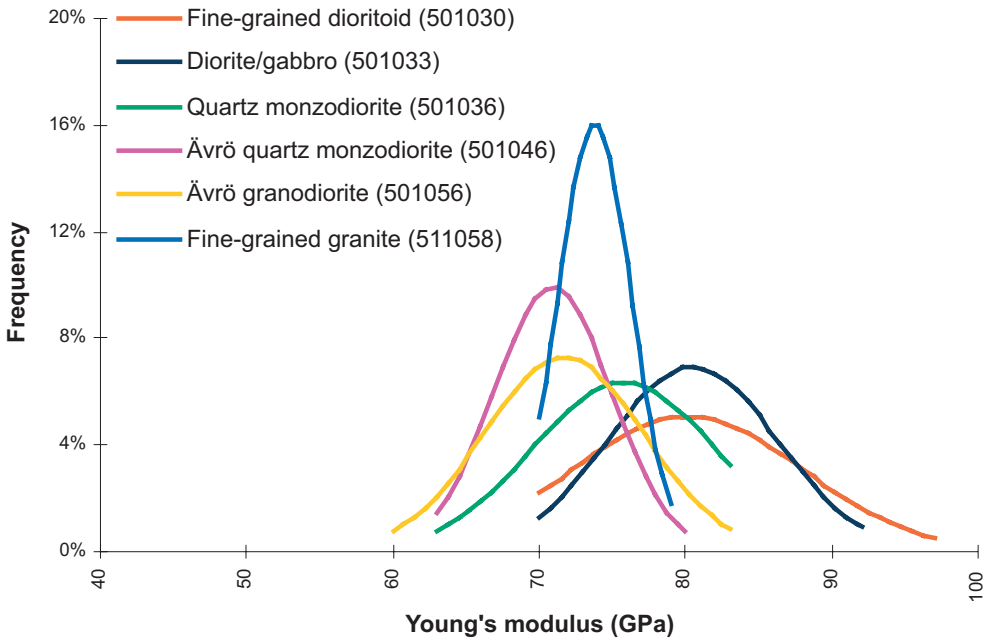

Figure 3-22. *Models for frequency distributions of the different rock codes for Young's modulus test samples; see Table 3-9, which gives the rock type name and corresponding mean standard deviation and truncation values.*

3.6 Model for spatial variation of UCS

3.6.1 Introduction

One issue in the design process of the repository is to estimate the degree of spalling in the deposition holes, i.e. estimation of loss of deposition holes, which is one factor that governs the space required. This estimation is based on the estimation of stress and the occurrence and strength of the intact rock of different types. In Laxemar, the stresses are not expected to be high, but the strength of some of the rock types is relatively low for crystalline rocks. Therefore, a geostatistical analysis which describes the expected spatial distribution of the uniaxial compressive strength (UCS) has been performed.

The main objectives of the stochastic simulation of UCS are:

1. To obtain a spatial statistical description of the uniaxial compressive strength of the rock domains for the Laxemar area. From these results, the amount of low strength rock in the model volume may be estimated.
2. To acquire an increased understanding of the spatial correlation structure of uniaxial compressive strength (UCS) of intact rock.
3. To visualise the spatial distribution of uniaxial compressive strength.
4. To provide the basis for further study of issues relating to the spatial variability of UCS in and around a repository, using the realisations produced by the simulation.

3.6.2 Strategy for modelling uniaxial compressive strength

The modelling approach used here is modified from that used for the modelling of thermal properties at Laxemar /Sundberg et al. 2008/ and described in the strategy report /Back and Sundberg 2007/. The approach as applied to the modelling of uniaxial compressive strength is summarised below.

Lithological simulations at 2 m scale were performed in the Laxemar area as part of the thermal modelling during stage SDM-Site and are the results are reported in /Sundberg et al. 2008/. Each realisation has a cell size of 2×2×2 m, and a simulation volume of 100×100×100 m. This simulation volume is assumed to be sufficiently large for the objectives of the simulations.

For the purpose of the lithological simulations rock types were grouped into a maximum of five rock classes (called thermal rock classes (TRCs) in thermal modelling) per rock domain. Each TRC comprises one or more rock types having similar lithological properties. The maximum number of classes that can be handled in the lithological simulations is five /Back and Sundberg 2007/. Therefore the rock types needed to be grouped into TRCs. Given that each TRC is generally dominated by a single rock type this simplification has little significance for the overall UCS model at domain level.

The basis for the stochastic simulation of UCS is spatial statistical models of UCS for each TRC, describing both probability distributions and spatial correlation. The models for a TRC are based on the dominant rock type in each TRC. The probability distribution models for different rock types, described in Section 3.5, are derived from UCS laboratory measurements. Spatial correlation models are defined by variograms based primarily on borehole loggings of density. A relationship between density and thermal conductivity for igneous rocks has been observed both between rock types and within rock types at Laxemar /Sundberg et al. 2008/, which is not surprising as both properties are closely associated with mineral composition. Thus, for the purposes of thermal modelling, it was reasonably assumed that density and thermal conductivity exhibit similar correlation structures /Back and Sundberg 2007/, which permitted the use of borehole density loggings for the construction of variogram models. It is assumed here that UCS also exhibit similar a correlation structure to density. Support for this assumption is provided by the existence of a correlation between wet density and the rock mechanic properties uniaxial compressive strength and indirect tensile strength for some rock types (Figure 3-1a and Figure 3-2a). Therefore, the variogram models defined for density can be used for simulation of UCS. The suitability of these models is tested by variogram analysis of the available UCS data.

Stochastic simulations of compressive strength were performed for each rock class (TRC). The simulation volume and resolution are the same as for the lithological simulations. Although the geostatistical simulations have a cell size of 2×2×2 m, UCS is a parameter that relates to intact rock at standard laboratory scale (dm). In other words, each 2 m cell is assigned *one* UCS value, corresponding to the UCS of a drill core size sample taken in the centre of the cell.

Lithological realisations and the compressive strength realisations are merged, i.e. each cell in the lithological realisation is filled with the appropriate compressive strength value in the corresponding position of the compressive strength realisations. Merging produces a set of realisations of compressive strength for each rock domain that considers the spatial variability both between TRCs and within TRCs; see Figure 3-23.

At Laxemar, three rock domains are of particular interest within the local model volume: domains RSMA01, RSMM01 and RSMD01. A uniaxial compressive strength model is presented for each rock domain.

3.6.3 Spatial statistical models of UCS

Probability distribution models

The classification of rock types into rock classes (TRCs) is shown in Table 3-11. The data indicate that oxidised quartz monzodiorite (501036) has a lower UCS than non-oxidised rock (Section 3.5). Therefore, oxidised quartz monzodiorite was treated as a separate rock class (TRC 136) both in the lithological simulations and compressive strength simulations. The statistical distribution models of UCS used in the simulations for a particular TRC are generally based on the dominant rock type in that TRC. Since data for rock type fine-grained diorite-gabbro (TRC 102) are not available, the model for TRC 102 was based on diorite-gabbro instead. Distribution models of UCS for rock types are presented in Figure 3-20.

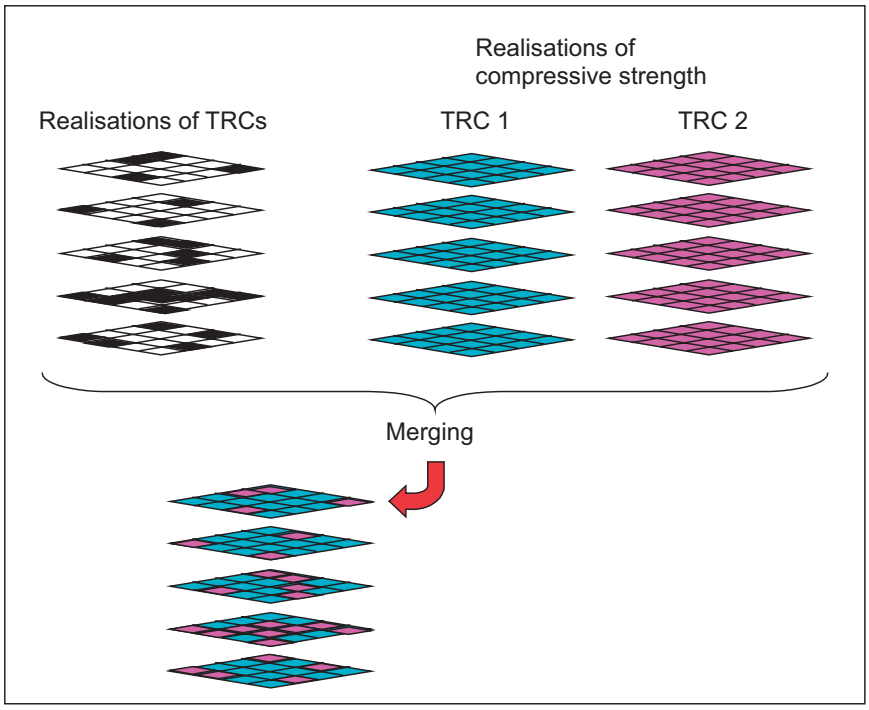

Figure 3-23. *Schematic description of the merging of lithological realisations and compressive strength realisations for two TRCs. A maximum of five TRCs can be modelled. The spatial variability of compressive strength within each TRC is not illustrated in the figure.*

Table 3-11. Classification of rock types into thermal rock classes (TRC). Dominant rock type in bold determines the statistical distribution. Summary statistical parameters of UCS probability distributions for all TRCs. Reduction in variance in resolution models compared to data is due to truncation. The expected volume occurrence of the rock types is given in Table 2-1.

TRC	Rock name/code	Present in rock domain	Mean (MPa)	St. dev. (MPa)	min (MPa)	max (MPa)	Variance reduction compared to data
36	**Quartz monzodiorite (501036)**	D	184	27	110	240	19%
	Fine-grained dioritoid (501030)						
46	**Ävrö quartz monzodiorite (501046)**	A, M	167	10	140	190	17%
56	**Ävrö granodiorite (501056)**	A, M	198	18	150	240	10%
	Granite (501058)						
136	**Oxidised Quartz monzodiorite (501036)**	D	171	26	102	223	19%
33	**Diorite-gabbro (501033)**	M	229	16	200	270	36%
	Fine-grained diorite-gabbro (505102)						
30	**Fine-grained dioritoid (501030)**	A	236	60	100	359	31%
	Quartz monzodiorite (501036)						
58	**Fine-grained granite (511058)**	A, D, M	280	34	210	350	43%
	Pegmatite (501061)						
102	**Fine-grained diorite-gabbro (505102)**	A, D	229	16	200	270	36%
	Diorite-gabbro (501033)						
	Dolerite (501027)						

They are truncated normal distributions based on frequency models presented for UCS laboratory data in Table 3-9. For oxidised quartz monzodiorite, the mean UCS is estimated to be 7% lower than the non-oxidised quartz monzodiorite, which includes both unaltered and saussuritised varieties (Table 3-9). The minimum and maximum values have also been reduced by 7% as has the variance giving the following model parameters: a normal distribution with a mean of 173 MPa and a standard deviation of 29 MPa, truncated at a minimum 102 MPa and a maximum 223 MPa. Due to the truncations, the resulting distribution models have means and standard deviations that differ slightly from the values that define the shape of the model distributions (Table 3-9) and the data (Table 3-2). The summary statistics for the distributions used in the spatial simulations are also given in Table 3-11. The reductions in variance caused by truncating the distributions are also quoted.

Spatial correlation models

Variograms are used to model the spatial correlation structure of UCS within a rock type. Variogram models for UCS are based on those produced for thermal modelling /Sundberg et al. 2008/ and are described in Table 3-12. They rely primarily on density logging data, in particular for defining the range of a variogram. Since density, which is closely related to mineral composition, displays a certain degree of correlation with UCS for some rock types (Figure 3-1a), the same variogram models used have been selected for modelling of compressive strength.

Validation of these variogram models for the simulation of compressive strength was possible with respect to short lag distances for the dominant rock types (TRCs) in each domain, namely quartz monzodiorite (501036), Ävrö quartz monzodiorite (501046) and Ävrö granodiorite (501056). This is exemplified for TRC 36 in Figure 3-24 and in Appendix 8 for other TRCs.

Table 3-12. Variogram model parameters used for modelling spatial correlation of UCS for each TRC. Semi-variance of variogram structures is standardised so that the sum of the semi-variance values for all structures is 1. The nugget is treated as a separate variogram structure with no range.

TRC	Rock type on which variogram is based (code)	Structure	Semi-variance (contribution, weight)	Range (m)
TRC 30	501036	Nugget	0.33	
		Spherical	0.67	75
TRC 33	501033 (type A)	Nugget	0.10	
		Exponential	0.30	3
		Spherical	0.60	22
TRC 36	501036	Nugget	0.33	
		Spherical	0.67	75
TRC 46	501046	Nugget	0.25	
		Spherical	0.28	1
		Spherical	0.47	35
TRC 56	501056	Nugget	0.60	
		Spherical	0.20	2
		Spherical	0.20	50
TRC 58	511058	Nugget	0.40	
		Exponential	0.60	6
TRC 102	505102	Nugget	0.10	
		Spherical	0.90	1.5
TRC 136	Same as TRC 36	Same as TRC 36		

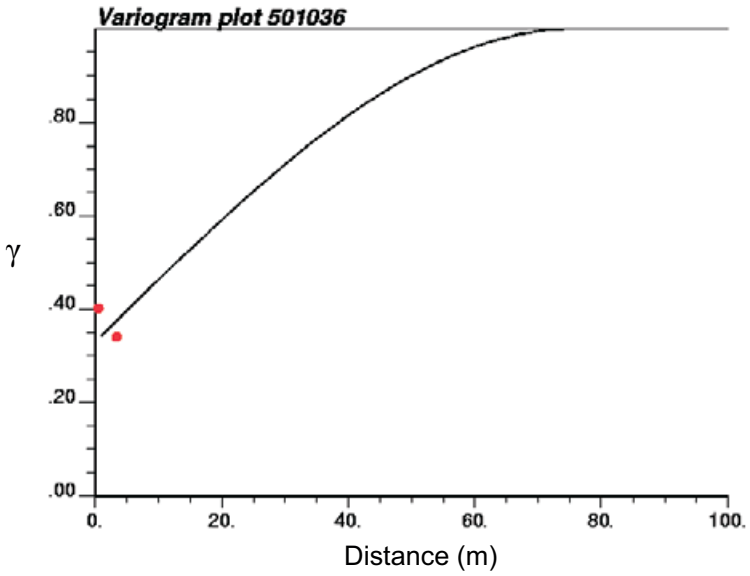

Figure 3-24. *Variogram model for TRC 36. Standardised semi-variance of UCS for quartz monzodiorite at lag distances of c. 0.5 m and 3 m is indicated by the red dots based on 22 and 14 data pairs respectively The sill level represents the total variance of the data. The scale of sample is c. 0.1 m.*

For other rock types (TRCs), there are not enough data pairs to make variogram analysis meaningful. Data for diorite-gabbro (501033) is also plotted although only four data pairs are available. There is generally insufficient data available to plot the semi-variance for longer lag distances. The variogram model adopted for TRC 136 (oxidised quartz monzodiorite) is the same as for TRC 36 (quartz monzodiorite). The variogram model for TRC 30 is based on rock type quartz monzodiorite (501036) and not fine-grained dioritoid (501030), the dominant rock type in TRC 30 /Sundberg et al. 2008/. It should be noted, however, that these two rock types are present in approximately equal amounts.

Based on the recognition of a low-density variety and a high-density variety of diorite-gabbro in TRC 33, two sub-TRCs were defined in the thermal modelling /Sundberg et al. 2008/. The limited UCS data for diorite-gabbro does not justify such a division for the simulation of UCS. The variogram model selected for UCS simulation is that describing TRC 33A in the thermal modelling, but the difference between variogram models for 33A and 33B is small (Appendix 8).

With the exception of TRC 56 (Ävrö granodiorite), the nugget of the variogram models are in general validated by the UCS data. For Ävrö granodiorite, the UCS data indicate that the nugget may be slightly lower than in the model. The lower nugget suggested by the UCS data may be partly due to the sampling procedure; rather homogenous sections of borehole core may have been selected for taking closely spaced samples, which would tend to give a higher apparent spatial dependency. Therefore no adjustment was made to the model. The distance over which spatial dependence occurs is given by the range of the variograms. The major rock types are modelled with ranges between 20 and 75 m. However, due to the paucity of data it is generally not possible to verify the range of the variogram models using UCS data.

It is acknowledged that support for assuming that UCS has a similar correlation structure to density is rather tentative. There may be other important factors controlling the spatial dependence of UCS for which it has not been possible to model. One such property is grain size. However, it can be stated with certainty that spatial correlation does exist. Given the lack of UCS data, the variograms used here represent a reasonable attempt to model this spatial dependence.

3.6.4 Stochastic simulation

Stochastic simulation of lithologies (TRCs)

Stochastic simulations of lithologies or TRCs for rock domains RSMA01, RSMM01 and RSMD01 were performed as part of the thermal modelling, stage SDM-Site /Sundberg et al. 2008/. The output from these simulations is also used in the modelling of compressive strength. Domains RSMA01 and RSMM01 were divided into more homogenous subdomains. A brief description of the lithological simulations is given in Appendix 8. One hundred realisations of geology for each rock domain were selected for the purpose of modelling UCS. Each realisation has dimensions 100×100×100 m and a resolution of 2 m.

Visualisations of example geology realisations for all three rock domains are presented in Appendix 8. A full account of the simulation results are presented in /Sundberg et al. 2008/. The borehole data used as input for lithological simulations have been processed to exclude the deterministically modelled deformation zones. The smaller MDZs have been retained which may result in a slightly higher proportion of oxidised quartz monzodiorite than would be the case if these zones were also excluded.

Stochastic simulation of UCS in each TRC

Stochastic simulation of compressive strength was performed for each TRC. The software used to perform the simulations is GSLIB /Deutsch and Journel 1998/. One hundred realisations were produced for each TRC. For each TRC the following plots and diagrams have been produced to illustrate the results and validate the method:

1. Histogram of simulated values in 100 realisations (Appendix 8). The results for TRC 36 are exemplified in Figure 3-25.
2. Variogram reproduction plots for 2 m resolution simulations based on individual realisations (Appendix 8).
3. Visual representation of simulation results at 2 m resolution. 2D slice through a 3D realisation (Appendix 8).

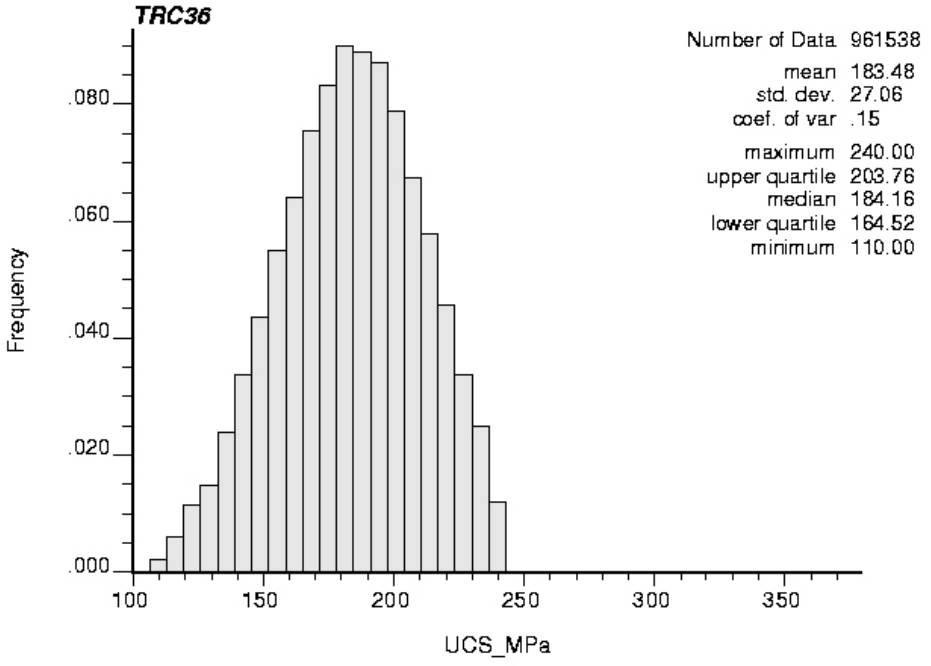

Figure 3-25. *Histograms of uniaxial compressive strength for TRC36 (dominated by quartz monzodiorite) based on stochastic simulation – 100 realisations.*

Analysis of results

- For each TRC, statistics of compressive strength based on results of the simulations are compared to the probability distributions used as input. It was found that the simulations have succeeded in reproducing the means and the standard deviations.
- Simulations have succeeded in reproducing rather well the spatial correlation models used as input in the simulations. The results of variogram reproduction are presented in Appendix 8. Plots compare the variograms calculated from the realisations with the model variograms on which simulations at 2 m resolution were based.

3.6.5 Rock domain model of uniaxial compressive strength

Rock domain modelling results

The results of compressive strength simulations at rock domain level for domains RSMA01, RSMM01 and RSMD01 are presented in this section.

The realisations of stochastic simulations of lithologies and the realisations of UCS are merged with each other as described in Section 3.6.2. Examples of 2D-visualisations of UCS at domain level and the corresponding geological realisations are presented in Figure 3-26 (More examples in Appendix 8).

Histograms of compressive strength for the modelled rock domains, each based on 100 realisations, are shown in Appendix 8. Summary statistics of the results of the simulations are presented in Table 3-13. The lower tails in domains RSMA01 and RSMM01 are mainly a result of TRC 46 which comprises Ävrö quartz monzodiorite, but the extremely low values between 100 and 140 MPa in RSMA01 are given exclusively by TRC 30, although the latter make up a very small proportion of the rock mass. Rocks making up the lower tail in domain RSMD01 are quartz monzodiorite (TRC 36) and oxidised quartz monzodiorite (TRC 136).

Evaluation of rock domain modelling results

All three rock domains have yielded similar mean UCS values. However, the histograms and the estimated 2.5 and 5 percentiles show that domain RSMD01 has a much pronounced lower tail, i.e. a higher proportion of rock with lower strengths (<150 MPa). The lower tail of the compressive strength distribution is of intrest for the design of a repository.

The domain histograms give a measure of the total spatial variability in UCS present within a rock domain. How this variability occurs spatially can to some extent be appreciated from an inspection of the 2D visualisations (Figure 3-26, Appendix 8).

Table 3-13. Summary statistics of results of simulation of UCS for domains RSMA01, RSMM01 and RSMD01.

Statistical parameter	RSMA01 (MPa)	RSMM01 (MPa)	RSMD01 (MPa)
Mean	193	187	187
Standard deviation	29	31	34
2.5-percentile	151	149	128
5-percentile	155	152	137
Proportion <150 MPa (%)	2.0%	3.2%	12.0%

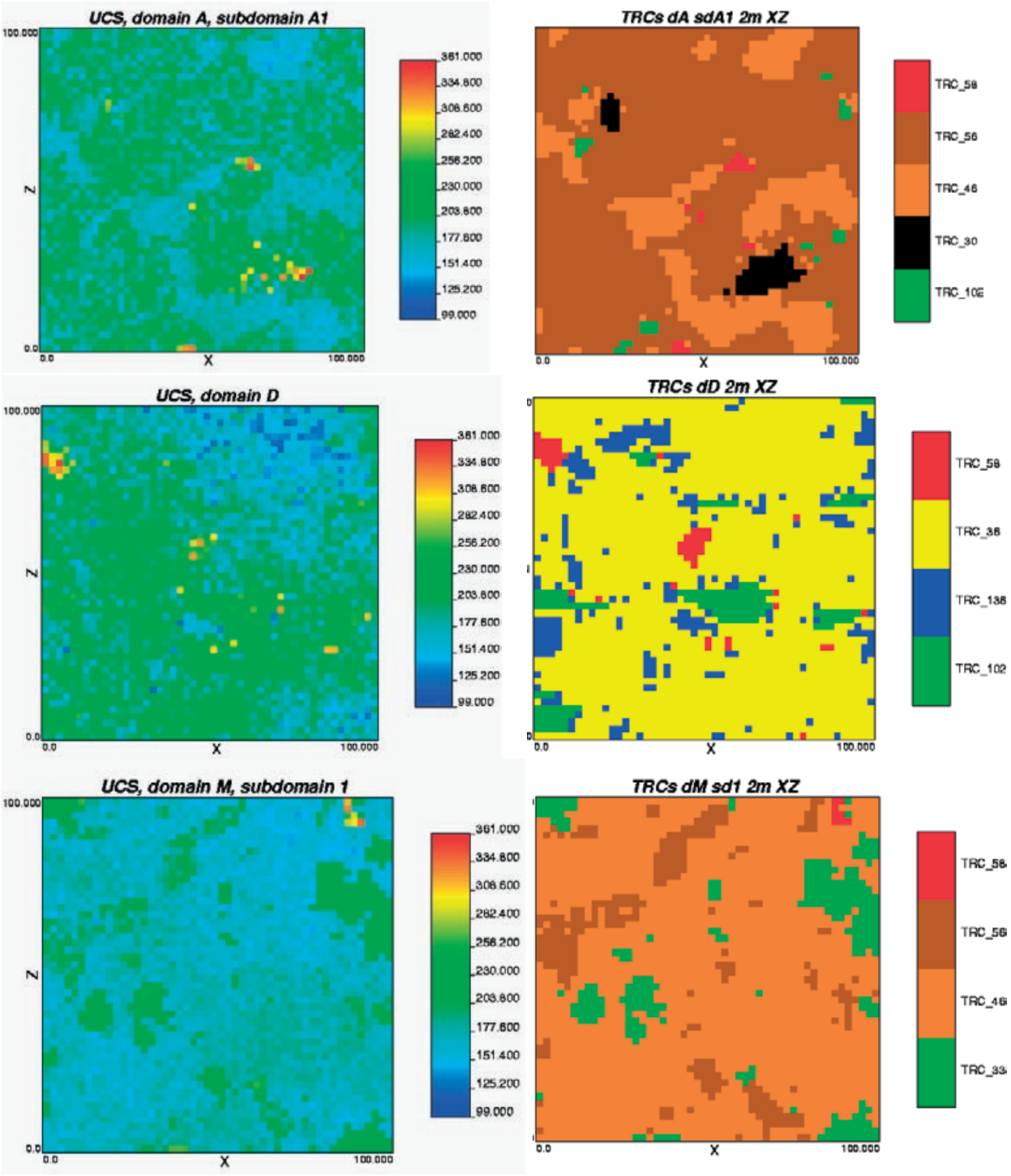

Figure 3-26. *Example 2D visualisations from 3D realisations (resolution = 2 m, xz-plane, distance in metres) illustrating the distribution of compressive strength in domain RSMA01, RSMM01 and RSMD01 (left) and corresponding realisations of lithology or TRCs (right).*

Uncertainties

The following main uncertainties have been identified.

1. The statistical distribution models of compressive strength are based on rather few data, and are therefore rather uncertain. In particular, the tails of the UCS distributions at domain level are affected by the chice of truncation levels – minimum and maximum UCS values – for each TRC.
2. Models of spatial correlation of compressive strength are based on the assumption that compressive strength exhibits a spatial correlation structure similar to that of density. Other characteristics (e.g. grain type, grain size and structural fabric) that may influence the UCS of rock have not been considered.
3. Uncertainties associated with the grouping of rock types into rock classes (TRC) are considered to be small given that each TRC is dominated by a single rock type.
4. Uncertainties related to the lithological simulations are discussed in /Sundberg et al. 2008/. These uncertainties are considered to have only a minor impact on the simulation results as regards the lower percentiles of UCS, whereas the mean UCS values in domains RSMA01 and RSMM01 are more sensitive.

3.6.6 Conclusions from simulations of spatial variation in UCS

The spatial variability of compressive strength within and between different rock types has been modelled for three rock domains within the local model volume at Laxemar. The output from modelling is sets of realisations of compressive strength generated by stochastic simulation.

The results of the geostatistical analysis and stochastic simulations reinforces the conclusions of the previous SDM site descriptive models, and confirms the spatial variability of UCS within rock type and rock domains. Despite the recognised uncertainties, the stochastic simulations have shown that spatial variability within individual rock types makes up a significant portion of the total variability observed in the measurement data.

According to the simulation results, all three modelled rock domains have similar mean compressive strengths. However, domain RSMD01 displays greater variability and has a larger proportion of rock with low compressive strength (<150 MPa). The estimated volume of rock with compressive strength values lower than 150 MPa estimated to 2% in rock domain RSMA01, 3% for RSMM01 and 12% for RSMD01. In both domains RSMA01 and RSMM01, the lower tail of the domain UCS distribution is mainly a result of Ävrö quartz monzodiorite, whereas for domain RSMD01, quartz monzodiorite, both fresh and altered, dominate the lower tail.

4 Single fracture mechanical properties

4.1 Overview of the primary data

In this chapter the laboratory strength and deformation properties of discrete fractures are presented and discussed. The available tests on fractures for the selected rock domains are listed in Table 4-1. The results from these tests are used in the theoretical approach to estimate the strength and deformation properties of the rock mass. This report also includes WellCad plots that show the sampling locations and results in relation to interpreted geological features (see Appendix 1).

The strength and deformability of the natural rock fractures was determined in two ways:

1. To get an overview of the variation in fracture properties along boreholes, tilt tests were performed, where shearing is induced by the self-weight of the upper block as the fracture is progressively tilted.
2. To get more detailed information on strength and deformability of the fractures, direct shear tests were performed on fractures from selected locations where shearing is induced by actuators that apply a load perpendicular and parallel to the fracture plane. Three different types of shear test configuration were used over time; these are referred to as Type I, Type II and Type III. The main differences between the different shear test configurations are explained in Section 4.4.

The methodology, standard and performance used for the laboratory testing are described in SKB's Method Description for each test:

- Tilt tests on fractures: SKB MD 190.006, ver 2.0 (SKB controlling document)
- Shear tests on fractures: SKB MD 190.005, ver 3.0 (SKB controlling document)

Tilt tests were performed on 199 fracture samples. All tilt tests were performed by the Norwegian Geological Institute Laboratory (NGI).

Table 4-1. Number of tested fractures for each testing method performed.

Borehole	Tilt tests on fractures	SKB report [1)]	Shear tests on open fractures	Shear tests on sealed fractures	Shear test method [2)]	SKB report [1)]
KAV01	26	P-04-42	5		I	P-05-05
KLX02	29	P-04-44	9		II	P-04-257
KLX03	18	P-05-02	8		II	P-05-92
KLX04	18	P-04-265	10		II	P-04-264
KLX06			6		III	P-05-146
KLX07A				3	III	P-05-209
KLX10	9	P-06-34	5		III	P-06-39
KLX12A			5		III	P-06-75
KLX13A				11	III	P-06-277
KSH01A	51	P-03-107	17		I	P-05-06
KSH02	48	P-04-10	6		I	P-05-07
Total	199		71	14		

1) For references, see Section 9.1.
2) See Section 4.4.

Direct shear tests were performed on 71 open fracture samples and 15 tests were performed on sealed fractures. The size of each sample was about 55 mm. All samples were tested by the Swedish National Testing and Research Institute (SP).

An inter-laboratory test series to check the quality in the direct shear tests by SP has been performed by NGI. These laboratory tests were performed on samples from Forsmark and have been reported by /Lanaro and Fredriksson 2005b/. This test series supported the development of changes in the test configuration mentioned above.

4.2 Sampling strategy

The sampling for the tilt tests was performed during the drill core logging. The strategy for ensuring that different fracture orientation were sampled was to aim at selection of fractures with a relative angle to the core axis in different intervals 0–30°, 30–60° and >60°.

Samples for the direct testing of normal stiffness and shear stress were intended to be collected from the same depth intervals as for testing of intact rock. Samples were typically taken from either gently dipping fractures, or steeply dipping fractures with a small angle to the core axis. In the latter case two to three samples could be taken from the same fracture.

4.3 Tilt test results

A number of tilt tests were performed on natural fractures in order to evaluate the strength of the fractures. The tilt tests are designed to allow the fracture parameter determination according to /Barton and Bandis 1990/. The shear strength of the fracture is a function of the normal stress σ_n as:

$$\tau = \sigma_n \tan\left[\phi_b^{BB} + JRC \log\left(\frac{JCS}{\sigma_n}\right)\right] \qquad \textit{Equation 4-1}$$

JRC is the Joint Roughness Coefficient that quantifies roughness, *JCS* is the Joint Wall Compression Strength of the rock surfaces (determined by a Schmidt hammer test /Chryssanthakis 2005/), and ϕ_b^{BB} is the basic friction angle on dry saw-cut surfaces. The residual friction angle ϕ_r^{BB} is used instead of ϕ_b^{BB} if the strength of wet surfaces is considered. The index notation *BB* is used to emphasise that the parameters relate to the Barton-Bandis model, to differentiate them from parameters in the Mohr-Coulomb model, discussed later. /Barton and Bandis 1990/ also suggested truncating the strength envelope as follows: τ/σ should always be smaller than tan (70°) and, in this case, the envelope should go through the origin ($\sigma_n = \tau = 0\ MPa$), in other words the cohesion is zero.

The *JRC* and *JCS* parameters are dependent on fracture length. The measured JRC_0 and JCS_0 values relate to fracture specimens of different lengths. Therefore, the measured values are normalised and extrapolated to values that relate to a standard fracture length of 100 mm, and hereafter referred to as JRC_{100} and JCS_{100} values.

For a certain level of stress, the relation in Equation 4-1 can be linearly approximated to determine the peak friction angle and cohesion of the Mohr-Coulomb Strength Criterion as:

$$\tau = c_p^{MC} + \sigma_n \tan\left(\phi_p^{MC}\right) \qquad \textit{Equation 4-2}$$

where, c_p^{MC} and ϕ_p^{MC} are peak cohesion and peak friction angle. Similarly, the residual cohesion c_r^{MC} and peak friction angle, ϕ_r^{MC} can be fitted by the Mohr-Coulomb residual envelope. The determined Mohr-Coulomb model parameters based on all tilt tests are presented in Table 4-2.

Table 4-2. Calculated results from all tilt tests made at Laxemar and Simpevarp (see Table 4-1), in total 199 tests.

Test	Minimum	Mean	Median	Maximum	Standard deviation
Basic friction angle, ϕ_b [°]	21.7	31.4	31.3	35.2	1.6
Residual friction angle, ϕ_r [°]	17.7	26.3	26.4	36.5	3.0
JRC_{100} [–]	1.8	6.1	6.3	9.5	1.4
JCS_{100} [MPa]	26	69	63	150	25
Peak friction angle, ϕ_p^{MC} [°]	25.9	34.0	34.0	38.8	1.8
Peak cohesion, c_p^{MC} [MPa]	0.1	0.5	0.5	0.8	0.1
Residual friction angle, ϕ_r^{MC} [°]	18.7	28.9	28.7	40.0	3.5
Residual cohesion, c_r^{MC} [MPa]	0.1	0.4	0.4	0.7	0.1

The linear Mohr-Coulomb envelope has been fitted to the curved Barton-Bandis envelope in the stress range from 0–20 MPa i.e. the same stress range as the direct shear stress envelope is fitted to measured data.

In Table 4-3, the tilt data are shown grouped into fracture sets according to the geological DFN model of Laxemar /La Pointe et al. 2008/. Tests that are not, or can not, be assigned to any fracture set, because they are sampled from boreholes outside the fracture domains (i.e. from Simpevarp boreholes), are denoted “not assigned” in the table. T he variation of the evaluated mechanical fracture parameters with depth are reported in Figure 4-1 to Figure 4-4. In general, the data are so scattered that no trends with depth or fracture sets can be recognised. The only clear difference that was found is a higher stiffness for the subhorizontal set compared to steeply dipping fractures.

4.4 Direct shear test results

Specimens containing a natural fracture from boreholes KAV01, KSH01A, KSH02, KLX02, KLX03, KLX04, KLX06, KLX10 and KLX12A were tested with normal stress and shear tests.

In the normal loading tests, the joints were loaded and unloaded twice up to a normal stress of 10 MPa. Direct shear tests with constant normal loading were carried out after the normal loading tests. Each fracture sample was sheared three times, at the normal stress levels 0.5, 5 and 20 MPa.

Table 4-3. Summary of the results of tilt tests performed on rock fractures grouped in different fracture sets.

Fracture set	Number of samples	ϕ_b [°]	ϕ_r [°]	JRC_{100} [–]	JCS_{100} [MPa]
		Mean/Std dev	Mean/Std dev	Mean/Std dev	Mean/Std dev
ENE	9	31.9/1.1	25.1/2.5	7.4/1.5	59.5/18
NS	17	31.5/0.9	27.0/2.6	6.5/1.8	80.0/22
WNW	14	31.4/1.0	25.2/2.8	6.8/1.2	65.8/25
SH	26	31.8/1.1	26.3/2.2	5.6/1.3	63.4/19
Not assigned	133	31.3/1.9	26.4/3.2	6.0/1.3	70.0/26
All fractures	199	31.4/1.6	26.3/3.0	6.1/1.4	69.0/25

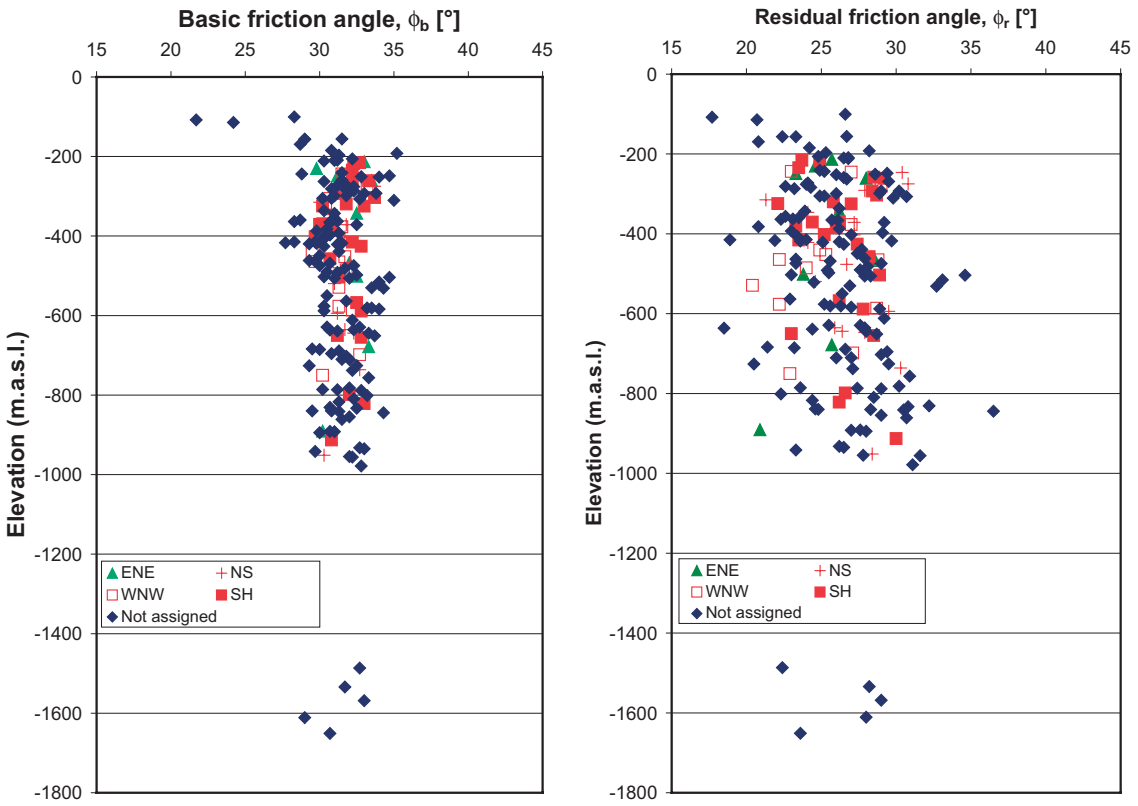

Figure 4-1. *Basic friction angle φ_b and residual friction angle ϕ_r versus elevation.*

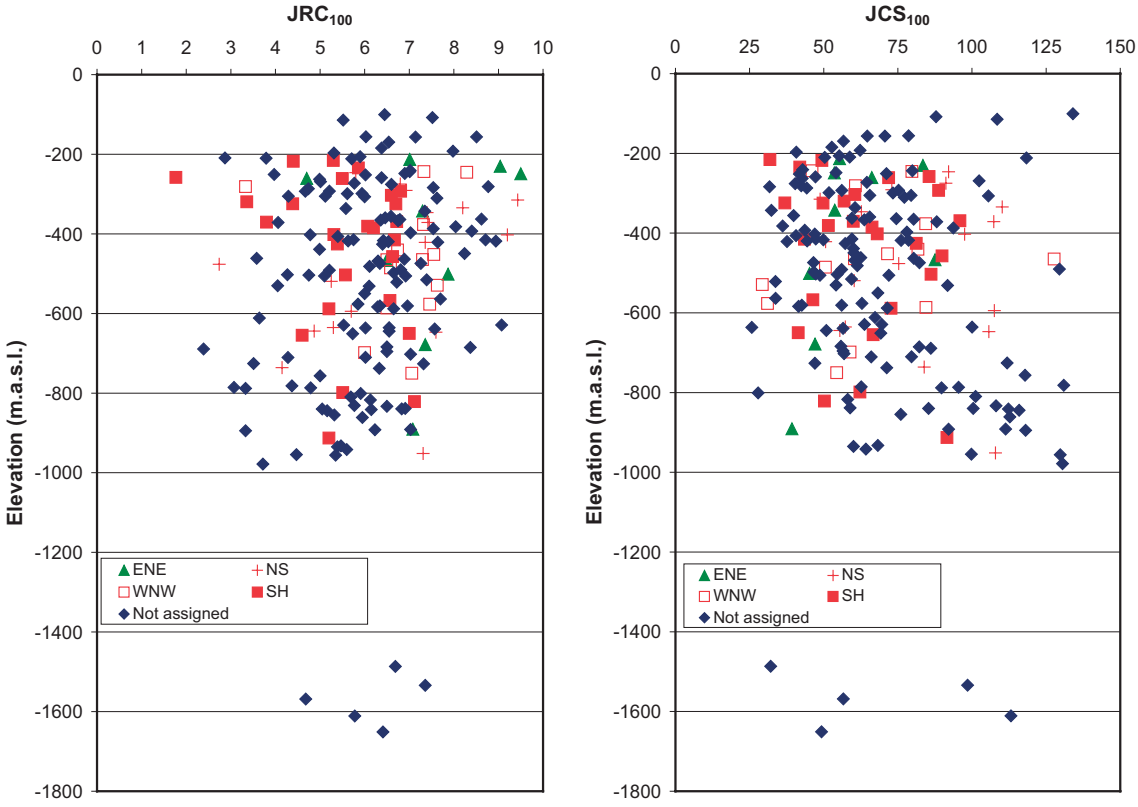

Figure 4-2. *JRC_{100} and JCS_{100} versus elevation.*

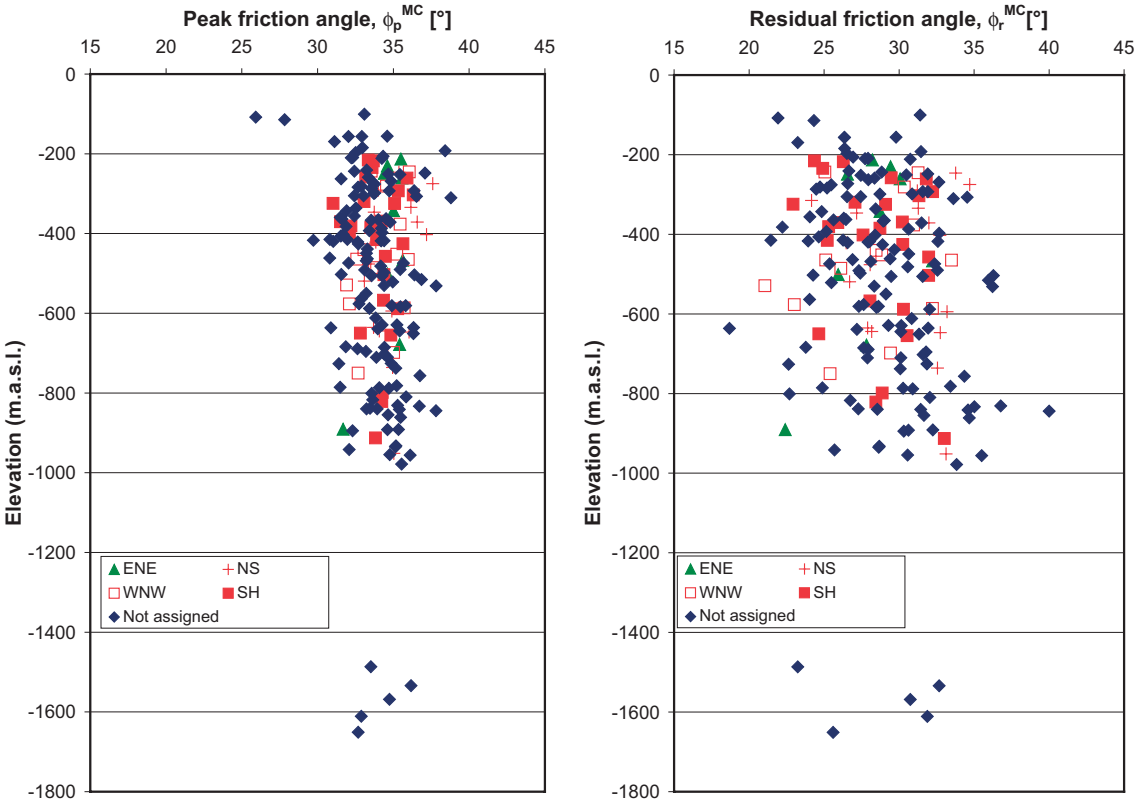

Figure 4-3. *Peak friction angle ϕ_p^{MC} and residual friction angle ϕ_r^{MC} versus elevation.*

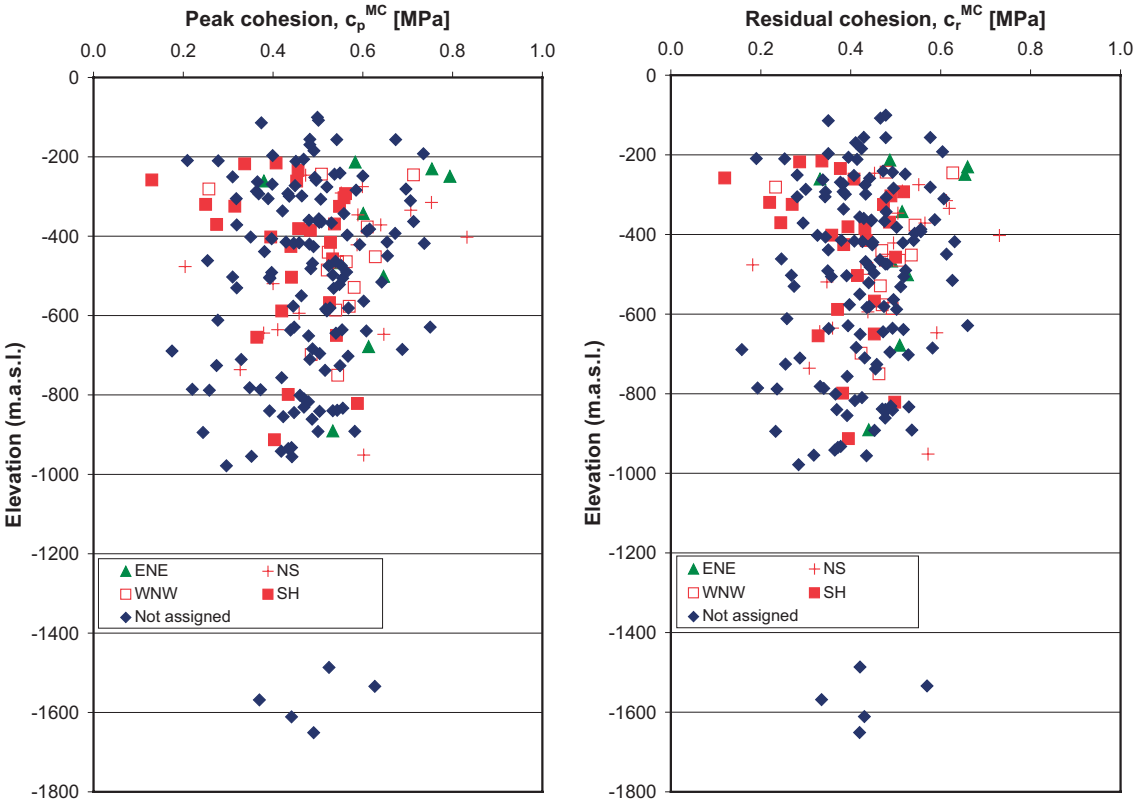

Figure 4-4. *Peak cohesion c_p^{MC} and residual cohesion c_r^{MC} versus elevation.*

To examine how the clamping of rock specimens in the laboratory test apparatus may influence test results, three different techniques were used. The main difference between the three methods is the casting material and size of the steel holders that are used to hold the specimen in the shear test apparatus. The three different test configurations are denoted Type I, Type II, and Type III, respectively, are briefly described below.

Type I: The aim was to use maximum fracture length resulting in various fracture lengths depending on their formation. The specimens were cast into specimen holders using a fast hardening anchoring grout. The normal deformation was measured using an indirect measurement method. A correction of the normal deformation values due to the cement deformation was subsequently carried out based on results from reference tests on steel specimens. The shear test started from an initial state corresponding to a mated fracture at the 0.5 and the 20 MPa normal stress level, but not on the 5 MPa level. This type of test was used on samples from boreholes KAV01, KSH01A and KSH02.

Type II: The aim was to use similar fracture areas in the different specimens and the fractures were therefore cut to a length between 50–60 mm. The specimens were also cut parallel to the fractures to obtain equal total heights. The specimens were cast into smaller specimen holders using an epoxy material. A correction of the normal deformation values due to the epoxy deformation was carried out based on results from reference tests on steel specimens. The shear test started from the initial state corresponding to a mated fracture at respective normal stress level. This test type was used on samples from borehole KLX02 and KLX04.

Type III: This configuration is similar to Type II. The difference is that specimens were partially cast into fast hardening anchoring grout for the normal loading test. A direct measurement of the normal deformation over the fracture was used. The specimens were removed from the holders after the test and cast into another set of specimen holders using an epoxy material. This configuration was used during the shear tests. The shear test started from an initial state corresponding to a mated fracture at respective normal stress level. This test type was used on samples from boreholes KLX03, KLX06, KLX10 and KLX12A.

The laboratory results were evaluated in terms of several different rock mechanical parameters that describe fracture strength and deformability. These parameters are summarised and analysed in the following sections.

Description of parameter evaluation

The secant normal stiffness K_N is determined as the secant evaluated between the unloaded state and full loading belonging to the loading path during the second load cycle.

The secant shear stiffness K_S is determined as the secant evaluated between 30% and 50% of the peak shear stress $\sigma_{s,max}$ at the loading path during the test at each of the three normal stress levels, 0.5, 5 and 20 MPa, respectively. The secant dilatancy angle Ψ is determined between 0.3 and 1.3 mm shear deformation at the 0.5 MPa normal stress level, between 0.5 and 1.9 mm shear deformation at the 5 MPa normal stress level and between 0.7 and 2.1 mm shear deformation at the 20 MPa normal stress level. Small modifications of the evaluation criteria were done in some cases. This is noted in conjunction with the result presentations.

The peak friction angle ϕ_p and cohesion c_p and the residual friction angle ϕ_r and cohesion c_r were determined by linear regression (least square fit) to the measured peak and residual shear stresses at the three normal stress levels.

Tests on open fractures

The test results are present in Table 4-4 to Table 4-6. The variation of the evaluated parameters with depth is shown in Figure 4-6 to Figure 4-11.

Table 4-4. Test results from Type I test (28 tests).

Parameter	Minimum	Mean	Median	Maximum	Standard deviation
Normal stiffness, K_N (MPa/mm)	50	139	103	882	155
Shear stiffness, $K_{S0.5}$ (MPa/mm)	1	8	7	21	6
Shear stiffness, K_{S5} (MPa/mm)	14	29	30	49	9
Shear stiffness, K_{S20} (MPa/mm)	6	30	31	48	10
Dilatancy angle, 0.5 MPa, $\psi_{0.5}$ (°)	5.1	13.9	15.0	21.9	4.6
Dilatancy angle, 5 MPa, ψ_5 (°)	0.1	3.5	3.6	7.4	2.2
Dilatancy angle, 20 MPa, ψ_{20} (°)	0.1	3.4	2.3	12.4	3.1
Peak friction angle, ϕ_p (°)	23.8	31.9	32.7	40.7	4.2
Peak cohesion, c_p (MPa)	0.1	0.5	0.5	1.7	0.3
Residual friction angle, ϕ_r (°)	21.5	30.8	31.2	40.5	4.6
Residual cohesion, c_r (MPa)	0.0	0.3	0.3	1.0	0.3

Table 4-5. Test results from Type II test (19 tests).

Parameter	Minimum	Mean	Median	Maximum	Standard deviation
Normal stiffness, K_N (MPa/mm)	150	239	226	512	78
Shear stiffness, $K_{S0.5}$ (MPa/mm)	3	10	11	18	5
Shear stiffness, K_{S5} (MPa/mm)	14	27	24	45	8
Shear stiffness, K_{S20} (MPa/mm)	16	43	45	62	13
Dilatancy angle, 0.5 MPa, $\psi_{0.5}$ (°)	4.1	13.7	15.1	22.0	5.8
Dilatancy angle, 5 MPa, ψ_5 (°)	2.7	8.3	8.4	15.4	3.7
Dilatancy angle, 20 MPa, ψ_{20} (°)	0.8	3.7	3.2	9.4	2.3
Peak friction angle, ϕ_p (°)	31.2	36.6	37.1	40.8	3.0
Peak cohesion, c_p (MPa)	0.3	0.8	0.9	1.6	0.4
Residual friction angle, ϕ_r (°)	27.5	34.0	34.7	39.5	3.3
Residual cohesion, c_r (MPa)	0.2	0.4	0.3	0.6	0.1

Table 4-6. Test results from Type III test (24 tests).

Parameter	Minimum	Mean	Median	Maximum	Standard deviation
Normal stiffness, K_N (MPa/mm)	240	850	791	2,059	408
Shear stiffness, $K_{S0.5}$ (MPa/mm)	1	10	9	26	6
Shear stiffness, K_{S5} (MPa/mm)	11	23	21	44	9
Shear stiffness, K_{S20} (MPa/mm)	25	38	36	58	8
Dilatancy angle, 0.5 MPa, $\psi_{0.5}$ (°)	6.5	15.0	12.7	57.5	9.8
Dilatancy angle, 5 MPa, ψ_5 (°)	2.5	8.3	8.0	14.7	2.9
Dilatancy angle, 20 MPa, ψ_{20} (°)	0.3	3.2	3.2	6.8	1.7
Peak friction angle, ϕ_p (°)	33.7	36.6	36.8	40.0	1.7
Peak cohesion, c_p (MPa)	0.4	0.9	0.8	2.5	0.6
Residual friction angle, ϕ_r (°)	31.5	35.0	35.0	39.2	1.8
Residual cohesion, c_r (MPa)	0.0	0.5	0.4	0.9	0.2

The influence of the deformations in the sample holder, in the anchoring grout and rock outside the fracture on the evaluated normal stiffness, K_{NM}, of the fracture can be expressed as:

$$K_{NM} = \frac{\sigma_n}{\delta_F + \delta_T} \qquad \textit{Equation 4-3}$$

where, δ_F is the normal deformation of the fracture, δ_T the deformation in the sample holder, the grout and the rock outside the fracture and σ_n is the normal stress. By rearranging Equation 4-3 the real normal stiffness, K_{NF}, of the fracture can be calculated if the stiffness of the holder and grout, K_{NT}, is known.

$$\frac{1}{K_{NF}} = \frac{1}{K_{NM}} - \frac{1}{K_{NT}} \qquad \textit{Equation 4-4}$$

The type III test gives the normal stiffness of the fracture, K_{NF}, as the deformation is measured directly over the fracture. By assuming that the mean real normal stiffness for the fractures tested by type I and type II tests shall be the same as measured by the type III test, the stiffness of the holder and grout, K_{NT}, can be calculated, see Table 4-7.

The measured normal stiffness, K_{NM}, by the type I and type II tests can be corrected by using Equation 4-4. The measured shear stiffness and friction angle by the type I and type II tests can also be corrected. The evaluated corrected parameters with respect to normal stiffness, peak friction angle and peak cohesion are presented in Table 4-8 and Figure 4-6 to Figure 4-11. The variation of the normal stiffness, K_N, is high compared with the variation in other parameters, the distribution in this case is also skewed (Figure 4-5).

Table 4-7. Mean real normal stiffness and calculated stiffness of the sample holder and grout.

Test type	Measured mean normal stiffness K_{NM} (MPa/mm)	Normal stiffness K_{NF} (MPa/mm)	Stiffness of holder, grout and rock K_{NT} (MPa/mm)
I	139	850	149.5
II	239	850	332.5
III	850	850	

Table 4-8. Test results from all tests (71 tests) (see text for explanation on how the tests from different test types were merged).

Test	Minimum	Mean	Median	Maximum	Standard deviation
Normal stiffness K_N (MPa/mm)	72	721	588	4,003	655
Shear stiffness $K_{S0.5}$ (MPa/mm)	1	9	9	26	6
Shear stiffness K_{S5} (MPa/mm)	11	26	24	49	9
Shear stiffness K_{S20} (MPa/mm)	14	39	39	62	10
Dilatancy angle, 0.5 MPa, $\psi_{0.5}$ (°)	4.1	14.2	13.8	57.5	7.0
Dilatancy angle, 5 MPa, ψ_5 (°)	2.5	8.3	8.1	15.4	2.9
Dilatancy angle, 20 MPa, ψ_{20} (°)	0.1	3.4	3.1	12.4	2.5
Peak friction angle, ϕ_p (°)	28.5	36.6	37.0	45.4	3.2
Peak cohesion, c_p (MPa)	0.3	0.9	0.9	2.5	0.4
Residual friction angle, ϕ_r (°)	25.7	34.7	34.9	44.7	3.5
Residual cohesion, c_r (MPa)	0.0	0.4	0.3	1.0	0.2

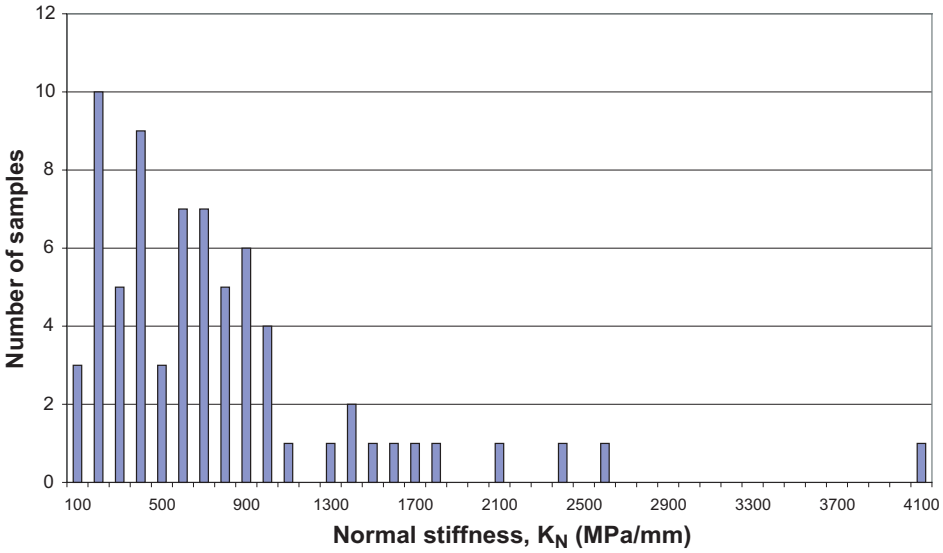

Figure 4-5. *Histogram of the normal stiffness data (cf Table 4-8).*

In Table 4-9, the shear test data are shown grouped into fracture sets according to the DFN model of the Site /La Pointe et al. 2008/. Tests that are not, or cannot, be assigned to any fracture set because they are sampled from boreholes outside the fracture domain are denoted "not assigned" in the table. The variation of the evaluated mechanical fracture parameters with depth are reported in Figure 4-6 to Figure 4-11. In general, the data are so scattered that no trends with depth can be recognised. As is also seen in the results from tilt tests, the direct test results do not exhibit any clear differences in properties between the sets, possibly with the exception of the normal stiffness for the subhorizontal set. In previous model version the potential correlation between cohesion and friction angle parameters was investigated, by no such correlation was found /Lanaro et al. 2006/. Since no significant difference was seen between sets or between the tests inside and outside Laxemar, all available data was utilized in the modelling of fracture strength properties.

Table 4-9. Summary of the results of shear tests performed on rock fractures grouped in different fracture sets.

Test	ENE mean/ std.dev.	NS mean/ std.dev	WNW mean/ std.dev.	SH mean/ std.dev	Not assigned mean/ std.dev.
Number of tests	**6**	**4**	**7**	**25**	**29**
Normal stiffness K_N (MPa/mm)	849/443	699/454	832/479	960/807	464/530
Shear stiffness $K_{S0.5}$ (MPa/mm)	9.7/7.8	9.9/4.5	8.1/4.2	10.3/6.0	8.1/6.0
Shear stiffness K_{S5} (MPa/mm)	25.8/9.8	22.6/7.1	21.2/2.8	25.3/9.3	29.1/8.8
Shear stiffness K_{S20} (MPa/mm)	39.3/8.9	32.4/10.8	37.1/6.7	41.8/10.9	39.1/10.9
Dilatancy angle, 0.5 MPa, $\psi_{0.5}$ (°)	21.6/17.9	13.4/7.4	14.3/5.1	13.0/4.7	13.9/4.4
Dilatancy angle, 5 MPa, ψ_5 (°)	10.2/3.1	8.5/3.6	8.4/3.3	7.8/3.3	8.3/2.2
Dilatancy angle, 20 MPa, ψ_{20} (°)	4.2/1.7	3.9/1.7	3.3/2.3	3.2/2.1	3.4/3.1
Peak friction angle, ϕ_p (°)	38.1/1.9	37.7/2.4	35.9/2.1	36.3/2.5	36.6/4.2
Peak cohesion, c_p (MPa)	1.0/0.8	0.8/0.3	0.8/0.3	0.8/0.5	0.9/0.3
Residual friction angle, ϕ_r (°)	34.7/1.0	35.8/1.2	33.5/2.1	34.8/3.0	34.9/4.6
Residual cohesion, c_r (MPa)	0.5/0.3	0.5/0.2	0.5/0.2	0.4/0.2	0.3/0.3

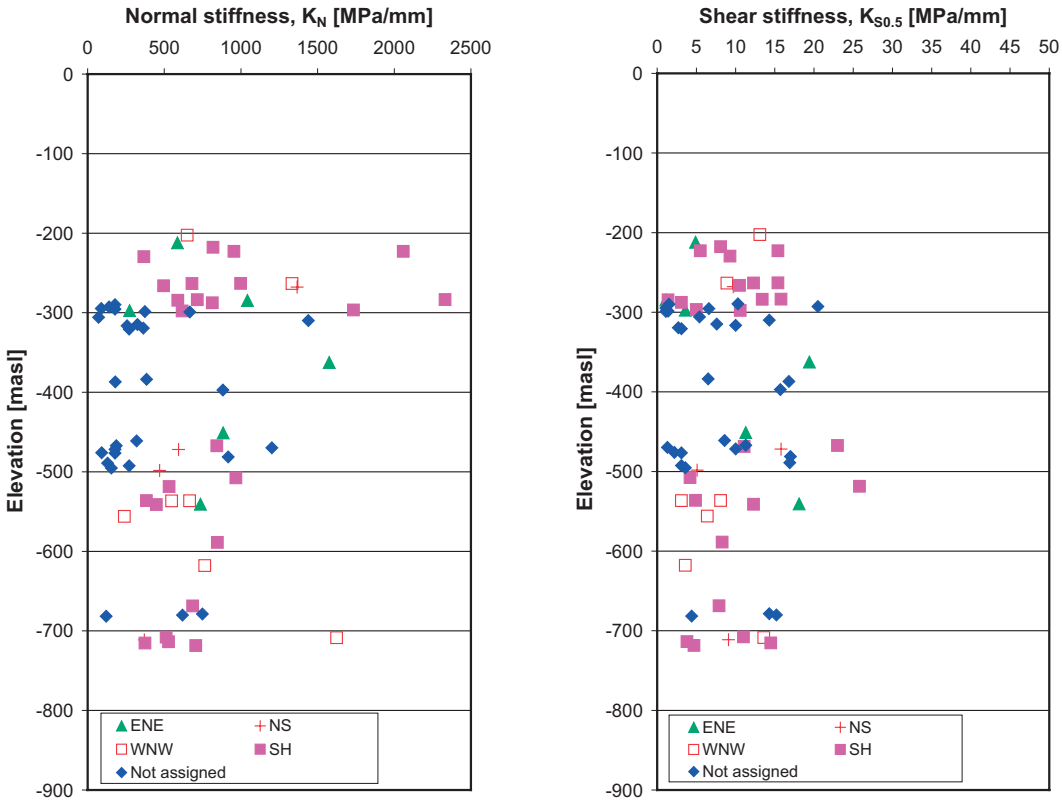

Figure 4-6. *Normal stiffness K_N and shear stiffness K_{S05} versus elevation.*

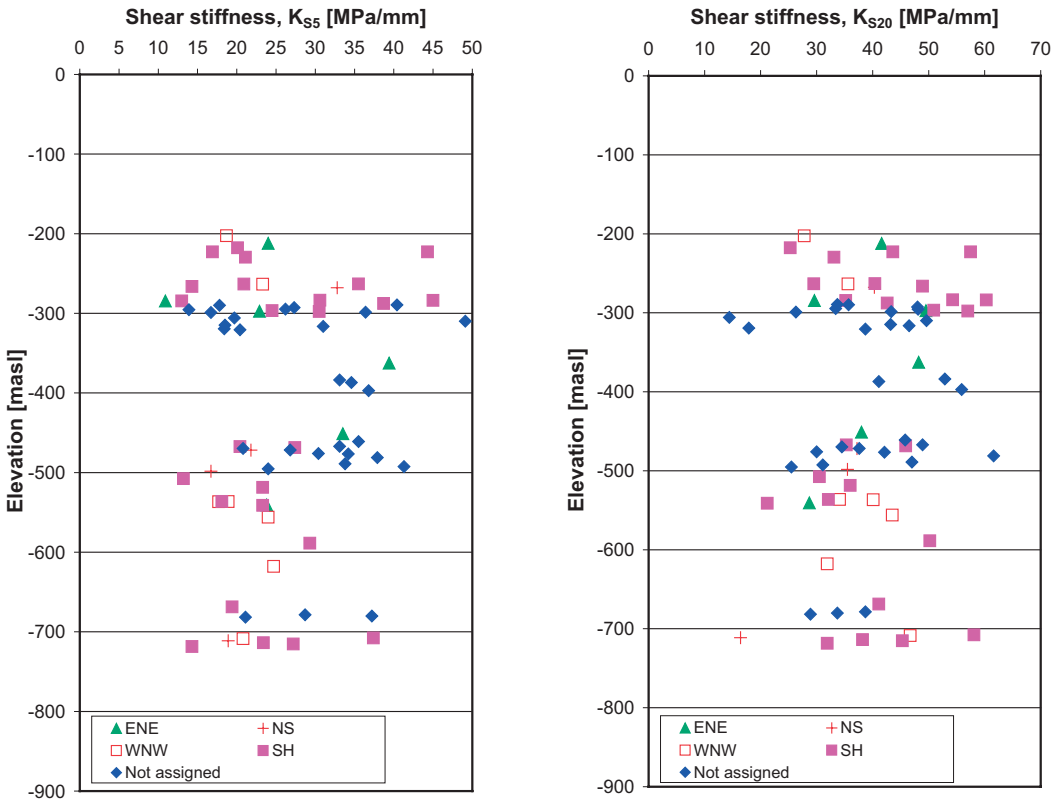

Figure 4-7. *Shear stiffness K_{S5} and shear stiffness K_{S20} versus elevation.*

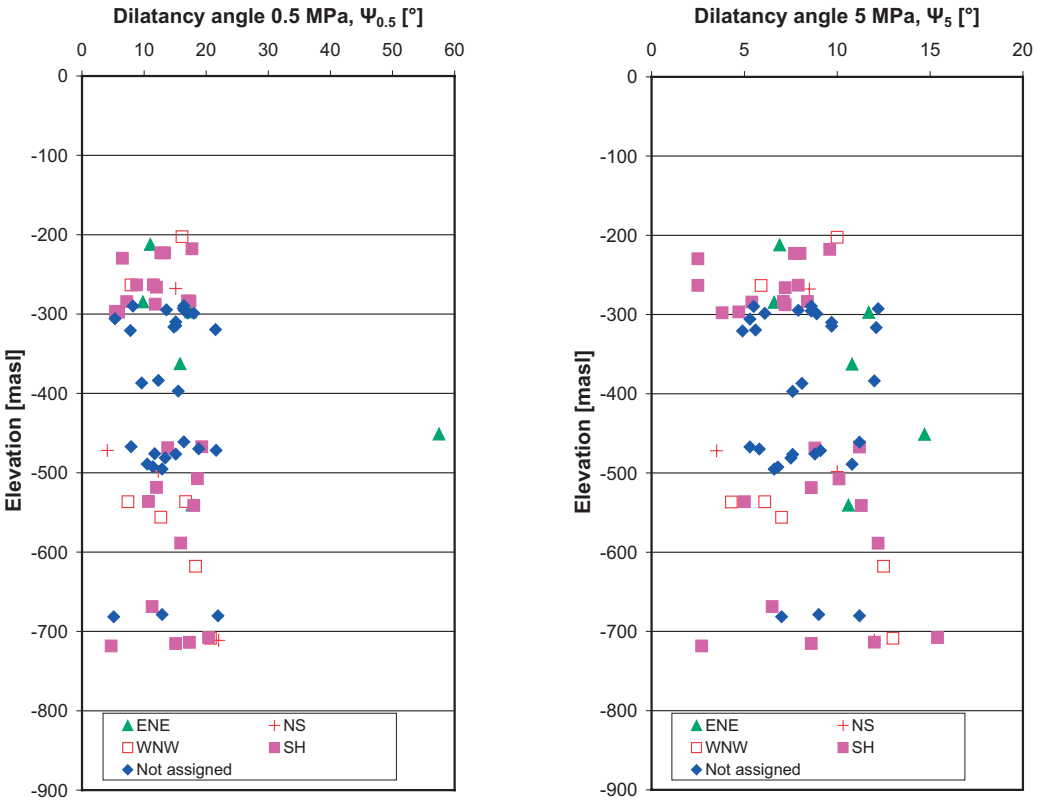

Figure 4-8. *Dilatancy angle at 0.5 MPa and Dilatancy angle at 5 MPa versus elevation.*

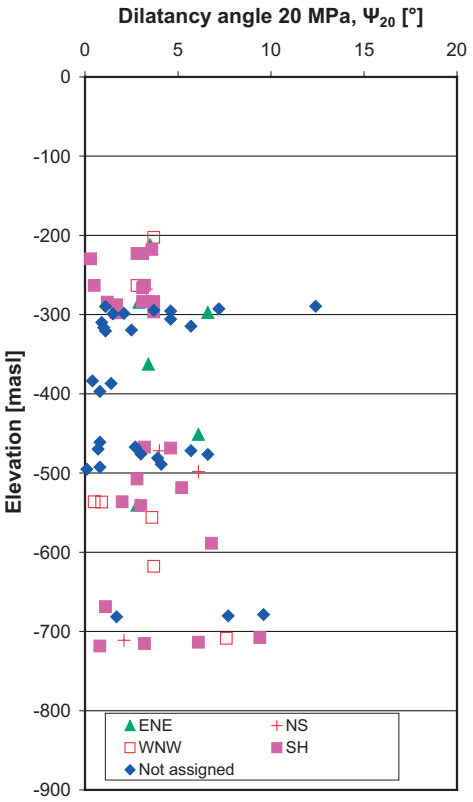

Figure 4-9. *Dilatancy angle at 20 MPa versus elevation.*

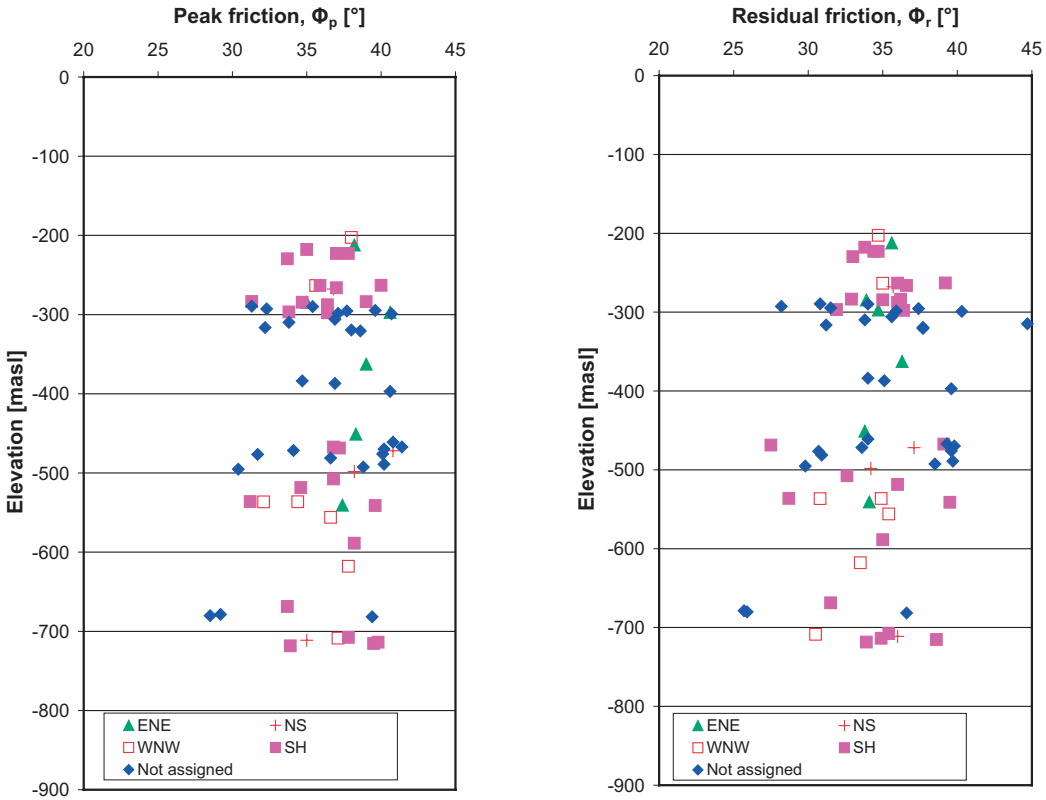

Figure 4-10. *Peak and residual friction angle versus elevation.*

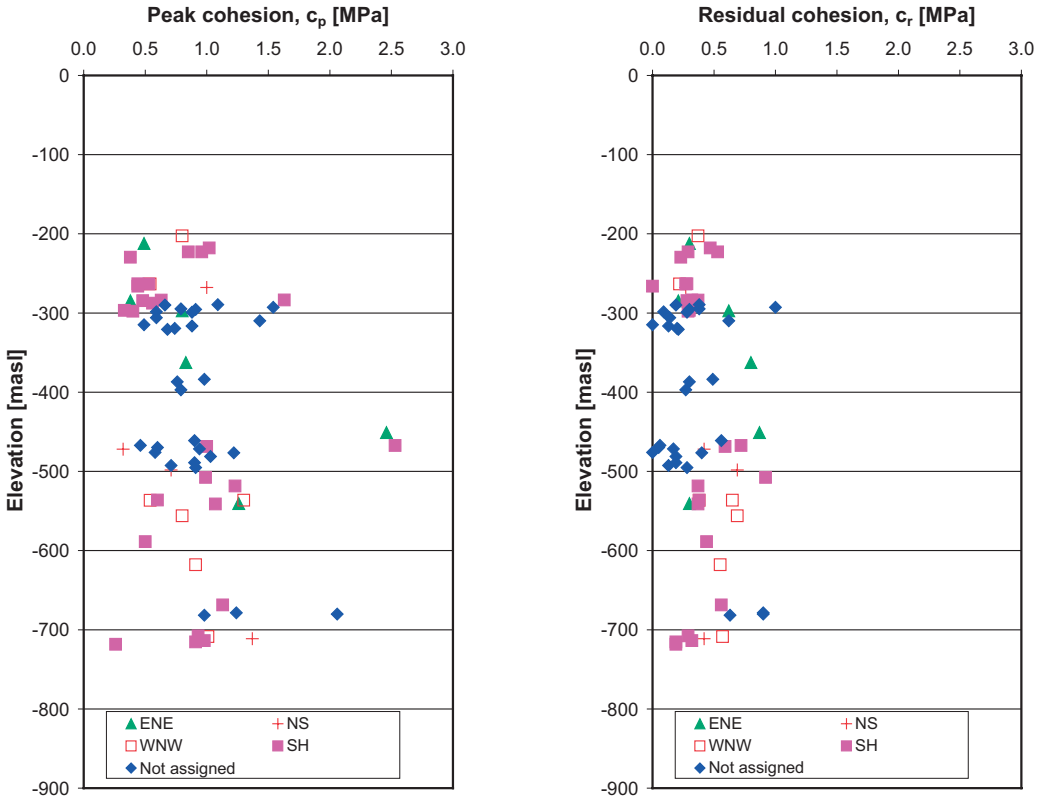

Figure 4-11. *Peak and residual cohesion versus elevation.*

Tests on sealed fractures

Shear tests on sealed fractures were performed on three sealed fractures from borehole KLX07A and eleven from KLX13A. Three specimens were prepared from each fracture and tested at three different normal stress levels. The initial test was followed by three shear cycles, at the normal stress levels 0.5, 5 and 20 MPa, on the open fracture that was created after breaking the sealed joint. The results from the tested sealed fractures are shown in Figure 4-12.

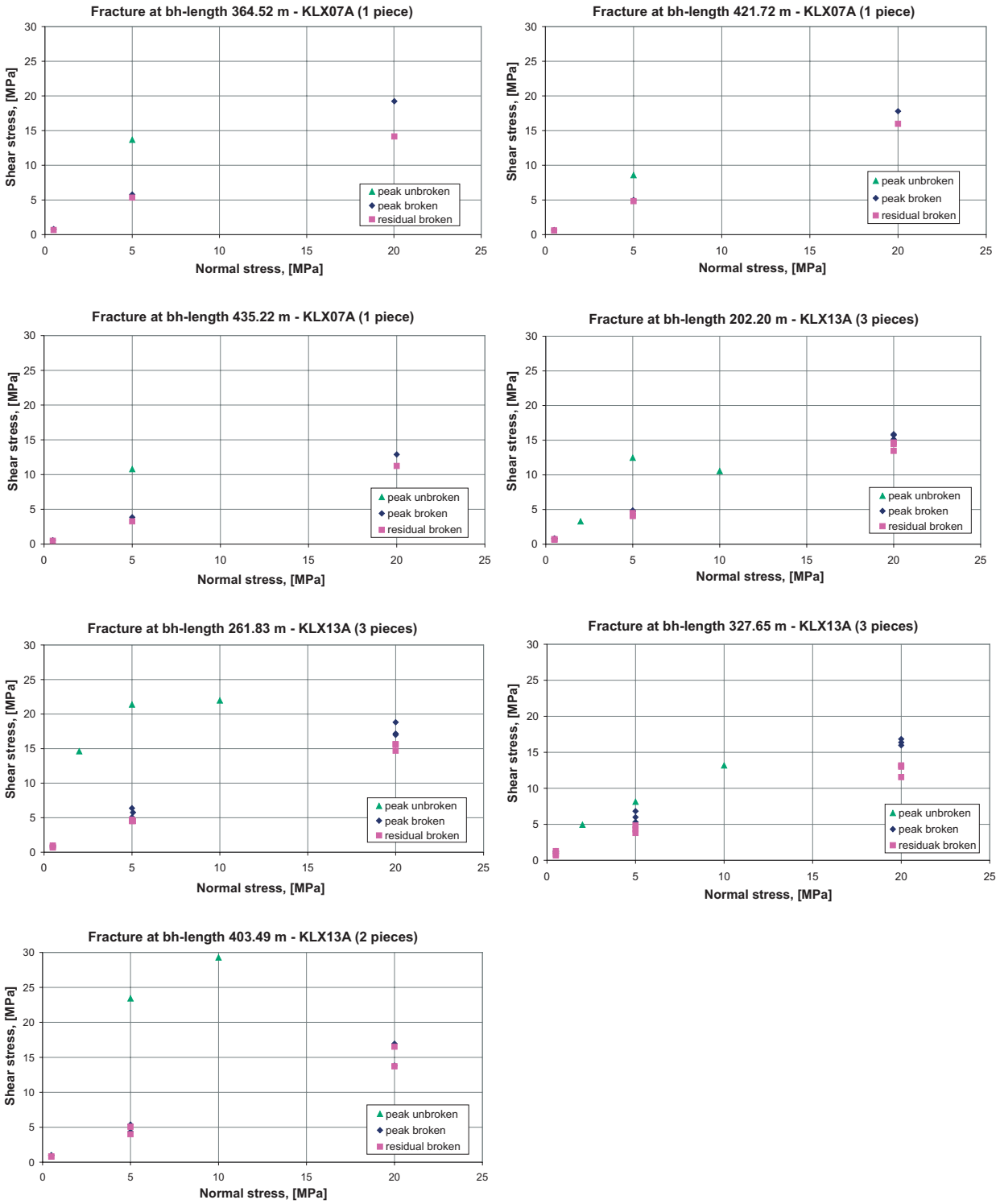

Figure 4-12. *Results from shear tests on sealed fractures. 14 successful tests from 7 different fractures sampled from KLX07A and KLX13A. For further description of the samples and tests see /Jacobsson and Flansbjer 2006a/ and /Jacobsson and Flansbjer 2006d/.*

Table 4-10. Summary of results from tests on sealed fractures (15 tests).

Test	Minimum	Mean	Median	Maximum	Standard deviation
Peak friction angle of sealed fractures (°)	37.8	42.5	42.9	46.3	4.2
Peak cohesion of sealed fractures (MPa)	2.9	6.7	4.6	14.6	5.3
Peak friction angle of broken fractures (°)	32.0	38.1	37.2	43.0	3.7
Peak cohesion of broken fractures (MPa)	0.4	0.8	0.7	1.4	0.3
Residual friction angle of broken fractures (°)	28.7	33.9	34.5	37.8	3.3
Residual cohesion of broken fractures (MPa)	0.3	0.7	0.6	1.1	0.3

The evaluated strength parameters are given in Table 4-10. The measured friction angles of the sealed fracture are lower that that of intact rock, 43° compared with 60° for intact rock. The measured cohesion is considerably lower, 7 MPa compared with 28 MPa for intact rock. The results from the shear tested after breaking the sealed fracture are similar to the results for the tests on open fractures.

4.5 Analysis of fracture property dependence on orientation

4.5.1 Statistical inference tests on fracture data

The strength and deformability data comprise several different rock mechanical parameters. These have been derived from three different laboratory test methods, which may entail systematic differences in results. The primary interest is to analyse if different fracture sets have significant differences in fracture strength and deformability. The objective is therefore to distinguish whether significant differences can be found in laboratory data, in terms of: 1) fracture sets, and 2) laboratory test methods.

In the statistical analyses the data can be grouped either by the laboratory test method used or by fracture sets. The parameters studied are the Mohr-Coulomb model parameters (c_p^{MC}, ϕ_p^{MC}, c_r^{MC}, ϕ_r^{MC}) and the Barton-Bandis model parameters (ϕ_b^{BB}, ϕ_r^{BB}, JRC_{100}, JCS_{100}). To clarify the statistical analyses, the data are referred to as x_{ij}, where x is the parameter studied, i is laboratory testing method used (Tilt and Shear) and j is its fracture set (ENE, NS, WNW and SH). The fracture sets are defined in /La Pointe et al. 2008/. The total number of samples is 270 and most of the data come from tilt tests (Table 4-11). The chance of finding significant differences in statistical tests increases with larger sample size; however, grouping data that do not belong to a homogeneous underlying population may lead to incorrect inference.

Table 4-11. Sample sizes, classified by test methods and fracture sets.

Set *j* \ Method *i*	Tilt	Shear	All methods
ENE	9	6	15
NS	17	4	21
WNW	14	7	21
SH	26	25	51
Outside assign area	133	29	162
All fractures	199	71	270

With respect to the number of data available, the following analyses are considered possible:

1) Analysing influence of laboratory tests method (for all fractures, regardless of fracture sets, i.e., comparing x_i, for all j combined)
2) Analysing differences between fracture sets (for Tilt test data alone).

The reason for excluding all shear test data in alternative (2) is that for some fracture sets only few data are available.

The full presentations of the statistical test performed and the results of the analysis are found in Appendix 2. The conclusions from the analysis are given in the following section.

4.5.2 Conclusions from statistcal inference tests on fracture data

A comparison of the results from tilt tests and shear tests shows a significant difference. For use in repository design and in the theoretical approach it is recommended to use the values from direct shear tests since they are based on direct measurements with a stress magnitude comparable to what is expected to be experienced at tentative repository depth.

The only significant difference from the tilt tests result on different fracture sets was observed for the peak and residual cohesion for the subhorizontal (SH) set. The number of data from each fracture sets are not the same and the number are few why the results from statistical tests are uncertain. It can therefore be inferred that all the fracture sets seem to have the same mechanical properties independently of the fracture set orientation. The direct shear testing results were too few to enable the comparison of properties of different fracture sets.

4.6 Mechanical properties of highly water conducting fractures

As a part of the hydrogeological modelling, sections in the boreholes with significant water inflow have been identified /Rhén et al. 2008/. These sections are identified by PFL (from the use of the Posiva Flow Log) and denoted conductive features or “PFL-f features” for short. Most of the features are single open flowing fractures (PFL-f fractures) and a fairly large part (about 45%) is attributed to a so called “crush” sections identified in the core logging, i.e. in these cases there is no individual fracture in the drill core coupled to the high inflow. The PFL-f features are located both inside interpreted deformation zones and outside. About 70% of the PFL features are found between deformation zones as defined in the ESHI.

In an attempt to analyse the mechanical properties of the water conductive fractures, that could possibly be of interest in future coupled hydro-mechanical analyses, the mechanical characteristics of PFL-f fractures identified in boreholes KLX07A–B, KLX10, KLX10B–C, KLX11A, KLX12A and were studied. It was found that the surface rougness and planarity was not different in this subgroup compared to the total population of fractures. The absolute majority of fractures are mapped as “rough” and “planar”.

Although the selection of fractures to be used for mechanical tests was not driven by hydraulic properties, a check was made whether any of the actually sampled fractures for mechanical tests were among the identified PFL-f fractures, but this was found not to be the case. It is of importance to remember that the number of PFL-fractures is much less than the total number of open fractures. For example, in borehole KLX12A the total number of mapped open fractures is 1,181 whereas 74 PFL-f fractures (out of totally 75 PFL-f features) are identified.

Although direct shear tests on highly water bearing fractures are not available from the Laxemar site investigation, such tests have been performed on a fracture at the Äspö Hard Rock Laboratory. /Mas Ivars and Norén 2006/ present results from laboratory shear-flow tests on three samples from the same highly water conducting fracture intersecting the APSE site at c. 450 m depth. These fracture surface samples are quadratic with 120 cm side length.

The normal stiffness of these samples varies from 75 to 108 MPa/mm and the shear stiffness from 1.05 to 1.52 MPa/mm (with initial normal load of 2 MPa). If this result is compared to the results in Section 4.4 it is clear that the fracture samples from the APSE site are about 10 times less stiff than the analysed non-conductive fractures in the Laxemar boreholes.

Most of the mapped fractures have an "aperture classification" in the range ≤0.5 mm /Rhén et al. 2008/ and this is also the case for all the mechanically tested fractures. The PFL-f fractures have a variation in mapped aperture (from the BIPS imaging); most have aperture classification ≤0.5 mm, but there is a correlation between the occurrence of larger apertures (i.e. >0.5 mm) and the occurrence of a PFL-f fracture (i.e. in many cases, not all, a larger aperture fracture is also identified as a PFL-f fracture).

However, even without direct evidence from the site data, it is reasonable to assume that the PFL-f fractures, on average, have a different aperture distribution than the "ordinary" (very frequent) fractures mapped as being open or partly open. This is reasonable since we know the flow is directly, and strongly, determined by the aperture distribution. Accepting this concept of a different aperture distribution for PFL-f fractures, it follows that the contact area distribution and the mean aperture should be different for PFL-f fractures.

The more complex PFL-f features associated with crush zones, are impossible to test mechanically, but there is no reason to believe that these features are stiffer or stronger than single fractures (if this single fracture has a small aperture), rather the opposite.

It is worth noting here that the Hydro-DFN model includes fractures of all sizes; from the typical borehole diameter to 1,000 m /Rhén et al. 2008/. Different models for size-transmissivity dependence are discussed in the latter report but the recommended model is where transmissivity is correlated to the fracture size. This idea is also supported by the "mechanical argument" that only fractures above a certain size can obtain, in their central parts, the shear displacement required to create large dilation (shear displacements in the order of cm, not mm or less).

The conclusion from the above arguments is that there are reasons to assume that the results presented in Sections 4.3 and 4.4, from tests on fracture samples of small apertures (well mated) should not be used to describe the expected mechanical properties for highly water conducting fractures.

Therefore, although there is a lack of data and an obvious uncertainty in the quantification, it is recommended that when mechanical properties for highly water conductive fractures are required, the stiffness values given for non-PFL fractures (Table 4-12 in Section 4.6) are reduced by a factor 10–100, and that sensitivity studies are performed. The friction and cohesion are also expected to be slightly lower compared to values given in Table 4-14 while the dilatancy angle may be of the same order as in Table 4-13.

4.7 Models for the mechanical properties of fractures and associated uncertaintes

Specifications of the uncertainties in the used laboratory methods are found in SKB's Method Descriptions and the underlying P-reports that present the laboratory results. Here, the uncertainty in the mechanical properties of fractures is expressed by means of a span for the expected mean values of the distribution. The uncertainty of the mean was quantified according to the "Central Limit Theorem" /Peebles 1993/ for a 95% confidence interval, based on observed test results. Minimum and maximum truncation values given in the tables below are based on the observed minimum and maximum for the tested populations.

It should be noted that the large-scale mechanical properties of fractures are expected to deviate from the results reported here on small specimens of 50–60 mm in size. Due to reduction in the effective roughness of the surface, JRC, most likely the shear strength of the large-scale fractures will be reduced as compared to the results from the tested samples /Bandis 1980/.

Due to the greater possibility of weakness in a large surface, it is also likely that the mean joint wall compressive strength, JCS, decreases with increasing scale /Barton and Bandis 1982/. There is also a possibility that the large-scale fractures will show differences between the fracture sets, although the differences in the small scale were found insignificant.

The fracture properties given in Table 4-12, Table 4-13 and Table 4-14 are recommended to be used in the design and safety assessment. These properties are expected to represent the properties of the majority of open single fractures. They are, however, not representing properties of the sealed fractures. The model may also not be considered to represent well the properties of the few highly conductive fractures at the site, which were not part of the tested population (see previous Section 4.6). Therefore the user should consider these limitations in the application of the models.

Table 4-12. Model for stiffness properties for single open fractures[1)] in all fracture domains.

	Normal stiffness K_N (MPa/mm)	**Shear stiffness $K_{S0.5}$ (MPa/mm)**	**Shear stiffness $K_{S5.0}$ (MPa/mm)**	**Shear stiffness $K_{S20.0}$ (MPa/mm)**
	Mean/std. dev. Min–max *Uncertainty of mean*	Mean/std. dev. Min–max *Uncertainty of mean*	Mean/std. dev. Min–max *Uncertainty of mean*	Mean/std. dev. Min–max *Uncertainty of mean*
All fracture domains	721/655 72–4,003 ±11%	9/6 1–26 ±15%	26/9 11–49 ±8%	39/10 14–62 ±6%

1) See text concerning limitations.

Table 4-13. Model for dilatancy in single open fractures[1)] in all fracture domains.

	Dilatancy angle $\psi_{0.5}$ (°)	**Dilatancy angle ψ_5 (°)**	**Dilatancy angle ψ_{20} (°)**
	Mean/std. dev. Min–max *Uncertainty of mean*	Mean/std. dev. Min–max *Uncertainty of mean*	Mean/std. dev. Min–max *Uncertainty of mean*
All fracture domains	14.2/7.0 4.1–57.5 ±11%	8.3/2.9 2.5–15.4 ±8%	3.3/2.5 0.1–12.4 ±17%

1) See text concerning limitations.

Table 4-14. Model for friction and cohesion in single open fractures[1)] in all fracture domains.

	Peak friction angle ϕ_p (°)	**Peak cohesion c_p, (MPa)**	**Residual friction angle ϕ_r (°)**	**Residual cohesion c_r (MPa)**
	Mean/std. dev. Min–max *Uncertainty of mean*	Mean/std. dev. Min–max *Uncertainty of mean*	Mean/std. dev. Min–max *Uncertainty of mean*	Mean/std. dev. Min–max *Uncertainty of mean*
All fracture domains	36.6/3.2 28.5–45.4 ±2%	0.9/0.4 0.3–2.5 ±11%	34.7/3.5 25.7–44.7 ±2%	0.4/0.2 0.0–1.0 ±14%

1) See text concerning limitations.

5 Rock mass mechanical properties

In this chapter the rock mass strength and deformation properties are estimated. The rock mass quality is used in the design of a repository to estimate the risk for stability problems and for the assessment of rock support requirements, cf. Section 1.3.

Two modelling approaches are utilised to estimate the rock mass properties, the empirical and the theoretical approach /Andersson et al. 2002/. The empirical approach estimates the rock mass mechanical properties based on classification systems and empirical relation (Section 5.1), while the theoretical approach (Section 5.2) estimates the properties of the rock mass by using numerical models. The final estimate of the rock mass properties is achieved by weighting the results from the two model approaches together, a process termed "harmonisation" (Section 5.3). The modelling of the mechanical properties of deterministic and minor deformation zones (DZ and MDZ) is presented in Section 5.4.

5.1 Empirical approach using classification systems

This section summarises the results of the rock mechanics characterisation of the rock mass along five boreholes (KLX02, KLX03, KLX04, KLX05 and KLX12A) by means of empirical methods. The detailed results from the characterisation of KLX05 and KLX12A are found in Appendix 3. Based on the correlations between the Rock Quality Designation (RQD) and the rock mass quality in terms of Q and RMR ratings, strength and deformability of the rock mass determined based on these five boreholes, the rock mass quality along borehole KLX10, KLX11A, KLX15A and KLX19A was also estimated.

The empirical characterisation was performed for borehole sections of 5 metres according to the Q and RMR systems. The methodology for the empirical characterisation is presented in the strategy document for rock mechanics modelling /Andersson et al. 2002, Röshoff et al. 2002/.

The well established formulae for the Rock Mass Rating (RMR) /Bienawski 1989/ and Rock Quality Index (Q) /Barton 2002/ are reported here for the convenience of the reader. The basic equation for the RMR is:

$$RMR = RMR_{strength} + RMR_{RQD} + RMR_{spacing} + RMR_{conditions} + \\ + RMR_{water} + RMR_{orientation}$$ *Equation 5-1*

where the subscripts refer to the strength of the intact rock; Rock Quality Designation; conditions and spacing of the fractures; groundwater conditions and the orientation of the fracture sets with respect to a hypothetical tunnel orientation.

The basic equation for Q is:

$$Q = \frac{RQD}{J_n} \times \frac{J_r}{J_a} \times \frac{J_w}{SRF}$$ *Equation 5-2*

where, J_n depends on the number of fracture sets; J_r and J_a on the roughness and alteration of the fractures; J_w on the groundwater conditions and a Stress Reduction Factor (SRF) that takes into account the stresses in the rock mass. The classification systems have been applied for obtaining the ratings independently on the water pressure (J_w = 1, RMR_{water} = 15) and possible orientation of the excavation ($RMR_{orientation}$ = 0) /Anderssson et al. 2002/. The effect of the stress state has been taken into account by assigning SRF =1 for rock mass outside deformation zones and SRF = 2.5 in deformation zones with markedly reduced RQD values.

The mechanical properties of the rock mass were estimated from the characterisation of the rock mass quality. In particular, focus was given to:

- The deformation modulus (E_m) and Poisson's ratio (ν_m) of the rock mass calculated by means of RMR.
- The equivalent uniaxial compressive strength and tensile strength of the rock mass determined by means of RMR, through GSI, and the Hoek-Brown's Failure Criterion.
- The friction angle (ϕ_m), cohesion (c_m) and apparent uniaxial compressive strength of the rock mass according to the Coulomb's Criterion also determined by means of RMR, through GSI, and the Hoek-Brown's Failure Criterion.

The empirical characterisation of the rock mass does not consider sealed or partly open fractures. Empirical methods are designed based on the occurrence of open fractures, which are the weakest component of the rock mass. However, since natural rocks often contain a mixture of open and sealed or partly open fractures, this does not mean that the empirical methods ignore their presence. In fact, the empirical methods are build on databases of real case histories where sealed or partly open fractures are present. Therefore, such fractures are implicitly considered, even if they are not directly analysed.

5.1.1 Estimation of Q and RMR based on RQD

The characterisation of borehole KLX02, KLX03, KLX04, KLX05 and KLX12A, was performed according to the Q and RMR systems. However, there are several boreholes at the site where the rock mass characterisation has not been performed. By exploiting the available geological information in previous boreholes, a correlation between the values of Q and RMR and RQD (Rock Quality Designation) has been established for borehole KLX10, KLX11A, KLX15A and KLX19A. These correlations are determined separately for each rock domain intercepted by the boreholes (RSMA01, RSMD01 and RSMM01). For example, for rock domain RSMA01, some correlations are shown in Figure 5-1. Similar correlations were obtained for each rock domain and rock mass mechanical parameter (uniaxial compressive strength, cohesion, friction angle, deformation modulus and Poisson's ratio) to take into account the particular rock types, fracture conditions and possible deformation zones. Thus, an equivalent set of parameters as for the boreholes characterised according to the Q and RMR systems was obtained.

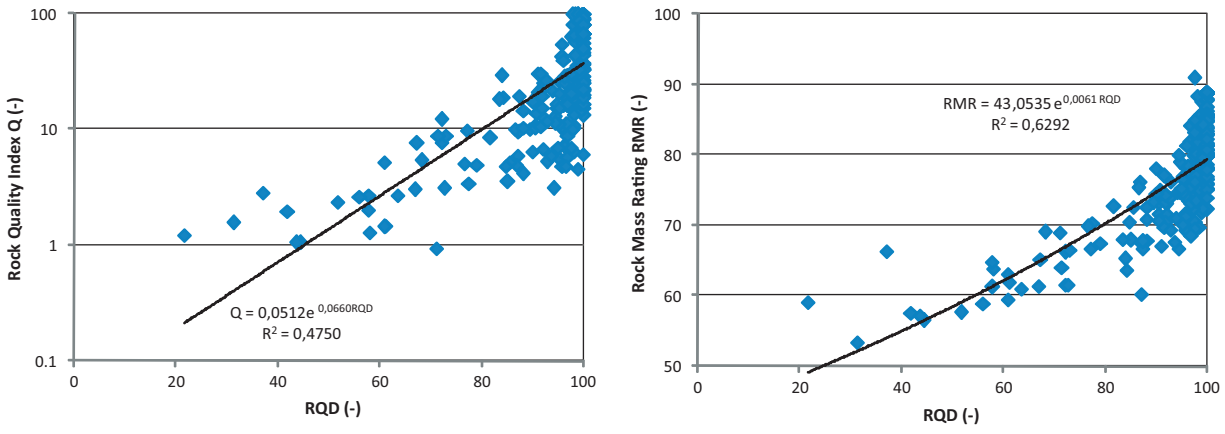

Figure 5-1. *Correlations between the values of the rock mass quality ratings and RQD: a) for the Rock Quality Index Q and; b) for the Rock Mass Rating RMR. The fitting of the data by means of exponential curves is also shown.*

All data, resulting from the characterisation and from the estimation, were then subdivided according to the fracture domains (FSM_C, FSM_W, FSM_N, FSM_EW007 and FSM_NE005) and deterministic and minor deformation zones, DZ and MDZ. Statistics of the rock mass quality ratings and mechanical properties can be calculated and are shown in Table 5-1 and Table 5-13.

5.1.2 Strength and deformation properties for the fracture domains

Six fracture domains were recognised at the site (see Figure 2-10). The rock mass property values were determined or estimated for five of them due to the availability of the data: FSM_C, FSM_W, FSM_N, FSM_EW007 and FSM_NE005 as reported in Table 5-1. It can be observed that these fracture domains can be divided into two groups, based on the values of the mechanical properties, FSM_C can be grouped with FSM_W and FSM_NE005, and FSM_N can be grouped with FSM_EW007, respectively. The statistics of the quality and mechanical properties of the rock mass in these two groups of fracture domains are summarised in Table 5-2 for the rock mass outside the deformation zones (all DZ found in ESHI).

Table 5-1. Estimated mechanical properties of the rock mass outside the deterministic deformation zones and MDZ in the fracture domains based on the empirical characterisation of the rock mass.

Fracture domain [1]	**FSM_C**	**FSM_W**	**FSM_N**	**FSM_EW007**	**FSM_NE005**
Properties of the rock mass	Mean/std. dev. Min–max	Mean/std. dev. Min–max	Mean/std. dev. Min–max	Mean/std. dev. Min–max	Mean/std. dev. Min–max
Q [2]	53.5 6.9–704	87.0 11.4–87.0	17.6 3.4–150	29.7 0.9–528	46.0 3.5–264.0
RMR	82.0/3.6 68.9–90.9	83.2/1.8 70.5–83.8	77.0/5.5 66.2–87.9	77.7/5.1 63.0–88.7	79.9/6.8 60.2–90.0
Deformation modulus [GPa]	62.3/10.1 29.6–78.0	64.6/4.3 33.8–66.1	49.3/15.3 25.4–78.0	50.5/13.1 21.1–78.0	55.4/16.3 18.0–80.0
Poisson's ratio [–]	0.20/0.04 0.08–0.27	0.23/0.02 0.12–0.24	0.13/0.04 0.07–0.21	0.15/0.04 0.06–0.24	0.21/0.06 0.06–0.33
Uniaxial compressive strength (Hoek-Brown) [MPa]	53.4/10.8 25.8–88.6	56.5/4.4 28.5–58.1	42.8/13.4 22.5–75.0	40.4/12.1 18.9–76.8	52.2/22.3 13.4–124.3
Tensile strength (Hoek-Brown) [MPa]	1.6/0.5 0.7–3.6	1.6/0.2 0.6–1.6	1.4/0.6 0.6–2.9	1.1/0.6 0.3–2.8	1.5/0.8 0.2–3.2
Friction angle [3] [°]	44.3/1.2 40.0–47.7	45.1/0.4 42.2–45.2	41.8/1.4 39.0–44.1	43.7/2.0 37.9–47.9	44.0/3.0 34.9–52.0
Cohesion [3] [MPa]	20.4/1.5 15.7–25.3	21.0/0.6 16.7–21.2	18.4/2.2 15.0–23.8	18.8/1.8 14.3–23.6	20.1/3.5 12.8–30.8
Uniaxial compressive strength (Mohr-Coulomb) [MPa]	97.4/9.7 67.5–122.6	101.6/3.9 75.2–103.0	82.9/12.3 63.1–112.3	88.3/12.1 58.3–116.9	96.5/24.1 49.0–178.8

1) The rock mass properties of the domains do not include the effects of DZ and MDZ. DZ and MDZ properties are described separately see Section 5.4.1.
2) For Q, the most frequent value is reported instead of the average.
3) For confinement stress between 10 and 30 MPa.

Table 5-2. Estimated mechanical properties of the rock mass outside the deterministic deformation zones and MDZ in two groups of fracture domains based on the empirical characterisation of the rock mass.

Fracture domains [1]	FSM_C FSM_W FSM_NE005	FSM_N FSM_EW007
Properties of the rock mass	Mean/std. dev. Min–max	Mean/std. dev. Min–max
Q [2]	66.0 3.5–704	26.3 0.9–528
RMR	81.7/4.6 60.2–90.9	77.6/5.1 63.0–88.7
Deformation modulus [GPa]	61.0/11.8 18.0–80.0	50.3/13.6 21.1–78.0
Poisson's ratio [–]	0.21/0.04 0.06–0.33	0.15/0.04 0.06–0.24
Uniaxial compressive strength (Hoek-Brown) [MPa]	53.9/14.2 13.4–124.3	40.8/12.4 18.9–76.8
Tensile strength (Hoek-Brown) [MPa]	1.6/0.6 0.2–3.6	1.1/0.6 0.3–2.9
Friction angle [3] [°]	44.4/1.9 34.9–52.0	43.3/2.0 37.9–47.9
Cohesion [3] [MPa]	20.5/2.2 12.8–30.8	18.7/1.9 14.3–23.8

1) The rock mass properties of the domains do not include the effects of DZ and MDZ. DZ and MDZ properties are described separately see Section 5.4.1.
2) For Q, the most frequent value is reported instead of the average.
3) For confinement stress between 10 and 30 MPa.

5.1.3 Uncertainties

For quantifying the uncertainty on the parameters of the rock mass, the correlations established in Section 5.1.1 were also applied to the boreholes where characterisation results directly obtained by means of Q and RMR were available. In this way, two sets of values of Q and RMR could be determined for each borehole interval of 5 metres. The difference between the two sets of values can be used to estimate the uncertainty of the mean value of the rock quality and related mechanical properties.

Thus, for each fracture domain, the difference between the values obtained from the characterisation and those estimated by means of the correlations are assumed to constitute a statistical population which standard deviation can be determined. Considering that between 38 and 188 values are available for each fracture domain, the 95% confidence interval of the mean value of each parameter can be calculated as in Table 5-3. For the groups of fracture domains the total number of available values increases to 639. The larger size of the sets of values contributes to larger standard deviations. This is the reason why the uncertainties presented in Table 5-3 and Table 5-4 do not differ much. For fracture domain FSM_W, the Q and RMR quantification based on the empirical characterisation is not available. The uncertainty in this domain is therefore larger but remains not quantified.

Table 5-3. Evaluation of the uncertainties of the mean values of the mechanical properties of the rock mass outside the deterministic deformation zones and MDZ in the fracture domains based on the empirical characterisation of the rock mass.

Fracture domain [1]	**FSM_C** [4]	**FSM_N** [5]	**FSM_EW007** [6]	**FSM_NE005** [7]
Property of the rock mass	Confidence interval of the mean value [2]	Confidence interval of the mean value [2]	Confidence interval of the mean value [2]	Confidence interval of the mean value [2]
Q	±31.5%	±48%	±42%	±22%
RMR	±0.5%	±2%	±1%	±1%
Deformation modulus [GPa]	±2%	±8%	±4%	±2.5%
Poisson's ratio [–]	±2%	±8%	±4%	±2.5%
Uniaxial compressive strength (Hoek-Brown) [MPa]	±3%	±8%	±5%	±4%
Tensile strength (Hoek-Brown) [MPa]	±5%	±14%	±9%	±5%
Friction angle [3] [°]	±0.5%	±1%	±7%	±0.5%
Cohesion [3] [MPa]	±1%	±3%	±10%	±1.5%

1) The rock mass properties of the domains do not include the effects of DZ and MDZ. DZ and MDZ properties are described separately see Section 5.4.1.
2) 95% confidence interval of the mean value (see Section 5.1.3)
3) For confinement stress between 10 and 30 MPa.
4) Uncertainty based on the empirical characterisation results of borehole KLX03 and KLX04.
5) Uncertainty based on the empirical characterisation results of borehole KLX04.
6) Uncertainty based on the empirical characterisation results of borehole KLX02, KLX04 and KLX10.
7) Uncertainty based on the empirical characterisation results of borehole KLX02, KLX05 and KLX12A.

Table 5-4. Evaluation of the uncertainties of the mean values of the mechanical properties of the rock mass outside the deformation zones in two groups of fracture domains based on the empirical characterisation of the rock mass.

Fracture domains [1]	**FSM_C FSM_W FSM_NE005**	**FSM_N FSM_EW007**
Property of the rock mass	Confidence interval of the mean value [2]	Confidence interval of the mean value [2]
Q	±18%	±38.5%
RMR	±0.5%	±1%
Deformation modulus [GPa]	±2%	±3.5%
Poisson's ratio [–]	±2%	±3.5%
Uniaxial compressive strength (Hoek-Brown) [MPa]	±3%	±4%
Tensile strength (Hoek-Brown) [MPa]	±3.5%	±7.5%
Friction angle [3] [°]	±0.5%	±0.5%
Cohesion [3] [MPa]	±1%	±1.5%

1) The rock mass properties of the domains do not include the effects of DZ and MDZ. DZ and MDZ properties are described separately see Section 5.4.1.
2) 95% confidence interval of the mean value (see Section 5.1.3)
3) For confinement stress between 10 and 30 MPa.

5.2 Theoretical approach using numerical models

This section summarises the results of the rock mechanics characterisation of the rock mass made using the approach of numerical simulations. The methodology has been developed for the purpose of site descriptive modelling and is built upon three different models: 1) the geological DFN model /La Pointe et al. 2008/ which is used to simulate the fracture network in the rock mass (see Section 2.1.5); 2) a discrete element numerical model, using the 3DEC software /Itasca 2008/, used to calculate the rock mass mechanical properties and 3) a statistical model for estimation of combined variability caused both from the variability in the fracture geometry and the variability in fracture properties /Olofsson and Fredriksson 2005/.

5.2.1 Assessment of mechanical properties for the fracture domains

Thin slabs (10×10×1 m) of fractured rock are numerically loaded to failure in one direction to failure while the boundaries in the perpendicular directions are held fixed. Ten geometrically different models, i.e. with different fracture patterns, were simulated for each calculation case. Different levels of confinement stress enabled the determination of the friction angle and cohesion of the rock mass.

The input to the DFN simulations is taken from /La Pointe et al. 2008/. An alternative model referred to as BMU, with unlinked traces and Euclidean scaling, has also been used. The input parameters for the DFN simulations in the fracture domains are shown in Table 5-5 to Table 5-7. Only open and partly open fractures are generated. In each fracture domain, which has different DFN models, 10 simulations of the fracture network have been generated in a 20×20×20 m block.

Table 5-5. DFN – Fracture set orientation, for all fracture domains.

Fracture set	Trend	Plunge	Fisher K
ENE	337	0.5	13.6
NS	269.8	1.6	9.6
WNW	26.2	2.3	10.1
SH	344.8	87.3	8.3

Table 5-6. DFN – Intensity of the open fractures, P_{32}.

Fracture set	FSM_C	FSM_EW007	FSM_NE005	FSM_W
ENE	0.539	0.666	0.459	0.379
NS	0.471	0.864	0.809	0.808
WNW	0.767	1.164	0.622	0.543
SH	0.484	1.093	0.898	0.865
Total	2.261	3.787	2.789	2.594

Table 5-7. DFN – Intensity of the open fractures, P_{32}.

Fracture set	FSM_C		FSM_EW007		FSM_NE005		FSM_W	
	r_{min}	exp. b	r_{min}	exp. b	r_{min}	exp. b	r_{min}	exp. b
ENE	1.191	4.0	0.972	4.0	1.392	4.0	1.694	4.0
NS	2.087	4.26	1.29	4.26	1.359	4.26	1.361	4.26
WNW	0.367	3.8	0.218	3.8	0.476	3.8	0.564	3.8
SH	1.228	4.31	0.659	4.31	0.765	4.31	0.788	4.31

For each DFN realisation, the average value of P_{10} (number of intersecting fracture per unit length) has been calculated along nine vertical lines evenly distributed in the model box. In Figure 5-2 the variation of P_{10} in the DFN simulations (variations along nine lines in each realisation) is shown for the different fracture domains. Notable is that the P_{10} in fracture domain FSM_EW007 from the DFN-model is about double than in P_{10} in FSM_C.

From each block, two vertical thin slices, parallel to the direction of the major and the minor principal stresses in the horizontal plane are extracted. The fracture traces in these slices are converted into fractures in the 3DEC model. An example of fracture traces is shown in Figure 5-3. The 3DEC model is loaded vertically under plane strain conditions. Examples of deformed model and stresses in the 3DEC model are shown in Figure 5-4 and Figure 5-5. The stresses and strains during loading are recorded, are shown for one example in Figure 5-6. From these curves the deformation modulus, Poisson's ratio and failure load are evaluated assuming that the rock mass is a linear-elastic isotropic and perfectly-plastic material.

Each model has been tested at three different horizontal stress levels to enable the study of stress dependence. One case with the horizontal stress parallel to the model (confining stress) equal to the approximate maximum horizontal stress at repository level (25.8 MPa and 10.5 MPa, depending on the model orientation, based on stress model for Laxemar version 1.2), one case with horizontal stress parallel to the model equal to 25% of this stress level and the last case with a horizontal stress equal to 2 MPa. The material properties used for the intact rock and fractures are shown in Table 5-8. Note that all fractures, irrespective of size, are given the same properties. This means that any potential effect of MDZ is not included in the simulations. The larger fracture sizes can not be included because of the scale of the numerical models.

The results show that the variation of the evaluated deformation modulus with confining stress is small, see Figure 5-7. The cohesion and friction angle has been evaluated by fitting a linear envelope to the results from these three tests, see Figure 5-8.

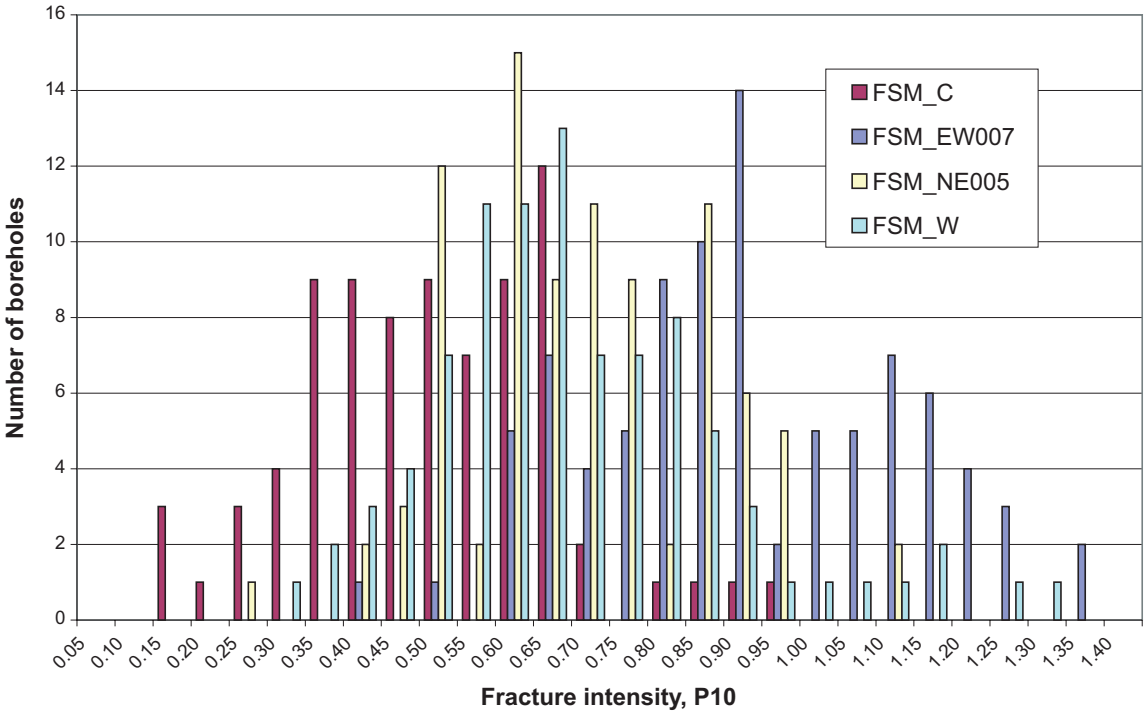

Figure 5-2. *Variation of P_{10} in different fracture domains from sampling of DFN simulations.*

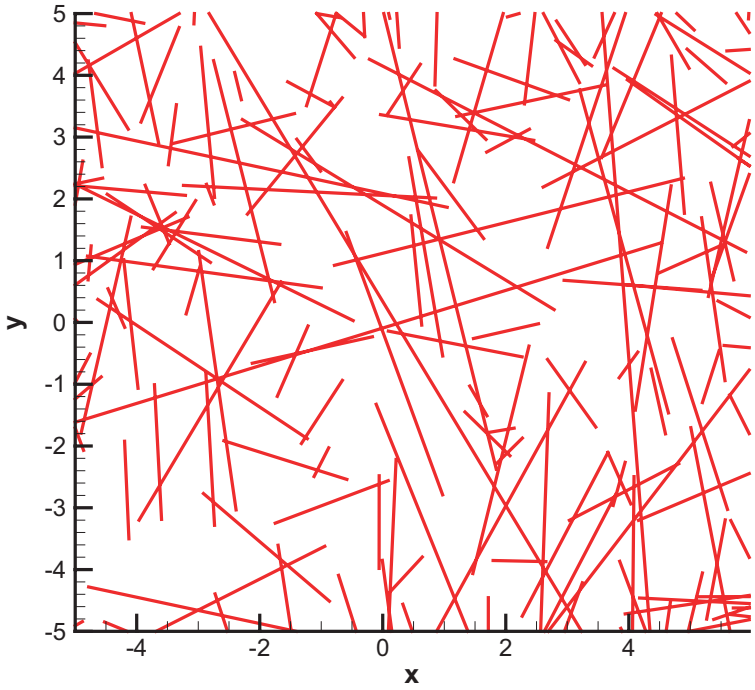

Figure 5-3. *An example of fracture traces. The fracture network is created from a realization of the DFN model for open fractures. (Block size 10×10 m.)*

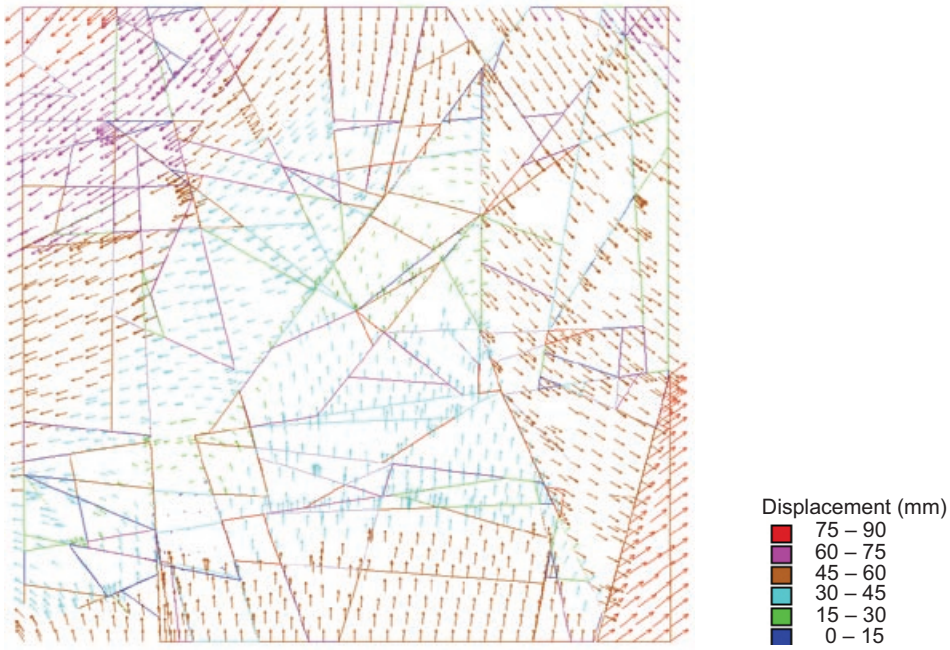

Figure 5-4. *An example of deformed model with 25.8 MPa horizontal confinement. Vectors show displacements, coloured by magnitude. (Block size 10×10 m.)*

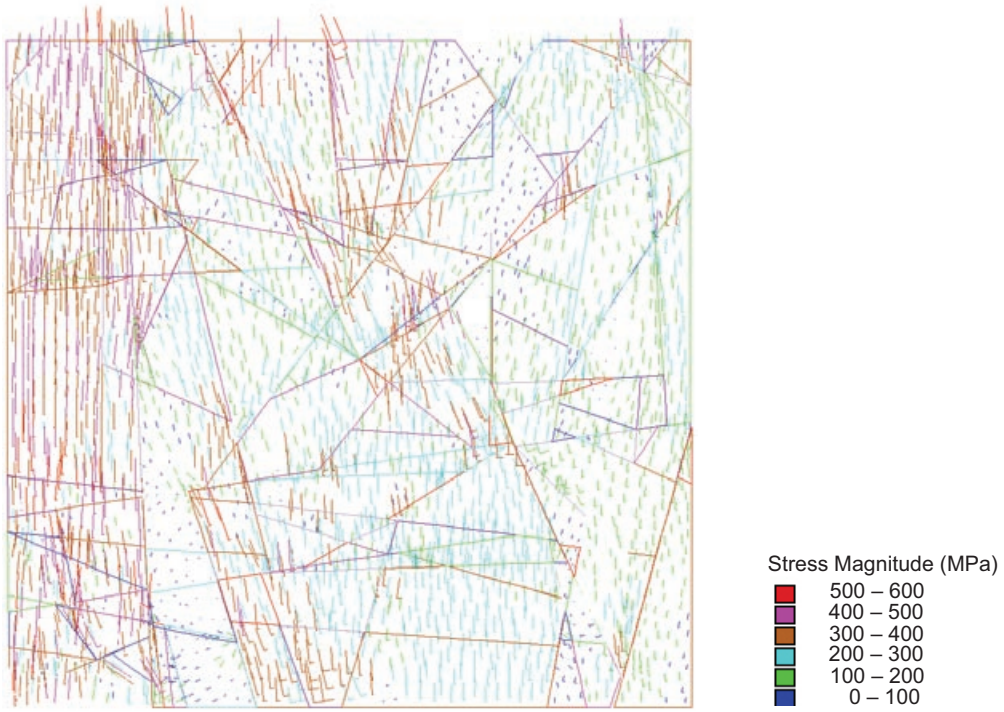

Figure 5-5. *An example of stresses in the model, with 25.8 MPa horizontal confinement, at failure. Symbols show principal stresses coloured by maximum compressive stress magnitude. (Block size 10×10 m.)*

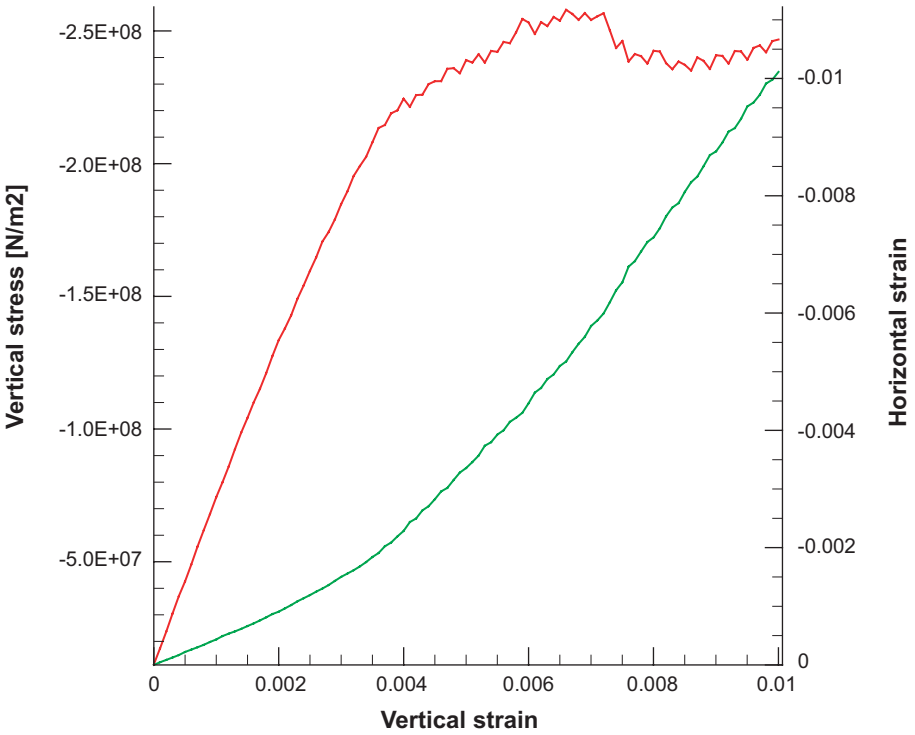

Figure 5-6. *An example of stress – strain curve. From the example model in Figure 5-4 and Figure 5-5.*

Table 5-8. Mean material properties used as model input (cf. Table 3-9 and Table 4-8).

Property	Ävrö quartz monzodiorite	Diorite to Gabbro	Quartz monzodiorite	Ävrö granodiorite
Intact rock				
Young´s modulus (GPa)	72.0	80.0	75.0	73.0
Poisson´s ratio	0.27	0.33	0.28	0.24
Cohesion (MPa)	24.0	30.3	26.0	24.0
Friction angle (°)	55	60	56	60.0
Tensile strength (MPa)	13.0	16.0	17.0	13.0
Fracture				
Normal stiffness (MPa/mm)	721.0	721.0	721.0	721.0
Shear stiffness (MPa/mm)	39.0	39.0	39.0	39.0
Cohesion (MPa)	0.9	0.9	0.9	0.9
Friction angle (°)	36.6	36.6	36.6	36.6
Dilatancy (°)	3.4	3.4	3.4	3.4

The different DFN simulations were performed by using mean values of all material data. The resulting variation of the evaluated parameters is only affected by the variation of the geometry of the fracture network of each model. Figure 5-9 shows the deformation modulus calculated assuming the DFN model for fracture domain FSM_C and assuming intact rock properties corresponding to different rock type in nine runs each. The resulting deformation modulus varies between 45 and 71 GPa.

Table 5-9 and Table 5-10 summarise all the evaluated parameters for the fracture domains. For FSM_C and FSM_W, where simulations have been done using different rock type materials, the results for each rock type are first presented separately, and then the results of the summed simulations are presented in column “Combined”. The deformation modulus and Poisson’s ratio are evaluated for a confining stress of 25.8 MPa. The results from each realisation, i.e. each run of the numerical model, are presented in Appendix 4.

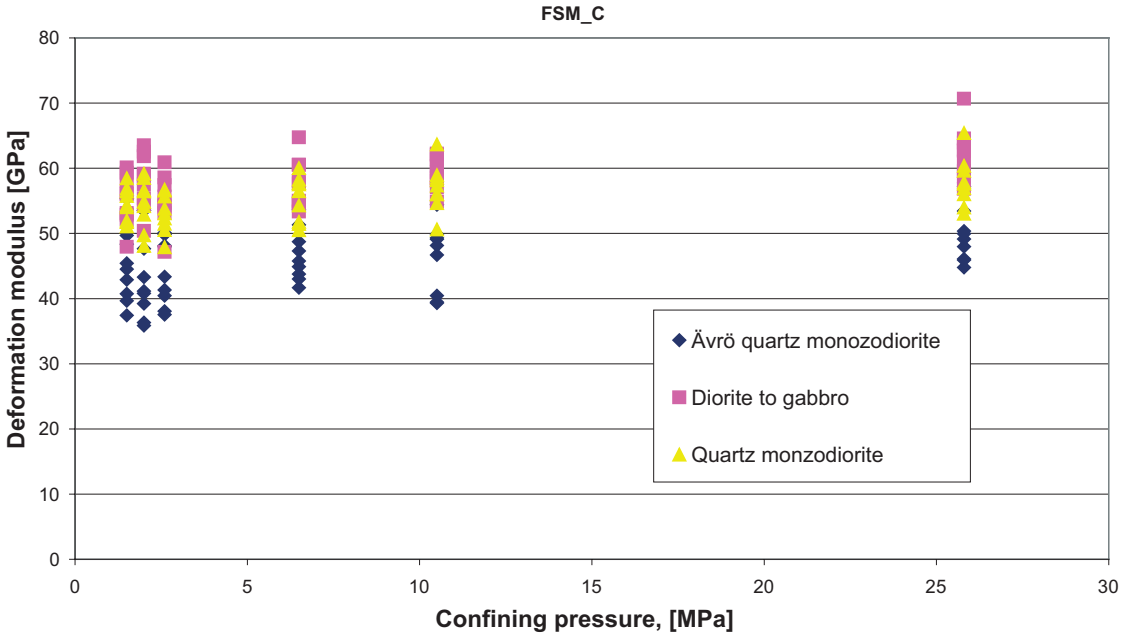

Figure 5-7. *Variation of evaluated deformation modulus with confining stress and intact rock type in fracture domain FSM_C.*

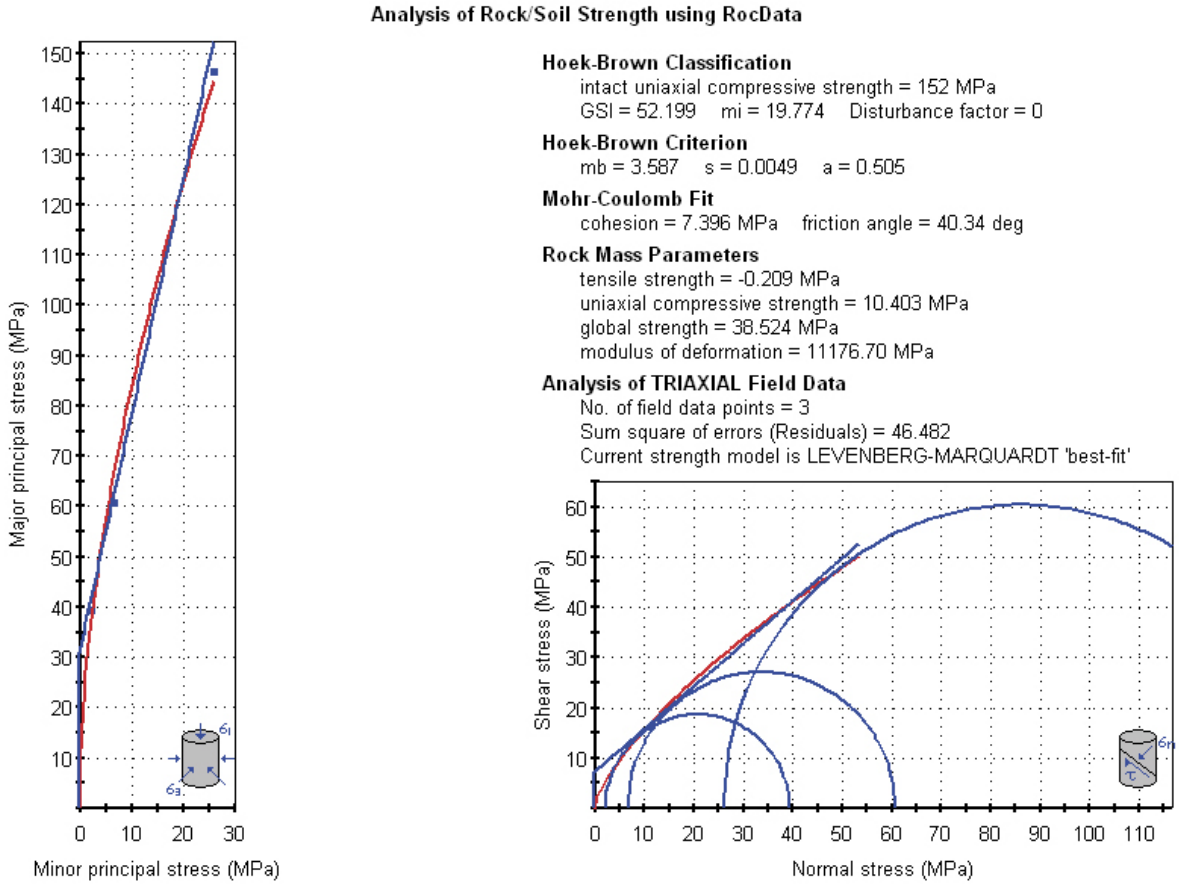

Figure 5-8. *The cohesion and friction angle has been evaluated by fitting a linear envelope to the results from the numerical compression tests with three different confing stresses.*

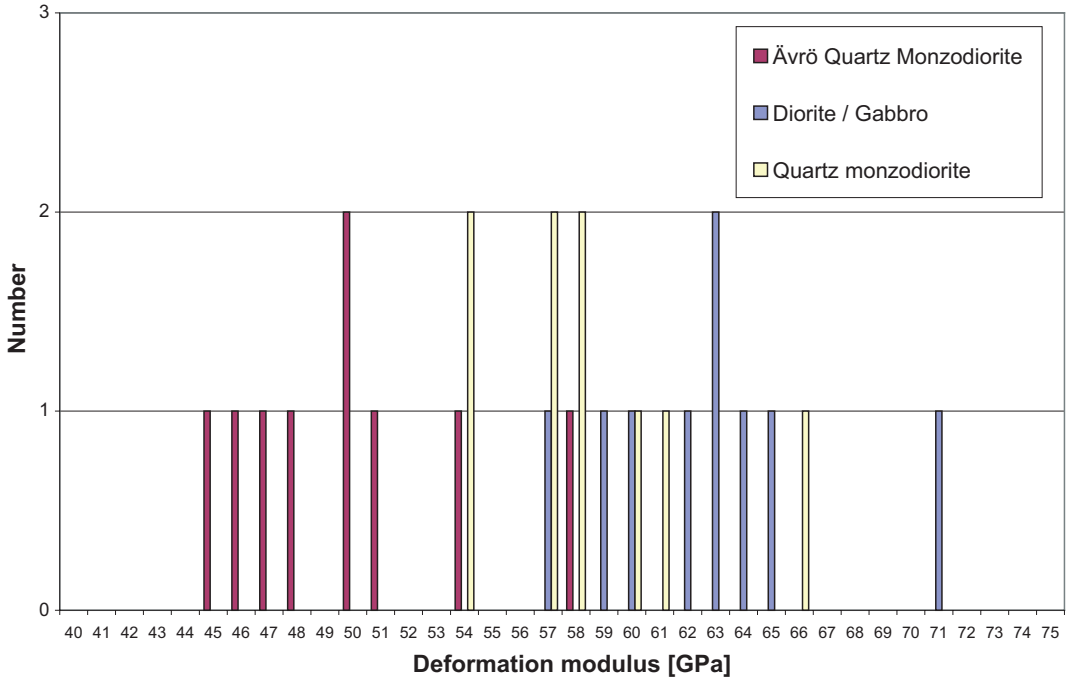

Figure 5-9. *Evaluated rock mass deformation modulus for the different 3DEC model runs. The variation is caused by the network variation in each DFN realization and intact rock type, respectively. The y-axis shows the number of model runs.*

Table 5-9. Resulting rock mass mechanical properties of fracture domain FSM_C based on the theoretical modelling.

Fracture domain [1]	FSM_C Ävrö quartz monzodiorite	FSM_C Diorite to gabbro	FSM_C Quartz monzodiorite	FSM_C Combined
Properties of the rock mass	Mean/std. dev. Min–max *Uncertainty of mean*	Mean/std. dev. Min–max *Uncertainty of mean*	Mean/std. dev. Min–max *Uncertainty of mean*	Mean/std. dev. Min–max *Uncertainty of mean*
Deformation modulus [GPa]	49.4/4.0 44.8–57.2 ±5%	62.3/4.0 56.8–70.7 ±4%	57.9/3.7 53.0–65.4 ±4%	56.5/6.6 44.8–70.7 ±4%
Poisson's ratio [–]	0.29/0.03 0.22–0.32 ±7%	0.35/0.01 0.35–0.36 ±2%	0.32/0.01 0.31–0.33 ±2%	0.32/0.03 0.22–0.36 ±4%
Uniaxial compressive strength [MPa] [2]	35.9/12.6 19.9–60.2 ±23%	56.2/10.4 42.9–76.5 ±12%	50.2/8.0 38.2–65.8 ±10%	47.4/13.3 19.9–76.5 ±11%
Friction angle [°] [3]	37.7/3.8 32.2–44.9 ±7%	45.0/2.5 41.5–49.3 ±4%	43.1/2.2 39.5–47.1 ±3%	41.9/4.2 32.2–49.3 ±4%
Cohesion [MPa] [3]	12.7/3.0 8.5–18.2 ±15%	17.1/2.0 14.4–20.8 ±8%	16.0/1.6 13.5–19.9 ±7%	15.3/2.9 8.5–20.8 ±7%

1) The rock mass properties in the domains do not include the effects of DZ and MDZ. DZ and MDZ properties are described by empirical approach see Section 5.4.1.
2) Estimated from fitting an average Mohr-Coulomb relationship in stress range 0–25.8 MPa.
3) For confinement stress between 10 and 30 MPa.

Table 5-10. Resulting rock mass mechanical properties of fracture domain FSM_EW007, FSM_NE005 and FSM_W based on the theoretical modelling.

Fracture domain [1]	FSM_EW007 Ävrö granodiotite	FSM_NE005 Ävrö granodiorite	FSM_W Ävrö granodiorite	FSM_W Quartz monzodiorite	FSM_W Combined
Properties of the rock mass	Mean/std. dev. Min–max *Uncertainty of mean*	Mean/std. dev. Min–max *Uncertainty of mean*	Mean/std. dev. Min–max *Uncertainty of mean*	Mean/std. dev. Min–max *Uncertainty of mean*	Mean/std. dev. Min–max *Uncertainty of mean*
Deformation modulus [GPa]	50.7/3.2 46.1–57.8 ±4%	51.0/4.2 44.7–56.9 ±5%	54.1/1.4 52.0–56.2 ±2%	54.7/1.7 52.2–57.0 ±2%	54.4/1.5 52.0–57.0 ±2%
Poisson's ratio [–]	0.30/0.01 0.29–0.31 ±2%	0.27/0.04 0.22–0.34 ±9%	0.29/0.01 0.26–0.30 ±2%	0.32/0.01 0.30–0.33 ±2%	0.30/0.02 0.26–0.33 ±3%
Uniaxial compressive strength [MPa] [2]	43.8/9.4 33.5–62.0 ±13%	53.1/10.9 34.4–70.8 ±13%	48.5/9.2 36.3–68.1 ±12%	46.5/7.5 35.1–60.0 ±11%	47.5/8.2 35.1–86.1 ±8%
Friction angle [°] [3]	41.2/2.8 37.8–46.4 ±4%	43.9/3.1 38.2–48.2 ±4%	42.7/2.6 38.9–46.7 ±4%	42.1/2.3 38.3–45.8 ±4%	42.3/2.4 38.3–47.7 ±3%
Cohesion [MPa] [3]	14.6/2.1 12.2–18.3 ±9%	16.5/2.2 12.5–19.8 ±8%	15.6/1.9 13.0–19.4 ±8%	15.3/1.6 12.7–17.9 ±7%	15.4/1.7 12.7–19.4 ±5%

1) The rock mass properties in the domains do not include the effects of DZ and MDZ. DZ and MDZ properties are described by empirical approach see Section 5.4.1.
2) Estimated from fitting an average Mohr-Coulomb relationship in stress range 0–25.8 MPa.
3) For confinement stress between 10 and 30 MPa.

5.3 Model for rock mass properties in fracture domains

In this section the results of the empirical and theoretical approaches are compared to achieve a "harmonised" description of the rock mass. The two approaches provide estimates of the rock mass properties that on the whole are completely independent from one another. Both methods involve elements of subjective judgement and assumptions which motivate a subsequent harmonisation step to guarantee the reliability of the modelling results.

When performing the harmonisation, there are some modelling parameters that differ between the two approaches and which must be placed on levelled terms. There are also some factors regarding the deformation zones that limit the possibility to perform a harmonisation.

Parameters that must be normalised are:

- *Modelling scale*. The empirical approach utilises borehole data divided into 5 m sections, whereas the theoretical approach is based on numerical modelling of blocks of 10×10×1 m.
- *Confining stress*. The empirical approach assumes no explicit stress dependence for the deformation modulus and Poisson's ratio while the confining stress is taken into account in the theoretical approach.
- *Fracture frequency*. The empirical approach uses a mean value based on 5 m sections (local fracture frequency) whereas the theoretical model is based on a mean value for the entire fracture domain.
- *Poisson's ratio*. In the empirical approach Poisson's ratio is limited to the value of intact rock while Poisson's ratio might be larger than the intact value in the theoretical approach.

Factors that limit the possibility to perform a complete harmonisation for the deformations zones are:

- Sealed fractures are not treated explicitly by the empirical approach whereas they are considered in the theoretical modelling of the deformations zones.
- The properties of the deformation zones are treated in an isotropic mode by the empirical approach while evaluated in parallel and perpendicular directions to the zone by the theoretical approach.

These differences regarding the deformation zones result in a parameter outcome from the two modelling approaches that slightly differ.

5.3.1 Harmonisation of results for fracture domains

The harmonisation of the results for the fracture domains were carried out essentially in accordance to the methodology used in the Laxemar model version 1.2 /SKB 2006b/. Based on the results from both the empirical and the theoretical approaches, it was concluded that the fracture domains could be divided in two different groups and that it would be sufficient to make one model for each of these groups.

The rock mass properties were assigned by making the following overall assumptions:

- The standard deviation describing the variation of the properties was mainly based on the empirical approach since it was judged that this approach better reflects the variation in fracture properties and fracture intensity.
- The minimum and maximum truncation values was selected to be plus/minus two times the standard deviation.
- The uncertainty values for the mean of the distribution were selected based on the difference seen in the two approaches and furthermore based on some judgement of the general confidence of the approaches for each specific parameter.

- The rock mass deformation modulus and uniaxial compressive strength were determined based on both approaches with the same weighting.
- The Poisson's ratio was estimated based on the theoretical approach results, since they were considered more reliable.
- The apparent cohesion and friction angle based on Mohr-Coulomb failure criterion were assumed to be directly comparable for confining pressure between 10 and 30 MPa. Averaging was applied to the mean values estimated by the two approaches (without weighting).
- The rock mass tensile strength is reported based on the empirical approach, since no value is evaluated from the theoretical approach.

In Figure 5-10 to Figure 5-14 the empirical and theoretical approaches (Section 5.1 and Section 5.2) for the different rock mechanics properties (deformation modulus, Poisson's ratio, UCS, Friction angle and cohesion) are compared with the harmonised model (see Table 5-1, Table 5-9, Table 5-10 and Table 5-11).

The resulting rock mechanics properties following harmonisation are presented in Table 5-11. Each parameter is given as a truncated normal distribution, describing the actually expected spatial variability within the domain. The model values in the table indicate parameter values recommended to be used for the rock mass outside deformation zones for design and the safety assessment work. The uncertainty of the model is described by a plus-minus span for the expected mean value of the normal distribution.

Note that 'rock mass' here excluds all DZ in ESHI, also the minor deformation zones (MDZ). MDZ are not included in the rock mass simulations made with the theoretical model, because it is not possible to include fractures of larger size due to the size of the numerical models. MDZ were also modelled separately in the empirical model approach. This means that the addition of MDZ compliance should not be forgotten if a response on a larger scale is to be analysed. (The properties of MDZ is separately estimated in Table 5-13 and the intensity of MDZ is estimated by the geological model, see Section 2.1.6).

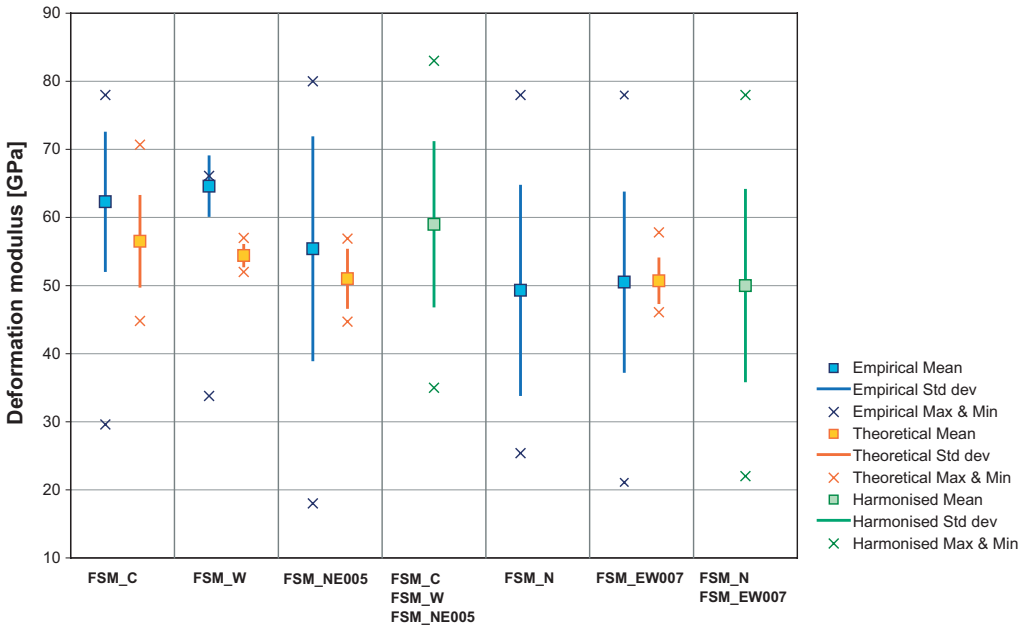

Figure 5-10. *The deformation modulus for the empirical and theoretical approaches is compared with the harmonised model for different fracture domains (see Table 5-1 and Table 5-9 to Table 5-11).*

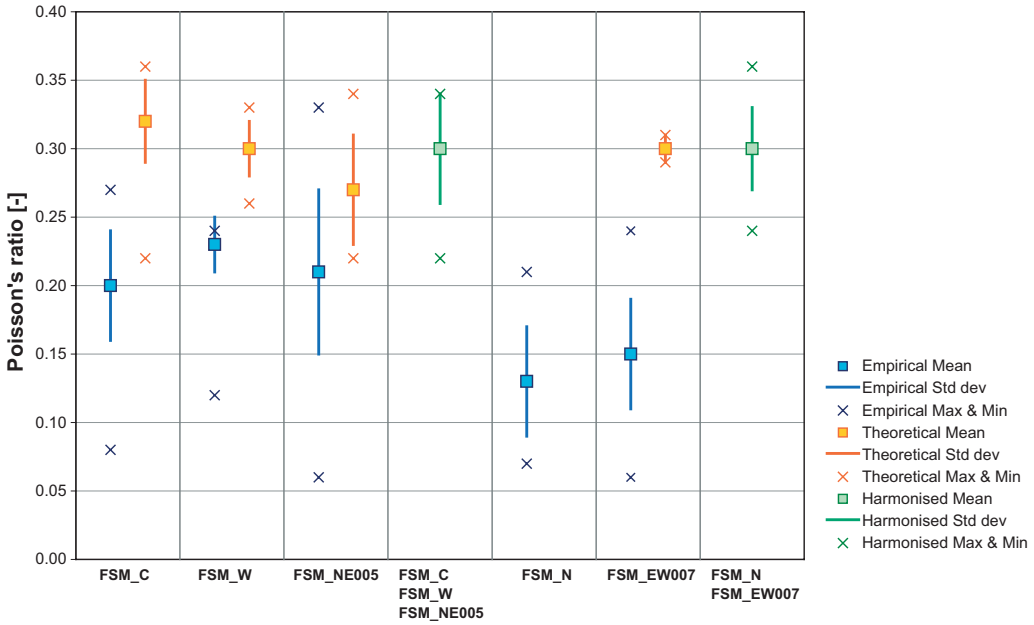

Figure 5-11. *Poissons ratio for the empirical and theoretical approaches is compared with the harmonised model for different fracture domains (see Table 5-1 and Table 5-9 to Table 5-11).*

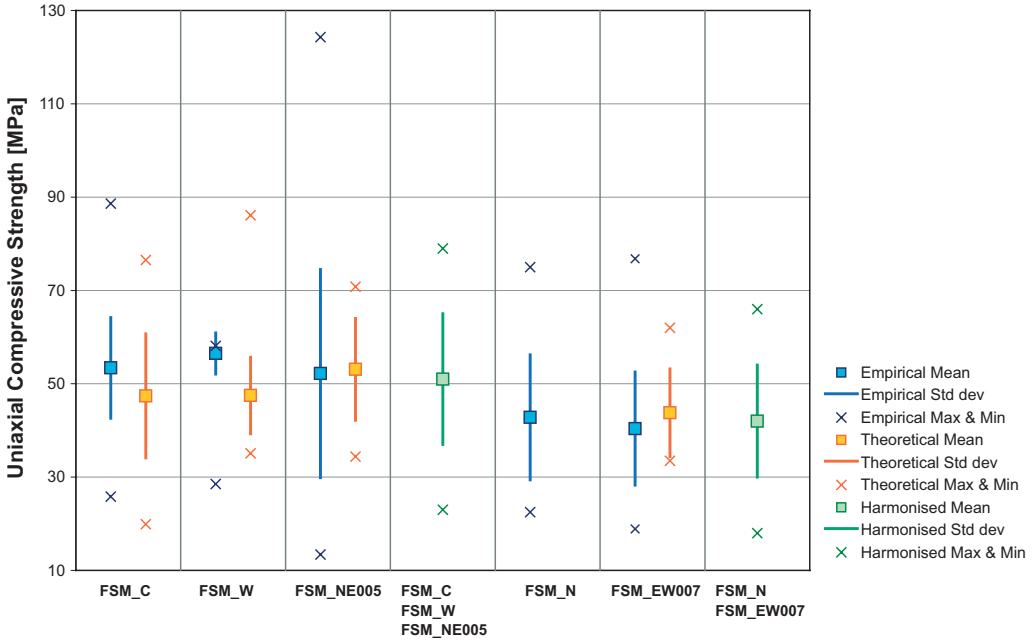

Figure 5-12. *Uniaxial compressive strength (Hoek & Brown) for the empirical and theoretical approaches is compared with the harmonised model for different fracture domains (see Table 5-1 and Table 5-9 to Table 5-11).*

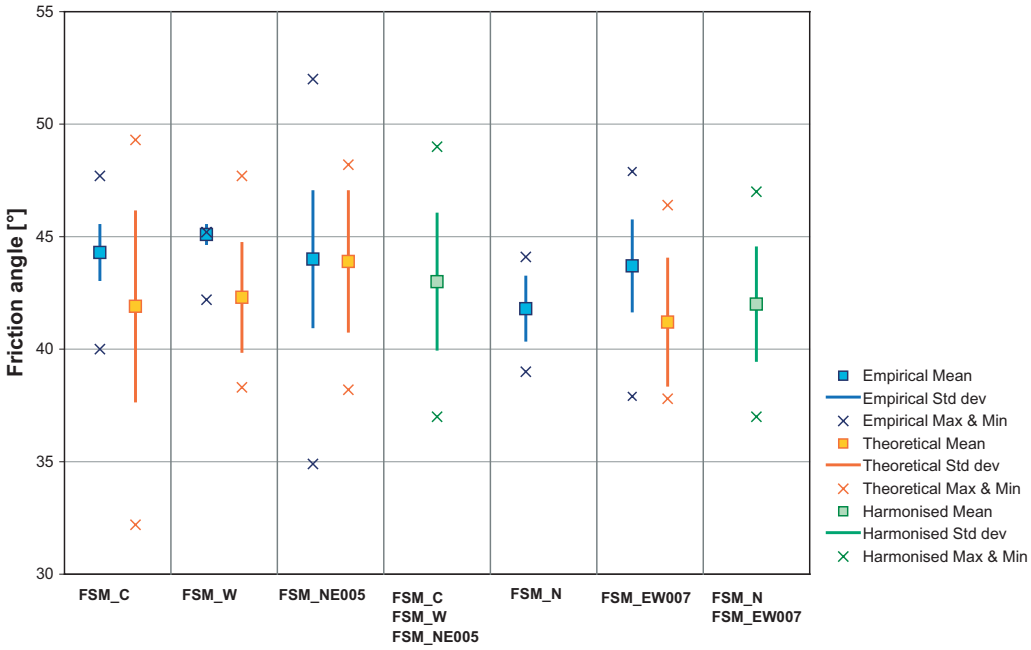

Figure 5-13. *Friction angle for the empirical and theoretical approaches is compared with the harmonised model for different fracture domains (see Table 5-1 and Table 5-9 to Table 5-11).*

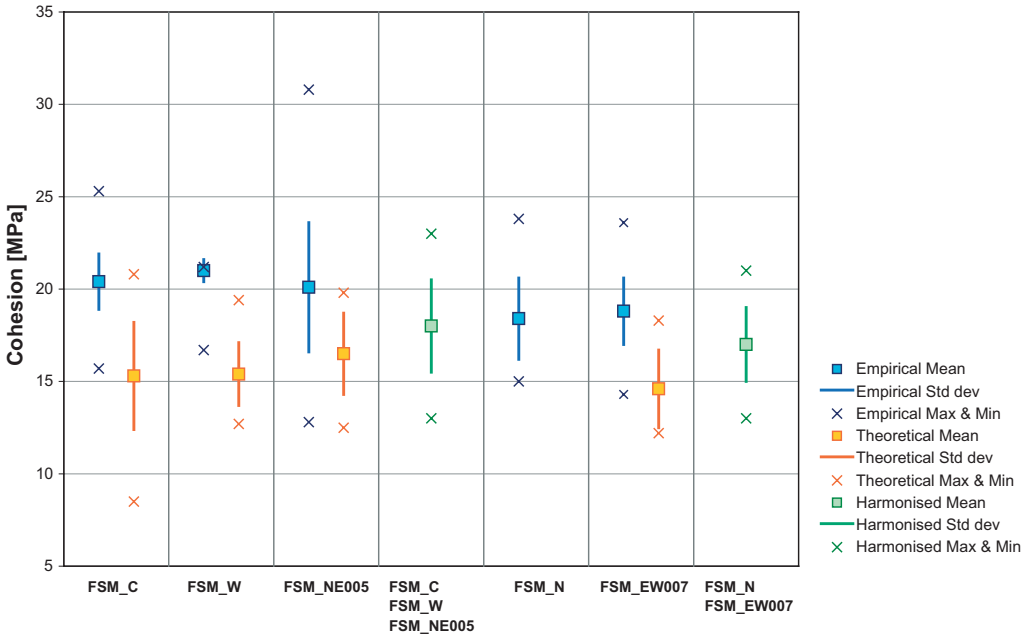

Figure 5-14. *Cohesion for the empirical and theoretical approaches is compared with the harmonised model for different fracture domains (see Table 5-1 and Table 5-9 to Table 5-11).*

Table 5-11. Harmonised model for mechanical properties of the rock mass for two groups of fracture domains. The models are truncaded normal distributions.

Properties of the rock mass	Fracture domains [1] FSM_C, FSM_W and FSM_NE005	Fracture domains [1] FSM_N and FSM_EW007
	Mean/std. dev. Min–max *Uncertainty in mean*	Mean/std. dev. Min–max *Uncertainty in mean*
Deformation modulus [GPa]	59/12 35–83 *±3%*	50/14 22–78 *±3%*
Poisson's ratio [–]	0.3/0.04 0.22–0.34 *±10%*	0.3/0.03 0.24–0.36 *±10%*
Uniaxial compressive strength (Hoek-Brown) [MPa]	51/14 23–79 *±14%*	42/12 18–66 *±14%*
Tensile strength (Hoek-Brown) [MPa]	1 0–8 [2] *0.5–5* [3]	0.5 0.2–1.5 [2] *0–2.5* [3]
Friction angle [4] [°]	43/3 37–49 *±3%*	42/2.5 37–47 *±3%*
Cohesion [4] [MPa]	18/2.5 13–23 *±7%*	17/2 13–21 *±7%*

1) The rock mass properties in the domains do not include the effects of DZ and MDZ. DZ and MDZ properties are described separately see Section 5.4.1.
2) Minimum and maximum expected tensile strength (the standard deviation is not given if the uncertainty is too large).
3) The mean tensile strength is expected in this range, which describes the uncertainty.
4) For confinement stress between 10 and 30 MPa.

5.4 Model for rock mechanics properties of deformation zones

The properties of the deformation zones have been estimated by two different approaches, the "empirical" and the "theoretical". In the first case, the properties are modelled in the same way as for the rock mass in fracture domains (described in Section 5.1), using the Q and RMR from boreholes intersecting the deformation zones. Only deformation zones with crush rock, higher fracture frequency and borehole interception longer than 1 metre were considered from a rock mechanics point of view. In the theoretical approach, the starting point has been the description of deformation zones in the geological modelling interms of fracture frequency, occurrence of crush and expected thickness of the deformation zones (found in Appendix 14 of the main geology report /Wahlgren et al. 2008/, see also Section 2.1.3). This information is used to estimate the equivalent mechanical properties of deformation zones when these are assumed to be large fracture planes.

It is recommended that users who apply the results evaluated for the deformation zones should consider which type of description of the zones that is most appropriate for the particular case: as volumes with weaker *rock mass* or as geometrically simplified large *fracture planes*. Depending on this choice, different parameter sets may be selected for the analysis.

5.4.1 Empirical approach

The nine characterised boreholes intercept a number of fractured zones. Such zones were characterised by the Geological Model /Wahlgren et al. 2008/ and can be divided into three categories:

- Deformation zones: Deterministically modelled and included in the deterministic Deformation Zone Model with an interpreted surface outcrop or lineament.
- Other deformation zones: All other deterministically modelled zones included in the deterministic Deformation Zone Model lacking an interpreted surface outcrop.
- Minor (local) deformation zones (MDZ): determined by the extended single-hole interpretation (ESHI) and often only observed in one borehole and not reaching the surface.

Table 5-12 shows the list of all deterministic (DZ) and minor deformation zones (MDZ) intercepting the boreholes characterised with the empirical approach for determining the rock mass quality. Within each deterministic deformation zone (DZ), the rock mass quality and mechanical parameters were determined for each 5 m section of the intersecting borehole. The summary statistics are presented for each zone. For some of the DZ and MDZ, only the lumped properties for all the different interceptions in different zones were determined and presented together. Such results can be found in Table 5-13.

Table 5-12. List of the deformation zones intercepted by the empirically characterised boreholes KLX02, KLX03, KLX04, KLX05 and KLX12A, and borehole KLX10, KLX11A, KLX15A and KLX19A for which the rock mass quality was estimated based on correlations with RQD.

Type	Borehole	Name (or ESHI identification)				
DZ	KLX02	ZSMEW007A	ZSMNE107A	ZSMNW928A		
	KLX03	ZSMEW946A				
	KLX04	ZSMEW007A	ZSMNW928A			
	KLX05	–				
	KLX12A	–				
	KLX10	ZSMEW946A	ZSMNE942A			
	KLX11A	–				
	KLX15A	ZSMNE107A	ZSMNW042A			
	KLX19A	ZSMNE942A				
Other DZ		KLX03_DZ1b	KLX03_DZ1c			
		KLX04_DZ6b	KLX04_DZ6c			
		KLX11_DZ11	HLX28_DZ1 (KLX11A)			
MDZ		KLX02/DZ2	KLX02/DZ4			
		KLX03/DZ1	KLX03/DZ4	KLX03/DZ8		
		KLX04/DZ1	KLX04/DZ2	KLX04/DZ3	KLX04/DZ6	KLX04/DZ16
		KLX05/DZ1	KLX05/DZ4	KLX05/DZ6	KLX05/DZ8	KLX05/DZ11
		KLX05/DZ12				
		KLX10/DZ8				
		KLX11A/DZ3	KLX11A/DZ4	KLX11A/DZ5	KLX11A/DZ6	KLX11A/DZ7
		KLX11A/DZ9	KLX11A/DZ10	KLX11A/DZ12	KLX11A/DZ13	KLX11A/DZ14
		KLX11A/DZ16	KLX11A/DZ18			
		KLX12A/DZ4	KLX12A/DZ10	KLX12A/DZ12		
		KLX15A/DZ2	KLX15A/DZ4	KLX15A/DZ8	KLX15A/DZ9	KLX15A/DZ10
		KLX15A/DZ11	KLX15A/DZ12	KLX15A/DZ14	KLX15A/DZ17	
		KLX19A/DZ2	KLX19A/DZ3	KLX19A/DZ5	KLX19A/DZ6	KLX19A/DZ7
		KLX19A/DZ9	KLX19A/DZ10			

Table 5-13. Estimated mechanical properties of the deformation zones intercepted by the empirically characterised boreholes listed in Table 5-12. Note that the rock mass is expected to have varying properties inside a zone, and that this variation in turn will be different between different zones.

Properties of the deformation zones	Q [1] [–]	RMR [–]	Deformation modulus [GPa]	Poisson's ratio [–]	Friction angle [2] [°]	Cohesion [2] [MPa]
	Mean/std. dev. Min–max [3]	Mean/std. dev. Min–max [3]	Mean/std. dev. Min–max [3]	Mean/std. dev. Min–max [3]	Mean/std. dev. Min–max [3]	Mean/std. dev. Min–max [3]
ZSMEW007A	13.0 1.2–97.8	73.6/7.2 59.0–85.7	42.0/16.7 16.8–77.9	0.11/0.04 0.04–0.21	41.0/2.0 36.9–44.1	17.3/2.2 13.6–21.9
ZSMEW946A	7.9 2.3–36.2	67.7/7.7 61.2–78.9	29.8/14.5 18.2–52.9	0.09/0.05 0.05–0.15	40.5/2.2 38.5–43.3	16.0/2.0 14.2–19.0
ZSMNE107A	7.7 0.7–87.0	67.7/7.1 53.3–83.8	30.3/12.8 12.1–66.1	0.10/0.05 0.04–0.24	40.3/2.2 35.9–45.2	15.9/1.9 12.8–21.2
ZSMNE942A	19.8 0.5–43.2	72.5/6.3 53.6–79.2	38.9/12.2 10.9–54.4	0.12/0.04 0.02–0.19	41.6/1.7 36.6–44.1	17.1/1.7 12.5–19.4
ZSMNW042A	31.6 0.6–59.2	72.2/10.4 55.3–81.1	38.7/23.9 0–59.5	0.14/0.08 0–0.21	42.6/2.3 38.8–44.6	17.4/3.0 12.6–20.2
Other DZ	10.5 0.6–87.0	70.9/9.7 53.3–84.4	37.6/20.2 0–72.3	0.12/0.08 0–0.24	41.3/3.2 35.2–46.7	16.9/2.9 12.5–21.2
MDZ	12.3 0.2–87.0	72.9/9.0 50.8–83.8	40.4/20.4 0–66.1	0.14/0.08 0–0.24	42.4/2.6 36.2–47.8	17.6/2.8 11.6–22.3

1) For Q, the most frequent value is reported instead of the average.
2) For confinement stress between 10 and 30 MPa.
3) Statistics made on all 5 m core sections from the borehole(s) intersecting each DZ (see text).

In a way similar to what is shown in Section 5.1.3, also the uncertainty in the rock mass quality and derived parameters can be determined by studying the difference between the Q and RMR results of the direct characterisation and their estimated values based on the correlations with RQD. Table 5-14 summarises the uncertainty of the mean of the parameters concerning the deterministic deformation zones and the minor deformation zones. It can be seen that the properties of deterministic deformation zones often exhibit lower uncertainty than the minor deformation zones. This can be explained by the fact that there are more data available on the deterministic deformation zones and their rock mass quality is lower and less variable from zone to zone.

5.4.2 Theoretical approach

In the numerical modelling of the influence of deformation zones on stress (Section 6.3), the deformation zones are modelled as fracture planes. The properties of the deformation zones are expressed by the normal and shear stiffness along with the strength in terms of cohesion and friction angle. To estimate the properties of the deformation zones an analytical approach was used. The estimations are only made for deformation zones where data are available from boreholes and for zones that are to be used in the stress modelling.

Table 5-14. Uncertainty of the mean values of the mechanical parameters of the deformation zones intercepted by the empirically characterised boreholes. (Note that the mean value is only relevant to use as an overall average representation of the whole zone thickness, including both the weaker and the stronger parts. Inside the zone the properties will vary as described with the min-max span given in Table 5-13).

Deformation zones	DZ Deterministic deformation zones	MDZ Minor deformation zones
Property of the rock mass	Confidence interval of the mean value [1]	Confidence interval of the mean value [1]
Q [2]	0.5 [4] – 30	0.2 [4] – 40
RMR	±4%	±5%
Deformation modulus [GPa]	±18%	±24%
Poisson's ratio [–]	±22%	±28%
Friction angle [3] [°]	±2%	±6%
Cohesion [3] [MPa]	±5%	±11%

1) 95% confidence interval of the mean value (see Section 5.1.3)
2) As interval of expected Q-values.
3) For confinement stress between 10 and 30 MPa.
4) Since the resulting uncertainty interval of the mean is very large, the minimum observed value of Q is assumed as lower limit.

A deformation zone is then divided into sections (with a width b) with constant fracture frequency, and the normal stiffness, K_n, and shear stiffness, K_s, are calculated using Equation 5-3 and Equation 5-4. For each section the constrained deformation modulus, M_i, and shear modulus, G_i, are taken from the 3DEC simulations (in Section 5.2). The shear strength of the deformation zones is assumed equal to the shear strength of the section with the smallest shear strength.

$$K_n = \frac{\sum_{i=1}^{n} b_i}{\sum_{i=1}^{n} \frac{b_i}{M_i}}$$

Equation 5-3

$$K_s = \frac{\sum_{i=1}^{n} b_i}{\sum_{i=1}^{n} \frac{b_i}{G_i}}$$

Equation 5-4

A compilation of the estimated properties for the deformation zones, regarded as equivalent single planar features, is given in Table 5-15. The stiffness of the deformation zones in Laxemar is lower than the corresponding parameters for deformation zones in Forsmark (with exception of the Singö deformation zone) /Glamheden et al. 2007/. The main reason for this is the difference in the larger thickness of the Laxemar deformation zones and the higher fracture frequency.

Table 5-15. Summary of the estimated properties of the majority of the deformation zones used in the stress modelling (Section 6.3). The deformation zons are regarded as single planar features with the listed equivalent properties.

Zone name	Normal stiffness K_n [MPa/m]	Shear stiffness K_s [MPa/m]	Friction angle ϕ [°]	Cohesion c [MPa]
ZSMEW007A	450	90	34.0	0.9
ZSMEW946A	2,960	470	34.0	0.9
ZSMNE107A	1,490	350	43.7	9.2
ZSMNE942A	2,730	510	34.0	0.9
ZSMNW042A	1,400	310	44.8	10.1
KLX07_DZ12	1,170	260	34.0	0.9
KLX07_DZ7	1,510	350	34.0	0.9
KLX07_DZ9	2,400	390	34.0	0.9
KLX09_DZ10	1,020	220	34.0	0.9
ZSMEW002A	390	70	34.0	0.9
ZSMEW013A	1,360	350	44.8	10.1
ZSMEW120A	380	50	34.0	0.9
KLX11_DZ11	2,690	580	34.0	0.9
ZSMNE004A	450	110	45.9	11.0
ZSMNE005A	200	50	42.6	8.2
ZSMNE006A	330	80	41.5	7.3
ZSMNE011A	610	160	44.8	10.1
ZSMNE012A	390	90	42.6	8.2
ZSMNE018A	1,230	310	44.8	10.1
ZSMNE021A	1,530	390	44.8	10.1
ZSMNE024A	460	120	40.5	6.4
KLX04_DZ6b	2,040	450	34.0	0.9
KLX04_DZ6c	910	190	34.0	0.9
KLX07_DZ13	3,020	580	34.0	0.9
ZSMNS001A–E	570	100	34.0	0.9
ZSMNS059A	780	170	34.0	0.9
KLX09E_DZ2	2,140	440	34.0	0.9
ZSMNW052A	1,940	280	34.0	0.9
ZSMNW928A	2,220	350	34.0	0.9
ZSMNW931A	1,230	310	44.8	10.1

6 In situ state of stress

6.1 Stress patterns at a larger scale

This section gives a short summary of what is found on seismicity and stress pattern in Section 3.6 of the report on the geological history, compiled for both Forsmark and Laxemar in /Söderbäck (ed.) 2008/. That chapter is in turn largely extracted from /Bödvarsson et al. 2006/.

Seismic events of lower magnitude are seen fairly frequently in Scandinavia (Figure 6-1). However, much of south-eastern Sweden, including both Forsmark and Laxemar-Simpevarp areas, show relatively little seismic activity. The maximum principal stress as inferred from the seismic data is oriented WNW-ESE. This direction is in accordance with that expected from plate tectonics deformation caused by the opening of the Atlantic, which dominates the current stress field in Sweden. Stresses due to postglacial rebound are expected to be much less significant today compared to the tectonic stresses /Bödvarsson et al. 2006/.

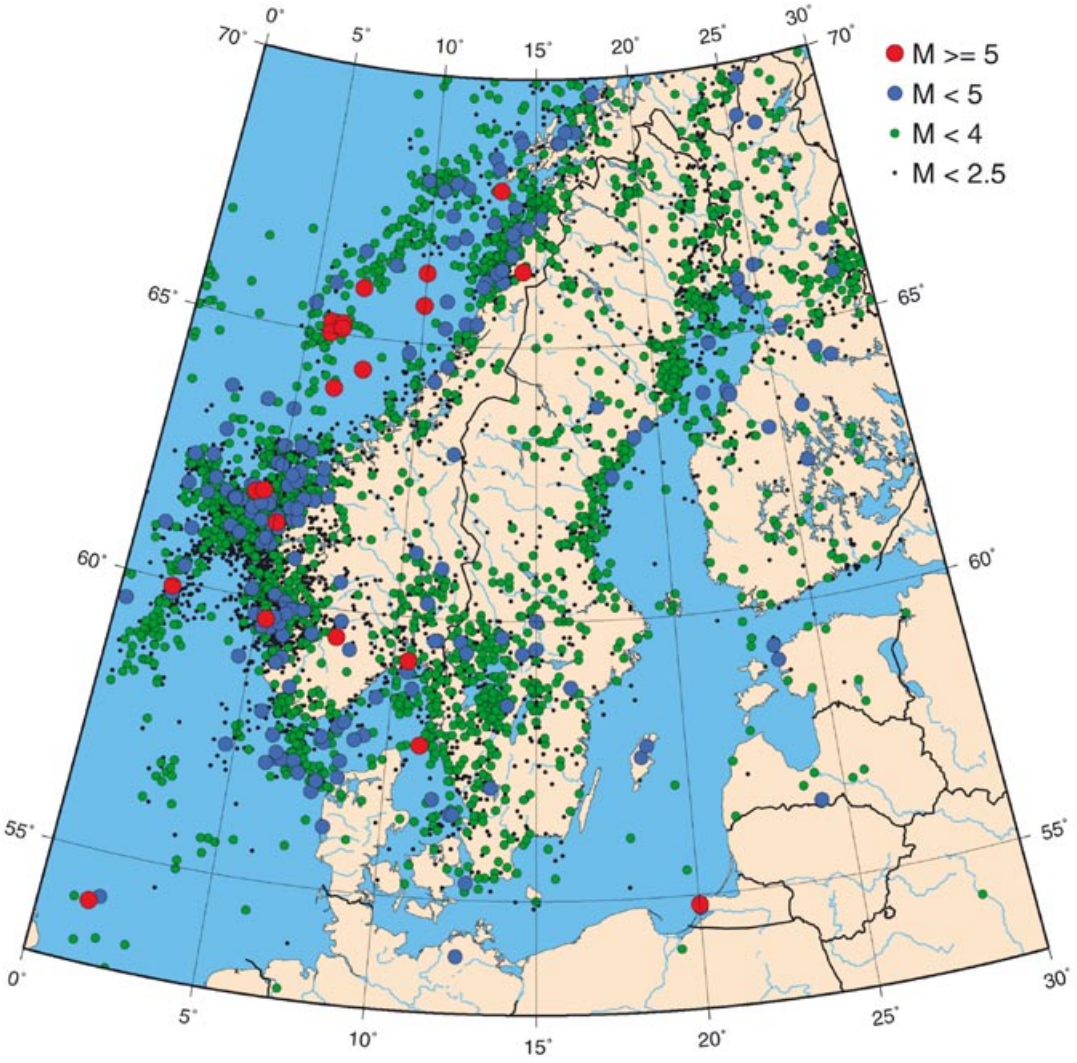

Figure 6-1. *Epicentre and magnitude of earthquakes in the northern part of Europe (Norden) between 1375 and 2005. Note that earthquake data for the neighbouring countries to the south of the Baltic Sea are not complete (modified after /Bödvarsson et al. 2006/).*

Although strike-slip movement is the dominant focal mechanism, irrespective of where in Sweden the seismic event occurred, there appears to be some tendency for a less varied pattern in fault plane solutions in northern Sweden relative to that observed in the southern part of the country. In northern Sweden, a dominant set of strike-slip and a subordinate set of reverse dip-slip fault solutions are present. This pertains to crustal stress at seismogenic depths, and much evidence points to a reverse state of stress in the uppermost part of the crust (c. 1,000 m) in large parts of Sweden (i.e. that the maximum and minimum horizontal stresses exceed the vertical stress).

An attempt to monitor *local* surface deformation with the help of detailed GPS measurements has recently been completed in the Laxemar-Simpevarp area /Sjöberg et al. 2004/. The results were only partly significant but were interpreted as a component of dextral strike-slip displacement of an E-W fault. This is consistent with the inferred general orientation of the current stress field in southern Sweden with the principal maximum stress in a WNW-ESE direction in the horizontal plane. However, there are intrinsic difficulties to relate ground measurements to deeper seismic or a seismic activity along active faults, since significant bedrock movements occur close to the ground surface related to release of stress and diminish rapidly at depth.

Compilations made by the World Stress Map Project /Reinecker et al. 2005/ show that the regional stress field in the southern part of Sweden is characterised by a general orientation of the major horizontal stress in the range of N130°–150°, see Figure 6-2. The stress directions indicated on this map are based on information from focal mechanism, borehole breakouts as well as direct measurements by overcoring and hydraulic fracturing.

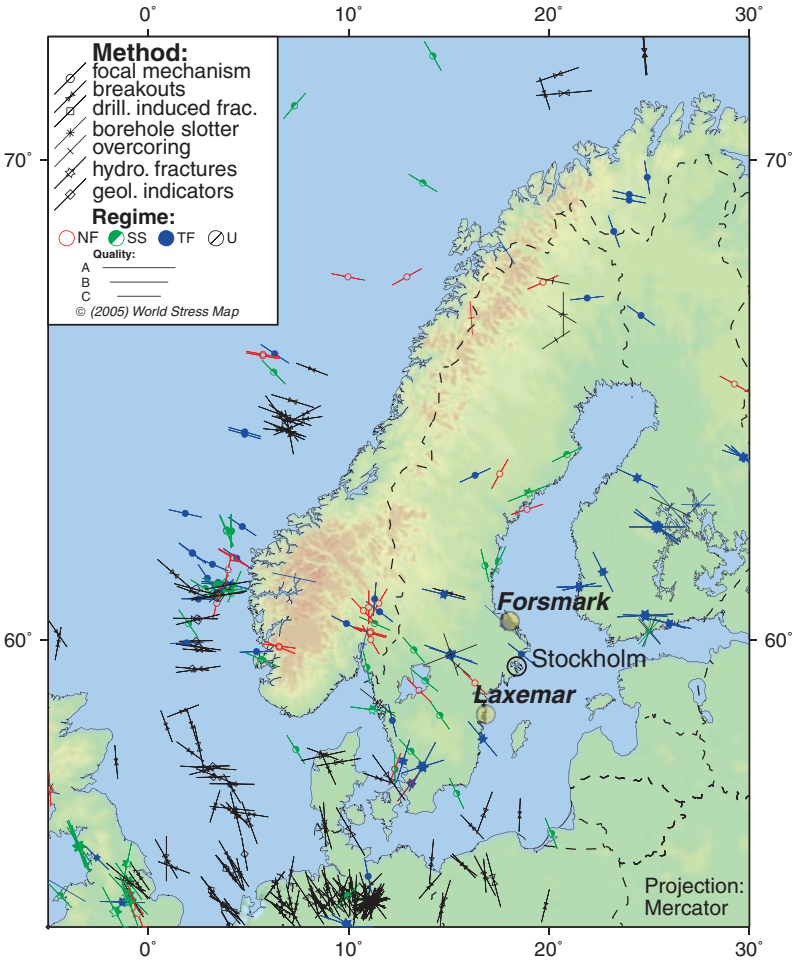

Figure 6-2. *Orientation of the major principal stress based on data from the World Stress Map Project /Reinecker et al. 2005/.*

/Stephansson et al. 1991/ summarised the state of stress in Fennoscandia using a rock stress database containing about 500 entries from more than 100 sites in Finland, Norway and Sweden. /Stephansson et al. 1991/ concluded that in the Fennoscandian shield there is a large horizontal stress component in the uppermost 1,000 m of bedrock, and that the maximum and minimum horizontal stresses exceed the vertical stress, assuming the vertical stress is estimated from the weight of the overburden. /Amadei and Stephanssons 1997/ emphasise that generic stress versus stress relationships should be used with caution as it is common with local variation of in situ stress and further they point to the fact that the ordering of in situ stresses (i.e. the stress regime) is not necessarily constant with depth.

6.2 Overview of the primary data on stress

6.2.1 Primary data locations

Methods used for direct stress measurements at Laxemar were borehole overcoring (OC), hydraulic fracturing (HF) and hydraulic testing on pre-existing fractures (HTPF). The boreholes utilised for the direct measurements, and the corresponding P-reports are listed in Table 6-1 and the measurement locations are shown in Figure 6-3.

Indirect observations of the in situ stress included borehole breakout studies, which has been done in all boreholes (see Section 6.2.4), and mapping of core disking performed in conjunction with the regular geological mapping of all core drilled holes, see Section 6.2.5. Furthermore, tests of microcrack porosity in laboratory samples from one borehole, KLX17 (reported in Section 3.4.1), may be used as an indirect indicator of the stress, see Section 6.2.5.

Table 6-1. Boreholes utilised for direct stress measurement using OverCoring (OC), Hydraulic Fracturing (HF) and Hydraulic Tests on Pre-existing Fractures (HTPF). A report list is provided at the end of the reference chapter (Section 9.1).

Borehole name	Measurement method		
	OC	HF	HTPF
PLU Laxemar subarea			
KLX04 [3)]	P-05-69	–	–
KLX12A [3)]	P-07-123	P-07-232	P-07-232
PLU Simpevarp subarea			
KAV04A [3)]	P-04-84	–	–
KSH01A [5)]	–	P-04-310	P-04-310
KSH02 [3)]	P-04-23	–	–
Older measurement in Laxemar subarea			
KLX02 [3)]	–	PR U-97-27	–
Äspö Hard Rock Laboratory			
KA3759G [6)]	IPR-01-67	–	–
KF0093A01 [6)]	R-02-26	IPR-02-02	–
KK0045G01 [6)]	R-02-26 IPR-01-67	–	–
KA3376B01 [6)]	IPR-03-16	–	–
KA2599G01 [6)]	– [1)]	IPR-02-02	–
Oskarshamn			
KOV01 [2) 4)]	IPR-02-18	IPR-02-01	–

1) Doorstopper data exist from KA2599G01 but are not used /Janson and Stigsson 2002/.
2) About 30 km south of Laxemar.
3) Data for boreholes KLX02, KLX04, KLX12A, KAV04A and KSH02 are from Sicada 2008-02-27.
4) Data for KOV01 are from Sicada 2008-04-01.
5) Data for KSH01A are from Sicada 2008-07-18.
6) Data for boreholes KA3759G, KF0093A01, KK0045G01, KA3376B01 and KA2599G01 are partly taken from Sicada 2008-02-27 and partly from the reports.

Figure 6-3. *Map with location marked for boreholes utilised for direct stress measurement (cf. Table 6-1). The area marked in red is the SDM-Site Laxemar local model area.*

The primary data available for rock mechanics modelling in the SKB database, Sicada, have been displayed in a series of WellCad plots, one for each cored borehole, see Appendix 5. These plots provide a good overview and a visual means of correlating in situ stress with geological mapping and the geological model. If desired, the corresponding rock mechanics data from laboratory testing, rock mass quality indices and P-wave velocity data may be easily collected from the WellCad plots in comparable format presented in Appendix 1.

6.2.2 Overcoring data

The data selected to be used as a basis for the model of this model version are data not older than from 1996, which means that the quality of the measurement procedures and documentations are well established. From the Äspö Hard Rock Laboratory only data from measurement points at a minimum distance of 10 m from excavations are included, to avoid any measurement being influenced by secondary stress field (stress redistribution caused by the excavations).

The overcoring data are normally ranked into categories depending on the quality or success of the measurement. Class A gives data with highest confidence and class B somewhat less confidence. Data ranked C in the measurement reports are not included in the database and do not constitute basis for the modelling. (If no ranking was made in Sicada the class was set to class B. The ranking appears in the plots in Appendix 5). No datum is excluded from the compilation of primary data based on the measurement value as such.

The results from the overcoring measurements from all boreholes are shown together in the diagrams of Figure 6-4 as the principal stress magnitudes versus depth. The corresponding orientations of measured principal stresses are found in the stereographic plots of Figure 6-5.

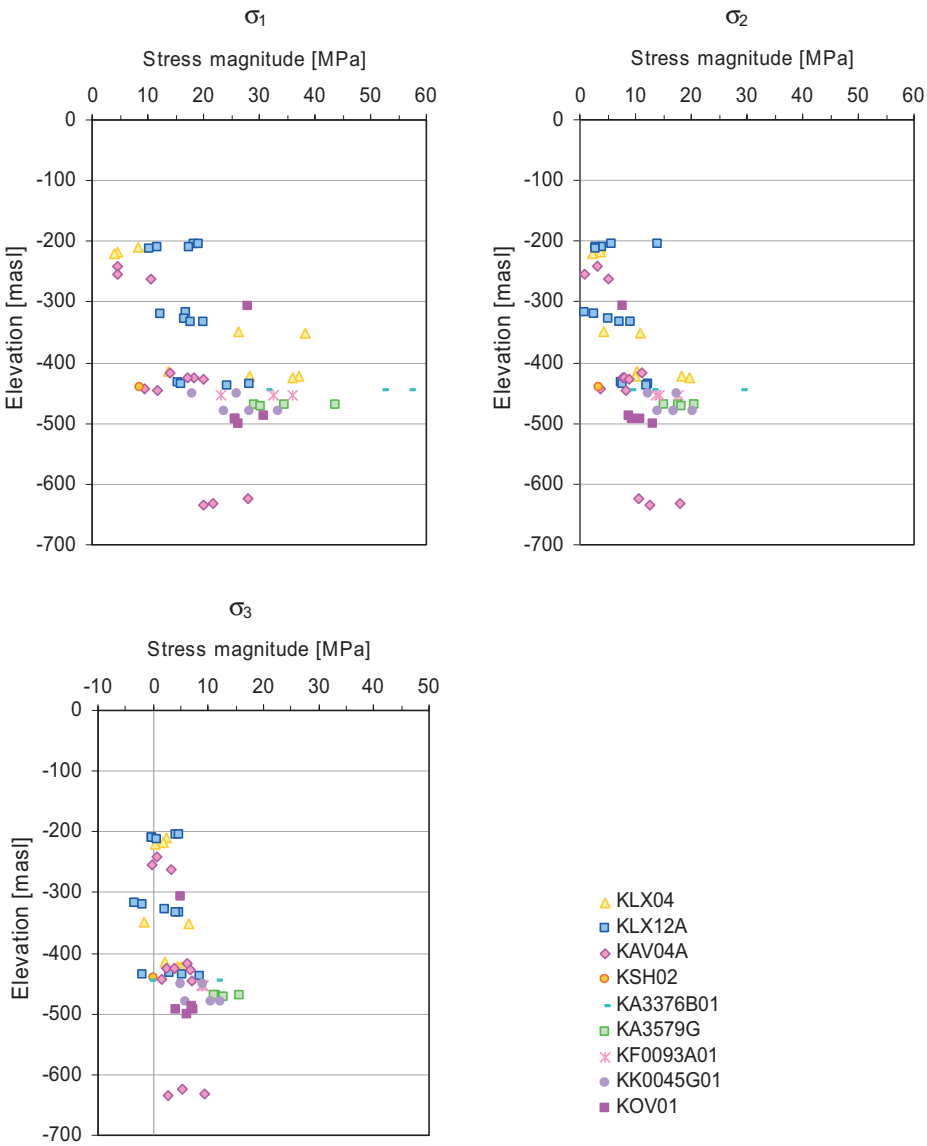

Figure 6-4. *Principal stress magnitudes versus depth from all available overcoring data in the region. Different boreholes are marked with different symbols. The location of boreholes is shown in Figure 6-3. (Corresponding plots for horizontal stresses and vertical stress are given in Appendix 6).*

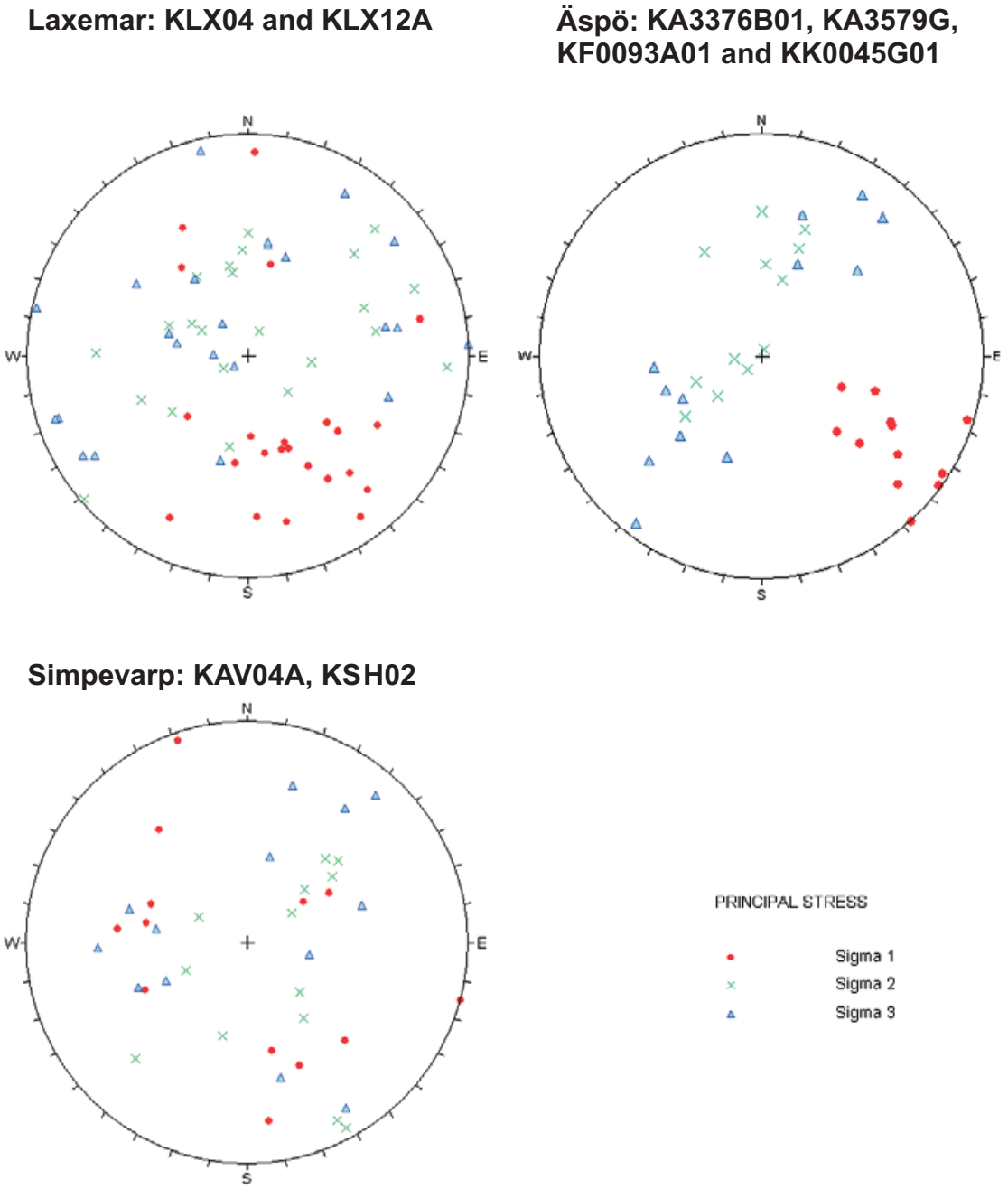

Figure 6-5. *Stereographic plots of principal stress orientations from overcoring measurements.*

Looking at all available overcoring data it may be concluded that values are quite scattered, both what concerns magnitudes and orientations. Within the Laxemar local model area there are two boreholes, KLX04 and KLX12A, where overcoring has been carried out, and the results from these two boreholes are presented separately in Figure 6-6 and Figure 6-7. From these diagrams a clear trend is seen for both orientation and magnitudes although the variation between single measurements is still quite significant. The direction of the maximum principal stress is NW-SE, as was expected due to the tectonic driving forces in the region (see Section 6.1). The average magnitudes of stresses, at least the maximum stress, seem to be constantly increasing with depth, which is also what is often seen in stress measurement campaigns.

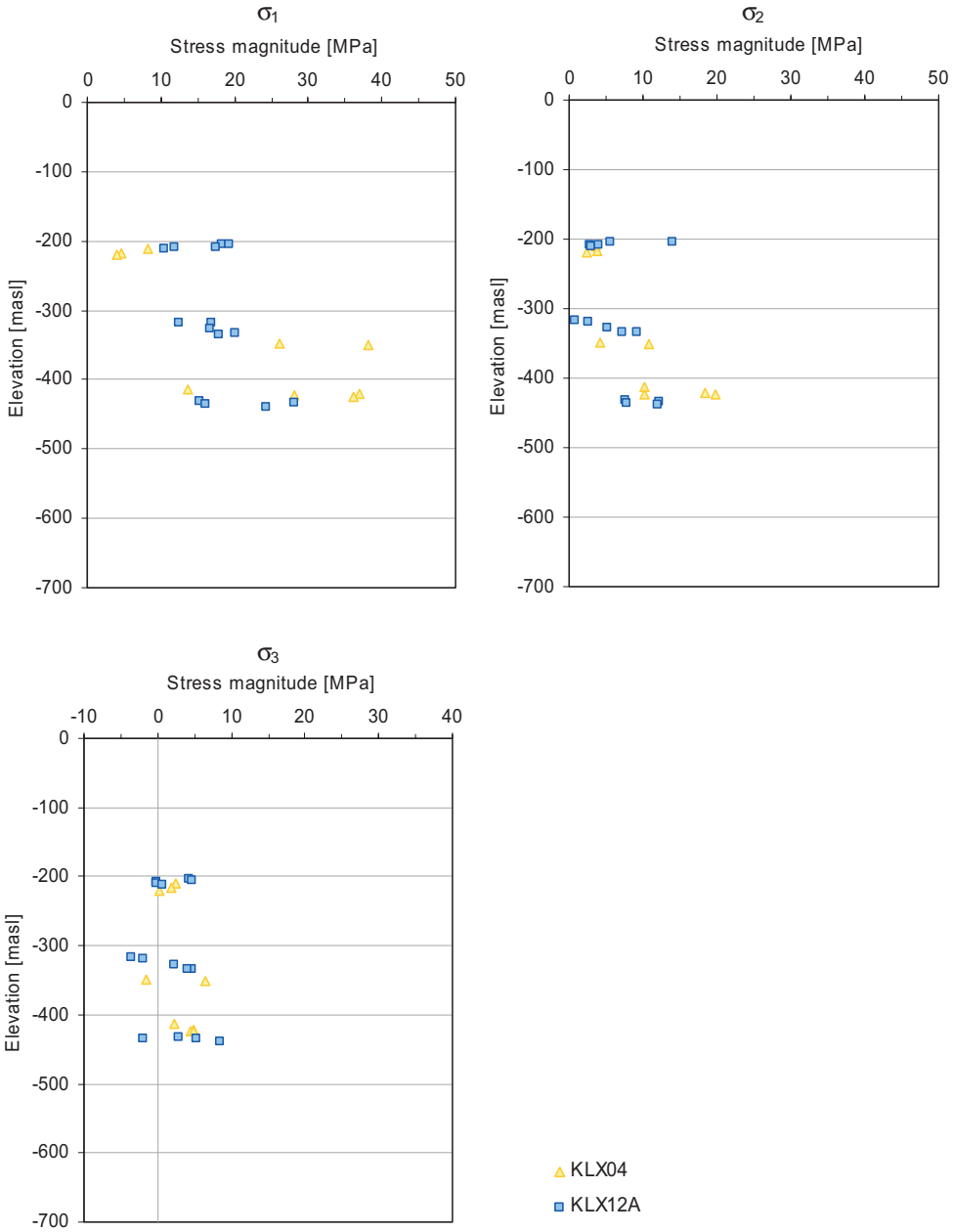

Figure 6-6. *Overcoring measurement result in KLX04 and KLX12A; Principal stresses. (Corresponding plots for horizontal stresses and vertical stress are given in Appendix 6).*

The stress in KLX04 is lower at about –200 m elevation, compared with the same depth in KLX12A, and is very scattered at about –400 m elevation. It is noteworthy (refer to Appendix 5) that in KLX04 there are deformation zones located at the upper measurement level which introduces the thought that this could be the cause of stress differences observed.

As already brought up in Section 6.1 it is of interest to try to categorise the general states of stress at a site or region, based on the general principal stress orientations. In a so called strike-slip regime the minor principal stress is oriented horizontally, while in a thrust (or reverse dip-slip) regime the vertical stress is the minor principal stress. The plots of Figure 6-5 show that most measurements indicate that the maximum stress is fairly horizontal, but the orientations for minimum and intermediate principal stresses are strongly varying, in particular at Äspö and in the Simpevarp subarea.

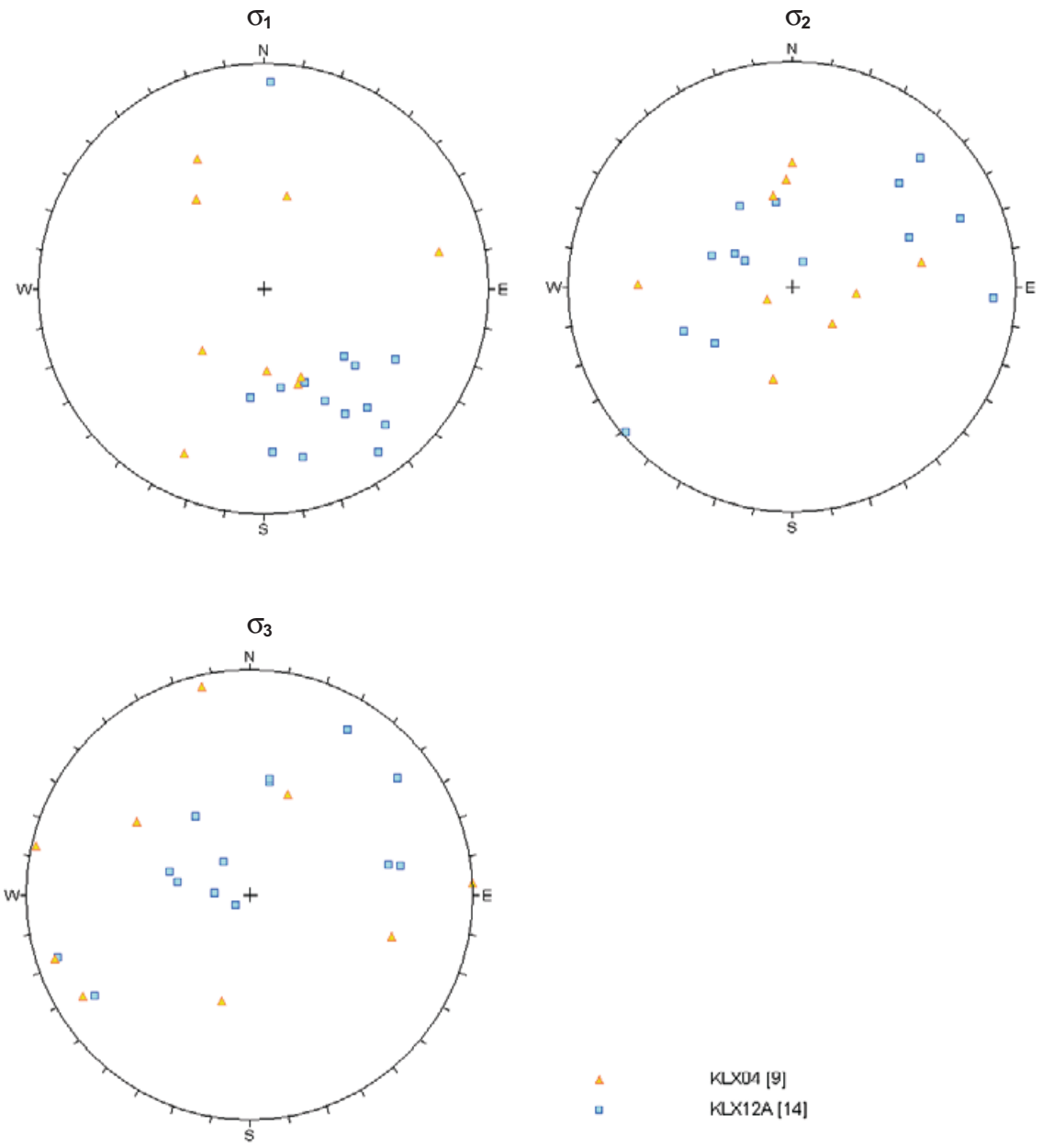

Figure 6-7. *Stereographic plots of principal stress orientations overcoring measurements in KLX04 and KLX12A (see also Appendix 5).*

Another way of presenting the measurement data is to compile the stress ratios between principal stresses. This is performed in Figure 6-9 and Figure 6-10. Again a great scatter may be noted (a few data also outside the ranges). Here it should be remembered that as for all measurements some of the scatter seen is a result of pure measurement technique errors, and not necessarily reflecting the actual stress field. However, the relative magnitudes are often considered more reliable than the absolute stress magnitudes (with the exception of points where the minor stress are very small (or close to zero or negative) in which cases the ratios become exceptional).

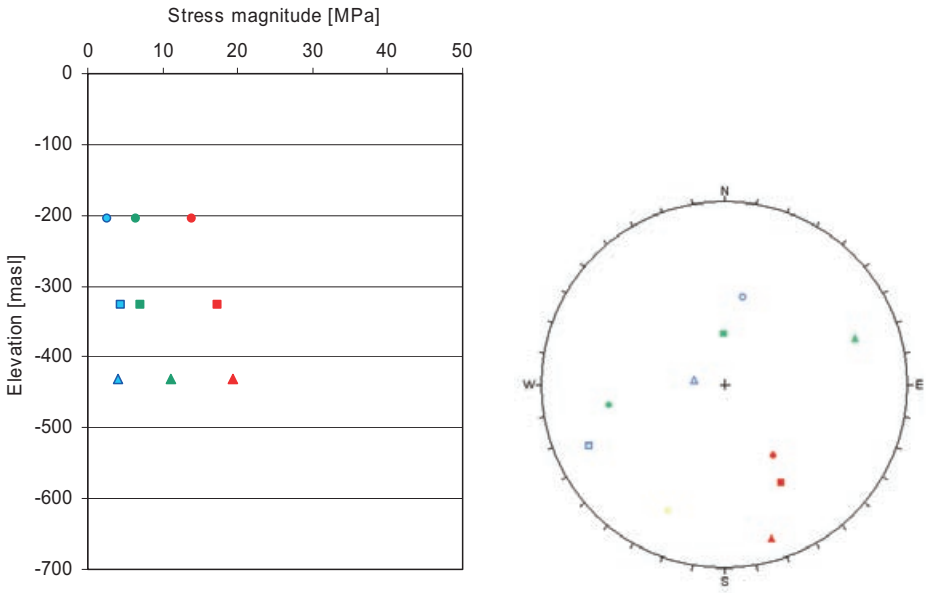

Figure 6-8. *The average values for principal stress in overcoring measurements in KLX12A a) variation of stress magnitude with depth and b) variation of stress orientation with depth; Red = σ_1, Green = σ_2 and Blue = σ_3, the symbols represent different depths (circle = –203 m, square = –326 m and triangle = –431 m). (See also Figure 6-5 and Figure 6-6 for all data in KLX12A.)*

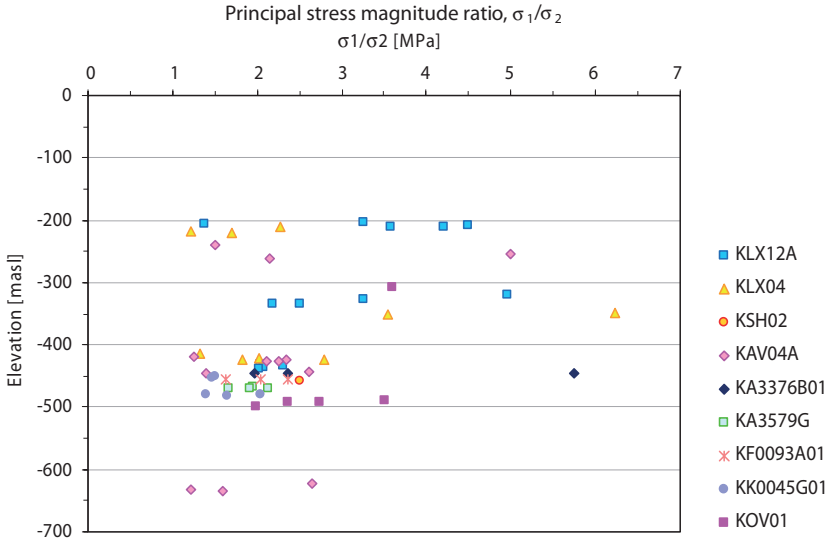

Figure 6-9. *The ratio between the maximum and the intermediate principal stresses in overcoring results from all available boreholes in the region. (One datum fall outside the x-axis range shown.)*

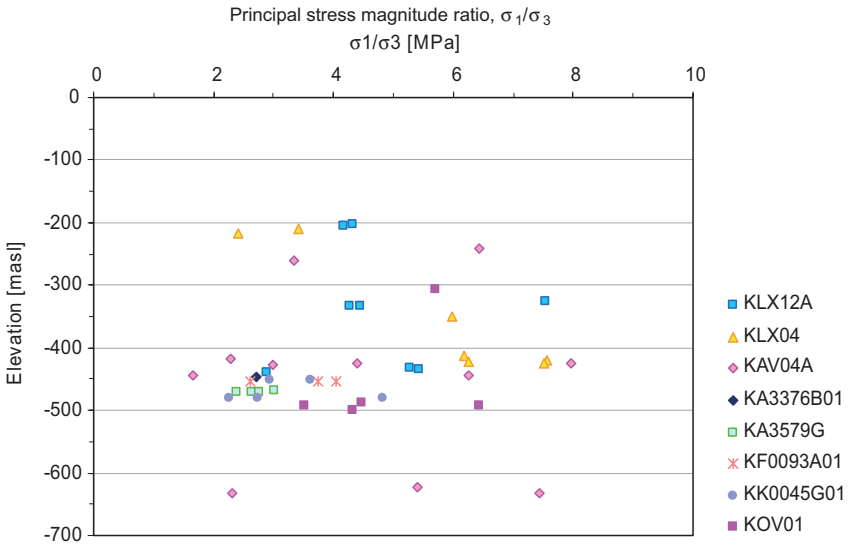

Figure 6-10. *The ratio between the maximum and the minimum principal stresses in overcoring results from all available boreholes in the region. (12 data fall outside the x-axis range shown, 8<0 and 4>10.)*

6.2.3 Hydraulic fracturing and HTPF data

Hydraulic fracturing and HTPF measurements have been performed in five boreholes. In the previous model version /SKB 2006b/ also some older HF measurements from the Äspö island (KAS02 and KAS03) were included, but to ensure similar quality on the data and they are excluded here.

The detailed primary results for hydraulic fracturing will not be presented here, but may be found in the corresponding P-reports (see Table 6-1 for reference). A compilation of all the data for the interpreted minimum principal stress is shown in Figure 6-11. The maximum horizontal stress evaluated from the traditional HF method is not used in the modelling, since there is a low confidence in this approach. (The maximum principal stress values interpreted from the measurements are presented in Appendix 6.) However, the HTPF results, i.e. the best fit inversion based on tests from two different depth intervals in KLX12A is shown for the maximum stress in Figure 6-12. The intermediate stress was assumed to be vertical and equal to the overburden in the interpretation, thus the HTPF in this case does not give any information regarding the actual dip of the principal stresses.

The orientation of the maximum horizontal stress according to the hydraulic measurements is also in the NW-SE direction, as was shown by the overcoring measurements (see Figure 6-8 and Appendix 6). The inversion results from borehole KLX12A, which is the borehole located inside the focused volume, has orientation of 132° (upper measurement level) and 161° (lower), respectively. However, hydraulic measurements are interpreted with the assumption that the major principal stresses are horizontal and vertical, and thus do not give anyu information on potential plunge in the stress field.

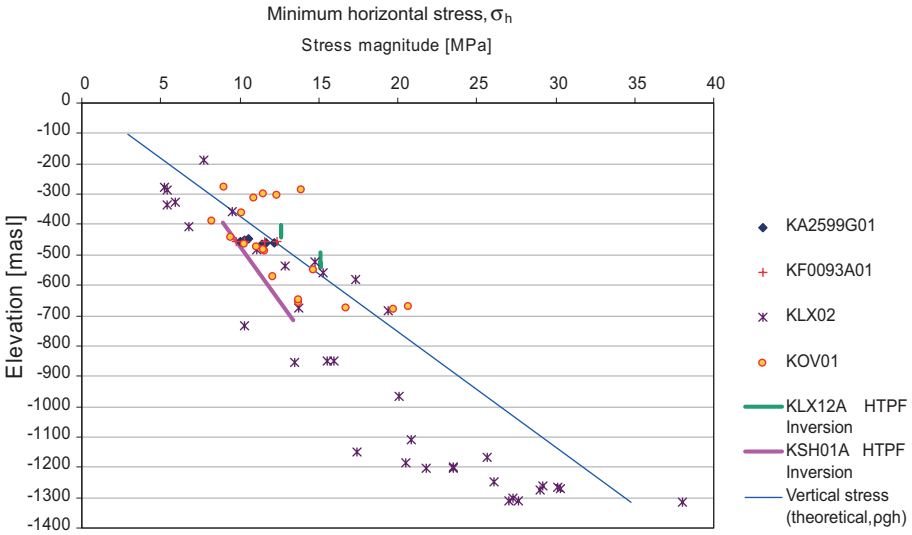

Figure 6-11. *Results from hydraulic fracturing stress measurements – Minimum horizontal stress. In KLX12A and KSH01A the result from an HTPF inversion of test results are shown.*

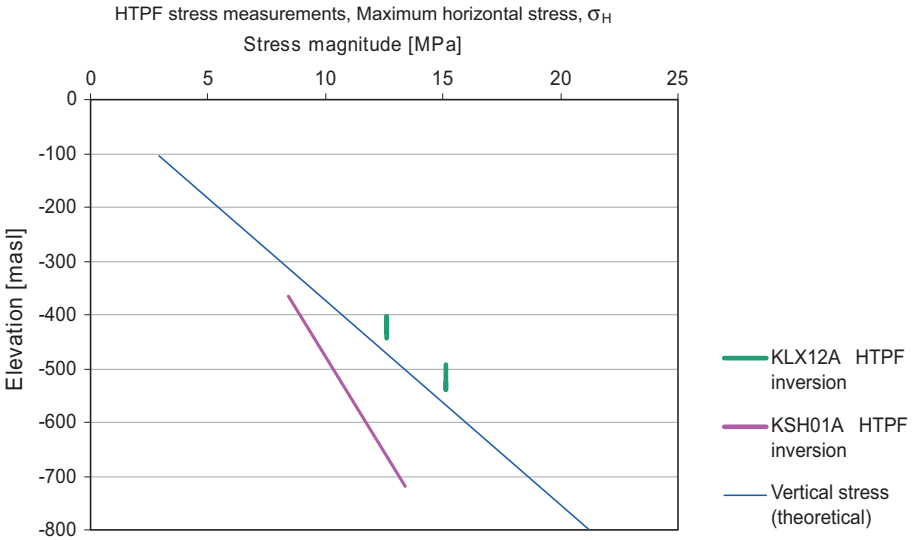

Figure 6-12. *HTPF (Hydraulic testing of pre-existing fractures) results from boreholes KLX12A and KSH01A. Maximum horizontal stress.*

6.2.4 Borehole breakout data

A methodology to infer relative stress levels from the borehole geometry was proposed for the Forsmark site by /Ask and Ask 2007/. Figure 6-13 shows examples of how the borehole breakouts may be recognised in the plots of the televiewer logging results. A visual inspection of all borehole logging plots revealed very few breakouts. In addition a detailed analysis making use of the televiewer raw data, was performed in six selected cored boreholes (KAV04A, KLX10, KLX11A, KLX12A, KLX15A and KLX18A) where breakouts were observed /Ringgaard 2009/. With the detailed analysis also the micro fallouts may be identified.

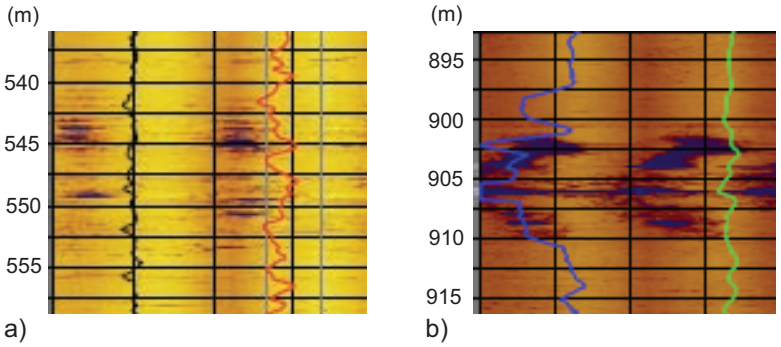

Figure 6-13. *Examples of the few breakout occurrences in the Laxemar area a) KLX12A at BH length 543 m /Nielsen and Ringgaard 2006/ and b) KLX03 at BH length 905 m /Nielsen and Horn 2004/. (See also Table 6-3.)*

All the observed borehole breakouts are listed in Table 6-2. The results from this detailed analysis, of the televiewer data are presented in Table 6-3 and in Figure 6-14 – Figure 6-19. In Figure 6-20a a rose diagram shows the orientations for the breakouts not associated with geological structures (see also Table 6-3). When the breakout is located at a structure (i.e. a fracture is intersecting) it is expected that the shape of the breakout will be influenced by the structure and therefore these cases are not reliable for the determination of in situ stress orientation. In Figure 6-20b the orientation is shown for micro fallouts (MF).

Table 6-2. Summary of all observations (including those associated with geological structures) of breakouts made in KAV04A, KLX10, KLX11A, KLX12A, KLX15A and KLX18A /Ringgaard 2009/ and KLX03, /Nielsen and Horn 2004/. The terminology used for classification of the breakouts (BB = classical borehole breakout, MF = Micro fallout, KS = Keyseat (breakout seen on only one side of the hole), WO = Washout) is defined in /Ringgaard 2009/. Classical refers to breakouts with obvious deep fallouts being located diametrically opposite to each other.

Borehole	BH Incl.	Survey length	Number of observations				Total length (m)				Mean Azimuth [1] (°)			
	(°)	(m)	BB	MF [2]	KS	WO	BB	MF	KS	WO	BB	MF	KS	WO
KAV04A	–84.90	904.0	17	8 (3)	4	0	17.1	29.2	0.4	–	58.7	42.0	45.5	–
KLX10	–85.18	901.2	3	2 (1)	0	1	26.6	16.7	–	5.8	65.3	26.0	–	0.0
KLX11A	–76.76	892.3	2	0	2	0	0.6	–	0.5	–	50.0	–	69.0	–
KLX12A	–75.30	502.3	2	6	3	0	3.1	18.0	0.6	–	84.5	76.7	56.0	–
KLX15A	–54.41	920.4	5	15 (2)	0	0	6.5	149.9	–	–	16.0	59.2	–	–
KLX18A	–82.10	511.3	0	3	0	0	–	20.2	–	–	–	38.0	–	–
KLX03 [3]	–74.92	900.4	1	–	–	–	7	–	–	–	50.0	–	–	–
Total		5,531.9	30	34 (6)	9	1	60.9	231.1	1.5	5.8				
% of survey length							1.1	4.2	0.02	0.1				
Mean of total (°)											53.1	56.4	54.2	0.0

1. The mean values are calculated as point values (not weighted with respect to breakout length).
2. Number of observations with no recorded azimuth is given in parenthesis.
3. This observation was made by visual inspection of the televiewer log /Nielsen and Horn 2004/. MF, KS and WO not studied.

Table 6-3. Classical borehole breakouts (BB) not associated with geological structures found in KAV04A, KLX03, KLX10, KLX11A, KLX12A and KLX15A (in KLX18A, there were no observations made) /Nielsen and Horn 2004/ and /Ringgaard 2009/. (See also Figure 6-20.)

Borehole	Azimuth (°)	BH length Secup	Seclow	Main rock type code[2] / Occurrence	In DZ (ESHI)
KAV04A	78	940.96	941.18	501030	No
	66	953.36	954.18	501044, 501036 / 511058 (veins)	No
	58	956.63	956.76	501036 / 511058 (vein)	No
	32	965.47	969.59	501036 / 511058 (veins), 501030	No
	46	971.89	973.18	501030 / 511058 (dyke and veins)	No
	46	986.00	986.72	511058	No
	48	999.10	999.60	501058 / 501058	No
	32	1,000.60	1,002.33	501058 / 501058	No
KLX03[1]	50	903	910	511058 / 511058 (veins)[3]	Possible DZ
KLX11A	32	417.80	418.25	501036	Possible DZ
KLX12A	75	542.96	545.40	501036 / 511058 (veins)	No
	94	548.95	549.65	501036 / 511058 (vein)	No
KLX15A	0	675.13	676.07	501044 / 511058, 501036	Possible DZ
	30	771.49	771.99	501036	Possible DZ (ZSMNE107A)
	8	939.22	940.55	501036	No
	26	984.47	985.81	501036 / 511058 (veins)	Possible DZ (ZSMNW042A)
	16	992.50	994.85	501036 / 511058 (veins)	Possible DZ (ZSMNW042A)

1. This observation was made by visual inspection of the televiewer log /Nielsen and Horn 2004/.
2. For the corresponding rock type name, see Table 2-1.
3. Several (N = 5) veins of 511058 surrounded by 501036.

Classical borehole breakouts not associated with geological structures tend to be more common in quartz monzodiorite (501036) with veins of fine-grained granite (511058), see Table 6-3. The general picture is that the number of micro fallout and breakout observations in KAV04A, KLX12A, KLX15A and KLX18A increase with depth (Figure 6-14 and Figure 6-17 to Figure 6-19). However, it may be concluded that in the Laxemar local model volume the occurrence of breakouts is very limited. In total about 1% of the surveyed length corresponds to breakouts, and these are for the most part located at great depth.

Due to the stress concentration on the borehole walls the orientation of the breakouts is expected to be in the direction perpendicular to the major horizontal stress. The confidence in the correlation between breakout orientation and in situ stress orientation is higher for the vertical (or subvertical) boreholes. Washouts, keyseats and breakouts associated with structures (fractures) may not be used as indicators for in situ stress conditions.

In the case of borehole KLX15A (Figure 6-18) the azimuth change with depth and the breakout azimuth is different compared to KLX12A. Two circumstances may be the explanation to this, borehole KLX15A is inclined and at the bottom of the borehole stresses may be influenced by the deformation zone ZSMNW042A.

It may be noted from the rose diagram in Figure 6-20a that the mean orientation is 43.4°, which means that the breakouts indicate a horizontal stress trending 133.4°. This NW-SE direction is in agreement with the direct stress measurement data.

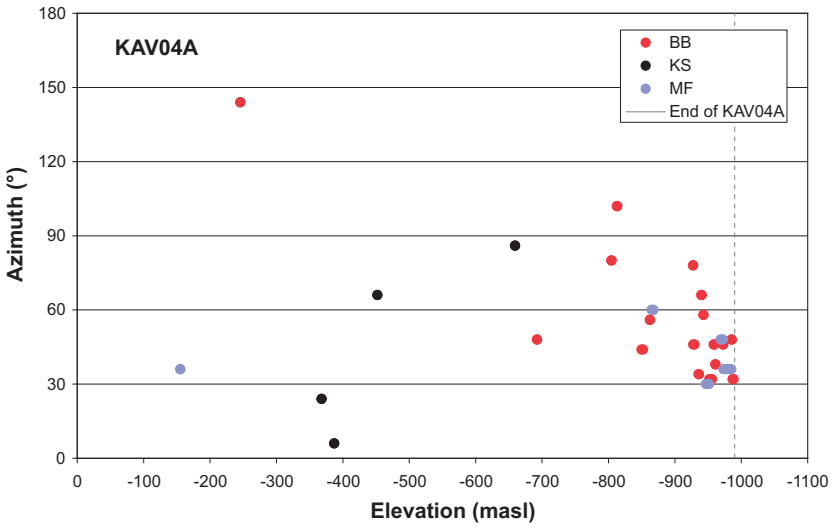

Figure 6-14. *Plot showing azimuth for all of the observed breakouts (with recorded azimuth) in KAV04A as a function of elevation, (BB = 17, MF = 5, KS = 4).*

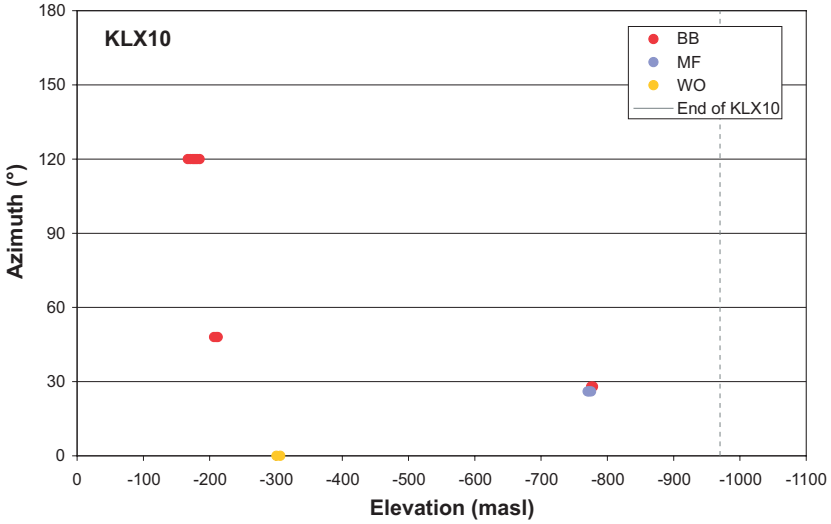

Figure 6-15. *Plot showing azimuth for all of the observed breakouts (with recorded azimuth) in KLX10 as a function of elevation, (BB = 3, MF = 1, WO = 1).*

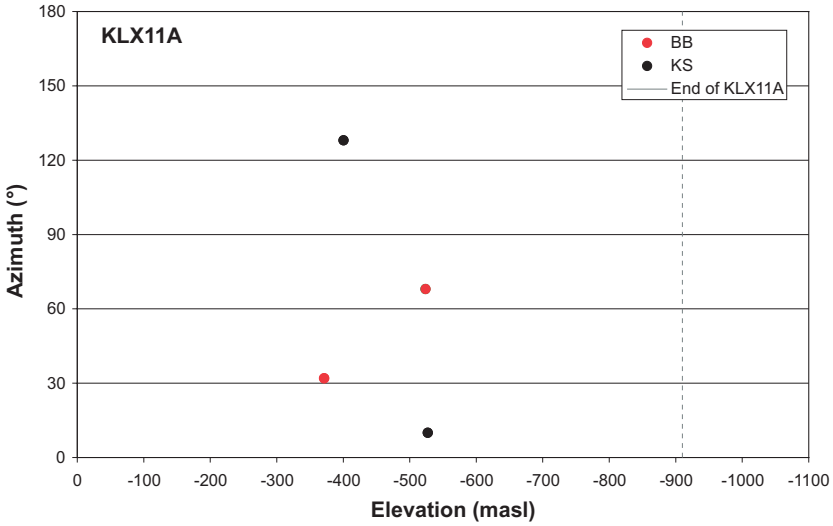

Figure 6-16. *Plot showing azimuth for all of the observed breakouts (with recorded azimuth) in KLX11A as a function of elevation, (BB = 2, KS = 2).*

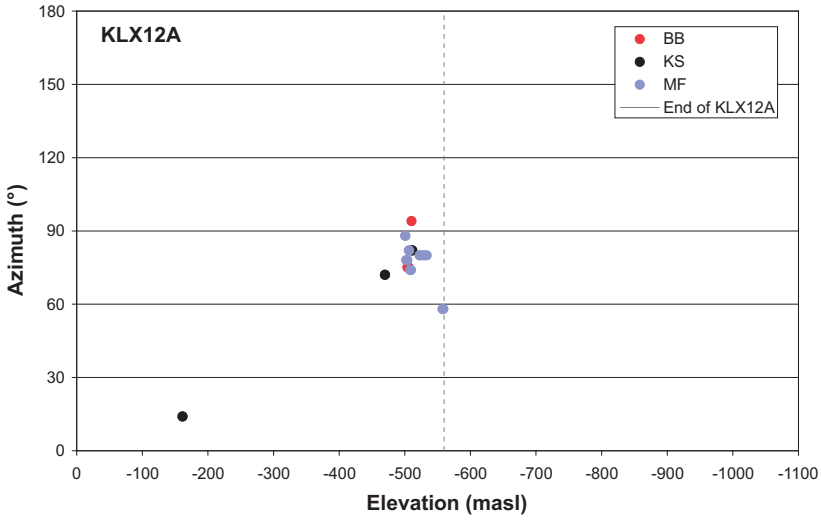

Figure 6-17. *Plot showing azimuth for all of the observed breakouts (with recorded azimuth) in KLX12A as a function of elevation, (BB = 2, MF = 6, KS = 3).*

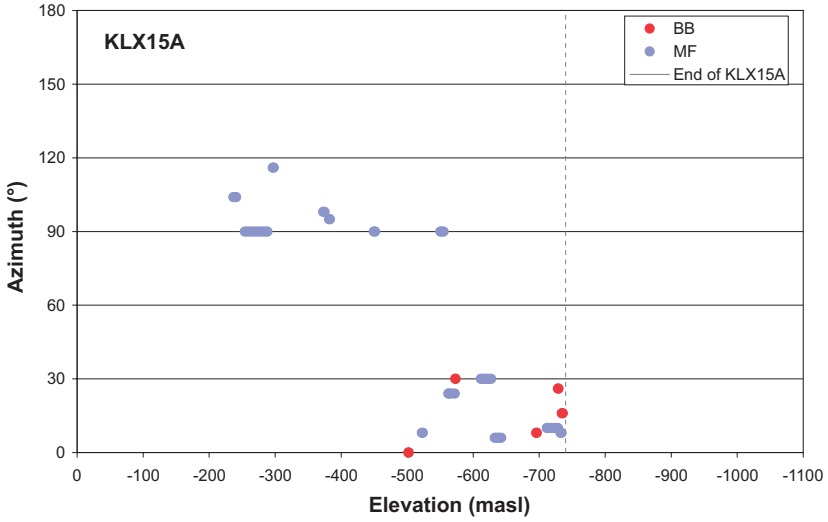

Figure 6-18. *Plot showing azimuth for all of the observed breakouts (with recorded azimuth) in KLX15A as a function of elevation, (BB = 5, MF = 13).*

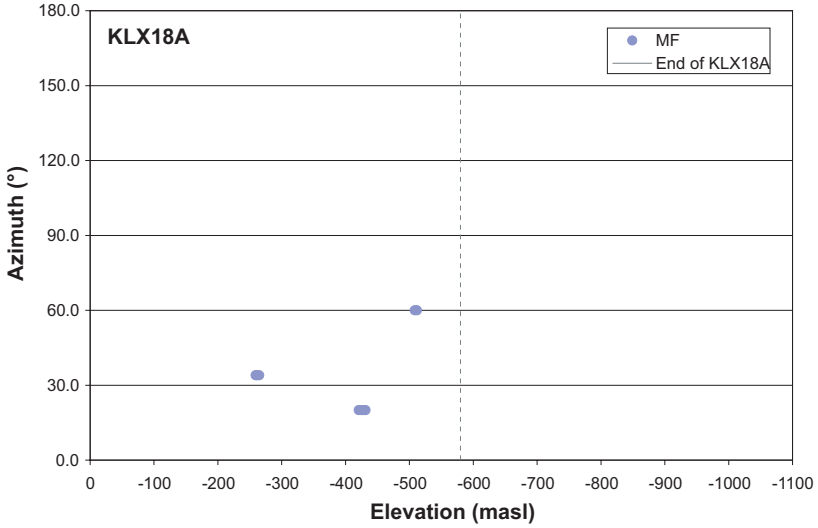

Figure 6-19. *Plot showing azimuth for all of the observed breakouts (with recorded azimuth) in KLX18A as a function of elevation, (MF = 3).*

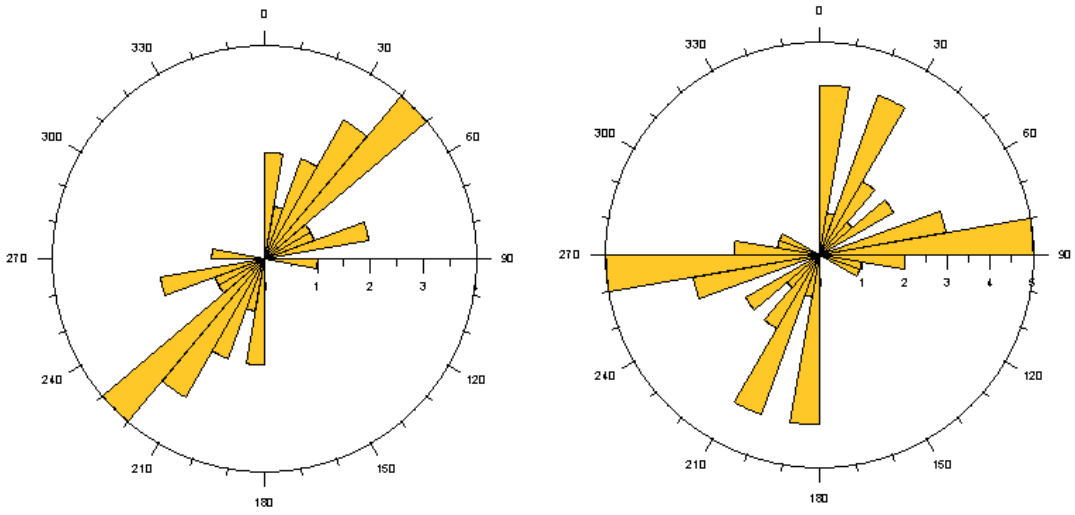

a) BB b) MF

Figure 6-20. *a) Classical borehole breakouts not associated with geological structures (17 BB) KAV04A, KLX03, KLX11A, KLX12A and KLX15A (Median=46°and Mean=43.4°) and b) Micro fallouts not associated with geological structures (26 MF) for boreholes KAV04A, KLX11A, KLX12A, KLX15A and KLX18A (Median=59° and Mean=57.0°). Note that the observations are not weighted with respect to length.*

6.2.5 Core disking and core damage

The phenomenon that the drill core is broken up in several cm-thick disks, separated by fresh fractures perpendicular to the borehole axis, is called "core disking" /e.g. Amadei and Stephansson 1997/. The disking is caused by tensile forces developing at the base of the core during the drilling. If the in situ stresses are high, the probability of core disking increases dramatically. This is why the identification of core disking during core mapping is important indirect information for the stress modelling.

Core disking has been noted in a total of 6 cored boreholes. The total extent of core disking is very limited, about 5 m in all, and the locations of the occurrences are listed in Table 6-4. The main occurrence is below 900 m borehole length in KLX03.

Table 6-4. List of core disking observed in all cored boreholes at Laxemar, as mapped in Boremap (Sicada).

Borehole	Borehole length (m)	Section length (m)	In DZ (ESHI)	Rock code (Table 1-3)
KLX03	901.90–902.05	0.15	No	511058
KLX03	903.20–903.96	0.76	No	511058
KLX03	903.96–904.40	0.44	DZ7	511058
KLX03	906.66–906.82	0.16	No	511058
KLX03	906.89–906.98	0.09	No	511058
KLX03	906.98–907.64	0.66	No	511058
KLX03	907.86–907.98	0.12	No	511058
KLX03	983.59–983.90	0.31	No	501061
KLX09	435.61–435.64	0.03	No	501044
KLX10	800.80–800.93	0.13	No	501044
KLX12A	549.23–549.40	0.17	No	501036
KLX15A	704.40–704.44	0.04	No	501061
KLX15A	992.93–993.24	0.31	DZ 20	501036 [1)]
Total		3.37		

1) Occurrence of two fine- to medium-grained granite (511058) veins and a quartz monzonite to monzodiordiorite (501036) ductile shear zone.

6.3 Evaluation of stress variability caused by major deformation zones

6.3.1 Modelling approach

The objective of the numerical modelling is to investigate how much stress variation that may be expected in the local model volume due to the configuration of major deformation zones that we have described (see Chapter 2). Stress data are available in some points in the area, as described in previous sections of this chapter, and the stress results in the numerical model will be compared to the measurements in an attempt to explain the observed differences in data. In this way we want to use numerical modelling to increase our understanding of the site, and as a tool in the estimation of a stress model to be used for future prediction of the in situ stress in the whole local model volume. The strategy for performing the numerical analyses for in situ stress variation is further described in /Hakami et al. 2002/.

The applied modelling sequence is the following:

- A numerical model geometry is built, using 3DEC /Itasca 2008/, that complies with the geometry of the major deformation zones in the area. The deformation zones are simulated as single fracture planes between deformable blocks.
- The properties of the fractures are all put to very high strength and stiffness values, making them "mechanically invisible" in the model.
- The properties of all the rock blocks between the deformation zones, cf. Table 6-4, are taken as being corresponding to an overall deformation modulus of 40 GPa, which is slightly lower than what is modelled for the fracture domains, but considered realistic for the large blocks, including the MDZ. The Poisson's ratio is 0.15 in the model of the rock blocks. The potential influence on stresses from stiffness differences, caused by rock type differences or fracturing difference, is thus not studied in this numerical model. The influence from stiffness differences are expected to be quite low since the stiffness differences are limited (see further /Hakami et al. 2002/).
- The model blocks are first initiated with isotropic stress levels equal to the gravitational forces, i.e. $\sigma_{1,2,3} = \rho g z$
- The model is run to equilibrium for a no-displacement boundary condition.
- The properties of the deformation zones are set to the lower values that are expected to correspond to the actual deformation zones (see Table 6-6). The properties were selected based on the estimation performed in Section 5.4.2.
- The model is run to equilibrium again, and thereafter the SE and NW boundaries are slowly moved towards the centre of the model, simulating the prevailing tectonic compression expected in the SE-NW direction. In this way the stresses inside the model blocks build up.
- The deformation zones and the blocks deform according to the stiffness parameters applied and at some of the deformation zone planes the shear stresses become high enough to cause the plane to slip. On these planes the deformation becomes larger and the stresses in the model have to redistribute more.
- After a certain displacement of the boundaries (most cases about 8 m) the movement is stopped and the model is run to equilibrium again. This amount of compression does not correspond to any actual known compression; it is merely a means of getting roughly the stress levels in the numerical model that we have observed in measurements.
- Different model cases using different properties on the deformation zones have been compared (see Table 6-5). The estimation of properties for deformation zones has a great deal of uncertainty and therefore alternative models were run for the friction and for the case of deformation zone properties assigned, cf. Table 6-6. It was assumed that some reduction of the friction angle was appropriate to assume, compared to the estimation in Section 5.4.2, due to the effect of pore pressure.

The different models run are listed in the Table 6-7. The results from each run are presented in Appendix 7.

Table 6-5. Material parameters used for different model cases (see Table 6-7). Every deformation zone is, for each run, assigned to a certain "material class, Jmat 1–4" (cf. Table 6-6).

Friction case	Rock mass [1] (not varied)	DZ Jmat 2	DZ Jmat 3	DZ Jmat 4
H (higher)	Density = 2,700 Bulk mod = 19.05e9 Shear mod = 17.39	Kn = 400e6 Ks = 100e6 ϕ = 37 Coh = 8e6	Kn = 1400e6 Ks = 310e6 ϕ = 29 Coh = 0.9e6	Kn = 400e6 Ks = 100e6 ϕ = 29 Coh = 0.9e6
L (lower)	Density = 2,700 Bulk mod= 19.05e9 Shear mod = 17.39	Kn = 400e6 Ks = 100e6 ϕ = 32 Coh = 8e6	Kn = 1400e6 Ks = 310e6 ϕ = 24 Coh = 0.9e6	Kn = 400e6 Ks = 100e6 ϕ = 24 Coh = 0.9e6

1) Rock mass = Jmat 1.

Table 6-6. Division of the 19 included deformation zones in three different property cases (Jmat) to be used in the numerical models. The parameter values for Jmat are given in Table 6-5.

DZ name	DZ material propery cases			Estimated Kn according to Section 5.4	Estimated ϕ according to Section 5.4
	I	II	III		
	[Jmat]	[Jmat]	[Jmat]	[MPa/m]	[°]
ZSMEW002A	4	4	4	390	34
ZSMEW007A	4	4	4	450	34
ZSMEW946A	3	3	3	2,960	34
KLX11_DZ11	3	3	3	2,690	34
ZSMNE004A	2	3	2	450	45.9
ZSMNE005A	2	2	2	200	42.5
ZSMNE006A	2	2	2	330	41.5
ZSMNE011A	2	2	2	610	44.8
ZSMNE012A	2	3	4	390	42.6
ZSMNE024A + ZSMNE031A	2	4	2	460	40.5
ZSMNE107A	2	2	2	1,490	43.7
ZSMNE942A	3	3	3	2,730	34
ZSMNS001A–E	4	4	4	570	34
ZSMNS059A	4	4	4	780	34
ZSMNW042A	2	4	4	1,400	44.8
ZSMNW052A	3	3	3	1,940	34
ZSMNW928A	3	3	3	2,220	34
ZSMNW900A	2	2	2	–	–
ZSMEW038A+ ZSMEW009A	2	2	2	1,360	44.8

Table 6-7. List of different 3DEC models analysed.

Model case	DZ friction case (Table 6-5)	DZ material property case (Table 6-6)	Model compression case Boundary maximum displacement (m)
Model 1	H	I	7.82
Model 2	L	II	7.82
Model 3	L	III	7.82
Model 4	L	I	7.82
Model 5	H	III	7.82
Model 6	H	II	7.82
Model 7	H	I	4.23
Model 8	H	I	11.45
Model 9	H	I	15.06

6.3.2 Geometry of the numerical model

Figure 6-21 shows the whole model block volume. The block is divided into regions with denser mesh in the central parts where the model is supposed to be demonstrating stress variation. The orientation of the outer boundaries are selected parallel to the assumed direction of compression, NW-SE (132°, based on the results from stress modelling in previous version Laxemar 1.2).

Figure 6-22 shows the deformation zones cutting the model block. The larger zones extend out to the borders of the Laxemar-Simpevarp regional model area. The location, orientation and terminations of these deformation zones, which are simulated as single fracture planes, are based on the deformation model (see Section 2.1.3 and /Wahlgren et al. 2008/). Figure 6-23 shows a similar, but more close up picture of the deformation zones in the numerical model.

The horizontal sections through the 3DEC model given in Figure 6-24 and Figure 6-25 may be compared with the horizontal sections through the geological deformation zone model shown in Figure 2-7.

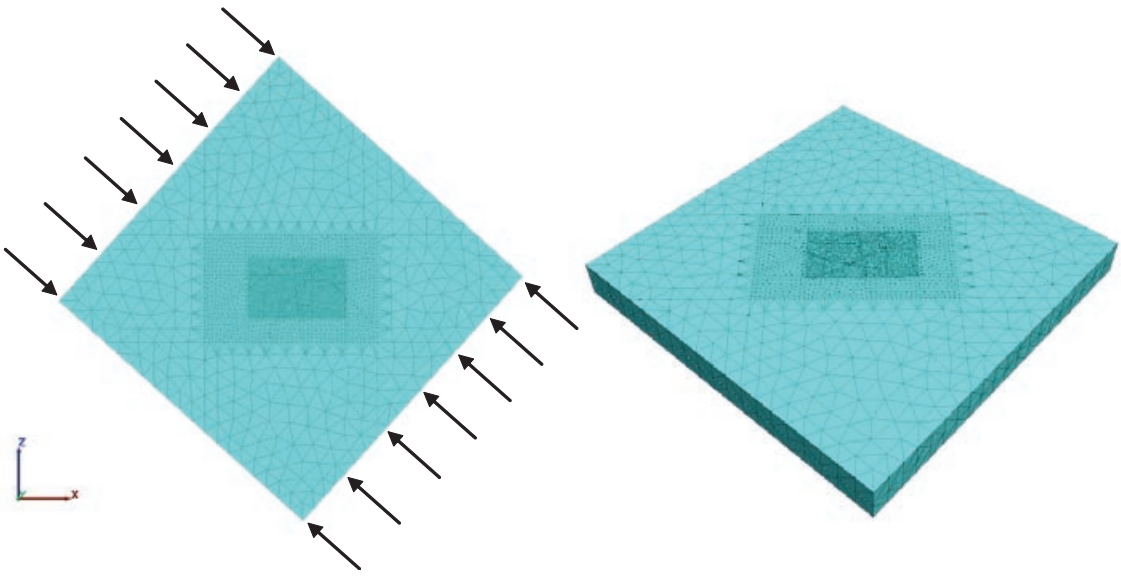

Figure 6-21. *The geometry of the numerical model built to simulate stress variation at the site. The size of the block is 40×40×4 km. The mesh is denser in the central parts were the Laxemar local model area is located.*

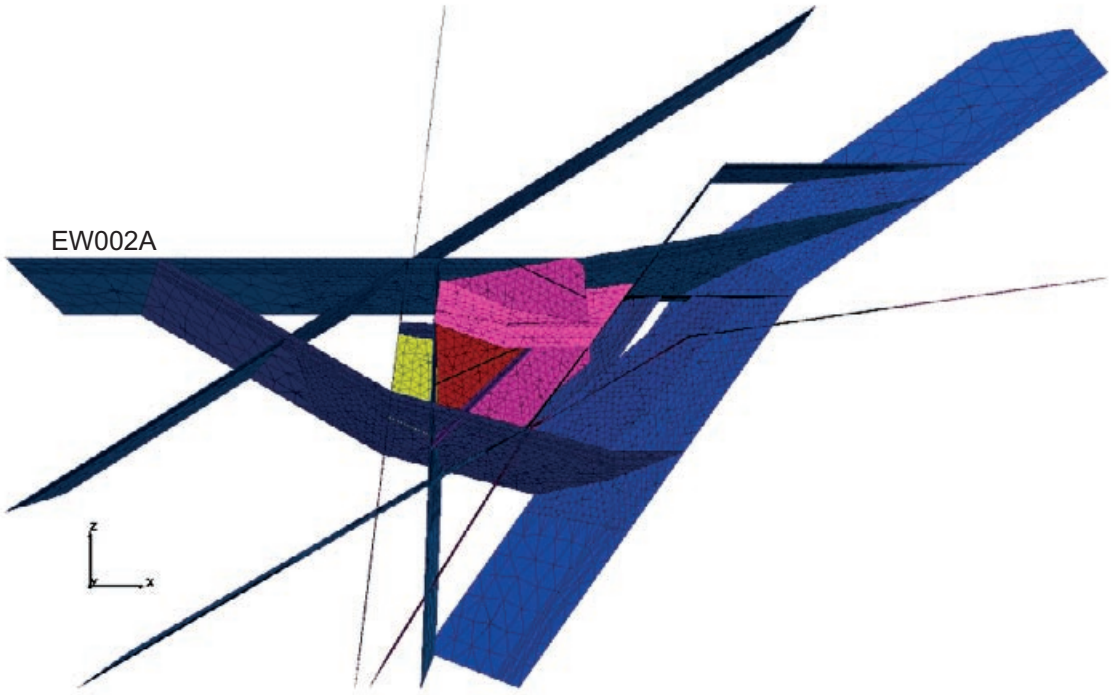

Figure 6-22. *The major deformation zones at the site are included in the numerical model (3DEC) as fracture planes (Plan view). The location and orientation of the zones is based on the deterministic deformation zone model. (Horizontal sections in Figure 6-24 and Figure 6-25 and horizontal sections including DZ names in Figure 1 a)–c) in Appendix 7.)*

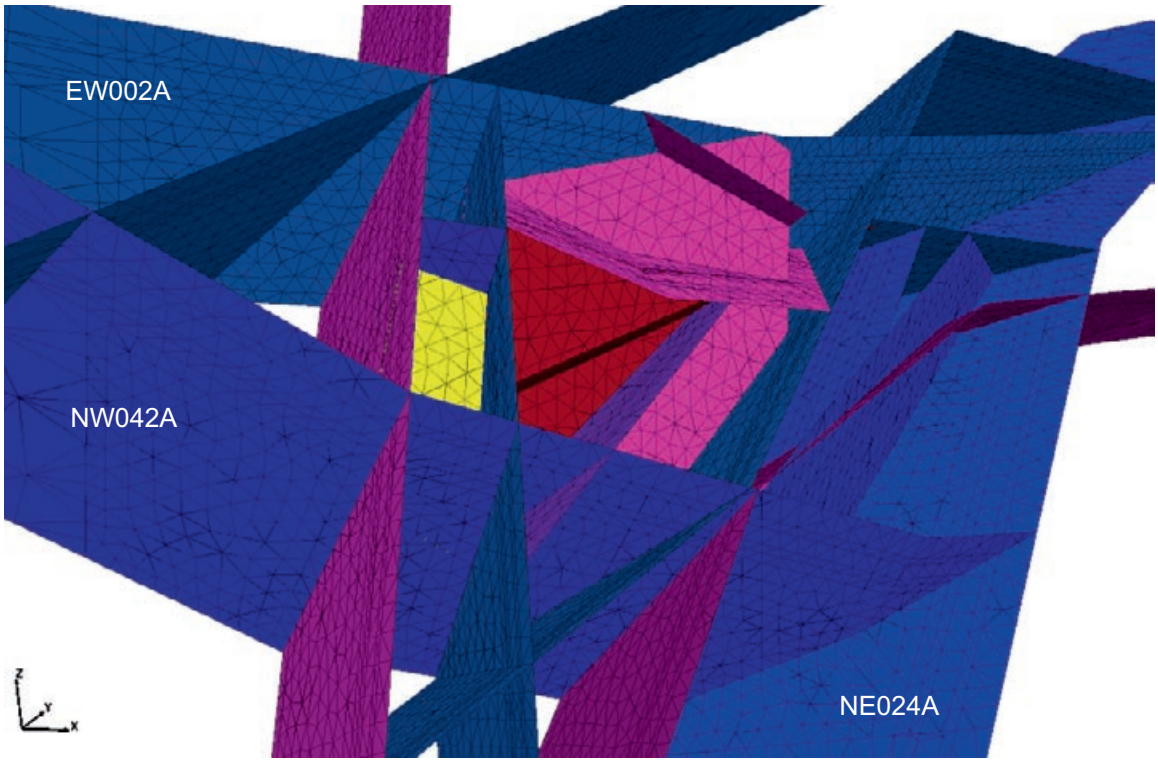

Figure 6-23. *A close up of the fracture planes simulating the deformation zones in the Laxemar area. (View towards north).*

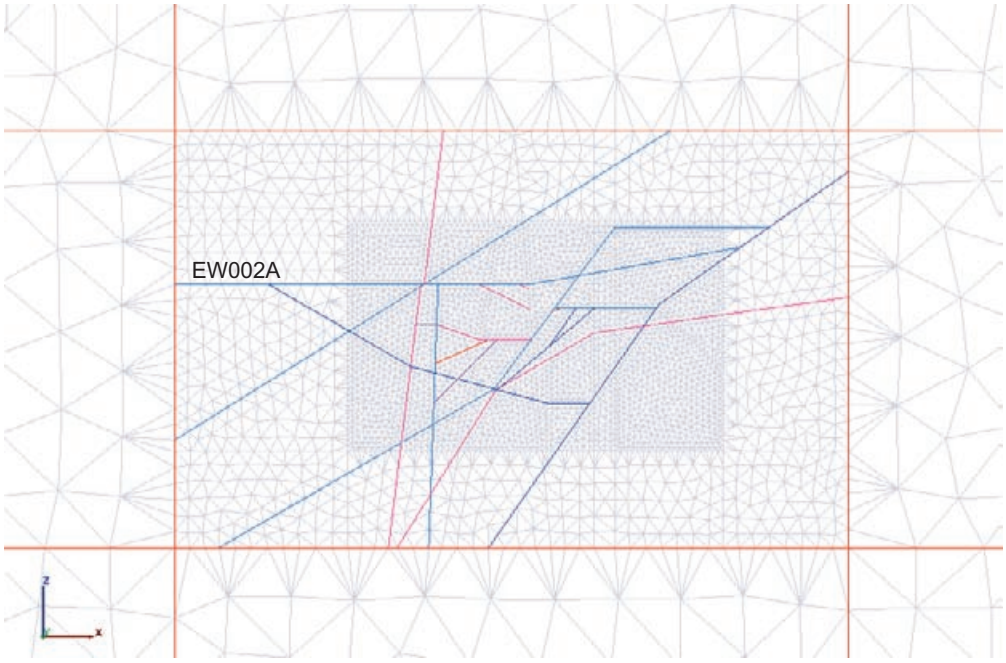

Figure 6-24. *Horizontal sections through the numerical model at ground surface; the outer red lines correspond to the region model area (13×21 km), and the major deformation zones are modelled to terminate against this boundary. (See Figure 1 (a)–(c) in Appendix 7 for DZ names.)*

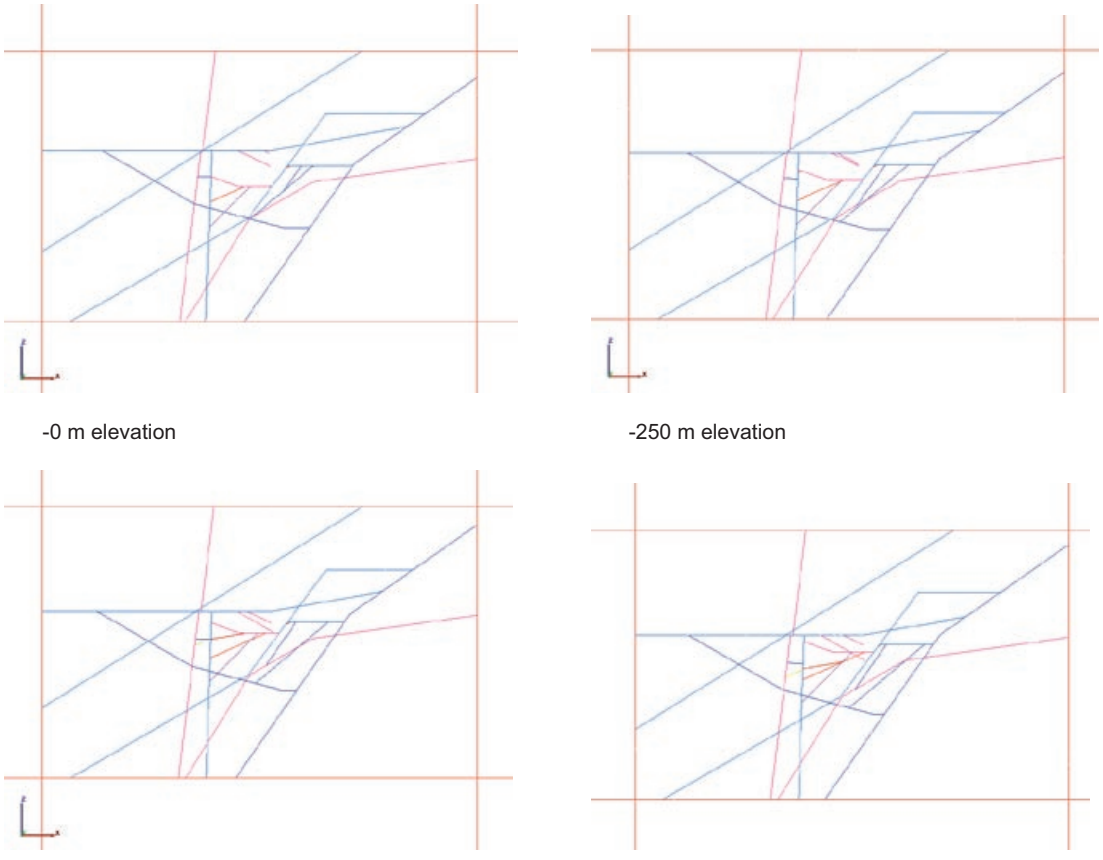

Figure 6-25. *Horizontal sections through the model at different elevations (cf. the horizontal sections through the DZ model). Compare with DZ model in Section 2.1.3. The red square is 13×21 km. (See Figure 1 (a)–(c) in Appendix 7 for DZ names.)*

6.3.3 Results from the numerical model

As an example of results from the numerical modelling the stress tensors calculated in a horizontal section through the numerical model at 200 m, 400 m and 600 m depth are shown in Figure 6-26 through Figure 6-28. The colour legend gives the maximum principal stress. It can be noted that within the focused volume the lowest σ_1 stress is in about 16 MPa and the highest σ_1 stress about 23 MPa, for 200 m depth. Similarly the spatial difference is from about 19 MPa to 26 MPa at 400 m depth and from 27 MPa to 34 MPa. The results from all models are given in Appendix 7.

Corresponding stress tensor plots in a vertical section through the same model (Model 2) is presented in Figure 6-29 and Figure 6-30. Due to the strong depth dependence, the relatively small spatial differences are almost not visible in the vertical sections. If zooming in (and changing legend) at the ground surface where EW007A intersects the Laxemar model volume, a change in stress may be noticed also in vertical section. Results from different model runs are presented as horizontal section in Appendix 7. There are no major differences between the different models that are compressed to the same degree (Model 1–6). However, since there is an agreement in the tendency for the major horizontal stress to plunge southeast, according to overcoring data in KLX12A, we consider the Model 2 that shows such influence from ZSMNW042A (Figure 6-30), to be the best fitting.

6.3.4 Comparison between numerical model results and primary data along boreholes

To enable a comparison with primary data, the results from the numerical models along the approximate locations of a number of actual boreholes, are plotted together with direct measurement results and the core disking and breakout information, in the same diagram. The approach for using the observation of stable cored boreholes (no breakouts) in the stress modelling is described in the following section.

Upper stress limit estimation based on borehole breakout observations

Based on the assumption that borehole breakout would actually occur at a certain point with known rock strength properties, the expected stress level needed to cause this borehole instability (borehole breakout) may be calculated. Since we generally do *not* observe any borehole breakouts (see Section 6.2.4) these stress values may be regarded as estimates of the very upper limit for the expected *actual* stress at this point in the borehole.

Two different strength criteria for the stress limits have been applied. The first criterion is empirical, introduced and described by /Martin 2007/ in the Forsmark modelling, and this empirical failure criterion assumes that the uniaxial compressive strength (UCS) will determine the stress value at borehole instability. Failure is according to the criterion expected when:

$$3\sigma_H - \sigma_h \geq UCS \times SR \qquad \text{Equation 6-1}$$

In our case a "spalling ratio" value SR = 0.56 was applied, based on experience from other sites /Martin 2007/. To solve for the stress magnitudes it is further needed to assume a certain ratio between the horizontal stresses, $\sigma_H/\sigma_h = R$. This breakout criterion does not involve any dependence of the vertical stress.

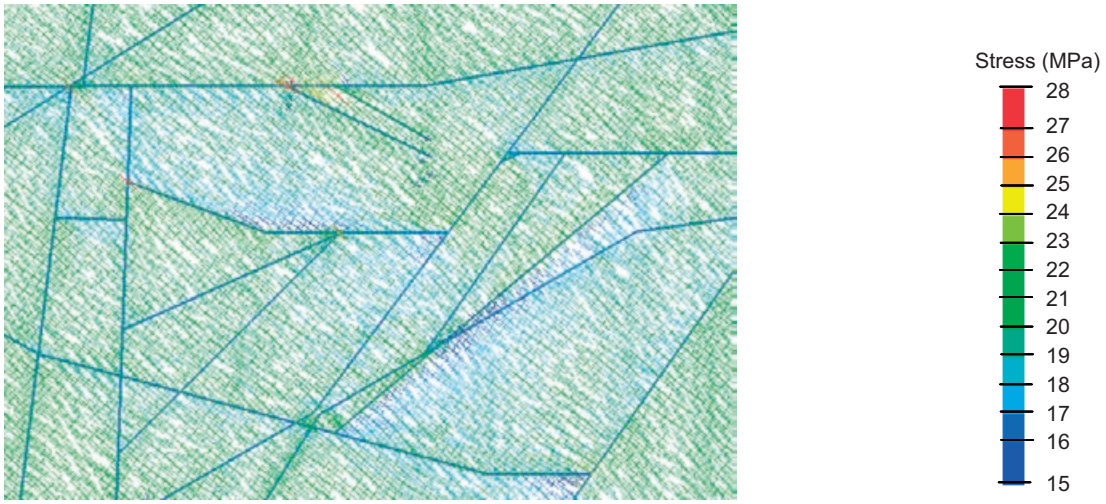

Figure 6-26. *Stress tensors coloured by magnitude of maximum principal stress in horizontal section at –200 m elevation (Model 2). (See Figure 1 (a)–(c) in Appendix 7 for DZ names.)*

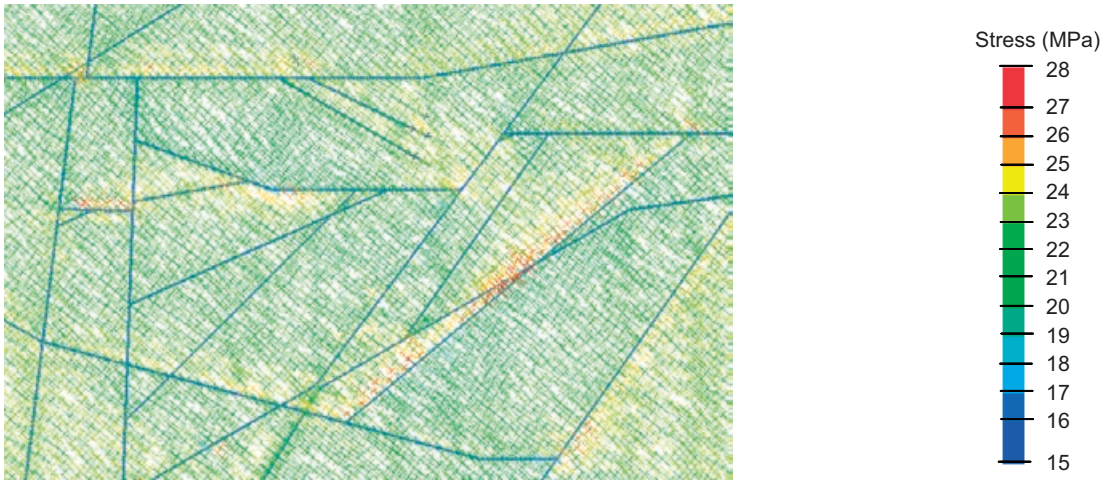

Figure 6-27. *Stress tensors coloured by magnitude of maximum principal stress in horizontal section at –400 m elevation (Model 2). (See Figure 1 (a)–(c) in Appendix 7 for DZ names.)*

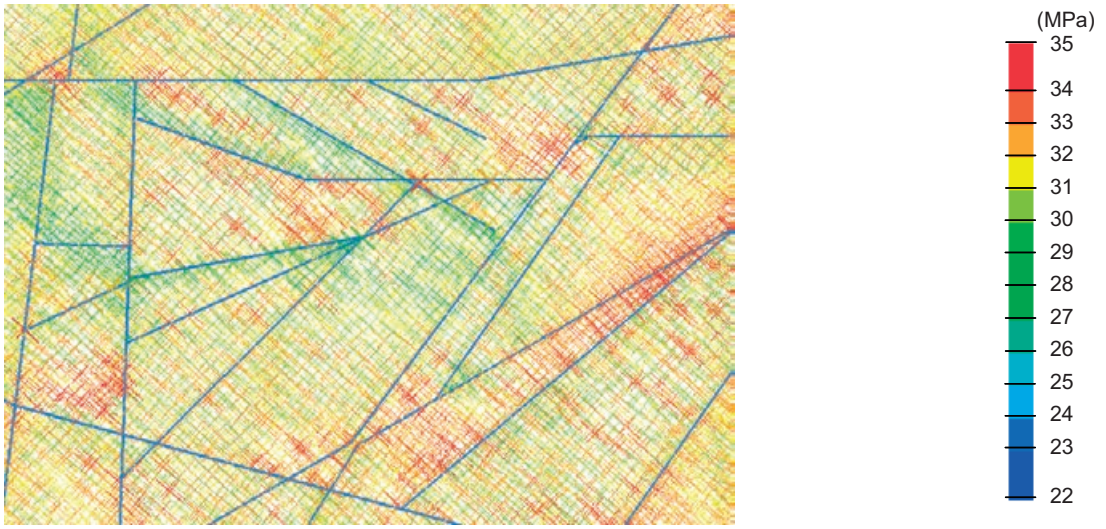

Figure 6-28. *Stress tensors coloured by magnitude of maximum principal stress in horizontal section at –600 m elevation (Model 2). (See Figure 1 (a)–(c) in Appendix 7 for DZ names.) Note the different legend.*

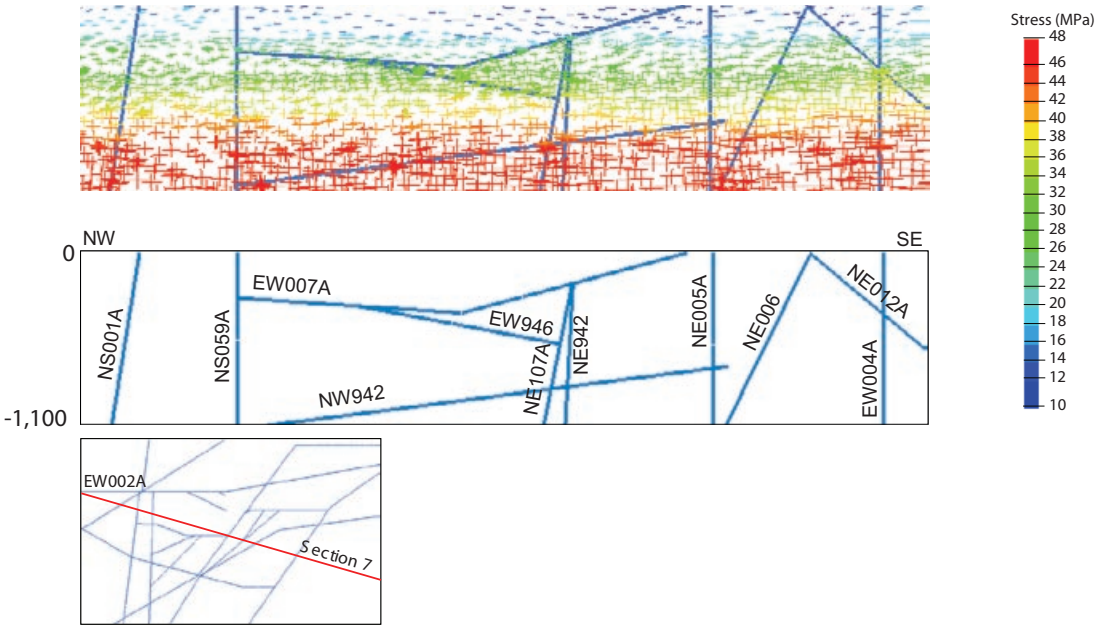

Figure 6-29. *Stress tensors coloured by magnitude of maximum principal stress in NW-SE vertical section (Section 7); looking northeast (Model 2).*

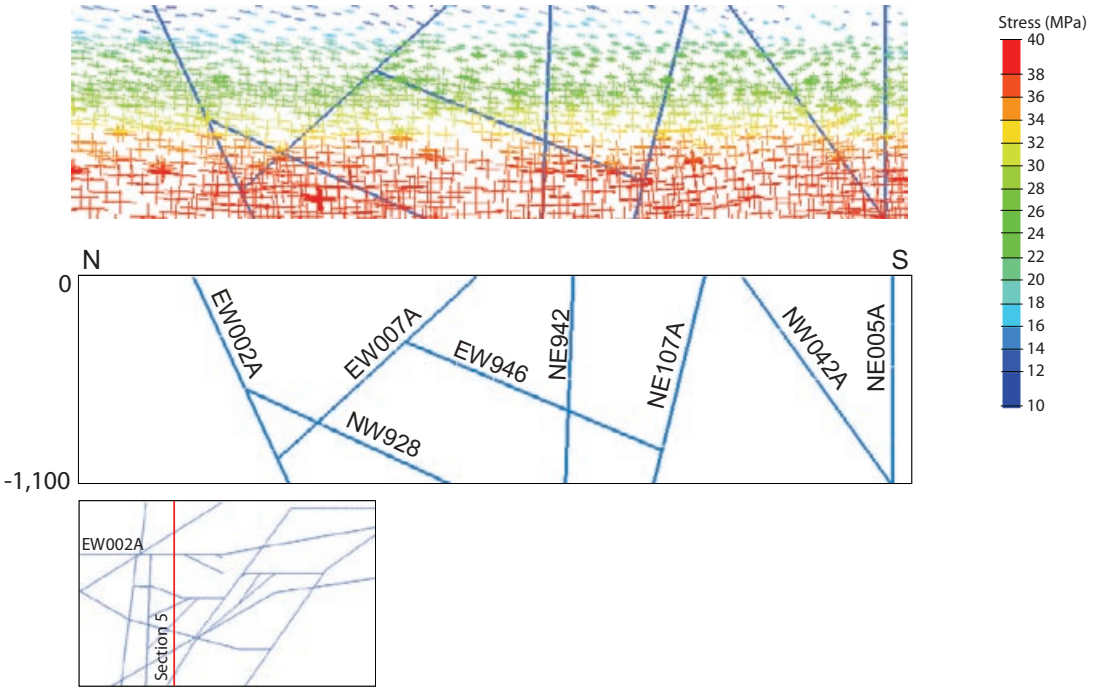

Figure 6-30. *Stress tensors coloured by magnitude of maximum principal stress in N-S vertical section (Section 5); looking east (Model 2).*

The second criteria applied is the Mogi-Coulomb criteria which states that the octahedral shear stress at failure is a function of the mean of σ_1 and σ_3, according to /Al-Ajmi and Zimmerman 2006/. The Mogi-Coulomb criterion is similar to the Mohr-Coulomb failure criterion extended to three dimensions, allowing the intermediate stress to have an influence on the failure stress. As σ_2 is assumed to be vertical in Laxemar, the borehole failure can be stated as in the following equation (note: derivation here is for Laxemar)

$$(A+B)^2 - 3(AB) = (a + bA)^2 \qquad \textit{Equation 6-2}$$

Where

$A = 3\sigma_H - \sigma_h$

$B = \sigma_v + 2\nu(\sigma_H - \sigma_h)$

$a = 2c\ Cos(\phi)\ ,\ \ b = Sin\ (\phi)$

where c and ϕ are the traditional cohesion and frictional coefficients that may be estimated from triaxial testing results for the appropriate confinement level. As in the empirical case one has to assume the ratio between horizontal stresses $\sigma_H / \sigma_h = R$ and solving the Equation 6-2 then yields σ_H and σ_h at failure.

Figure 6-31 shows a comparison of the resulting maximum horizontal stress (σ_H) at failure, when applying the two critera, for different rock types (assuming the same value on R = 3.7 in both cases). Figure 6-32 gives the correponding comparison for the minimum horizontal stress at failure, σ_h.

Figure 6-33 shows the influence on caluculated failure stresses for different R values for rock type Ävrö granodiorite, while Figure 6-34 shows the influence of different spalling ratios in the empirical criterion (Equation 6-1), assuming a constant value 3.7 for R.

Table 6-8 shows the values on c, ϕ and UCS used for each rock type. Note that these values on the cohesion and friction angle are not the same as in Table 3-9 (which gives the different parameter models for intact rock) because in the case of the boreholes stability at depth we want to have the cohesion and friction that gives us the strength that expected for high confining stress conditions (around 20 MPa), while in Table 3-9 the parameters at selected to give a fair fit to the span 0–15 MPa confinement (see Section 3.2.4).

Figure 6-31 to Figure 6-34 indicate how sensitive the results are to the input parameters. It seems that among them the strength parameters, i.e. the rock type (or actually the mean compressive strength of the actual rock type), is what is the most important to get the right estimation. If this is assumed well known the uncertainty in R could give a variation of σ_H from 38 to 41 MPa as R changes from 2 to 4 at 500 m depth (Figure 6-33). The ratio σ_H/σ_h is, in the following comparison for the Laxemar case, assumed to be 3.7, the basis for this particular choice is however quite weak, see Figure 6-10. (The previous stress model (Laxemar version 1.2 /SKB 2006b/) gave this ratio at 500 m depth and this is the explanation of the picked number).

From Figure 6-34 it may be noted that σ_H is shifted from 36 MPa to 43 MPa when the spalling ratio (SR) changes from two extreme values in the expected range, 0.5 and 0.6 at 500 m. In the following comparison the value 0.56 is applied, following the suggestion of /Martin 2007/. It may also be noted that, in general, the difference between the two approaches, Mogi-Coulomb and the empirical failure criterion, decreases with depth.

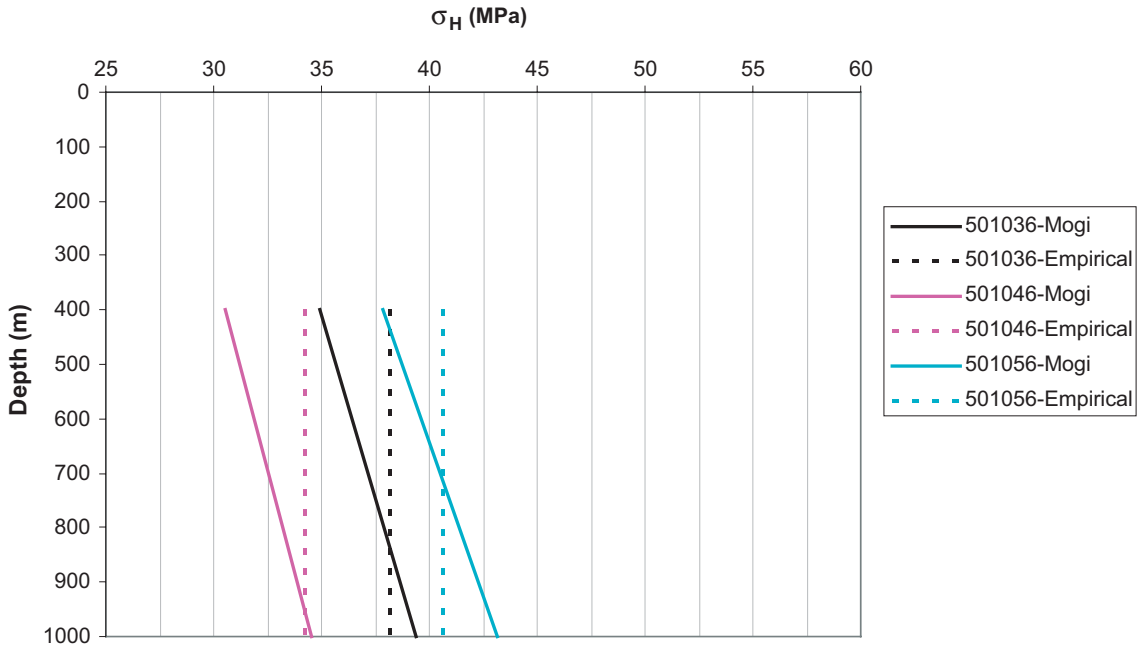

Figure 6-31. *Variation of the upper limit of σ_H, as a result of the Mogi-Coulomb criterion for failure (Equation 6-2) and the empirical criterion for failure (Equation 6-1), for different rock types. (Table 1-3 gives the rock types for the rock codes in the legend).*

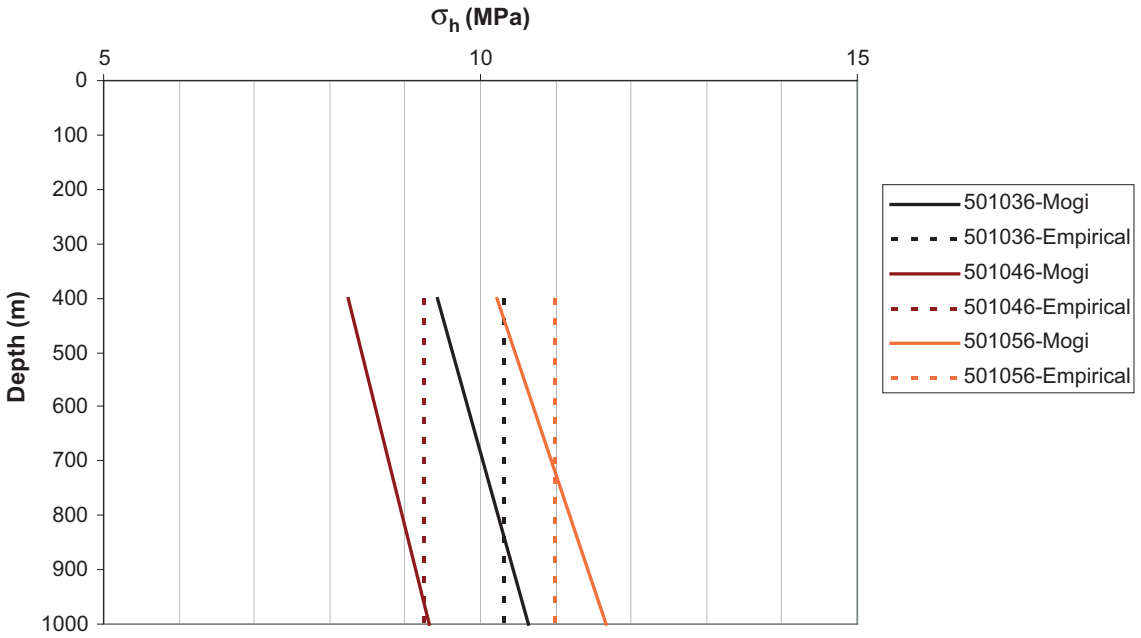

Figure 6-32. *Variation of the upper limit of σ_h, as a result of the Mogi criterion for borehole failure (Equation 6-2) and the empirical criterion for failure (Equation 6-1), for different rock types. (Table 1-3 gives the rock types for the rock codes in the legend).*

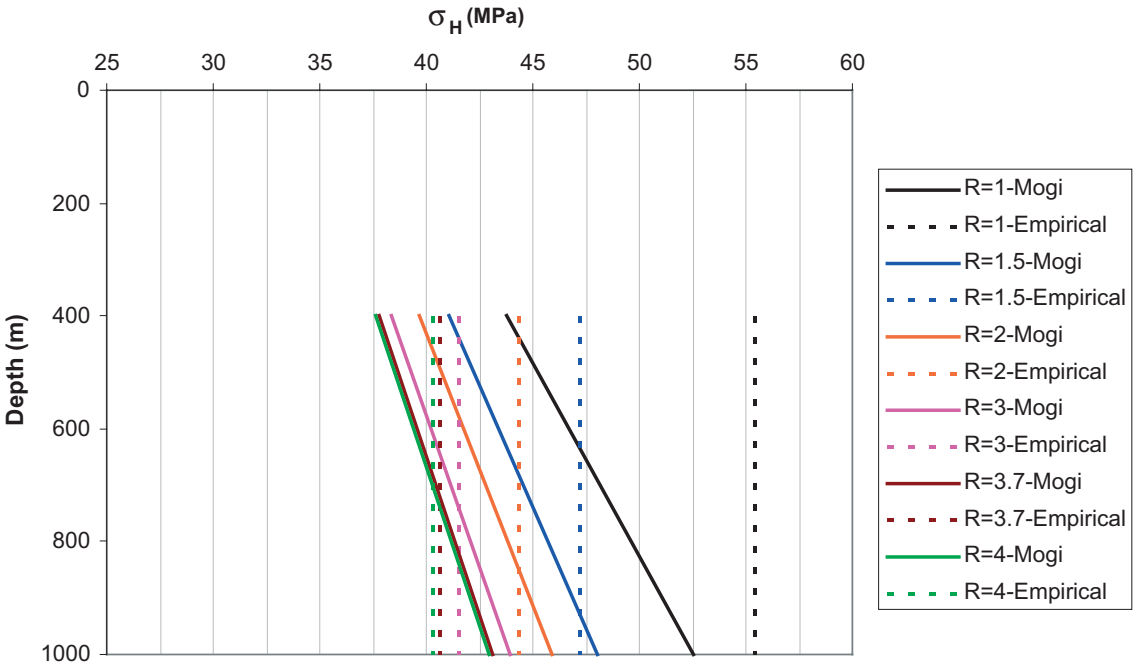

Figure 6-33. *The effect of R ($R = \sigma_H / \sigma_h$) on the caluculated maximum horizontal stress at boreholes failure, in the case of Ävrö granodiorite (501056).*

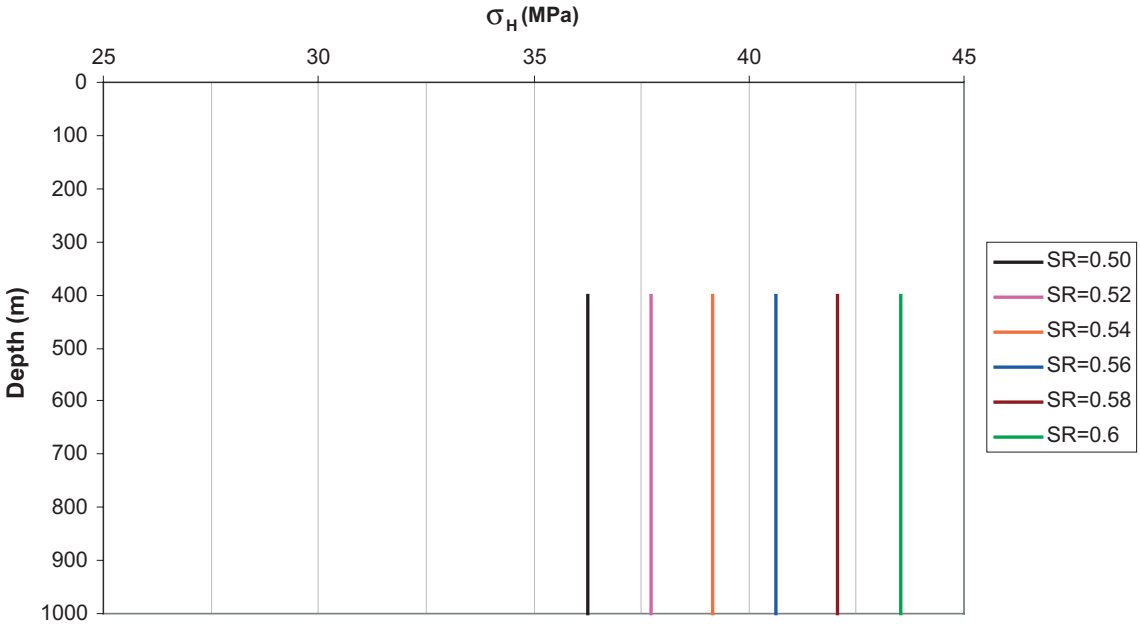

Figure 6-34. *The effect of "spalling ratio" (SR in Equation 6-1,) for Ävrö granodiorite (501056) and R=3.7.*

Table 6-8 Strength parameters used for the different rocks included in the estimation of upper bound of the stress based on the two failure criteria. The UCS values are the mean values from intact rock models (Table 3-9). The cohesion and friction angles were selected to fit to the strength seen in triaxial results at high confing stresses (see text and cf. Figure 3-12 to Figure 3-15).

Rock type (Rock code)	UCS (MPa)	C (Mogi) (MPa)	ϕ (Mogi) (degrees)
Quartz monzodiorite (501036)	186	14.4	42.4
Ävrö quartz monzodiorite (501046)	167	12.8	41.7
Ävrö granodiorite (501056)	198	15.8	43.0

Results from borehole KLX12A

Borehole KLX12A is the borehole where most stress information is available in Laxemar. Both overcoring and hydraulic stress measurements were performed. It may be noted in Figure 6-35 that the difference between the two different direct measurement methods is not large. The 3DEC models 1–6 (which have the same amount of compression of the model boundaries, the minor differences is only in DZ properties) gives the overall stress magnitude that is closest to the measurement data.

The comparison for the maximum horizontal stresses shows a fairly good agreement between the overcoring and the hydraulic results. The overcoring has a fairly large spread in the individual measurement points, but there is a consistent increasing trend with depth. At about –440 m elevation the HTPF values fall within the wide range of overcoring measurements. Unfortunately there are no overcoring measurements at about –520 m elevation to be directly compared with the HTPF results.

Both methods show stress levels down to an elevation of –500 masl that are below what can be expected as an upper limit for expected maximum horizontal stress when no breakout is observed. The limit lines introduced in the figure correspond roughly to the strength expected for the weakest rock type, Ävrö quartz monzodiorite, which is dominating in the lower part of KLX12A.

At –540 masl elevation there is a short section with both breakout and core disking. This section is not located in a deformation zone. It may thus be expected that the stresses at this depth should not be very far from the limits at this point. The lines indicating the estimated breakout limits in Figure 6-35 are showing a higher stress than the HTPF, but it fits that the breakouts and core disking do occur when there is a change in rock type, to the weaker Ävrö quartz monzodiorite. The fact that only these very short sections show these phenomenons, and not the whole continuation of the borehole at deeper sections, can probably be explained by a locally slightly even weaker rock at this point, possibly also in combination with some additional thermal loading due to the drilling. Unfortunately, the KLX12A borehole has a lowest elevation of about –560 masl, and therefore it is not possible to infer the stress increase based on additional observations at greater depth.

When comparing the orientation of maximum horizontal stress in KLX12A, as interpreted from different methods (Figure 6-8, Table 6-3, and Appendix 6, respectively) it may be noted that there is a certain spread, both within the same method and between methods. At level c. –440 masl HTPF indicates 132° while the OC gives 162° as a mean for this depth level. At depth level c. –520 masl the HTPF gives 161° and there is two breakouts, one giving 165° and the other 184°. The 3DEC model, that does not include any minor deformation zones, does not show any significant variation in orientation, see Appendix 7. The potential variation in orientation due to minor fracture is discussed in Section 6.4.

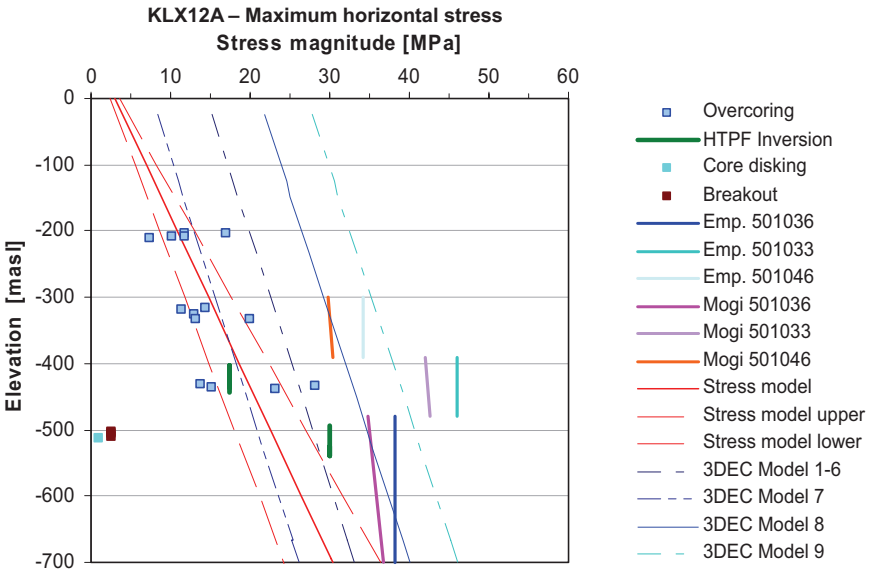

Figure 6-35. *Comparison between direct and indirect stress data from KLX12A and the numerical model results along a scanline at approximately the same location as KLX12A – Maximum horizontal stress. Two models for stress criterion for borehole breakout stress limits are also given (see text). Note that the borehole itself ends at elevation –560 masl.*

The comparison of the minimum principal stress between overcoring and HTPF is also fairly good (Figure 6-36), but lower values are being obtained from the overcoring. The poor depth overlap in the measurements makes the comparison of methods uncertain. The final stress model for the minimum stress was selected such that the uncertainty span should include the hydraulic results, while the overcoring results, at some points showing even negative minimum horizontal stress, were considered not to be representative for the average minimum stress in the whole area. The five measurement points around –320 masl is located just at a minor deformation zone, according to the single hole interpretation (Appendix 5). The other two measurements levels are not located at deformation zones.

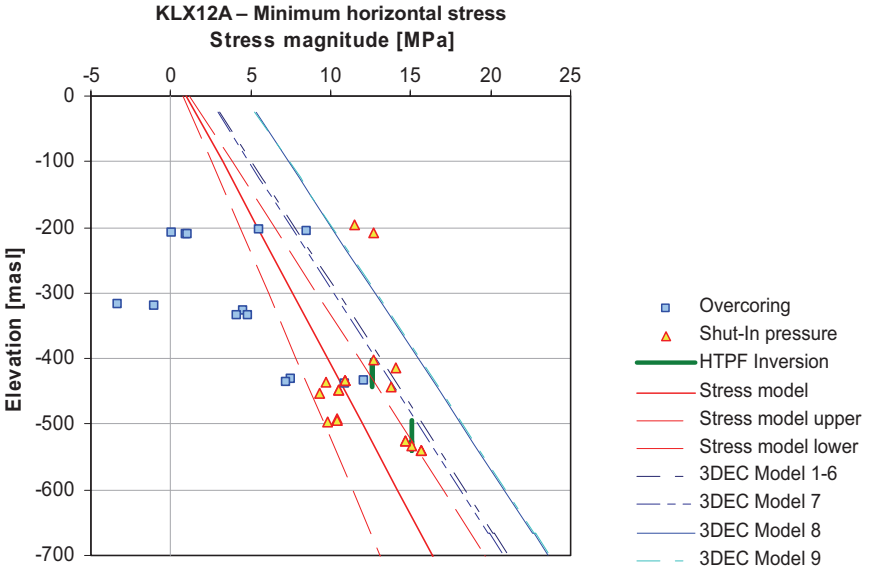

Figure 6-36. *Comparison between direct and indirect stress data of different kinds from KLX12A, together with numerical model results along a scanline at approximately the same location as KLX12A – Minimum horizontal stress.*

Results from borehole KLX04

A similar comparison may be made for borehole KLX04 data and modelling results (Figure 6-37). This borehole intersects with deformation zone EW007A (complex structure) at about –200 m elevation accordning to DZ model but in the 3DEC model, due to geometrical simlifications, the intersection is at –440 m elevation. The influence from the zone gives a slight increase in stress below the zone in both measurements and model, but the influence is less strong in the numerical model.

KLX04 is a deep borehole and as such constitutes a main reason for selecting the stress gradient. The stress model, indicated with a red line, will at 1,000 m depth give stresses that are expected to cause borehole breakouts.

Results from borehole KLX02

In KLX02, a deep borehole drilled before the start of the site investigations, hydraulic fracturing data are available but no overcoring is performed. The updated core mapping was made only down to elevation –980 masl. But core disking has been observed in previous documentation of the borehole /Ekman 2001/. Also, no detailed caliper logging (acoustic televiewer) was performed in KLX02, but information concerning the breakouts for this borehole has been gathered from /Ekman 2001/, based on BIPS analyses.

In Figure 6-38 the interpreted minimum horizontal stress from the hydraulic fracturing tests are given together with the minimum principal stress of the numerical models. The 3DEC models seems to overestimate the minium stress compared to the HF data, but the final stress model chosen, mainly based on KLX12A, is not far from the KLX02 HF data at repository depth. It should be remembered that borehole KLX02 intersects major deformation zones, EW007A at ca –200 masl and NE107A at –750 to –950 masl, and also six MDZ, which possibly explain the non-linear behaviour of the stress data. The deeper parts of borehole KLX02 (below FSM_EW007) are located in FSM_C, i.e. in the focused volume.

In Figure 6-39 the maximum horizontal stress from numerical modelling and the hydraulic fracturing is shown togheter with the core disking, breakouts and the final stress model chosen. The maximum stress estimation from hydraulic fracturing is not judged to be a reliable method for maximum stress. This borehole is however, since it is so deep, of particular interest for the study of borehole stability. If we compare the upper limits from the Empirical ad Mogi-Coulomb

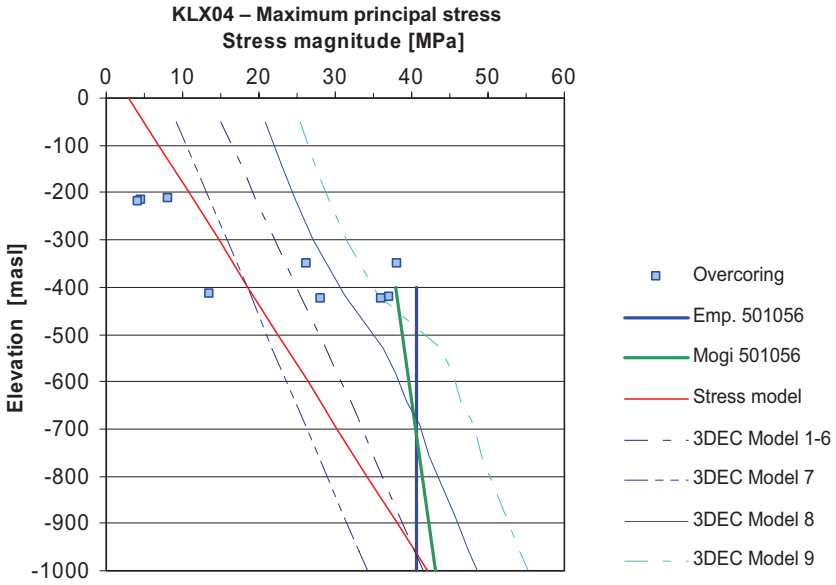

Figure 6-37. *Comparison between direct and indirect stress data from KLX04 and the numerical model results along a scanline at approximately the same location as KLX04 – Maximum principal stress. Two models for stress criterion for borehole breakout stress limits are also given.*

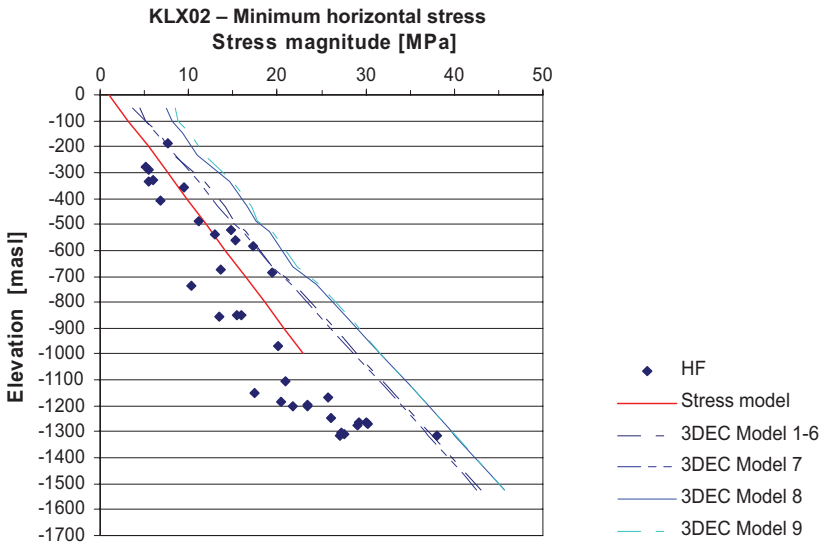

Figure 6-38. *Data from hydraulic fracturing stress measurement (interpreted minimum horizontal stress) together with results from numerical models (σ_2 which is horizontal in the models) versus elevation along approximate location of KLX02. The borehole extends down to –1,700 masl, but the mapping (Appendix 5) is made down to –1,000 masl.*

estimation of stress needed for breakouts with the actual situation we can notice that, below say elevation –900 masl the stress model is crossing the upper limits. The actual observation of some borehole instability and core disking at deep locations supports the idea that these phenomena are indicators of high stress, but it seems that we are still not clear above this limit since it is only at some part of the borehole that they occur. If it is correct that the vertical stress has an influence on the borehole stability (the Mogi-Coulomb criterion), a fairly limited stress gradient with depth could possibly explain the stable conditions towards the bottom of the very deep hole. (Here in the figure the stress model is extrapolated along the hole borehole depth (to enable comparisons) but actually the model is meant to be valid only at 400–700 m depth and the uncertainty span at very deep location at the site should be considered higher than what this model gives.)

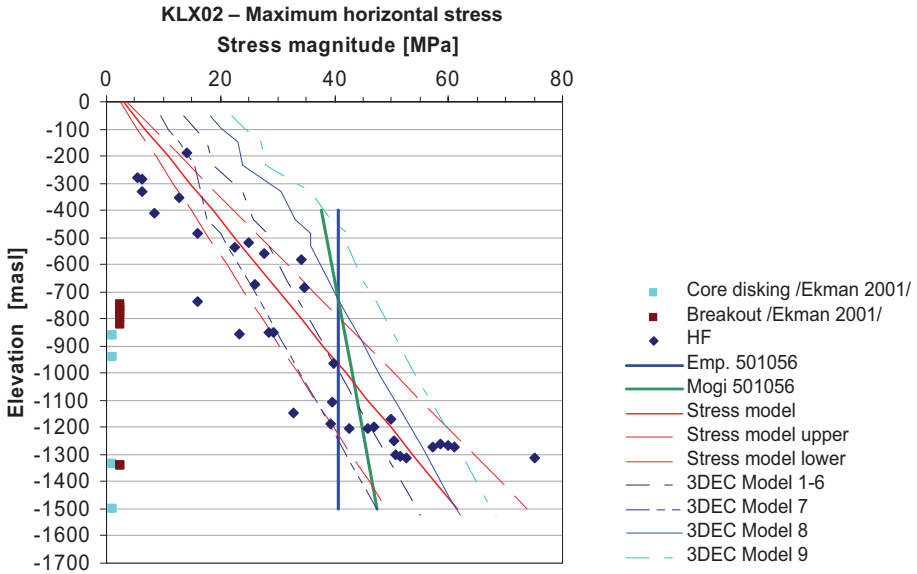

Figure 6-39. *Data from hydraulic fracturing stress measurement (interpreted maximum horizontal stress) together with results from numerical models (σ_1 which is horizontal in the models) versus elevation along approximate location of KLX02. The borehole extends down to –1,700 masl, but the updated mapping (Appendix 5) is made down to –1,000 masl.*

Results from borehole KLX03 and KLX11A

Only one occurrence of breakout at about –860 masl elevation, located in a short section of fine grained granite, is seen in borehole KLX03 (Figure 6-40). Also core disking is occurring at exactly the same location (see also WellCad plot in Appendix 5). At this point there is a section of fine-grained granite in the geological mapping. It is thus probable that the rock material at this location is different than in the surrounding rock and that this is why both the disking and the breakouts have occurred at this spot. It is also possible that some additional drilling load (thermal and/or purely mechanical load) had been created associated with the change in rock type at this depth.

The stress model span chosen, which is based on the OC results in KLX12A, fits with this upper limit given by the almost non-existence of borehole breakouts in the entire borehole. The same observation can be made for KLX04 and KLX12A.

Results from Äspö Hard Rock Laboratory

In the literature three stress models proposed for Äspö Hard Rock Laboratory may be found. /Andersson 2007/ and /Jonsson et al. 2009/ used convergence measurements and so called back-analysis to estimate the stress level. These results are shown in Figure 6-42 together with the direct measurements from Äspö (performed after 1996) and the model based on interpretation of Äspö measurements made by /Ask 2006/. There is no major difference between the three models of stress levels in the literature; they lie in the span from 24 MPa to 30 MPa for the maximum principal stress. Again it may be noted that the 3DEC Model 2 is the numerical model compression case that gives a stress level close to the observed, at the level of the laboratory. Since we do not have any deeper boreholes data there is no possibility to draw strong conclusion on the stress gradient towards depth below the laboratory level. The 3DEC model probably gives a little too high stresses towards ground surface compared to reality since both gradients from /Ask 2006/ are higher than the model gradients.

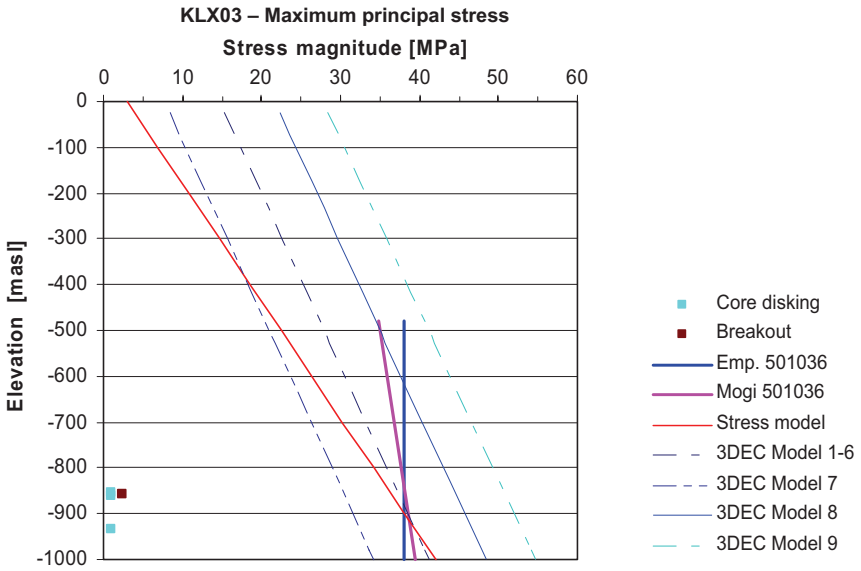

Figure 6-40. *Results from numerical models versus elevation along scanline KLX03 and the location for observed croe disking and borehole breakouts in the borehole. (The borehole itself ends at elevation –950 masl.)*

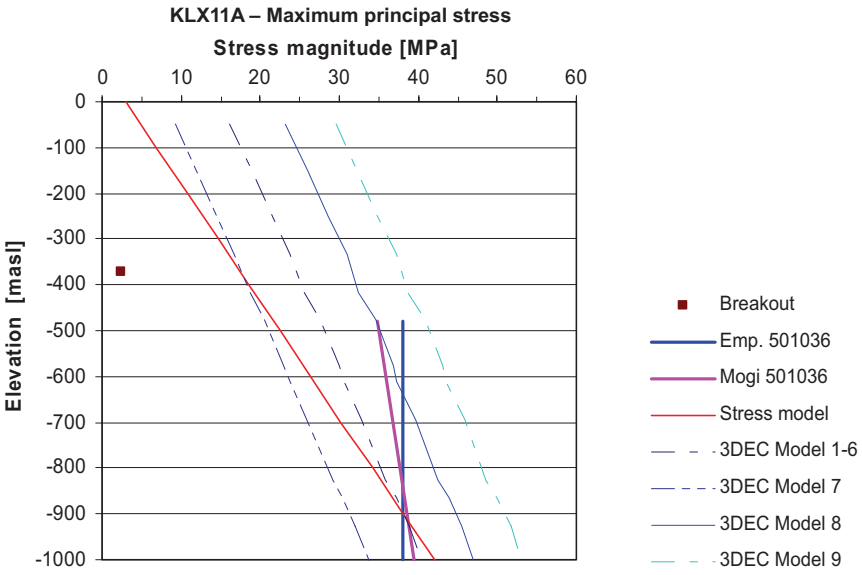

Figure 6-41. *Results from numerical models versus elevation along scanline KLX11A and the location for observed borehole breakout in the borehole. (The borehole itself ends at elevation –992 masl.)*

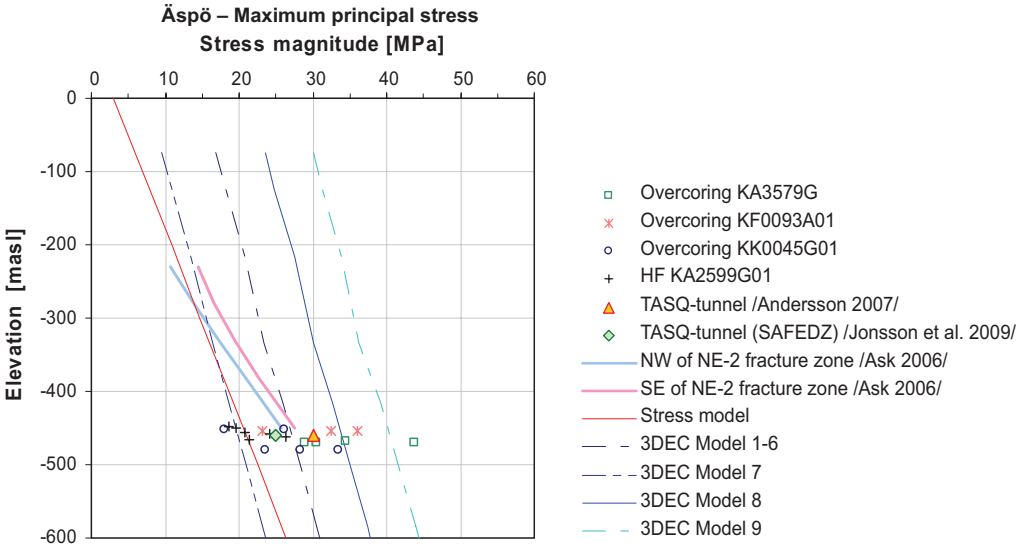

Figure 6-42. *Data from stress measurements (overcoring and hydraulic fracturing) are compared with the three stress models proposed for Äspö HRL /Andersson 2007/, /Ask 2006/ and /Jonsson et al. 2009/ and the 3DEC numerical models (Model 1–6, 7, 8 and 9). (Note: For hydraulic fracturing, the stress magnitude is based on σ_H, for the rest it is based on σ_1.) At Äspö HRL we do not have information on core disking mapped or boreholes breakouts. No information available at depth deeper than –480 (masl).*

Results from Simpevarp subarea – boreholes KAV04A, KSH01A and KSH02

In the Simpevarp subarea there are three boreholes with some stress measurements, overcoring in KAV04A and (only one single point) in KSH02. Hydraulic fracturing and HTPF is performed in KSH01A, and the inversion is made on both results. The comparison with 3DEC model results and breakout observations are shown in Figure 6-43. No core disking was observed during mapping of any of these boreholes. The linear function that was finally selected as the most likely mean stress value for Laxemar is also put in the figure for comparison. It may be noted that the low stress measured with the overcoring in KAV04A can not be explained by the 3DEC model, the stresses in the model is higher. The 3DEC fit to the boreholes KSH01A

and KSH02 is better. The explanation to the results in KAV04A could possibly be that the borehole is located in such proximity to the deformation zone NE012A that the stress situation is complex and the stress measured is only a very local situation. The very scattered orientation of stresses also points to this possibility. Another explation could be that the geometry of the DZ in the 3DEC model, based on the geological DZ model, actually does not well represent the actual geometry of major DZ in this area. However, the breakout occurrence at the bottom of the borehole fits well with the hypothesis of stress release above NE012A, giving an expected higher stress below the zone. The middle of the wide zone intersects at –850 masl according to the single hole interpretation.

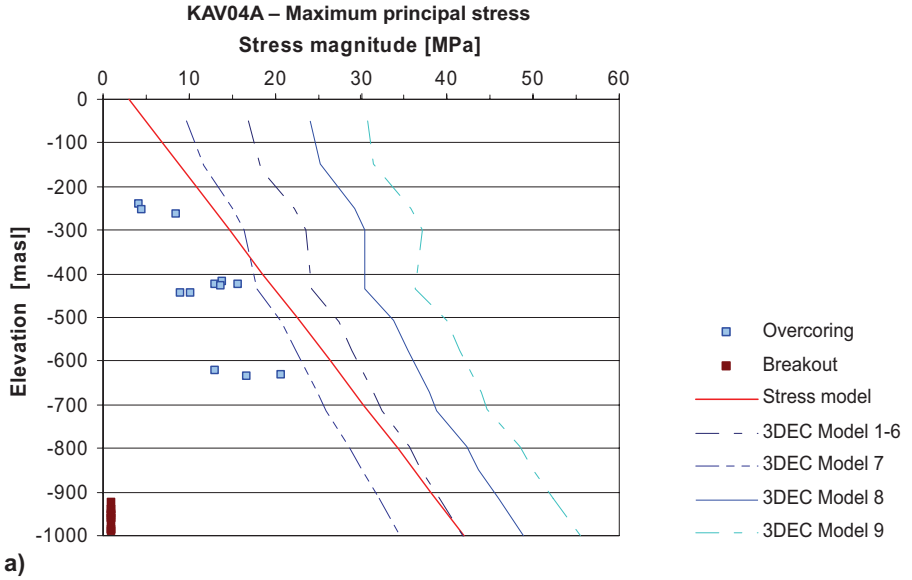

a)

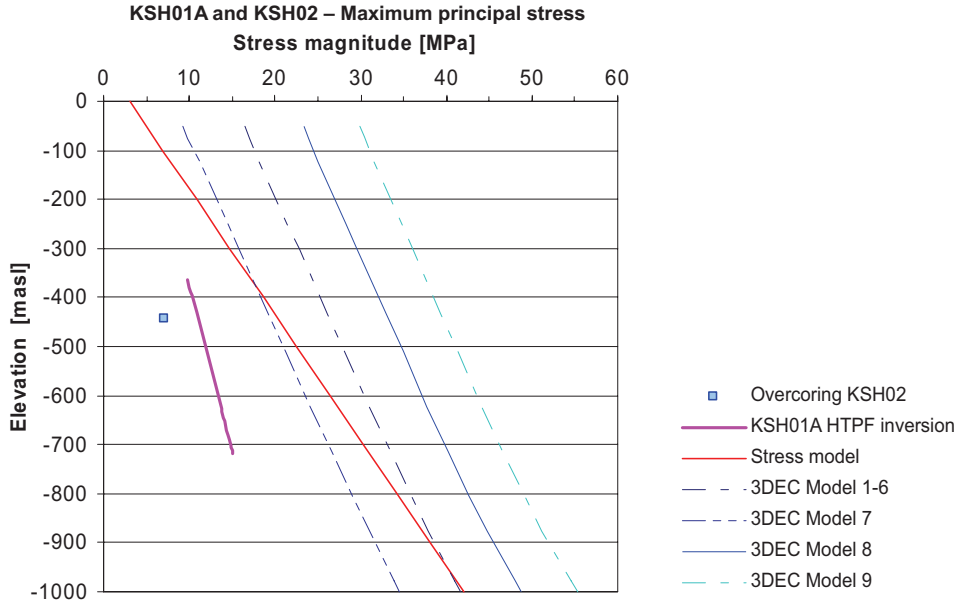

b)

Figure 6-43. *Data from stress measurements (overcoring and HTPF inversion) are compared with the 3DEC numerical models along the locations for Simpevarp boreholes a) KAV04A and, b) KSH01A and KSH02. (The 3DEC results are almost identical for KSH01A and KSH02). All three boreholes extend down to –970 to –990 masl. The stress model chosen for the focused area of Laxemar is given as the red line for comparison.*

6.4 Stress variability due to discrete fractures

The potential variation in magnitude of the principal stresses, at the scale of a 5 m diameter deposition tunnel, was examined by applying the mean principal stresses at repository depth to a 3DEC model containing a discrete fracture network model. The methodology used in these analyses is similar to that presented in Section 5.2. A 10×10×1 m plane strain block model was populated with fractures based on a DFN model taken from /La Pointe et al. 2008/. The Base Case model, unlinked traces and Euclidean scaling has been used. The sides of the box were aligned parallel with the principal stresses. The fractures and the intact rock in this 3DEC model were given mean properties described in Section 5.2.1. The mean principal stresses were applied to the boundaries of the model and the program was iterated to equilibrium.

The 3DEC model was divided into approximately 500 intact rock blocks. The mesh generated in these blocks produced some 3,000 sampling points equating to a sampling volume of approximately 0.03 m^3. This volume is approximately the same as that associated with an overcoring test (0.01–0.08 m^3). Hence, the variability in magnitude and orientation at these sampling points (see Figure 6-44 and Figure 6-45) is, approximately, what could be expected from overcore stress measurements. The variation in the stress magnitudes and orientations is attributed to stress perturbations caused by the discrete fractures in the sampled volume.

Figure 6-44 and Figure 6-45 show the variation in magnitude and orientation of the major principal stress due to the discrete fractures at 400–500 m depth in the 3DEC model. The variation in magnitudes and orientation for all three principal stresses are presented in Table 6-9 and Table 6-10. The analyses indicate that for the rock mass conditions expected in Laxemar σ_1 obtained from overcoring tests, could be expected to vary spatially by ±5 MPa in magnitude and ±9 degrees in orientation. /Martin et al. 1990/ clearly showed that as the sampling volume increased from a 96-mm-diameter overcoring test to the tunnel scale, the mean stress remained relatively constant while the variability in the magnitudes decreased dramatically. Hence, the variability in the stress magnitudes and orientations from this 3DEC simulation is considered to represent the variation only at the local scale (single measurement scale) for the Laxemar rock mass at the repository depth containing a discrete fracture network. The estimation of large-scale variability is discussed in Section 6.3.

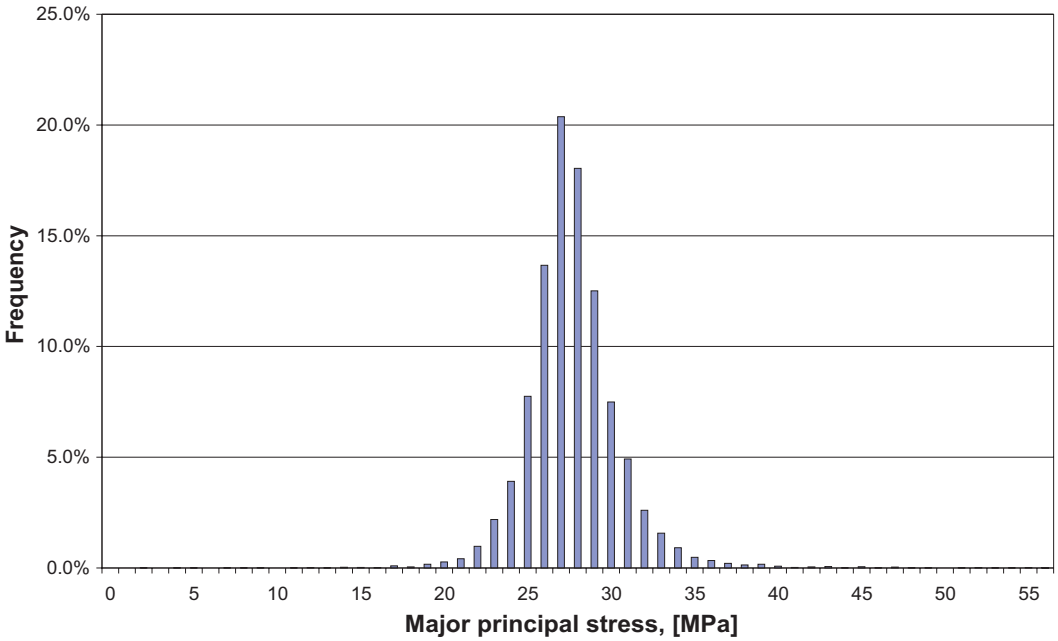

Figure 6-44. *Histogram of the major principal stress in the calculation zones of a numerical model (3DEC) simulating the stress variation due to the fractures in the rock mass. The histogram includes the sum of data from five numerical models with different fracture networks in each, based on the same DFN model.*

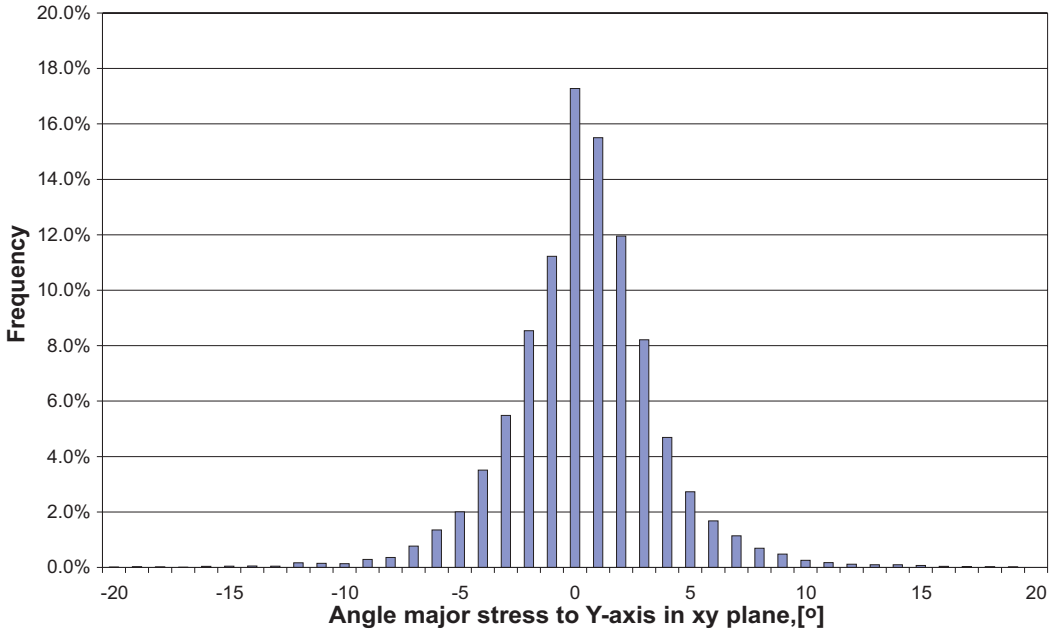

Figure 6-45. *Variation in orientation of the major principal stress in the calculation zones of the models (see Figure 6-44).*

Table 6-9. Summary of the results regarding variation in magnitude of the principal stresses.

Principal stress component	Mean magnitude (MPa)	Standard deviation (MPa)
σ_1	27.2	3.4
σ_2	12.6	1.6
σ_3	10.5	1.2

Table 6-10. Summary of the results regarding variation in orientation of the principal stresses in relation to applied boundary stresses.

Principal stress component	Mean orientation (°)	Standard deviation (°)
σ_1 – y-axis in xy plane	0.7	4.3
σ_3 – x-axis in xy plane	–0.4	4.6
σ_1 – y-axis in yz plane	–0.2	4.2
σ_2 – z-axis in yz plane	0.1	4.1
σ_3 – x-axis in xz plane	–4.4	18.2
σ_2 – z-axis in xz plane	2.9	18.1

6.5 Model of the in situ stress

It is clear from the number of direct measurements within the Laxemar local model area and from the total spread seen in the measurement data that the final model for the stress magnitudes can not be very certain. However, the numerical model, for different cases, has also indicated that even if an influence in stress field from deformation zones is to be expected, this influence should not give a large scale spatial variation within the focused volume (i.e. the volumes defined by fracture domains FSM_C, FSM_W and FSM_NE005) that is more than about ±4 MPa (Figure 6-25 and Appendix 7).

The selected model function for these domains is based on the overcoring data from KLX12A only, when it concerns the maximum horizontal stress. These data were considered more undisturbed than the data from KLX04, and most representative for the volume. A simple visual fit of a linearly increasing magnitude with depth was adopted. This level of magnitude was also supported roughly by the HF/HTPF results, and the uncertainty span was selected such that also the HF/HTPF results were within the uncertainty span.

The minimum horizontal stress was selected to lie between the data from the HF/HTPF and overcoring results in KLX12A, with the uncertainty span covering both. The vertical stress is estimated to be corresponding to the overburden. This means that the minor horizontal and vertical stresses at about 200–400 m depth are estimated to be of the same magnitude. Deeper down the minor horizontal stress is estimated to be slightly lower than the vertical stress. This is supported by the deep data for the minimum horizontal stress in KLX02.

The upper limits for the stresses based on the analysis borehole stability were used as a guide in the selection of the model function uncertainty span. Since the model concerns the stresses at the planned repository depth (400–700 m) the upper limits from the Mogi-Coulomb criterion was selected as an upper truncation limit for the expected stresses. The uncertainty in the assumption of the calculated liming functions has also been considered. At very deep levels the assumed input parameters to the limit calculations (SR value, σ_H/σ_h-ratio and the rock strength parameters c and ϕ) may not be the most representative, or at least the uncertainty is higher.

The uncertainty finally chosen for the most likely value of major and minor horizontal stresses magnitudes are presented in Table 6-11. A quantification has also been made of the expected small scale spread around the mean value due to the fracturing. These values are given as standard deviations of a normal distribution, and were selected based on the results in the numerical modelling of a confined fractured rock block, which is presented in Section 6.4. The resulting uncertainty spans at elevations –400 masl, –500 masl and –600 masl from the functions in Table 6-11 are given in Table 6-12.

Table 6-11. Stress model for domains FSM_C, FSM_W, FSM_NE005, at –400 to –700 masl elevation. The stress magnitude is modelled as a function with the depth z.

Parameter	Most likely value (mean value)	Estimated uncertainty (in the mean value)	Upper limit at –400 masl elevation	Local stress variability (expressed as St. dev. Of a normal distribution around the local mean value)
Magnitude				
Major horizontal stress, σ_H	0.039z + 3 MPa	±20%	31–34 MPa [1)]	12%
Minor horizontal stress, σ_h	0.022z + 1 MPa	±20%		13%
Vertical stress, σ_v	0.027z MPa	±3%		15%
Orientation				
Major horizontal stress trend, σ_H	135°	±15°		±15°

1) Depending on the rock type, lower value in RSMM01 and higher in RSMD01.

Table 6-12. Stress model for domains FSM_C, FSM_W, FSM_NE005. The stress magnitudes and orientations are here given as uncertainty span for the mean stress values at three different elevations (cf. Table 6-11).

Elevation	–400 masl	–500 masl	–600 masl
Magnitude			
Major horizontal stress, σ_H [MPa]	14.9–22.3	18.0–27.0	21.1–31.7
Minor horizontal stress, σ_h [MPa]	7.8–11.8	9.6–14.4	11.4–17.0
Vertical stress, σ_v [MPa]	10.5–11.1	13.1–13.9	15.7–16.7
Orientation			
Major horizontal stress trend, σ_H [°]	120–150	120–150	120–150

7 Summary of the rock mechanics model

7.1 Intact rock properties

The results from laboratory testing have shown that there is a clear relationship between rock density and strength properties for the Ävrö granite (501044). Therefore, and in conformity to the geological description, a division of Ävrö granite into two varieties, Ävrö quartz monzodiorite (501046, quartz poor and with higher density) and Ävrö granodiorite (501056, quartz richer and with lower density), was introduced based on density. As a result of this division a clear difference is seen in the average properties of the two rock type varieties, and the expected spread in the compressive strength decreased, which makes the division justified.

The modelling of the six most frequently occurring rock types in Laxemar shows that the strength is high but with a fairly large spread. The mean uniaxial compressive strength (UCS) is 186 MPa for the fresh quartz monzodiorite (501036), which is dominant in the southern rock domain RSMD01, 198 MPa for Ävrö granodiorite (501056 dominating RSMA01 in the north), 167 MPa for fresh Ävrö quartz monzodiorite (501046) and 225 MPa for diorite/gabbro (501033), both parts of RSMM01. The less frequently occurring fine-grained dioritoid (501030) and fine-grained granite (511058) have a mean uniaxial compressive strength of 239 MPa and 280 MPa, respectively. The uncertainty of the mean UCS values is estimated at 3–5% for the three main rock types, and the standard deviation in the expected normal distribution is 11–30 MPa.

The average Young's modulus for all the rock types is between 71 and 80 GPa, with an uncertainty of the mean values about 3–5%. Poisson's ratio varies between 0.25 and 0.33. A clearer difference can be noted in the tensile strength where, for fresh samples, fine-grained dioritoid is the strongest with a mean tensile strength of 19 MPa and Ävrö quartz monzodiorite is the weakest with 13 MPa.

An improvement in the current description compared to the previous model versions is that the effect of oxidation is modelled. About 10% of the rock in RSMD01 and 14% of RSMM01, outside deformation zones, is expected to be oxidised to some degree (mostly faintly or weakly) /Wahlgren et al. 2008/. The results from laboratory testing has shown that the tensile strength of oxidised rock is reduced roughly by 20%, the Young's modulus reduced by 14% and the Poisson's ratio is increased by 8% compared to fresh samples. No significant influence is seen from saussuritisation of quartz monzodiorite or from oxidation of Ävrö granodiorite, and therefore these two types of alteration are included in the description of fresh rock.

The crack initiation stress (σ_{ci}) is seen to be correlated with the uniaxial compressive strength, such that σ_{ci} on the average reaches 110 MPa for Quartz monzodiorite (58% of UCS), 88 MPa for Ävrö granodiorite (52% of UCS) and to 104 MPa for Ävrö granodiorite (52% of UCS).

The core samples tested in the laboratory always have a slightly higher porosity compared to in situ rock conditions, due to the stress relief. If in situ stresses or thermal stresses due to the drilling are high at the sampling point, the rock core will be damaged to some extent leading to an increase of the porosity. In Laxemar, a slight core damage increasing with depth in the form of microcracking has been observed from microcrack volume determinations performed on samples from borehole KLX17A. However, this kind of minor core damage does not seem to affect the strength of the rock samples, since no depth trend is observed in strength data.

The overall confidence in the models for intact rock is judged to be high due to several reasons. Firstly, the test methods used are standard methods, which imply that the parameters as such are well known and understood. A comparative study with testing at different laboratories has been carried out with satisfactory results. Secondly, the number of tests is large enough to enable sufficiently reliable statistics, at least for the fresh and most frequent rock types. Thirdly, the spatial distribution of the sampling points is quite good, from KLX11A in the west to KLX21B in the east of Laxemar local model volume. The mechanical models are also supported by previous results from Simpevarp and Äspö Hard Rock Laboratory.

7.2 Fracture properties

The mechanical properties of single fractures have been modelled based on two types of tests; direct shear and normal stiffness tests on small fracture samples in the laboratory and so-called tilt tests, also performed on small fracture samples from the drill cores.

The small size of the drill core and the sampling and testing procedure introduces strong limitations on the type of fractures that can be tested. Only fractures that may be considered fairly mated and undisturbed by the drilling process can be tested. According to the geological DFN description /La Pointe et al. 2008/ all sizes of single fractures exist, also very large size structures (but assumed bounded by size of 1,000 m, corresponding to a radius of 564.2 m – larger structures are modelled deterministically). The largest fractures in the DFN are expected to be represented in the geological single-hole interpretation by thin crush zones, or as fractures of comparatively large physical aperture, or even mapped as minor deformation zones. The current mechanical descriptive model for fractures is however limited in application only to the much more frequent smaller size (radius) part of the fracture population.

The results from the tilt tests are considered less reliable than the results from direct shear testing with regards to actual parameter values. However, since the number of tilt tests is larger, these results have been used in support of the assessment of variability. The only significant difference between different fracture sets that is observed from the tilt tests results is a lower peak and residual cohesion for the subhorizontal set.

The results from the direct tests has been studied separately for fracture sets of different orientation but no clear differences were found, apart from a higher stiffness for the subhorizontal set compared to steeply dipping fracture sets. The surface characteristics of the tested samples have been compared with the total fracture statistics of surface characteristics and no bias in the sampling was found. Furthermore, no clear correlation between mapped surface characteristics and the shear test results was found.

The mean peak friction angle, for all tested samples (excluding the sealed fracture samples), is 37° with a standard deviation of 3.2°. The mean peak cohesion is 0.9 MPa. The normal stiffness of a single fracture increases with normal stress and number of test cycles, and therefore the definition of the parameter used in the description become important. In this case the normal stiffness was evaluated between unloaded and fully loaded state, during the second cycle. The mean normal stiffness for all samples is 720 MPa/mm with a large min–max span of 70 to 4,000 MPa/mm. The shear stiffness is here evaluated as the secant between 30% and 50% of the peak shear stress, and the mean value for shear stiffness is modelled to be 26 MPa/mm at a normal stress of 5 MPa.

Direct tests on sealed fractures also enabled modelling of these fairly frequently occurring fractures. The sealed fractures are unsurprisingly stronger than the open ones (or broken originally sealed fractures). The mean peak friction angle for sealed fractures is 42.5° end the mean peak cohesion is 6.7 MPa. The available samples did not enable assessment of the effects of different fracture infillings.

The overall confidence in the single fracture mechanical model is moderately high. The factor that contributes to confidence is the fairly large number of tests performed (71 direct shear tests) and the fairly consistent and reasonable results from the tests. The circumstance that lowers the confidence is the inherent limitations associated with tests on drill core samples and the lack of knowledge regarding scale effects for the described parameters.

7.3 Rock mass properties

Two different approaches have been applied to evaluate the mechanical properties of the rock mass, i.e. the strength and the deformation properties of both intact rock and fracture network at a larger scale. The first approach was to use the empirical rock classification systems and empirical relationships based on them. The second approach was to try to calculate a larger scale

behaviour based on our models for intact rock and single fractures and the model for the geometrical properties of the fracture network (the DFN model). This second approach is referred to as "theoretical".

The empirical characterisation was performed along five boreholes within the Laxemar subarea. Indices Q and RMR were determined for each 5 m long core section, according to the developed methodology. For another four boreholes the indices were estimated by first finding an empirical relation between RQD from the first five boreholes. The deformation modulus and Poisson's ratio were calculated by means of RMR. The equivalent uniaxial compressive strength and tensile strength were also determined by means of RMR, through GSI and the Hoek-Brown failure criterion. Results were analysed for the different fracture domains defined.

The theoretical approach involved numerical analysis using a discrete element code (3DEC /Itasca 2008/) to simulate loading of 10×10×1 m slices of synthetic rock mass. The frequency, size and orientation of the fracture sets were based on the specific geological DFN model, as presented for each fracture domain. The intact rock properties and the fracture properties were assumed to be equal to the mean values in the models. The influences of confining stress, loading direction on the rock slices and the type of intact rock, were studied in different cases. Different network geometries by means of Monte-Carlo simulations of the same DFN model were then studied for each case. The results were analysed and merged in order to represent the actual variation of each fracture domain.

As was discussed for the single fractures, the influence of the few larger structures in the DFN, was not simulated in the theoretical approach. Therefore, the variation in actual mechanical properties may be underestimated to some extent.

The results from the empirical and the theoretical approaches agree quite well and indicate both that the five fracture domains studied can be divided into two groups with similar properties. Fracture domains in a central volume (FSM_W, FSM_C and FSM_NE005) have a somewhat higher rock quality compared to the fracture domains in the north (FSM_N and FSM_EW007). In the final proposed model, based on both approaches, the mean deformation modulus is estimated to be 59 GPa for the first group and 50 GPa for the latter, with standard deviation in the expected distributions of 12 GPa and 14 GPa, respectively. The uncertainty of the mean estimates is about 3%.

The mean uniaxial strength for the rock mass between interpreted deformation zones is modelled at 51 MPa for fracture domains FSM_W, FSM_C and FSM_NE005 and 42 MPa for FSM_N and FSM_EW007, assuming the Hoek-Brown's failure criterion. A similar difference is observed in the model for friction angle and cohesion assuming the Mohr-Coulomb's failure criterion for confining stress between 10 and 30 MPa. The first group of fracture domains presents mean values of 43° and 18 MPa while the second group has mean values of 42° and 17 MPa, respectively. The uncertainty in the friction angle is estimated to be 3% and for the cohesion 7%.

Using both the empirical and the theoretical approaches, the properties for the rock mass inside interpreted deformation zones have also been modelled. The properties vary according to the inferred size of the deformation zones and the strength and stiffness increase from the regional deterministic zones to the shorter minor deformation zones (MDZ).

The overall confidence in the model of mechanical properties of the rock mass is high as long as it concerns the fracture domains, i.e. the rock mass between interpreted deformation zones, and excluding the effect of the minor deformation zones. Since the fracture domains do not exhibit a strong anisotropy in terms of fracturing, it is believed that the simplifications made in the modelling of the rock mass mechanical properties are plausible and justifiable. The confidence in the rock mass properties of the interpreted deformation zones is considered moderate, since the detailed internal structure of the deformation zones is highly complex and their large-scale mechanical behaviour is not well known.

7.4 In situ state of stress

Two different direct stress measurement methods have been applied at Laxemar. Overcoring was performed in two boreholes within the local model volume (KLX04 and KLX12A) and hydraulic fracturing tests and HTPF were performed in boreholes KLX02 and KLX12A. The results from the measurements in KLX12A agree fairly well between the two different methods. The difference between the values of the maximum and minimum horizontal stresses obtained by the two methods is in the order of 3 MPa at a –440 masl elevation with HTPF giving the highest values.

Very little core disking has been observed in the drill cores from the site investigations at Laxemar. The total length of disking is about 5 m and most of this is atttributed to a section at about 900 m depth in borehole KLX03, consisting of fine-grained granite.

Borehole breakouts, observed from televiewer borehole logs, are also very scarcely found in the boreholes in Laxemar. The total length of breakouts is 61 m. Most of these observations are in subordinate rock types or in deformation zones.

Numerical modelling was performed to analyse the potential influence on the stress field of the interpreted major deformation zones in the area. Results from the modelling supports the observations from the direct measurement data, in that a spatial variation of the in situ stresses may be expected due to stress redistributions associated with the deformation zones.

Two different approaches have been taken to make an estimation of the expected upper limit of the in situ stresses, considering the lack of borehole failures (breakouts) in the boreholes. The first approach was to apply an empirical criterion from /Martin 2007/ which utilises UCS of the intact rock and an empirical factor as an input. A second approach was to use the Mogi-Coulomb's failure criterion from /Al-Ajmi and Zimmerman 2006/, which uses the friction angle and cohesion from the triaxial tests at the appropriate stress level. Both methods use the same assumptions regarding stress ratios and vertical stress. The two approaches give similar results at repository depth
(–500 masl elevation).

The stress model predicts a most likely value for the maximum horizontal stress of 23 MPa at –500 masl elevation in fracture domains FSM_W, FSM_C and FSM_NE005. The uncertainty in this value is estimated at ±20%. The minimum horizontal stress at repository level is modelled to most likely be 12 MPa. The uncertainty in this value is estimated at ±20%. The most likely vertical stress is corresponding to the weight of the overburden, 13.5 MPa at –500 masl elevation.

Locally, at the scale of a single overcoring measurement, the stress may vary around the mean with about ±12%. This value is based on a numerical analysis of the stress variability in a fractured rock block. The variation is supported by the large spread seen in closely spaced direct measurement data.

The very upper limit for the mean maximum stress is estimated from the observation of stable drill holes. These upper limits are 31 MPa at –400 masl, and at 35 MPa at –700 masl elevation, in the part of the focused volume that is located in the rock domain RSMM01, and about 5 MPa higher in rock domain RSMD01.

The overall confidence in the stress model is moderately high for the absolute stress magnitudes. The reason for this is that the number of direct stress measurements carried out is limited. However, the confidence in the upper limits of the stresses is higher because the number of deep cored boreholes within the Laxemar local model volume is large and the estimation is based on two independent approaches that provide similar results.

8 Conclusions

Given the above summary and discussion, the following general conclusions are drawn:

- The properties of the intact rock in Laxemar are well known. Compared to the previous model version the division of Ävrö granite into Ävrö granodiorite and Ävrö quartz monzodiorite constitutes a major improvement. The influence of oxidation is also quantified and is shown to decrease rock strength somewhat,
- The most frequently occurring fractures, typically characterised by smaller size (radius) and aperture (transmissivity) are considered sufficiently described by the results of the performed laboratory testing of fractures. However, and by consequence, the former description is not considered valid for the less frequent main water-conductors (associated with larger size, crush),
- The properties of the most frequently occurring single fractures, which are expected to be fairly small in size, are well described. This description does not apply to large aperture, water bearing single structures,
- The modelled mechanical properties of the rock mass, subdivided in terms of fracture domains, as well as the mechanical properties of the deformation zones, are judged to satisfy the needs of repository design and safety assessment,
- The confidence in the developed stress model has been improved due to additional stress measurements and a significant increase in the number of deep cored boreholes.

9 References

Al-Ajmi A M, Zimmerman R W, 2006. Stability analysis of vertical boreholes using the Mogi-Coulomb failure criterion. Int. J. Rock Mech.

Andersson J, Ström A, Svemar C, Almén K-E, Ericsson L-O, 2000. What requirements does the KBS-3 repository make on the host rock? Geoscientific suitability indicators and criteria for siting and site evaluation. SKB TR-00-12, Svensk Kärnbränslehantering AB.

Andersson J, Christiansson R, Hudson J, 2002. Site investigations. Strategy for Rock Mechanics Site Descriptive Model. SKB TR-02-01, Svensk Kärnbränslehantering AB.

Andersson J C, 2007. Äspö Hard Rock Laboratory. Äspö Pillar Stability Experiment, Final report. Rock mass response to coupled mechanical thermal loading. SKB TR-07-01, Svensk Kärnbränslehantering AB.

Amadei A, Stephansson O, 1997. Rock stress and its measurement, Chapman and Hall, London, ISBN 0412447002.

Ask D, 2006. New developments in the integrated Stress Determination Method and their application to rock stress data at the Äspö HRL, Sweden. International Journal of Rock Mechanics and Mining Sciences, Volume 43, Issue 1, January 2006, pp. 107–126.

Ask M V S, Ask D, 2007. Detection of potential borehole breakouts in boreholes KFM01A and KFM01B. Forsmark site investigation. SKB P-07-235, Svensk Kärnbränslehantering AB

Ask D, Cornet F, Brunet C, Fontbonne F, 2007. Stress measurements with hydraulic methods in borehole KLX12A. Oskarshamn site investigation. SKB P-07-232, Svensk Kärnbränslehantering AB.

Back P-E, Sundberg J, 2007. Thermal Site Descriptive Model. A Strategy for the Model Development during Site Investigations. Version 2.0. SKB R-07-42, Svensk Kärnbränslehantering AB.

Bandis N, 1880. Experimental studies of scale effects on shear strength, and deformation of rock joints. Ph.D. thesis, University of Leeds.

Barton N, Bandis S, 1982. Effects of block size on shear behavior of jointed rock. 23rd U.S. symp. on rock mechanics, Berkeley, pp. 739–760.

Barton N, Bandis S, 1990. Review of predictive capabilities of JRC-JCS model in engineering practice. In Rock joints, proc. Int. symp. on rock joints, Loen, Norway, pp 603–610. Balkema.

Barton N, 2002. Some new Q-value correlations to assist in site characterisation and tunnel design, I.J. Rock Mech. & Min. Eng., Vol. 39, pp 185–216.

Bienawski Z T, 1989. Engineering rock mass classifications. John Wiley & Sons.

Bruner W M, 1976. Comment on "Seismic velocity in dry and cracked solids" by Richard J. O'Connell and Bernard Budiansky. Journal of Geophysical Research, 81(14), pp 2573–2576.

Bödvarsson R, Lund B, Roberts R, Slunga S, 2006. Earthquake activity in Sweden. Study in connection with a proposed nuclear waste repository in Forsmark or Oskarshamn. SKB R-06-67, Svensk Kärnbränslehantering AB.

Chryssanthakis P, 2003. Borehole: KSH01A. Results of tilt testing. Oskarshamn site investigation. SKB P-03-107, Svensk Kärnbränslehantering AB.

Chryssanthakis P, 2004a. Borehole: KSH02. Results of tilt testing. Oskarshamn site investigation. SKB P-04-10, Svensk Kärnbränslehantering AB.

Chryssanthakis P, 2004b. Borehole: KAV01. Results of tilt testing. Oskarshamn site investigation. SKB P-04-42, Svensk Kärnbränslehantering AB.

Chryssanthakis P, 2004c. Borehole: KLX02. Results of tilt testing. Oskarshamn site investigation. SKB P-04-44, Svensk Kärnbränslehantering AB.

Chryssanthakis P, 2004d. Borehole KLX04A. Tilt testing. Oskarshamn site investigation. SKB P-04-265, Svensk Kärnbränslehantering AB.

Chryssanthakis P, 2005. Borehole KLX03A. Tilt testing. Oskarshamn site investigation. SKB P-05-02, Svensk Kärnbränslehantering AB.

Chryssanthakis P, 2006. Borehole KLX10. Tilt testing. Oskarshamn site investigation. SKB P-06-34, Svensk Kärnbränslehantering AB.

Davis J C, 2002. Statistics and data analysis in geology – 3rd ed. John Whiley & Sons, Inc. New York.

Deere D U, 1964. Technical description of rock cores for engineering purposes. Rock Mech. Rock Engineering, 1(1), pp 17–22.

Dearman W R, 1974. Weathering classification in the characterization of rock for engineering purposes in British Practice. Bull. Int. Assoc. Eng. Geol. 9, pp 33–42.

Dearman W R, Baynes F J, Irfan T Y, 1978. Engineeringgrading of weathered granite. Eng. Geol. 12, pp 345–374.

Deutsch C, Journel A, 1998. GS-LIB: Geostatistical Software Library and User´s Guide. Second edition. Oxford University Press.

Drake H, Tullborg E-L, 2006. Mineralogical, chemical and redox features of red-staining adjacent to fractures – Results from drill core KLX04. Oskarshamn site investigation. SKB P-06-02, Svensk Kärnbränslehantering AB.

Ekman L, 2001. Project Deep Drilling KLX02 – Phase 2. Methods, scope of activities and results. Summary report. SKB TR-01-11, Svensk Kärnbränslehantering AB.

Eloranta P, 2004a. Drill hole KSH01A. Uniaxial compression test (HUT). Oskarshamn site investigation. SKB P-04-182, Svensk Kärnbränslehantering AB.

Eloranta P, 2004b. Drill hole KSH01A. Triaxial compression test (HUT). Oskarshamn site investigation. SKB P-04-183, Svensk Kärnbränslehantering AB.

Eloranta P, 2004c. Drill hole KSH01A: Indirect tensile strength test (HUT). Oskarshamn site investigation. SKB P-04-184, Svensk Kärnbränslehantering AB.

Fälth B, Hökmark H, 2006. Seismically induced slip on rock fractures. Results from dynamic discrete fracture modeling. SKB R-06-48, Svensk Kärnbränslehantering AB.

Glamheden R, Fredriksson A, Röshoff K, Karlsson J, Hakami H, Christiansson R, 2007. Rock Mechanics Forsmark. Site descriptive modelling. Forsmark stage 2.2. SKB R-07-31, Svensk Kärnbränslehantering AB.

Glamheden R, Lanaro F, Karlsson J, Lindberg U, Wrafter J, Hakami H, Johansson M, 2008. Rock mechanics Forsmark. Modelling stage 2.3. Complementary analysis and verification of the rock mechanics model. SKB R-08-66, Svensk Kärnbränslehantering AB.

Hakami E, Hakami H, Cosgrove J, 2002. Strategy for a Rock Mechanics Site Descriptive Model. Development and testing of an approach to modelling the state of stress. SKB R-02-03, Svensk Kärnbränslehantering AB.

Hermanson J, Fox A, Öhman J, Rhén I, 2008. Compilation of data used for the analysis of the geological and hydrogeological DFN models. Site descriptive modelling. SDM-Site Laxemar. SKB R-08-56, Svensk Kärnbränslehantering AB.

Hoek E, Carranza-Torres C, Corkum B, 2002. The Hoek-Brown Failure Criterion – 2002 Edition. 5th North American Rock Mech. Symp. And 17th Tunneling Ass. of Canada Conf. NARMS-TAC, pp 267–271.

Hökmark H, Fälth B, Wallroth T, 2006. T-H-M couplings in rock. Overview of results of importance to the SR-Can safety assessment. SKB R-06-88, Svensk Kärnbränslehantering AB.

Itasca Consulting Group, Inc., 2008. 3DEC version 4.1, Minneapolis, USA

Jacobsson L, 2004a. Drill hole KSH01A. Indirect tensile strength test. Oskarshamn site investigation. SKB P-04-62, Svensk Kärnbränslehantering AB.

Jacobsson L, 2004b. Drill hole KSH02. Indirect tensile strenght test. Oskarshamn site investigation. SKB P-04-63, Svensk Kärnbränslehantering AB.

Jacobsson L, 2004c. Drill hole KSH01A. Uniaxial compression test of intact rock. Oskarshamn site investigation. SKB P-04-207, Svensk Kärnbränslehantering AB.

Jacobsson L, 2004d. Drill hole KSH01A. Triaxial compression test of intact rock. Oskarshamn site investigation. SKB P-04-208, Svensk Kärnbränslehantering AB.

Jacobsson L, 2004e. Drill hole KSH02A. Uniaxial compression test of intact rock. Oskarshamn site investigation. SKB P-04-209, Svensk Kärnbränslehantering AB.

Jacobsson L, 2004f. Drill hole KSH02A. Triaxial compression test of intact rock. Oskarshamn site investigation. SKB P-04-210, Svensk Kärnbränslehantering AB.

Jacobsson L, 2004g. Borehole KLX02. Uniaxial compression test of intact rock. Oskarshamn site investigation. SKB P-04-255, Svensk Kärnbränslehantering AB.

Jacobsson L, 2004h. Drill hole KLX02. Indirect tensile strength test. Oskarshamn site investigation. SKB P-04-256, Svensk Kärnbränslehantering AB.

Jacobsson L, 2004i. Borehole KLX02. Normal stress and shear tests on joints. Oskarshamn site investigation. SKB P-04-257, Svensk Kärnbränslehantering AB.

Jacobsson L, 2004j. Borehole KLX04A Uniaxial compression test of intact rock. Oskarshamn site investigation. SKB P-04-261, Svensk Kärnbränslehantering AB.

Jacobsson L, 2004k. Borehole KLX04A Triaxial compression test of intact rock. Oskarshamn site investigation. SKB P-04-262, Svensk Kärnbränslehantering AB.

Jacobsson L, 2004l. Drill hole KLX04A: Indirect tensile strength test. Oskarshamn site investigation. SKB P-04-263, Svensk Kärnbränslehantering AB.

Jacobsson L, 2004m. Borehole KLX04A. Normal stress and shear tests on joints. Oskarshamn site investigation. SKB P-04-264, Svensk Kärnbränslehantering AB.

Jacobsson L, 2005a. Drill hole KAV01. Normal loading and shear tests on joints. Oskarshamn site investigation. SKB P-05-05, Svensk Kärnbränslehantering AB.

Jacobsson L, 2005b. Drill hole KSH01A. Normal loading and shear tests on joints. Oskarshamn site investigation. SKB P-05-06, Svensk Kärnbränslehantering AB.

Jacobsson L, 2005c. Drill hole KSH02A. Normal loading and shear tests on joints. Oskarshamn site investigation. SKB P-05-07, Svensk Kärnbränslehantering AB.

Jacobsson L, 2005d. Borehole KLX03A. Uniaxial compression test of intact rock. Oskarshamn site investigation. SKB P-05-90, Svensk Kärnbränslehantering AB.

Jacobsson L, 2005e. Drill hole KLX03A. Indirect tensile strength test. Oskarshamn site investigation. SKB P-05-91, Svensk Kärnbränslehantering AB.

Jacobsson L, 2005f. Borehole KLX03A. Triaxial compression test of intact rock. Oskarshamn site investigation. SKB P-05-96, Svensk Kärnbränslehantering AB.

Jacobsson L, 2005g. Borehole KLX06A. Triaxial compression test of intact rock. Oskarshamn site investigation. SKB P-05-128, Svensk Kärnbränslehantering AB.

Jacobsson L, Flansbjer M, 2005a. Borehole KLX03A. Normal loading and shear tests on joints. Oskarshamn site investigation. SKB P-05-92, Svensk Kärnbränslehantering AB.

Jacobsson L, Flansbjer M, 2005b. Borehole KLX06A. Normal loading and shear tests on joints. Oskarshamn site investigation. SKB P-05-146, Svensk Kärnbränslehantering AB.

Jacobsson L, 2006a. Borehole KLX08. Uniaxial compression test of intact rock. Oskarshamn site investigation. SKB P-06-32, Svensk Kärnbränslehantering AB.

Jacobsson L, 2006b. Borehole KLX10. Uniaxial compression test of intact rock. Oskarshamn site investigation. SKB P-06-37, Svensk Kärnbränslehantering AB.

Jacobsson L, 2006c. Drill hole KLX10. Indirect tensile strength test. Oskarshamn site investigation. SKB P-06-38, Svensk Kärnbränslehantering AB.

Jacobsson L, 2006d. Borehole KLX10. Triaxial compression test of intact rock. Oskarshamn site investigation. SKB P-06-40, Svensk Kärnbränslehantering AB.

Jacobsson L, 2006e. Borehole KLX12A. Uniaxial compression test of intact rock. Oskarshamn site investigation. SKB P-06-73, Svensk Kärnbränslehantering AB.

Jacobsson L, 2006f. Drill hole KLX12A. Indirect tensile strength test. Oskarshamn site investigation. SKB P-06-74, Svensk Kärnbränslehantering AB.

Jacobsson L, 2006g. Borehole KLX12A. Triaxial compression test of intact rock. Oskarshamn site investigation. SKB P-06-76, Svensk Kärnbränslehantering AB.

Jacobsson L, 2006h. Borehole KLX11A. Uniaxial compression test of intact rock. Oskarshamn site investigation. SKB P-06-270, Svensk Kärnbränslehantering AB.

Jacobsson L, 2006i. Drill hole KLX11A. Indirect tensile strength test. Oskarshamn site investigation. SKB P-06-271, Svensk Kärnbränslehantering AB.

Jacobsson L, 2006j. Borehole KLX11A. Triaxial compression test of intact rock. Oskarshamn site investigation. SKB P-06-272, Svensk Kärnbränslehantering AB.

Jacobsson L, 2006k. Drill hole KLX13A. Indirect tensile strength test. Oskarshamn site investigation. SKB P-06-276, Svensk Kärnbränslehantering AB.

Jacobsson L, 2006l. Drill hole KLX05. Indirect tensile strength. Oskarshamn site investigation. SKB P-06-299, Svensk Kärnbränslehantering AB.

Jacobsson L, 2006m. Boreholes KLX05 and KLX13A. Uniaxial compression test of intact rock. Oskarshamn site investigation. SKB P-06-300, Svensk Kärnbränslehantering AB.

Jacobsson L, Flansbjer M, 2006a. Borehole KLX07A. Shear tests on sealed joints. Oskarshamn site investigation. SKB P-05-209, Svensk Kärnbränslehantering AB.

Jacobsson L, Flansbjer M, 2006b. Borehole KLX10. Normal loading and shear tests on joints. Oskarshamn site investigation. SKB P-06-39, Svensk Kärnbränslehantering AB.

Jacobsson L, Flansbjer M, 2006c. Borehole KLX12A. Normal loading and shear tests on joints. Oskarshamn site investigation. SKB P-06-75, Svensk Kärnbränslehantering AB.

Jacobsson L, Flansbjer M, 2006d. Borehole KLX13A. Shear tests on sealed joints. Oskarshamn site investigation. SKB P-06-277, Svensk Kärnbränslehantering AB.

Jacobsson L, 2007a. Borehole KLX17A. Microcrack volume measurements and triaxial compression test on intact rock. Oskarshamn site investigation. SKB P-07-140, Svensk Kärnbränslehantering AB.

Jacobsson L, 2007b. Borehole KLX16A. Indirect tensile strength test. Oskarshamn site investigation. SKB P-07-142, Svensk Kärnbränslehantering AB.

Jacobsson L, 2007c. Borehole KLX16A. Uniaxial compression test of intact rock. Oskarshamn site investigation. SKB P-07-143, Svensk Kärnbränslehantering AB.

Jacobsson L, 2007d. Boreholes KLX17A, KLX18A and KLX21B. Uniaxial compression test of intact rock. Oskarshamn site investigation. SKB P-07-217, Svensk Kärnbränslehantering AB.

Jaeger J C, Cook N G W, Zimmerman R W, 2007. Fundamentals of rock mechanics. Blackwell publishing, Victoria.

Jansson T, Stigsson M, 2002. Test with different stress measurement methods in two orthogonal bore holes in Äspö HRL. SKB R-02-26, Svensk Kärnbränslehantering AB.

Jonsson M, Berglund J, Bäckström A, Christiansson R, Johansson M, Mas Ivars D, Olsson M, Feng Q, 2009. ÄSPÖ Hard Rock Laboratory Studies of factors that affect and controls the Excavation Disturbance/Deformation Zone. SKB R-09-17, Svensk Kärnbränslehantering AB.

Klasson H, Persson M, Ljunggren C, 2001. Overcoring rock stress measurements at Äspö HRL. Prototype Repository: Borehole KA3579G (Revised data) and K-tunnel: Borehole KK0045G01. SKB IPR-01-67, Svensk Kärnbränslehantering AB.

Klasson H, Lindblad K, Lindfors U, Andersson S, 2002. Äspö Hard Rock Laboratory. Overcoring rock stress measurements in borehole KOV01, Oskarshamn. SKB IPR-02-18, Svensk Kärnbränslehantering AB.

Klee G, Rummel F, 2002. Äspö Hard Rock Laboratory. Rock Stress measurements at the Äspö HRL. Hydraulic fracturing in boreholes KA2599G01 and KF0093A01. SKB IPR-02-02, Svensk Kärnbränslehantering AB.

Lanaro F, Bäckström A, 2005. Rock mechanics characterisation of borehole KSH01A and B, KSH02, KSH03A and B, KAV01 and KLX02. Oskarshamn site investigation. SKB P-05-283, Svensk Kärnbränslehantering AB.

Lanaro F, Fredriksson A, 2005a. Rock mechanics characterization of the rock mass – Summary of primary data, Preliminary site description, Simpevarp subarea – version 1.2. SKB R-05-21, Svensk Kärnbränslehantering AB.

Lanaro F, Fredriksson A, 2005b. Rock Mechanics Model – Summary of the primary data. Forsmark site investigation. SKB R-05-83, Svensk Kärnbränslehantering AB.

Lanaro F, Bäckström A, 2006a. Empirical characterization of the rock mass along borehole KBH02 and comparison with the results of the EXPECT project. SKB R-06-74, Svensk Kärnbränslehantering AB.

Lanaro F, Bäckström A, 2006b. Rock mechanics characterisation of borehole KLX01, KLX03, KLX04 and KAV04. Oskarshamn site investigation. SKB P-06-323, Svensk Kärnbränslehantering AB.

Lanaro F, Öhman J, Fredriksson A, 2006. Rock mechanics modelling of rock mass properties – Summery of primary data. Preliminary site description subarea – version 1.2. SKB R-06-15, Svensk Kärnbränslehantering AB.

La Pointe P, Fox A, Hermanson J, Öhman J, 2008. Site Descriptive Modeling, SDM Site Laxemar. Geological discrete fracture network model for the Laxemarsite. SKB R-08-55, Svensk Kärnbränslehantering AB.

Lindfors U, 2004. Hydraulic fracturing and HTPF rock stress measurements in borehole KSH01A. Oskarshamn site investigation. SKB P-04-310, Svensk Kärnbränslehantering AB.

Lindfors U, Perman F, 2007. Overcoring rock stress measurements in borehole KLX12A. Oskarshamn site investigation. SKB P-07-123, Svensk Kärnbränslehantering AB.

Ljunggren C, Klasson H, 1997. Drilling KLX02 – Phase 2 Lilla Laxemar Oskarshamn – Deep hydraulic fracturing Rock stress measurements in borehole KLX02, Laxemar. SKB PR U-97-27, Svensk Kärnbränslehantering AB.

Lucas-Girot A, Langlois P, Sangleboeuf J C, Ouammou A, Rouxel T, Gaude J, 2002. A synthetic aragonite-based bioceramic: influence of process parameters on porosity and compressive strength. Elsivier Biomaterials 23, pp 503–510.

Martin C D, Read R S, Chandler N A, 1990. Does scale influence in situ stress measurements? – Some findings at the Underground Research Laboratory. In Proc. First Int. Workshop on Scale Effects in Rock Masses, Loen, Norway (Ed. da Cunha AP), pp 307–316, A.A. Balkema, Rotterdam.

Martin C D, Christiansson R, Söderhäll J, 2001. Rock stability considerations for siting and constructing a KBS-3 repository. Based on experiences from Äspö HRL, AECL's URL, tunnelling and mining. SKB TR-01-38, Svensk Kärnbränslehantering AB.

Martin C D, 2007. Quantifying in-situ stress magnitudes and orientations at Forsmark for Design Step D2. SKB R-07-26, Svensk Kärnbränslehantering AB.

Mas Ivars D, Norén K, 2006. Äspö Hard Rock Laboratory. Äspö Pillar Stability Experiment. Coupled Stress-flow tests on large fracture samples from the APSE site. (In prep), Svensk Kärnbränslehantering AB.

Nielsen U T, Horn F, 2004. Oskarshamn site investigation. Geophysical borehole logging in borehole KLX03, HLX21, HLX22, HLX23, HLX24 and HLX 25. SKB P-04-280, Svensk Kärnbränslehantering AB.

Nielsen U T, Ringgaard J, 2006. Geophysical borehole logging in boreholes KLX12A, KLX09G, KLX10B and KLX10C. Oskarshamn site investigation. SKB P-06-198, Svensk Kärnbränslehantering AB.

Olofsson I, Fredriksson A, 2005. Strategy for a numerical Rock Mechanics Site descriptive Model. SKB R-05-43, Svensk Kärnbränslehantering AB.

Olofsson I, Simeonov A, Stephens M, Follin S, Nilsson A-C, Röshoff K, Lindberg U, Lanaro F, Fredriksson A, Persson L, 2007. Site descriptive modelling Forsmark, stage 2.2. A fracture domain concept as a basis for the statistical modelling of fractures and minor deformation zones, and interdisciplinary coordination. SKB R-07-15, Svensk Kärnbränslehantering AB.

Peebles P Z, 1993. Probability, random variables and random signal functions, McGraw.

Reinecker J, Heidbach O, Tingay M, Sperner B, Müller B, 2005. The 2005 release of the World Stress Map (available online at www.world-stress-map.org).

Rhén I, Forsmark T, Hartley L, Jackson P, Roberts D, Swan D, Gylling B, 2008. Bedrock hydrogeology: data interpretation and model parameterisation. Site descriptive modelling, SDM-Site Laxemar. SKB R-08-78, Svensk Kärnbränslehantering AB

Ringgaard J, 2009. Mapping of borehole breakouts. Processing of acoustical televiewer data from KAV04A, KLX10, KLX11A, KLX12A, KLX15A and KLX18A. Oskarshamn site investigation. SKB P-09-31, Svensk Kärnbränslehantering AB.

Rummel F, Klee G, Weber U, 2002. Äspö Hard Rock Laboratory. Rock Stress measurements in Oskarshamn. Hydraulic fracturing and core testing in borehole KOV01. SKB IPR-02-01, Svensk Kärnbränslehantering AB.

Röshoff K, Lanaro F, Jing L, 2002. Strategy for a Rock Mechanics Site Descriptive Model. Development and testing of the empirical approach. SKB R-02-01, Svensk Kärnbränslehantering AB.

Salganik R L, 1973. Mechanics of bodies with many cracks. Mechanics of solids, 8(4) pp 135–143.

Sjöberg J, 2003. Äspö Hard Rock Laboratory. Äspö Pillar Stability Experiment. 3D overcoring rock stress measurements in borehole KA3376B01 ät Äspö HRL. SKB IPR-03-16, Svensk Kärnbränslehantering AB.

Sjöberg J, 2004. Overcoring rock stress measurements in borehole KSH02. Oskarshamn site investigation. SKB P-04-23, Svensk Kärnbränslehantering AB.

Sjöberg J, 2004. Overcoring rock stress measurements in borehole KAV04. Oskarshamn site investigation. SKB P-04-84, Svensk Kärnbränslehantering AB.

Sjöberg J, Perman F, 2005. Overcoring rock stress measurements in borehole KLX04. Oskarshamn site investigation. SKB P-05-69, Svensk Kärnbränslehanntering AB.

Sjöberg L E, Pan M, Asenjo E, 2004. Oskarshamn site investigation. A deformation analysis of the Äspö GPS monitoring network from 2000 to 2004. SKB P-04-196, Svensk Kärnbränslehantering AB.

SKB, 2000. Geoscientific programme for investigation and evaluation of sites for the deep repository. SKB TR-00-20, Svensk Kärnbränslehantering AB.

SKB, 2001. Site investigations. Investigation methods and general execution programme. SKB TR-01-29, Svensk Kärnbränslehantering AB.

SKB, 2006a. Long-term safety for KBS-3 repositories at Forsmark and Laxemar – a first evaluation. Main Report of the SR-Can project. SKB TR-06-09, Svensk Kärnbränslehantering AB.

SKB, 2006b. Preliminary site description. Laxemar subarea – version 1.2. SKB R-06-10, Svensk Kärnbränslehantering AB.

SKB, 2006c. Data report for the safety assessment SR-Can. SKB TR-06-25, Svensk Kärnbränslehantering AB.

SKB, 2008. Site descriptive modelling Forsmark SDM Site. SKB TR-08-05, Svensk Kärnbränslehantering AB.

SKB, 2009. Site description of Laxemar at completion of the site investigation phase (SDM-Site Laxemar). SKB TR-09-01, Svensk Kärnbränslehantering AB.

Stephansson O, Ljunggren C, Jing L, 1991. Stress measurements and tectonic implications for Fennoscandia. Tectonophysics 189, pp 317–322.

Sundberg J, Wrafter J, Back P-E, Rosén L, 2008. Thermal properties Laxemar, Site descriptive modelling, SDM-Site Laxemar Thermal modelling SDM-Site Laxemar. SKB R-08-61, Svensk Kärnbränslehantering AB.

Söderbäck (ed.), 2008. Geological evolution, palaeoclimate and historic development of the Forsmark and Laxemar-Simpevarp areas. Site descriptive modelling SDM-Site. SKB R-08-19, Svensk Kärnbränslehantering AB.

U.S. Bureau of Mines, 1996. Dictionary of Mining, Mineral and Related Terms, CD-ROM, Second Edition, U.S. Bureau of Mines, U.S. Dept. of the Interior, USA.

Viola G, Venvik Ganerod G, 2007. Oskarshamn site investigation. Structural analysis of brittle deformation zones in the Simpevarp-Laxemar area, Oskarshamn, southeast Sweden. SKB P-07-41, Svensk Kärnbränslehantering AB.

Wahlgren C-H, Curtis P, Hermanson J, Forssberg O, Öhman J, Drake H, Fox A, La Pointe P, Triumf C-A, Mattsson H, Thunehed H, 2008. Geology Laxemar, Site descriptive modelling, SDM-Site Laxemar. SKB R-08-54, Svensk Kärnbränslehantering AB.

Zimmerman R W, 1991. Compressiblity of Sand Stones. Elsevier, Amsterdam.

9.1 List of SKB report references

P-03-107 **Chryssanthakis P, 2003.** Borehole: KSH01A. Results of tilt testing. Oskarshamn site investigation. Svensk Kärnbränslehantering AB.

P-04-10 **Chryssanthakis P, 2004a.** Borehole: KSH02. Results of tilt testing. Oskarshamn site investigation. Svensk Kärnbränslehantering AB.

P-04-23 **Sjöberg J, 2004.** Overcoring rock stress measurements in borehole KSH02. Oskarshamn site investigation. Svensk Kärnbränslehantering AB.

P-04-42 **Chryssanthakis P, 2004b.** Borehole: KAV01. Results of tilt testing. Oskarshamn site investigation. Svensk Kärnbränslehantering AB.

P-04-44 **Chryssanthakis P, 2004c.** Borehole: KLX02. Results of tilt testing. Oskarshamn site investigation. Svensk Kärnbränslehantering AB.

P-04-62 **Jacobsson L, 2004a.** Drill hole KSH01A. Indirect tensile strength test. Oskarshamn site investigation. Svensk Kärnbränslehantering AB.

P-04-63 **Jacobsson L, 2004b.** Drill hole KSH02. Indirect tensile strenght test. Oskarshamn site investigation. Svensk Kärnbränslehantering AB.

P-04-84 **Sjöberg J, 2004.** Overcoring rock stress measurements in borehole KAV04. Oskarshamn site investigation. Svensk Kärnbränslehantering AB.

P-04-182 **Eloranta P, 2004.** Drill hole KSH01A. Uniaxial compression test (HUT). Oskarshamn site investigation. Svensk Kärnbränslehantering AB.

P-04-183 **Eloranta P, 2004b.** Drill hole KSH01A. Triaxial compression test (HUT). Oskarshamn site investigation. Svensk Kärnbränslehantering AB.

P-04-184 **Eloranta P, 2004c.** Drill hole KSH01A: Indirect tensile strength test (HUT). Oskarshamn site investigation. Svensk Kärnbränslehantering AB.

P-04-196 **Sjöberg L E, Pan M, Asenjo E, 2004.** Oskarshamn site investigation. A deformation analysis of the Äspö GPS monitoring network from 2000 to 2004. Svensk Kärnbränslehantering AB.

P-04-207 **Jacobsson L, 2004c.** Drill hole KSH01A. Uniaxial compression test of intact rock. Oskarshamn site investigation. Svensk Kärnbränslehantering AB.

P-04-208 **Jacobsson L, 2004d.** Drill hole KSH01A. Triaxial compression test of intact rock. Oskarshamn site investigation. Svensk Kärnbränslehantering AB.

P-04-209 **Jacobsson L, 2004e.** Drill hole KSH02A. Uniaxial compression test of intact rock. Oskarshamn site investigation. Svensk Kärnbränslehantering AB.

P-04-210 **Jacobsson L, 2004f.** Drill hole KSH02A. Triaxial compression test of intact rock. Oskarshamn site investigation. Svensk Kärnbränslehantering AB.

P-04-255 **Jacobsson L, 2004g.** Borehole KLX02. Uniaxial compression test of intact rock. Oskarshamn site investigation. Svensk Kärnbränslehantering AB.

P-04-256 **Jacobsson L, 2004h.** Drill hole KLX02. Indirect tensile strength test. Oskarshamn site investigation. Svensk Kärnbränslehantering AB.

P-04-257 **Jacobsson L, 2004i.** Borehole KLX02. Normal stress and shear tests on joints. Oskarshamn site investigation. Svensk Kärnbränslehantering AB.

P-04-261 **Jacobsson L, 2004j.** Borehole KLX04A Uniaxial compression test of intact rock. Oskarshamn site investigation. Svensk Kärnbränslehantering AB.

P-04-262 **Jacobsson L, 2004k.** Borehole KLX04A Triaxial compression test of intact rock. Oskarshamn site investigation. Svensk Kärnbränslehantering AB.

P-04-263 **Jacobsson L, 2004l.** Drill hole KLX04A: Indirect tensile strength test. Oskarshamn site investigation. Svensk Kärnbränslehantering AB.

P-04-264 **Jacobsson L, 2004m.** Borehole KLX04A. Normal stress and shear tests on joints. Oskarshamn site investigation. Svensk Kärnbränslehantering AB.

P-04-265 **Chryssanthakis P, 2004d.** Borehole KLX04A. Tilt testing. Oskarshamn site investigation. Svensk Kärnbränslehantering AB.

P-04-280 **Nielsen U T, Horn F, 2004.** Oskarshamn site investigation. Geophysical borehole logging in borehole KLX03, HLX21, HLX22, HLX23, HLX24 and HLX 25. Svensk Kärnbränslehantering AB.

P-04-310 **Lindfors U, 2004.** Hydraulic fracturing and HTPF rock stress measurements in borehole KSH01A. Oskarshamn site investigation. Svensk Kärnbränslehantering AB.

P-05-02 **Chryssanthakis P, 2005.** Borehole KLX03A. Tilt testing. Oskarshamn site investigation. Svensk Kärnbränslehantering AB.

P-05-05 **Jacobsson L, 2005a.** Drill hole KAV01. Normal loading and shear tests on joints. Oskarshamn site investigation. Svensk Kärnbränslehantering AB.

P-05-06 **Jacobsson L, 2005b.** Drill hole KSH01A. Normal loading and shear tests on joints. Oskarshamn site investigation. Svensk Kärnbränslehantering AB.

P-05-07 **Jacobsson L, 2005c.** Drill hole KSH02A. Normal loading and shear tests on joints. Oskarshamn site investigation. Svensk Kärnbränslehantering AB.

P-05-69 **Sjöberg J, Perman F, 2005.** Overcoring rock stress measurements in borehole KLX04. Oskarshamn site investigation. Svensk Kärnbränslehanntering AB.

P-05-90 **Jacobsson L, 2005d.** Borehole KLX03A. Uniaxial compression test of intact rock. Oskarshamn site investigation. Svensk Kärnbränslehantering AB.

P-05-91 **Jacobsson L, 2005e.** Drill hole KLX03A. Indirect tensile strength test. Oskarshamn site investigation. Svensk Kärnbränslehantering AB.

P-05-92 **Jacobsson L, Flansbjer M, 2005a.** Borehole KLX03A. Normal loading and shear tests on joints. Oskarshamn site investigation. Svensk Kärnbränslehantering AB.

P-05-96 **Jacobsson L, 2005f.** Borehole KLX03A. Triaxial compression test of intact rock. Oskarshamn site investigation. Svensk Kärnbränslehantering AB.

P-05-128 **Jacobsson L, 2005g.** Borehole KLX06A. Triaxial compression test of intact rock. Oskarshamn site investigation. Svensk Kärnbränslehantering AB.

P-05-146 **Jacobsson L, Flansbjer M, 2005b.** Borehole KLX06A. Normal loading and shear tests on joints. Oskarshamn site investigation. Svensk Kärnbränslehantering AB.

P-05-209 **Jacobsson L, Flansbjer M, 2006a.** Borehole KLX07A. Shear tests on sealed joints. Oskarshamn site investigation. Svensk Kärnbränslehantering AB.

P-05-283 **Lanaro F, Bäckström A, 2005.** Rock mechanics characterisation of borehole KSH01A and B, KSH02, KSH03A and B, KAV01 and KLX02. Oskarshamn site investigation. Svensk Kärnbränslehantering AB.

P-06-02 **Drake H, Tullborg E-L, 2006.** Mineralogical, chemical and redox features of red-staining adjacent to fractures – Results from drill core KLX04. Oskarshamn site investigation. Svensk Kärnbränslehantering AB.

P-06-32 **Jacobsson L, 2006a.** Borehole KLX08. Uniaxial compression test of intact rock. Oskarshamn site investigation. Svensk Kärnbränslehantering AB.

P-06-34 **Chryssanthakis P, 2006.** Borehole KLX10. Tilt testing. Oskarshamn site investigation. Svensk Kärnbränslehantering AB.

P-06-37 **Jacobsson L, 2006b.** Borehole KLX10. Uniaxial compression test of intact rock. Oskarshamn site investigation. Svensk Kärnbränslehantering AB.

P-06-38 **Jacobsson L, 2006c.** Drill hole KLX10. Indirect tensile strength test. Oskarshamn site investigation. Svensk Kärnbränslehantering AB.

P-06-39 **Jacobsson L, Flansbjer M, 2006b.** Borehole KLX10. Normal loading and shear tests on joints. Oskarshamn site investigation. Svensk Kärnbränslehantering AB.

P-06-40 **Jacobsson L, 2006d.** Borehole KLX10. Triaxial compression test of intact rock. Oskarshamn site investigation. Svensk Kärnbränslehantering AB.

P-06-73 **Jacobsson L, 2006e.** Borehole KLX12A. Uniaxial compression test of intact rock. Oskarshamn site investigation. Svensk Kärnbränslehantering AB.

P-06-74 **Jacobsson L, 2006f.** Drill hole KLX12A. Indirect tensile strength test. Oskarshamn site investigation. Svensk Kärnbränslehantering AB.

P-06-75 **Jacobsson L, Flansbjer M, 2006c.** Borehole KLX12A. Normal loading and shear tests on joints. Oskarshamn site investigation. Svensk Kärnbränslehantering AB.

P-06-76 **Jacobsson L, 2006g.** Borehole KLX12A. Triaxial compression test of intact rock. Oskarshamn site investigation. Svensk Kärnbränslehantering AB.

P-06-198 **Nielsen U T, Ringgaard J, 2006.** Geophysical borehole logging in boreholes KLX12A, KLX09G, KLX10B and KLX10C. Oskarshamn site investigation. Svensk Kärnbränslehantering AB.

P-06-270 **Jacobsson L, 2006h.** Borehole KLX11A. Uniaxial compression test of intact rock. Oskarshamn site investigation. Svensk Kärnbränslehantering AB.

P-06-271 **Jacobsson L, 2006i.** Drill hole KLX11A. Indirect tensile strength test. Oskarshamn site investigation. Svensk Kärnbränslehantering AB.

P-06-272 **Jacobsson L, 2006j.** Borehole KLX11A. Triaxial compression test of intact rock. Oskarshamn site investigation. Svensk Kärnbränslehantering AB.

P-06-276 **Jacobsson L, 2006k.** Drill hole KLX13A. Indirect tensile strength test. Oskarshamn site investigation. Svensk Kärnbränslehantering AB.

P-06-277 **Jacobsson L, Flansbjer M, 2006d.** Borehole KLX13A. Shear tests on sealed joints. Oskarshamn site investigation. Svensk Kärnbränslehantering AB.

P-06-299 **Jacobsson L, 2006l.** Drill hole KLX05. Indirect tensile strength. Oskarshamn site investigation. Svensk Kärnbränslehantering AB.

P-06-300 **Jacobsson L, 2006m.** Boreholes KLX05 and KLX13A. Uniaxial compression test of intact rock. Oskarshamn site investigation. Svensk Kärnbränslehantering AB.

P-06-323 **Lanaro F, Bäckström A, 2006b.** Rock mechanics characterisation of borehole KLX01, KLX03, KLX04 and KAV04. Oskarshamn site investigation. Svensk Kärnbränslehantering AB.

P-07-41 **Viola G, Venvik Ganerod G, 2007a.** Oskarshamn site investigation. Structural analysis of brittle deformation zones in the Simpevarp-Laxemar area, Oskarshamn, southeast Sweden. Svensk Kärnbränslehantering AB.

P-07-123 **Lindfors U, Perman F, 2007.** Overcoring rock stress measurements in borehole KLX12A. Oskarshamn site investigation. Svensk Kärnbränslehantering AB.

P-07-140 **Jacobsson L, 2007a.** Borehole KLX17A. Microcrack volume measurements and triaxial compression test on intact rock. Oskarshamn site investigation. Svensk Kärnbränslehantering AB.

P-07-142 **Jacobsson L, 2007b.** Borehole KLX16A. Indirect tensile strength test. Oskarshamn site investigation. Svensk Kärnbränslehantering AB.

P-07-143 **Jacobsson L, 2007c.** Borehole KLX16A. Uniaxial compression test of intact rock. Oskarshamn site investigation. Svensk Kärnbränslehantering AB.

P-07-217 **Jacobsson L, 2007d.** Boreholes KLX17A, KLX18A and KLX21B. Uniaxial compression test of intact rock. Oskarshamn site investigation. Svensk Kärnbränslehantering AB.

P-07-232 **Ask D, Cornet F, Brunet C, Fontbonne F, 2007.** Stress measurements with hydraulic methods in borehole KLX12A. Oskarshamn site investigation. Svensk Kärnbränslehantering AB.

P-07-235 **Ask MVS, Ask D, 2007.** Detection of potential borehole breakouts in boreholes KFM01A and KFM01B. Forsmark site investigation. Svensk Kärnbränslehantering AB.

P-09-31 **Ringgaard J, 2009.** Mapping of borehole breakouts. Processing of acoustical televiewer data from KAV04A, KLX10, KLX11A, KLX12A, KLX15A and KLX18A. Oskarshamn site investigation. Svensk Kärnbränslehantering AB.

R-02-01 **Röshoff K, Lanaro F, Jing L, 2002.** Strategy for a Rock Mechanics Site Descriptive Model. Development and testing of the empirical approach. Svensk Kärnbränslehantering AB.

R-02-03 **Hakami E, Hakami H, Cosgrove J, 2002.** Strategy for a Rock Mechanics Site Descriptive Model. Development and testing of an approach to modelling the state of stress. Svensk Kärnbränslehantering AB.

R-02-26 **Jansson T, Stigsson M, 2002.** Test with different stress measurement methods in two orthogonal bore holes in Äspö HRL. Svensk Kärnbränslehantering AB.

R-05-21 **Lanaro F, Fredriksson A, 2005.** Rock mechanics characterization of the rock mass – Summary of primary data, Preliminary site description, Simpevarp subarea – version 1.2. Svensk Kärnbränslehantering AB.

R-05-43 **Olofsson I, Fredriksson A, 2005.** Strategy for a numerical Rock Mechanics Site descriptive Model. Svensk Kärnbränslehantering AB.

R-05-83 **Lanaro F, Fredriksson A, 2005.** Rock Mechanics Model – Summary of the primary data. Forsmark site investigation. Svensk Kärnbränslehantering AB.

R-06-10 **SKB, 2006b.** Preliminary site description. Laxemar subarea – version 1.2. Svensk Kärnbränslehantering AB.

R-06-15 **Lanaro F, Öhman J, Fredriksson A, 2006.** Rock mechanics modelling of rock mass properties – Summery of primary data. Preliminary site description subarea – version 1.2. Svensk Kärnbränslehantering AB.

R-06-48 **Fälth B, Hökmark H, 2006.** Seismically induced slip on rock fractures. Results from dynamic discrete fracture modeling. Svensk Kärnbränslehantering AB.

R-06-67 **Bödvarsson R, Lund B, Roberts R, Slunga S, 2006.** Earthquake activity in Sweden. Study in connection with a proposed nuclear waste repository in Forsmark or Oskarshamn. Svensk Kärnbränslehantering AB.

R-06-74 **Lanaro F, Bäckström A, 2006a.** Empirical characterization of the rock mass along borehole KBH02 and comparison with the results of the EXPECT project. Svensk Kärnbränslehantering AB.

R-06-88 **Hökmark, H, Fälth, B, Wallroth, T, 2006.** T-H-M couplings in rock. Overview of results of importance to the SR-Can safety assessment. Svensk Kärnbränslehantering AB.

R-07-15 **Olofsson I, Simeonov A, Stephens M, Follin S, Nilsson A-C, Röshoff K, Lindberg U, Lanaro F, Fredriksson A and Persson L, 2007.** Site descriptive modelling Forsmark, stage 2.2. A fracture domain concept as a basis for the statistical modelling of fractures and minor deformation zones, and interdisciplinary coordination. Svensk Kärnbränslehantering AB.

R-07-26 **Martin C D, 2007**. Quantifying in-situ stress magnitudes and orientations at Forsmark for Design Step D2. Svensk Kärnbränslehantering AB.

R-07-31 **Glamheden R, Fredriksson A, Röshoff K, Karlsson J, Hakami H, Christiansson R, 2007.** Rock Mechanics Forsmark. Site descriptive modelling. Forsmark stage 2.2. Svensk Kärnbränslehantering AB.

R-07-42 **Back P-E, Sundberg J, 2007.** Thermal Site Descriptive Model. A Strategy for the Model Development during Site Investigations. Version 2.0. Svensk Kärnbränslehantering AB.

R-08-19 **Söderbäck (ed.), 2008.** Geological evolution, palaeoclimate and historic development of the Forsmark and Laxemar-Simpevarp areas. Site descriptive modelling SDM-Site. Svensk Kärnbränslehantering AB.

R-08-54 **Wahlgren C-H, Curtis P, Hermanson J, Forssberg O, Öhman J, Drake H, Fox A, La Pointe P, Triumf C-A, Mattsson H, Thunehed H, 2008**. Geology Laxemar, Site descriptive modelling, SDM-Site Laxemar. Svensk Kärnbränslehantering AB.

R-08-55 **La Pointe P, Fox A, Hermanson J, Öhman J, 2008.** Site Descriptive Modeling, SDM Site Laxemar. Geological discrete fracture network model for the Laxemar site. Svensk Kärnbränslehantering AB.

R-08-56 **Hermanson J, Fox A, Öhman J, Rhén I, 2008.** Compilation of data used for the analysis of the geological and hydrogeological DFN models. Site descriptive modelling. SDM-Site Laxemar. Svensk Kärnbränslehantering AB.

R-08-61 **Sundberg J, Wrafter J, Back P-E, Rosén L, 2008.** Thermal properties Laxemar, Site descriptive modelling, SDM-Site Laxemar Underlagsrapport Thermal modelling SDM-Site Laxemar. Svensk Kärnbränslehantering AB.

R-08-66 **Glamheden R, Lanaro F, Karlsson J, Lindberg U, Wrafter J, Hakami H, Johansson M, 2008.** Rock mechanics Forsmark. Modelling stage 2.3. Complementary analysis and verification of the rock mechanics model. Svensk Kärnbränslehantering AB.

R-08-78 **Rhén I, Forsmark T, Hartley L, Jackson P, Roberts D, Swan D, Gylling B, 2008.** Bedrock hydrogeology: data interpretation and model parameterization. Site descriptive modelling. SDM-Site Laxemar. Svensk Kärnbränslehantering AB.

R-09-17 **Jonsson M, Berglund J, Bäckström A, Christiansson R, Johansson M, Mas Ivars D, Olsson M, Feng Q, 2009.** ÄSPÖ Hard Rock Laboratory Studies of factors that affect and controls the Excavation Disturbance/Deformation Zone. SKB R-09-17, Svensk Kärnbränslehantering AB.

TR-00-12 **Andersson J, Ström A, Svemar C, Almén K-E, Ericsson L-O, 2000.** What requirements does the KBS-3 repository make on the host rock? Geoscientific suitability indicators and criteria for siting and site evaluation. Svensk Kärnbränslehantering AB.

TR-00-20 **SKB, 2000.** Geoscientific programme for investigation and evaluation of sites for the deep repository. Svensk Kärnbränslehantering AB.

TR-01-11 **Ekman L, 2001.** Project Deep Drilling KLX02 – Phase 2. Methods, scope of activities and results. Summary report. Svensk Kärnbränslehantering.

TR-01-29 **SKB, 2001.** Site investigations. Investigation methods and general execution programme. Svensk Kärnbränslehantering AB.

TR-01-38 **Martin C D, Christiansson R, Söderhäll J, 2001.** Rock stability considerations for siting and constructing a KBS-3 repository. Based on experiences from Äspö HRL, AECL's URL, tunnelling and mining. Svensk Kärnbränslehantering AB.

TR-02-01 **Andersson J, Christiansson R, Hudson J, 2002.** Site investigations. Strategy for Rock Mechanics Site Descriptive Model. Svensk Kärnbränslehantering AB.

TR-06-09 **SKB, 2006a.** Long-term safety for KBS-3 repositories at Forsmark and Laxemar – a first evaluation. Main Report of the SR-Can project. Svensk Kärnbränslehantering AB.

TR-06-25 **SKB, 2006c**. Data report for the safety assessment SR-Can. Svensk Kärnbränslehantering AB.

TR-07-01 **Andersson J C, 2007.** Äspö Hard Rock Laboratory. Äspö Pillar Stability Experiment, Final report. Rock mass response to coupled mechanical thermal loading. Svensk Kärnbränslehantering AB.

TR-08-05 **SKB, 2008**. Site description of Forsmark at completion of the site investigation phase. Svensk Kärnbränslehantering AB.

TR-09-01 **SKB, 2009.** Site description of Laxemar at completion of the site investigation phase (SDM-Site Laxemar). SKB TR-09-01. Svensk Kärnbränslehantering AB

PR U-97-27 **Ljunggren C, Klasson H, 1997.** Drilling KLX02 – Phase 2 Lilla Laxemar Oskarshamn – Deep hydraulic fracturing Rock stress measurements in borehole KLX02, Laxemar. Svensk Kärnbränslehantering AB.

IPR-01-67 **Klasson H, Persson M, Ljunggren C, 2001.** Overcoring rock stress measurements at Äspö HRL. Prototype Repository: Borehole KA3579G (Revised data) and K-tunnel: Borehole KK0045G01. Svensk Kärnbränslehantering AB.

IPR-02-01 **Rummel F, Klee G, Weber U, 2002.** Äspö Hard Rock Laboratory. Rock Stress measurements in Oskarshamn. Hydraulic fracturing and core testing in borehole KOV01. Svensk Kärnbränslehantering AB.

IPR-02-02 **Klee G, Rummel F, 2002.** Äspö Hard Rock Laboratory. Rock Stress measurements at the Äspö HRL. Hydraulic fracturing in boreholes KA2599G01 and KF0093A01. Svensk Kärnbränslehantering AB.

IPR-02-18 **Klasson H, Lindblad K, Lindfors U, Andersson S, 2002.** Äspö Hard Rock Laboratory. Overcoring rock stress measurements in borehole KOV01, Oskarshamn. Svensk Kärnbränslehantering AB.

IPR-03-16 **Sjöberg J, 2003.** Äspö Hard Rock Laboratory. Äspö Pillar Stability Experiment. 3D overcoring rock stress measurements in borehole KA3376B01 ät Äspö HRL. Svensk Kärnbränslehantering AB.

Appendix 1

WellCad diagrams for rock mechanics data

WellCad diagrams for the cored boreholes were rock mechanical measurements have been performed, showing a selected suite of rock mechanical data in the context of some base geological and geophysical data.

Note:

- BH length (m. f. ToC) vs. Elevation (m.a.s.l.) – BH length is the borehole length in meters from Top of Casing (ToC is different for every borehole and is shown in the heading as Elevation (m.a.s.l. ToC)) and Elevation is the vertical depth in meters above sea level.
- P-wave velocity – The blue line is the sonic velocity log, the same as in Appendix 5. The green (maximum) and red (minimum) dots shows measurements of p-wave velocities made on the drill core.
- If the columns are blank this means that there are no sample taken or no observation made.
- The notation NO DATA means that no such study is performed in this borehole.
- The boreholes with no specific “rock mechanic” information is not included in the appendix but WellCad plots for all boreholes is found in /Hermanson et al. 2008/.
- For borehole locations see Figure 2–2.

Title ROCK MECHANICS KAV01

Site	ÄVRÖ	Bearing [°]	225.61	Northing [m]	6367257.52	Date of mapping	2003-10-07 00:00:00
Borehole	KAV01	Inclination [°]	-89.19	Easting [m]	1553084.92	Plot Date	2008-11-03 23:04:19
Diameter [mm]	56	Elevation [m.a.s.l.ToC]	14.10	Drilling Start Date	1977-04-21 00:00:00		
Length [m.f.ToC]	757.310	Coordinate System	RT90-RHB70	Drilling Stop Date	1977-05-16 00:00:00		

ROCK TYPE ÄVRÖ
- Fine-grained granite
- Granite
- Ävrö granite
- Fine-grained dioritoid
- Fine-grained diorite-gabbro

ROCK UNIT
- High confidence

DEFORMATION ZONE
- High confidence

TENSILE STRENGTH

TRIAXIAL COMPRESSIVE STRENGTH
(confinement stress MPa)

Q Value
- < 1 Very poor
- 1 - 4 Poor
- 4 - 10 Fair
- 10 - 40 Good
- > 40 Very good

RMR
- < 20 Very poor
- 21 - 40 Poor
- 41 - 60 Fair
- 61 - 80 Good
- 81 - 100 Very good

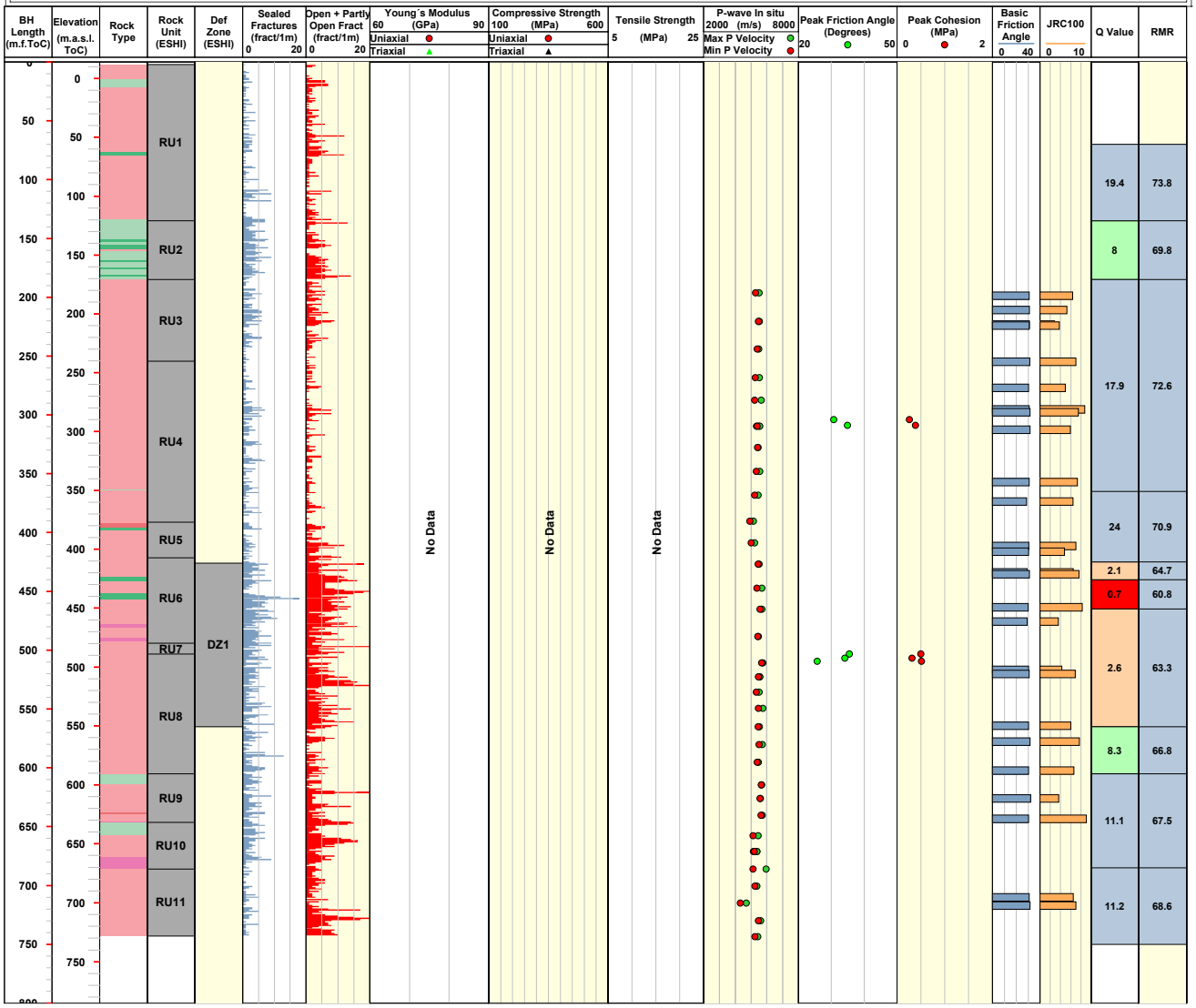

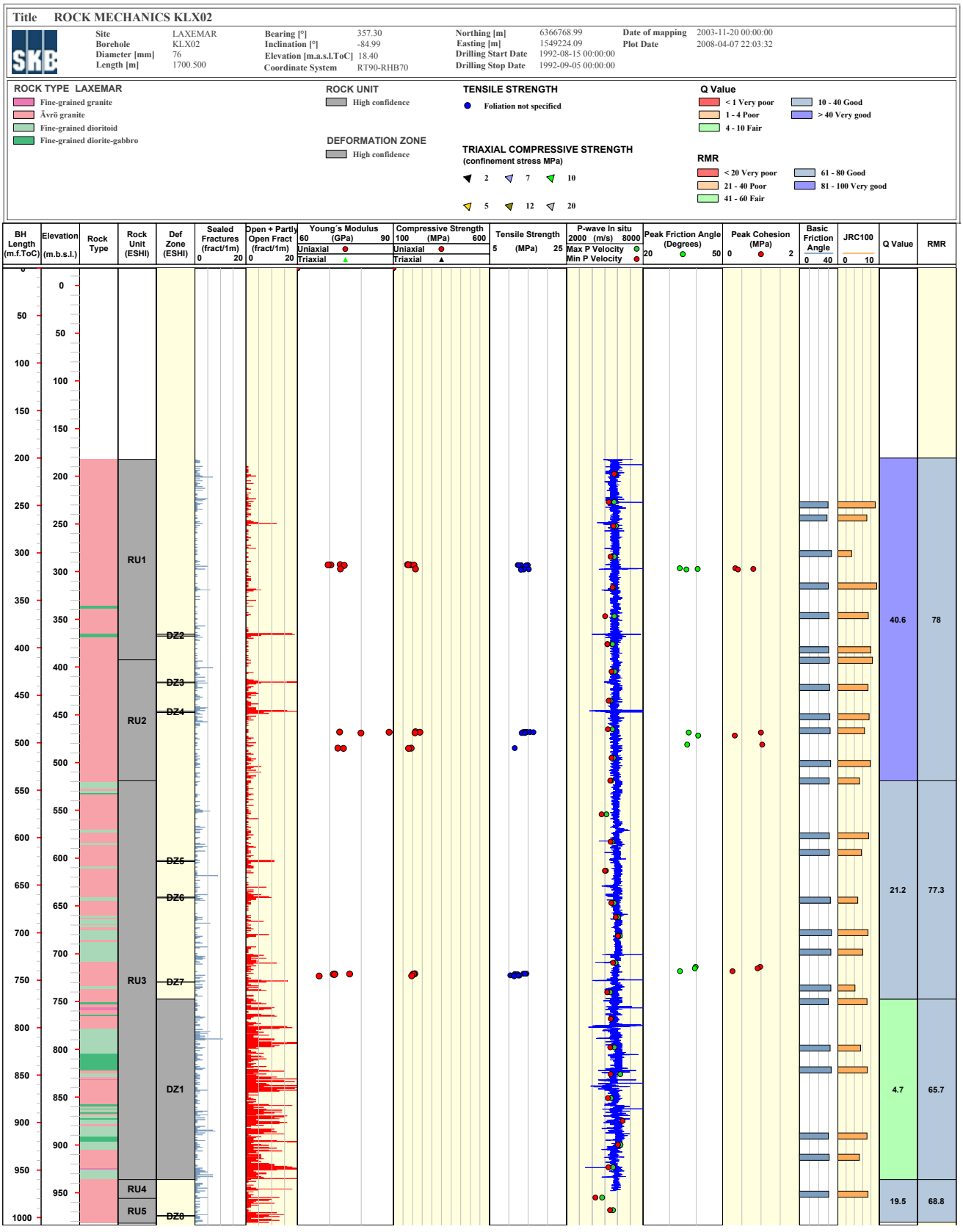
Title ROCK MECHANICS KLX02
Site LAXEMAR
Borehole KLX02
Diameter [mm] 76
Length [m] 1700.500
Bearing [°] 357.30
Inclination [°] -84.99
Elevation [m.a.s.l.ToC] 18.40
Coordinate System RT90-RHB70
Northing [m] 6366768.99
Easting [m] 1549224.09
Drilling Start Date 1992-08-15 00:00:00
Drilling Stop Date 1992-09-05 00:00:00
Date of mapping 2003-11-20 00:00:00
Plot Date 2008-04-07 22:03:32
ROCK TYPE LAXEMAR
Fine-grained granite
Åvrö granite
Fine-grained dioritoid
Fine-grained diorite-gabbro
ROCK UNIT
High confidence
DEFORMATION ZONE
High confidence
TENSILE STRENGTH
Foliation not specified
TRIAXIAL COMPRESSIVE STRENGTH
(confinement stress MPa)
2 7 10
5 12 20
Q Value
< 1 Very poor
1 - 4 Poor
4 - 10 Fair
10 - 40 Good
> 40 Very good
RMR
< 20 Very poor
21 - 40 Poor
41 - 60 Fair
61 - 80 Good
81 - 100 Very good
BH Length (m.f.ToC)
Elevation (m.b.s.l.)
Rock Type
Rock Unit (ESHI)
Def Zone (ESHI)
Sealed Fractures (fract/1m) 0 20
Open + Partly Open Fract (fract/1m) 0 20
Young´s Modulus 60 (GPa) 90
Uniaxial
Triaxial
Compressive Strength 100 (MPa) 600
Uniaxial
Triaxial
Tensile Strength 5 (MPa) 25
P-wave In situ 2000 (m/s) 8000
Max P Velocity
Min P Velocity
Peak Friction Angle (Degrees) 20 50
Peak Cohesion (MPa) 0 2
Basic Friction Angle 0 40
JRC100 0 10
Q Value
RMR
RU1
RU2
RU3
RU4
RU5
DZ2
DZ3
DZ4
DZ5
DZ6
DZ7
DZ1
DZ0
40.6
78
21.2
77.3
4.7
65.7
19.5
68.8

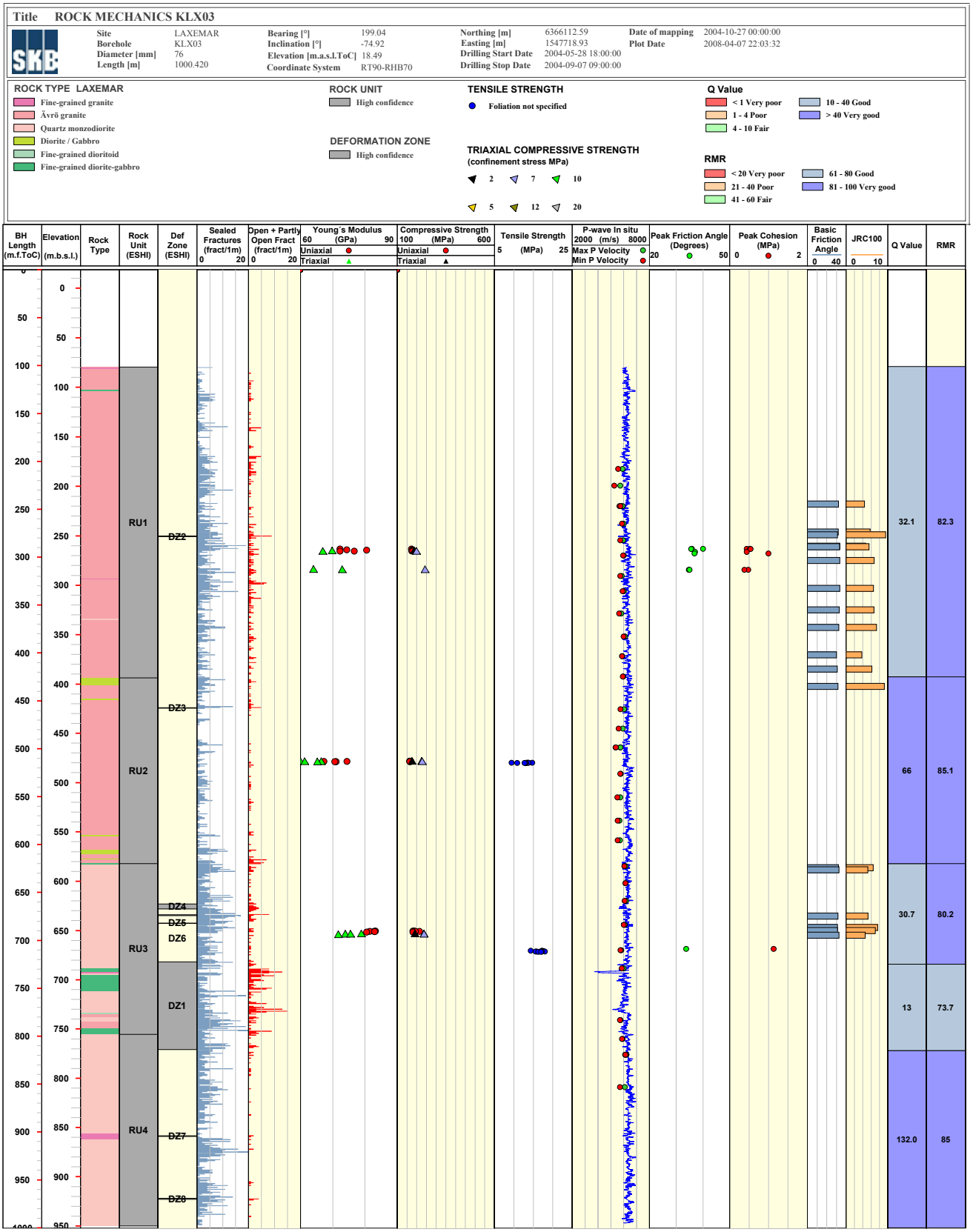
Title ROCK MECHANICS KLX03
Site LAXEMAR
Borehole KLX03
Diameter [mm] 76
Length [m] 1000.420
Bearing [°] 199.04
Inclination [°] -74.92
Elevation [m.a.s.l.ToC] 18.49
Coordinate System RT90-RHB70
Northing [m] 6366112.59
Easting [m] 1547718.93
Drilling Start Date 2004-05-28 18:00:00
Drilling Stop Date 2004-09-07 09:00:00
Date of mapping 2004-10-27 00:00:00
Plot Date 2008-04-07 22:03:32
ROCK TYPE LAXEMAR
Fine-grained granite
Ävrö granite
Quartz monzodiorite
Diorite / Gabbro
Fine-grained dioritoid
Fine-grained diorite-gabbro
ROCK UNIT
High confidence
DEFORMATION ZONE
High confidence
TENSILE STRENGTH
Foliation not specified
TRIAXIAL COMPRESSIVE STRENGTH
(confinement stress MPa)
2 7 10
5 12 20
Q Value
< 1 Very poor
1 - 4 Poor
4 - 10 Fair
10 - 40 Good
> 40 Very good
RMR
< 20 Very poor
21 - 40 Poor
41 - 60 Fair
61 - 80 Good
81 - 100 Very good
BH Length (m.f.ToC)
Elevation (m.b.s.l.)
Rock Type
Rock Unit (ESHI)
Def Zone (ESHI)
Sealed Fractures (fract/1m) 0 20
Open + Partly Open Fract (fract/1m) 0 20
Young´s Modulus 60 (GPa) 90
Uniaxial
Triaxial
Compressive Strength 100 (MPa) 600
Uniaxial
Triaxial
Tensile Strength 5 (MPa) 25
P-wave In situ 2000 (m/s) 8000
Max P Velocity
Min P Velocity
Peak Friction Angle (Degrees) 20 50
Peak Cohesion (MPa) 0 2
Basic Friction Angle 0 40
JRC100 0 10
Q Value
RMR
RU1
RU2
RU3
RU4
DZ2
DZ3
DZ4
DZ5
DZ6
DZ1
DZ7
DZ8
32.1
82.3
66
85.1
30.7
80.2
13
73.7
132.0
85

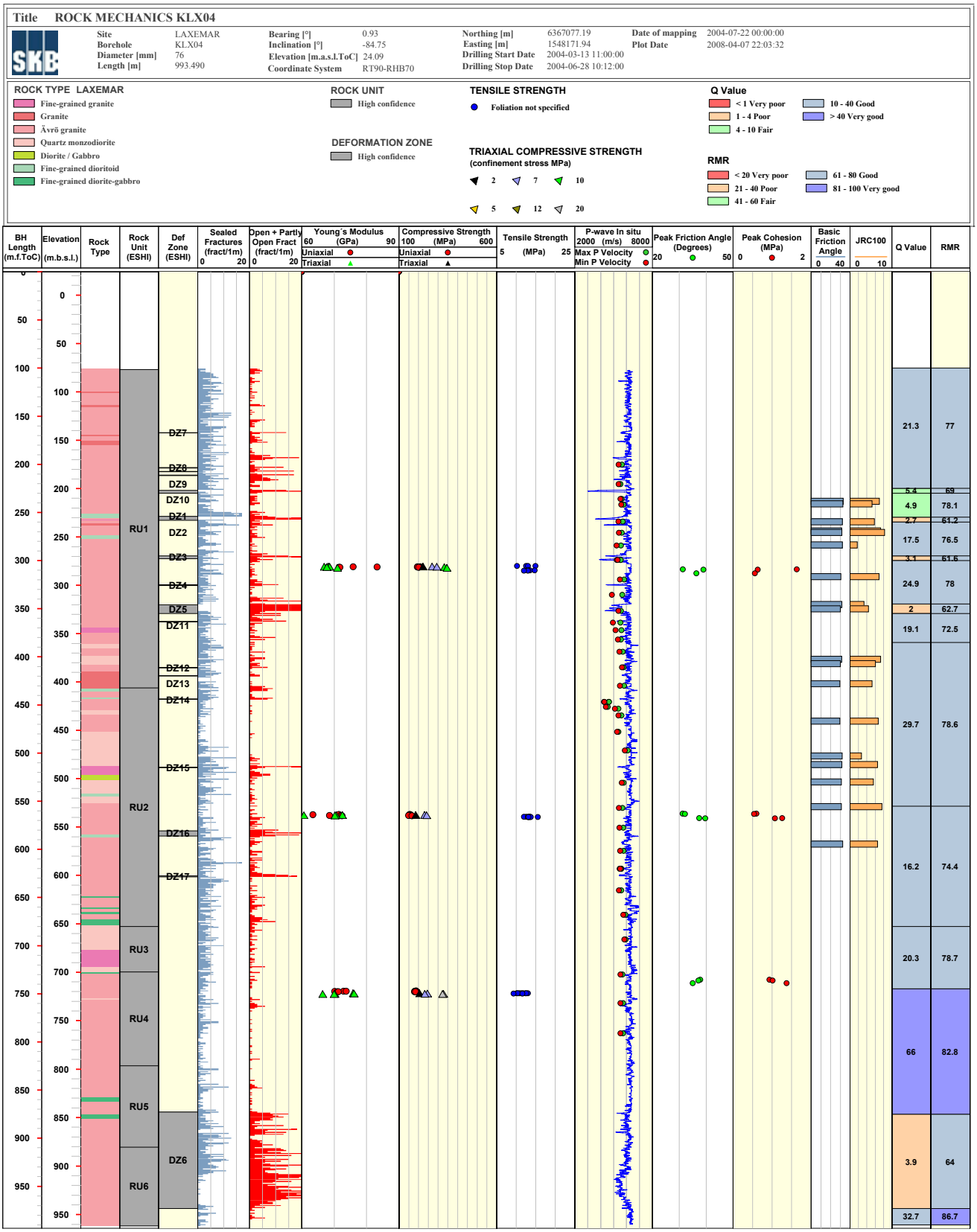
Title ROCK MECHANICS KLX04
Site LAXEMAR
Borehole KLX04
Diameter [mm] 76
Length [m] 993.490
Bearing [°] 0.93
Inclination [°] -84.75
Elevation [m.a.s.l.ToC] 24.09
Coordinate System RT90-RHB70
Northing [m] 6367077.19
Easting [m] 1548171.94
Drilling Start Date 2004-03-13 11:00:00
Drilling Stop Date 2004-06-28 10:12:00
Date of mapping 2004-07-22 00:00:00
Plot Date 2008-04-07 22:03:32
ROCK TYPE LAXEMAR
Fine-grained granite
Granite
Ävrö granite
Quartz monzodiorite
Diorite / Gabbro
Fine-grained dioritoid
Fine-grained diorite-gabbro
ROCK UNIT
High confidence
DEFORMATION ZONE
High confidence
TENSILE STRENGTH
Foliation not specified
TRIAXIAL COMPRESSIVE STRENGTH
(confinement stress MPa)
2 7 10
5 12 20
Q Value
< 1 Very poor
1 - 4 Poor
4 - 10 Fair
10 - 40 Good
> 40 Very good
RMR
< 20 Very poor
21 - 40 Poor
41 - 60 Fair
61 - 80 Good
81 - 100 Very good
BH Length (m.f.ToC)
Elevation (m.b.s.l.)
Rock Type
Rock Unit (ESHI)
Def Zone (ESHI)
Sealed Fractures (fract/1m) 0 20
Open + Partly Open Fract (fract/1m) 0 20
Young´s Modulus 60 (GPa) 90
Uniaxial
Triaxial
Compressive Strength 100 (MPa) 600
Uniaxial
Triaxial
Tensile Strength 5 (MPa) 25
P-wave In situ 2000 (m/s) 8000
Max P Velocity
Min P Velocity
Peak Friction Angle (Degrees) 20 50
Peak Cohesion (MPa) 0 2
Basic Friction Angle 0 40
JRC100 0 10
Q Value
RMR
RU1
RU2
RU3
RU4
RU5
RU6
DZ7
DZ8
DZ9
DZ10
DZ1
DZ2
DZ3
DZ4
DZ5
DZ11
DZ12
DZ13
DZ14
DZ15
DZ16
DZ17
DZ6
21.3 77
5.4 69
4.9 78.1
2.7 61.2
17.5 76.5
3.1 61.6
24.9 78
2 62.7
19.1 72.5
29.7 78.6
16.2 74.4
20.3 78.7
66 82.8
3.9 64
32.7 86.7

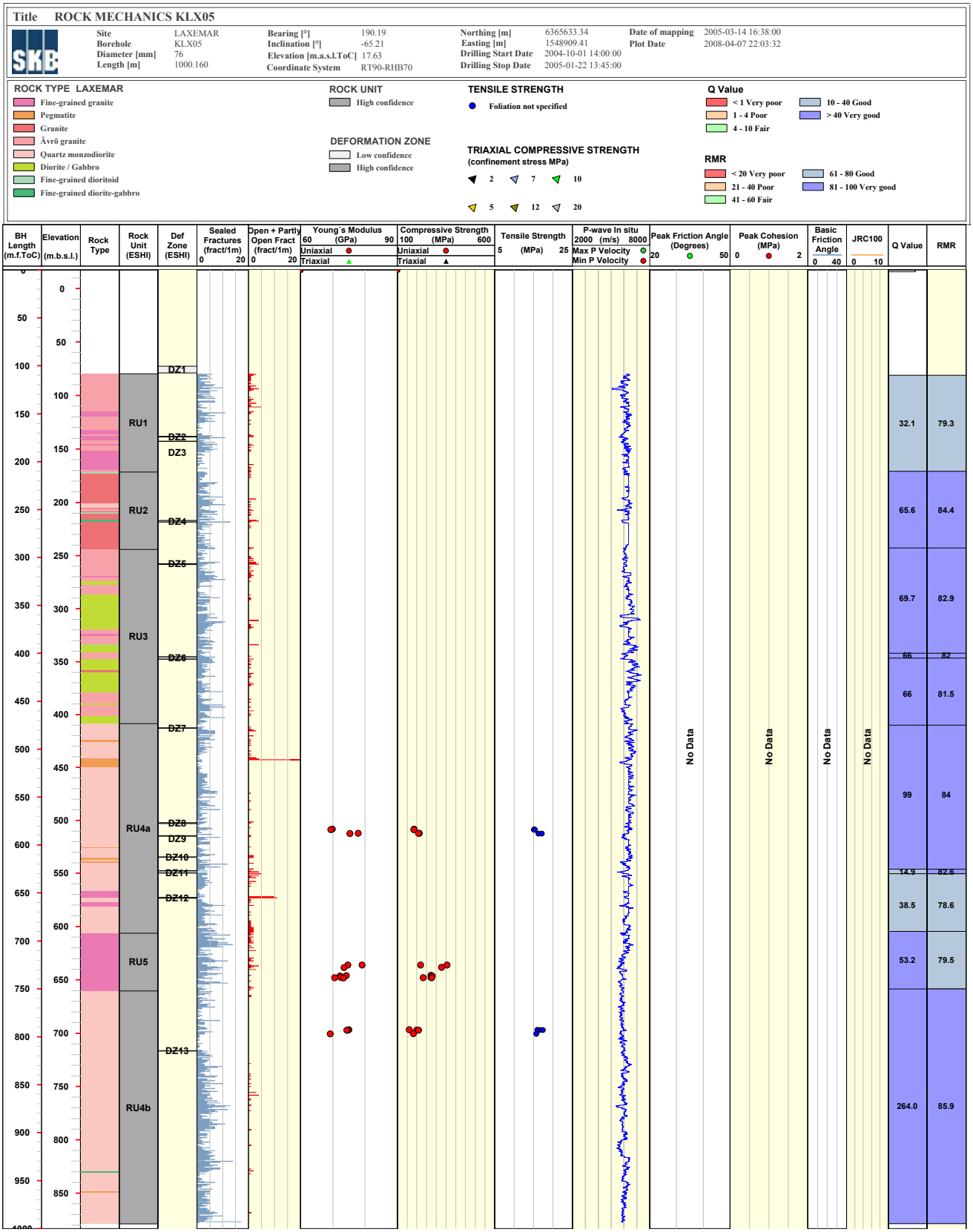
Title ROCK MECHANICS KLX05
Site LAXEMAR
Borehole KLX05
Diameter [mm] 76
Length [m] 1000.160
Bearing [°] 190.19
Inclination [°] -65.21
Elevation [m.a.s.l.ToC] 17.63
Coordinate System RT90-RHB70
Northing [m] 6365633.34
Easting [m] 1548909.41
Drilling Start Date 2004-10-01 14:00:00
Drilling Stop Date 2005-01-22 13:45:00
Date of mapping 2005-03-14 16:38:00
Plot Date 2008-04-07 22:03:32
ROCK TYPE LAXEMAR
Fine-grained granite
Pegmatite
Granite
Ävrö granite
Quartz monzodiorite
Diorite / Gabbro
Fine-grained dioritoid
Fine-grained diorite-gabbro
ROCK UNIT
High confidence
DEFORMATION ZONE
Low confidence
High confidence
TENSILE STRENGTH
Foliation not specified
TRIAXIAL COMPRESSIVE STRENGTH
(confinement stress MPa)
2 7 10
5 12 20
Q Value
< 1 Very poor
1 - 4 Poor
4 - 10 Fair
10 - 40 Good
> 40 Very good
RMR
< 20 Very poor
21 - 40 Poor
41 - 60 Fair
61 - 80 Good
81 - 100 Very good
BH Length (m.f.ToC)
Elevation (m.b.s.l.)
Rock Type
Rock Unit (ESHI)
Def Zone (ESHI)
Sealed Fractures (fract/1m)
Open + Partly Open Fract (fract/1m)
Young´s Modulus (GPa)
Uniaxial
Triaxial
Compressive Strength (MPa)
Tensile Strength (MPa)
P-wave In situ (m/s)
Max P Velocity
Min P Velocity
Peak Friction Angle (Degrees)
Peak Cohesion (MPa)
Basic Friction Angle
JRC100
Q Value
RMR
RU1
RU2
RU3
RU4a
RU5
RU4b
DZ1
DZ2
DZ3
DZ4
DZ5
DZ6
DZ7
DZ8
DZ9
DZ10
DZ11
DZ12
DZ13
No Data
32.1
79.3
65.6
84.4
69.7
82.9
66
82
66
81.5
99
84
14.9
82.6
38.5
78.6
53.2
79.5
264.0
85.9

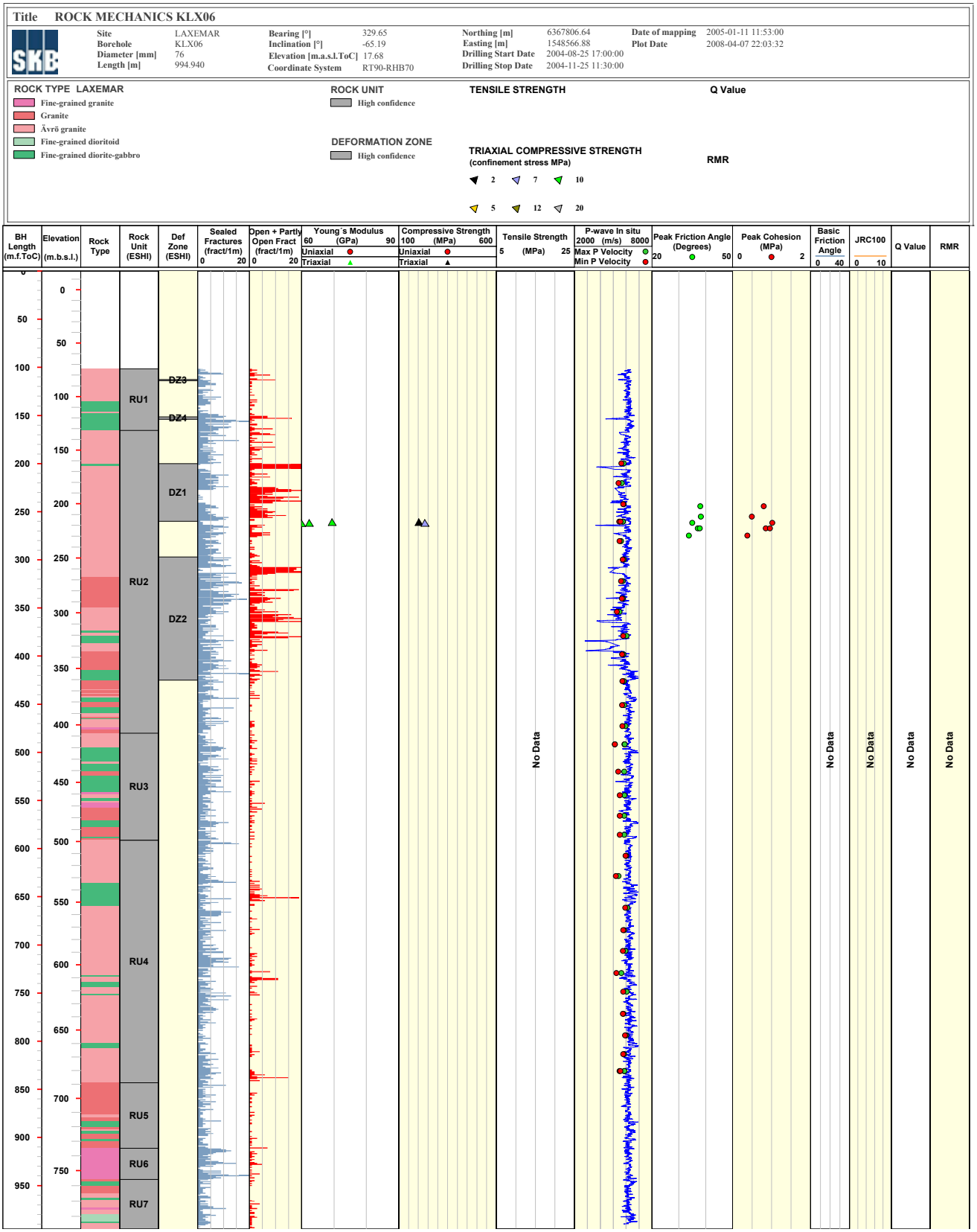
Title ROCK MECHANICS KLX06
Site LAXEMAR
Borehole KLX06
Diameter [mm] 76
Length [m] 994.940
Bearing [°] 329.65
Inclination [°] -65.19
Elevation [m.a.s.l.ToC] 17.68
Coordinate System RT90-RHB70
Northing [m] 6367806.64
Easting [m] 1548566.88
Drilling Start Date 2004-08-25 17:00:00
Drilling Stop Date 2004-11-25 11:30:00
Date of mapping 2005-01-11 11:53:00
Plot Date 2008-04-07 22:03:32
ROCK TYPE LAXEMAR
Fine-grained granite
Granite
Ävrö granite
Fine-grained dioritoid
Fine-grained diorite-gabbro
ROCK UNIT
High confidence
DEFORMATION ZONE
High confidence
TENSILE STRENGTH
TRIAXIAL COMPRESSIVE STRENGTH
(confinement stress MPa)
2 7 10
5 12 20
Q Value
RMR
BH Length (m.f.ToC)
Elevation (m.b.s.l.)
Rock Type
Rock Unit (ESHI)
Def Zone (ESHI)
Sealed Fractures (fract/1m) 0 20
Open + Partly Open Fract (fract/1m) 0 20
Young´s Modulus (GPa) 60 90
Uniaxial
Triaxial
Compressive Strength (MPa) 100 600
Uniaxial
Triaxial
Tensile Strength (MPa) 5 25
No Data
P-wave In situ (m/s) 2000 8000
Max P Velocity
Min P Velocity
Peak Friction Angle (Degrees) 20 50
Peak Cohesion (MPa) 0 2
Basic Friction Angle 0 40
No Data
JRC100 0 10
No Data
Q Value
No Data
RMR
No Data
RU1
RU2
RU3
RU4
RU5
RU6
RU7
DZ3
DZ4
DZ1
DZ2

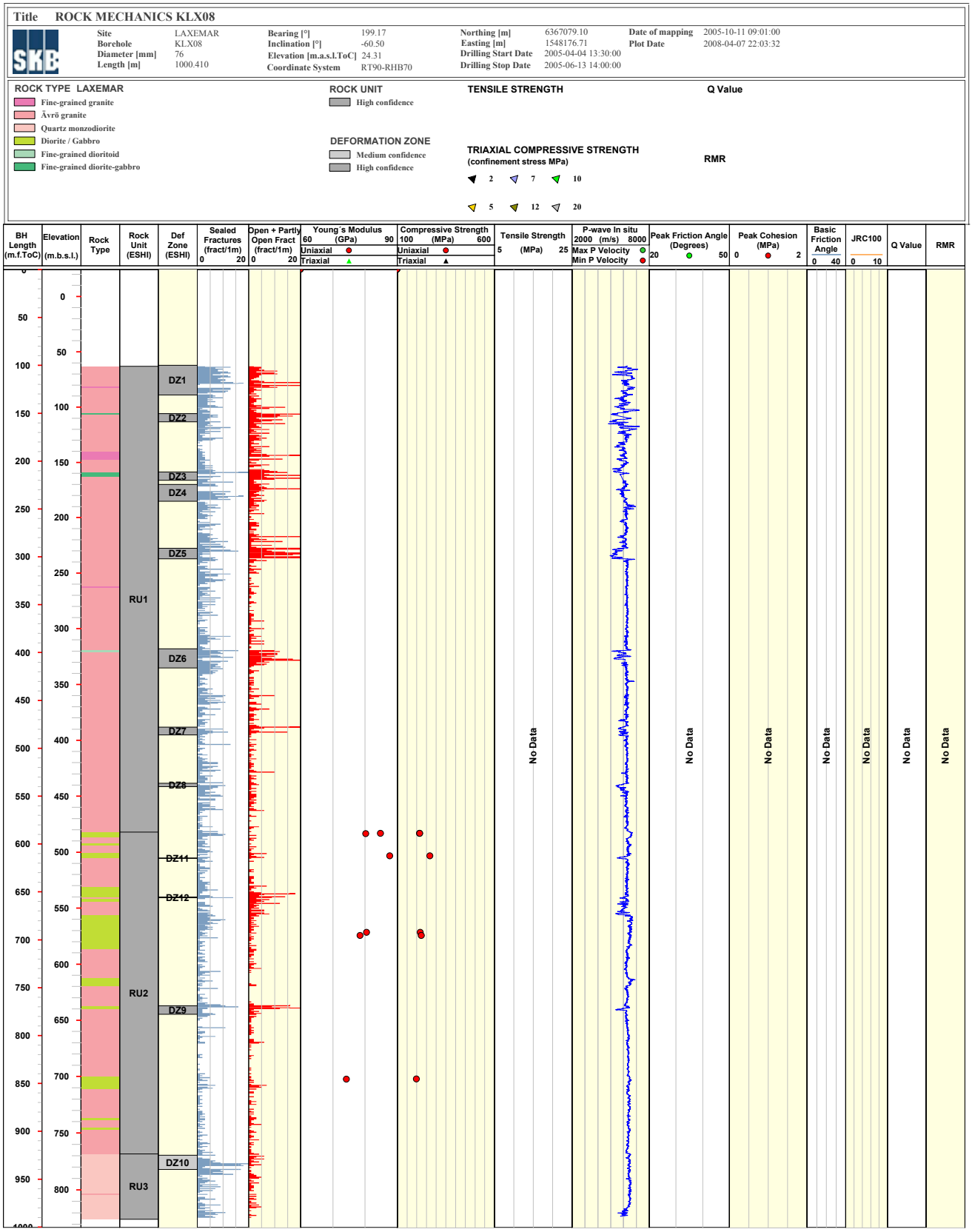
Title ROCK MECHANICS KLX08
Site LAXEMAR
Borehole KLX08
Diameter [mm] 76
Length [m] 1000.410
Bearing [°] 199.17
Inclination [°] -60.50
Elevation [m.a.s.l.ToC] 24.31
Coordinate System RT90-RHB70
Northing [m] 6367079.10
Easting [m] 1548176.71
Drilling Start Date 2005-04-04 13:30:00
Drilling Stop Date 2005-06-13 14:00:00
Date of mapping 2005-10-11 09:01:00
Plot Date 2008-04-07 22:03:32
ROCK TYPE LAXEMAR
Fine-grained granite
Ävrö granite
Quartz monzodiorite
Diorite / Gabbro
Fine-grained dioritoid
Fine-grained diorite-gabbro
ROCK UNIT
High confidence
DEFORMATION ZONE
Medium confidence
High confidence
TENSILE STRENGTH
TRIAXIAL COMPRESSIVE STRENGTH
(confinement stress MPa)
2 7 10
5 12 20
Q Value
RMR
BH Length (m.f.ToC)
Elevation (m.b.s.l.)
Rock Type
Rock Unit (ESHI)
Def Zone (ESHI)
Sealed Fractures (fract/1m) 0 20
Open + Partly Open Fract (fract/1m) 0 20
Young´s Modulus 60 (GPa) 90
Uniaxial
Triaxial
Compressive Strength 100 (MPa) 600
Uniaxial
Triaxial
Tensile Strength 5 (MPa) 25
P-wave In situ 2000 (m/s) 8000
Max P Velocity
Min P Velocity
Peak Friction Angle (Degrees) 20 50
Peak Cohesion (MPa) 0 2
Basic Friction Angle 0 40
JRC100 0 10
Q Value
RMR
DZ1
DZ2
DZ3
DZ4
DZ5
DZ6
DZ7
DZ8
DZ11
DZ12
DZ9
DZ10
RU1
RU2
RU3
No Data

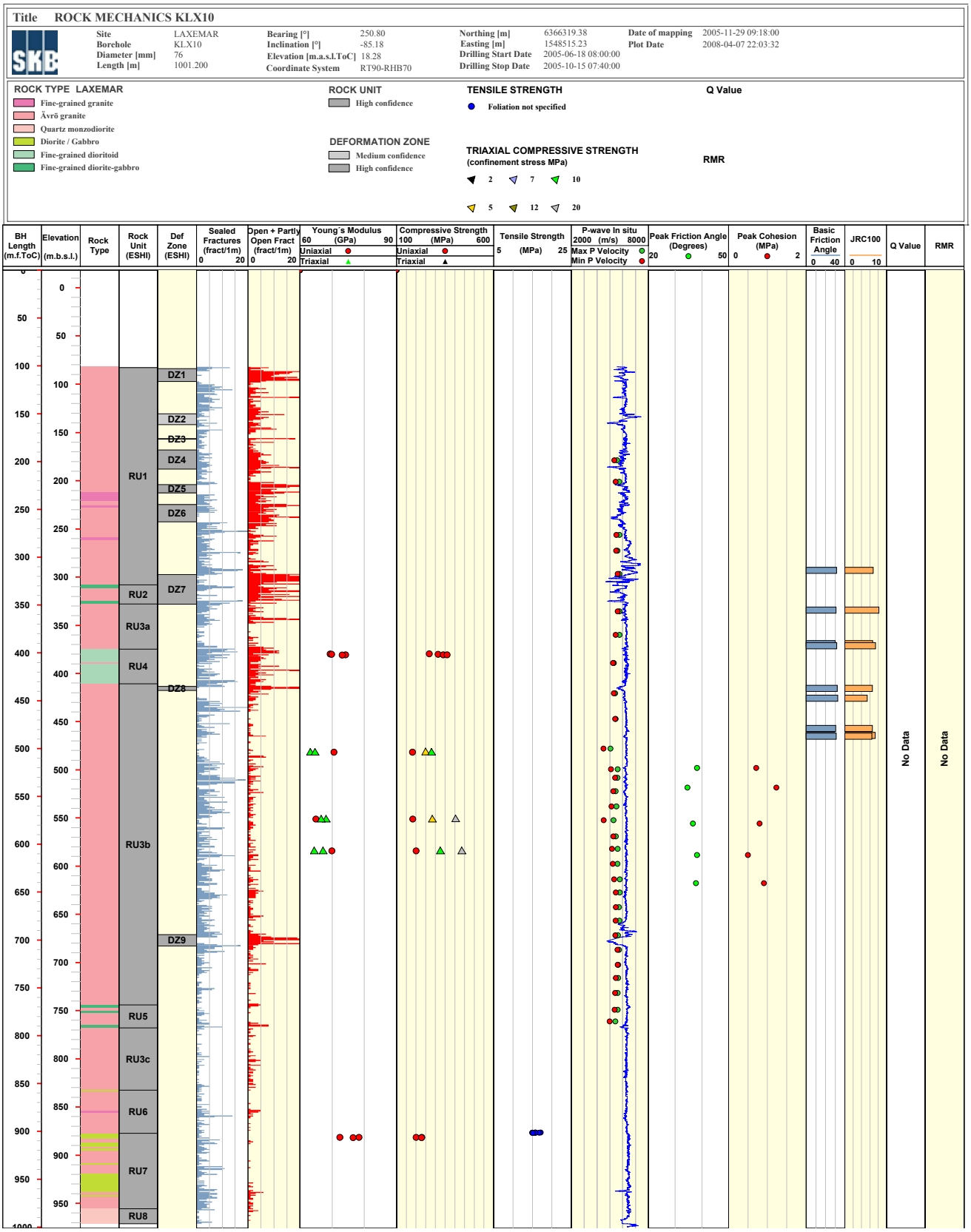
Title ROCK MECHANICS KLX10
Site LAXEMAR
Borehole KLX10
Diameter [mm] 76
Length [m] 1001.200
Bearing [°] 250.80
Inclination [°] -85.18
Elevation [m.a.s.l.ToC] 18.28
Coordinate System RT90-RHB70
Northing [m] 6366319.38
Easting [m] 1548515.23
Drilling Start Date 2005-06-18 08:00:00
Drilling Stop Date 2005-10-15 07:40:00
Date of mapping 2005-11-29 09:18:00
Plot Date 2008-04-07 22:03:32
ROCK TYPE LAXEMAR
Fine-grained granite
Åvrö granite
Quartz monzodiorite
Diorite / Gabbro
Fine-grained dioritoid
Fine-grained diorite-gabbro
ROCK UNIT
High confidence
DEFORMATION ZONE
Medium confidence
High confidence
TENSILE STRENGTH
Foliation not specified
TRIAXIAL COMPRESSIVE STRENGTH
(confinement stress MPa)
2 7 10
5 12 20
Q Value
RMR
BH Length (m.f.ToC)
Elevation (m.b.s.l.)
Rock Type
Rock Unit (ESHI)
Def Zone (ESHI)
Sealed Fractures (fract/1m) 0 20
Open + Partly Open Fract (fract/1m) 0 20
Young´s Modulus (GPa) 60 90
Uniaxial
Triaxial
Compressive Strength (MPa) 100 600
Uniaxial
Triaxial
Tensile Strength (MPa) 5 25
P-wave In situ 2000 (m/s) 8000
Max P Velocity
Min P Velocity
Peak Friction Angle (Degrees) 20 50
Peak Cohesion (MPa) 0 2
Basic Friction Angle 0 40
JRC100 0 10
Q Value
RMR
DZ1
DZ2
DZ3
DZ4
DZ5
DZ6
DZ7
DZ8
DZ9
RU1
RU2
RU3a
RU4
RU3b
RU5
RU3c
RU6
RU7
RU8
No Data
No Data

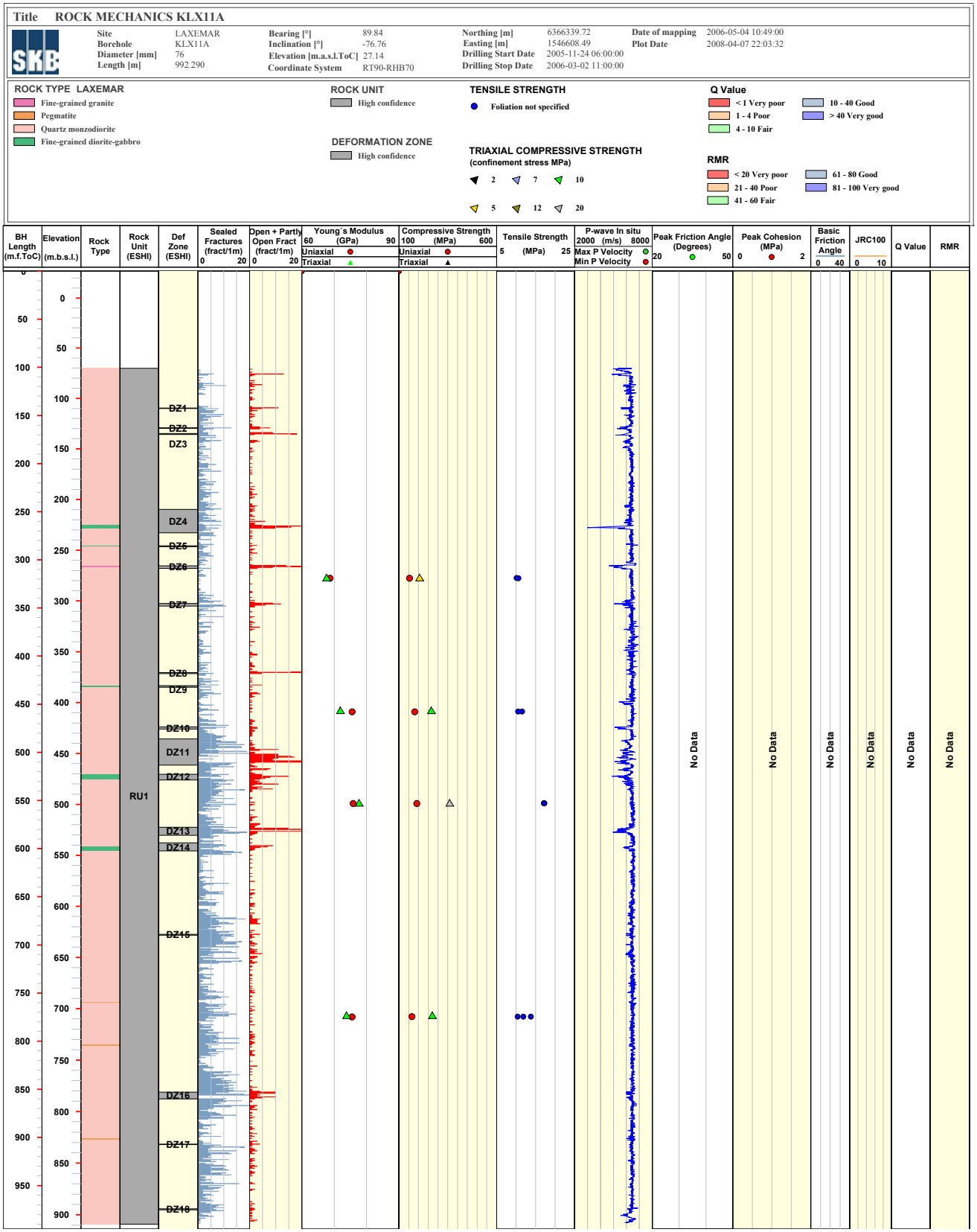
Title ROCK MECHANICS KLX11A
Site LAXEMAR
Borehole KLX11A
Diameter [mm] 76
Length [m] 992.290
Bearing [°] 89.84
Inclination [°] -76.76
Elevation [m.a.s.l.ToC] 27.14
Coordinate System RT90-RHB70
Northing [m] 6366339.72
Easting [m] 1546608.49
Drilling Start Date 2005-11-24 06:00:00
Drilling Stop Date 2006-03-02 11:00:00
Date of mapping 2006-05-04 10:49:00
Plot Date 2008-04-07 22:03:32
ROCK TYPE LAXEMAR
Fine-grained granite
Pegmatite
Quartz monzodiorite
Fine-grained diorite-gabbro
ROCK UNIT
High confidence
DEFORMATION ZONE
High confidence
TENSILE STRENGTH
Foliation not specified
TRIAXIAL COMPRESSIVE STRENGTH
(confinement stress MPa)
2 7 10
5 12 20
Q Value
< 1 Very poor
1 - 4 Poor
4 - 10 Fair
10 - 40 Good
> 40 Very good
RMR
< 20 Very poor
21 - 40 Poor
41 - 60 Fair
61 - 80 Good
81 - 100 Very good
BH Length (m.f.ToC)
Elevation (m.b.s.l.)
Rock Type
Rock Unit (ESHI)
Def Zone (ESHI)
Sealed Fractures (fract/1m) 0 20
Open + Partly Open Fract (fract/1m) 0 20
Young´s Modulus (GPa) 60 90
Uniaxial
Triaxial
Compressive Strength (MPa) 100 600
Uniaxial
Triaxial
Tensile Strength (MPa) 5 25
P-wave In situ 2000 (m/s) 8000
Max P Velocity
Min P Velocity
Peak Friction Angle (Degrees) 20 50
Peak Cohesion (MPa) 0 2
Basic Friction Angle 0 40
JRC100 0 10
Q Value
RMR
RU1
DZ1
DZ2
DZ3
DZ4
DZ5
DZ6
DZ7
DZ8
DZ9
DZ10
DZ11
DZ12
DZ13
DZ14
DZ15
DZ16
DZ17
DZ18
No Data

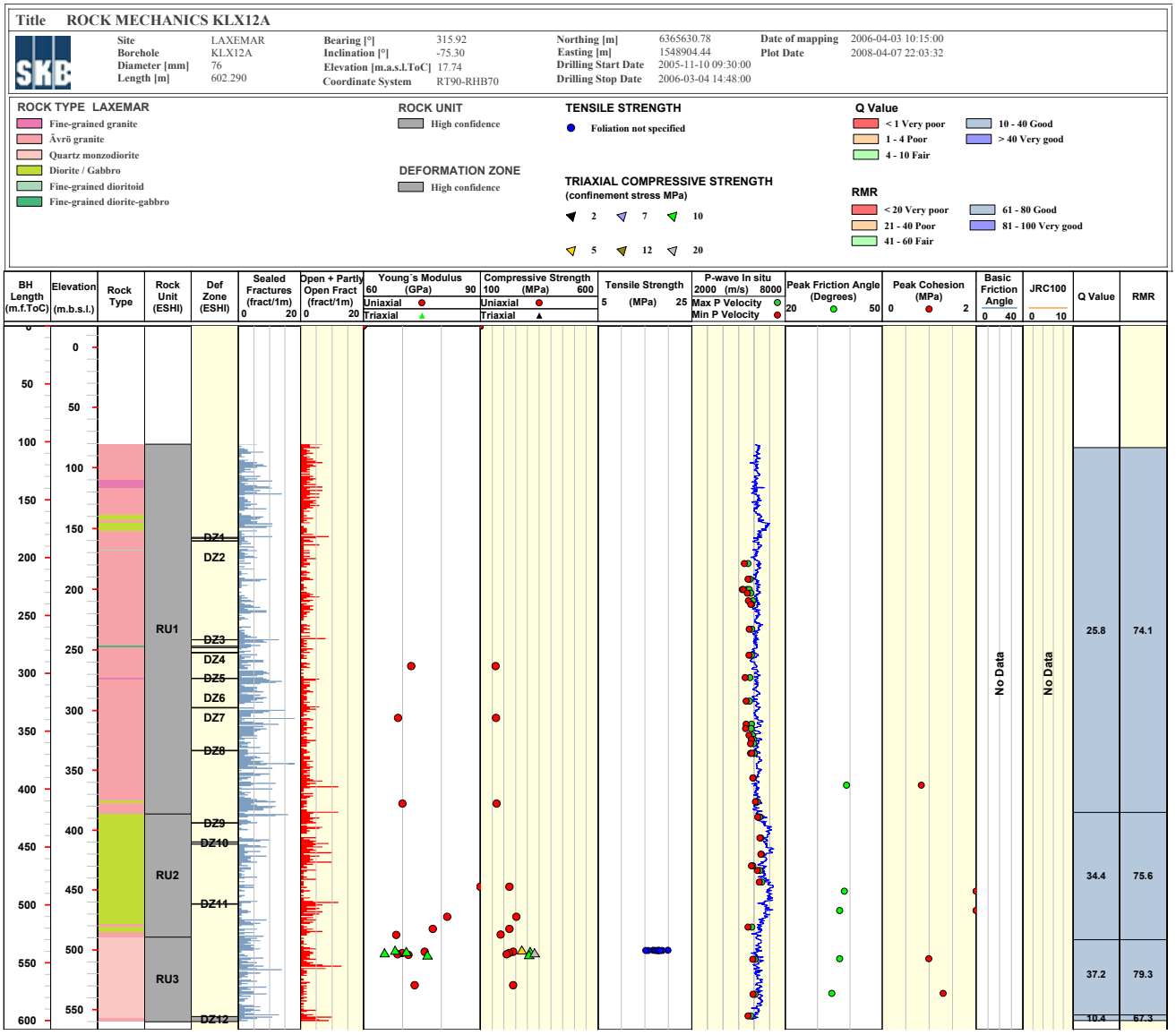
Title ROCK MECHANICS KLX12A
Site LAXEMAR
Borehole KLX12A
Diameter [mm] 76
Length [m] 602.290
Bearing [°] 315.92
Inclination [°] -75.30
Elevation [m.a.s.l.ToC] 17.74
Coordinate System RT90-RHB70
Northing [m] 6365630.78
Easting [m] 1548904.44
Drilling Start Date 2005-11-10 09:30:00
Drilling Stop Date 2006-03-04 14:48:00
Date of mapping 2006-04-03 10:15:00
Plot Date 2008-04-07 22:03:32
ROCK TYPE LAXEMAR
Fine-grained granite
Ävrö granite
Quartz monzodiorite
Diorite / Gabbro
Fine-grained dioritoid
Fine-grained diorite-gabbro
ROCK UNIT
High confidence
DEFORMATION ZONE
High confidence
TENSILE STRENGTH
Foliation not specified
TRIAXIAL COMPRESSIVE STRENGTH
(confinement stress MPa)
2 7 10
5 12 20
Q Value
< 1 Very poor
1 - 4 Poor
4 - 10 Fair
10 - 40 Good
> 40 Very good
RMR
< 20 Very poor
21 - 40 Poor
41 - 60 Fair
61 - 80 Good
81 - 100 Very good
BH Length (m.f.ToC)
Elevation (m.b.s.l.)
Rock Type
Rock Unit (ESHI)
Def Zone (ESHI)
Sealed Fractures (fract/1m)
Open + Partly Open Fract (fract/1m)
Young´s Modulus (GPa)
Uniaxial
Triaxial
Compressive Strength (MPa)
Uniaxial
Triaxial
Tensile Strength (MPa)
P-wave In situ (m/s)
Max P Velocity
Min P Velocity
Peak Friction Angle (Degrees)
Peak Cohesion (MPa)
Basic Friction Angle
JRC100
No Data
No Data
Q Value
RMR
RU1
RU2
RU3
DZ1
DZ2
DZ3
DZ4
DZ5
DZ6
DZ7
DZ8
DZ9
DZ10
DZ11
DZ12
25.8
74.1
34.4
75.6
37.2
79.3
10.4
67.3

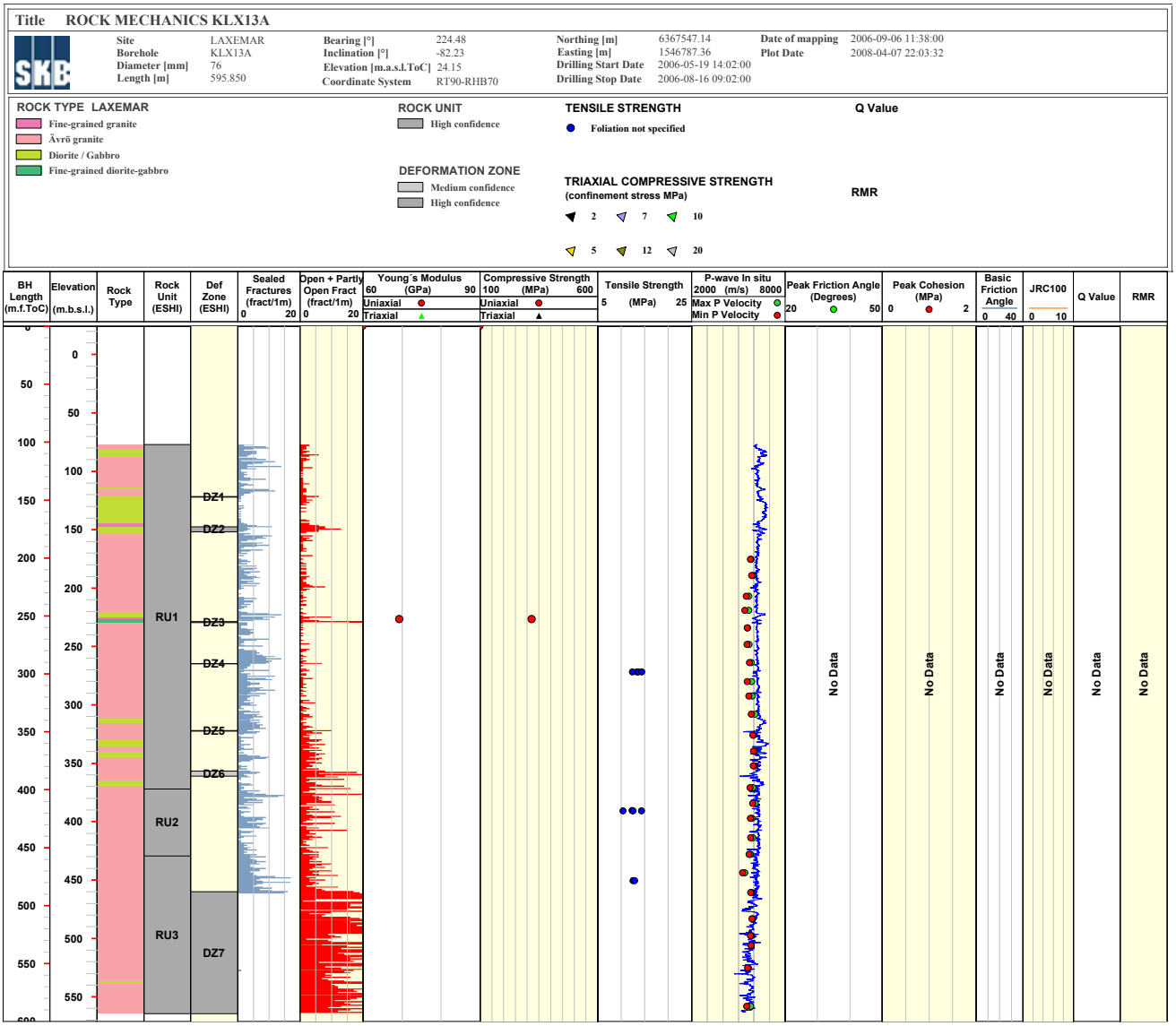
Title ROCK MECHANICS KLX13A
Site LAXEMAR
Borehole KLX13A
Diameter [mm] 76
Length [m] 595.850
Bearing [°] 224.48
Inclination [°] -82.23
Elevation [m.a.s.l.ToC] 24.15
Coordinate System RT90-RHB70
Northing [m] 6367547.14
Easting [m] 1546787.36
Drilling Start Date 2006-05-19 14:02:00
Drilling Stop Date 2006-08-16 09:02:00
Date of mapping 2006-09-06 11:38:00
Plot Date 2008-04-07 22:03:32
ROCK TYPE LAXEMAR
Fine-grained granite
Ävrö granite
Diorite / Gabbro
Fine-grained diorite-gabbro
ROCK UNIT
High confidence
DEFORMATION ZONE
Medium confidence
High confidence
TENSILE STRENGTH
Foliation not specified
TRIAXIAL COMPRESSIVE STRENGTH
(confinement stress MPa)
2 7 10
5 12 20
Q Value
RMR
BH Length (m.f.ToC)
Elevation (m.b.s.l.)
Rock Type
Rock Unit (ESHI)
Def Zone (ESHI)
Sealed Fractures (fract/1m)
Open + Partly Open Fract (fract/1m)
Young´s Modulus (GPa)
Uniaxial
Triaxial
Compressive Strength (MPa)
Tensile Strength (MPa)
P-wave In situ (m/s)
Max P Velocity
Min P Velocity
Peak Friction Angle (Degrees)
Peak Cohesion (MPa)
Basic Friction Angle
JRC100
Q Value
RMR
RU1
RU2
RU3
DZ1
DZ2
DZ3
DZ4
DZ5
DZ6
DZ7
No Data

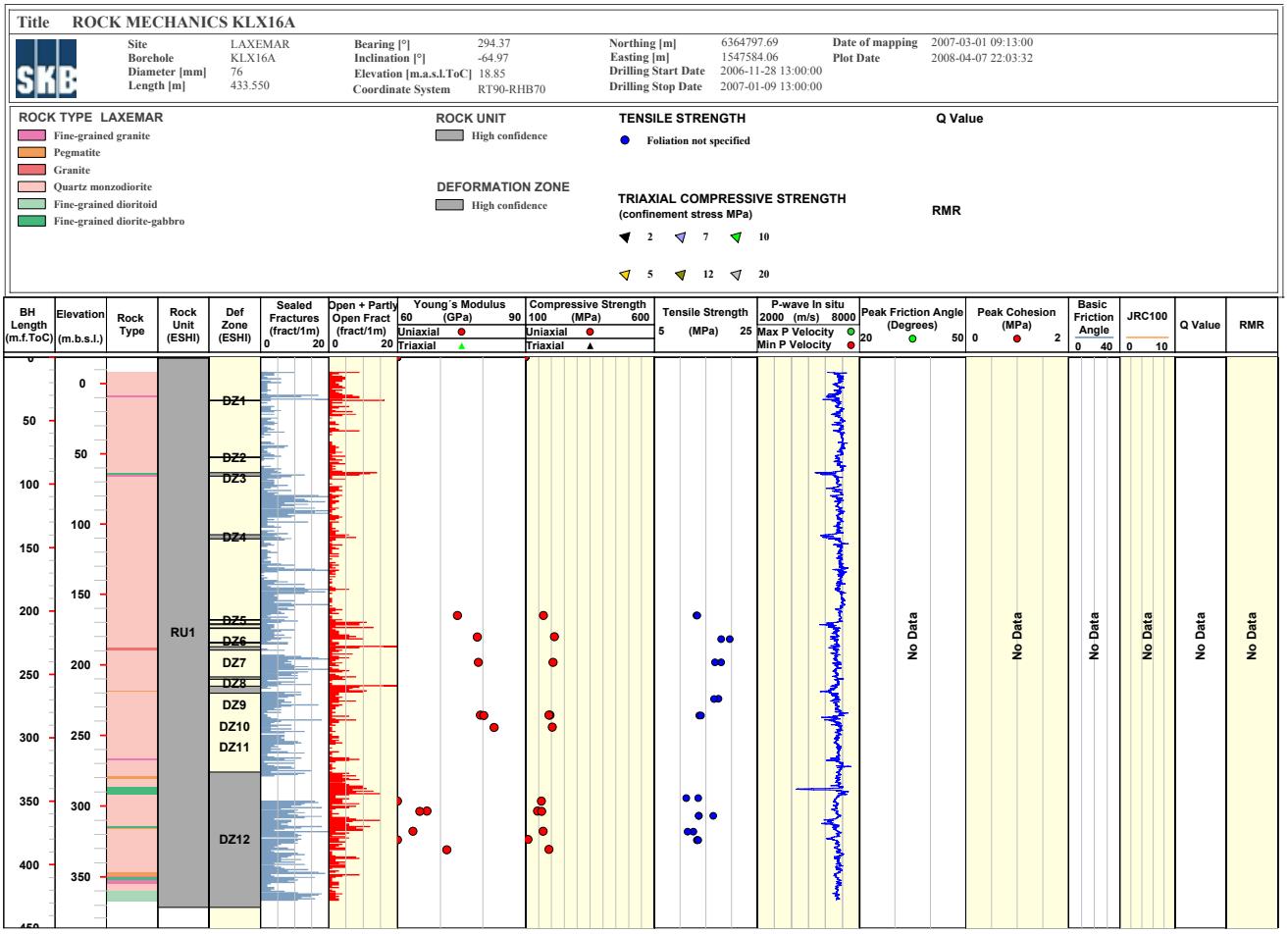
Title ROCK MECHANICS KLX16A
Site LAXEMAR
Borehole KLX16A
Diameter [mm] 76
Length [m] 433.550
Bearing [°] 294.37
Inclination [°] -64.97
Elevation [m.a.s.l.ToC] 18.85
Coordinate System RT90-RHB70
Northing [m] 6364797.69
Easting [m] 1547584.06
Drilling Start Date 2006-11-28 13:00:00
Drilling Stop Date 2007-01-09 13:00:00
Date of mapping 2007-03-01 09:13:00
Plot Date 2008-04-07 22:03:32
ROCK TYPE LAXEMAR
Fine-grained granite
Pegmatite
Granite
Quartz monzodiorite
Fine-grained dioritoid
Fine-grained diorite-gabbro
ROCK UNIT
High confidence
DEFORMATION ZONE
High confidence
TENSILE STRENGTH
Foliation not specified
TRIAXIAL COMPRESSIVE STRENGTH
(confinement stress MPa)
2 7 10
5 12 20
Q Value
RMR
BH Length (m.f.ToC)
Elevation (m.b.s.l.)
Rock Type
Rock Unit (ESHI)
Def Zone (ESHI)
Sealed Fractures (fract/1m)
Open + Partly Open Fract (fract/1m)
Young´s Modulus (GPa)
Uniaxial
Triaxial
Compressive Strength (MPa)
Uniaxial
Triaxial
Tensile Strength (MPa)
P-wave In situ (m/s)
Max P Velocity
Min P Velocity
Peak Friction Angle (Degrees)
Peak Cohesion (MPa)
Basic Friction Angle
JRC100
Q Value
RMR
RU1
DZ1
DZ2
DZ3
DZ4
DZ5
DZ6
DZ7
DZ8
DZ9
DZ10
DZ11
DZ12
No Data

Title ROCK MECHANICS KLX17A

Site	LAXEMAR	Bearing [°]	11.21	Northing [m]	6366848.75	Date of mapping	2006-12-06 11:49:00
Borehole	KLX17A	Inclination [°]	-61.33	Easting [m]	1546862.09	Plot Date	2008-04-07 22:03:32
Diameter [mm]	76	Elevation [m.a.s.l.ToC]	27.63	Drilling Start Date	2006-09-13 06:00:00		
Length [m]	701.080	Coordinate System	RT90-RHB70	Drilling Stop Date	2006-10-23 09:30:00		

ROCK TYPE LAXEMAR
- Fine-grained granite
- Ävrö granite
- Diorite / Gabbro
- Fine-grained diorite-gabbro

ROCK UNIT
- High confidence

DEFORMATION ZONE
- High confidence

TENSILE STRENGTH

TRIAXIAL COMPRESSIVE STRENGTH (confinement stress MPa)
2 7 10
5 12 20

Q Value

RMR

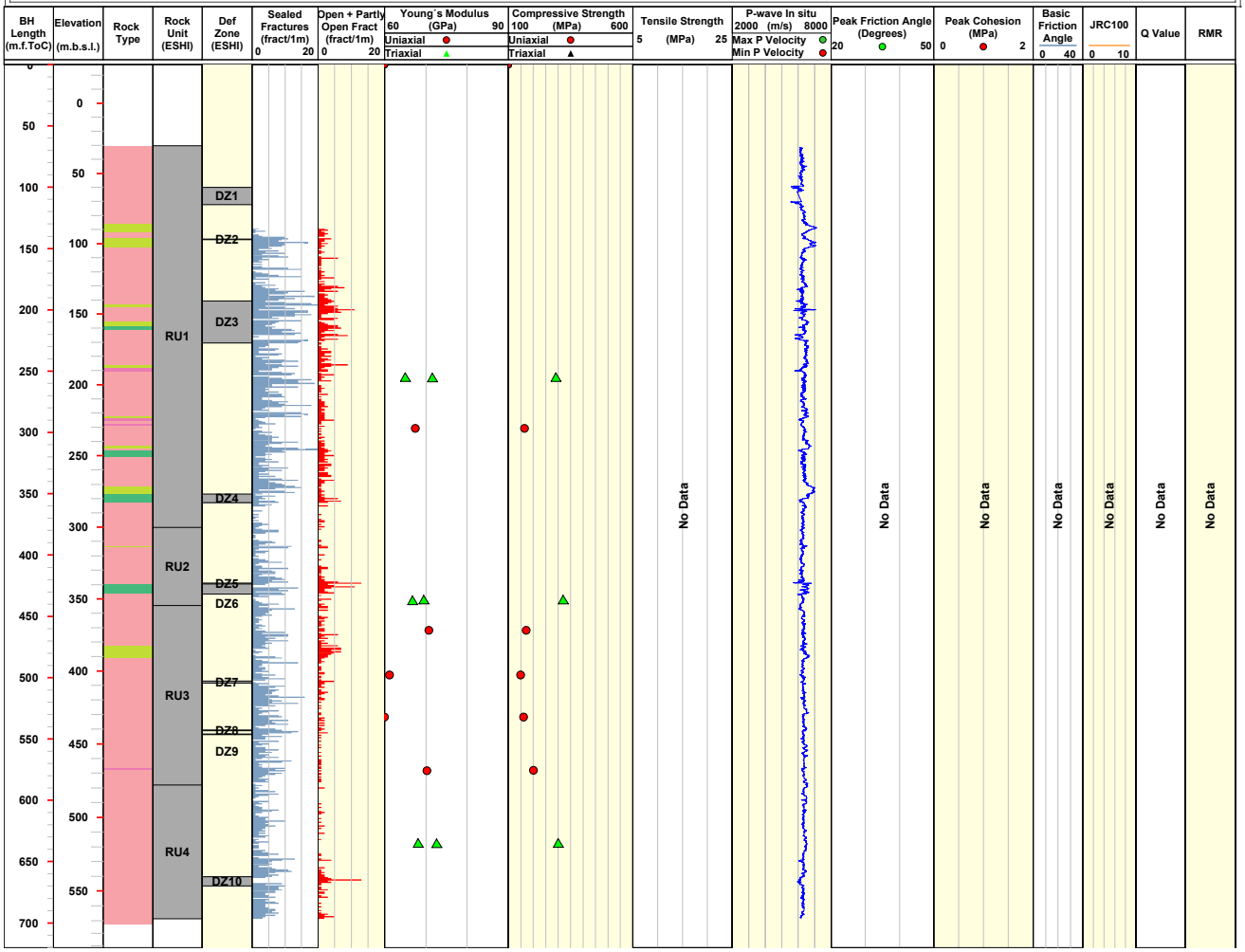

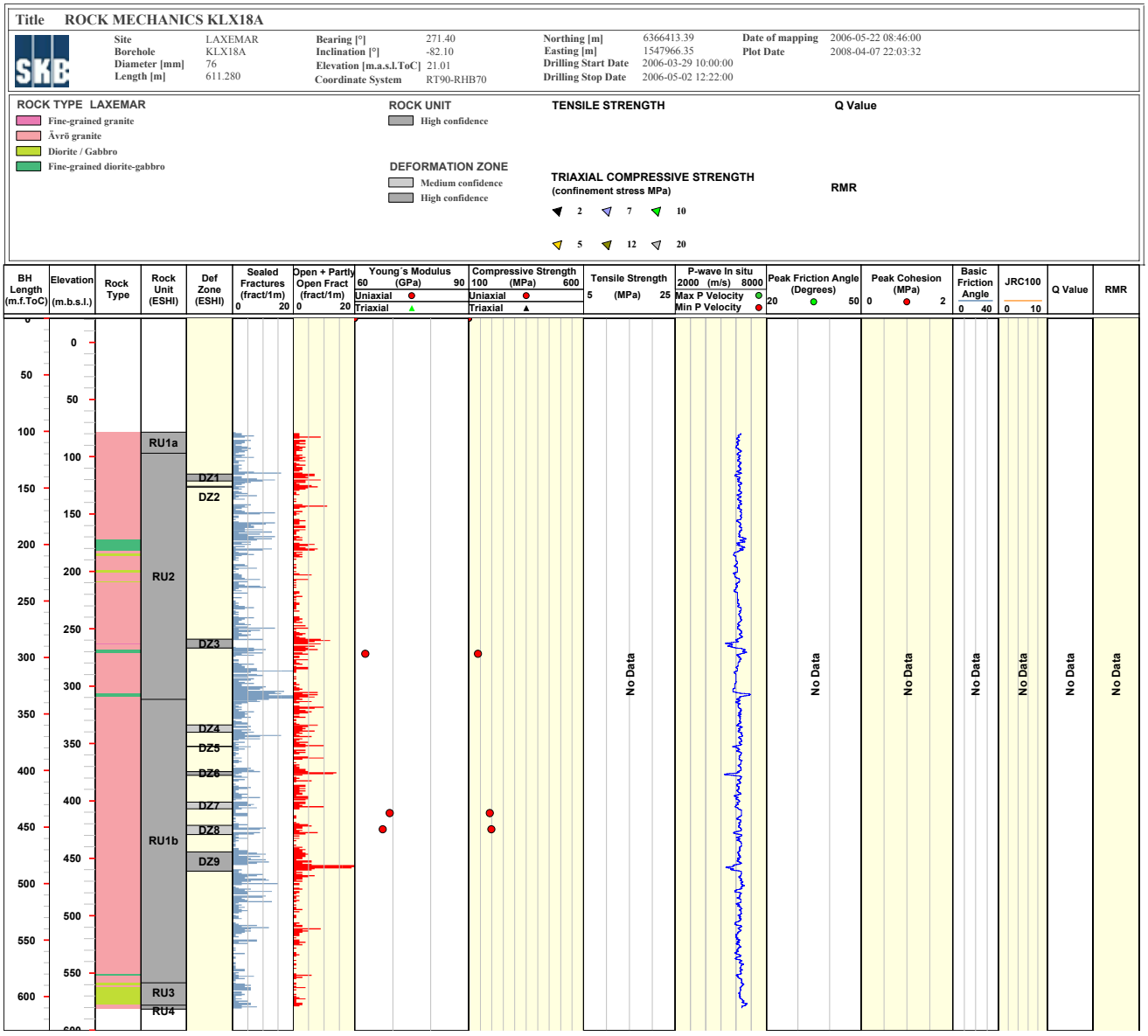
Title ROCK MECHANICS KLX18A
Site LAXEMAR
Borehole KLX18A
Diameter [mm] 76
Length [m] 611.280
Bearing [°] 271.40
Inclination [°] -82.10
Elevation [m.a.s.l.ToC] 21.01
Coordinate System RT90-RHB70
Northing [m] 6366413.39
Easting [m] 1547966.35
Drilling Start Date 2006-03-29 10:00:00
Drilling Stop Date 2006-05-02 12:22:00
Date of mapping 2006-05-22 08:46:00
Plot Date 2008-04-07 22:03:32
ROCK TYPE LAXEMAR
Fine-grained granite
Ävrö granite
Diorite / Gabbro
Fine-grained diorite-gabbro
ROCK UNIT
High confidence
DEFORMATION ZONE
Medium confidence
High confidence
TENSILE STRENGTH
TRIAXIAL COMPRESSIVE STRENGTH
(confinement stress MPa)
2 7 10
5 12 20
Q Value
RMR
BH Length (m.f.ToC)
Elevation (m.b.s.l.)
Rock Type
Rock Unit (ESHI)
Def Zone (ESHI)
Sealed Fractures (fract/1m) 0 20
Open + Partly Open Fract (fract/1m) 0 20
Young´s Modulus 60 (GPa) 90
Uniaxial
Triaxial
Compressive Strength 100 (MPa) 600
Uniaxial
Triaxial
Tensile Strength 5 (MPa) 25
P-wave In situ 2000 (m/s) 8000
Max P Velocity
Min P Velocity
Peak Friction Angle (Degrees) 20 50
Peak Cohesion (MPa) 0 2
Basic Friction Angle 0 40
JRC100 0 10
Q Value
RMR
RU1a
RU2
RU1b
RU3
RU4
DZ1
DZ2
DZ3
DZ4
DZ5
DZ6
DZ7
DZ8
DZ9
No Data

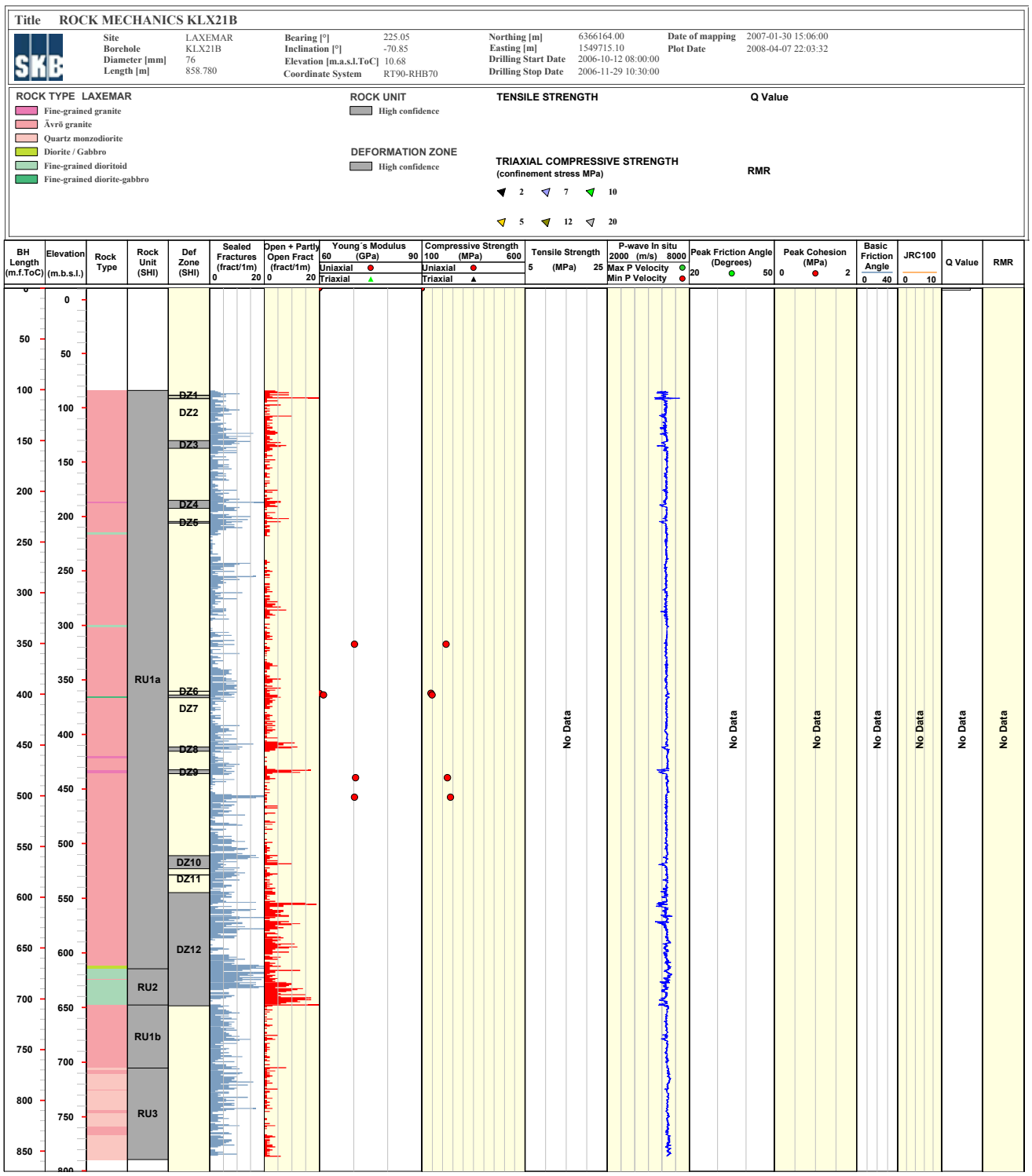
Title ROCK MECHANICS KLX21B
Site LAXEMAR
Borehole KLX21B
Diameter [mm] 76
Length [m] 858.780
Bearing [°] 225.05
Inclination [°] -70.85
Elevation [m.a.s.l.ToC] 10.68
Coordinate System RT90-RHB70
Northing [m] 6366164.00
Easting [m] 1549715.10
Drilling Start Date 2006-10-12 08:00:00
Drilling Stop Date 2006-11-29 10:30:00
Date of mapping 2007-01-30 15:06:00
Plot Date 2008-04-07 22:03:32
ROCK TYPE LAXEMAR
Fine-grained granite
Ävrö granite
Quartz monzodiorite
Diorite / Gabbro
Fine-grained dioritoid
Fine-grained diorite-gabbro
ROCK UNIT
High confidence
DEFORMATION ZONE
High confidence
TENSILE STRENGTH
TRIAXIAL COMPRESSIVE STRENGTH
(confinement stress MPa)
2 7 10
5 12 20
Q Value
RMR
BH Length (m.f.ToC)
Elevation (m.b.s.l.)
Rock Type
Rock Unit (SHI)
Def Zone (SHI)
Sealed Fractures (fract/1m) 0 20
Open + Partly Open Fract (fract/1m) 0 20
Young´s Modulus 60 (GPa) 90
Uniaxial
Triaxial
Compressive Strength 100 (MPa) 600
Uniaxial
Triaxial
Tensile Strength 5 (MPa) 25
P-wave In situ 2000 (m/s) 8000
Max P Velocity
Min P Velocity
Peak Friction Angle (Degrees) 20 50
Peak Cohesion (MPa) 0 2
Basic Friction Angle 0 40
JRC100 0 10
Q Value
RMR
DZ1
DZ2
DZ3
DZ4
DZ5
DZ6
DZ7
DZ8
DZ9
DZ10
DZ11
DZ12
RU1a
RU2
RU1b
RU3
No Data

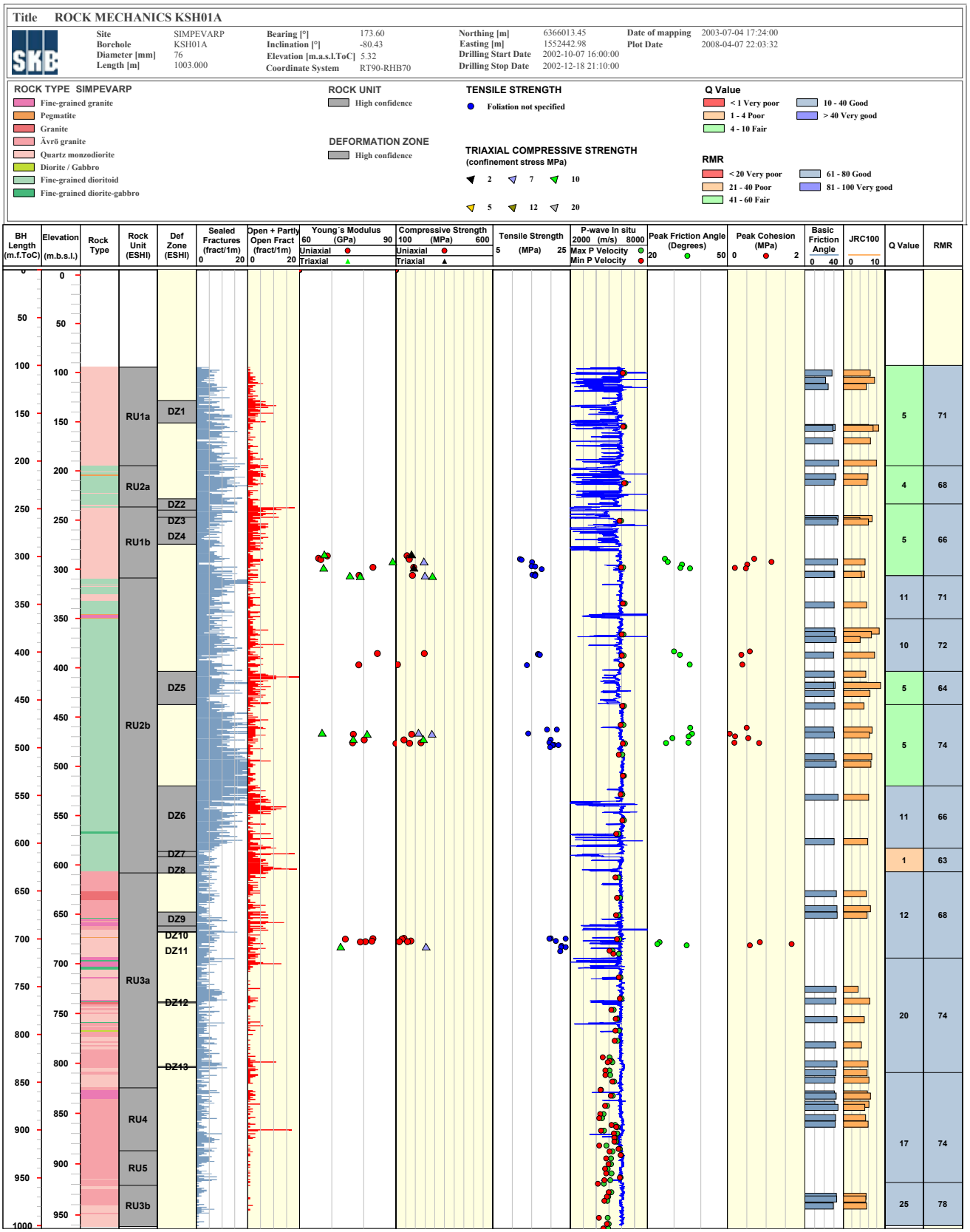
Title ROCK MECHANICS KSH01A
Site SIMPEVARP
Borehole KSH01A
Diameter [mm] 76
Length [m] 1003.000
Bearing [°] 173.60
Inclination [°] -80.43
Elevation [m.a.s.l.ToC] 5.32
Coordinate System RT90-RHB70
Northing [m] 6366013.45
Easting [m] 1552442.98
Drilling Start Date 2002-10-07 16:00:00
Drilling Stop Date 2002-12-18 21:10:00
Date of mapping 2003-07-04 17:24:00
Plot Date 2008-04-07 22:03:32
ROCK TYPE SIMPEVARP
Fine-grained granite
Pegmatite
Granite
Ävrö granite
Quartz monzodiorite
Diorite / Gabbro
Fine-grained dioritoid
Fine-grained diorite-gabbro
ROCK UNIT
High confidence
DEFORMATION ZONE
High confidence
TENSILE STRENGTH
Foliation not specified
TRIAXIAL COMPRESSIVE STRENGTH
(confinement stress MPa)
2 7 10
5 12 20
Q Value
< 1 Very poor
1 - 4 Poor
4 - 10 Fair
10 - 40 Good
> 40 Very good
RMR
< 20 Very poor
21 - 40 Poor
41 - 60 Fair
61 - 80 Good
81 - 100 Very good
BH Length (m.f.ToC)
Elevation (m.b.s.l.)
Rock Type
Rock Unit (ESHI)
Def Zone (ESHI)
Sealed Fractures (fract/1m) 0 20
Open + Partly Open Fract (fract/1m) 0 20
Young´s Modulus 60 (GPa) 90
Uniaxial
Triaxial
Compressive Strength 100 (MPa) 600
Uniaxial
Triaxial
Tensile Strength 5 (MPa) 25
P-wave In situ 2000 (m/s) 8000
Max P Velocity
Min P Velocity
Peak Friction Angle (Degrees) 20 50
Peak Cohesion (MPa) 0 2
Basic Friction Angle 0 40
JRC100 0 10
Q Value
RMR
RU1a
RU2a
RU1b
RU2b
RU3a
RU4
RU5
RU3b
DZ1
DZ2
DZ3
DZ4
DZ5
DZ6
DZ7
DZ8
DZ9
DZ10
DZ11
DZ12
DZ13
5 71
4 68
5 66
11 71
10 72
5 64
5 74
11 66
1 63
12 68
20 74
17 74
25 78

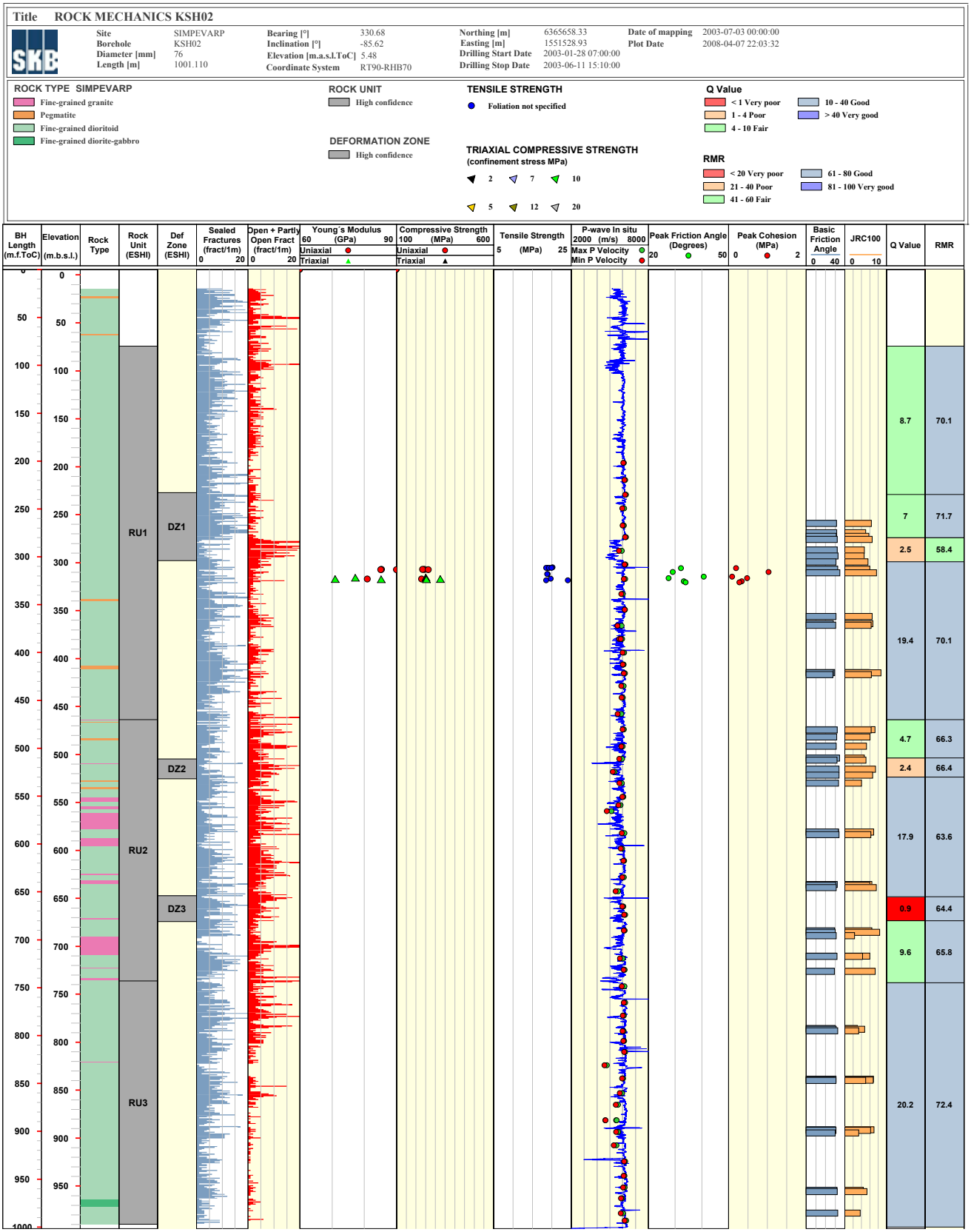
Title ROCK MECHANICS KSH02
Site SIMPEVARP
Borehole KSH02
Diameter [mm] 76
Length [m] 1001.110
Bearing [°] 330.68
Inclination [°] -85.62
Elevation [m.a.s.l.ToC] 5.48
Coordinate System RT90-RHB70
Northing [m] 6365658.33
Easting [m] 1551528.93
Drilling Start Date 2003-01-28 07:00:00
Drilling Stop Date 2003-06-11 15:10:00
Date of mapping 2003-07-03 00:00:00
Plot Date 2008-04-07 22:03:32
ROCK TYPE SIMPEVARP
Fine-grained granite
Pegmatite
Fine-grained dioritoid
Fine-grained diorite-gabbro
ROCK UNIT
High confidence
DEFORMATION ZONE
High confidence
TENSILE STRENGTH
Foliation not specified
TRIAXIAL COMPRESSIVE STRENGTH
(confinement stress MPa)
2 7 10
5 12 20
Q Value
< 1 Very poor
1 - 4 Poor
4 - 10 Fair
10 - 40 Good
> 40 Very good
RMR
< 20 Very poor
21 - 40 Poor
41 - 60 Fair
61 - 80 Good
81 - 100 Very good
BH Length (m.f.ToC)
Elevation (m.b.s.l.)
Rock Type
Rock Unit (ESHI)
Def Zone (ESHI)
Sealed Fractures (fract/1m)
Open + Partly Open Fract (fract/1m)
Young´s Modulus (GPa)
Uniaxial
Triaxial
Compressive Strength (MPa)
Uniaxial
Triaxial
Tensile Strength (MPa)
P-wave In situ (m/s)
Max P Velocity
Min P Velocity
Peak Friction Angle (Degrees)
Peak Cohesion (MPa)
Basic Friction Angle
JRC100
Q Value
RMR
RU1
RU2
RU3
DZ1
DZ2
DZ3
8.7 70.1
7 71.7
2.5 58.4
19.4 70.1
4.7 66.3
2.4 66.4
17.9 63.6
0.9 64.4
9.6 65.8
20.2 72.4

Appendix 2

Analysis of fracture sets

The full presentations of the statistical test performed on fracture sets and the results of the analysis are found in this appendix. (See also Section 4.5.)

Contents

A2.1 Analysis of fracture property dependence on orientation

A2.1.1 Statistical inference tests on fracture data

The strength and deformability data comprise several different rock mechanical parameters. These have been derived from three different laboratory test methods, which may entail systematic differences in results. The primary interest is to analyze if different fracture sets have significant differences in fracture strength and deformability. The objective is therefore to distinguish whether significant differences can be found in laboratory data, in terms of: 1) fracture sets, and 2) laboratory test methods.

In the statistical analyses the data can be grouped either by the laboratory test method used or by fracture sets. The parameters studied are the Mohr-Coulomb model parameters (c_p^{MC}, Φ_p^{MC}, c_r^{MC}, Φ_r^{MC}) and the Barton-Bandis model parameters (Φ_b^{BB}, Φ_r^{BB}, JRC_{100}, JCS_{100}). To clarify the statistical analyses, the data is referred to as x_{ij}, where x is the parameter studied, i is laboratory testing method used (Tilt, and Shear) and j is its fracture set (ENE, NS, WNW and SH). The fracture sets are defined in /La Pointe et al. 2008/. The total number of samples is 270 and most of the data come from tilt tests (Table A2-1). The chance of finding significant differences in statistical tests improves with larger sample sizes; however, grouping data that do not belong to a homogeneous underlying population may lead to incorrect inference.

With respect to the number of data available, the following analyses are considered possible:

1) Analyzing influence of laboratory tests method (for all fractures, regardless of fracture sets, i.e., comparing x_i, for all j combined).
2) Analyzing differences between fracture sets (for Tilt test data alone).

The reason for excluding all shear test data in alternative (2) is that for some fracture sets only few data is available.

A2.1.2 Statistical tests used

The following three types of parametric tests were used: *t*-test, for pair-wise sample mean comparison, *F*-test, for pair-wise sample variance comparison, and ANOVA (Analysis of variance) /e.g. Davis 2002/. These are all parametric tests, which require that the underlying distributions of data are normal. Normality can be tested by various methods, including probability plots, Chi-squared, and Kolmogorov-Smirnov tests. In this study, normality was only estimated roughly by visual inspections of the data plotted as histograms (Figure A2-1 to Figure A2-3). Yet another requirement for these tests is that the sample variances and sample sizes should not be too different from each other.

If the underlying distributions prove not to be normal, non-parametric tests must be used. Therefore, the Mann-Whitney test is also used for pair-wise sample mean comparisons of sample medians (as alternative to the *t*-test) /e.g. Davis 2002/. The drawback of many non-parametric tests is that they generally require large sample sizes to be powerful.

Table A2-1. Sample sizes, classified by test methods and fracture sets.

Set *j* \ Method *i*	Tilt	Shear	All methods
ENE	9	6	15
NS	17	4	21
WNW	14	7	21
SH	26	25	51
Outside assign area	133	29	162
All fractures	199	71	270

The tests use a significance level $\alpha = 0.05$ (Type I error; the risk of erroneously rejecting a true null-hypothesis). The risk of the statistical tests not being powerful enough to reveal a true significant difference between data sets (Type II error) is not addressed in this study. The inference tests are finally reported in terms of *p*-values, which are defined as the smallest level of significance at which the null hypothesis would be rejected for a specific test (Table A2-2 to Table A2-6). In other words, a low *p*-value (i.e., $p < 0.05$) signifies that two data sets are likely to be significantly different, in terms of the specific test used.

t-test; pair-wise comparison of sample means

The t-test is used to test if there is a significant difference in mean values of two data sets. The two data sets are assumed to belong to two populations that are normally distributed and have unknown and unequal variances.

$x_1 \sim N(\mu_1,\sigma_1^2)$ and $x_2 \sim N(\mu_2,\sigma_2^2)$

The population means are estimated by the sample means ($\mu_1 \approx \bar{x}_1$ and $\mu_2 \approx \bar{x}_1$) and population variances are estimated by sample variances ($\sigma_1 \approx s_1$ and $\sigma_2 \approx s_2$).

Two hypotheses are set up: the null-hypothesis and the alternative hypothesis

$H_0 : \mu_1 - \mu_2 = \delta$ and $H_1 : \mu_1 - \mu_2 \neq \delta;\ \delta = 0$

The test statistics used for a two-sided t-test at significance level $\alpha = 0.05$ is:

$$t = \frac{(\bar{x}_1 - \bar{x}_2 - \delta)}{\sqrt{(s_1^2 / n_1 + s_2^2 / n_2)}}$$

Then, the hypothesis H_{A0} can be rejected at significance level $\alpha = 0.05$, if:

$$|t| \geq \frac{w_1 t_1 + w_2 t_2}{w_1 + w_2}$$

where, $w_1 = s_1^2 / n_1$ and $w_2 = s_2^2 / n_1$

$t_1 = t_{1-\alpha/2,n_1-1} = t_{0.975,n_1-1}$ and $t_2 = t_{1-\alpha/2,n_2-1} = t_{0.975,n_2-1}$

The two data sets must have 'similar' variance, if the number of data, n<30. Also, the number of available data of the two data sets should not differ hugely.

F-test; pair-wise comparison of sample variances

The *F*-test is used to test if there is a significant difference in variance of two data sets. As above, two hypotheses are set up: the null-hypothesis and the alternative hypothesis

$H_0 : \sigma_1^2 = \sigma_2^2 \qquad H_1 : \sigma_1^2 \neq \sigma_2^2$

In this case, the test statistics used for a one-sided F-test at significance level $\alpha = 0.05$ is

$F_c = s_1^2 / s_2^2 ; \qquad s_1^2 > s_2^2$

where F_c is F-distributed with n_1-1 and n_2-1 degrees of freedom. The null hypothesis H_0 is therefore rejected if

$F_c > F_{1-\alpha,n_1-1,n_2-1}$

ANOVA; simultaneous analysis of variance

The *t*- and *F*-tests can only infer differences between two data sets, at a time. The present data set can be divided into several different groups (fracture sets and laboratory test methods). Thus, the *t*- and *F*-tests require many pair-wise test combinations, either between a global group and a subgroup, or between two subgroups. The benefit of the ANOVA test is that it can compare sample mean values of several different subgroups at the time. The one-way ANOVA test uses the null hypothesis that there is no difference between any of the subgroups being compared. It then uses the F-test statistics to compare whether the ratio (variance between groups/variance within sample groups) exceeds its critical value for rejecting its null hypothesis. The drawback is that it can only reject or accept its null hypothesis that all subgroups share the same mean; it cannot infer if a particular group is different.

A2.1.3 Comparison of the different laboratory techniques on natural fractures

Statistical inference tests were used to evaluate the influence that different laboratory test techniques may have on results. The fracture properties studied are primarily the Mohr-Coulomb model parameters: peak cohesion c_p, peak friction angle Φ_p, residual cohesion c_r, and residual friction angle Φ_r determined from tilt and shear tests. In this inference test, the data are only grouped in terms of laboratory testing technique, i.e., no distinction was made regarding fracture sets ($\bar{x}_i = \Sigma_j x_{ij}/n_j$). The differences between fracture sets are addressed in the next section.

The distributions of x_i were plotted as histograms to examine normality, which is required for parametric tests, see Figure A2-1 The distributions appear to bee normal, see Figure A2-1. The Tilt data was compared to the Shear data. The results of the *t*-tests (H_{A0}: $\mu_{Tilt} = \mu_{Shear}$) and *F*-tests (H_{B0}: $\sigma_{Tilt} = \sigma_{Shear}$) yield significant differences for all parameters, see Table A2-2.

Table A2-2. Inference tests on laboratory test methods; tilt data and shear data.

	Average, $\bar{x}_i$					Standard Deviation, s_i			
	n_i	c_p^{MC}	Φ_p^{MC}	c_r^{MC}	Φ_r^{MC}	c_p^{MC}	Φ_p^{MC}	c_r^{MC}	Φ_r^{MC}
Tilt data	199	0.49	33.97	0.43	28.88	0.12	1.76	0.10	3.47
All Shear data	71	0.88	36.63	0.38	34.73	0.43	3.21	0.23	3.49

Statistical inference between Tilt and all shear data (rejection risk)				
	c_p^{MC}	Φ_p^{MC}	c_r^{MC}	Φ_r^{MC}
t-test: H_{A0}	0.00*	0.00*	0.01*	0.00*
F-test: H_{B0}	0.0*	0.0*	0.0*	0.46*

* significance level α = 0.05.

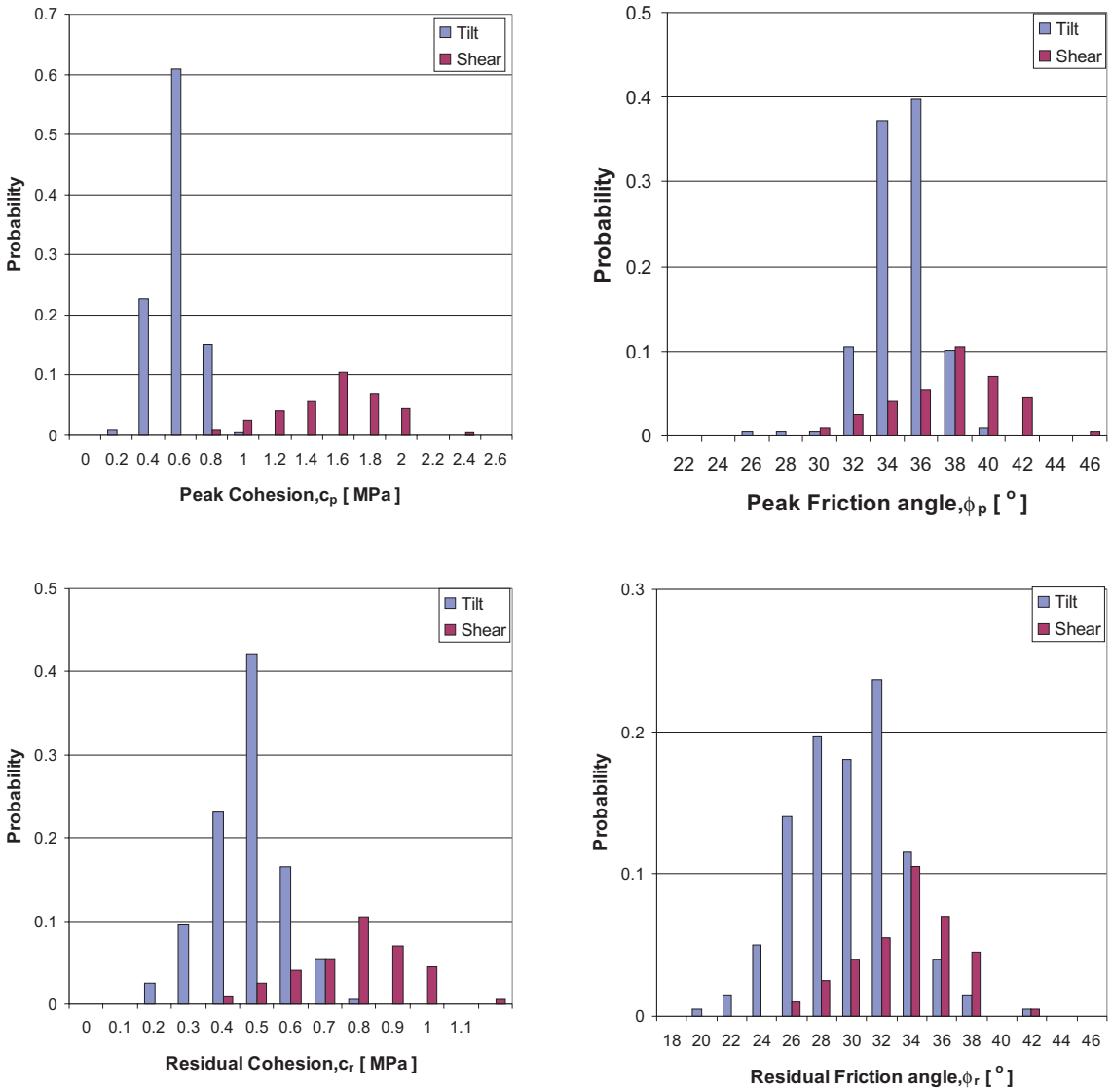

Figure A2-1. *Exploring normality in parameter distributions of Tilt test data and Shear test data. The Tilt data appears normally distributed.*

A2.1.4 Comparing fracture set properties: Mohr-Coulomb model parameters

Only the tilt-test data set was used to analyse the differences between fractures of different sets. The reason for selecting the tilt-test data set is that it is the largest homogeneous data set (Table A2-1). In this section, the fracture set properties are compared in terms of Mohr-Coulomb model parameters; an analogous study, in terms of Barton-Bandis model parameters, is given in the following section. As above, the distributions of $x_{Tilt,j}$ were plotted as histograms to examine normality (Figure A2-2). The overall impression is that the data appears not to deviate remarkably from multi-normality.

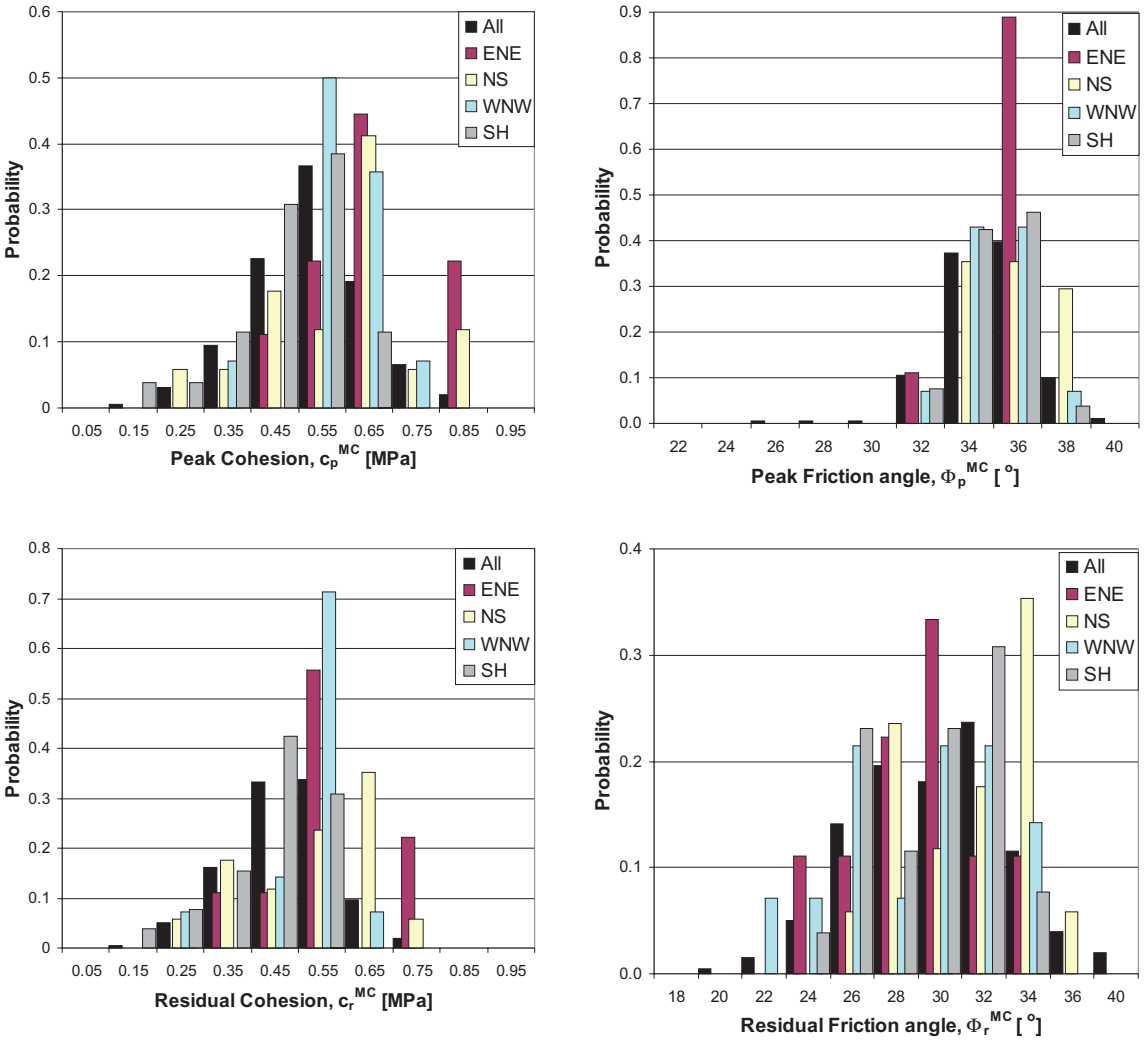

Figure A2-2. *Exploring normality of Mohr-Coulomb model parameter distributions in the Tilt-test data set.*

The ANOVA test is first used for simultaneous comparisons between the individual fracture sets. The ANOVA-test (Table A2-3) gives a difference in peak and residual cohesion between the fracture sets. Next, all tilt-test data are combined to form a reference data set, x_{all}, which contains data from all fracture sets. The properties of each individual fracture set are then compared to this reference data set, by means of *t*-tests (H_{A0}: $\mu_j = \mu_{all}$) and *F*-tests (H_{B0}: $\sigma_j = \sigma_{all}$). No significant differences are found for all parameters between the fracture sets; the only exception being peak and residual cohesion for some fracture sets (Table A2-3).

Next, the properties of the individual fracture sets were pair-wise compared, by means of *t*-tests (H_0: $\mu_{j1} = \mu_{j2}$) and *F*-tests (H_0: $\sigma_{j1} = \sigma_{j2}$). A significant difference in mean peak and residual cohesion was found between the subhorizontal set (SH) and all other sets (Table A2-4).

Table A2-3. Inference tests on fracture set properties of the Mohr-Coulomb model; pair-wise tests between individual fracture set, x_j, and total data set, x_{all}.

	Average, $\overline{x}_j$					t-test; risk of rejecting H_0 [2]			
	n_j	c_p^{MC}	Φ_p^{MC}	c_r^{MC}	Φ_r^{MC}	c_p^{MC}	Φ_p^{MC}	c_r^{MC}	Φ_r^{MC}
ENE	9	0.60	34.7	0.51	27.9	**0.02**	0.12	**0.04**	0.35
NS	17	0.54	34.9	0.48	30.4	0.22	**0.03**	0.18	0.08
WNW	14	0.54	34.1	0.47	27.9	0.07	0.72	0.11	0.36
SH	26	0.44	33.9	0.39	28.5	**0.04**	0.87	**0.03**	0.53
All	199	0.48	34.0	0.43	28.9				
ANOVA test; risk of rejecting H_0						**0.003**[1]	0.14[1]	**0.005**[1]	0.11[1]

	Standard Deviation, s_j					F-test; risk of rejecting H_0 [2]			
	n_j	c_p^{MC}	Φ_p^{MC}	c_r^{MC}	Φ_r^{MC}	c_p^{MC}	Φ_p^{MC}	c_r^{MC}	Φ_r^{MC}
ENE	9	0.12	1.23	0.10	2.79	0.56	0.13	0.50	0.26
NS	17	0.16	1.45	0.14	3.16	**0.04**	0.19	**0.04**	0.35
WNW	14	0.10	1.48	0.09	3.68	0.20	0.25	0.21	0.34
SH	26	0.11	1.32	0.10	2.86	0.26	**0.04**	0.33	0.12
All	199	0.12	1.76	0.10	3.47				

1) ANOVA test
2) significance level α = 0.05.

Table A2-4. Inference tests on fracture set properties of the Mohr-Coulomb model; pair-wise tests between individual fracture sets, x_{j1} and x_{j2}.

t-test of sample means; risk of rejecting H_0: $\mu_{j1} = \mu_{j2}$							
c_p^{MC}	NS	WNW	SH	Φ_p^{MC}	NS	WNW	SH
ENE	0.26	0.22	**0.00**	ENE	0.80	0.32	0.13
NS		0.95	**0.03**	NS		0.19	0.04
WNW			**0.01**	WNW			0.67
c_r^{MC}	NS	WNW	SH	Φ_r^{MC}	NS	WNW	SH
ENE	0.51	0.35	**0.01**	S_A	0.06	0.99	0.62
NS		0.85	**0.02**	S_B		0.06	0.06
WNW			**0.01**	S_C			0.62
F-test of sample variance; risk of rejecting H_0: $\sigma_{j1} = \sigma_{j2}$							
c_p^{MC}	NS	WNW	SH	Φ_p^{MC}	NS	WNW	SH
ENE	0.21	0.25	0.32	ENE	0.32	0.30	0.45
NS		0.04	0.04	NS		0.46	0.32
WNW			0.37	WNW			0.29
c_r^{MC}	NS	WNW	SH	Φ_r^{MC}	NS	WNW	SH
ENE	0.18	0.29	0.41	ENE	0.37	0.22	0.51
NS		0.04	0.05	NS		0.29	0.32
WNW			0.33	WNW			0.13

A2.1.5 Comparing fracture set properties: Barton-Bandis model parameters

In this section, fracture set properties is compared in terms of Barton-Bandis model parameters (analogous to the approach above). By visual inspection, only the distribution of joint compressive strength, JCS_{100}, appears to deviate particularly from normality. For consistency, it is treated with the same tests as in the previous section, although results from the parametric *t*- and *F*-tests should be treated with caution.

The ANOVA-test shows differences in JRC_{100}, see Table A2-5. Differences in mean JRC_{100} are found between SH (subhorizontal) and ENE, and between SH and WNW, see Table A2-6.

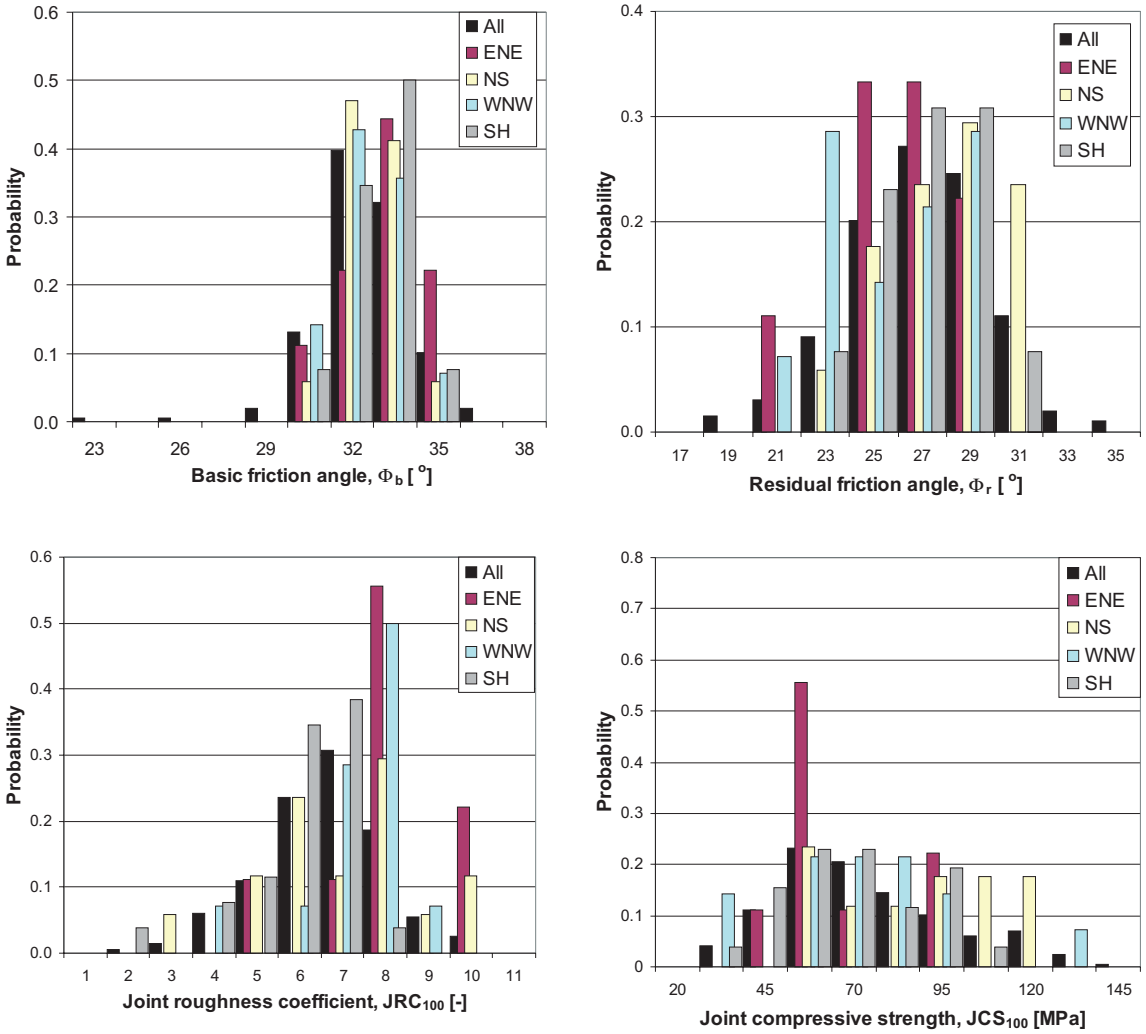

Figure A2-3. *Exploring normality of the Barton-Bandis model parameter distributions in the Tilt-test data set. Comparison between three steeply dipping fracture sets and one subhorizontal (SH).*

Table A2-5. Inference tests on fracture set properties of the Barton-Bandis model in Equation 4-1; pair-wise tests between individual fracture set, x_j, and total data set, x_{all}.

	Average, $\overline{x}_j$					t-test; risk of rejecting H_0			
	n_j	Φ_b^{BB}	Φ_r^{BB}	JRC_{100}	JCS_{100}	Φ_b^{BB}	Φ_r^{BB}	JRC_{100}	JCS_{100}
ENE	9	32.0	25.2	7.4	59.0	0.21	0.23	**0.03**	0.11
NS	17	31.5	27.0	6.6	81.6	0.68	0.29	0.36	0.05
WNW	14	31.4	25.1	6.8	65.8	0.94	0.18	0.05	0.62
SH	26	31.8	26.3	5.6	63.4	0.14	0.98	**0.03**	0.15
All	199	31.4	26.3	6.1	69.3				
ANOVA test; risk of rejecting H_0						0.52[1]	0.15[1]	**0.003**[1]	0.02[1]

	Standard Deviation, s_j					F-test; risk of rejecting H_0			
	n_j	Φ_b^{BB}	Φ_r^{BB}	JRC_{100}	JCS_{100}	Φ_b^{BB}	Φ_r^{BB}	JRC_{100}	JCS_{100}
ENE	9	1.3	2.4	1.4	16.8	0.27	0.26	0.55	0.11
NS	17	0.9	2.6	1.8	22.5	0.01	0.25	0.08	0.33
WNW	14	1.0	2.8	1.2	25.4	0.03	0.44	0.22	0.42
SH	26	1.1	2.2	1.3	18.8	0.02	0.04	0.27	0.05
All	199	1.7	3.0	1.4	25.0				

1) ANOVA test.

Table A2-6. Inference tests on fracture set properties of the Barton-Bandis model; pair-wise tests between individual fracture sets, x_{j1} and x_{j2}.

t-test of sample means; risk of rejecting H_0: $\mu_{j1} = \mu_{j2}$							
Φ_b^{BB}	NS	WNW	SH	Φ_r^{BB}	NS	WNW	SH
ENE	0.32	0.28	0.65	ENE	0.09	0.98	0.26
NS		0.82	0.39	NS		0.08	0.36
WNW			0.32	WNW			0.22
JRC_{100}	NS	WNW	SH	**JCS_{100}**	NS	WNW	SH
ENE	0.21	0.35	**0.004**	ENE	0.01	0.45	0.53
NS		0.61	0.05	NS		0.08	0.01
WNW			**0.003**	WNW			0.76
F-test of sample variance; risk of rejecting H_0: $\sigma_{j1} = \sigma_{j2}$							
Φ_b^{BB}	NS	WNW	SH	Φ_r^{BB}	NS	WNW	SH
ENE	0.10	0.20	0.27	ENE	0.44	0.33	0.37
NS		0.32	0.18	NS		0.36	0.26
WNW			0.26	WNW			0.15
JRC_{100}	NS	WNW	SH	**JCS_{100}**	NS	WNW	SH
ENE	0.26	0.27	0.33	ENE	0.20	0.12	0.39
NS		0.07	0.07	NS		0.32	0.20
WNW			0.38	WNW			0.09

A2.1.6 Conclusions

Comparing the results from tilt tests and shear tests shows a significant difference. For use in design and in the theoretical approach it is recommended to use the values from direct shear tests since they are based on direct measurements with a stress magnitude comparable to what is expected to be found at tentative repository depth.

The only significant difference from the tilt tests result on different fracture sets was observed for the peak and residual cohesion for the subhorizontal (SH) set. The number of data from each fracture sets are not the same and the number are few why the results from statistical tests are uncertain. It can therefore bee inferred that all the fracture sets seem to have the same mechanical properties independently of the set orientation. The direct shear testing results were too few to enable the comparison of different fracture sets.

Appendix 3

Empirical characterisation of the rock mass along borehole KLX05 and KLX12A

This appendix presents the empirical characterization performed for boreholes KLX05 and KLX12A following the methodology described in /Röshoff et al. 2002/. For the other boreholes used in the modelling, described in Section 5.1, the corresponding information is found in P-reports (KLX02 in /Lanaro and Bäckström 2005/; KLX01, KLX03 and KLX04 in /Lanaro and Bäckström 2006b/). Further comments to the methodology and results may be found in these reports.

Contents

A3.1 KLX05

Table A3-1. Partitioning of borehole KLX05; rock units, deformation and crush zones used in the empirical characterization (based on Sicada_08_018, p_eshi.xls).

Rock Unit	BH length (m)/Section 1 m	5 m	Deformation zones	BH length (m)/Section 1 m	5 m	Crushed Zones	BH length (m)/Section 1 m	5 m
	Outside mapping section		DZ 1	101–108	101–110			
RU 1	108–212	110–215	DZ 2	(173.8–173.9)				
			DZ 3	(178.7–178.8)				
RU 2	212–293	215–295	DZ 4	261–263				
RU 3	293–474	295–480	DZ 5	306–307		Crush Zone 1	(391.8–391.9)	
			DZ 6	403–407	400–405			
RU 4a	474–693	475–695	DZ 7	477–478		Crush Zone 2	511–512	510–515
			DZ 8	576–577				
			DZ 9	590–591				
			DZ 10	612–613				
			DZ 11	626–629	625–630			
			DZ 12	654–655		Crush Zone 3	654–655	650–655
RU 5	693–753	695–755						
RU 4b	753–995	755–995	DZ 13	814–815		–		

A3.1.1 Fracture orientation

Table A3-2. a) Set identification from the open fracture orientation mapped for borehole KLX05A used in the empirical characterization (Sicada, 07-11-26). The orientations are given as strike/dip (right-hand rule). b) Fisher's constant of the fracture sets identified for borehole KLX05 (Sicada, 07-11-26).

BH length (m)	No. of fractures	Fracture orientation (Strike/Dip) SH	WNW	ENE	NS	Fisher's constant SH	WNW	ENE	NS
108–211	61	149/6	79/87	105/90	9/87	34	21	25	14
211–292	28	65/16	225/76	285/84	351/83	19	166	34	5
292–473	63	140/9	246/80	117/85	353/87	17	15	37	8
473–692	88	136/7	70/88	112/86	354/87	23	11	19	11
692–752	42		73/75	112/89	353/83		11	29	16
752–995	26		62/74	113/80	343/74		5	9	21

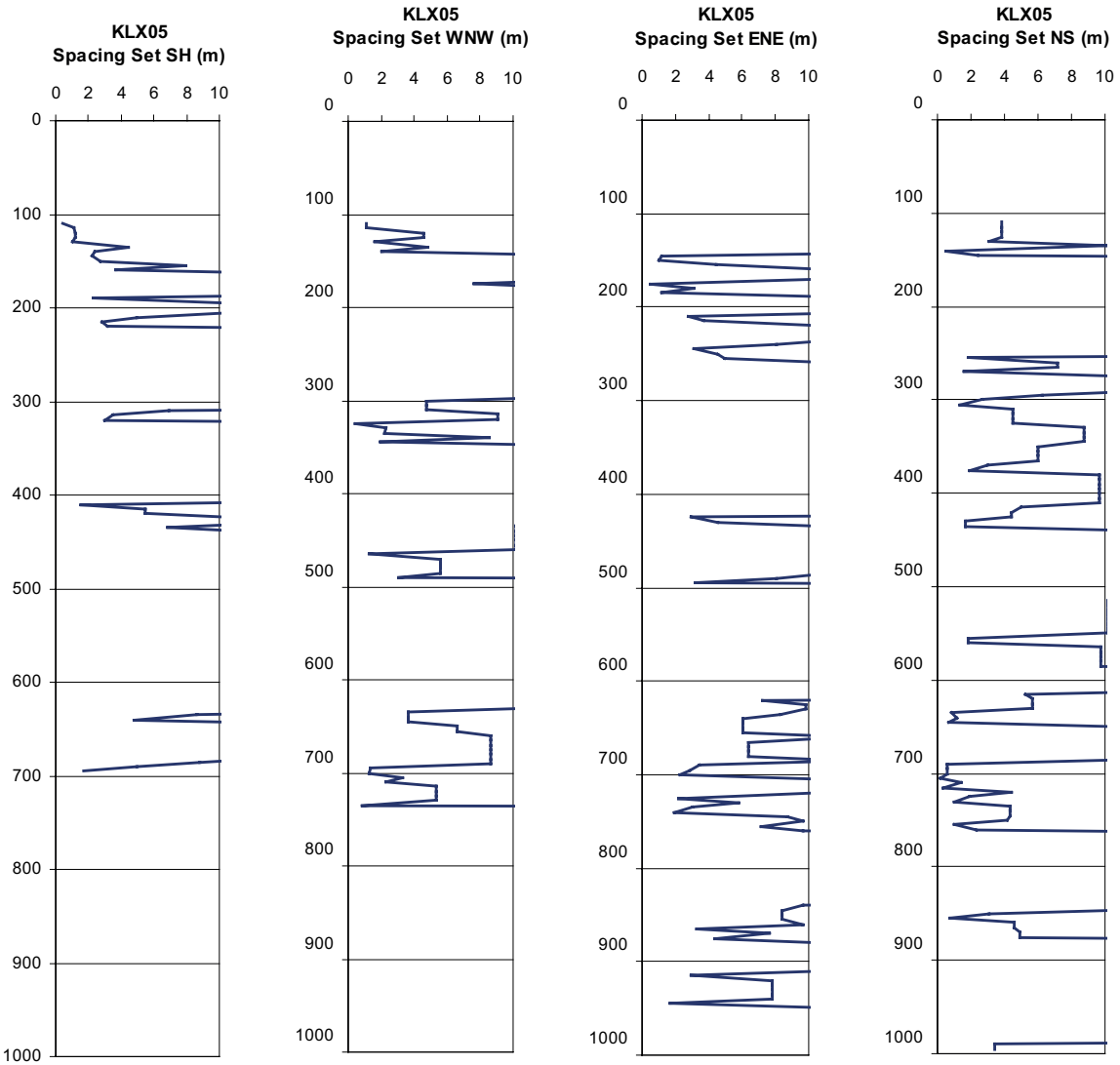

Figure A3-1. *Fracture spacing with depth for the four facture sets in borehole KLX05. The values are averaged for each 5 m length of borehole. Y-axis shows borehole length in meters.*

A3.1.2 RMR

Table A3-3. RMR values along borehole KLX05 (core sections of 5 m).

Rock Unit	BH length (m)	Min RMR	Mean RMR	Frequent RMR	Max RMR	Std. dev. RMR	Min possible RMR	Max possible RMR
RU 1.1	110–210	67.0	79.3	78.8	90.0	6.3	58.2	90.0
RU 2.1	210–290	75.0	84.4	82.8	89.5	5.0	62.3	90.0
RU 3.1	290–400	65.7	82.9	82.0	89.6	6.3	56.3	90.0
DZ 6	400–405	82.0	82.0	82.0	82.0	–	79.4	82.6
RU 3.3	405–475	73.9	81.5	81.5	89.6	4.9	64.4	90.0
RU 4a.1	*475–510*	*80.6*	*82.4*	*82.0*	*85.5*	*1.7*	*71.9*	*86.9*
Crush Zone 2	*510–515*	*70.7*	*70.7*	*70.7*	*70.7*	–	*52.3*	*82.0*
RU 4a.3	*515–625*	*74.5*	*85.1*	*88.5*	*88.9*	*4.5*	*54.8*	*90.0*
RU 4a (incl. crush zone)	475–625	70.7	84.0	84.1	88.9	4.8	52.3	90.0
DZ 11	625–630	82.6	82.6	82.6	82.6	–	72.6	86.9
RU 4a.6	*630–650*	*72.4*	*77.7*	*74.8*	*89.0*	*7.7*	*53.8*	*89.9*
Crush Zone 3	*650–655*	*72.2*	*72.2*	*72.2*	*72.2*	–	*56.6*	*82.0*
RU 4a.7	*655–690*	*67.9*	*79.9*	*80.1*	*88.5*	*6.3*	*53.9*	*89.9*
RU 4a (incl. crush zone)	630–690	67.9	78.6	79.1	89.0	6.6	53.8	89.9
RU 5	690–750	69.1	79.5	78.5	89.0	6.8	61.8	89.0
RU 4b.1	750–995	75.2	85.9	88.5	88.7	3.9	68.1	89.9
RU 3	290–400 and 405–475	65.7	82.4	81.7	89.6	5.8	56.3	90.0
RU 4a	470–510, 515–625, 630–650 and 655–690	67.9	83.0	82.8	89.0	5.4	53.8	90.0
DZ zones	400–405 and 625–630	82.0	82.3	82.3	82.6	0.5	72.6	86.9
Crush zones	510–515 and 650–655	70.7	71.5	71.5	72.2	1.1	52.3	82.0
Competent rock		65.7	83.1	82.8	90.0	5.7	53.8	90.0
Deformation & Crush Zones		70.7	76.9	77.1	82.6	6.3	52.3	86.9
Whole borehole		65.7	83.1	82.6	90.0	5.7	52.3	90.0

DZ 1 is situated outside the mapping section, the following DZ were only included in the 1 m core sections; DZ 4 (1.7 m), DZ 5 (0.86 m), DZ 7 (0.6 m), DZ 8 (1 m), DZ 9 (0.5 m), Not included; DZ 2 (0.1 m), DZ 3 (0.8 m), DZ 10 (0.2 m) and Crush Zone 1 (0.7 m). DZ 12 (1.1 m) mainly coincides with Crush Zone 3 (0.9 m).

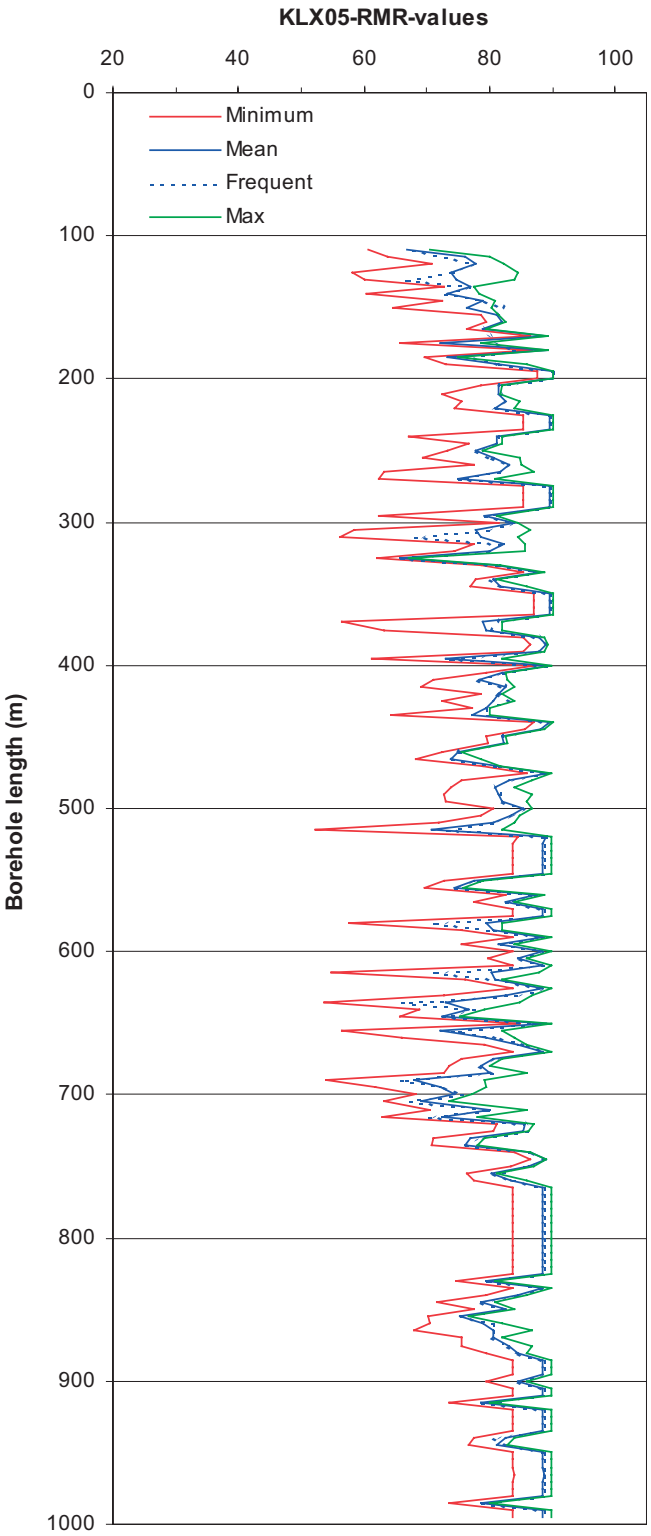

Figure A3-2. *Variation of RMR with depth for borehole KLX05; the values are given every 5 m.*

A3.1.3 Q

Table A3-4. Q values along borehole KLX05 (core sections of 5 m).

Rock Unit	BH length (m)	Min Q	Mean Q	Frequent Q	Max Q	Std. dev. Q	Min possible Q	Max possible Q
RU 1.1	110–210	3.6	61.4	32.1	200.0	71.2	2.0	200.0
RU 2.1	210–290	7.5	116.0	65.6	264.0	99.4	4.3	264.0
RU 3.1	290–400	5.9	131.8	69.7	264.0	114.8	1.1	264.0
DZ 6	400–405	66.0	66.0	66.0	66.0	–	13.2	132.0
RU 3.3	405–475	13.4	96.9	66.0	264.0	95.7	1.8	264.0
RU 4a.1	*475–510*	*29.3*	*83.9*	*79.2*	*132.0*	*30.7*	*5.3*	*132.0*
Crush Zone 2	*510–515*	*14.5*	*14.5*	*14.5*	*14.5*	–	*0.1*	*49.5*
RU 4a.3	*515–625*	*21.4*	*181.0*	*264.0*	*264.0*	*103.3*	*12.2*	*264.0*
RU 4a (incl. crush zone)	475–625	14.5	152.8	99.0	264.0	101.6	0.1	264.0
DZ 11	625–630	14.9	14.9	14.9	14.9	–	2.2	198.0
RU 4a.6	*630–650*	*7.4*	*78.5*	*21.3*	*264.0*	*124.2*	*4.4*	*264.0*
Crush Zone 3	*650–655*	*3.8*	*3.8*	*3.8*	*3.8*	–	*0.1*	*12.4*
RU 4a.7	*655–690*	*3.5*	*77.6*	*66.0*	*264.0*	*86.2*	*2.2*	*264.0*
RU 4a (incl. crush zone)	630–690	3.5	71.8	38.5	264.0	93.4	0.1	264.0
RU 5	690–750	4.8	57.9	53.2	132.0	42.0	2.9	132.0
RU 4b.1	750–995	29.3	196.0	264.0	264.0	95.5	7.5	264.0
RU 3	290–400 and 405–475	5.9	118.3	66.0	264.0	107.8	1.1	264.0
RU 4a	475–510, 515–625, 630–650 and 655–690	3.5	135.7	83.6	264.0	103.9	2.2	264.0
DZ zones	400–405 and 625–630	14.9	40.4	40.4	66.0	36.2	2.2	198.0
Crush zones	510–515 and 650–655	3.8	9.1	9.1	14.5	7.6	0.1	49.5
Competent rock		3.5	132.9	79.2	264.0	105.3	1.1	264.0
Deformation & Crush Zones		3.8	24.8	14.7	66.0	28.0	0.1	198.0
Whole borehole		3.5	131.2	77.1	264.0	105.2	0.1	264.0

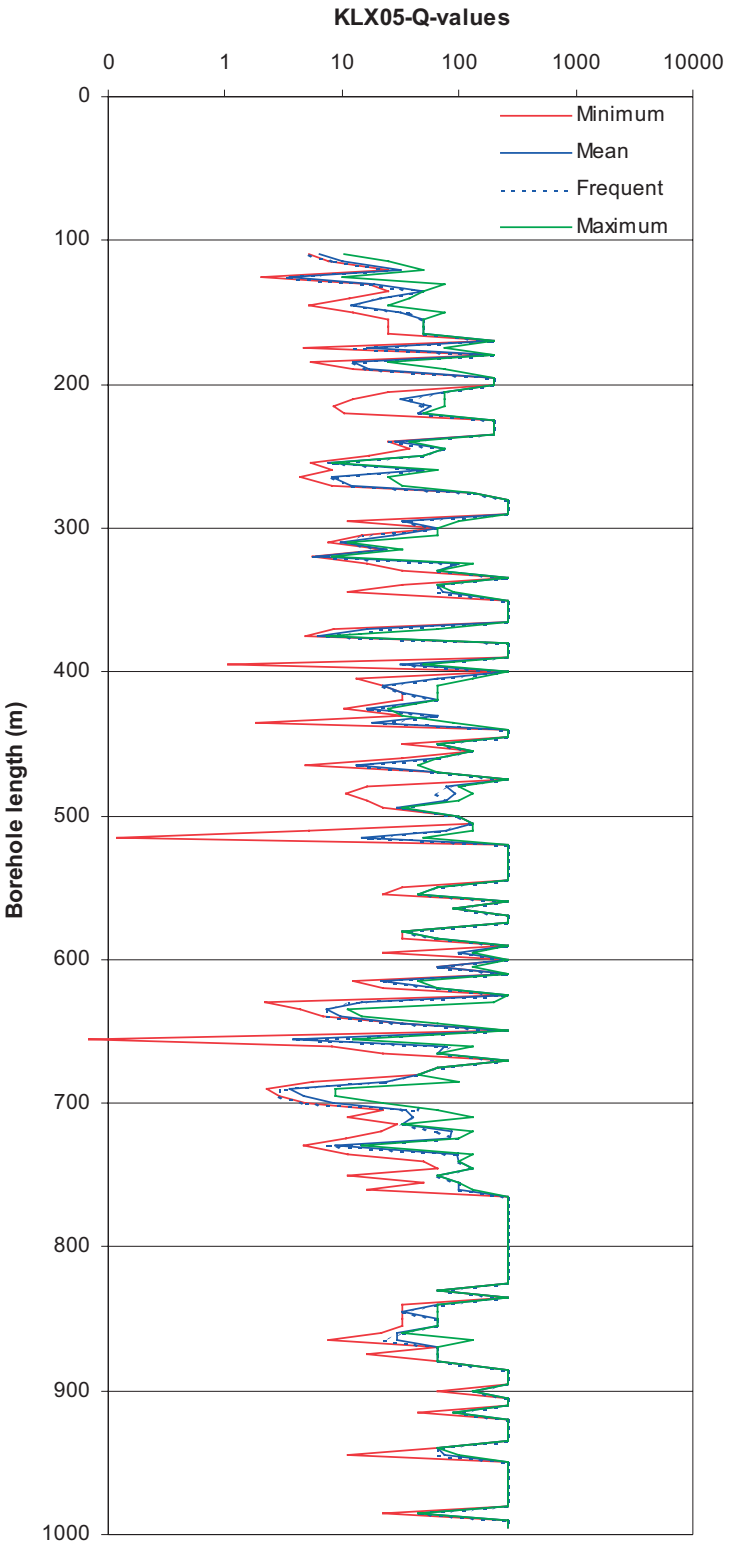

Figure A3-3. *Variation of Q with depth for borehole KLX05; the values are given every 5 m.*

A3.1.4 Rock mass properties

Deformation modulus

RMR

Table A3-5. Deformation modulus Em derived from RMR along for borehole KLX05 (core sections of 5 m).

Rock Unit	BH length (m)	Min Em (GPa)	Mean Em (GPa)	Frequent Em (GPa)	Max Em (GPa)	Std. dev. Em (GPa)	Min possible Em (GPa)	Max possible Em (GPa)
RU 1.1	110–210	26.6	52.9	52.4	73.0	13.8	16.0	80.0
RU 2.1	210–290	42.2	65.6	66.2	75.0	10.3	20.3	85.0
RU 3.1	290–400	24.7	62.9	63.3	80.0	14.8	14.4	93.0
DZ 6	400–405	63.1	63.1	63.1	63.1	–	54.3	65.3
RU 3.3	405–475	39.6	60.1	61.3	80.0	12.3	22.9	93.0
RU 4a.1	*475–510*	*58.2*	*64.7*	*63.2*	*75.0*	*5.9*	*35.4*	*83.0*
Crush Zone 2	*510–515*	*32.9*	*32.9*	*32.9*	*32.9*	–	*11.4*	*63.1*
RU 4a.3	*515–625*	*40.9*	*67.9*	*75.0*	*75.0*	*10.5*	*13.2*	*83.0*
RU 4a (incl. crush zone)	475–625	32.9	66.0	71.1	75.0	11.3	11.4	83.0
DZ 11	625–630	65.5	65.5	65.5	65.5	–	36.7	83.0
RU 4a.6	*630–650*	*36.4*	*48.6*	*41.9*	*74.4*	*17.7*	*12.4*	*81.8*
Crush Zone 3	*650–655*	*35.9*	*35.9*	*35.9*	*35.9*	–	*14.6*	*63.1*
RU 4a.7	*655–690*	*28.0*	*56.7*	*56.6*	*75.0*	*15.5*	*12.5*	*83.0*
RU 4a (incl. crush zone)	630–690	28.0	52.3	53.3	75.0	16.1	12.4	83.0
RU 5	690–750	30.0	54.8	51.9	73.0	17.3	19.7	79.0
RU 4b.1	750–995	42.8	69.9	75.0	75.0	8.8	28.3	83.0
RU 3	290–400 and 405–475	24.7	61.8	62.0	80.0	13.8	14.4	93.0
RU 4a	470–510, 515–625, 630–650 and 655–690	28.0	63.4	65.9	75.0	13.0	12.4	83.0
DZ zones	400–405 and 625–630	63.1	64.3	64.3	65.5	1.7	36.7	83.0
Crush zones	510–515 and 650–655	32.9	34.4	34.4	35.9	2.1	11.4	63.1
Competent rock		24.7	63.2	66.2	80.0	13.4	12.4	93.0
Deformation & Crush Zones		32.9	49.4	49.5	65.5	17.3	11.4	83.0
Whole borehole		24.7	63.1	65.5	80.0	13.3	11.4	93.0

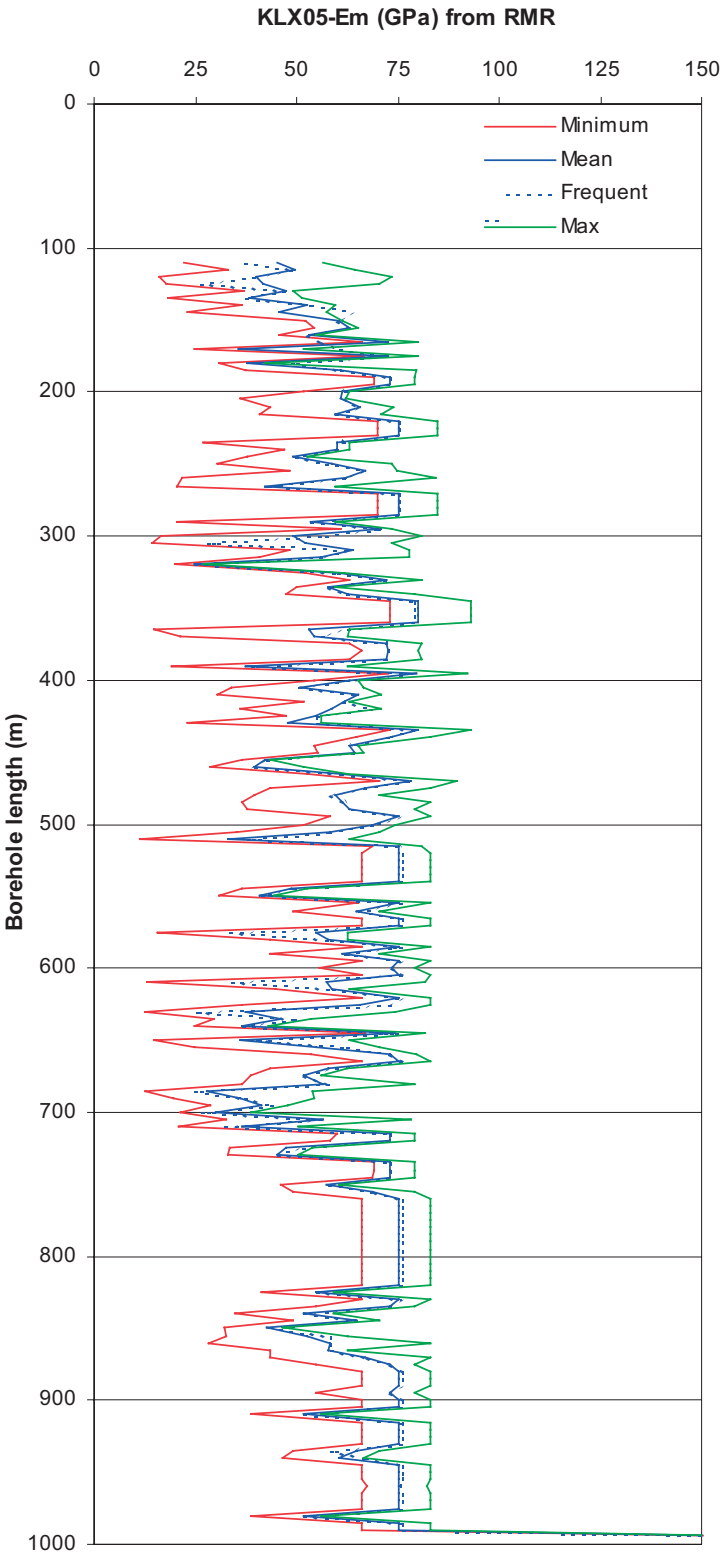

Figure A3-4. *Variation of the deformation modulus of the rock mass obtained from RMR with depth for borehole KLX05. The values are given every 5 m.*

Q

Table A3-6. Deformation modulus Em derived from Q along borehole KLX05 (core sections of 5 m).

Rock Unit	BH length (m)	Min Em (GPa)	Mean Em (GPa)	Frequent Em (GPa)	Max Em (GPa)	Std. dev. Em (GPa)	Min possible Em (GPa)	Max possible Em (GPa)
RU 1.1	110–210	18.3	43.3	41.2	73.0	17.5	14.5	80.0
RU 2.1	210–290	25.0	55.1	51.7	75.0	18.8	19.4	85.0
RU 3.1	290–400	21.7	54.5	51.8	80.0	20.7	12.2	89.1
DZ 6	400–405	48.0	48.0	48.0	48.0	–	27.1	62.7
RU 3.3	405–475	28.3	51.6	50.3	80.0	16.7	15.4	89.1
RU 4a.1	*475–510*	*38.2*	*53.0*	*52.7*	*62.5*	*7.4*	*18.5*	*68.4*
Crush Zone 2	*510–515*	*30.7*	*30.7*	*30.7*	*30.7*	–	*5.5*	*50.5*
RU 4a.3	*515–625*	*34.5*	*63.8*	*75.0*	*75.0*	*14.5*	*24.9*	*83.0*
RU 4a (incl. crush zone)	475–625	30.7	60.1	56.8	75.0	14.7	5.5	83.0
DZ 11	625–630	30.2	30.2	30.2	30.2	–	13.7	78.1
RU 4a.6	*630–650*	*23.9*	*41.0*	*32.8*	*74.4*	*23.3*	*17.4*	*81.8*
Crush Zone 3	*650–655*	*22.1*	*22.1*	*22.1*	*22.1*	–	*5.3*	*35.3*
RU 4a.7	*655–690*	*18.7*	*47.3*	*49.6*	*75.0*	*17.7*	*13.8*	*83.0*
RU 4a (incl. crush zone)	630–690	18.7	43.1	41.4	75.0	19.3	5.3	83.0
RU 5	690–750	22.8	50.6	53.0	72.3	16.5	17.4	77.7
RU 4b.1	750–995	37.9	66.2	75.0	75.0	12.9	20.7	83.0
RU 3	290–400 and 405–475	21.7	53.4	51.8	80.0	19.1	12.2	89.1
RU 4a	475–510, 515–625, 630–650 and 655–690	18.7	56.7	55.0	75.0	16.8	13.8	83.0
DZ zones	400–405 and 625–630	30.2	39.1	39.1	48.0	12.6	13.7	78.1
Crush zones	510–515 and 650–655	22.1	26.4	26.4	30.7	6.1	5.3	50.5
Competent rock		18.3	56.5	54.8	80.0	17.9	12.2	89.1
Deformation & Crush Zones		22.1	32.8	30.5	48.0	10.9	5.3	78.1
Whole borehole		18.3	56.2	54.6	80.0	17.9	5.3	89.1

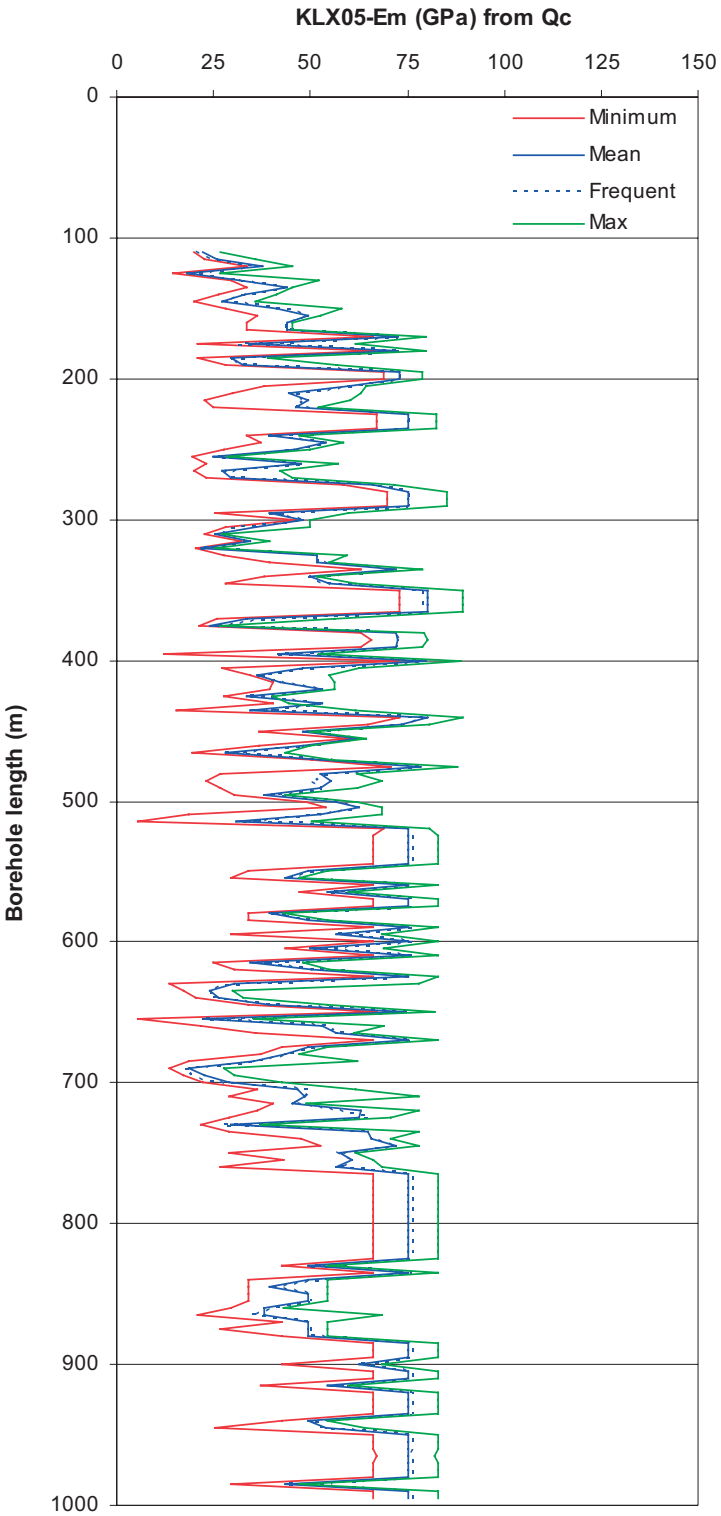

Figure A3-5. *Variation of the deformation modulus of the rock mass obtained from Q with depth for borehole KLX05. The values are given every 5 m.*

Poisson's ratio

RMR

Table A3-7. Poisson's ratio, v, derived from RMR along borehole KLX05 (core sections of 5 m).

Rock Unit	BH length (m)	Min v (–)	Mean v (–)	Frequent v (–)	Max v (–)	Std. dev. v (–)	Min possible v (–)	Max possible v (–)
RU 1.1	110–210	0.10	0.20	0.20	0.28	0.05	0.03	0.32
RU 2.1	210–290	0.13	0.21	0.21	0.23	0.03	0.04	0.31
RU 3.1	290–400	0.09	0.25	0.25	0.33	0.06	0.03	0.39
DZ 6	400–405	0.24	0.24	0.24	0.24	–	0.09	0.27
RU 3.3	405–475	0.15	0.24	0.24	0.33	0.05	0.05	0.39
RU 4a.1	*475–510*	*0.22*	*0.24*	*0.24*	*0.28*	*0.02*	*0.10*	*0.33*
Crush Zone 2	*510–515*	*0.13*	*0.13*	*0.13*	*0.13*	–	*0.04*	*0.28*
RU 4a.3	*515–625*	*0.15*	*0.25*	*0.28*	*0.29*	*0.04*	*0.04*	*0.35*
RU 4a (incl. crush zone)	475–625	0.1	0.2	0.3	0.3	0.0	0.0	0.4
DZ 11	625–630	0.24	0.24	0.24	0.24	–	0.11	0.33
RU 4a.6	*630–650*	*0.14*	*0.18*	*0.16*	*0.28*	*0.07*	*0.04*	*0.33*
Crush Zone 3	*650–655*	*0.14*	*0.14*	*0.14*	*0.14*	–	*0.05*	*0.26*
RU 4a.7	*655–690*	*0.10*	*0.21*	*0.21*	*0.28*	*0.06*	*0.04*	*0.33*
RU 4a (incl. crush zone)	630–690	0.1	0.2	0.2	0.3	0.1	0.0	0.3
RU 5	690–750	0.12	0.21	0.20	0.28	0.07	0.06	0.32
RU 4b.1	750–995	0.16	0.26	0.28	0.29	0.03	0.08	0.34
RU 3	290–400 and 405–475	0.09	0.24	0.24	0.33	0.06	0.03	0.39
RU 4a	475–510, 515–625, 630–650 and 655–690	0.10	0.24	0.25	0.29	0.05	0.04	0.35
DZ zones	400–405 and 625–630	0.24	0.24	0.24	0.24	0.01	0.09	0.33
Crush zones	510–515 and 650–655	0.13	0.13	0.13	0.14	0.00	0.04	0.28
Competent rock		0.09	0.24	0.24	0.33	0.05	0.03	0.39
Deformation & Crush Zones		0.13	0.19	0.19	0.24	0.06	0.04	0.33
Whole borehole		0.09	0.24	0.24	0.33	0.05	0.03	0.39

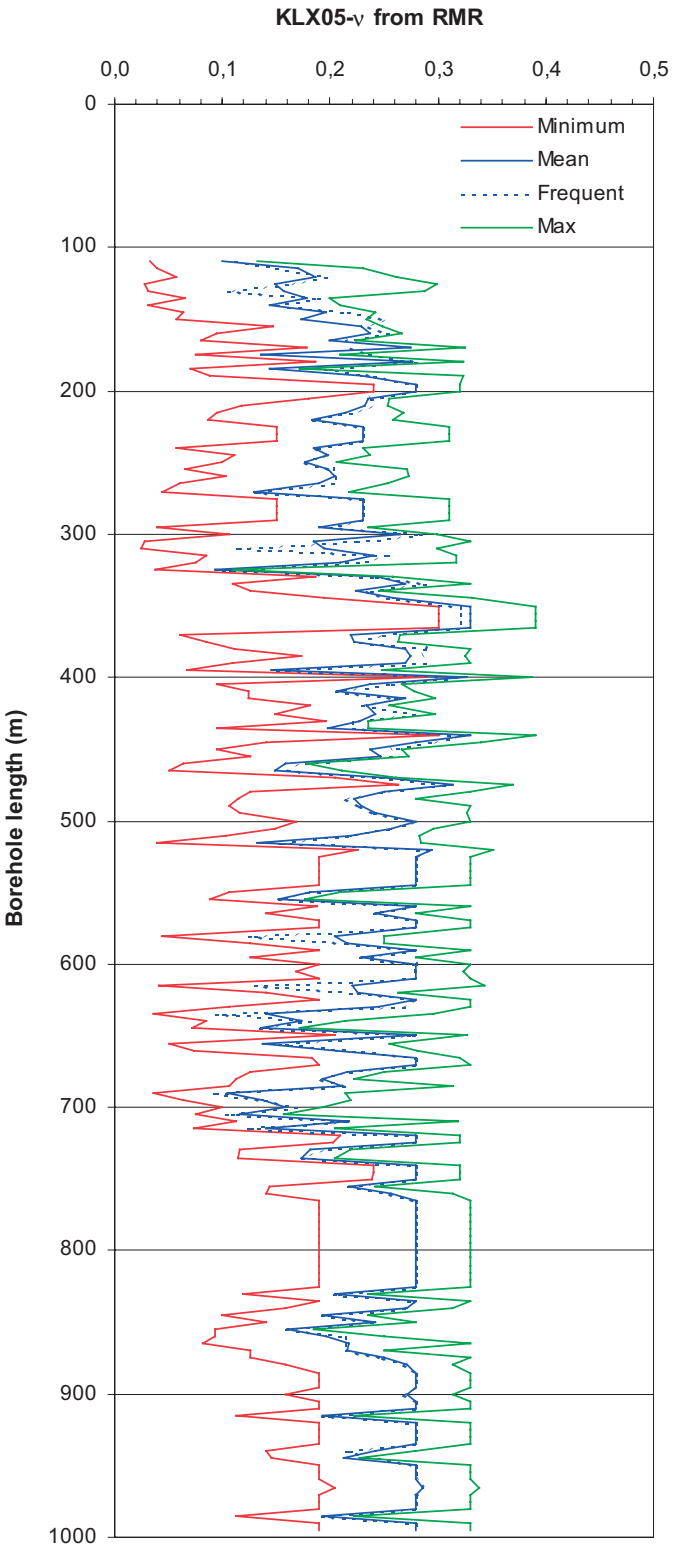

Figure A3-6. *Variation of Poisson's ratio (v) with depth for borehole KLX05 (Hoek-Brown's a = 0.5). The values are given every 5 m.*

Uniaxial compressive strength

RMR

Table A3-8. Summary of the uniaxial compressive strength of the rock mass derived from RMR for borehole KLX05 (core sections of 5 m, Hoek-Brown's a = 0.5).

Rock Unit	BH length (m)	Min UCS (MPa)	Mean UCS (MPa)	Frequent UCS (MPa)	Max UCS (MPa)	Std. dev. UCS (MPa)	Min possible UCS (MPa)	Max possible UCS (MPa)
RU 1.1	110–210	20.31	55.84	41.04	124.30	31.15	11.20	154.72
RU 2.1	210–290	41.54	72.23	66.35	92.99	20.08	13.97	121.69
RU 3.1	290–400	15.84	61.65	54.82	96.06	23.83	10.08	116.47
DZ 6	400–405	46.81	46.81	46.81	46.81	–	36.42	53.87
RU 3.3	405–475	29.88	57.81	56.85	96.06	18.44	19.67	116.47
RU 4a.1	*475–510*	*48.03*	*53.28*	*52.96*	*62.62*	*5.08*	*19.12*	*88.17*
Crush Zone 2	*510–515*	*29.73*	*29.73*	*29.73*	*29.73*	–	*7.48*	*72.45*
RU 4a.3	*515–625*	*33.91*	*63.29*	*73.97*	*80.14*	*14.23*	*7.83*	*110.45*
RU 4a (incl. crush zone)	475–625	29.7	59.8	58.4	80.1	14.2	7.5	110.5
DZ 11	625–630	53.43	53.43	53.43	53.43	–	19.51	88.17
RU 4a.6	*630–650*	*30.28*	*47.00*	*34.71*	*88.30*	*27.75*	*6.86*	*119.30*
Crush Zone 3	*650–655*	*46.26*	*46.26*	*46.26*	*46.26*	–	*14.93*	*99.15*
RU 4a.7	*655–690*	*23.57*	*52.71*	*47.03*	*88.12*	*21.45*	*6.91*	*119.52*
RU 4a (incl. crush zone)	630–690	23.6	50.3	46.3	88.3	21.7	6.9	119.5
RU 5	690–750	38.94	73.50	66.05	117.58	27.69	16.41	146.36
RU 4b.1	750–995	35.42	65.81	73.97	76.54	12.23	15.19	106.81
RU 3	290–400 and 405–475	15.84	60.16	55.69	96.06	21.70	10.08	116.47
RU 4a	475–510, 515–625, 630–650 and 655–690	23.57	58.06	53.75	88.30	16.74	6.86	119.52
DZ zones	400–405 and 625–630	46.81	50.12	50.12	53.43	4.68	19.51	88.17
Crush zones	510–515 and 650–655	29.73	38.00	38.00	46.26	11.68	7.48	99.15
Competent rock		15.84	62.78	60.87	124.30	20.67	6.86	154.72
Deformation & Crush Zones		29.73	44.06	46.53	53.43	10.09	7.48	99.15
Whole borehole		15.84	62.59	60.29	124.30	20.47	6.86	154.72

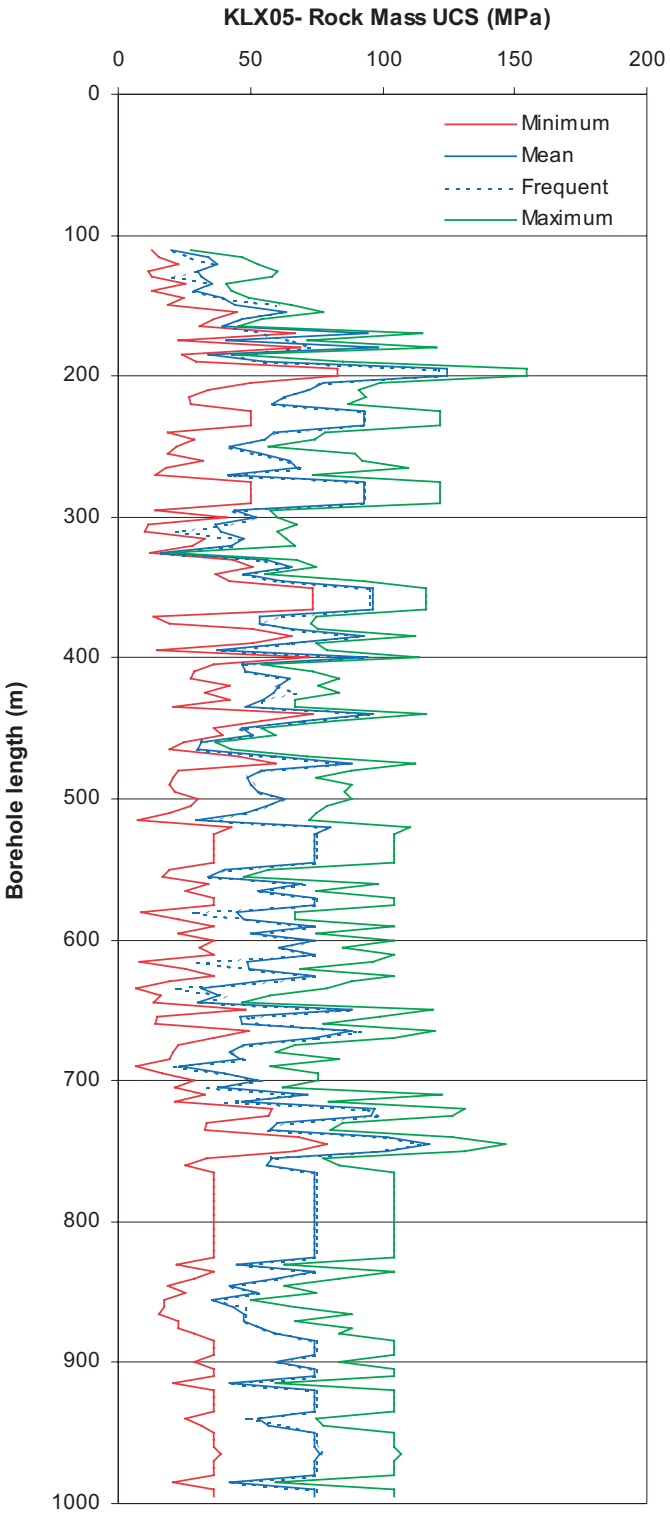

Figure A3-7. *Variation of the uniaxial compressive strength of the rock mass with depth for borehole KLX05 (Hoek-Brown's a = 0.5). The values are given every 5 m.*

Friction angle and cohesion of the rock mass

RMR

Table A3-9. Summary of the friction angle (ϕ') of the rock mass derived from RMR for borehole KLX05 (10–30 MPa) (core sections of 5 m, Hoek-Brown's a = 0.5).

Rock Unit	BH length (m)	Min ϕ' (°)	Mean ϕ' (°)	Frequent ϕ' (°)	Max ϕ' (°)	Std. dev. ϕ' (°)	Min possible ϕ' (°)	Max possible ϕ' (°)
RU 1.1	110–210	49.67	52.38	52.33	56.91	2.77	50.82	59.28
RU 2.1	210–290	51.75	53.67	54.17	54.65	1.05	46.88	57.03
RU 3.1	290–400	47.03	51.69	52.28	54.19	2.18	46.14	56.70
DZ 6	400–405	49.67	49.67	49.67	49.67	–	50.82	50.47
RU 3.3	405–475	49.67	52.47	53.55	54.25	1.93	47.35	56.79
RU 4a.1	*475–510*	*50.68*	*50.84*	*50.85*	*51.02*	*0.11*	*48.14*	*53.00*
Crush Zone 2	*510–515*	*51.66*	*51.66*	*51.66*	*51.66*	–	*48.06*	*54.79*
RU 4a.3	*515–625*	*50.50*	*50.71*	*50.54*	*51.13*	*0.23*	*47.87*	*53.66*
RU 4a (incl. crush zone)	475–625	50.5	50.8	50.8	51.7	0.3	47.9	54.8
DZ 11	625–630	50.81	50.81	50.81	50.81	–	48.24	52.09
RU 4a.6	*630–650*	*80.97*	*51.42*	*51.03*	*52.64*	*0.81*	*48.26*	*54.43*
Crush Zone 3	*650–655*	*57.08*	*57.08*	*57.08*	*57.08*	–	*52.85*	*59.27*
RU 4a.7	*655–690*	*50.50*	*51.72*	*50.93*	*56.27*	*2.03*	*48.08*	*58.55*
RU 4a (incl. crush zone)	630–690	50.5	52.1	51.0	57.1	2.2	48.01	59.3
RU 5	690–750	55.11	56.74	56.85	57.12	0.54	51.46	59.47
RU 4b.1	750–995	50.20	50.68	50.50	53.83	0.49	48.03	55.88
RU 3	290–400 and 405–475	47.03	51.99	53.10	54.25	2.09	46.14	56.79
RU 4a	475–510, 515–625, 630–650 and 655–690	50.50	50.98	50.86	56.27	0.94	47.87	58.55
DZ zones	400–405 and 625–630	49.67	50.24	50.24	50.81	0.81	48.24	52.09
Crush zones	510–515 and 650–655	51.66	54.37	54.37	57.08	3.83	48.06	59.27
Competent rock		47.03	51.92	50.88	57.12	2.17	46.14	59.47
Deformation & Crush Zones		49.67	52.30	51.23	57.08	3.29	48.06	59.27
Whole borehole		47.03	51.94	50.88	57.12	2.19	46.14	59.47

Table A3-10. Summary of the cohesion (c') of the rock mass derived from RMR for borehole KLX05 under confinement stress between 10 and 30 MPa) (core sections of 5 m, Hoek-Brown's a = 0.5).

Rock Unit	BH length (m)	Min c' (°)	Mean c' (°)	Frequent c' (°)	Max c' (°)	Std. dev. c' (°)	Min possible c' (°)	Max possible c' (°)
RU 1.1	110–210	20.91	24.64	23.19	32.15	3.74	21.46	35.86
RU 2.1	210–290	23.14	26.50	26.22	28.31	1.82	18.85	31.99
RU 3.1	290–400	18.85	24.59	23.74	28.36	2.75	18.28	31.40
DZ 6	400–405	22.14	22.14	22.14	22.14	–	22.22	23.11
RU 3.3	405–475	21.25	24.75	25.38	28.36	2.13	19.78	31.40
RU 4a.1	*475–510*	*22.97*	*23.30*	*23.34*	*23.92*	*0.34*	*19.74*	*27.09*
Crush Zone 2	*510–515*	*22.50*	*22.50*	*22.50*	*22.50*	–	*19.33*	*27.10*
RU 4a.3	*515–625*	*22.22*	*24.11*	*24.86*	*25.62*	*1.02*	*19.47*	*29.71*
RU 4a (incl. crush zone)	475–625	22.2	23.9	23.7	25.6	1.0	19.3	29.7
DZ 11	625–630	23.27	23.27	23.27	23.27	–	19.75	26.90
RU 4a.6	*630–650*	*22.08*	*23.44*	*22.26*	*27.16*	*2.48*	*19.48*	*30.87*
Crush Zone 3	*650–655*	*27.61*	*27.61*	*27.61*	*27.61*	–	*23.00*	*32.17*
RU 4a.7	*655–690*	*21.85*	*23.93*	*22.90*	*29.18*	*2.49*	*19.49*	*32.94*
RU 4a (incl. crush zone)	630–690	21.9	24.1	22.9	29.2	2.5	19.5	32.9
RU 5	690–750	25.62	28.83	28.41	31.61	1.70	21.93	35.21
RU 4b.1	750–995	22.29	24.29	24.86	25.52	0.91	19.63	28.99
RU 3	290–400 and 405–475	18.85	24.65	24.79	28.36	2.49	18.28	31.40
RU 4a	475–510, 515–625, 630–650 and 655–690	21.85	23.87	23.36	29.18	1.45	19.47	32.94
DZ zones	400–405 and 625–630	22.14	22.71	22.71	23.27	0.80	19.75	26.90
Crush zones	510–515 and 650–655	22.50	25.06	25.06	27.61	3.62	19.33	32.17
Competent rock		18.85	24.83	24.86	32.15	2.39	18.28	35.86
Deformation & Crush Zones		22.14	23.88	22.89	27.61	2.53	19.33	32.17
Whole borehole		18.85	24.83	24.56	32.15	2.38	18.28	35.86

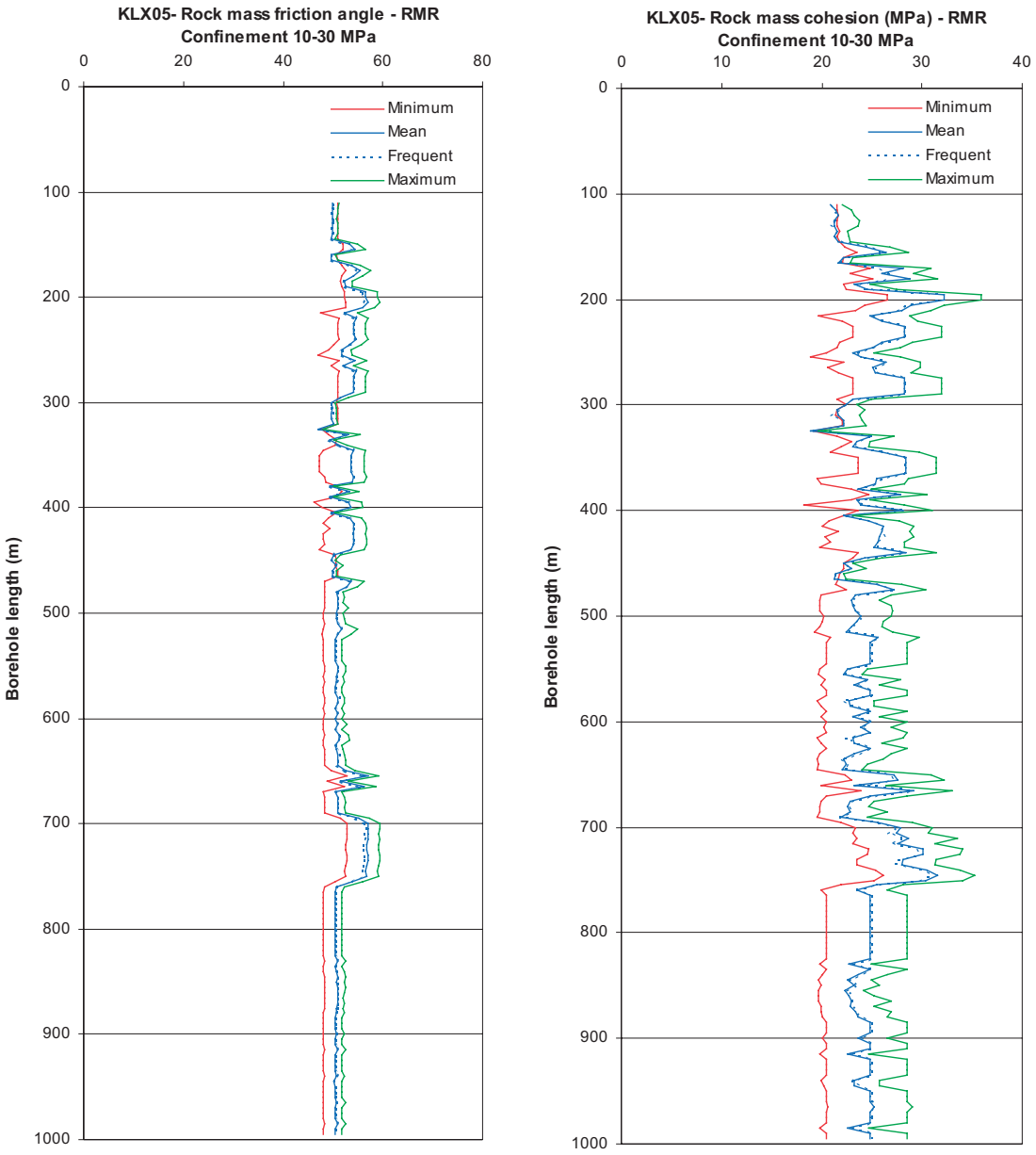

Figure A3-8. *Variation of a) the rock mass friction angle ϕ' and b) the rock mass cohesion c' from RMR for borehole KLX05 under stress confinement 10–30 MPa (Hoek-Brown's a = 0.5).*

A3.2 KLX12A

Table A3-11. Partitioning of borehole KLX12A used in the empirical characterization rock units, deformation and crush zones (based on Sicada_08_018, p_eshi.xls).

Rock Unit	BH length (m)/Section 1 m	5 m	Deformation Zones	BH length (m)/Section 1 m	5 m	Crushed Zones	BH length (m)/Section 1 m
RU 1	103–423	105–425	DZ 1	182–183			
			DZ 2	(185.4–185.7)			
			DZ 3	(270.7–271.1)			
			DZ 4	277–278			
			DZ 5	(282.0–282.4)			
			DZ 6	(304.4–304.5)			
			DZ 7	(329.4–329.7)		Crush Zone 1	(420.09–420.13)
			DZ 8	366–367			
RU 2	423–529	425–530	DZ 9	(429.0–429.4)		Crush Zone 2	(447.46–477.50)
			DZ 10	445–448		Crush Zone 3	(498.9–499.0)
			DZ 11	499–500			
RU 3	529–601	530–600	DZ 12	596–601	595–600		

A3.2.1 Fracture orientation

Table A3-12. a) Set identification from the open fracture orientation mapped for borehole KLX12A (Sicada, 07-11-26). The orientations are given as strike/dip (right-hand rule). b) Fisher's constant of the fracture sets identified for borehole KLX12A (Sicada, 07-11-26).

BH length (m)	No. of fractures	Fracture orientation (Strike/Dip) SH	WNW	ENE	NS	Fisher's constant SH	WNW	ENE	NS
102–183	229	154/08	18/84	107/67	341/68	32	25	23	57
183–184	7	115/18				90			
184–185	3	306/10				10,000			
185–186	2	88/29				10,000			
186–271	149	167/2	15/89	108/76	342/70	22	36	44	49
271–272	7	67/23				112			
272–277	7	104/7		106/78		35		10,000	
277–278	3	69/25		112/67		10,000		10,000	
278–282	7	136/10				31			
282–283	3	68/27				10,000			
283–304	20	88/14				30			
304–329	59	114/10		114/70	2/80	25		42	506
329–366	74	168/2	210/84	117/54	343/85	23	61	10,000	10,000
366–367	1	189/7				10,000			
367–422	135	29/6	23/84	112/70	347/73	23	22	73	29
422–429	28	81/13	31/86		357/55	54	17		10,000
429–430	2	39/23				10,000			
430–446	39	47/24	19/83	116/86	334/77	91	26	10,000	42
446–448	10	218/10		120/65		674		33	
448–499	114	69/11	25/70	116/73	337/74	24	40	29	23
499–500	4	38/16				10,000			
500–528	83	42/5	214/88	114/64	342/87	21	85	22	1,463
528–597	130	83/3	19/85	98/72	336/73	22	17	14	39
597–601	29	97/16			335/69	19			21

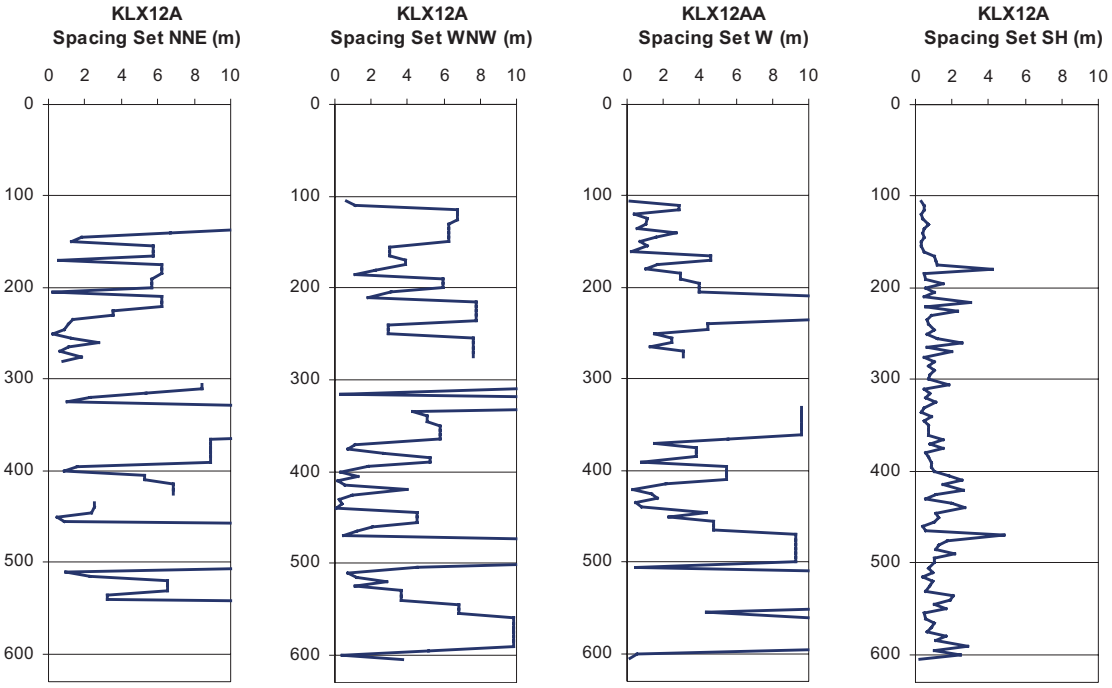

Figure A3-9. *Fracture spacing with depth for the four facture sets in borehole KLX12A. The values are averaged for each 5 m length of borehole. Y-axis shows borehole length in meters.*

A3.2.2 RMR

Table A3-13. RMR values along borehole KLX12A (core sections of 5 m).

Rock Unit	BH length (m)	Min RMR	Mean RMR	Frequent RMR	Max RMR	Std. dev. RMR	Min possible RMR	Max possible RMR
RU 1	105–420	68.9	74.1	73.8	83.7	3.4	51.9	86.6
RU 2	420–525	68.5	75.6	75.5	85.6	4.3	49.6	89.8
RU 3	525–595	72.2	79.3	79.0	85.5	3.8	52.3	88.9
DZ 10	595–605	63.8	67.3	67.3	70.8	4.9	49.8	80.1
Competent rock		68.5	75.1	74.5	85.6	4.0	49.6	89.8
Whole borehole		63.8	75.0	74.4	85.6	4.2	49.6	89.8

* The following DZ were only included in the 1 m core sections; DZ 1 (0.7 m), DZ 4 (1.1 m), DZ 8 (0.6 m), DZ 10 (1.9 m), DZ 11 (0.7 m), Not included at all; DZ 2 (0.3 m), DZ 3 (0.4 m), DZ 5 (0.4 m) DZ 6 (0.04 m), DZ 7 (0.5 m), DZ 9 (0.5 m), and Crush Zone 1 (0.04 m), Crush Zone 2 (0.04) and Crush Zone 3 (0.08).

A3.2.3 Q

Table A3-14. Q values along borehole KLX12A (core sections of 5 m).

Rock Unit	BH length (m)	Min Q	Mean Q	Frequent Q	Max Q	Std. dev. Q	Min possible Q	Max possible Q
RU 1	105–420	9.9	29.0	25.8	66.0	14.3	0.3	100.0
RU 2	420–525	4.0	33.8	34.4	132.0	27.5	0.2	198.0
RU 3	525–595	12.2	37.1	37.2	63.0	12.8	1.6	198.0
DZ 10	595–605	4.9	10.4	10.4	15.8	7.7	0.6	32.7
Competent rock		4.0	31.1	29.3	132.0	18.0	0.2	198.0
Whole borehole		4.0	30.7	28.8	132.0	18.1	0.2	198.0

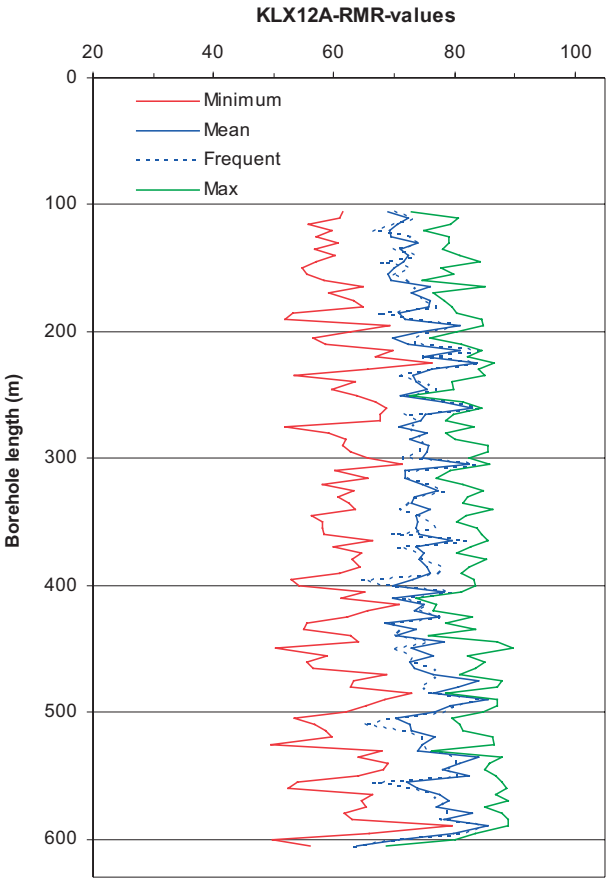

Figure A3-10. *Variation of RMR with depth for borehole KLX12A. The values are given every 5 m.*

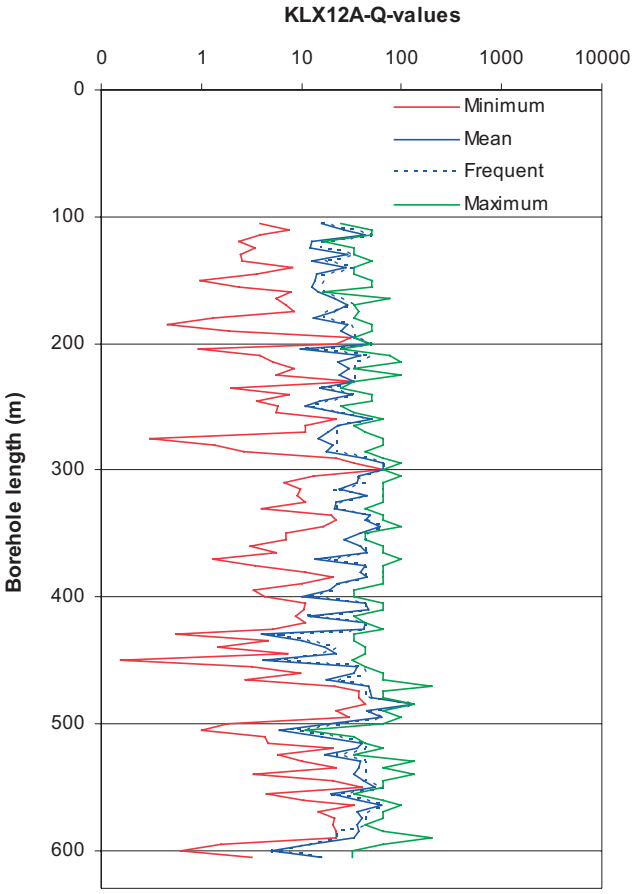

Figure A3-11. *Variation of Q with depth for borehole KLX12A. The values are given every 5 m.*

A3.2.4 Rock mass properties

Deformation modulus

RMR

Table A3-15. Deformation modulus Em derived from RMR along for borehole KLX12A (core sections of 5 m).

Rock Unit	BH length (m)	Min Em (GPa)	Mean Em (GPa)	Frequent Em (GPa)	Max Em (GPa)	Std. dev. Em (GPa)	Min possible Em (GPa)	Max possible Em (GPa)
RU 1	105–420	29.7	40.8	39.3	69.4	8.7	11.1	81.0
RU 2	420–525	29.0	45.1	43.4	77.6	12.0	9.8	93.0
RU 3	525–595	35.8	55.1	53.0	75.0	11.6	11.4	83.0
DZ 10	595–605	22.1	27.6	27.6	33.1	7.7	9.9	56.5
Competent rock		29.0	43.6	40.9	77.6	11.0	9.8	93.0
Whole borehole		22.1	43.3	40.8	77.6	11.1	9.8	93.0

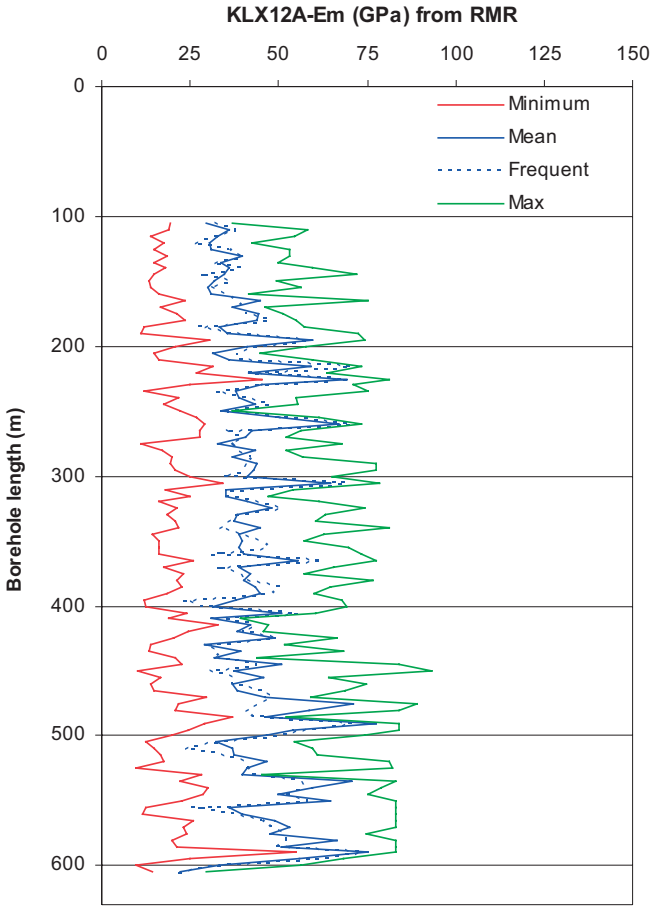

Figure A3-12. *Variation of the deformation modulus of the rock mass obtained from RMR with depth for borehole KLX12A. The values are given every 5 m.*

Q

Table A3-16. Deformation modulus Em derived from Q along borehole KLX12A (core sections of 5 m).

Rock Unit	BH length (m)	Min Em (GPa)	Mean Em (GPa)	Frequent Em (GPa)	Max Em (GPa)	Std. dev. Em (GPa)	Min possible Em (GPa)	Max possible Em (GPa)
RU 1	105–420	25.5	35.9	35.7	48.0	6.1	7.7	58.1
RU 2	420–525	20.8	39.4	41.1	66.8	10.9	6.8	81.0
RU 3	525–595	28.2	40.3	41.0	48.8	5.2	12.4	78.1
DZ 10	595–605	20.7	25.3	25.3	29.9	6.5	9.3	41.7
Competent rock		20.8	37.2	37.7	66.8	7.5	6.8	81.0
Whole borehole		20.7	37.0	37.1	66.8	7.6	6.8	81.0

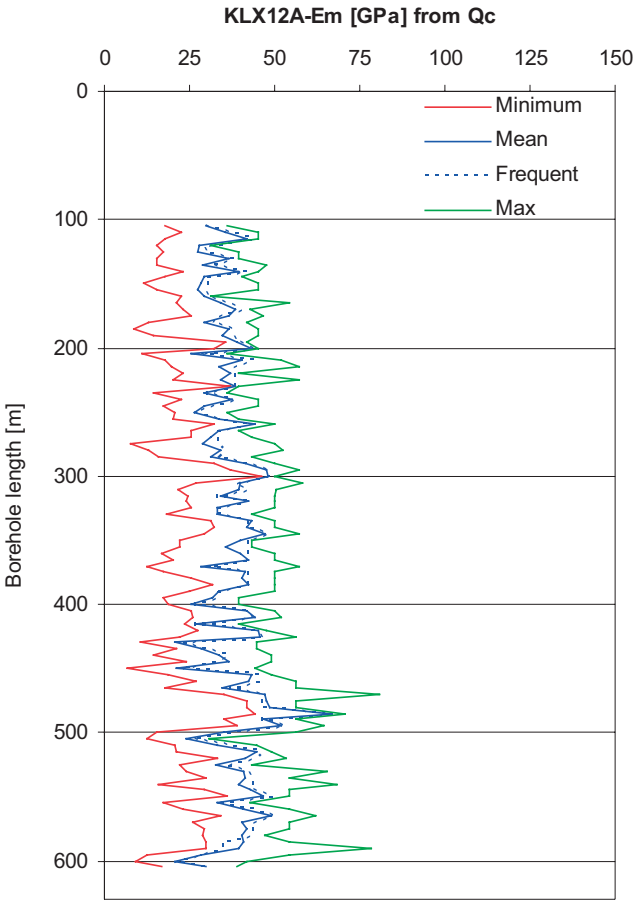

Figure A3-13. *Variation of the deformation modulus of the rock mass obtained from Q with depth for borehole KLX12A. The values are given every 5 m.*

Poisson's ratio

RMR

Table A3-17. Summary of Poisson's ratio (*v*) derived from RMR for borehole KLX12A (core sections of 5 m, Hoek-Brown's a = 0.5).

Rock Unit	BH length (m)	Min ν (–)	Mean ν (–)	Frequent ν (–)	Max ν (–)	Std. dev. ν (–)	Min possible ν (–)	Max possible ν (–)
RU 1	105–420	0.11	0.15	0.15	0.26	0.03	0.02	0.33
RU 2	420–525	0.12	0.18	0.17	0.32	0.05	0.03	0.39
RU 3	525–595	0.13	0.21	0.20	0.28	0.04	0.03	0.33
DZ 10	595–605	0.08	0.10	0.10	0.12	0.03	0.02	0.23
Competent rock		0.11	0.17	0.15	0.32	0.04	0.02	0.39
Whole borehole		0.08	0.17	0.15	0.32	0.04	0.02	0.39

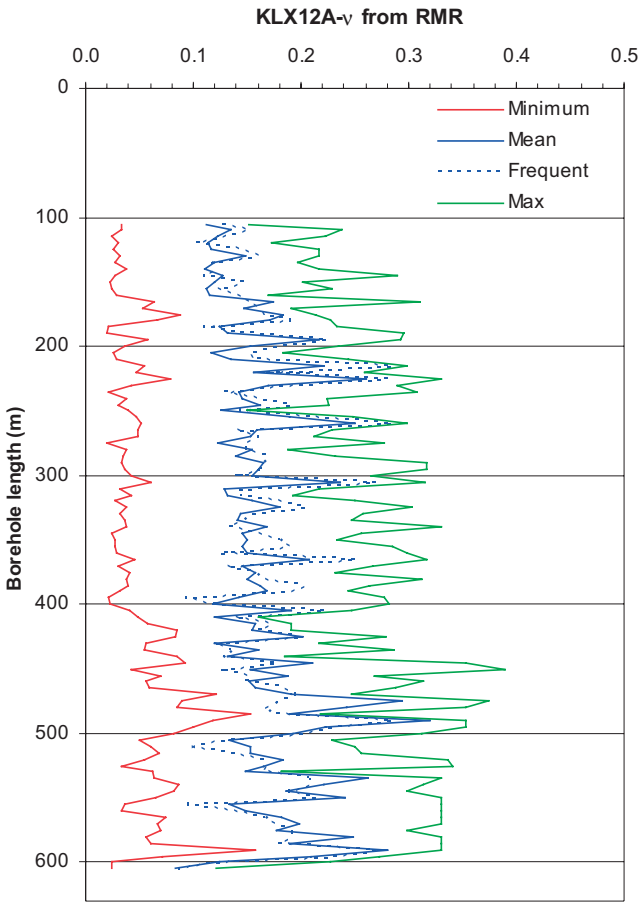

Figure A3-14. *Variation of Poisson's ratio (v) with depth for borehole KLX12A (Hoek-Brown's a = 0.5). The values are given every 5 m.*

Uniaxial compressive strength

RMR

Table A3-18. Summary of the uniaxial compressive strength of the rock mass derived from RMR for borehole KLX12A (core sections of 5 m, Hoek-Brown's a = 0.5).

Rock Unit	BH length (m)	Min UCS (MPa)	Mean UCS (MPa)	Frequent UCS (MPa)	Max UCS (MPa)	Std. dev. UCS (MPa)	Min possible UCS (MPa)	Max possible UCS (MPa)
RU 1	105–420	22.6	31.6	30.2	51.4	6.8	7.9	73.7
RU 2	420–525	29.7	44.7	40.5	76.9	12.1	8.5	115.2
RU 3	525–595	29.9	45.4	43.6	62.6	9.5	6.3	98.5
DZ 10	595–605	17.0	21.9	21.9	26.7	6.8	6.1	55.5
Competent rock		22.6	36.3	32.9	76.9	10.6	6.3	115.2
Whole borehole		17.0	36.0	32.9	76.9	10.8	6.1	115.2

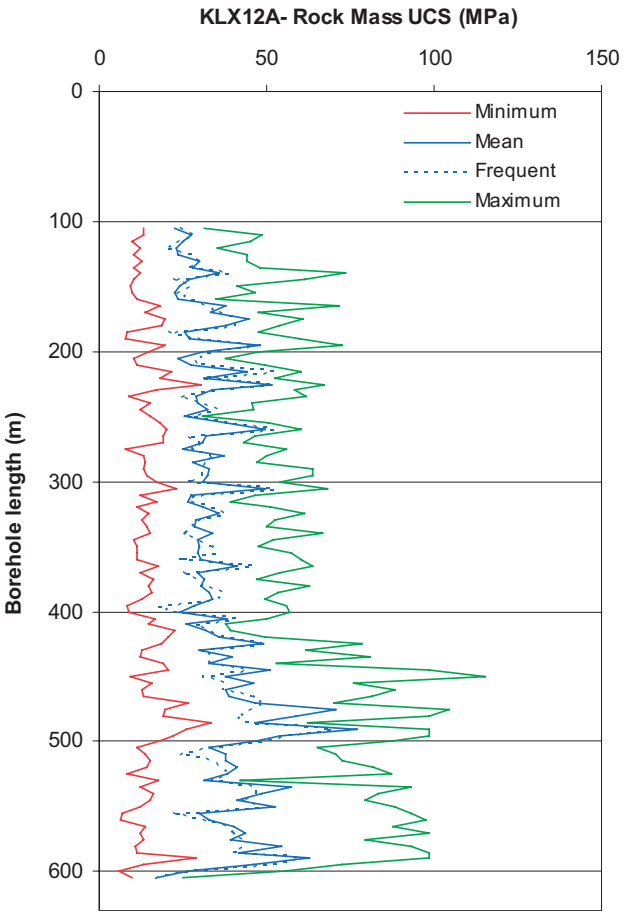

Figure A3-15. *Variation of the uniaxial compressive strength of the rock mass with depth for borehole KLX12A (Hoek-Brown's a = 0.5). The values are given every 5 m.*

Friction angle of the rock mass

RMR

Table A3-19. Summary of the friction angle (ϕ') of the rock mass derived from RMR for borehole KLX12A (10–30 MPa) (core sections of 5 m, Hoek-Brown's a = 0.5).

Rock Unit	BH length (m)	Min ϕ' (°)	Mean ϕ' (°)	Frequent ϕ' (°)	Max ϕ' (°)	Std. dev. ϕ' (°)	Min possible ϕ' (°)	Max possible ϕ' (°)
RU 1	105–420	49.6	50.2	49.9	54.7	1.0	48.3	57.0
RU 2	420–525	50.4	53.9	54.2	54.3	0.9	48.1	56.8
RU 3	525–595	50.7	50.9	50.9	51.0	0.1	48.2	52.3
DZ 10	595–605	49.9	50.3	50.3	50.6	0.5	49.4	51.8
Competent rock		49.6	51.1	49.9	54.7	1.8	48.1	57.0
Whole borehole		49.6	51.1	49.9	54.7	1.8	48.1	57.0

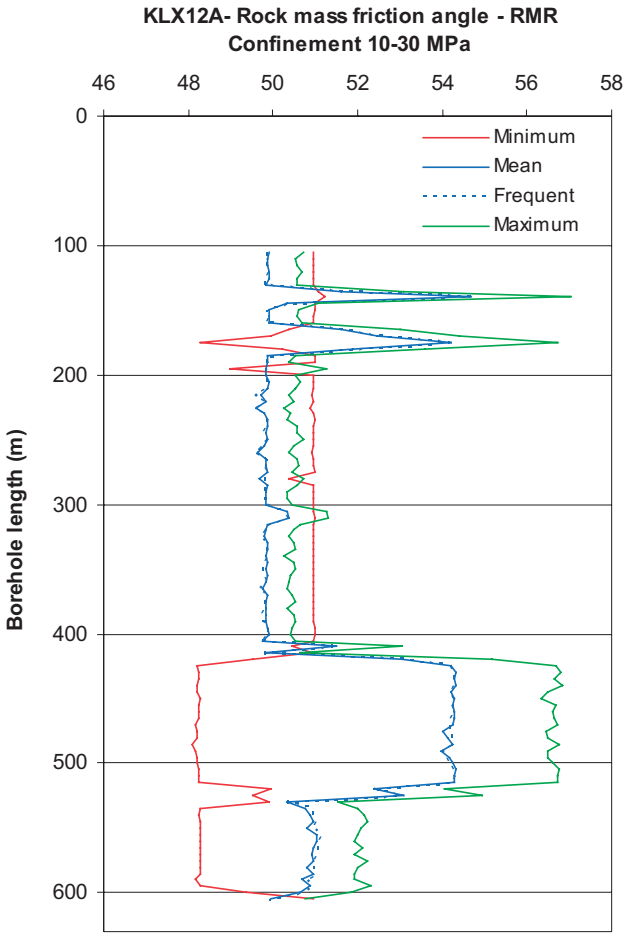

Figure A3-16. *Variation of the rock mass friction angle ϕ' from RMR for borehole KLX12A under stress confinement 10–30 MPa (Hoek-Brown's a = 0.5).*

Cohesion of the rock mass

Table A3-20. Summary of the cohesion (c') of the rock mass derived from RMR for borehole KLX12A under confinement stress between 10 and 30 MPa) (core sections of 5 m, Hoek-Brown's a = 0.5).

Rock Unit	BH length (m)	Min c' (°)	Mean c' (°)	Frequent c' (°)	Max c' (°)	Std. dev. c' (°)	Min possible c' (°)	Max possible c' (°)
RU 1	105–420	21.0	21.6	21.3	25.1	0.9	19.8	28.8
RU 2	420–525	21.6	24.9	24.9	26.9	1.0	19.5	31.3
RU 3	525–595	22.1	22.8	22.7	23.9	0.5	19.5	27.9
DZ 10	595–605	20.8	21.2	21.2	21.7	0.6	20.2	24.0
Competent rock		21.0	22.5	21.6	26.9	1.6	19.5	31.3
Whole borehole		20.8	22.5	21.6	26.9	1.6	19.5	31.3

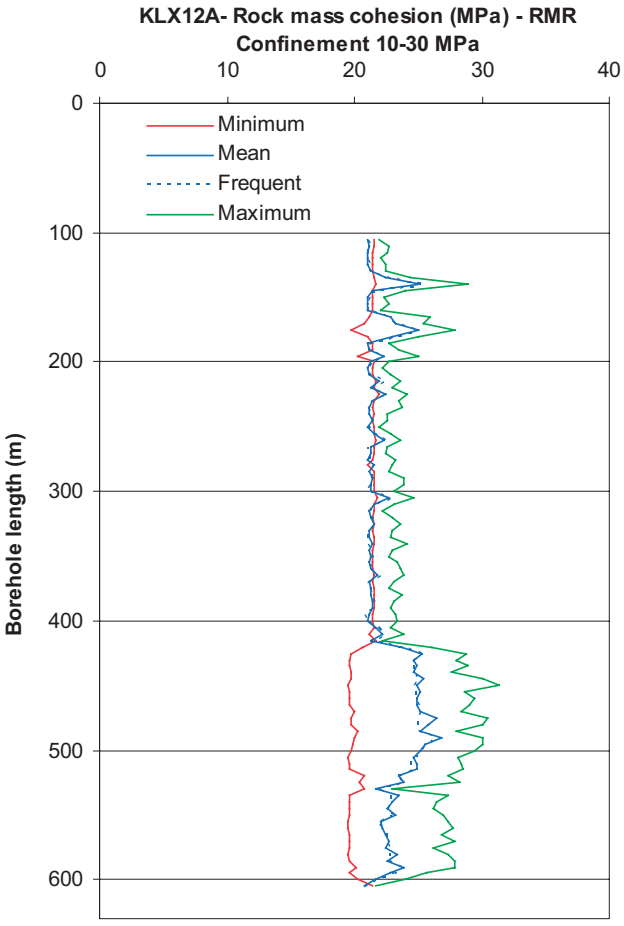

Figure A3-17. *Variation of the rock mass cohesion c' from RMR for borehole KLX12A under stress confinement 10–30 MPa (Hoek-Brown's a = 0.5).*

Appendix 4

Result tables from the theoretical modelling of rock mass properties

In this appendix results from the theoretical modelling of rock mass properties for each realisation, i.e. each numerical model run, for fracture domains FSM_C, FSM_EW007, FSM_NE005 and FSM_W are shown. (See also Section 5.2)

Contents

A4.1 Results from theoretical model

A4.1.1 FSM_C, intact rock Ävrö quartz monzodiorite, parallel to σ_H

Table A4-1. Poisson's ratio, deformation modulus and vertical stress at failure for all DFN realisations, FSM_C, intact rock Ävrö quartz monzodiorite, parallel to σ_H, stress level 25.8 MPa.

DFN realisation	P_{10}	Poisson's ratio, ν_m	Deformation modulus, E_m, (GPa)	Vertical stress at failure, σ_{vf}, (MPa)
1	0.59	0.32	53.45	245.30
2	0.46	0.28	47.97	142.20
3	0.49	0.30	44.77	146.60
4	0.49	0.22	45.91	118.20
5	0.47	0.29	49.95	160.20
6	0.44	0.30	50.37	151.80
7	0.49	0.30	46.09	188.00
8	0.50	0.30	57.17	213.30
10	0.48	0.30	49.15	151.30
Mean	**0.49**	**0.29**	**49.43**	**168.54**
Standard dev.	**0.04**	**0.03**	**3.95**	**39.73**
Min.	**0.44**	**0.22**	**44.77**	**118.20**
Max	**0.59**	**0.32**	**57.17**	**245.30**

Table A4-2. Poisson's ratio, deformation modulus and vertical stress at failure for all DFN realisations, FSM_C, intact rock Ävrö quartz monzodiorite, parallel to σ_H, stress level 6.5 MPa.

DFN realisation	P_{10}	Poisson's ratio, ν_m	Deformation modulus, E_m, (GPa)	Vertical stress at failure, σ_{vf}, (MPa)
1	0.59	0.34	51.30	105.40
2	0.46	0.29	44.90	57.20
3	0.49	0.31	41.66	60.70
4	0.49	0.21	43.02	45.05
5	0.47	0.27	48.75	66.50
6	0.44	0.29	47.30	60.90
7	0.49	0.28	43.78	66.30
8	0.50	0.25	53.63	82.60
10	0.48	0.28	45.78	67.80
Mean	**0.49**	**0.28**	**46.68**	**68.05**
Standard dev.	**0.04**	**0.04**	**3.96**	**17.19**
Min.	**0.44**	**0.21**	**41.66**	**45.05**
Max	**0.59**	**0.34**	**53.63**	**105.40**

Table A4-3. Poisson's ratio, deformation modulus and vertical stress at failure for all DFN realisations, FSM_C, intact rock Ävrö quartz monzodiorite, parallel to σ_H, stress level 2.0 MPa.

DFN realisation	P_{10}	Poisson's ratio, ν_m	Deformation modulus, E_m, (GPa)	Vertical stress at failure, σ_{vf}, (MPa)
1	0.59	0.33	53.49	73.60
2	0.46	0.30	41.16	35.30
3	0.49	0.29	47.65	29.30
4	0.49	0.28	35.87	25.80
5	0.47	0.34	39.23	33.60
6	0.44	0.36	36.33	31.90
7	0.49	0.31	40.79	39.20
8	0.50	0.25	53.55	68.10
10	0.48	0.33	43.29	35.60
Mean	**0.49**	**0.31**	**43.48**	**41.38**
Standard dev.	**0.04**	**0.03**	**6.70**	**17.20**
Min.	**0.44**	**0.25**	**35.87**	**25.80**
Max	**0.59**	**0.36**	**53.55**	**73.60**

Table A4-4. Uniaxial compressive strength, friction angle (MC) and cohesion (MC) for FSM_C with Ävrö quartz monzodiorite parallel to σ_H.

DFN realisation	Uniaxial compressive strength, (MPa) [1)]	Friction angle,(°) [2)] Mohr-Coulomb	Cohesion, (MPa) [2)] Mohr-Coulomb
1	60.2	44.9	18.2
2	28.0	35.4	10.9
3	28.8	35.7	11.1
4	19.9	32.2	8.5
5	33.0	37.0	12.1
6	30.3	36.3	11.5
7	39.4	39.7	13.8
8	51.6	41.8	16.7
10	31.6	36.6	11.9
Mean	**35.9**	**37.7**	**12.7**
Standard dev.	**12.6**	**3.8**	**3.0**
Min.	**19.9**	**32.2**	**8.5**
Max	**60.2**	**44.9**	**18.2**

1) Estimated from fitting an average Mohr-Coulomb relationship in stress range 0–25.8 MPa.
2) For confinement stress between 10 and 30 MPa.

A4.1.2 FSM_C, intact rock Ävrö quartz monzodiorite, parallel to σ_h

Table A4-5. Poisson's ratio, deformation modulus and vertical stress at failure for all DFN realisations, FSM_C, intact rock Ävrö quartz monzodiorite, parallel to σ_h, stress level 10.5 MPa.

DFN realisation	P_{10}	Poisson's ratio, ν_m	Deformation modulus, E_m, (GPa)	Vertical stress at failure, σ_{vf}, (MPa)
1	0.59	0.29	39.46	80.60
2	0.46	0.28	40.46	77.70
3	0.49	0.30	49.33	55.30
4	0.49	0.26	49.11	121.30
5	0.47	0.31	54.41	114.20
6	0.44	0.28	48.14	67.70
7	0.49	0.36	46.69	50.30
8	0.50	0.32	49.89	105.90
9	0.52	0.29	39.32	79.10
Mean	**0.50**	**0.30**	**46.31**	**83.57**
Standard dev.	**0.04**	**0.03**	**5.35**	**25.20**
Min.	**0.44**	**0.26**	**39.32**	**50.30**
Max	**0.59**	**0.36**	**54.41**	**121.30**

Table A4-6. Poisson's ratio, deformation modulus and vertical stress at failure for all DFN realisations, FSM_C, intact rock Ävrö quartz monzodiorite, parallel to σ_h, stress level 2.6 MPa.

DFN realisation	P_{10}	Poisson's ratio, ν_m	Deformation modulus, E_m, (GPa)	Vertical stress at failure, σ_{vf}, (MPa)
1	0.59	0.28	38.06	37.00
2	0.46	0.26	41.32	39.80
3	0.49	0.40	50.10	26.00
4	0.49	0.22	49.85	64.20
5	0.47	0.33	48.11	58.50
6	0.44	0.28	47.95	35.50
7	0.49	0.20	40.44	22.10
8	0.50	0.24	43.36	51.40
9	0.52	0.29	37.54	41.70
Mean	**0.50**	**0.28**	**44.08**	**41.80**
Standard dev.	**0.04**	**0.06**	**5.01**	**14.04**
Min.	**0.44**	**0.20**	**37.54**	**22.10**
Max	**0.59**	**0.40**	**50.10**	**64.20**

Table A4-7. Poisson's ratio, deformation modulus and vertical stress at failure for all DFN realisations, FSM_C, intact rock Ävrö quartz monzodiorite, parallel to σ_h, stress level 1.5 MPa.

DFN realisation	P_{10}	Poisson's ratio, ν_m	Deformation modulus, E_m, (GPa)	Vertical stress at failure, σ_{vf}, (MPa)
1	0.59	0.27	42.90	30.90
2	0.46	0.29	40.73	35.50
3	0.49	0.38	48.35	25.10
4	0.49	0.22	49.69	56.30
5	0.47	0.30	55.35	48.40
6	0.44	0.30	45.41	27.70
7	0.49	0.20	39.68	17.70
8	0.50	0.25	44.52	43.60
9	0.52	0.30	37.44	35.70
Mean	**0.50**	**0.28**	**44.90**	**35.66**
Standard dev.	**0.04**	**0.05**	**5.58**	**12.10**
Min.	**0.44**	**0.20**	**37.44**	**17.70**
Max	**0.59**	**0.38**	**55.35**	**56.30**

Table A4-8. Uniaxial compressive strength, friction angle (MC) and cohesion (MC) for FSM_C with Ävrö quartz monzodiorite parallel to σ_h.

DFN realisation	Uniaxial compressive strength, (MPa) [1)]	Friction angle, (°) [2)] Mohr-Coulomb	Cohesion, (MPa) [2)] Mohr-Coulomb
1	19.9	46.2	4.0
2	24.0	43.8	5.1
3	16.0	36.8	4.0
4	38.9	52.2	6.7
5	33.2	51.8	5.7
6	19.3	41.8	4.3
7	11.0	36.8	2.8
8	29.0	50.8	5.2
9	24.7	44.2	5.2
Mean	**24.5**	**44.8**	**4.9**
Standard dev.	**9.2**	**6.3**	**1.2**
Min.	**11.0**	**36.8**	**2.8**
Max	**38.9**	**52.2**	**6.7**

1) Estimated from fitting an average Mohr-Coulomb relationship in stress range 0–10.5 MPa.
2) For confinement stress between 0 and 10.5 MPa.

A4.1.3 FSM_C, intact rock Diorite to gabbro, parallel to σ_H

Table A4-9. Poisson's ratio, deformation modulus and vertical stress at failure for all DFN realisations, FSM_C, intact rock Diorite to gabbro, parallel to σ_H, stress level 25.8 MPa.

DFN realisation	P_{10}	Poisson's ratio, ν_m	Deformation modulus, E_m, (GPa)	Vertical stress at failure, σ_{vf}, (MPa)
1	0.59	0.36	64.6	310.5
2	0.46	0.35	62.8	258.9
3	0.49	0.36	56.8	248.2
4	0.49	0.35	62.7	224.3
5	0.47	0.35	63.9	225.5
6	0.44	0.36	59.5	202.9
7	0.49	0.36	58.7	241.3
8	0.50	0.35	70.7	265.2
10	0.48	0.35	61.0	272.6
Mean	**0.49**	**0.35**	**62.3**	**249.9**
Standard dev.	**0.04**	**0.01**	**4.0**	**31.7**
Min.	**0.44**	**0.35**	**56.8**	**202.9**
Max	**0.59**	**0.36**	**70.7**	**310.5**

Table A4-10. Poisson's ratio, deformation modulus and vertical stress at failure for all DFN realisations, FSM_C, intact rock Diorite to gabbro, parallel to σ_H, stress level 6.5 MPa.

DFN realisation	P_{10}	Poisson's ratio, ν_m	Deformation modulus, E_m, (GPa)	Vertical stress at failure, σ_{vf}, (MPa)
1	0.59	0.35	60.5	129.3
2	0.46	0.35	57.7	102.7
3	0.49	0.36	53.3	88.4
4	0.49	0.37	55.0	75.8
5	0.47	0.35	60.6	89.8
6	0.44	0.35	54.6	75.1
7	0.49	0.36	54.7	86.2
8	0.50	0.33	64.7	110.8
10	0.48	0.35	58.0	104.9
Mean	**0.49**	**0.35**	**57.7**	**95.9**
Standard dev.	**0.04**	**0.01**	**3.7**	**17.6**
Min.	**0.44**	**0.33**	**53.3**	**75.1**
Max	**0.59**	**0.37**	**64.7**	**129.3**

Table A4-11.Poisson's ratio, deformation modulus and vertical stress at failure for all DFN realisations, FSM_C, Diorite to gabbro, parallel to σ_H, stress level 2.0 MPa.

DFN realisation	P_{10}	Poisson's ratio, ν_m	Deformation modulus, E_m, (GPa)	Vertical stress at failure, σ_{vf}, (MPa)
1	0.59	0.38	58.7	94.2
2	0.46	0.39	50.4	59.3
3	0.49	0.36	57.5	45.7
4	0.49	0.37	55.4	44.5
5	0.47	0.35	63.5	44.6
6	0.44	0.35	59.2	42.5
7	0.49	0.37	54.2	57.1
8	0.50	0.36	62.5	73.0
10	0.48	0.35	61.8	59.9
Mean	**0.49**	**0.36**	**58.1**	**57.9**
Standard dev.	**0.04**	**0.02**	**4.3**	**16.9**
Min.	**0.44**	**0.35**	**50.4**	**42.5**
Max	**0.59**	**0.39**	**63.5**	**94.2**

Table A4-12. Uniaxial compressive strength, friction angle (MC) and cohesion (MC) for FSM_C with Diorite to gabbro parallel to σ_H.

DFN realisation	Uniaxial compressive strength, (MPa) [1]	Friction angle, (°) [2] Mohr-Coulomb	Cohesion, (MPa) [2] Mohr-Coulomb
1	76.5	49.2	20.8
2	59.0	45.9	17.7
3	54.4	44.7	16.8
4	45.0	42.1	14.9
5	49.4	43.4	15.8
6	42.9	41.5	14.4
7	53.4	44.5	16.6
8	62.5	46.7	18.3
10	62.4	46.7	18.3
Mean	**56.2**	**45.0**	**17.1**
Standard dev.	**10.4**	**2.5**	**2.0**
Min.	**42.9**	**41.5**	**14.4**
Max	**76.5**	**49.2**	**20.8**

1) Estimated from fitting an average Mohr-Coulomb relationship in stress range 0–25.8 MPa.
2) For confinement stress between 10 and 30 MPa.

A4.1.4 FSM_C, intact rock Diorite to gabbro, parallel to σ_h

Table A4-13.Poisson's ratio, deformation modulus and vertical stress at failure for all DFN realisations, FSM_C, intact rock Diorite to gabbro, parallel to σ_h, stress level 10.5 MPa.

DFN realisation	P_{10}	Poisson's ratio, ν_m	Deformation modulus, E_m, (GPa)	Vertical stress at failure, σ_{vf}, (MPa)
1	0.59	0.36	57.1	167.6
2	0.46	0.35	58.6	162.0
3	0.49	0.36	54.9	108.2
4	0.49	0.34	62.2	181.7
5	0.47	0.34	62.1	137.5
6	0.44	0.35	61.4	125.9
7	0.49	0.35	60.3	126.0
8	0.50	0.35	59.4	153.5
9	0.52	0.36	58.1	155.3
Mean	**0.50**	**0.35**	**59.3**	**146.4**
Standard dev.	**0.04**	**0.01**	**2.5**	**23.6**
Min.	**0.44**	**0.34**	**54.9**	**108.2**
Max	**0.59**	**0.36**	**62.2**	**181.7**

Table A4-14. Poisson's ratio, deformation modulus and vertical stress at failure for all DFN realisations, FSM_C, intact rock Diorite to gabbro, parallel to σ_h, stress level 2.6 MPa.

DFN realisation	P_{10}	Poisson's ratio, ν_m	Deformation modulus, E_m, (GPa)	Vertical stress at failure, σ_{vf}, (MPa)
1	0.59	0.37	54.6	84.2
2	0.46	0.35	58.6	87.2
3	0.49	0.39	47.2	59.9
4	0.49	0.37	60.9	88.6
5	0.47	0.36	57.4	58.6
6	0.44	0.37	54.3	63.9
7	0.49	0.38	53.9	61.3
8	0.50	0.37	55.6	74.5
9	0.52	0.38	53.1	83.9
Mean	**0.50**	**0.37**	**55.1**	**73.6**
Standard dev.	**0.04**	**0.01**	**3.9**	**12.7**
Min.	**0.44**	**0.35**	**47.2**	**58.6**
Max	**0.59**	**0.39**	**60.9**	**88.6**

Table A4-15. Poisson's ratio, deformation modulus and vertical stress at failure for all DFN realisations, FSM_C, intact rock Diorite to gabbro, parallel to σ_h, stress level 1.5 MPa.

DFN realisation	P_{10}	Poisson's ratio, ν_m	Deformation modulus, E_m, (GPa)	Vertical stress at failure, σ_{vf}, (MPa)
1	0.59	0.37	53.1	69.0
2	0.46	0.35	58.0	80.6
3	0.49	0.39	47.9	47.9
4	0.49	0.34	60.1	80.3
5	0.47	0.36	59.3	56.9
6	0.44	0.37	56.2	49.6
7	0.49	0.36	56.0	54.0
8	0.50	0.35	52.9	57.1
9	0.52	0.38	52.2	70.7
Mean	**0.50**	**0.36**	**55.1**	**62.9**
Standard dev.	**0.04**	**0.02**	**3.9**	**12.6**
Min.	**0.44**	**0.34**	**47.9**	**47.9**
Max	**0.59**	**0.39**	**60.1**	**80.6**

Table A4-16. Uniaxial compressive strength, friction angle (MC) and cohesion (MC) for FSM_C with Diorite to gabbro parallel to σ_h.

DFN realisation	Uniaxial compressive strength, (MPa) [1]	Friction angle, (°) [2] Mohr-Coulomb	Cohesion, (MPa) [2] Mohr-Coulomb
1	47.2	58.3	6.7
2	55.9	56.4	8.4
3	34.4	50.3	6.2
4	53.2	59.2	7.3
5	35.0	55.5	5.4
6	34.3	54.0	5.6
7	35.8	53.6	5.9
8	39.0	57.6	5.7
9	49.8	56.4	7.5
Mean	**42.7**	**55.7**	**6.5**
Standard dev.	**8.8**	**2.7**	**1.0**
Min.	**34.3**	**50.3**	**5.4**
Max	**55.9**	**59.2**	**8.4**

1) Estimated from fitting an average Mohr-Coulomb relationship in stress range 0–10.5 MPa.
2) For confinement stress between 0 and 10.5 MPa.

A4.1.5 FSM_C, intact rock Quartz monzodiorite, parallel to σ_H

Table A4-17. Poisson's ratio, deformation modulus and vertical stress at failure for all DFN realisations, FSM_C, intact rock Quartz monzodiorite, parallel to σ_H, stress level 25.8 MPa.

DFN realisation	P_{10}	Poisson's ratio, ν_m	Deformation modulus, E_m, (GPa)	Vertical stress at failure, σ_{vf}, (MPa)
1	0.59	0.32	60.4	278.9
2	0.46	0.31	57.6	219.9
3	0.49	0.33	53.0	226.2
4	0.49	0.32	57.0	200.7
5	0.47	0.32	59.6	210.3
6	0.44	0.33	54.0	181.1
7	0.49	0.33	56.0	213.5
8	0.50	0.31	65.4	242.5
10	0.48	0.32	57.9	241.0
Mean	**0.49**	**0.32**	**57.9**	**223.8**
Standard dev.	**0.04**	**0.01**	**3.7**	**28.2**
Min.	**0.44**	**0.31**	**53.0**	**181.1**
Max	**0.59**	**0.33**	**65.4**	**278.9**

Table A4-18. Poisson's ratio, deformation modulus and vertical stress at failure for all DFN realisations, FSM_C, intact rock Quartz monzodiorite, parallel to σ_H, stress level 6.5 MPa.

DFN realisation	P_{10}	Poisson's ratio, ν_m	Deformation modulus, E_m, (GPa)	Vertical stress at failure, σ_{vf}, (MPa)
1	0.59	0.33	57.5	110.6
2	0.46	0.32	56.5	91.9
3	0.49	0.32	51.5	81.5
4	0.49	0.34	51.8	75.9
5	0.47	0.33	57.7	80.4
6	0.44	0.31	54.3	71.1
7	0.49	0.31	50.5	91.9
8	0.50	0.27	58.3	104.3
10	0.48	0.30	60.0	93.9
Mean	**0.49**	**0.31**	**55.3**	**89.1**
Standard dev.	**0.04**	**0.02**	**3.4**	**13.1**
Min.	**0.44**	**0.27**	**50.5**	**71.1**
Max	**0.59**	**0.34**	**60.0**	**110.6**

Table A4-19. Poisson's ratio, deformation modulus and vertical stress at failure for all DFN realisations, FSM_C, Quartz monzodiorite, parallel to σ_H, stress level 2.0 MPa.

DFN realisation	P_{10}	Poisson's ratio, ν_m	Deformation modulus, E_m, (GPa)	Vertical stress at failure, σ_{vf}, (MPa)
1	0.59	0.33	58.5	73.3
2	0.46	0.33	54.2	49.5
3	0.49	0.32	54.8	43.7
4	0.49	0.36	48.1	44.9
5	0.47	0.30	52.9	45.3
6	0.44	0.31	56.6	40.7
7	0.49	0.31	49.7	48.7
8	0.50	0.22	56.5	61.7
10	0.48	0.31	59.2	54.1
Mean	**0.49**	**0.31**	**54.5**	**51.3**
Standard dev.	**0.04**	**0.04**	**3.8**	**10.4**
Min.	**0.44**	**0.22**	**48.1**	**40.7**
Max	**0.59**	**0.36**	**59.2**	**73.3**

Table A4-20. Uniaxial compressive strength, friction angle (MC) and cohesion (MC) for FSM_C with Quartz monzodiorite parallel to σ_H.

DFN realisation	Uniaxial compressive strength, (MPa) [1]	Friction angle, (°) [2] Mohr-Coulomb	Cohesion, (MPa) [2] Mohr-Coulomb
1	65.8	47.1	19.0
2	49.6	43.1	16.0
3	49.4	43.0	15.9
4	43.4	41.2	14.6
5	46.0	42.0	15.2
6	38.2	39.5	13.4
7	48.2	42.7	15.6
8	56.6	45.0	17.3
10	54.5	44.5	16.9
Mean	**50.2**	**43.1**	**16.0**
Standard dev.	**8.0**	**2.2**	**1.6**
Min.	**38.2**	**39.5**	**13.4**
Max	**65.8**	**47.1**	**19.0**

1) Estimated from fitting an average Mohr-Coulomb relationship in stress range 0–25.8 MPa.
2) For confinement stress between 10 and 30 MPa.

A4.1.6 FSM_C, intact rock Quartz monzodiorite, parallel to σ_h

Table A4-21. Poisson's ratio, deformation modulus and vertical stress at failure for all DFN realisations, FSM_C, intact rock Quartz monzodiorite, parallel to σ_h, stress level 10.5 MPa.

DFN realisation	P_{10}	Poisson's ratio, ν_m	Deformation modulus, E_m, (GPa)	Vertical stress at failure, σ_{vf}, (MPa)
1	0.59	0.33	54.7	168.7
2	0.46	0.31	57.4	133.6
3	0.49	0.33	50.6	100.3
4	0.49	0.32	63.7	153.2
5	0.47	0.31	58.2	122.0
6	0.44	0.28	56.1	112.4
7	0.49	0.32	59.0	109.0
8	0.50	0.31	58.6	136.1
9	0.52	0.32	56.0	142.7
Mean	**0.50**	**0.31**	**57.1**	**130.9**
Standard dev.	**0.04**	**0.01**	**3.5**	**22.2**
Min.	**0.44**	**0.28**	**50.6**	**100.3**
Max	**0.59**	**0.33**	**63.7**	**168.7**

Table A4-22. Poisson's ratio, deformation modulus and vertical stress at failure for all DFN realisations, FSM_C, intact rock Quartz monzodiorite, parallel to σ_h, stress level 2.6 MPa.

DFN realisation	P_{10}	Poisson's ratio, ν_m	Deformation modulus, E_m, (GPa)	Vertical stress at failure, σ_{vf}, (MPa)
1	0.59	0.34	51.5	79.6
2	0.46	0.30	56.7	79.1
3	0.49	0.35	47.9	49.9
4	0.49	0.29	55.7	85.6
5	0.47	0.32	56.6	60.1
6	0.44	0.31	53.8	55.4
7	0.49	0.35	53.1	54.0
8	0.50	0.31	52.3	65.4
9	0.52	0.35	50.5	81.2
Mean	**0.50**	**0.33**	**53.1**	**67.8**
Standard dev.	**0.04**	**0.02**	**2.9**	**13.7**
Min.	**0.44**	**0.29**	**47.9**	**49.9**
Max	**0.59**	**0.35**	**56.7**	**85.6**

Table A4-23. Poisson's ratio, deformation modulus and vertical stress at failure for all DFN realisations, FSM_C, intact rock Quartz monzodiorite, parallel to σ_h, stress level 1.5 MPa.

DFN realisation	P_{10}	Poisson's ratio, ν_m	Deformation modulus, E_m, (GPa)	Vertical stress at failure, σ_{vf}, (MPa)
1	0.59	0.33	51.1	66.4
2	0.46	0.32	55.8	67.4
3	0.49	0.33	52.0	39.4
4	0.49	0.24	54.0	72.6
5	0.47	0.33	56.4	47.4
6	0.44	0.31	56.9	40.6
7	0.49	0.31	58.5	45.0
8	0.50	0.29	54.3	53.2
9	0.52	0.33	51.8	72.2
Mean	**0.50**	**0.31**	**54.5**	**56.0**
Standard dev.	**0.04**	**0.03**	**2.6**	**13.7**
Min.	**0.44**	**0.24**	**51.1**	**39.4**
Max	**0.59**	**0.33**	**58.5**	**72.6**

Table A4-24. Uniaxial compressive strength, friction angle (MC) and cohesion (MC) for FSM_C with Quartz monzodiorite parallel to σ_h.

DFN realisation	Uniaxial compressive strength, (MPa) [1]	Friction angle, (°) [2] Mohr-Coulomb	Cohesion, (MPa) [2] Mohr-Coulomb
1	44.2	58.7	6.2
2	49.9	52.7	8.4
3	26.8	50.0	4.9
4	52.0	55.8	8.0
5	32.3	53.6	5.3
6	28.1	52.6	4.8
7	30.3	51.3	5.3
8	35.7	55.4	5.6
9	51.9	54.0	8.4
Mean	**39.0**	**53.8**	**6.3**
Standard dev.	**10.5**	**2.6**	**1.5**
Min.	**26.8**	**50.0**	**4.8**
Max	**52.0**	**58.7**	**8.4**

1) Estimated from fitting an average Mohr-Coulomb relationship in stress range 0–10.5 MPa.
2) For confinement stress between 0 and 10.5 MPa.

A4.1.7 FSM_EW007, intact rock Ävrö grantodiorite, parallel to σ_H

Table A4-25. Poisson's ratio, deformation modulus and vertical stress at failure for all DFN realisations, FSM_EW007, intact rock Ävrö granodiorite, parallel to σ_H, stress level 25.8 MPa.

DFN realisation	P_{10}	Poisson's ratio, ν_m	Deformation modulus, E_m, (GPa)	Vertical stress at failure, σ_{vf}, (MPa)
1	0.85	0.29	52.2	198.1
2	0.98	0.31	48.5	174.8
3	0.87	0.31	46.1	182.1
4	1.04	0.29	52.9	232.6
5	0.78	0.31	50.1	219.5
6	0.99	0.31	51.5	174.0
7	0.91	0.31	49.5	186.0
8	0.88	0.29	57.8	266.7
9	0.88	0.31	49.5	205.1
10	0.85	0.30	48.4	222.7
Mean	**0.90**	**0.30**	**50.7**	**206.2**
Standard dev.	**0.08**	**0.01**	**3.2**	**29.6**
Min.	**0.78**	**0.29**	**46.1**	**174.0**
Max	**1.04**	**0.31**	**57.8**	**266.7**

Table A4-26. Poisson's ratio, deformation modulus and vertical stress at failure for all DFN realisations, FSM_EW0007, intact rock Ävrö granodiorite, parallel to σ_H, stress level 6.5 MPa.

DFN realisation	P_{10}	Poisson's ratio, ν_m	Deformation modulus, E_m, (GPa)	Vertical stress at failure, σ_{vf}, (MPa)
1	0.85	0.29	54.0	61.4
2	0.98	0.30	48.8	51.5
3	0.87	0.30	45.9	51.2
4	1.04	0.28	53.4	104.2
5	0.78	0.30	47.9	75.5
6	0.99	0.32	46.8	60.6
7	0.91	0.32	48.9	66.0
8	0.88	0.28	56.1	101.2
9	0.88	0.32	47.8	78.9
10	0.85	0.31	45.6	73.8
Mean	**0.90**	**0.30**	**49.5**	**72.4**
Standard dev.	**0.08**	**0.01**	**3.7**	**18.5**
Min.	**0.78**	**0.28**	**45.6**	**51.2**
Max	**1.04**	**0.32**	**56.1**	**104.2**

Table A4-27. Poisson's ratio, deformation modulus and vertical stress at failure for all DFN realisations, FSM_EW007, Ävrö granodiorite, parallel to σ_H, stress level 2.0 MPa.

DFN realisation	P_{10}	Poisson's ratio, ν_m	Deformation modulus, E_m, (GPa)	Vertical stress at failure, σ_{vf}, (MPa)
1	0.85	0.26	52.7	31.9
2	0.98	0.28	50.3	25.4
3	0.87	0.29	47.0	26.8
4	1.04	0.29	52.3	64.0
5	0.78	0.28	51.6	41.6
6	0.99	0.36	43.0	36.5
7	0.91	0.35	45.8	30.2
8	0.88	0.28	54.9	71.4
9	0.88	0.33	45.6	50.7
10	0.85	0.32	45.9	37.5
Mean	**0.90**	**0.30**	**48.9**	**41.6**
Standard dev.	**0.08**	**0.03**	**3.9**	**15.7**
Min.	**0.78**	**0.26**	**43.0**	**25.4**
Max	**1.04**	**0.36**	**54.9**	**71.4**

Table A4-28. Uniaxial compressive strength, friction angle (MC) and cohesion (MC) for FSM_EW007 with Ävrö granodiorite parallel to σ_H.

DFN realisation	Uniaxial compressive strength, (MPa) [1]	Friction angle, (°) [2] Mohr-Coulomb	Cohesion, (MPa) [2] Mohr-Coulomb
1	40.3	40.2	13.9
2	33.5	37.8	12.2
3	35.2	38.4	12.7
4	55.3	44.4	17.1
5	47.0	42.4	15.4
6	34.9	38.4	12.6
7	37.7	39.4	13.3
8	62.0	46.4	18.3
9	45.0	41.7	15.0
10	47.3	42.5	15.4
Mean	**43.8**	**41.1**	**14.6**
Standard dev.	**9.4**	**2.8**	**2.0**
Min.	**33.5**	**37.8**	**12.2**
Max	**62.0**	**46.4**	**18.3**

1) Estimated from fitting an average Mohr-Coulomb relationship in stress range 0–25.8 MPa.
2) For confinement stress between 10 and 30 MPa.

A4.1.8 FSM_EW007, intact rock Ävrö grantodiorite, parallel to σ_h

Table A4-29. Poisson's ratio, deformation modulus and vertical stress at failure for all DFN realisations, FSM_EW007, intact rock Ävrö granodiorite, parallel to σ_h, stress level 10.5 MPa.

DFN realisation	P_{10}	Poisson's ratio, ν_m	Deformation modulus, E_m, (GPa)	Vertical stress at failure, σ_{vf}, (MPa)
1	0.85	0.32	47.2	97.5
2	0.98	0.32	42.3	85.4
3	0.87	0.32	46.8	93.2
4	1.04	0.31	48.7	114.7
5	0.78	0.31	49.8	104.8
6	0.99	0.31	44.8	89.1
7	0.91	0.29	55.4	112.0
8	0.88	0.28	52.5	101.1
9	0.88	0.31	50.3	111.6
10	0.85	0.30	48.0	93.9
Mean	**0.90**	**0.31**	**48.6**	**100.3**
Standard dev.	**0.08**	**0.01**	**3.7**	**10.2**
Min.	**0.78**	**0.28**	**42.3**	**85.4**
Max	**1.04**	**0.32**	**55.4**	**114.7**

Table A4-30. Poisson's ratio, deformation modulus and vertical stress at failure for all DFN realisations, FSM_EW007, intact rock Ävrö granodiorite, parallel to σ_h, stress level 2.6 MPa.

DFN realisation	P_{10}	Poisson's ratio, ν_m	Deformation modulus, E_m, (GPa)	Vertical stress at failure, σ_{vf}, (MPa)
1	0.85	0.31	49.7	38.8
2	0.98	0.32	42.6	47.8
3	0.87	0.30	45.5	38.3
4	1.04	0.31	46.8	49.1
5	0.78	0.33	46.6	42.8
6	0.99	0.30	47.5	37.3
7	0.91	0.30	53.6	52.2
8	0.88	0.27	48.0	49.4
9	0.88	0.31	44.5	41.1
10	0.85	0.30	45.1	37.4
Mean	**0.90**	**0.30**	**47.0**	**43.4**
Standard dev.	**0.08**	**0.02**	**3.1**	**5.7**
Min.	**0.78**	**0.27**	**42.6**	**37.3**
Max	**1.04**	**0.33**	**53.6**	**52.2**

Table A4-31. Poisson's ratio, deformation modulus and vertical stress at failure for all DFN realisations, FSM_EW007, intact rock Ävrö granodiorite, parallel to σ_h, stress level 1.5 MPa.

DFN realisation	P_{10}	Poisson's ratio, ν_m	Deformation modulus, E_m, (GPa)	Vertical stress at failure, σ_{vf}, (MPa)
1	0.85	0.22	48.2	33.0
2	0.98	0.29	49.4	34.5
3	0.87	0.23	39.2	30.6
4	1.04	0.23	40.9	43.9
5	0.78	0.23	43.0	33.6
6	0.99	0.25	41.6	27.8
7	0.91	0.21	44.5	45.6
8	0.88	0.21	47.1	47.1
9	0.88	0.26	41.3	31.1
10	0.85	0.30	50.7	26.7
Mean	**0.90**	**0.24**	**44.6**	**35.4**
Standard dev.	**0.08**	**0.03**	**4.0**	**7.4**
Min.	**0.78**	**0.21**	**39.2**	**26.7**
Max	**1.04**	**0.30**	**50.7**	**47.1**

Table A4-32. Uniaxial compressive strength, friction angle (MC) and cohesion (MC) for FSM_EW007 with Ävrö granodiorite parallel to σ_h.

DFN realisation	Uniaxial compressive strength, (MPa) [1]	Friction angle, (°) [2] Mohr-Coulomb	Cohesion, (MPa) [2] Mohr-Coulomb
1	21.2	50.1	3.8
2	25.4	46.4	5.1
3	20.0	49.4	3.7
4	27.0	53.0	4.5
5	23.2	51.2	4.1
6	18.7	48.6	3.5
7	29.6	52.0	5.1
8	30.9	49.1	5.8
9	24.2	51.7	4.2
10	19.7	49.2	3.7
Mean	**24.0**	**50.1**	**4.3**
Standard dev.	**4.2**	**1.9**	**0.7**
Min.	**18.7**	**46.4**	**3.5**
Max	**30.9**	**53.0**	**5.8**

1) Estimated from fitting an average Mohr-Coulomb relationship in stress range 0–10.5 MPa.
2) For confinement stress between 0 and 10.5 MPa.

A4.1.9 FSM_NE005, intact rock Ävrö grantodiorite, parallel to σ_H

Table A4-33. Poisson's ratio, deformation modulus and vertical stress at failure for all DFN realisations, FSM_NE005, intact rock Ävrö granodiorite, parallel to σ_H, stress level 25.8 MPa.

DFN realisation	P_{10}	Poisson's ratio, ν_m	Deformation modulus, E_m, (GPa)	Vertical stress at failure, σ_{vf}, (MPa)
1	0.72	0.29	53.3	240.4
2	0.72	0.29	55.7	259.6
3	0.69	0.29	54.9	258.6
4	0.62	0.32	51.9	233.0
5	0.76	0.30	53.1	177.2
6	0.67	0.31	45.8	183.3
7	0.70	0.27	57.2	250.7
8	0.64	0.28	57.9	249.3
9	0.62	0.29	54.2	228.9
10	0.76	0.28	57.9	301.0
Mean	**0.69**	**0.29**	**54.2**	**238.2**
Standard dev.	**0.05**	**0.01**	**3.6**	**36.4**
Min.	**0.62**	**0.27**	**45.8**	**177.2**
Max	**0.76**	**0.32**	**57.9**	**301.0**

Table A4-34. Poisson's ratio, deformation modulus and vertical stress at failure for all DFN realisations, FSM_NE005, intact rock Ävrö granodiorite, parallel to σ_H, stress level 6.5 MPa.

DFN realisation	P_{10}	Poisson's ratio, ν_m	Deformation modulus, E_m, (GPa)	Vertical stress at failure, σ_{vf}, (MPa)
1	0.72	0.33	47.6	85.0
2	0.72	0.31	53.1	110.2
3	0.69	0.30	52.2	97.7
4	0.62	0.34	49.1	77.6
5	0.76	0.32	49.2	56.2
6	0.67	0.31	44.0	58.9
7	0.70	0.27	57.1	91.9
8	0.64	0.26	54.9	101.3
9	0.62	0.28	51.2	91.8
10	0.76	0.28	57.1	118.2
Mean	**0.69**	**0.30**	**51.6**	**88.9**
Standard dev.	**0.05**	**0.02**	**4.2**	**20.2**
Min.	**0.62**	**0.26**	**44.0**	**56.2**
Max	**0.76**	**0.34**	**57.1**	**118.2**

Table A4-35. Poisson's ratio, deformation modulus and vertical stress at failure for all DFN realisations, FSM_NE005, Ävrö granodiorite, parallel to σ_H, stress level 2.0 MPa.

DFN realisation	P_{10}	Poisson's ratio, ν_m	Deformation modulus, E_m, (GPa)	Vertical stress at failure, σ_{vf}, (MPa)
1	0.72	0.28	55.0	49.9
2	0.72	0.22	52.0	68.9
3	0.69	0.22	45.4	59.2
4	0.62	0.34	47.5	47.5
5	0.76	0.29	54.5	29.9
6	0.67	0.30	44.7	28.2
7	0.70	0.28	56.9	57.5
8	0.64	0.24	49.9	60.4
9	0.62	0.28	50.0	60.6
10	0.76	0.26	53.8	70.2
Mean	**0.69**	**0.27**	**51.0**	**53.2**
Standard dev.	**0.05**	**0.04**	**4.2**	**14.6**
Min.	**0.62**	**0.22**	**44.7**	**28.2**
Max	**0.76**	**0.34**	**56.9**	**70.2**

Table A4-36. Uniaxial compressive strength, friction angle (MC) and cohesion (MC) for FSM_NE005 with Ävrö granodiorite parallel to σ_H.

DFN realisation	Uniaxial compressive strength, (MPa) [1)]	Friction angle, (°) [2)] Mohr-Coulomb	Cohesion, (MPa) [2)] Mohr-Coulomb
1	53.1	44.1	16.6
2	60.8	46.1	18.1
3	58.8	45.6	17.7
4	50.6	43.4	16.1
5	34.4	38.2	12.5
6	36.3	38.9	13.0
7	56.4	45.0	17.3
8	57.4	45.3	17.5
9	52.1	43.9	16.4
10	70.8	48.2	19.8
Mean	**53.1**	**43.9**	**16.5**
Standard dev.	**10.9**	**3.1**	**2.2**
Min.	**34.4**	**38.2**	**12.5**
Max	**70.8**	**48.2**	**19.8**

1) Estimated from fitting an average Mohr-Coulomb relationship in stress range 0–25.8 MPa.
2) For confinement stress between 10 and 30 MPa.

A4.1.10 FSM_NE005, intact rock Ävrö grantodiorite, parallel to σ_h

Table A4-37. Poisson's ratio, deformation modulus and vertical stress at failure for all DFN realisations, FSM_NE005, intact rock Ävrö granodiorite, parallel to σ_h, stress level 10.5 MPa.

DFN realisation	P_{10}	Poisson's ratio, ν_m	Deformation modulus, E_m, (GPa)	Vertical stress at failure, σ_{vf}, (MPa)
1	0.72	0.31	50.3	138.0
2	0.72	0.30	55.6	159.1
3	0.69	0.32	48.4	91.5
4	0.62	0.32	49.1	101.6
5	0.76	0.33	48.3	79.7
6	0.67	0.30	53.0	143.6
7	0.70	0.30	52.9	115.6
8	0.64	0.32	46.2	105.9
9	0.62	0.33	45.5	90.3
10	0.76	0.28	58.1	133.2
Mean	**0.69**	**0.31**	**50.7**	**115.9**
Standard dev.	**0.05**	**0.02**	**4.1**	**26.4**
Min.	**0.62**	**0.28**	**45.5**	**79.7**
Max	**0.76**	**0.33**	**58.1**	**159.1**

Table A4-38. Poisson's ratio, deformation modulus and vertical stress at failure for all DFN realisations, FSM_NE005, intact rock Ävrö granodiorite, parallel to σ_h, stress level 2.6 MPa.

DFN realisation	P_{10}	Poisson's ratio, ν_m	Deformation modulus, E_m, (GPa)	Vertical stress at failure, σ_{vf}, (MPa)
1	0.72	0.30	48.9	59.9
2	0.72	0.26	58.1	87.7
3	0.69	0.32	44.0	39.8
4	0.62	0.34	42.2	40.8
5	0.76	0.35	46.1	31.0
6	0.67	0.31	51.6	64.6
7	0.70	0.30	53.8	50.0
8	0.64	0.35	43.1	57.3
9	0.62	0.35	43.2	38.7
10	0.76	0.28	53.9	78.5
Mean	**0.69**	**0.32**	**48.5**	**54.8**
Standard dev.	**0.05**	**0.03**	**5.6**	**18.4**
Min.	**0.62**	**0.26**	**42.2**	**31.0**
Max	**0.76**	**0.35**	**58.1**	**87.7**

Table A4-39. Poisson's ratio, deformation modulus and vertical stress at failure for all DFN realisations, FSM_NE005, intact rock Ävrö granodiorite, parallel to σ_h, stress level 1.5 MPa.

DFN realisation	P_{10}	Poisson's ratio, ν_m	Deformation modulus, E_m, (GPa)	Vertical stress at failure, σ_{vf}, (MPa)
1	0.72	0.35	44.9	49.1
2	0.72	0.27	56.0	86.0
3	0.69	0.35	39.9	30.1
4	0.62	0.37	40.1	36.4
5	0.76	0.29	53.0	23.7
6	0.67	0.28	48.4	46.1
7	0.70	0.29	55.4	39.2
8	0.64	0.29	50.4	46.3
9	0.62	0.29	51.2	29.0
10	0.76	0.25	57.5	58.9
Mean	**0.69**	**0.30**	**49.7**	**44.5**
Standard dev.	**0.05**	**0.04**	**6.3**	**18.0**
Min.	**0.62**	**0.25**	**39.9**	**23.7**
Max	**0.76**	**0.37**	**57.5**	**86.0**

Table A4-40. Uniaxial compressive strength, friction angle (MC) and cohesion (MC) for FSM_NE005 with Ävrö granodiorite parallel to σ_h.

DFN realisation	Uniaxial compressive strength, (MPa) [1)]	Friction angle, (°) [2)] Mohr-Coulomb	Cohesion, (MPa) [2)] Mohr-Coulomb
1	33.4	55.7	5.2
2	60.2	55.3	9.4
3	19.7	49.3	3.7
4	22.6	50.8	4.0
5	15.5	46.6	3.1
6	34.8	56.1	5.3
7	26.8	53.0	4.5
8	32.8	50.1	6.0
9	19.3	49.0	3.6
10	44.3	53.8	7.3
Mean	**30.9**	**52.0**	**5.2**
Standard dev.	**13.5**	**3.3**	**1.9**
Min.	**15.5**	**46.6**	**3.1**
Max	**60.2**	**56.1**	**9.4**

1) Estimated from fitting an average Mohr-Coulomb relationship in stress range 0–10.5 MPa.
2) For confinement stress between 0 and 10.5 MPa.

A4.1.11 FSM_W, intact rock Ävrö grantodiorite, parallel to σ_H

Table A4-41. Poisson's ratio, deformation modulus and vertical stress at failure for all DFN realisations, FSM_W, intact rock Ävrö granodiorite, parallel to σ_H, stress level 25.8 MPa.

DFN realisation	P_{10}	Poisson's ratio, ν_m	Deformation modulus, E_m, (GPa)	Vertical stress at failure, σ_{vf}, (MPa)
1	0.72	0.29	55.0	245.3
3	0.78	0.28	55.4	293.5
4	0.70	0.29	53.2	185.9
5	0.55	0.26	52.0	209.6
6	0.62	0.29	56.2	225.4
7	0.52	0.29	53.7	178.5
8	0.65	0.29	55.0	209.1
9	0.69	0.29	52.9	231.1
10	0.71	0.30	53.2	231.9
Mean	**0.66**	**0.29**	**54.1**	**223.4**
Standard dev.	**0.08**	**0.01**	**1.4**	**34.2**
Min.	**0.52**	**0.26**	**52.0**	**178.5**
Max	**0.78**	**0.30**	**56.2**	**293.5**

Table A4-42. Poisson's ratio, deformation modulus and vertical stress at failure for all DFN realisations, FSM_W, intact rock Ävrö granodiorite, parallel to σ_H, stress level 6.5 MPa.

DFN realisation	P_{10}	Poisson's ratio, ν_m	Deformation modulus, E_m, (GPa)	Vertical stress at failure, σ_{vf}, (MPa)
1	0.72	0.31	51.3	80.7
3	0.78	0.29	53.3	110.8
4	0.70	0.30	52.9	67.7
5	0.55	0.30	46.2	86.1
6	0.62	0.31	55.4	79.8
7	0.52	0.32	50.0	65.7
8	0.65	0.29	54.4	72.2
9	0.69	0.31	50.5	75.1
10	0.71	0.31	47.0	87.2
Mean	**0.66**	**0.30**	**51.2**	**80.6**
Standard dev.	**0.08**	**0.01**	**3.1**	**13.6**
Min.	**0.52**	**0.29**	**46.2**	**65.7**
Max	**0.78**	**0.32**	**55.4**	**110.8**

Table A4-43. Poisson's ratio, deformation modulus and vertical stress at failure for all DFN realisations, FSM_W, Ävrö granodiorite, parallel to σ_H, stress level 2.0 MPa.

DFN realisation	P_{10}	Poisson's ratio, ν_m	Deformation modulus, E_m, (GPa)	Vertical stress at failure, σ_{vf}, (MPa)
1	0.72	0.27	51.1	39.8
3	0.78	0.27	55.9	66.2
4	0.70	0.25	47.6	36.1
5	0.55	0.26	53.3	50.4
6	0.62	0.29	55.9	44.2
7	0.52	0.27	49.8	31.8
8	0.65	0.29	54.1	44.5
9	0.69	0.27	52.0	39.0
10	0.71	0.28	52.3	51.2
Mean	**0.66**	**0.27**	**52.4**	**44.8**
Standard dev.	**0.08**	**0.01**	**2.7**	**10.2**
Min.	**0.52**	**0.25**	**47.6**	**31.8**
Max	**0.78**	**0.29**	**55.9**	**66.2**

Table A4-44. Uniaxial compressive strength, friction angle (MC) and cohesion (MC) for FSM_W with Ävrö granodiorite parallel to σ_H.

DFN realisation	Uniaxial compressive strength, (MPa) [1]	Friction angle, (°) [2] Mohr-Coulomb	Cohesion, (MPa) [2] Mohr-Coulomb
1	52.8	44.1	16.6
3	68.1	47.7	19.4
4	38.5	39.6	13.5
5	46.7	42.3	15.3
6	49.0	43.0	15.8
7	36.3	38.9	13.0
8	44.5	41.6	14.8
9	49.3	43.1	15.9
10	51.7	43.7	16.3
Mean	**48.5**	**42.7**	**15.6**
Standard dev.	**9.2**	**2.6**	**1.9**
Min.	**36.3**	**38.9**	**13.0**
Max	**68.1**	**47.7**	**19.4**

1) Estimated from fitting an average Mohr-Coulomb relationship in stress range 0–25.8 MPa.
2) For confinement stress between 10 and 30 MPa.

A4.1.12 FSM_W, intact rock Ävrö grantodiorite, parallel to σ_h

Table A4-45. Poisson's ratio, deformation modulus and vertical stress at failure for all DFN realisations, FSM_W, intact rock Ävrö granodiorite, parallel to σ_h, stress level 10.5 MPa.

DFN realisation	P_{10}	Poisson's ratio, ν_m	Deformation modulus, E_m, (GPa)	Vertical stress at failure, σ_{vf}, (MPa)
1	0.72	0.33	47.5	225.2
2	0.84	0.33	54.7	325.2
3	0.78	0.33	48.4	140.4
4	0.70	0.34	54.7	133.2
6	0.62	0.29	56.1	266.2
7	0.52	0.25	52.2	282.1
8	0.65	0.29	52.6	343.1
10	0.71	0.30	52.2	221.5
Mean	**0.69**	**0.31**	**52.3**	**242.1**
Standard dev.	**0.10**	**0.03**	**3.0**	**77.6**
Min.	**0.52**	**0.25**	**47.5**	**133.2**
Max	**0.84**	**0.34**	**56.1**	**343.1**

Table A4-46. Poisson's ratio, deformation modulus and vertical stress at failure for all DFN realisations, FSM_W, intact rock Ävrö granodiorite, parallel to σ_h, stress level 2.6 MPa.

DFN realisation	P_{10}	Poisson's ratio, ν_m	Deformation modulus, E_m, (GPa)	Vertical stress at failure, σ_{vf}, (MPa)
1	0.72	0.30	54.4	124.8
2	0.84	0.32	47.4	113.2
3	0.78	0.31	51.2	134.8
4	0.70	0.31	53.9	93.0
6	0.62	0.29	54.5	101.8
7	0.52	0.31	54.5	130.0
8	0.65	0.30	51.8	101.0
10	0.71	0.26	62.0	154.9
Mean	**0.69**	**0.30**	**53.7**	**119.2**
Standard dev.	**0.10**	**0.02**	**4.1**	**20.8**
Min.	**0.52**	**0.26**	**47.4**	**93.0**
Max	**0.84**	**0.32**	**62.0**	**154.9**

Table A4-47. Poisson's ratio, deformation modulus and vertical stress at failure for all DFN realisations, FSM_W, intact rock Ävrö granodiorite, parallel to σ_h, stress level 1.5 MPa.

DFN realisation	P_{10}	Poisson's ratio, ν_m	Deformation modulus, E_m, (GPa)	Vertical stress at failure, σ_{vf}, (MPa)
1	0.72	0.33	50.6	39.6
2	0.84	0.32	43.5	42.8
3	0.78	0.33	49.1	48.5
4	0.70	0.31	45.2	31.5
6	0.62	0.32	49.0	35.4
7	0.52	0.25	53.8	75.0
8	0.65	0.34	45.2	31.6
10	0.71	0.24	54.7	75.8
Mean	**0.69**	**0.30**	**48.9**	**47.5**
Standard dev.	**0.10**	**0.04**	**4.1**	**18.1**
Min.	**0.52**	**0.24**	**43.5**	**31.5**
Max	**0.84**	**0.34**	**54.7**	**75.8**

Table A4-48. Uniaxial compressive strength, friction angle (MC) and cohesion (MC) for FSM_W with Ävrö granodiorite parallel to σ_h.

DFN realisation	Uniaxial compressive strength, (MPa) [1]	Friction angle, (°) [2] Mohr-Coulomb	Cohesion, (MPa) [2] Mohr-Coulomb
1	48.1	59.6	6.5
2	80.8	63.2	9.6
3	62.1	53.3	10.3
4	34.6	56.1	5.3
6	45.2	59.0	6.3
7	79.9	63.1	9.5
8	80.6	63.2	9.6
10	70.2	62.3	8.6
Mean	**62.7**	**60.0**	**8.2**
Standard dev.	**18.2**	**3.7**	**1.9**
Min.	**34.6**	**53.3**	**5.3**
Max	**80.8**	**63.2**	**10.3**

1) Estimated from fitting an average Mohr-Coulomb relationship in stress range 0–10.5 MPa.
2) For confinement stress between 0 and 10.5 MPa.

A4.1.13 FSM_W, intact rock Quartz monzodiorite, parallel to σ_H

Table A4-49. Poisson's ratio, deformation modulus and vertical stress at failure for all DFN realisations, FSM_W, intact rock Quartz monzodiorite, parallel to σ_H, stress level 25.8 MPa.

DFN realisation	P_{10}	Poisson's ratio, ν_m	Deformation modulus, E_m, (GPa)	Vertical stress at failure, σ_{vf}, (MPa)
1	0.72	0.32	56.1	241.5
3	0.78	0.31	56.4	257.9
4	0.70	0.33	54.5	194.0
5	0.55	0.30	52.2	204.2
6	0.62	0.32	57.0	217.4
7	0.52	0.33	52.9	173.9
8	0.65	0.32	55.8	198.4
9	0.69	0.32	53.7	219.6
10	0.71	0.32	53.6	227.3
Mean	**0.66**	**0.32**	**54.7**	**214.9**
Standard dev.	**0.08**	**0.01**	**1.7**	**25.6**
Min.	**0.52**	**0.30**	**52.2**	**173.9**
Max	**0.78**	**0.33**	**57.0**	**257.9**

Table A4-50. Poisson's ratio, deformation modulus and vertical stress at failure for all DFN realisations, FSM_W, intact rock Quartz monzodiorite, parallel to σ_H, stress level 6.5 MPa.

DFN realisation	P_{10}	Poisson's ratio, ν_m	Deformation modulus, E_m, (GPa)	Vertical stress at failure, σ_{vf}, (MPa)
1	0.72	0.35	48.8	79.6
3	0.78	0.32	54.1	102.9
4	0.70	0.35	50.0	70.4
5	0.55	0.34	43.7	85.8
6	0.62	0.34	53.7	78.8
7	0.52	0.34	49.6	59.9
8	0.65	0.31	56.6	71.2
9	0.69	0.33	53.8	78.9
10	0.71	0.33	56.5	86.9
Mean	**0.66**	**0.33**	**51.8**	**79.4**
Standard dev.	**0.08**	**0.01**	**4.2**	**12.1**
Min.	**0.52**	**0.31**	**43.7**	**59.9**
Max	**0.78**	**0.35**	**56.6**	**102.9**

Table A4-51. Poisson's ratio, deformation modulus and vertical stress at failure for all DFN realisations, FSM_W, Quartz monzodiorite, parallel to σ_H, stress level 2.0 MPa.

DFN realisation	P_{10}	Poisson's ratio, ν_m	Deformation modulus, E_m, (GPa)	Vertical stress at failure, σ_{vf}, (MPa)
1	0.72	0.34	51.7	42.3
3	0.78	0.32	51.4	66.2
4	0.70	0.35	47.5	36.7
5	0.55	0.32	51.3	51.5
6	0.62	0.32	57.4	47.2
7	0.52	0.34	49.9	36.2
8	0.65	0.33	56.4	36.3
9	0.69	0.34	51.4	41.1
10	0.71	0.34	52.5	53.3
Mean	**0.66**	**0.33**	**52.2**	**45.6**
Standard dev.	**0.08**	**0.01**	**3.1**	**10.0**
Min.	**0.52**	**0.32**	**47.5**	**36.2**
Max	**0.78**	**0.35**	**57.4**	**66.2**

Table A4-52. Uniaxial compressive strength, friction angle (MC) and cohesion (MC) for FSM_W with Quartz monzodiorite parallel to σ_H.

DFN realisation	Uniaxial compressive strength, (MPa) [1]	Friction angle, (°) [2] Mohr-Coulomb	Cohesion, (MPa) [2] Mohr-Coulomb
1	52.2	43.8	16.5
3	60.0	45.8	17.9
4	40.6	40.2	14.0
5	45.7	41.9	15.1
6	47.3	42.4	15.5
7	35.1	38.3	12.7
8	39.6	39.9	13.8
9	47.5	42.5	15.5
10	50.9	43.5	16.2
Mean	**46.5**	**42.0**	**15.2**
Standard dev.	**7.5**	**2.3**	**1.6**
Min.	**35.1**	**38.3**	**12.7**
Max	**60.0**	**45.8**	**17.9**

1) Estimated from fitting an average Mohr-Coulomb relationship in stress range 0–25.8 MPa.
2) For confinement stress between 10 and 30 MPa.

A4.1.14 FSM_W, intact rock Quartz monzodiorite, parallel to σ_h

Table A4-53. Poisson's ratio, deformation modulus and vertical stress at failure for all DFN realisations, FSM_W, intact rock Quartz monzodiorite, parallel to σ_h, stress level 10.5 MPa.

DFN realisation	P_{10}	Poisson's ratio, ν_m	Deformation modulus, E_m, (GPa)	Vertical stress at failure, σ_{vf}, (MPa)
1	0.72	0.32	58.6	122.8
2	0.84	0.32	52.8	112.1
3	0.78	0.33	54.3	125.7
4	0.70	0.32	53.8	96.9
6	0.62	0.31	57.3	105.7
7	0.52	0.34	56.1	121.6
8	0.65	0.31	53.6	90.3
10	0.71	0.29	60.8	146.7
Mean	**0.69**	**0.32**	**55.9**	**115.2**
Standard dev.	**0.10**	**0.01**	**2.8**	**18.0**
Min.	**0.52**	**0.29**	**52.8**	**90.3**
Max	**0.84**	**0.34**	**60.8**	**146.7**

Table A4-54. Poisson's ratio, deformation modulus and vertical stress at failure for all DFN realisations, FSM_W, intact rock Quartz monzodiorite, parallel to σ_h, stress level 2.6 MPa.

DFN realisation	P_{10}	Poisson's ratio, ν_m	Deformation modulus, E_m, (GPa)	Vertical stress at failure, σ_{vf}, (MPa)
1	0.72	0.32	58.1	51.1
2	0.84	0.33	48.2	54.0
3	0.78	0.35	50.7	64.7
4	0.70	0.32	54.2	41.4
6	0.62	0.31	57.4	43.4
7	0.52	0.27	54.5	83.7
8	0.65	0.32	52.4	39.6
10	0.71	0.28	58.1	91.6
Mean	**0.69**	**0.32**	**54.2**	**58.7**
Standard dev.	**0.10**	**0.03**	**3.6**	**19.7**
Min.	**0.52**	**0.27**	**48.2**	**39.6**
Max	**0.84**	**0.35**	**58.1**	**91.6**

Table A4-55. Poisson's ratio, deformation modulus and vertical stress at failure for all DFN realisations, FSM_W, intact rock Quartz monzodiorite, parallel to σ_h, stress level 1.5 MPa.

DFN realisation	P_{10}	Poisson's ratio, ν_m	Deformation modulus, E_m, (GPa)	Vertical stress at failure, σ_{vf}, (MPa)
1	0.72	0.34	52.1	40.6
2	0.84	0.35	43.3	41.8
3	0.78	0.35	50.4	50.0
4	0.70	0.33	51.9	34.8
6	0.62	0.34	52.7	35.8
7	0.52	0.28	54.3	78.0
8	0.65	0.37	45.5	34.7
10	0.71	0.29	57.6	81.4
Mean	**0.69**	**0.33**	**51.0**	**49.6**
Standard dev.	**0.10**	**0.03**	**4.6**	**19.2**
Min.	**0.52**	**0.28**	**43.3**	**34.7**
Max	**0.84**	**0.37**	**57.6**	**81.4**

Table A4-56. Uniaxial compressive strength, friction angle (MC) and cohesion (MC) for FSM_W with Quartz monzodiorite parallel to σ_h.

DFN realisation	Uniaxial compressive strength, (MPa) [1)]	Friction angle, (°) [2)] Mohr-Coulomb	Cohesion, (MPa) [2)] Mohr-Coulomb
1	28.6	53.7	4.7
2	28.2	52.4	4.8
3	34.9	53.9	5.7
4	21.6	50.2	3.9
6	23.8	51.4	4.2
7	63.7	46.3	12.8
8	21.8	48.5	4.1
10	62.0	53.0	10.4
Mean	**35.6**	**51.2**	**6.3**
Standard dev.	**17.4**	**2.7**	**3.4**
Min.	**21.6**	**46.3**	**3.9**
Max	**63.7**	**53.9**	**12.8**

1) Estimated from fitting an average Mohr-Coulomb relationship in stress range 0–10.5 MPa.
2) For confinement stress between 0 and 10.5 MPa.

Appendix 5

WellCad diagrams for in situ stress data

WellCad diagrams for the cored boreholes where in situ stress measurements have been performed, showing the in situ stress data in the context of some base geological and geophysical data. For borehole locations see Figure 2–2.

Note:

- BH length (m. f. ToC) vs. Elevation (m.a.s.l.) – BH length is the borehole length in meters from Top of Casing (ToC is different for every borehole and is shown in the heading as Elevation (m.a.s.l. ToC)) and Elevation is the vertical length in meters above sea level.
- Sonic Velocity P-wave – The ultra sonic wave velocity log (part of the geophysical logging) made in the borehole.
- Rating A and B – Rating of data quality where A has the higher quality than B.
- The corresponding measurement reports for all measurements are given in Table 6-1. There is one single measurement point with overcoring in KSH02 but this borehole is not included in this appendix (see Appendix 6 for the KSH02 results).
- HTPF inversion – Inversion method based on results from Hydraulic testing of pre-existing fractures and Hydraulic fracturing (inducing new fractures) (see /Ask et al. 2007/).
- Borehole geometry – Detailed analysis of televiewer logging data has been performed in 6 boreholes: KAV04A, KLX10, KLX12A, KLX15A (shown in this appendix and Section 6.2.4), KLX11A and KLX18A (results shown only in Section 6.2.4).
- Core disking is a phenomenon where the drill core is broken up in several cm-thick disks, separated by fresh fractures perpendicular to the borehole axis. It is caused by tensile forces developing at the base of the core during the drilling (Section 6.2.5). Saddle denotes the case when the disk has a saddle shape and petal when disk is “s-shaped”.
- If the columns are blank this means that there is no observation of the phenomenon made along this borehole.
- The notation NO DATA means that no such studies or no such measurements are performed in this borehole.
- Psi in the column for Hydraulic Fracturing is the Shut in pressure.

Title INSITU STRESS DATA KAV04A

Site	ÄVRÖ	**Bearing [°]**	77.03	**Northing [m]**	6366795.76
Borehole	KAV04A	**Inclination [°]**	-84.90	**Easting [m]**	1552475.00
Diameter [mm]	76	**Date of mapping**	2004-06-01 00:00:00	**Elevation [m.a.s.l. ToC]**	10.35
BH length [m. f. ToC]	1004.000	**Coordinate System**	RT90-RHB70	**Drilling Start Date**	2003-12-10 13:55:00
				Drilling Stop Date	2004-05-03 14:53:00

ROCKTYPE ÄVRÖ
- Fine-grained granite
- Pegmatite
- Granite
- Ävrö granite
- Quartz monzodiorite
- Diorite / Gabbro
- Fine-grained dioritoid
- Fine-grained diorite-gabbro

DEFORMATION ZONE (DZ)
- High confidence

OVERCORING (OC)
- Sigma 3 Rating A
- Sigma 1 Rating B
- Sigma 2 Rating B
- Sigma 3 Rating B
- Mean stress
- Sigma 1 Rating A
- Sigma 2 Rating A

HYDRAULIC FRACTURING (HF)

CORE DISKING

HTPF INVERSION

BOREHOLE GEOMETRY
- Borehole breakout
- Micro fallout
- Key seat
- Washout
- Mean breakout orientation

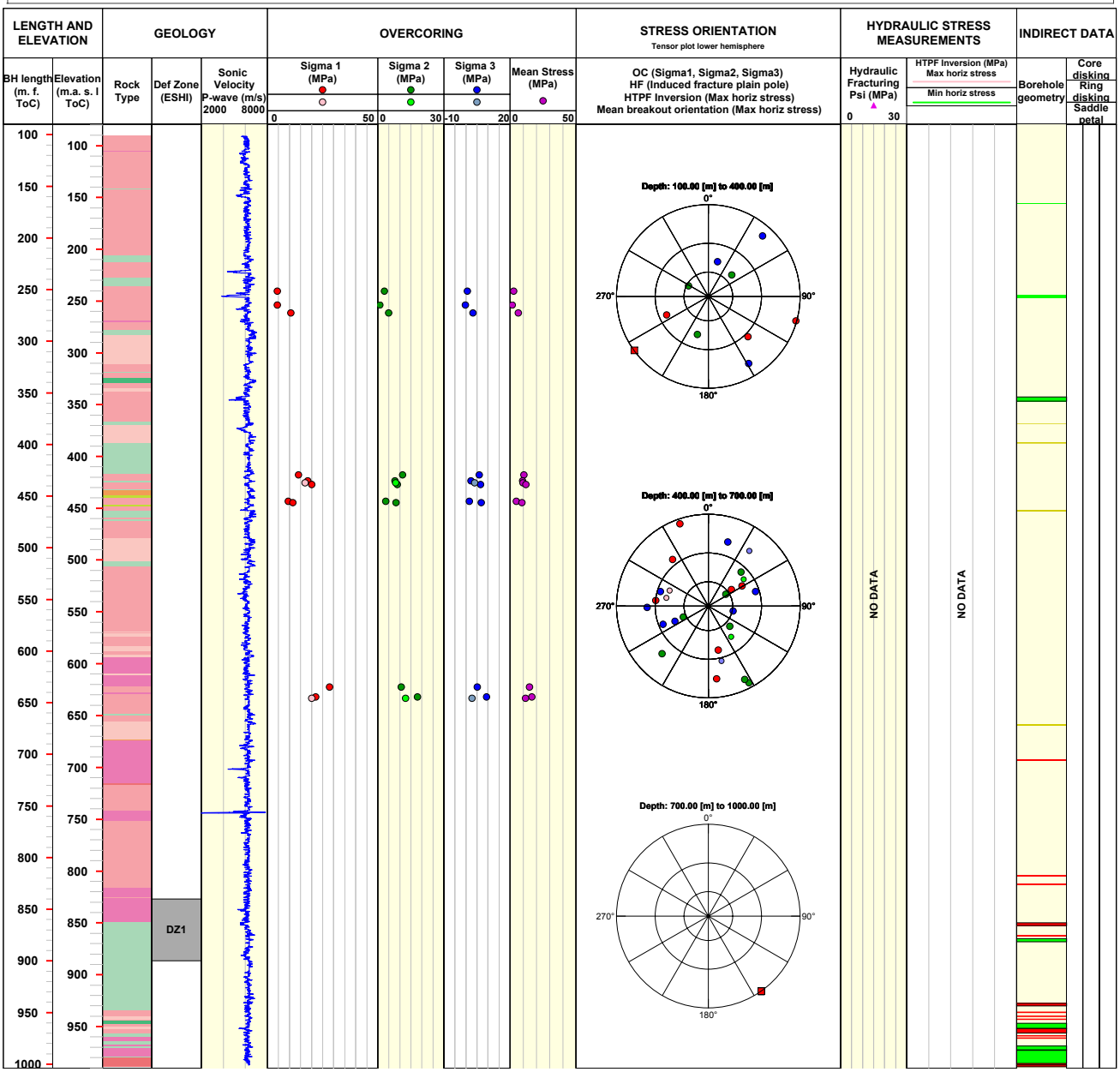

Title INSITU STRESS DATA KLX02

Site	LAXEMAR	**Bearing [°]**	357.30	**Northing [m]**	6366768.99
Borehole	KLX02	**Inclination [°]**	-84.99	**Easting [m]**	1549224.09
Diameter [mm]	76	**Date of mapping**	2003-11-20 00:00:00	**Elevation [m.a.s.l. ToC]**	18.40
BH length [m. f. ToC]	1700.500	**Coordinate System**	RT90-RHB70	**Drilling Start Date**	1992-08-15 00:00:00
				Drilling Stop Date	1992-09-05 00:00:00

ROCKTYPE LAXEMAR
- Fine-grained granite
- Ävrö granite
- Fine-grained dioritoid
- Fine-grained diorite-gabbro

DEFORMATION ZONE (DZ)
- High confidence

OVERCORING (OC)

HYDRAULIC FRACTURING (HF)
- Min horizotal stress

HTPF INVERSION

BOREHOLE GEOMETRY

CORE DISKING

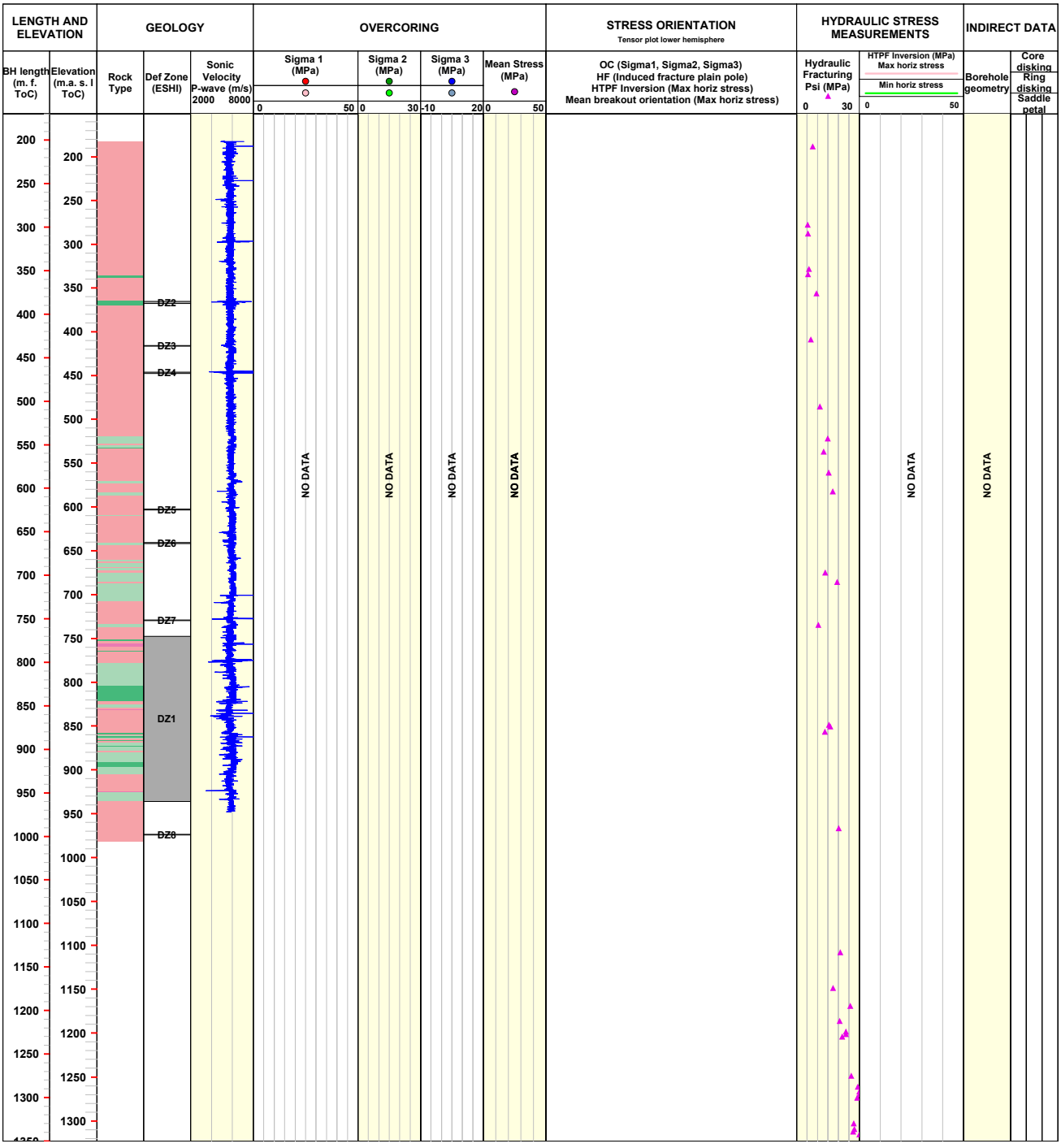

Title INSITU STRESS DATA KLX03

Site	LAXEMAR	**Bearing [°]**	199.04	**Northing [m]**	6366112.59
Borehole	KLX03	**Inclination [°]**	-74.92	**Easting [m]**	1547718.93
Diameter [mm]	76	**Date of mapping**	2004-10-27 00:00:00	**Elevation [m.a.s.l. ToC]**	18.49
BH length [m. f. ToC]	1000.420	**Coordinate System**	RT90-RHB70	**Drilling Start Date**	2004-05-28 18:00:00
				Drilling Stop Date	2004-09-07 09:00:00

ROCKTYPE LAXEMAR
- Fine-grained granite
- Ävrö granite
- Quartz monzodiorite
- Diorite / Gabbro
- Fine-grained dioritoid
- Fine-grained diorite-gabbro

OVERCORING (OC)

HTPF INVERSION

BOREHOLE GEOMETRY

HYDRAULIC FRACTURING (HF)

CORE DISKING
- Core disking > 4 per section
- Saddle/Petal shaped > 4 per section

DEFORMATION ZONE (DZ)
- High confidence

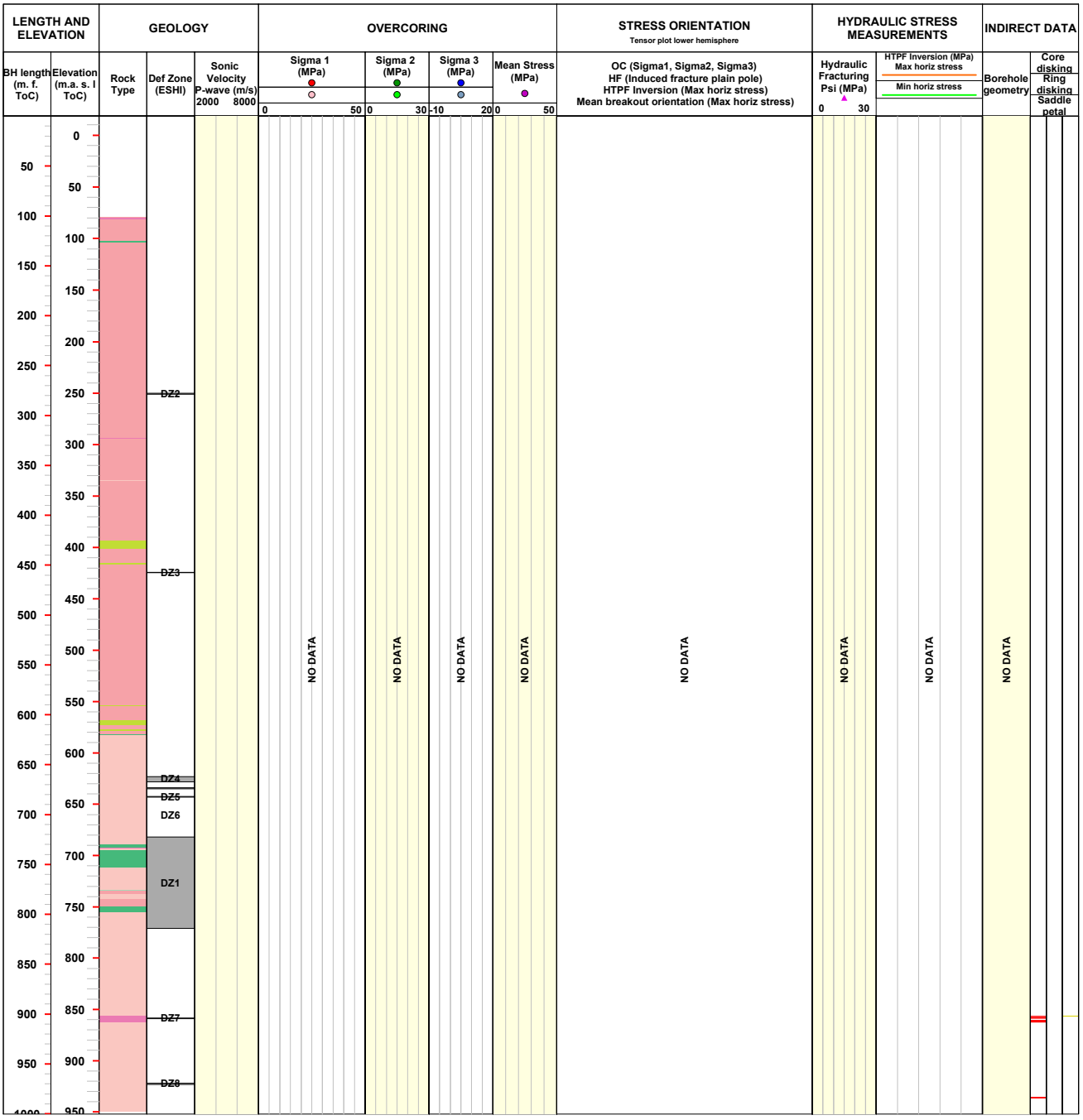

Title INSITU STRESS DATA KLX04

Site	LAXEMAR	**Bearing [°]**	0.93	**Northing [m]**	6367077.19
Borehole	KLX04	**Inclination [°]**	-84.75	**Easting [m]**	1548171.94
Diameter [mm]	76	**Date of mapping**	2004-07-22 00:00:00	**Elevation [m.a.s.l. ToC]**	24.09
BH length [m. f. ToC]	993.490	**Coordinate System**	RT90-RHB70	**Drilling Start Date**	2004-03-13 11:00:00
				Drilling Stop Date	2004-06-28 10:12:00

ROCKTYPE LAXEMAR
- Fine-grained granite
- Granite
- Ävrö granite
- Quartz monzodiorite
- Diorite / Gabbro
- Fine-grained dioritoid
- Fine-grained diorite-gabbro

OVERCORING (OC)
- Sigma 3 Rating A
- Sigma 1 Rating B
- Sigma 2 Rating B
- Sigma 3 Rating B
- Mean stress
- Sigma 1 Rating A
- Sigma 2 Rating A

HTPF INVERSION

BOREHOLE GEOMETRY

HYDRAULIC FRACTURING (HF)

CORE DISKING

DEFORMATION ZONE (DZ)
- High confidence

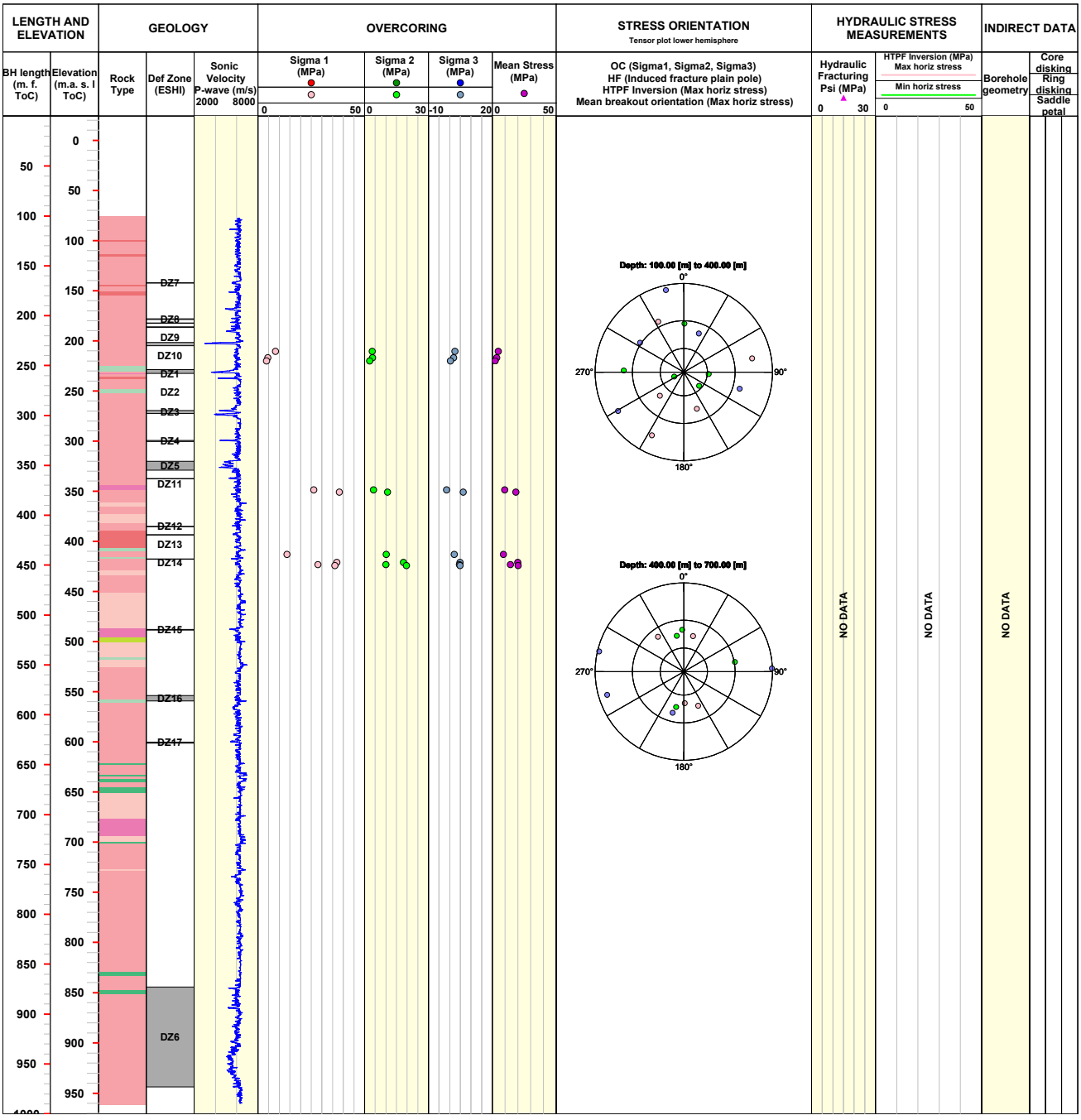

Title INSITU STRESS DATA KLX09

Site	LAXEMAR	**Bearing [°]**	267.41	**Northing [m]**	6367323.45
Borehole	KLX09	**Inclination [°]**	-84.93	**Easting [m]**	1548863.18
Diameter [mm]	76	**Date of mapping**	2006-02-02 14:40:00	**Elevation [m.a.s.l. ToC]**	23.45
BH length [m. f. ToC]	880.380	**Coordinate System**	RT90-RHB70	**Drilling Start Date**	2005-08-26 09:30:00
				Drilling Stop Date	2005-10-15 12:00:00

ROCKTYPE LAXEMAR
- Fine-grained granite
- Ävrö granite
- Quartz monzodiorite
- Diorite / Gabbro
- Fine-grained dioritoid
- Fine-grained diorite-gabbro

OVERCORING (OC)

HTPF INVERSION

BOREHOLE GEOMETRY

HYDRAULIC FRACTURING (HF)

CORE DISKING
- Core disking < 4 per section

DEFORMATION ZONE (DZ)
- High confidence

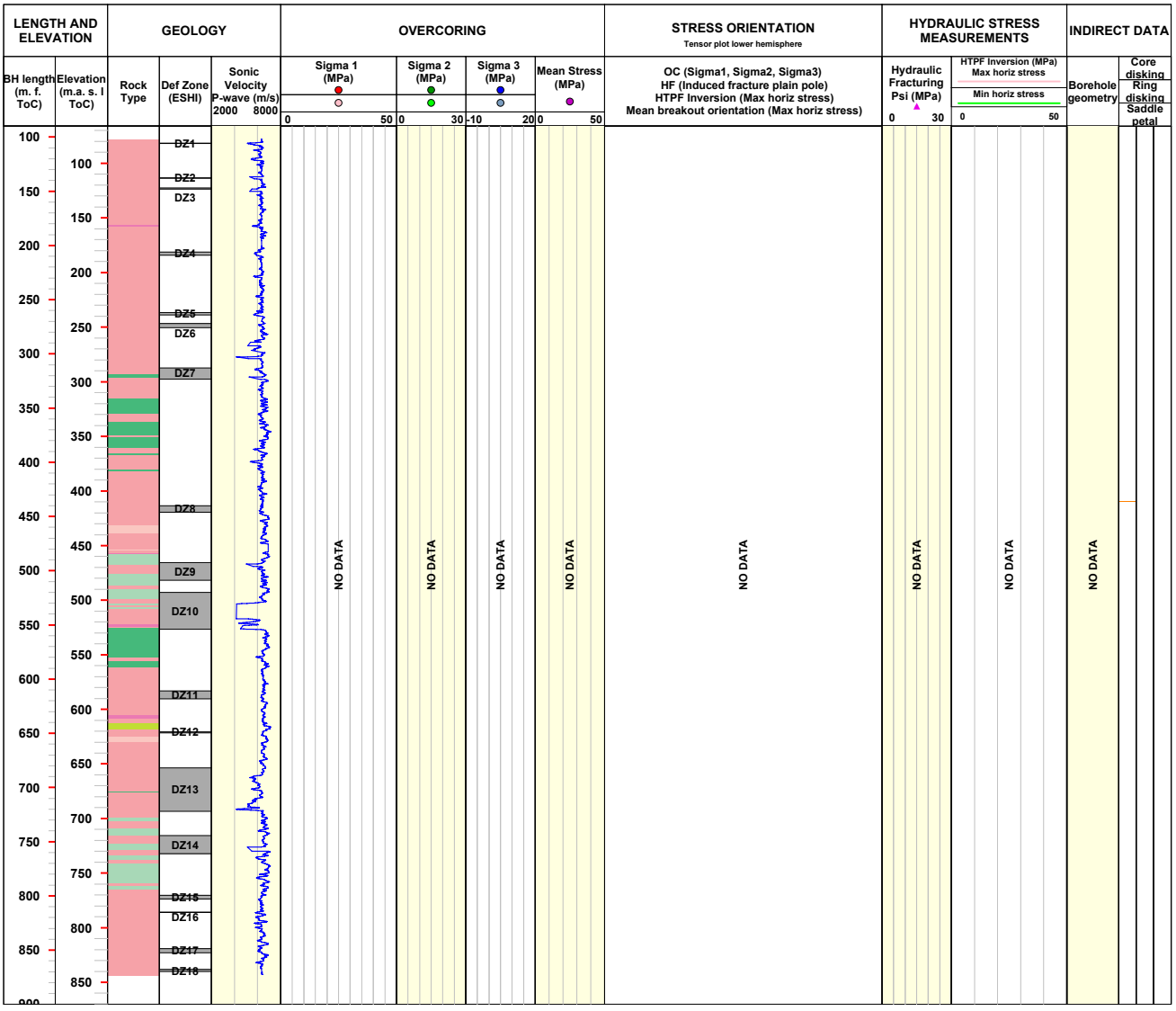

Title INSITU STRESS DATA KLX10

Site	LAXEMAR	**Bearing [°]**	250.80	**Northing [m]**	6366319.38
Borehole	KLX10	**Inclination [°]**	-85.18	**Easting [m]**	1548515.23
Diameter [mm]	76	**Date of mapping**	2005-11-29 09:18:00	**Elevation [m.a.s.l. ToC]**	18.28
BH length [m. f. ToC]	1001.200	**Coordinate System**	RT90-RHB70	**Drilling Start Date**	2005-06-18 08:00:00
				Drilling Stop Date	2005-10-15 07:40:00

ROCKTYPE LAXEMAR
- Fine-grained granite
- Ävrö granite
- Quartz monzodiorite
- Diorite / Gabbro
- Fine-grained dioritoid
- Fine-grained diorite-gabbro

DEFORMATION ZONE (DZ)
- Medium confidence
- High confidence

OVERCORING (OC)

HYDRAULIC FRACTURING (HF)

HTPF INVERSION

BOREHOLE GEOMETRY
- Borehole breakout
- Micro fallout
- Key seat
- Washout
- Mean breakout orientation

CORE DISKING
- Core disking > 4 per section

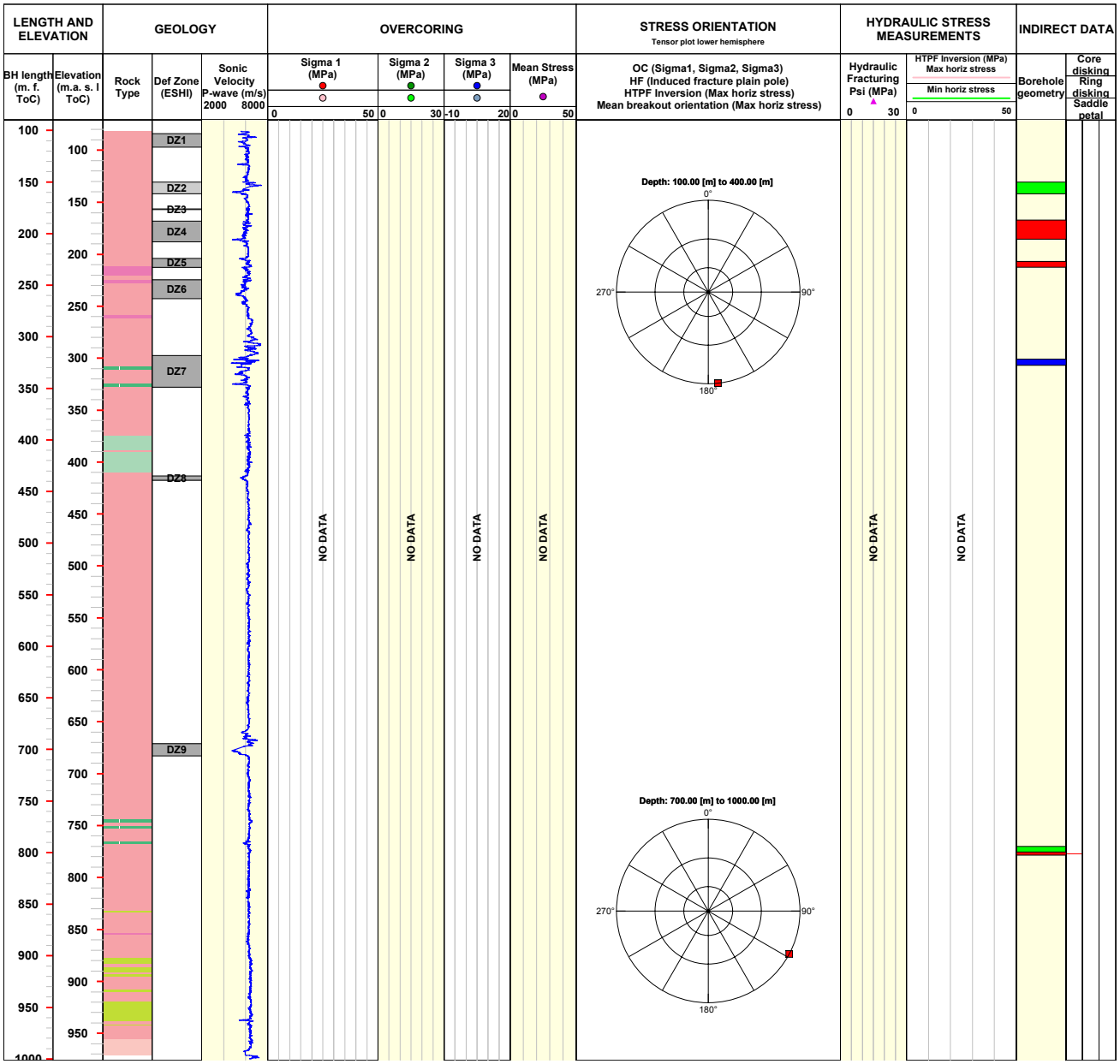

Title INSITU STRESS DATA KLX12A

Site	LAXEMAR	**Bearing [°]**	315.92	**Northing [m]**	6365630.78
Borehole	KLX12A	**Inclination [°]**	-75.30	**Easting [m]**	1548904.44
Diameter [mm]	76	**Date of mapping**	2006-04-03 10:15:00	**Elevation [m.a.s.l. ToC]**	17.74
BH length [m. f. ToC]	602.290	**Coordinate System**	RT90-RHB70	**Drilling Start Date**	2005-11-10 09:30:00
				Drilling Stop Date	2006-03-04 14:48:00

ROCKTYPE LAXEMAR
- Fine-grained granite
- Ävrö granite
- Quartz monzodiorite
- Diorite / Gabbro
- Fine-grained dioritoid
- Fine-grained diorite-gabbro

DEFORMATION ZONE (DZ)
- High confidence

OVERCORING (OC)
- Sigma 3 Rating A
- Sigma 1 Rating B
- Sigma 2 Rating B
- Sigma 3 Rating B
- Mean stress
- Sigma 1 Rating A
- Sigma 2 Rating A

HYDRAULIC FRACTURING (HF)
- Min horizotal stress
- Theoretical vert stress

HTPF INVERSION
- Max horizontal stress

BOREHOLE GEOMETRY
- Borehole breakout
- Micro fallout
- Key seat
- Washout
- Mean breakout orientation

CORE DISKING
- Core disking > 4 per section
- Saddle/Petal shaped < 4 per section

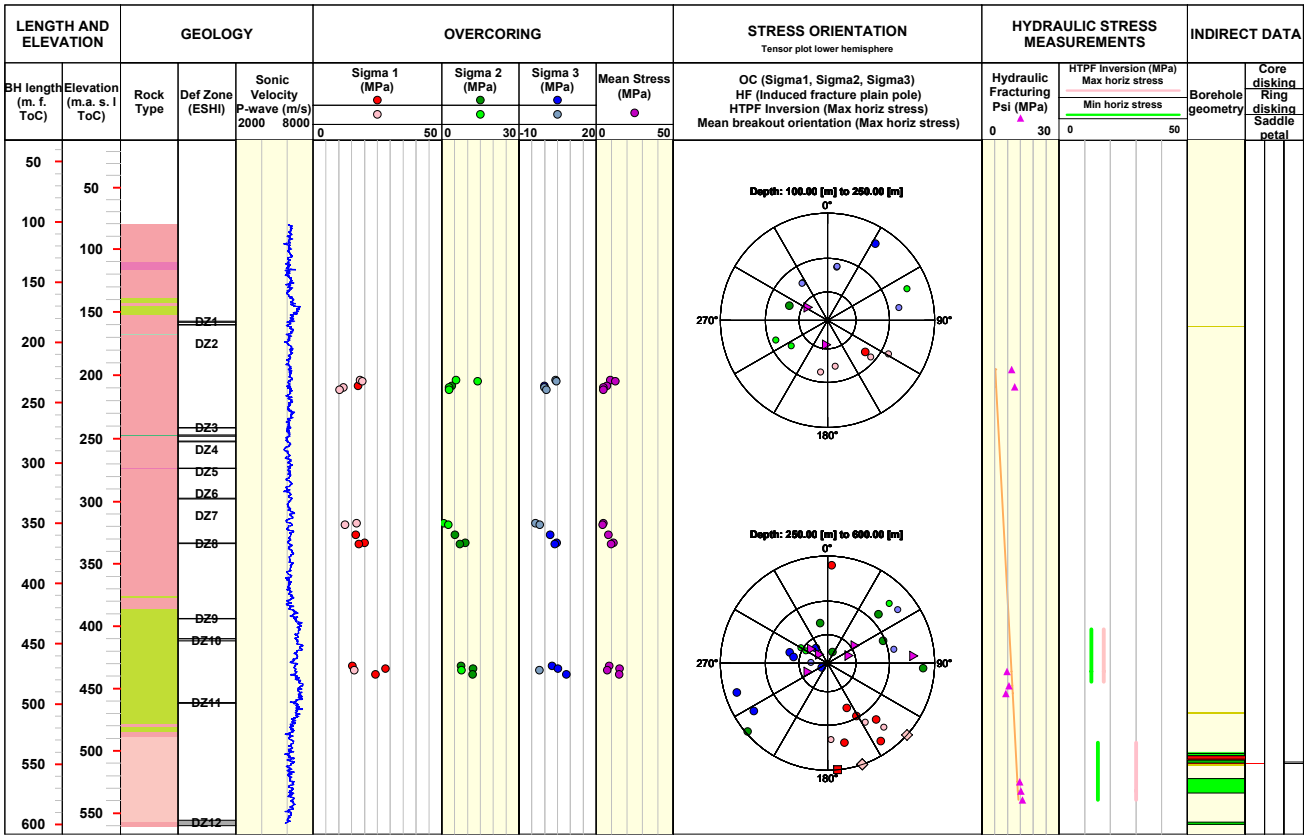

Title INSITU STRESS DATA KLX15A

Site	LAXEMAR	**Bearing [°]**	198.83	**Northing [m]**	6365614.17
Borehole	KLX15A	**Inclination [°]**	-54.41	**Easting [m]**	1547987.47
Diameter [mm]	76	**Date of mapping**	2007-04-04 16:08:00	**Elevation [m.a.s.l. ToC]**	14.59
BH length [m. f. ToC]	1000.430	**Coordinate System**	RT90-RHB70	**Drilling Start Date**	2007-01-17 10:30:00
				Drilling Stop Date	2007-02-25 20:00:00

ROCKTYPE LAXEMAR
- Fine-grained granite
- Pegmatite
- Granite
- Ävrö granite
- Quartz monzodiorite
- Fine-grained diorite-gabbro

OVERCORING (OC)

HTPF INVERSION

BOREHOLE GEOMETRY
- Borehole breakout
- Micro fallout
- Key seat
- Washout
- Mean breakout orientation

HYDRAULIC FRACTURING (HF)

CORE DISKING
- Core disking > 4 per section

DEFORMATION ZONE (DZ)
- High confidence

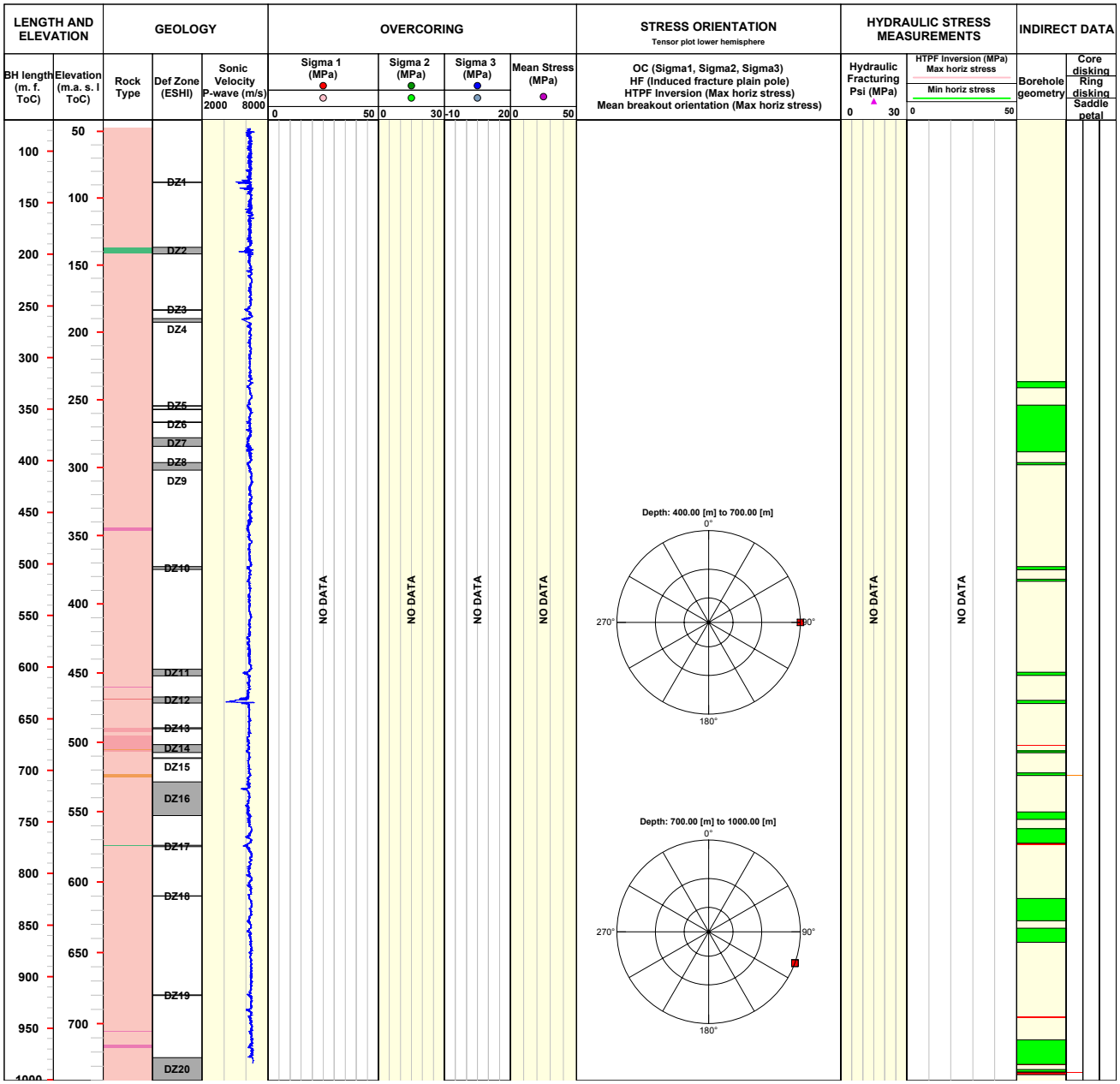

Title INSITU STRESS DATA KSH01A

Site	SIMPEVARP	**Bearing [°]**	173.60	**Northing [m]**	6366013.45
Borehole	KSH01A	**Inclination [°]**	-80.43	**Easting [m]**	1552442.98
Diameter [mm]	76	**Date of mapping**	2003-07-04 17:24:00	**Elevation [m.a.s.l. ToC]**	5.32
BH length [m. f. ToC]	1003.000	**Coordinate System**	RT90-RHB70	**Drilling Start Date**	2002-10-07 16:00:00
				Drilling Stop Date	2002-12-18 21:10:00

ROCKTYPE SIMPEVARP
- Fine-grained granite
- Pegmatite
- Granite
- Ävrö granite
- Quartz monzodiorite
- Diorite / Gabbro
- Fine-grained dioritoid
- Fine-grained diorite-gabbro

DEFORMATION ZONE (DZ)
- High confidence

OVERCORING (OC)

HYDRAULIC FRACTURING (HF)
- Min horizotal stress
- Theoretical vert stress

HTPF INVERSION
- Max horizontal stress

BOREHOLE GEOMETRY

CORE DISKING

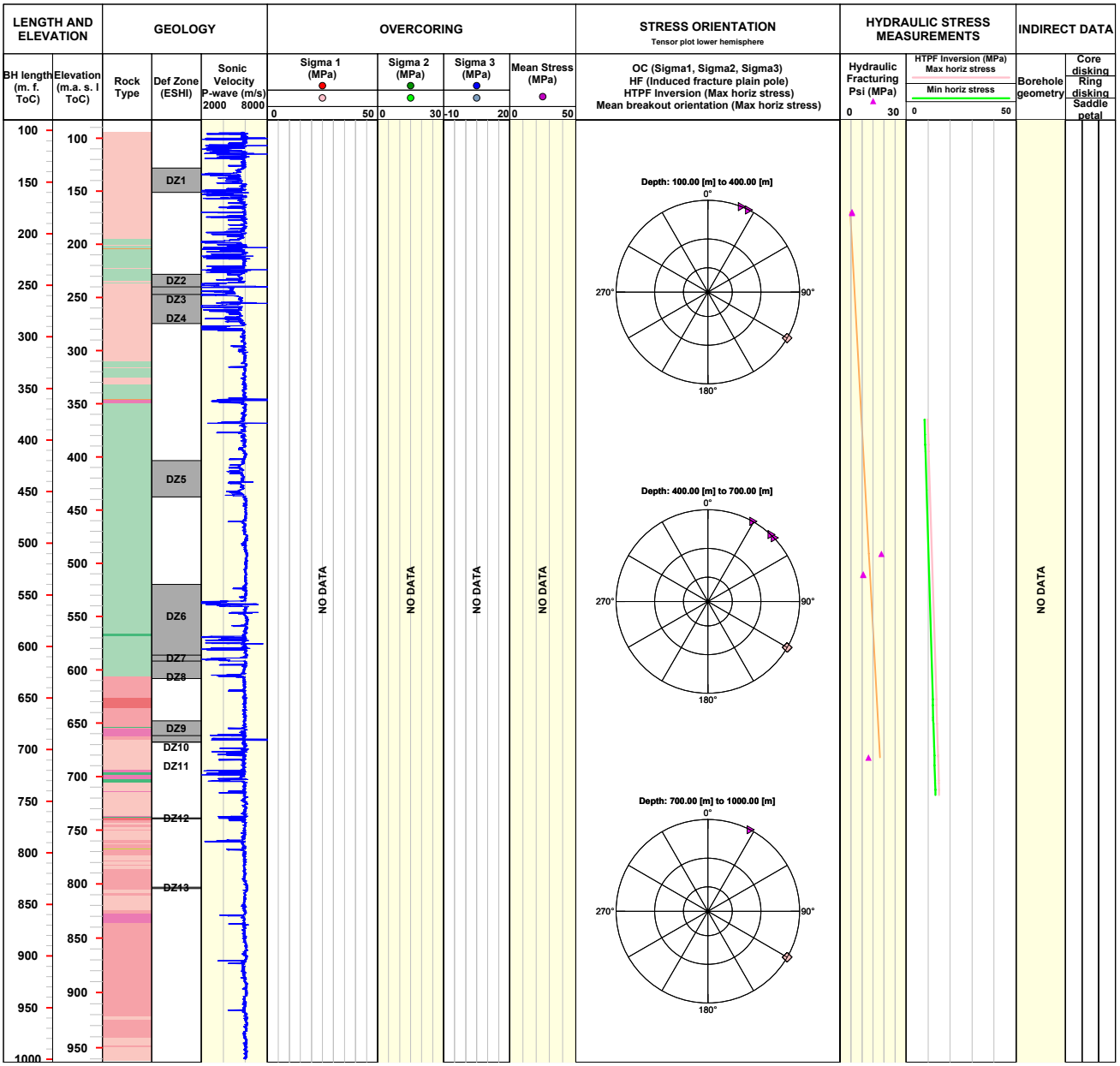

Appendix 6

Stress data compilation diagrams

Stress plots for 1) overcoring measurements and 2) hydraulic measurements (Hydraulic Fracturing and Hydraulic Testing of Pre-existing Fractures) are shown in this appendix.

Notes:

- The diagrams are compilation of data collected from Sicada (2008-02-19).
- All data from 1997 or more recent are included. Older measurement data are available in Sicada, but not included here.
- Borehole KOV01 is located in Oskarshamn.
- Boreholes KLX04, KLX12A, KAV04A and KSH02 locations are given by Figure 6-3 in the report.
- KAx, KFx, and KKx boreholes are located in Äspö Hard Rock Laboratory.
- The elevation is plotted for the upper level of the overcoring section (elevation_secup column in Sicada).
- Location of measurements in relation to geology given in WellCad plots for KLX02, KLX04, KLX12A, and KAV04A in Appendix 5.
- In the overcoring diagrams showing σ_1/σ_2 five data fall below zero (negative $\sigma_{3)}$ but these are not shown.
- In the overcoring diagrams showing σ_1/σ_3 two data fall below –20 and one value is high above 16 (KSH02), but these are not shown.
- For boreholes from Äspö (KA3376B01, KA3579A, KF0093A01 and KK0045G01) the measured stress values are taken from the reports (see Table 6-1).
- The corresponding measurement reports for all measurements are given in Table 6-1. (If there should be any difference in values between reports and Sicada data base, Sicada values has been used, except for Äspö.)
- Doorstopper measurements (2d-measurements, KA2599G01) carried out in ÄHRL are not included. These data are not regarded reliable /Jansson and Stigsson 2002/.
- Overcoring results shown inside report, Section 6.2.3.
- Hydraulic fracturing and HTPF (Hydraulic testing on pre-existing fractures) results shown inside report, Section 6.2.3.

All overcoring data – Horizontal and vertical components

Maximum horizontal stress, σ_H

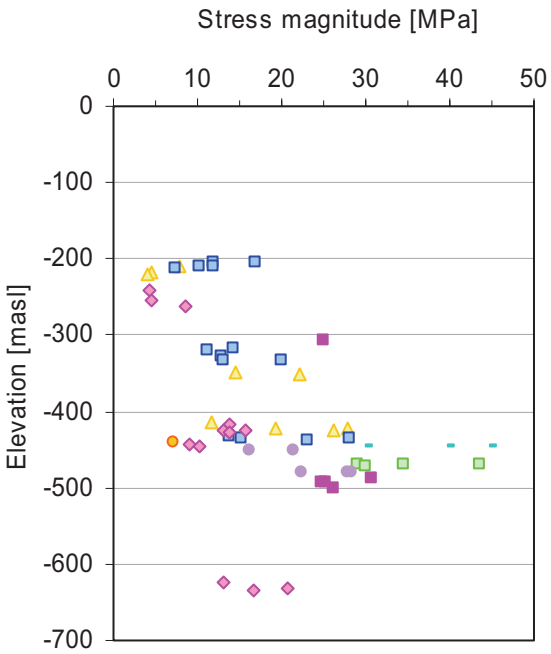

Minimum horizontal stress, σ_h

Vertical stress, σ_v

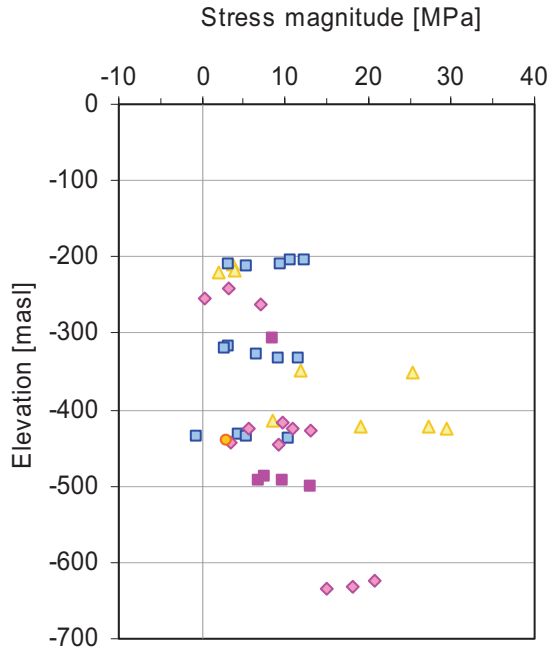

All overcoring data – Principal stress components

Maximum principal stress, σ_1

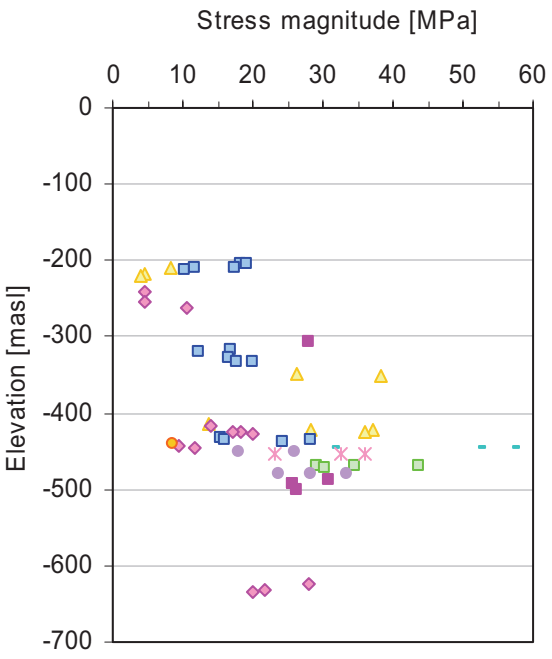

Intermediate principal stress, σ_2

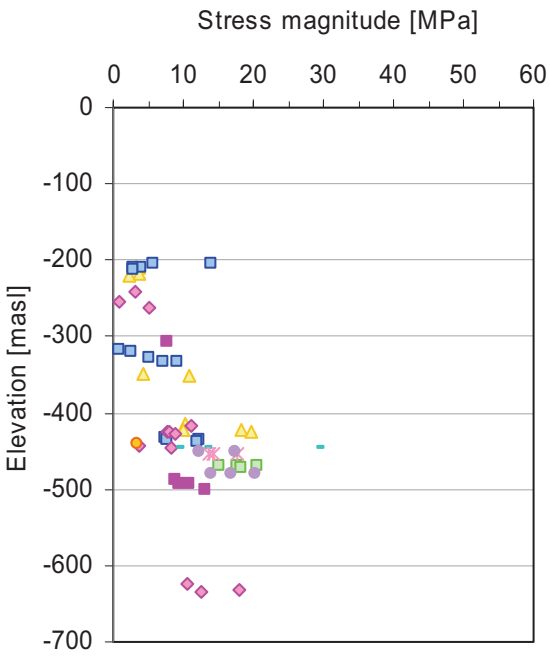

Minimum principal stress, σ_3

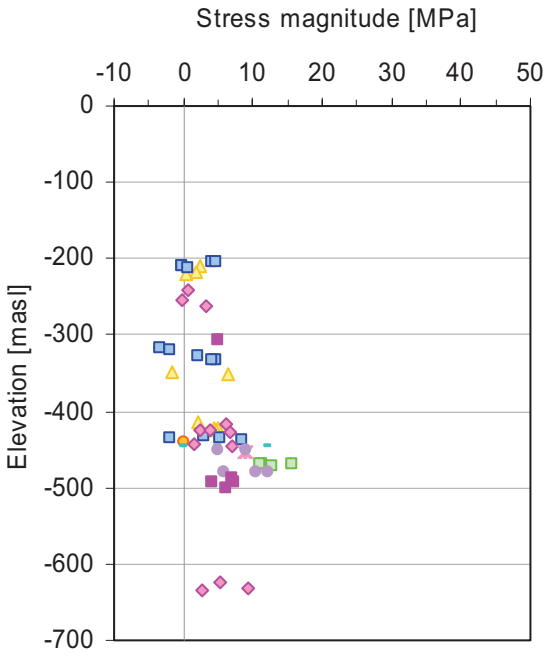

All overcoring data – Mean principal stress

Mean principal stress magnitude

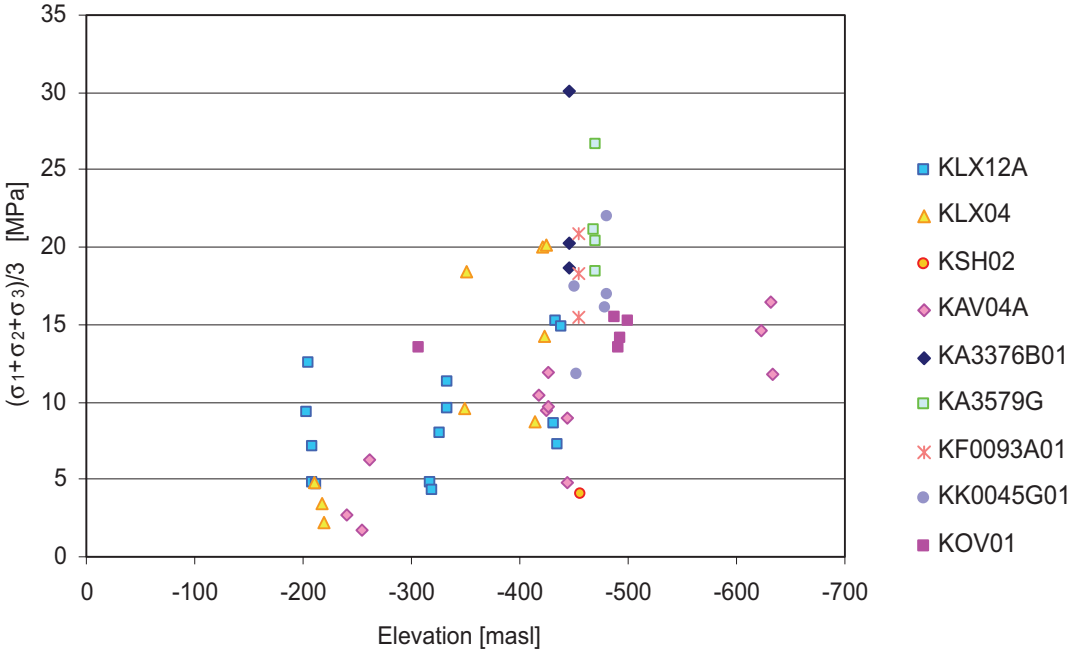

All overcoring data – Stress ratios

Principal stress magnitude ratio, σ_1/σ_2

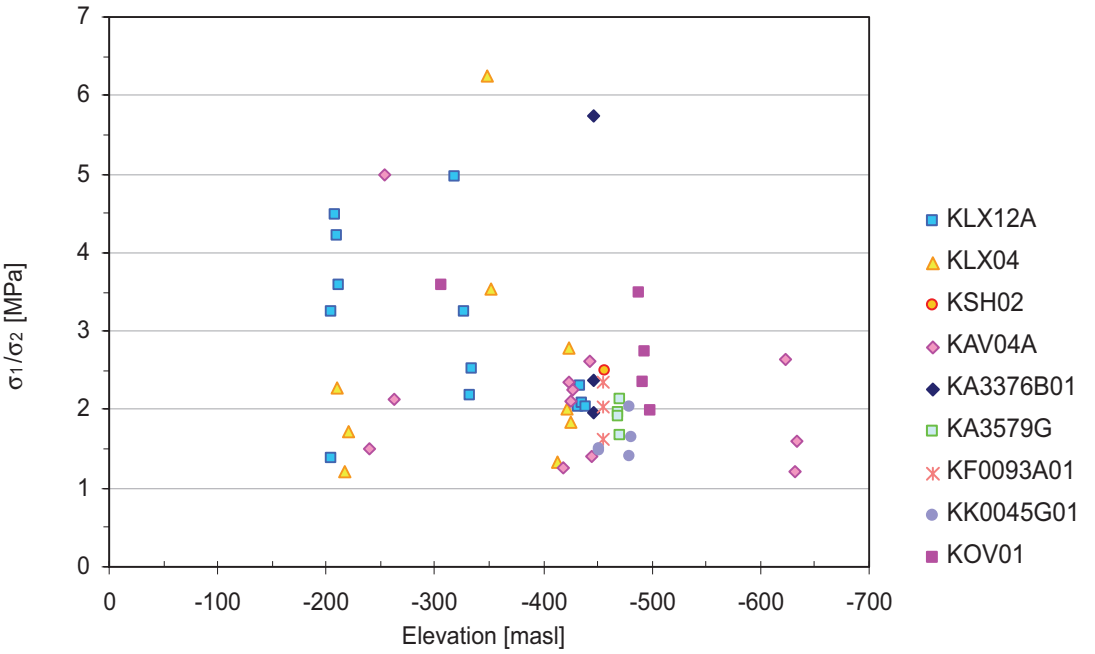

Principal stress magnitude ratio, σ_1/σ_3

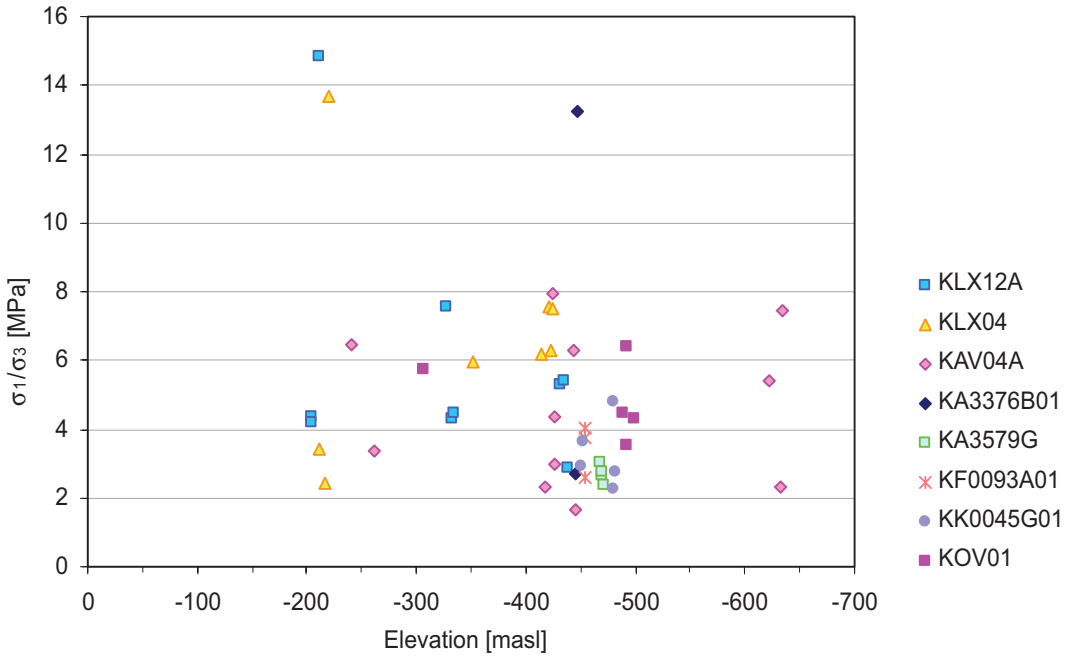

Ratio between maximum and minimum horizontal stress, σ_H/σ_h

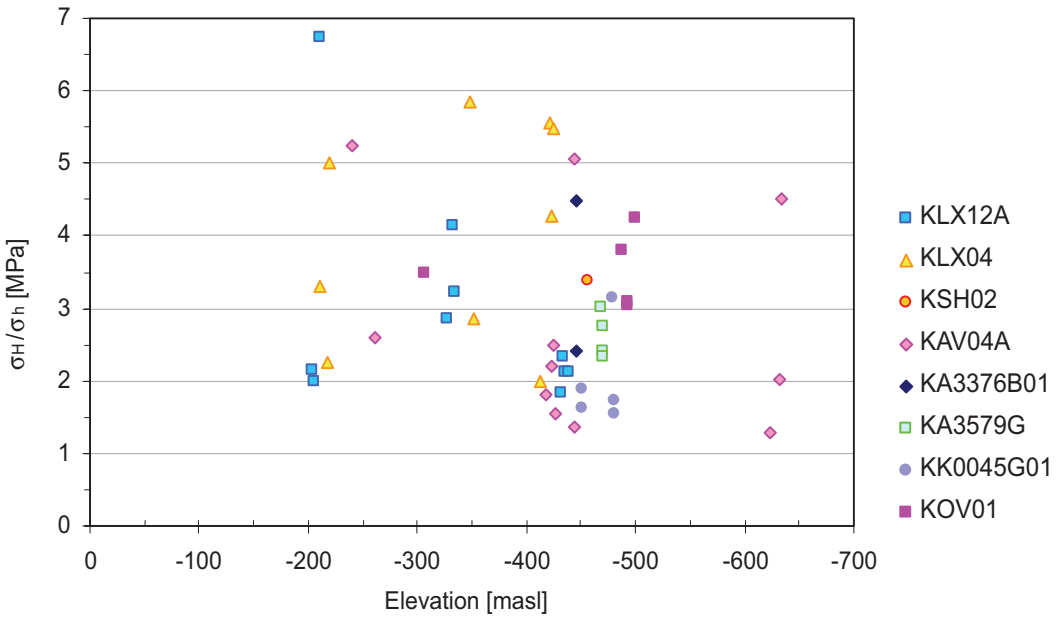

Ratio between maximum horizontal and vertical stress, σ_H/σ_v

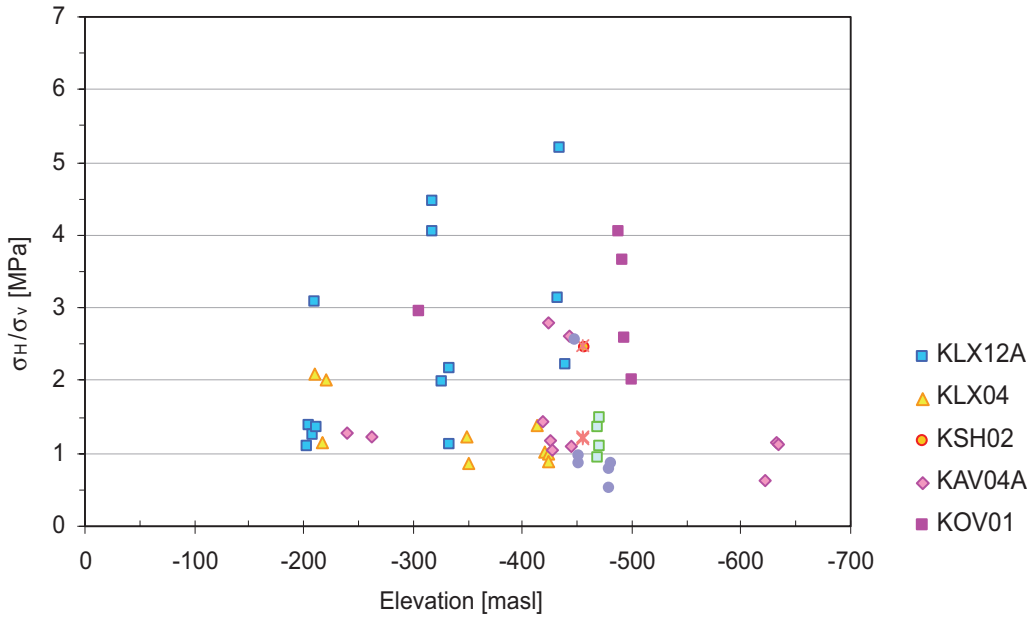

All Hydraulic stress measurement data (HF and HTPF) – Horizontal components

Maximum horizontal stress, σ_H

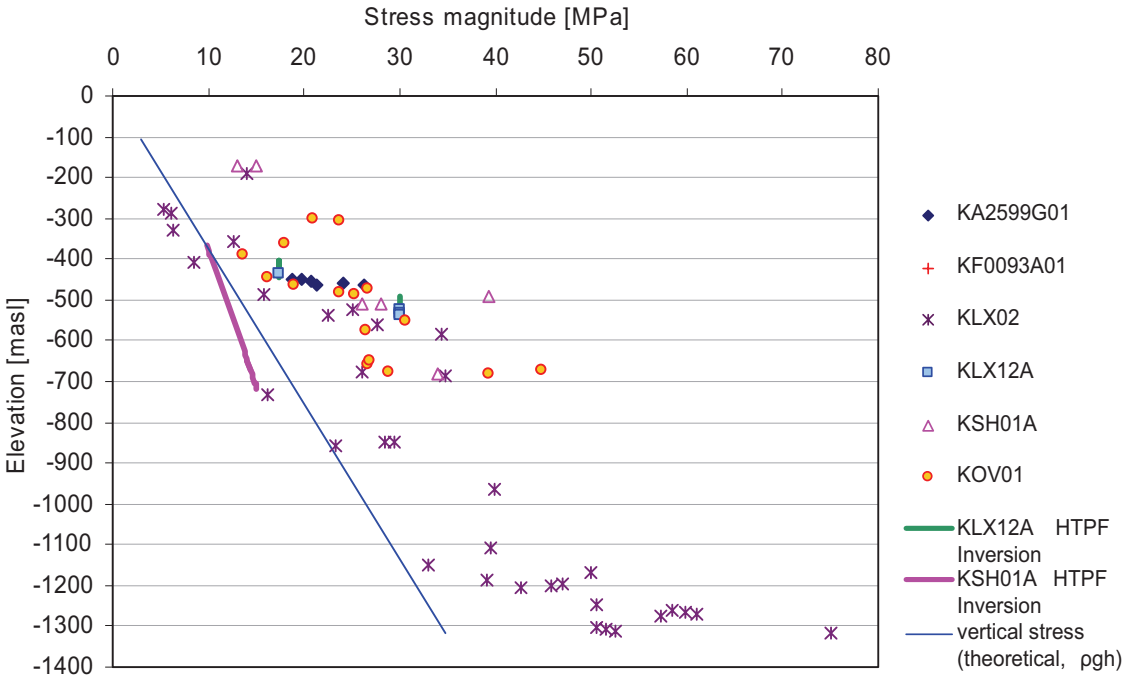

Minimum horizontal stress, σ_h

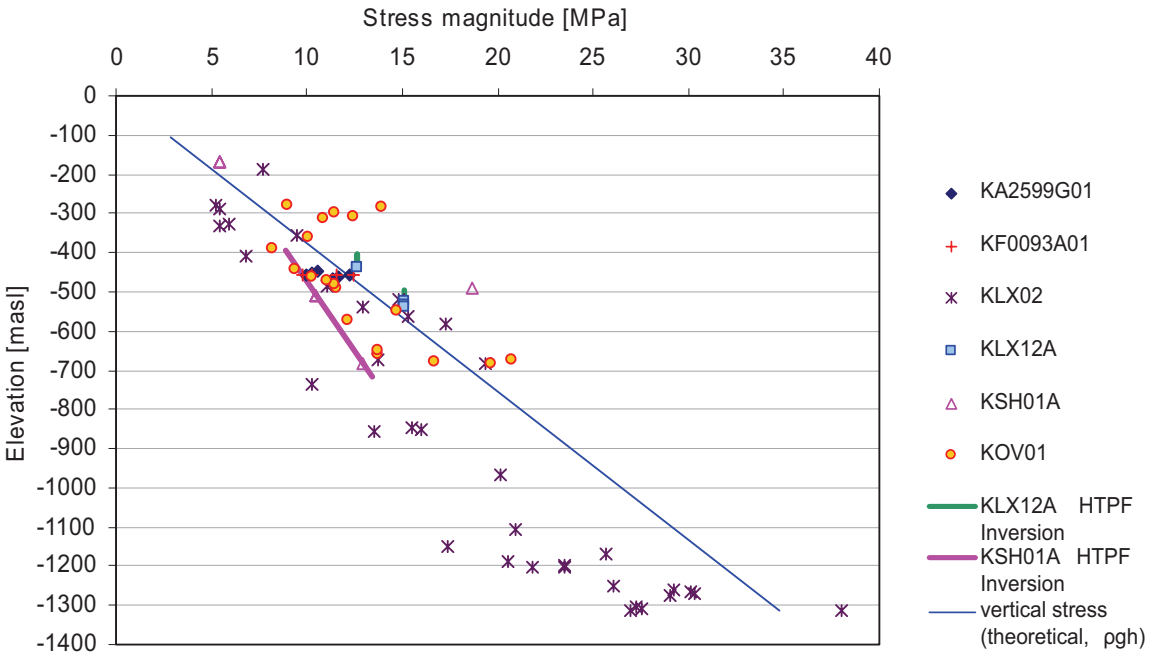

All Hydraulic stress measurement data (HF and HTPF) – Orientation of σ_H

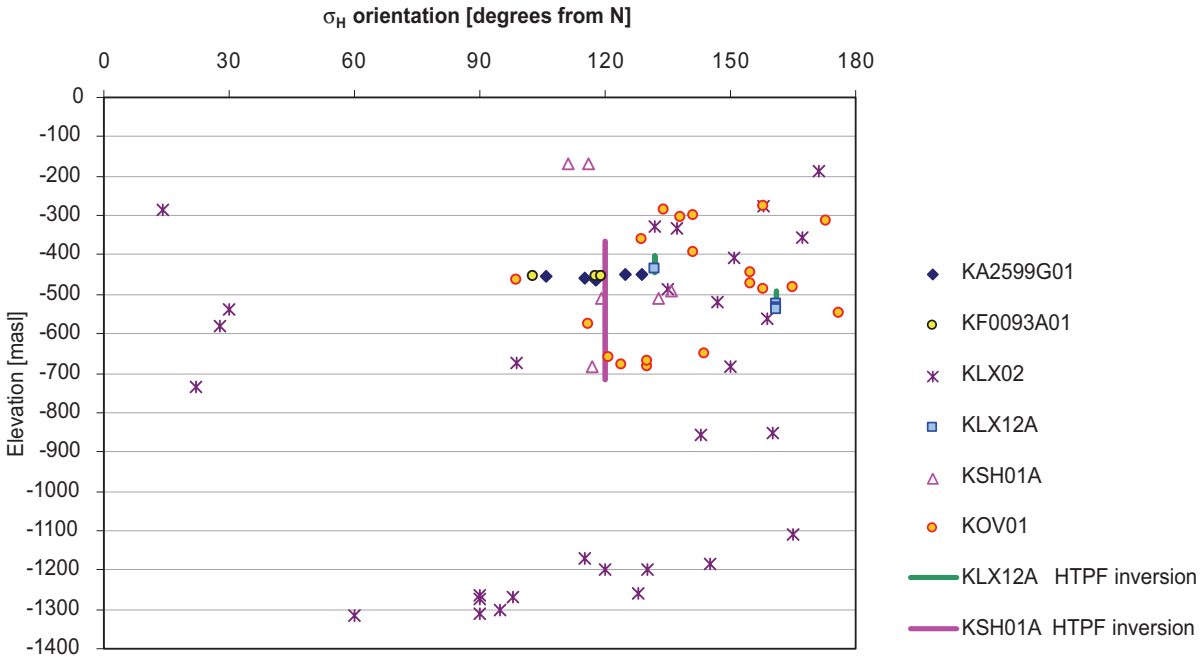

Laxemar: KLX04 and KLX12A

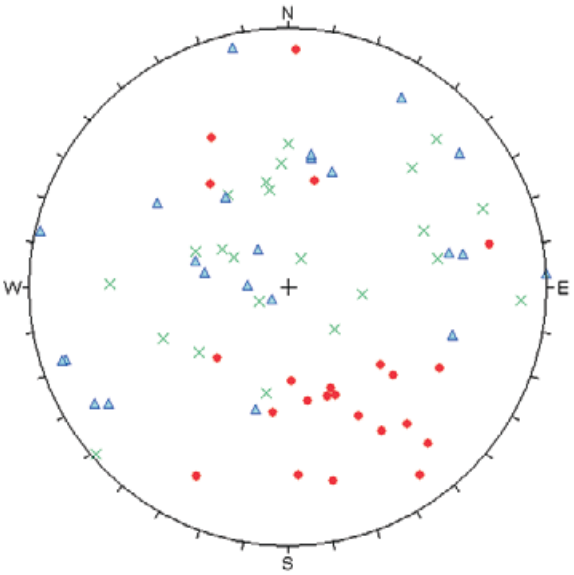

Äspö: KA3376B01, KA3579G, KF0093A01 and KK0045G01

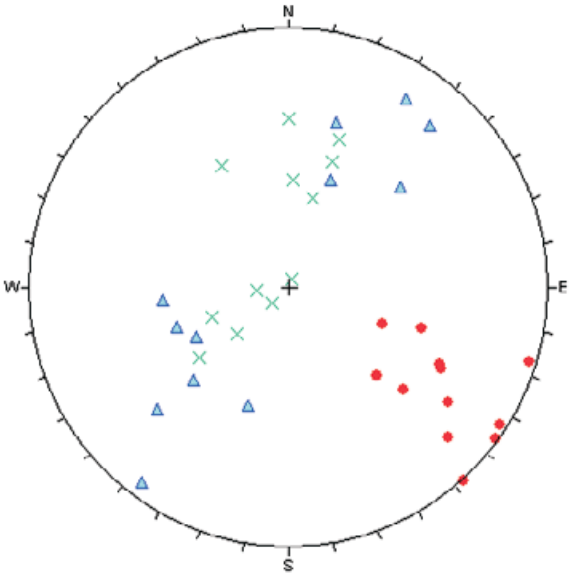

Simpevarp: KAV04A, KSH02

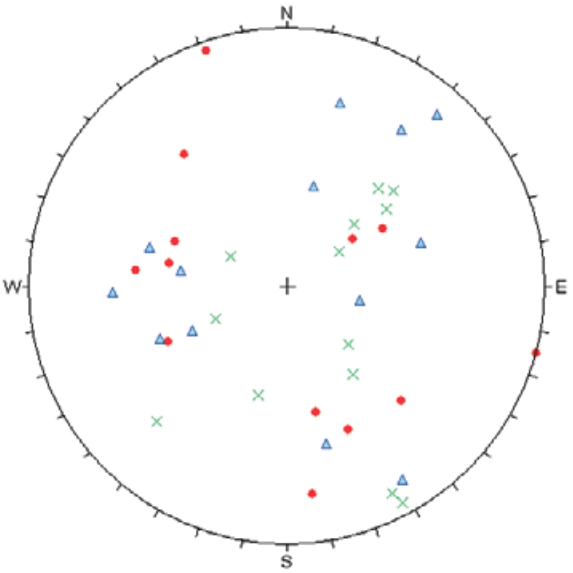

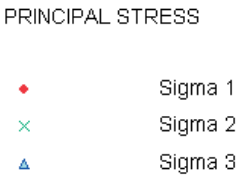

Appendix 7

Numerical modelling results

Numerical modelling results (3DEC) for Model cases 1–9 (see Section 6.3) are presented in this appendix. The aim of these calculations is to estimate the potential spatial difference in stress field to be expected inside Laxemar local model volume, due to the major deformation zones. The mechanical properties are varied between cases since the actual mechanical properties are uncertain.

Notes:

- See Table 6-4 and Table 6-5 of the main report for properties assigned to Model cases 1–9. The same geometry (extent strike and dip) for deformation zones is assumed in all models.
- The results from the different Model cases have been taken out from each model along vertical lines, having a zone roughly every 50–100 m from ground surface down to 1,000 m depth, at the same locations as some of the boreholes at Laxemar (KLX02, KLX03, KLX04, KLX11A and KLX12A) and in the Simpevarp area (KAV04A, KSH01A and KSH02) and at a scanline going through the Äspö hard rock laboratory (scanline denoted "Äspö") (See Figure 6-3). The inclination of the boreholes has not been taken into account, but is insignificant to inferences made.
- Figure 1 a)–c) shows the modelled zones and their names at three different elevations; top of the model (0 masl), –400 masl and –600 masl.
- Figure 2 a) shows the model representation of the SDM Site Laxemar deformation zone model and the locations of the points in the 3DEC model where the stress data has been collected (several points from elevation 0 masl to –1,000 masl), the locations can be compared with the boreholes in Figure 1-3. In Figure 2 b) and c) the points locations towards the depth is shown.
- Note that the legends for stress plots at the levels –400 masl and –600 masl are the same for the same Model case, but they can differ between different Model cases.
- At the end of the appendix, the stresses (σ_1, σ_2 and σ_3 magnitudes) for all Model cases (1–9) together are plotted for each "borehole" location, respectively.

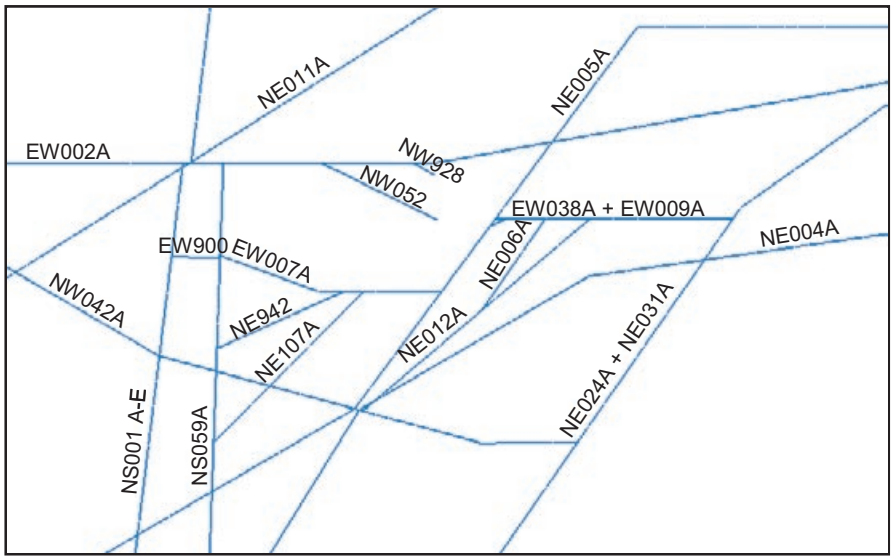

1 a) Deformation zones at the top of the model (elevation = 0 masl)

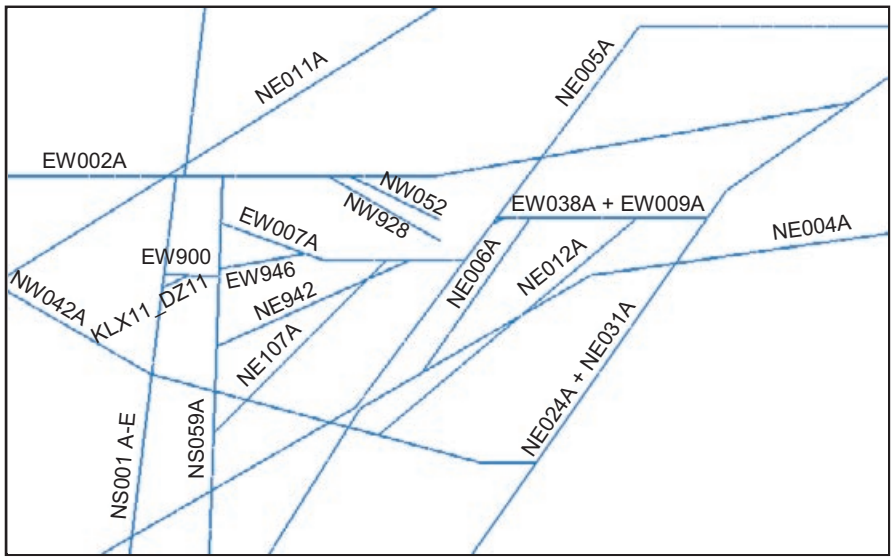

1 b) Deformation zones at elevation -400 masl.

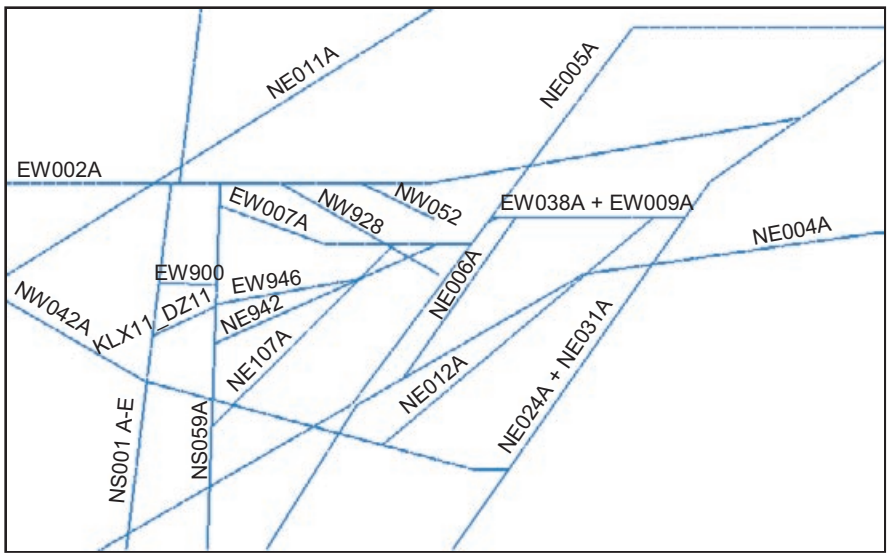

1 c) Deformation zones at elevation -600 masl

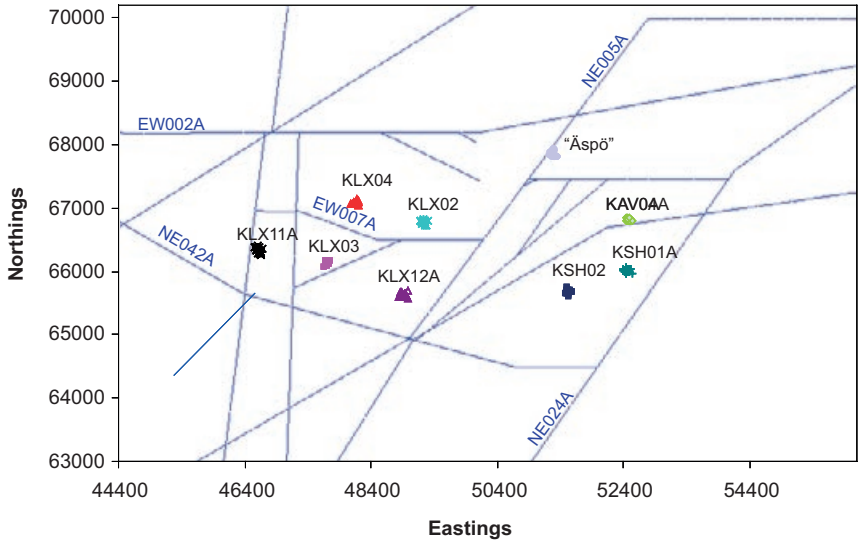

2 a) Shows the location (in the 3DEC model) of the modelled deformation zones and the fictitious boreholes (the scanlines where the stress data was collected). There are several points for every scanline from elevation 0 masl to -1000 masl.

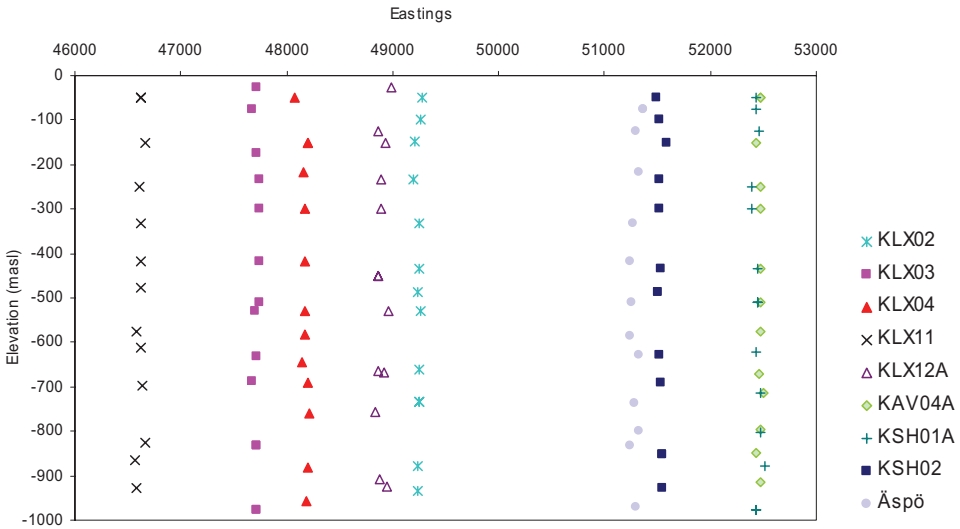

2 b) Shows for the different scanlines what eastings and elevation coordinate the stress data was collected from.

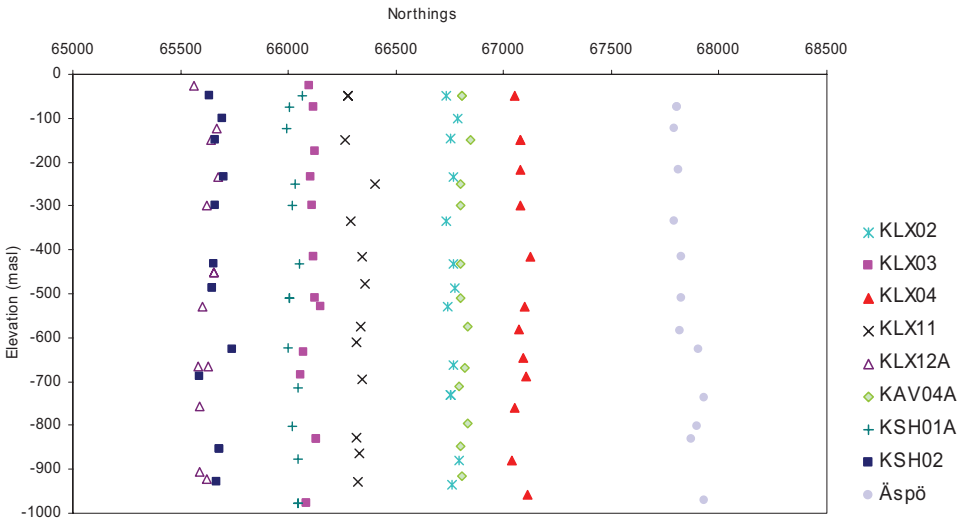

2 c) Shows for the different scanlines what northings and elevation coordinate the stress data was collected from.

Model 1

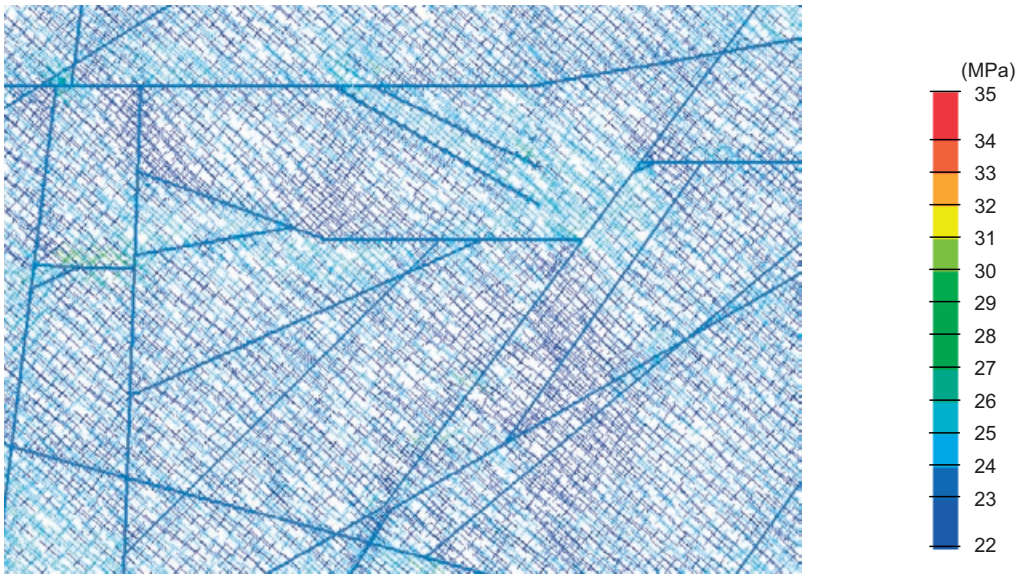

Model 1 a) Principal stress plot coloured by σ_1 – Elevation = -400 masl

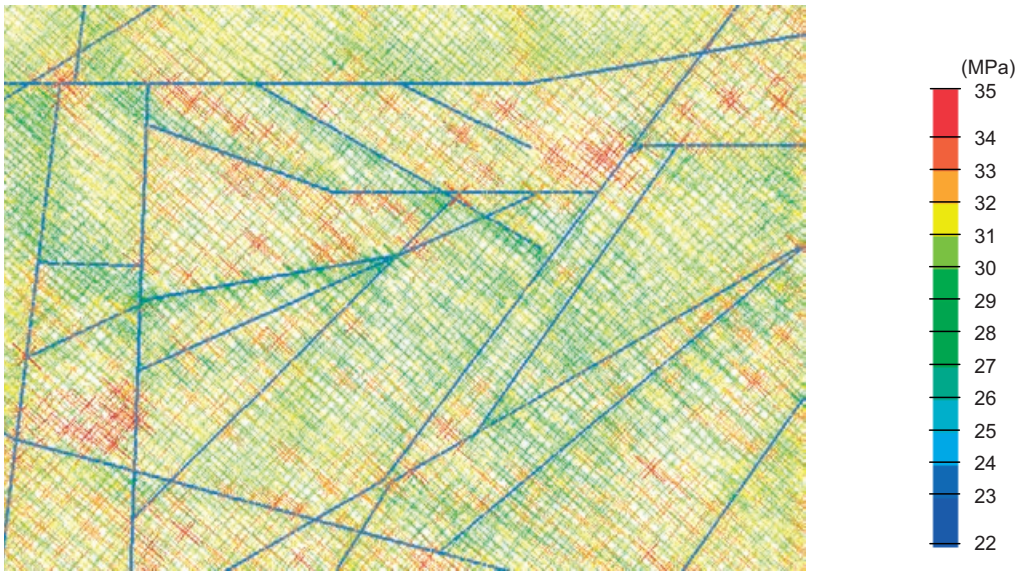

Model 1 b) Principal stress plot coloured by σ_1 – Elevation = -600 masl

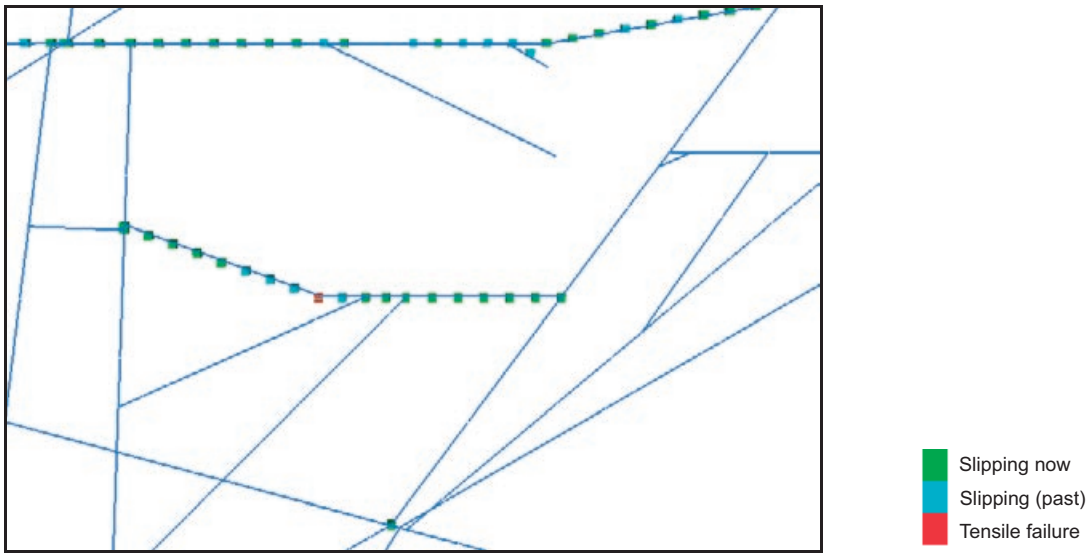

Model 1 c) Joint slip – Elevation = 0 masl

Model 1

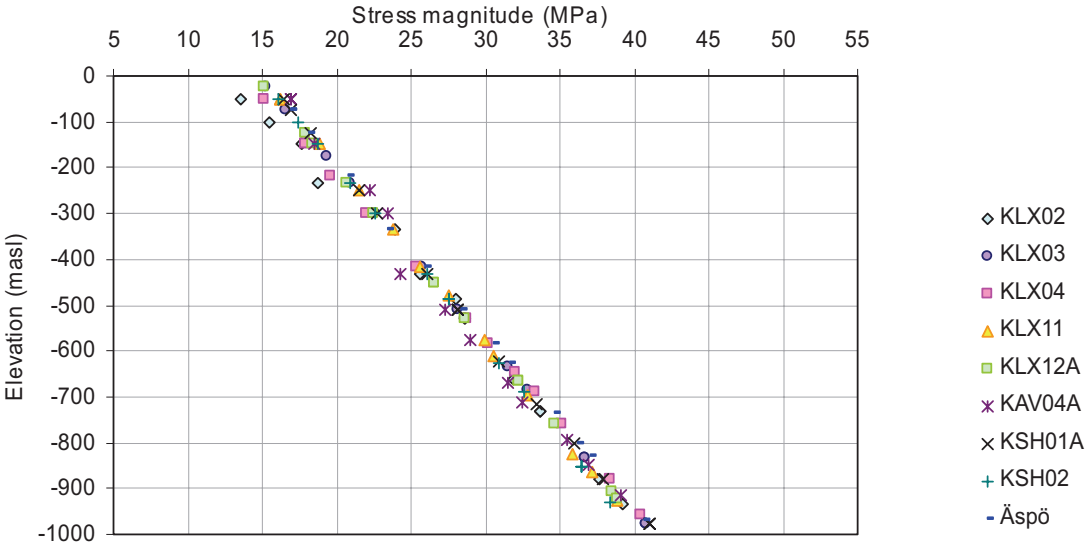

Model 1 d) Stress magnitude plot showing how σ_1 varies with elevation in different boreholes.

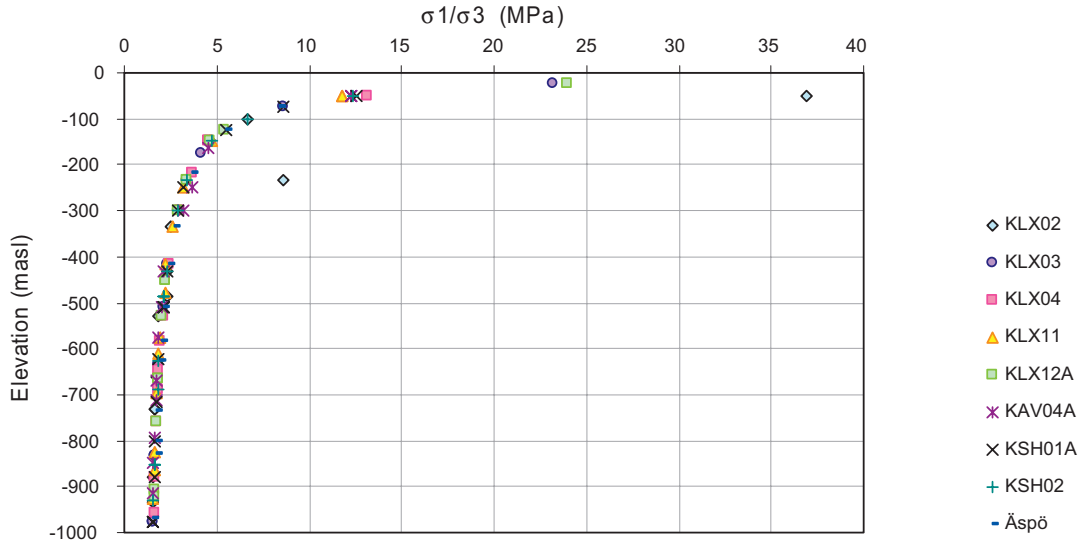

Model 1 e) Plot showing how σ_1/σ_3 varies with elevation in different boreholes

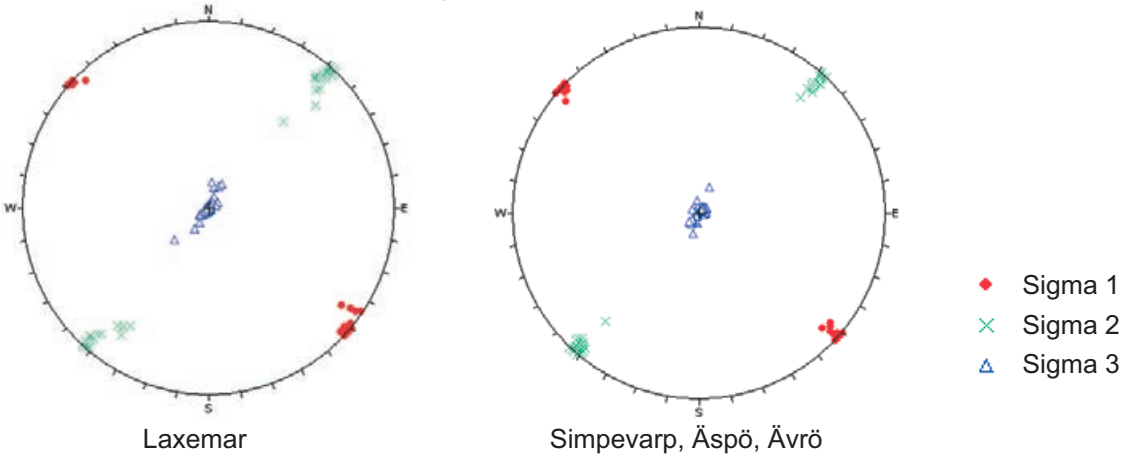

Model 1 f) Pole plots showing the simulated principal stress orientations for Model 1. The left plot shows the results from the Laxemar "boreholes"; KLX02, KLX03, KLX04, KLX11 and KLX12A and the right plot shows the results for the "boreholes" in Simpevarp, Äspö and Ävrö; KSH01A, KSH02, "Äspö", KAV04A.

Model 2

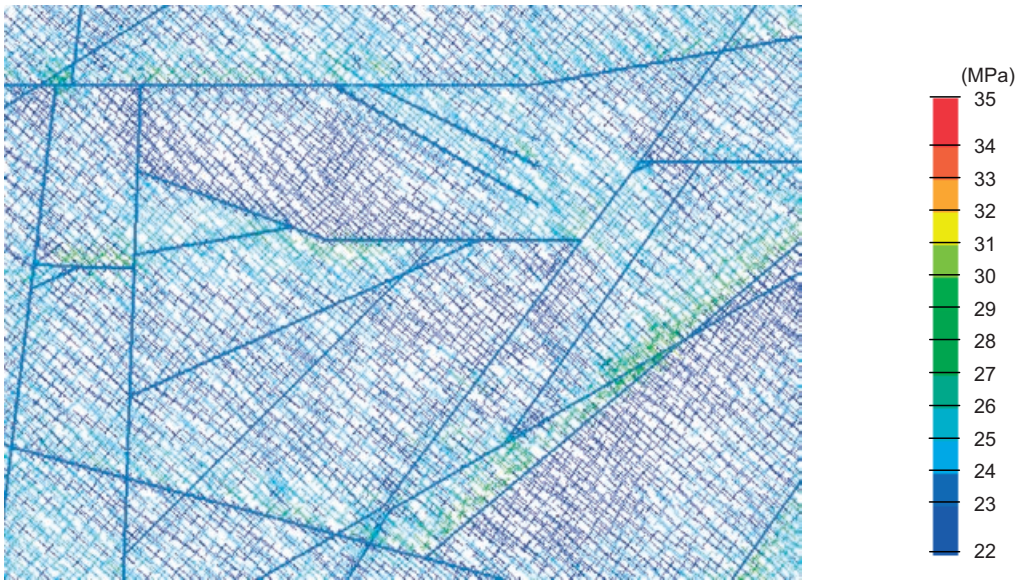

Model 2 a) Principal stress plot coloured by σ_1 – Elevation = -400 masl

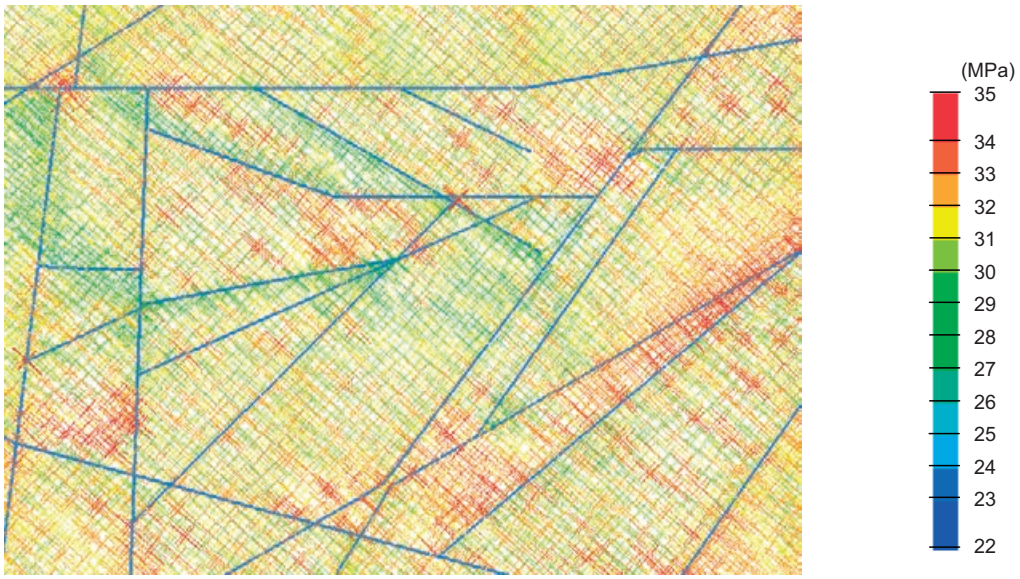

Model 2 b) Principal stress plot coloured by σ_1 – Elevation = -600 masl

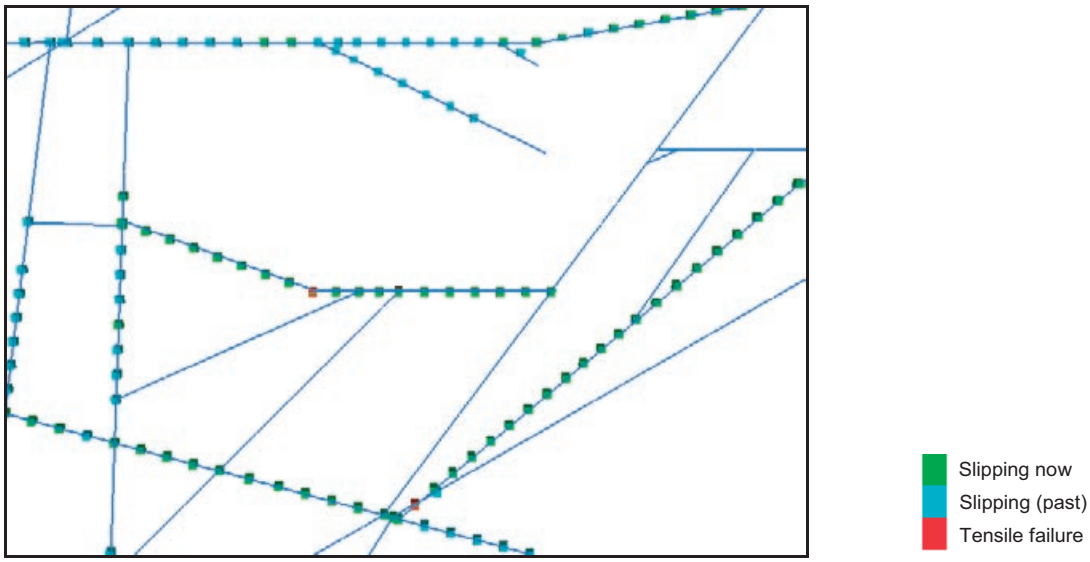

Model 2 c) Joint slip – Elevation = 0 masl

Model 2

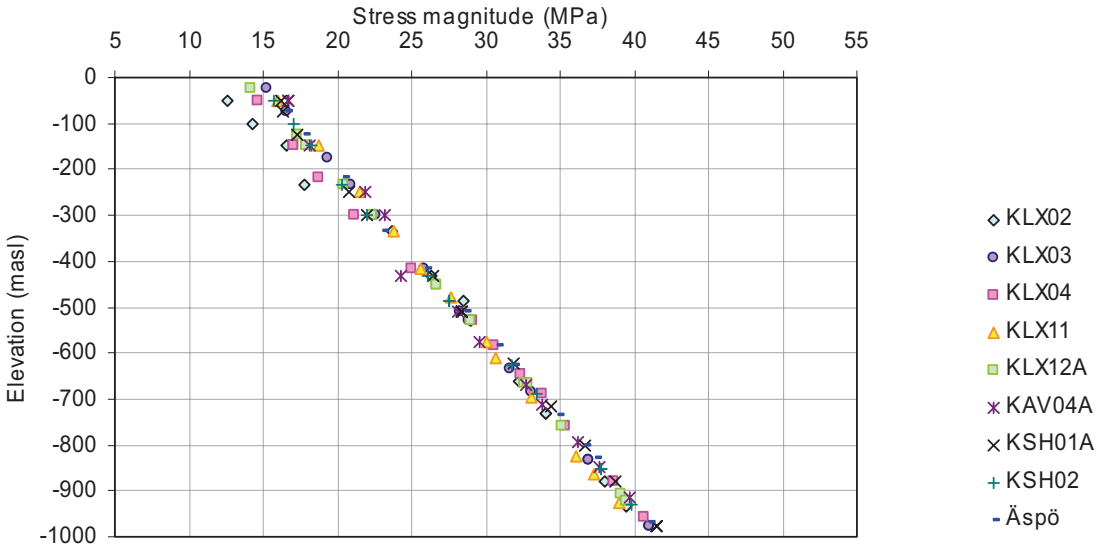

Model 2 d) Stress magnitude plot showing how σ_1 varies with elevation in different boreholes.

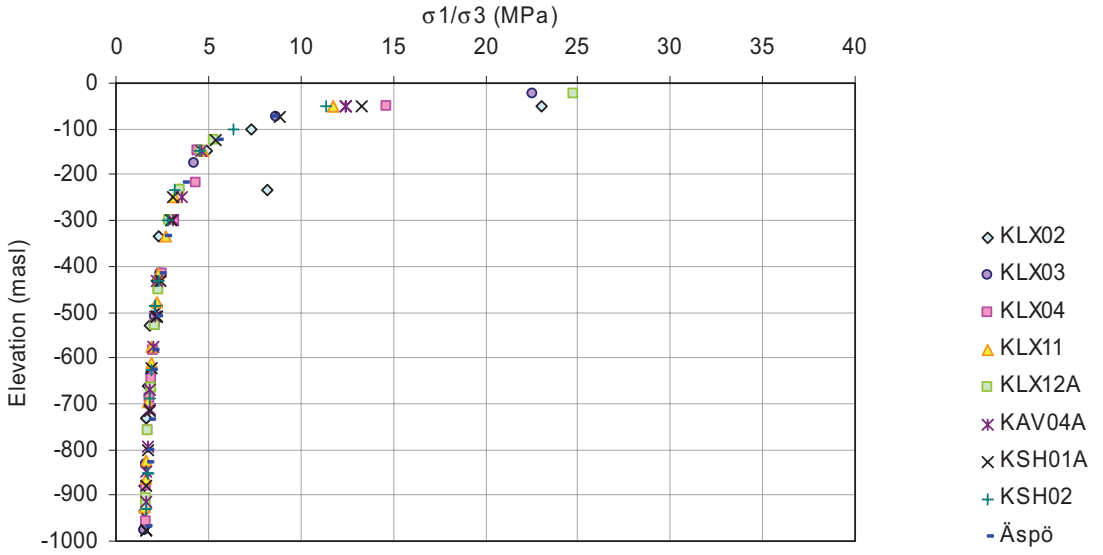

Model 2 e) Plot showing how the σ_1/σ_3 varies with elevation in different boreholes

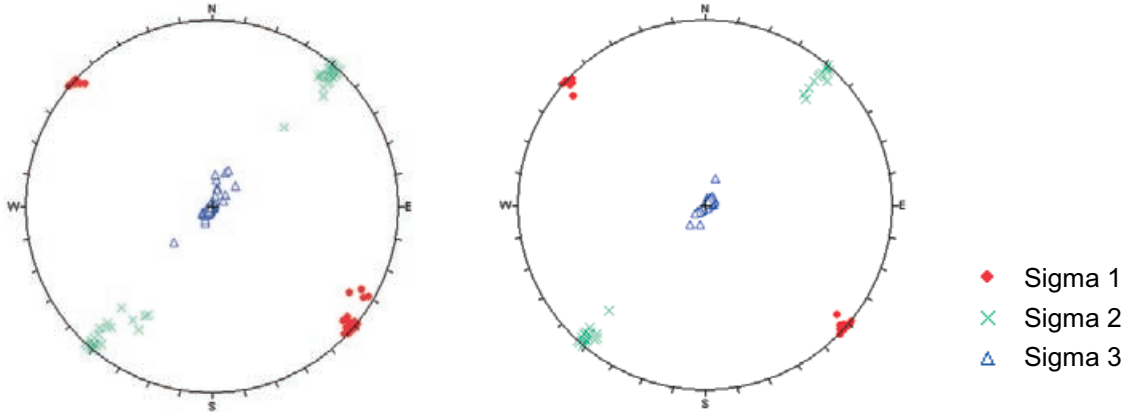

Laxemar *Simpevarp, Äspö, Ävrö*

Model 2 f) Pole plots showing the simulated principal stress orientations for Model 2. The left plot shows the results from the Laxemar boreholes; KLX02, KLX03, KLX04, KLX11 and KLX12A and the right plot shows the results for the boreholes in Simpevarp, Äspö and Ävrö; KSH01A, KSH02, "Äspö", KAV04A.

Model 3

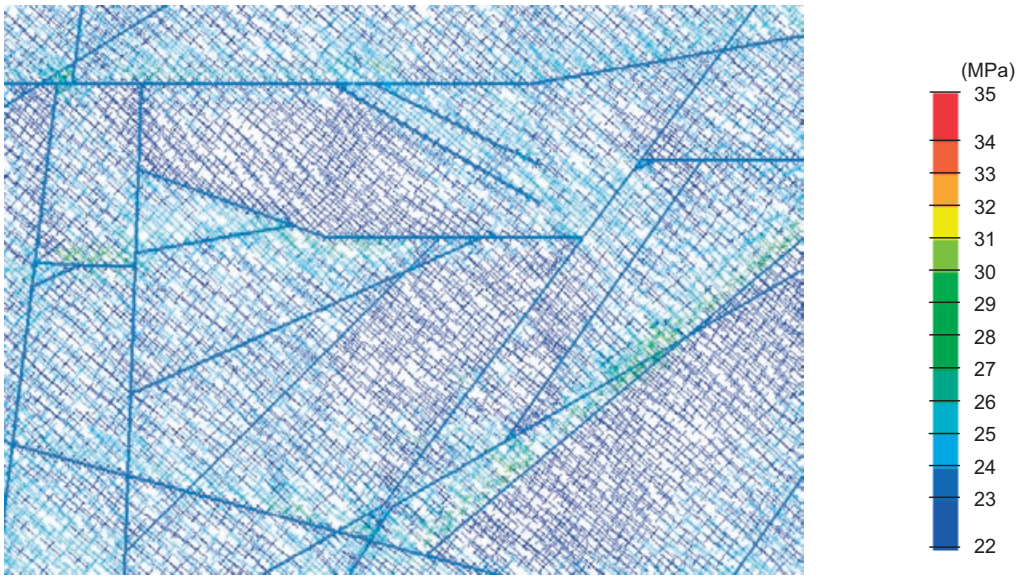

Model 3 a) Principal stress plot coloured by σ_1 – Elevation = -400 masl

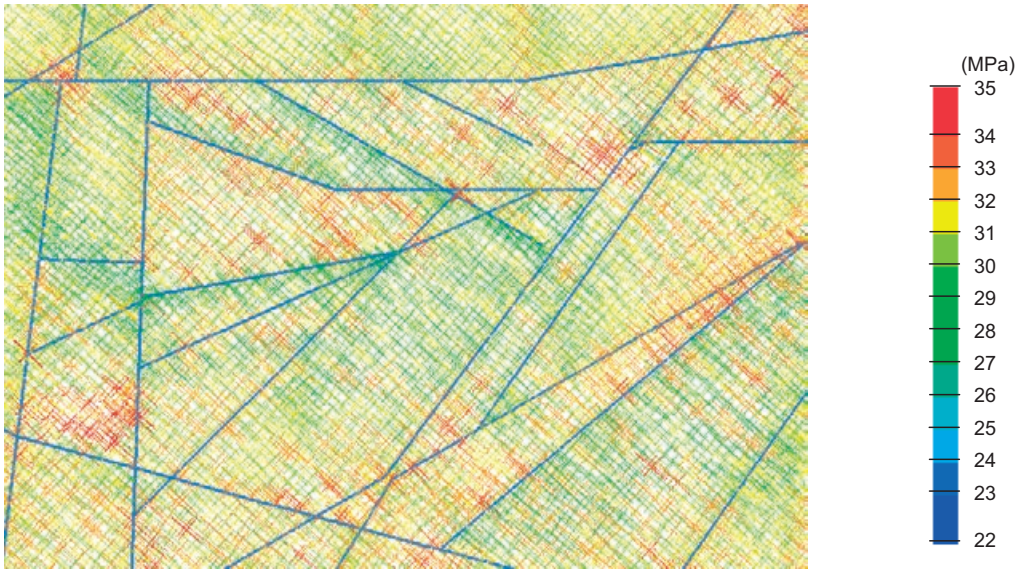

Model 3 b) Principal stress plot coloured by σ_1 – Elevation = -600 masl

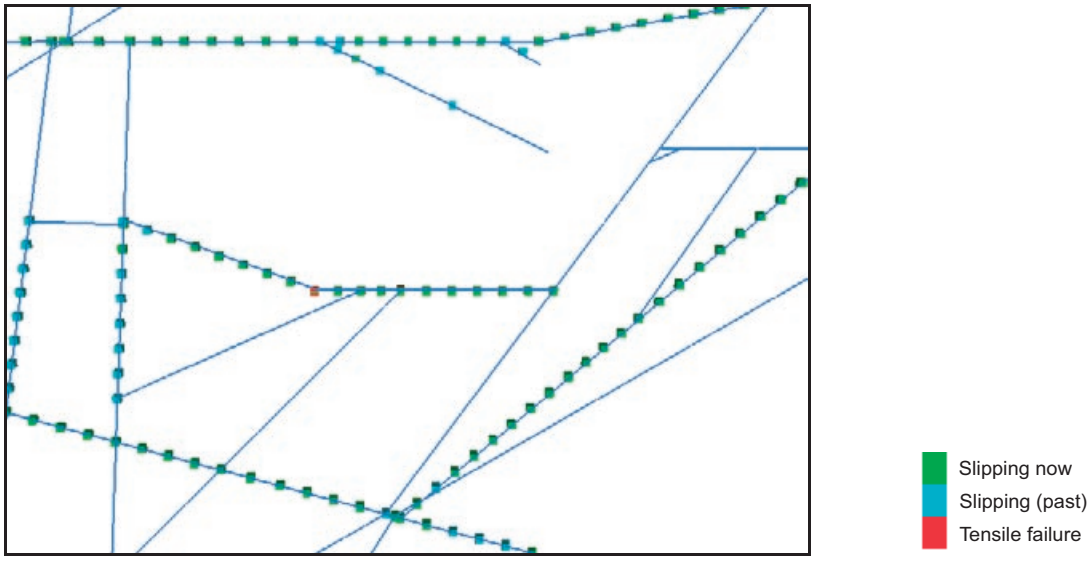

Model 3 c) Joint slip – Elevation = 0 masl

Model 3

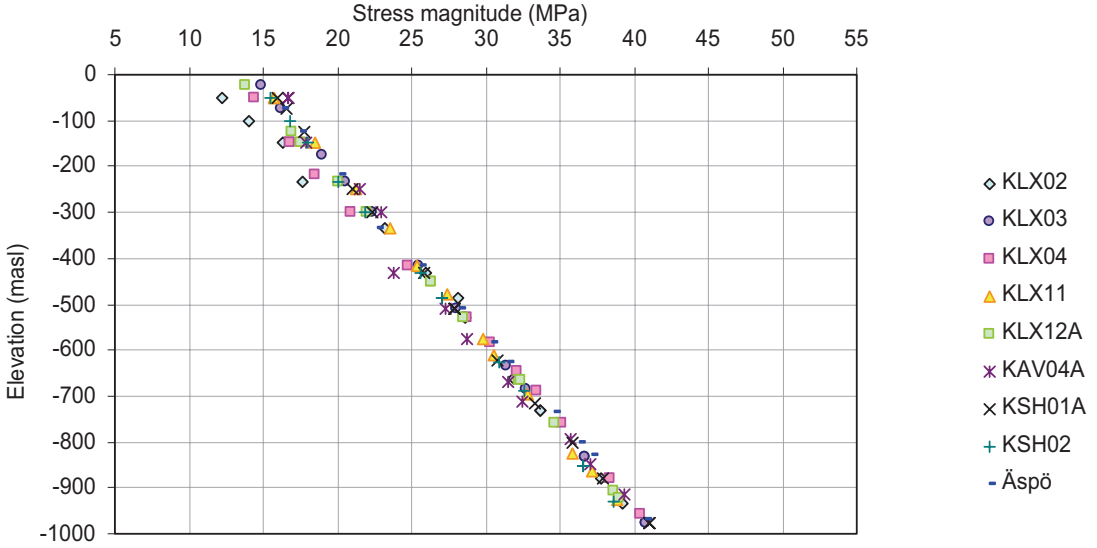

Model 3 d) Stress magnitude plot showing how σ_1 varies with elevation in different boreholes.

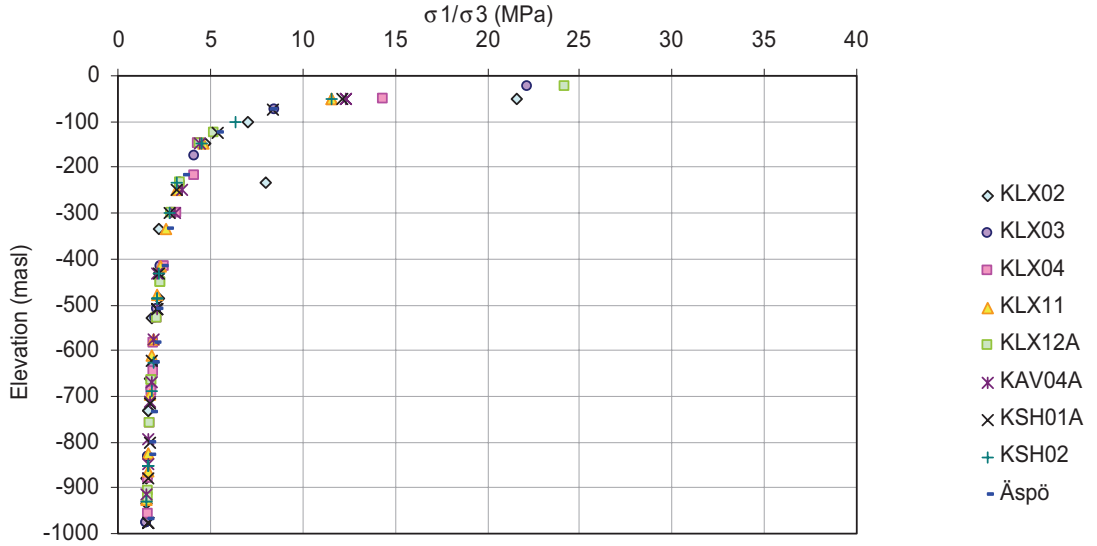

Model 3 e) Plot showing how the σ_1/σ_3 varies with elevation in different boreholes

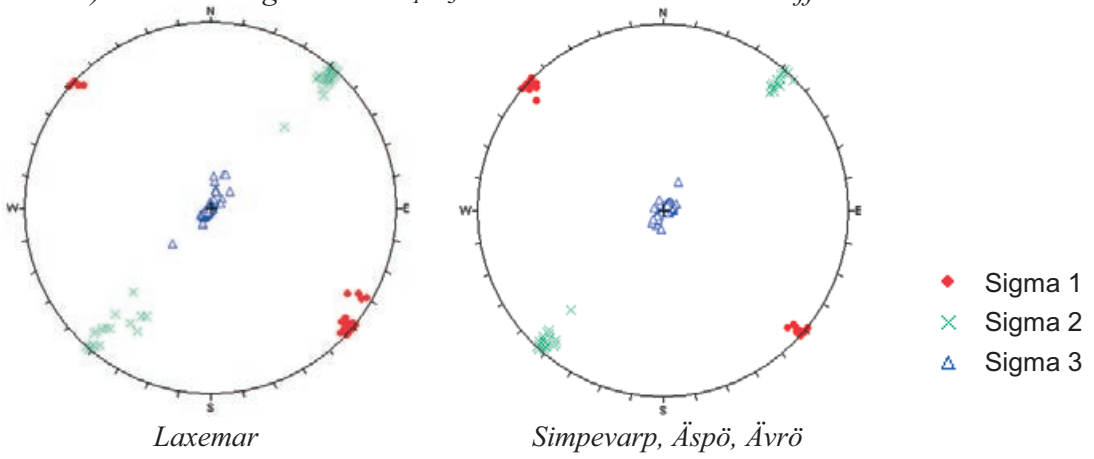

Laxemar *Simpevarp, Äspö, Ävrö*

Model 3 f) Pole plots showing the simulated principal stress orientations for Model 3. The left plot shows the results from the Laxemar boreholes; KLX02, KLX03, KLX04, KLX11 and KLX12A and the right plot shows the results for the boreholes in Simpevarp, Äspö and Ävrö; KSH01A, KSH02, "Äspö", KAV04A.

Model 4

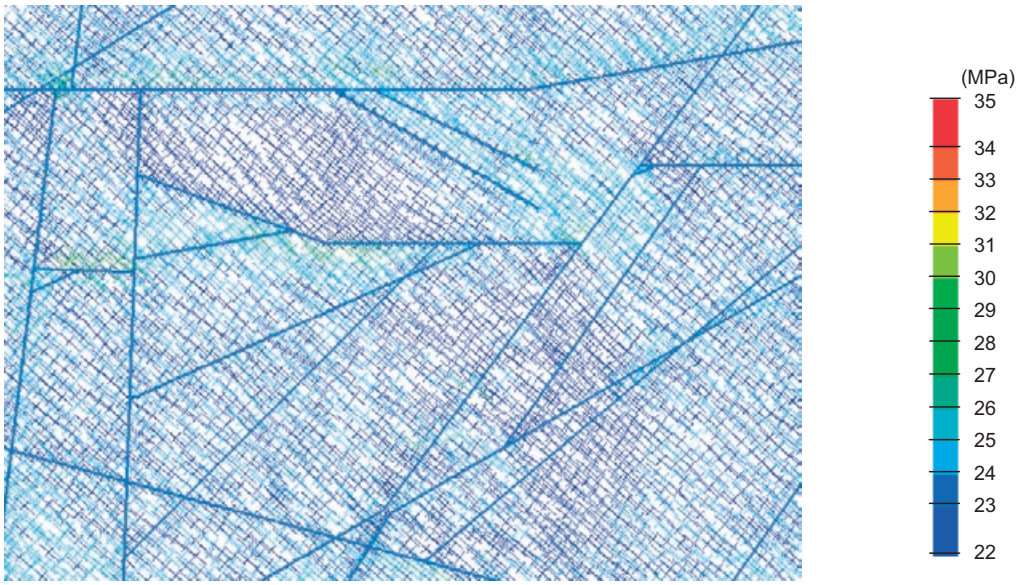

Model 4 a) Principal stress plot coloured by σ_1 – Elevation = -400 masl

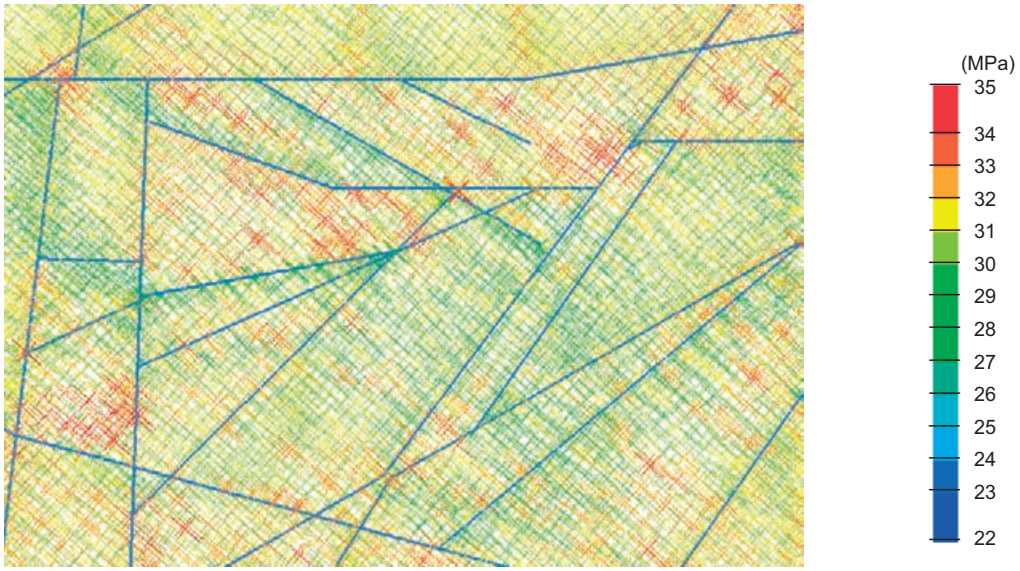

Model 4 b) Principal stress plot coloured by σ_1– Elevation = -600 masl

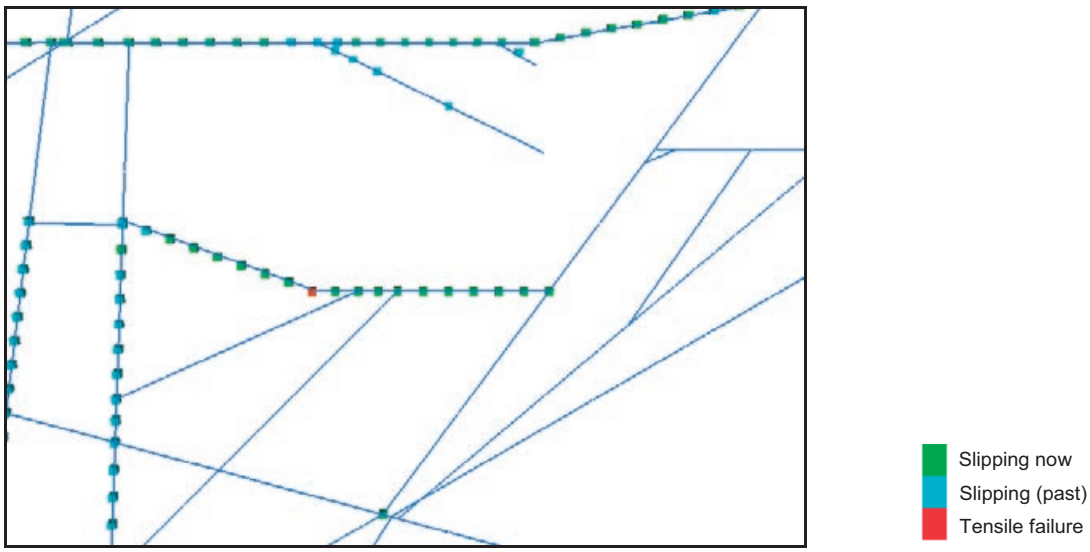

Model 4 c) Joint slip – Elevation = 0 masl

Model 4

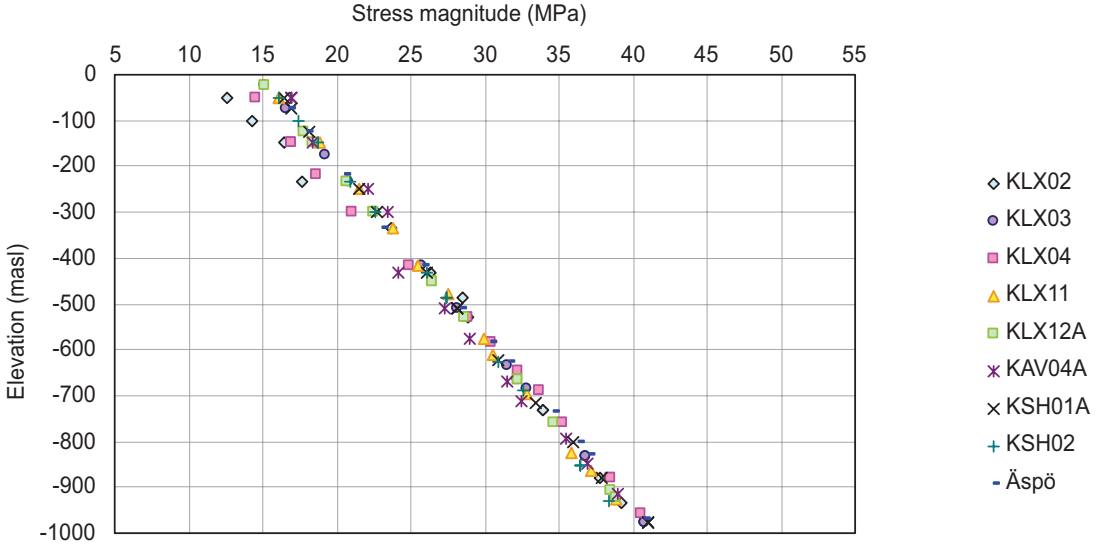

Model 4 d) Stress magnitude plot showing how σ_1 varies with elevation in different boreholes.

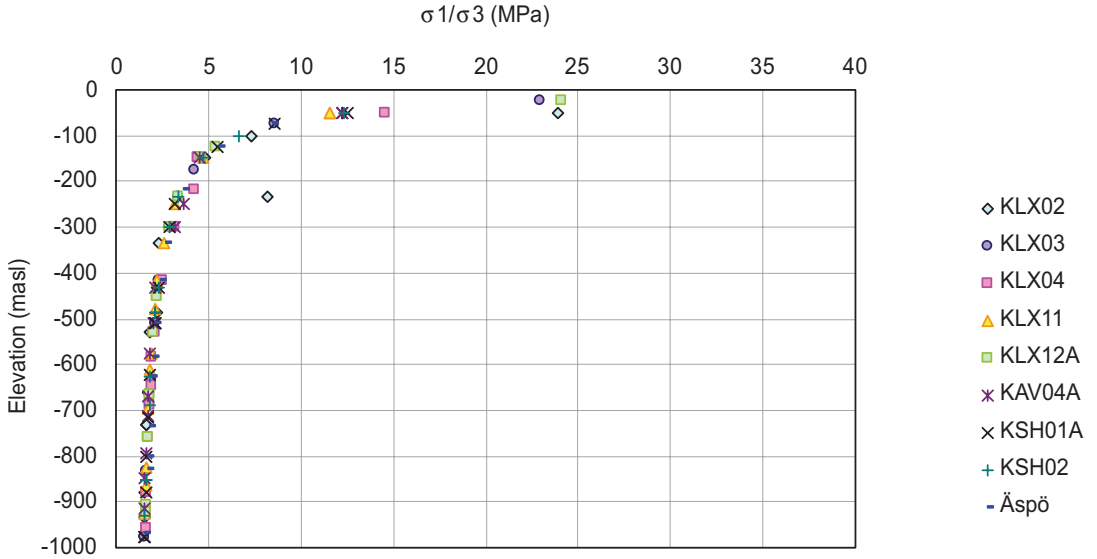

Model 4 e) Plot showing how the σ_1/σ_3 varies with elevation in different boreholes

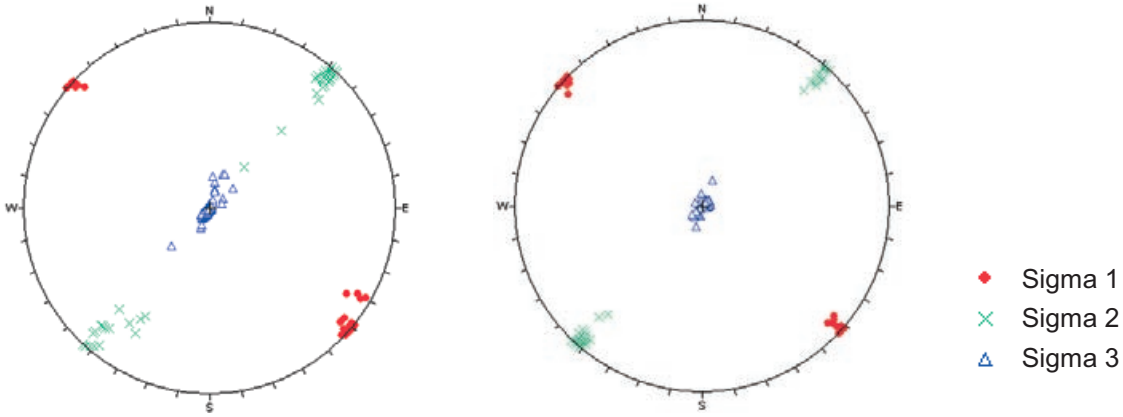

Laxemar *Simpevarp, Äspö, Ävrö*

Model 4 f) Pole plots showing the simulated principal stress orientations for Model 4. The left plot shows the results from the Laxemar boreholes; KLX02, KLX03, KLX04, KLX11 and KLX12A and the right plot shows the results for the boreholes in Simpevarp, Äspö and Ävrö; KSH01A, KSH02, "Äspö", KAV04A.

Model 5

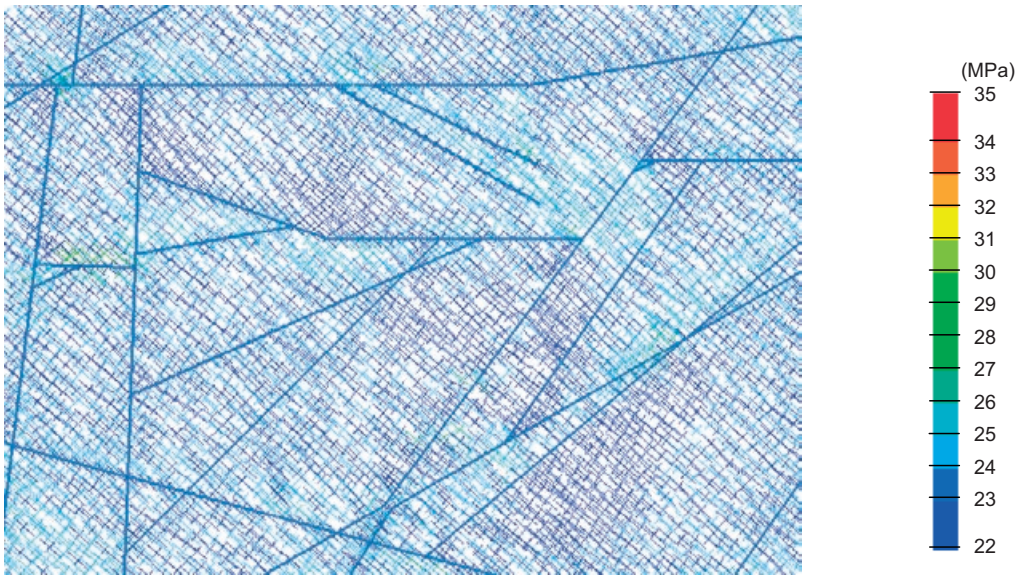

Model 5 a) Principal stress plot coloured by σ_1 – Elevation = -400 masl

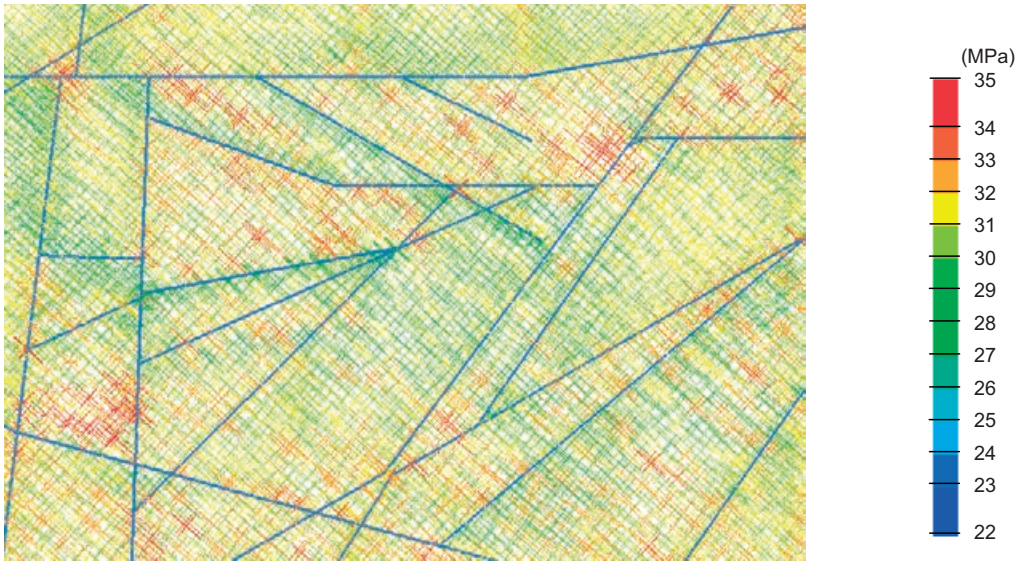

Model 5 b) Principal stress plot coloured by σ_1 – Elevation = -600 masl

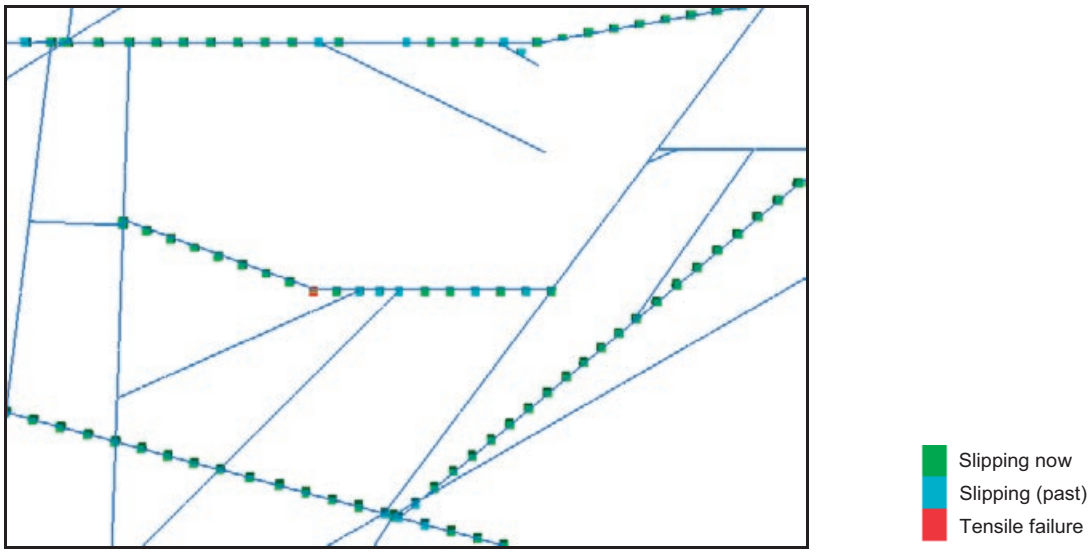

Model 5 c) Joint slip – Elevation = 0 masl

Model 5

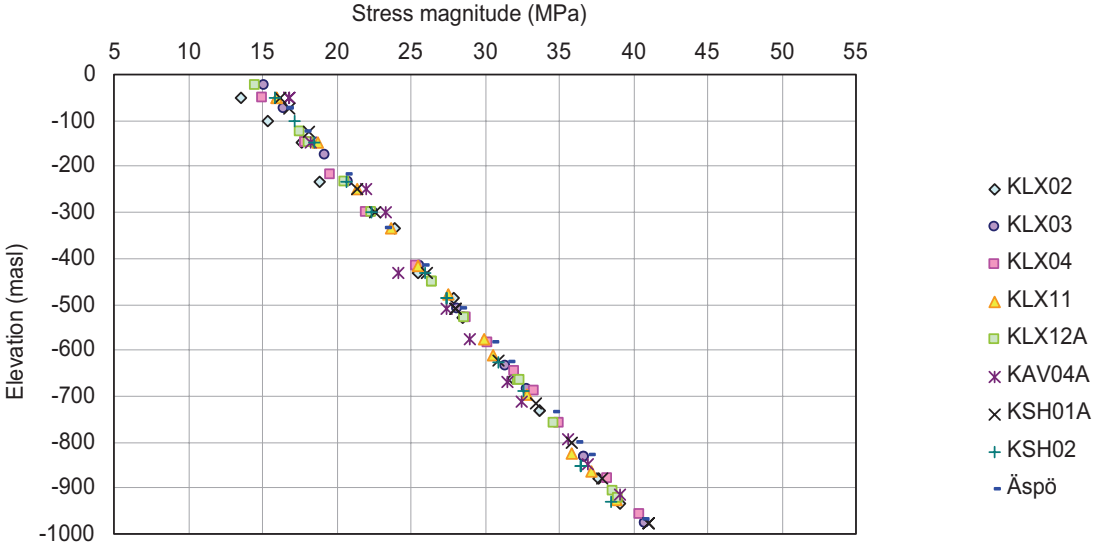

Model 5 d) Stress magnitude plot showing how σ_1 varies with elevation in different boreholes.

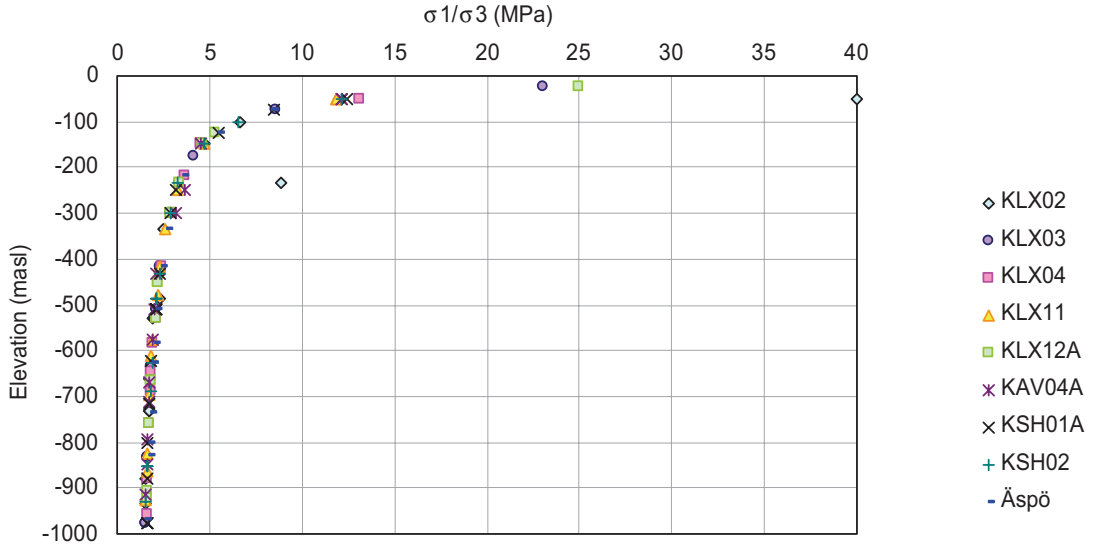

Model 5 e) Plot showing how the σ_1/σ_3 varies with elevation in different boreholes

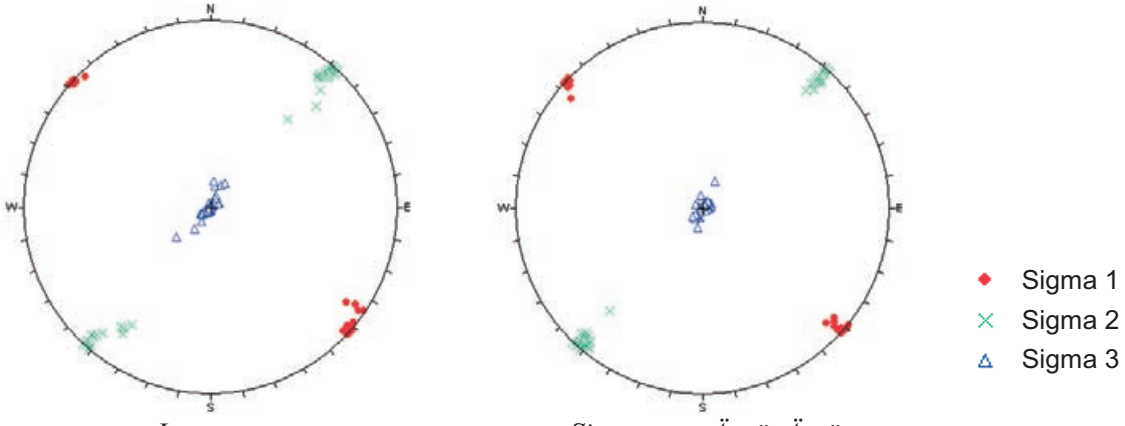

Laxemar *Simpevarp, Äspö, Ävrö*

Model 5 f) Pole plots showing the simulated principal stress orientations for Model 5. The left plot shows the results from the Laxemar boreholes; KLX02, KLX03, KLX04, KLX11 and KLX12A and the right plot shows the results for the boreholes in Simpevarp, Äspö and Ävrö; KSH01A, KSH02, "Äspö", KAV04A.

Model 6

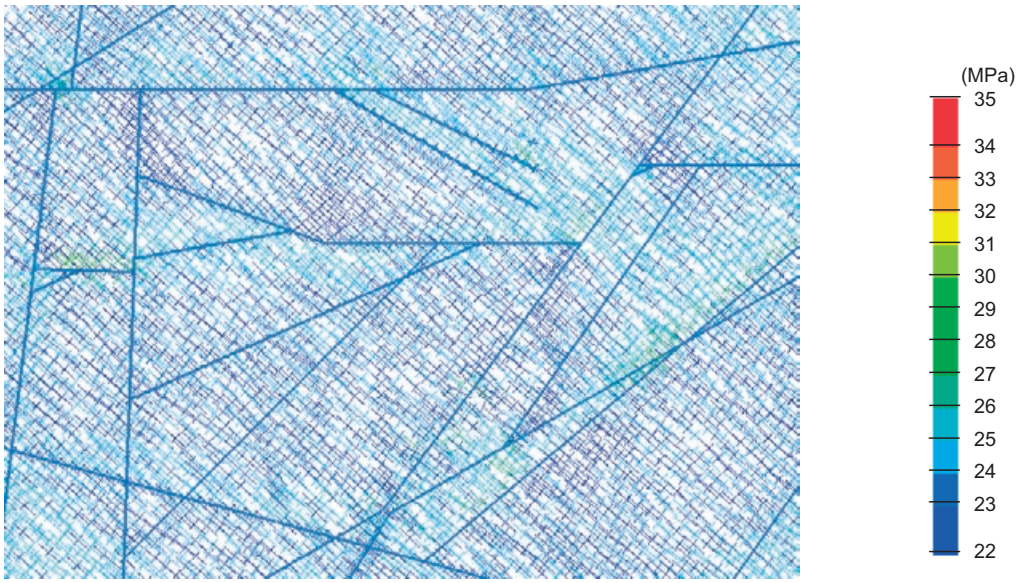

Model 6 a) Principal stress plot coloured by σ_1 – Elevation = -400 masl

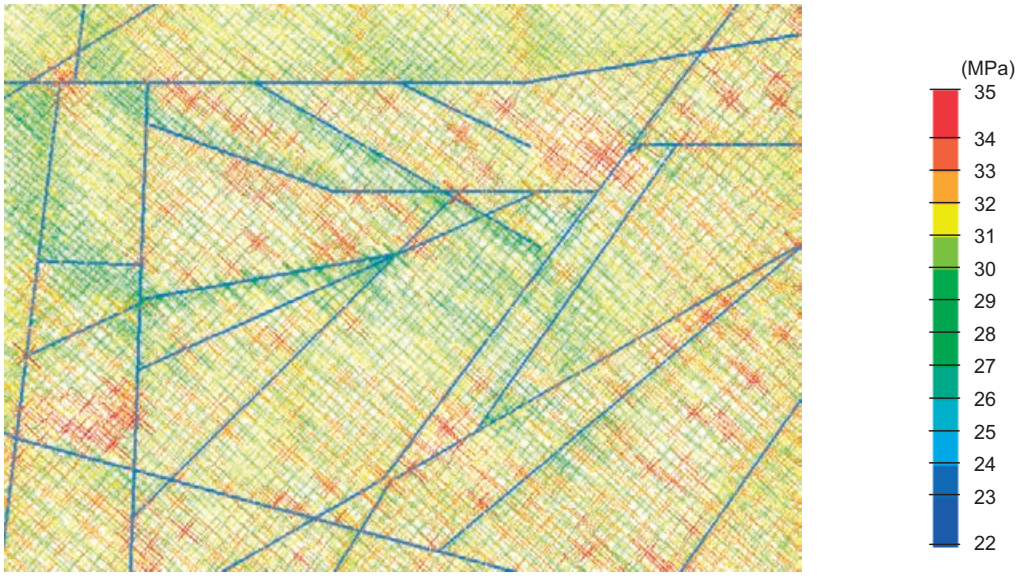

Model 6 b) Principal stress plot coloured by σ_1 – Elevation = -600 masl

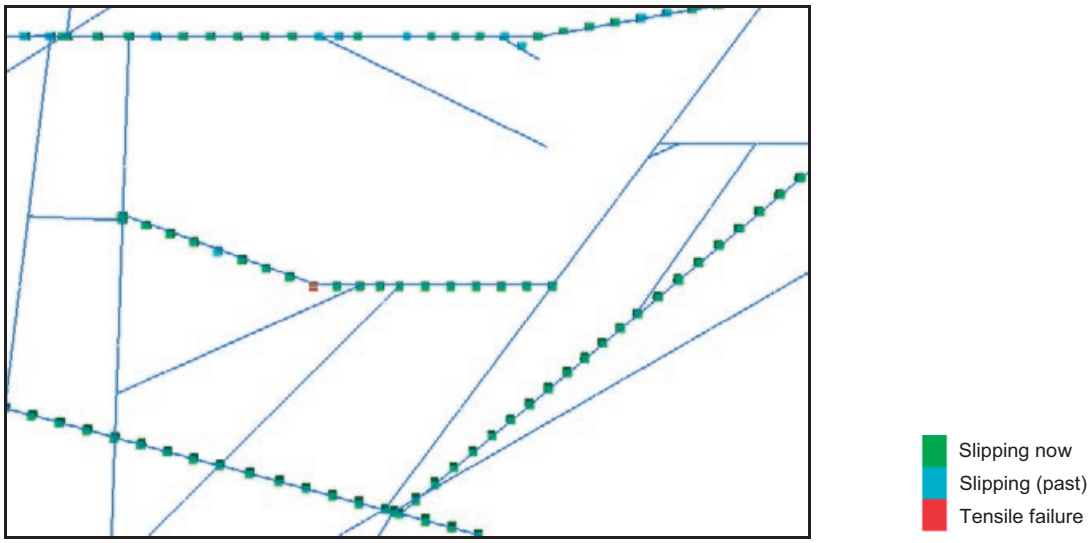

Model 6 c) Joint slip – Elevation = 0 masl

Model 6

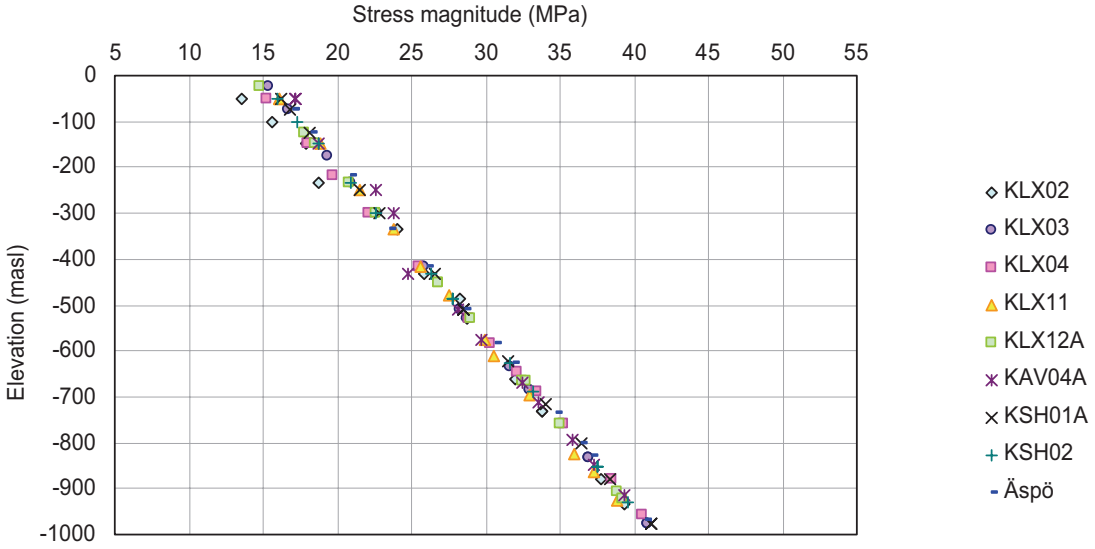

Model 6 d) Stress magnitude plot showing how σ_1 varies with elevation in different boreholes.

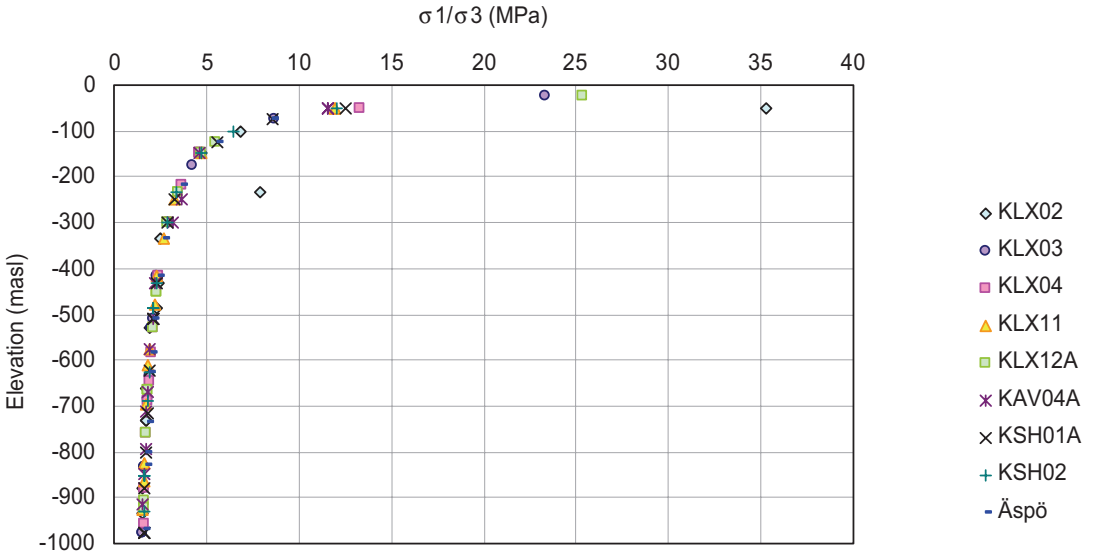

Model 6 e) Plot showing how the σ_1/σ_3 varies with elevation in different boreholes

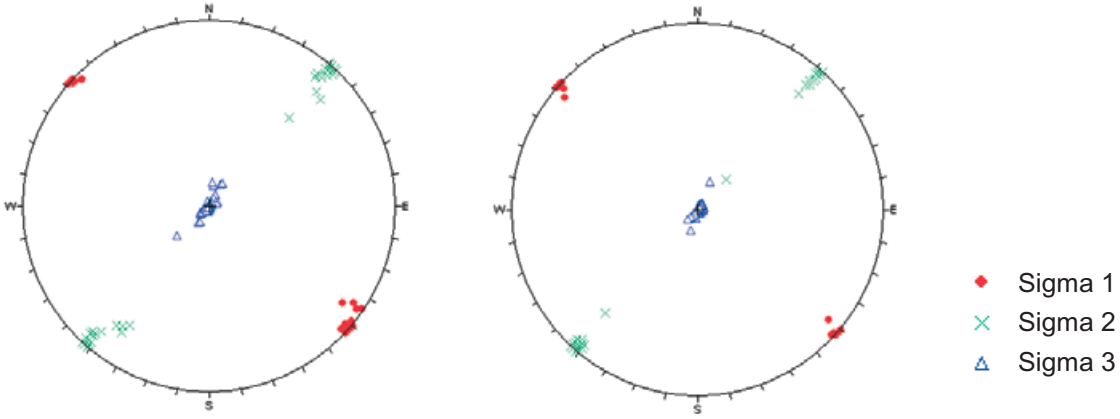

Laxemar *Simpevarp, Äspö, Ävrö*

Model 6 f) Pole plots showing the simulated principal stress orientations for Model 6. The left plot shows the results from the Laxemar boreholes; KLX02, KLX03, KLX04, KLX11 and KLX12A and the right plot shows the results for the boreholes in Simpevarp, Äspö and Ävrö; KSH01A, KSH02, "Äspö", KAV04A.

Model 7

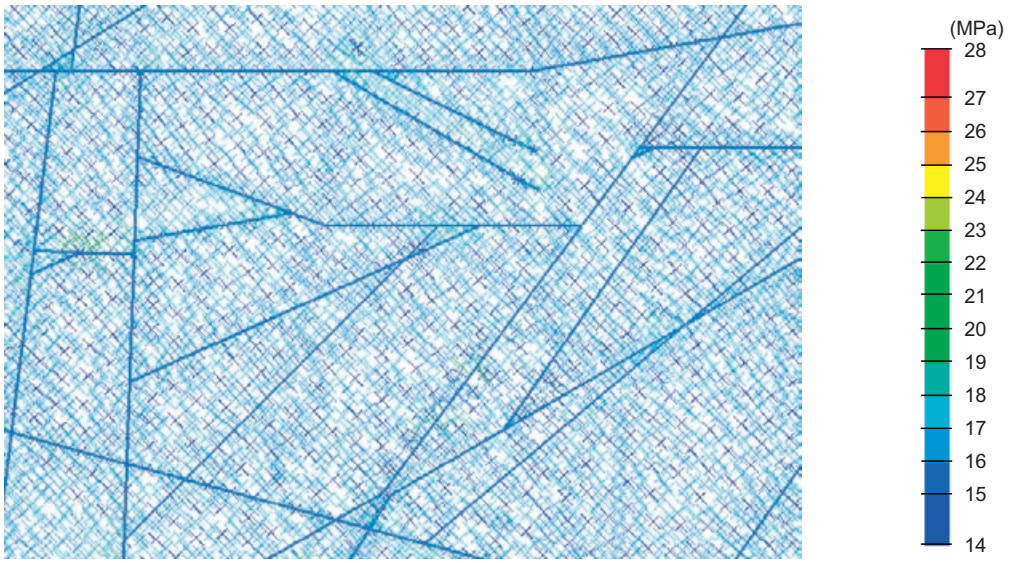

Model 7 a) Principal stress plot coloured by σ_1 – Elevation = -400 masl (Note: Different legend)

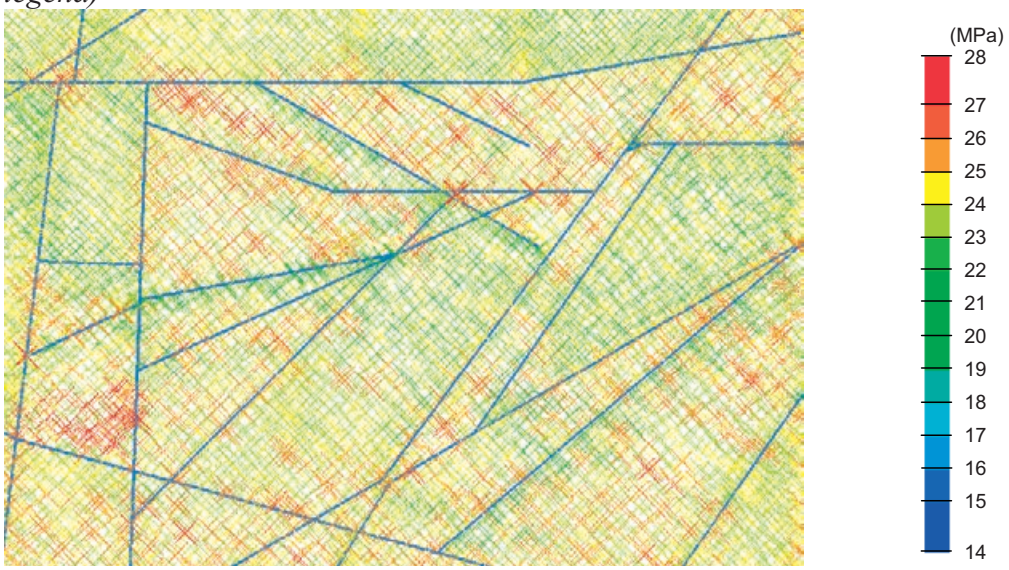

Model 7 b) Principal stress plot coloured by σ_1 – Elevation = -600 masl (Note: Different legend)

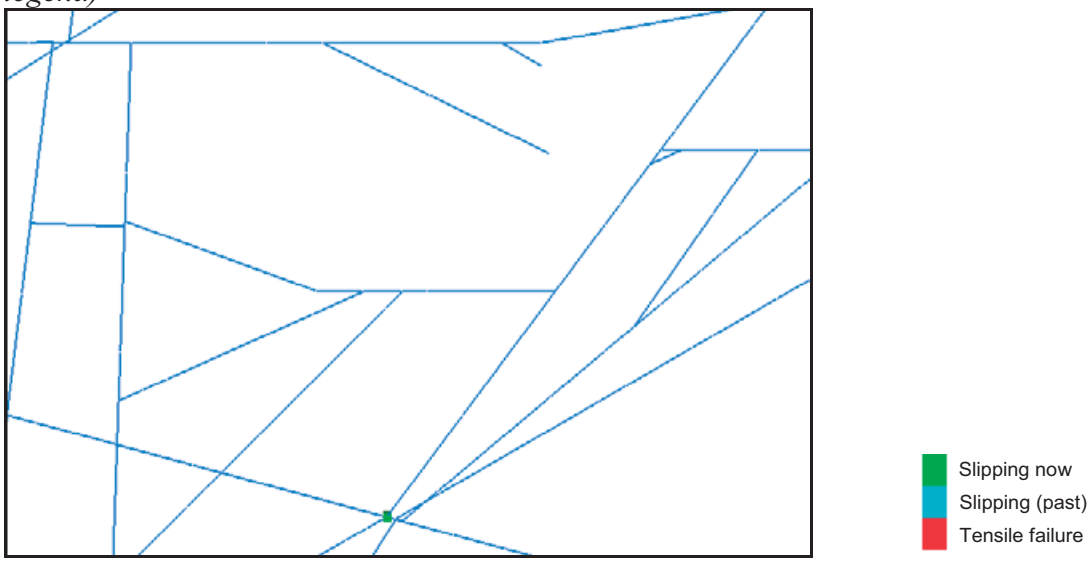

Model 7 c) Joint slip – Elevation = 0 masl

Model 7

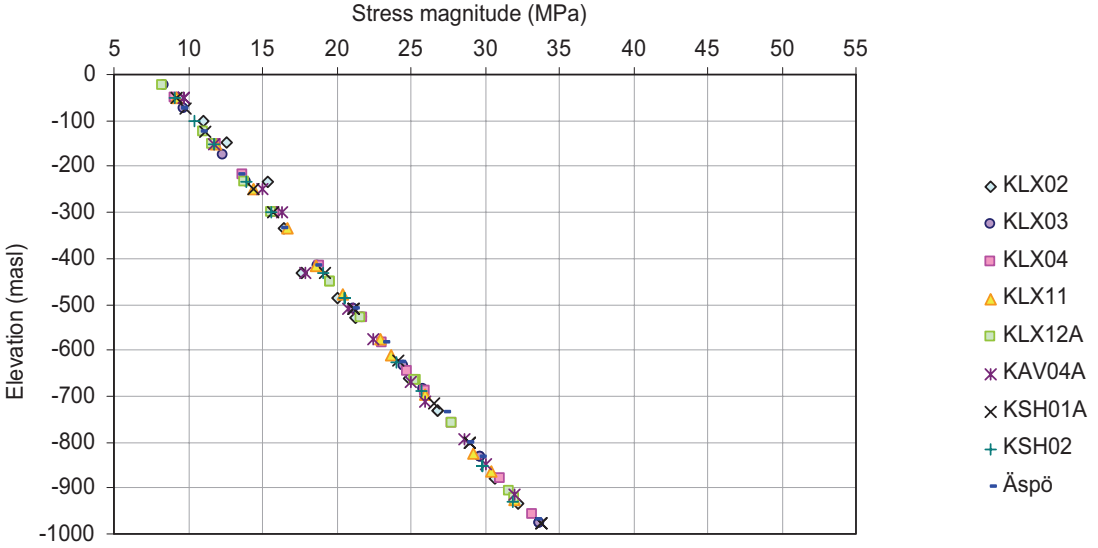

Model 7 d) Stress magnitude plot showing how σ_1 varies with elevation in different boreholes.

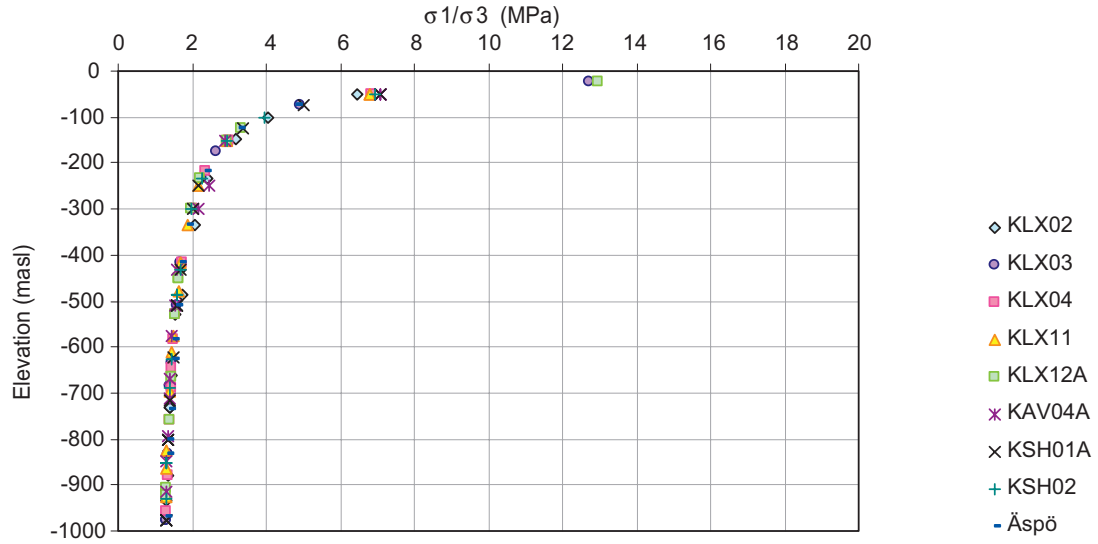

Model 7 e) Plot showing how the σ_1/σ_3 varies with elevation in different boreholes.

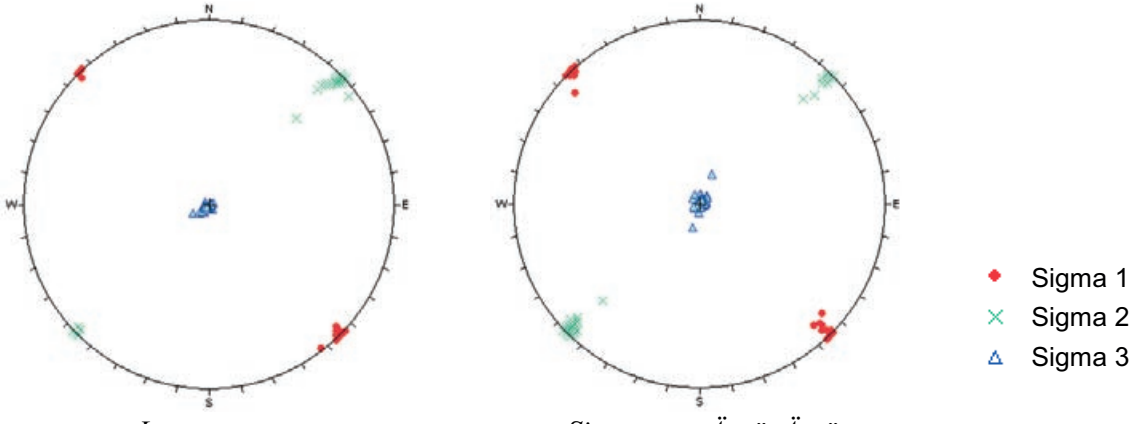

Laxemar *Simpevarp, Äspö, Ävrö*

Model 7 f) Pole plots showing the simulated principal stress orientations for Model 7. The left plot shows the results from the Laxemar boreholes; KLX02, KLX03, KLX04, KLX11 and KLX12A and the right plot shows the results for the boreholes in Simpevarp, Äspö and Ävrö; KSH01A, KSH02, "Äspö", KAV04A.

Model 8

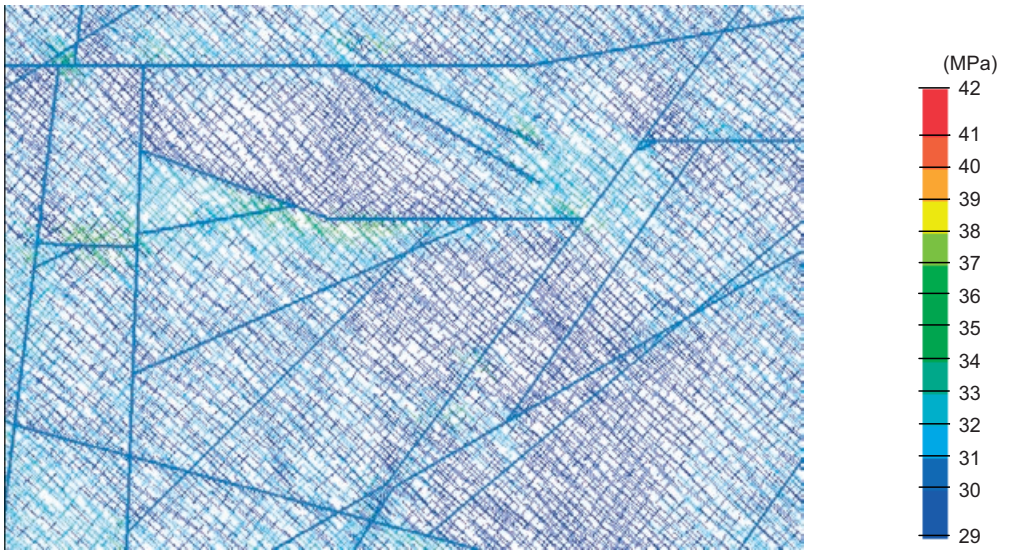

Model 8 a) Principal stress plot coloured by σ_1 – Elevation = -400 masl (Note: Different legend)

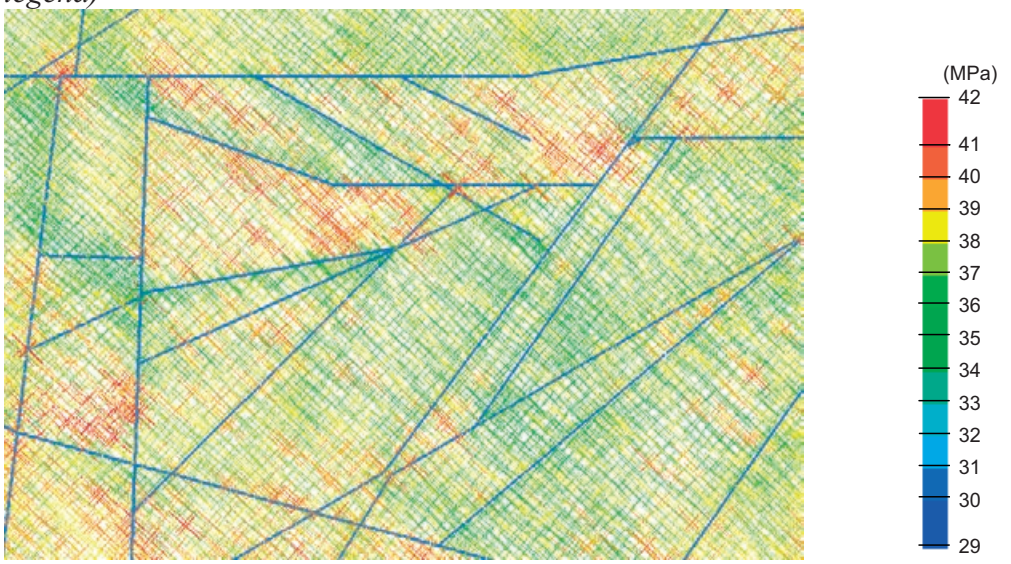

Model 8 b) Principal stress plot coloured by σ_1 – Elevation = -600 masl (Note: Different legend)

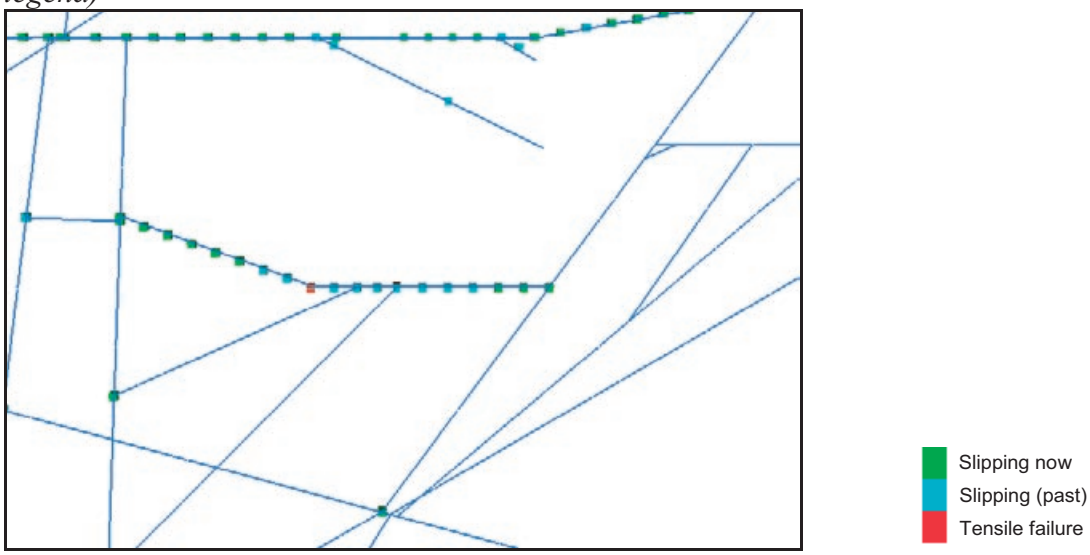

Model 8 c) Joint slip – Elevation = 0 masl

Model 8

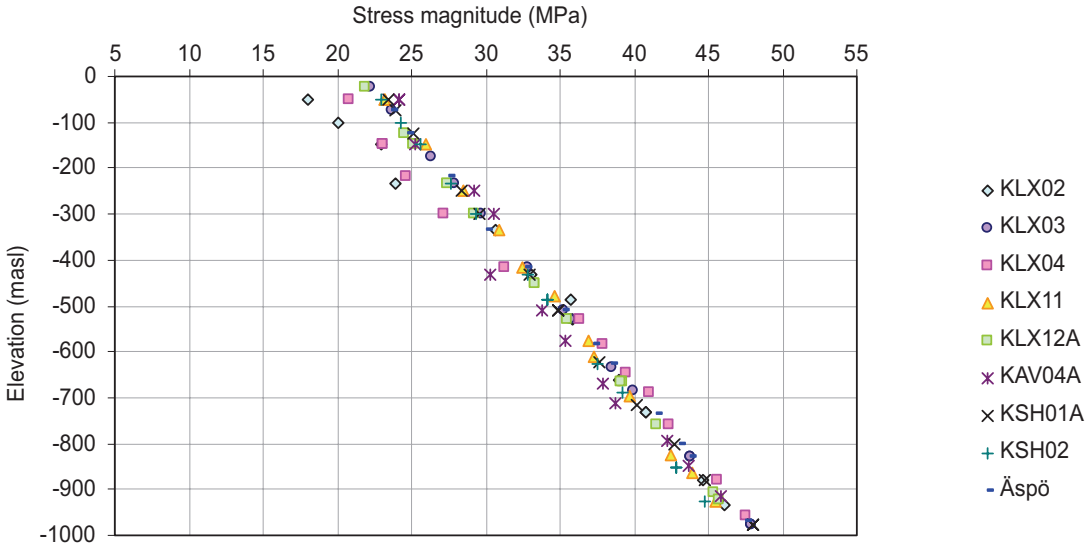

Model 8 d) Stress magnitude plot showing how σ_1 varies with elevation in different boreholes.

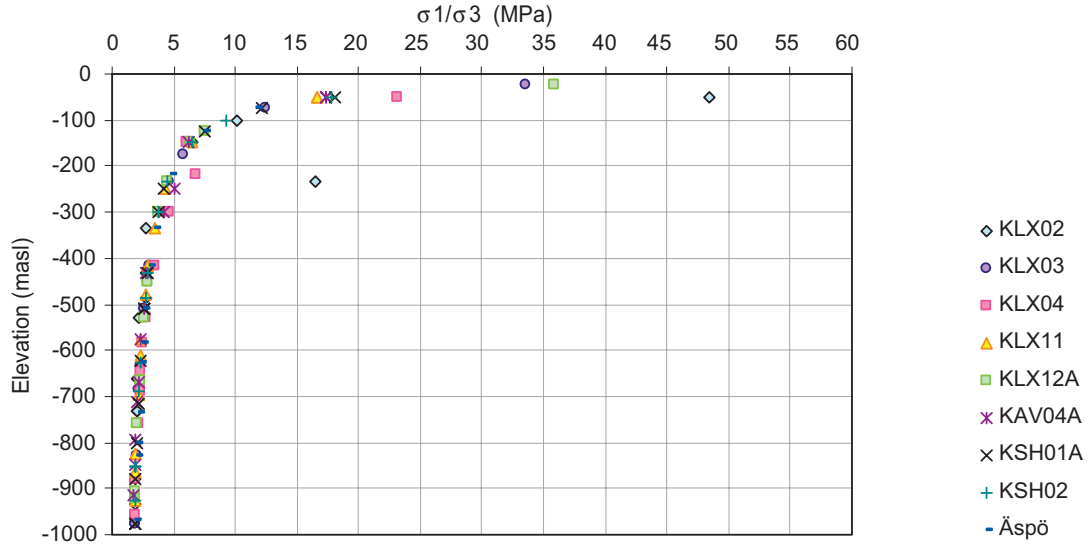

Model 8 e) Plot showing how the σ_1/σ_3 varies with elevation in different boreholes

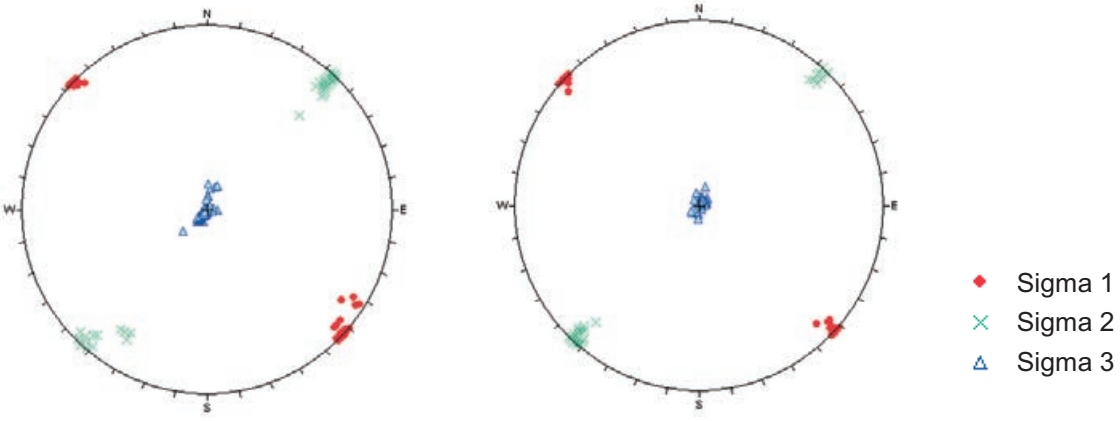

Laxemar *Simpevarp, Äspö, Ävrö*

Model 8 f) Pole plots showing the simulated principal stress orientations for Model 8. The left plot shows the results from the Laxemar boreholes; KLX02, KLX03, KLX04, KLX11 and KLX12A and the right plot shows the results for the boreholes in Simpevarp, Äspö and Ävrö; KSH01A, KSH02, "Äspö", KAV04A.

Model 9

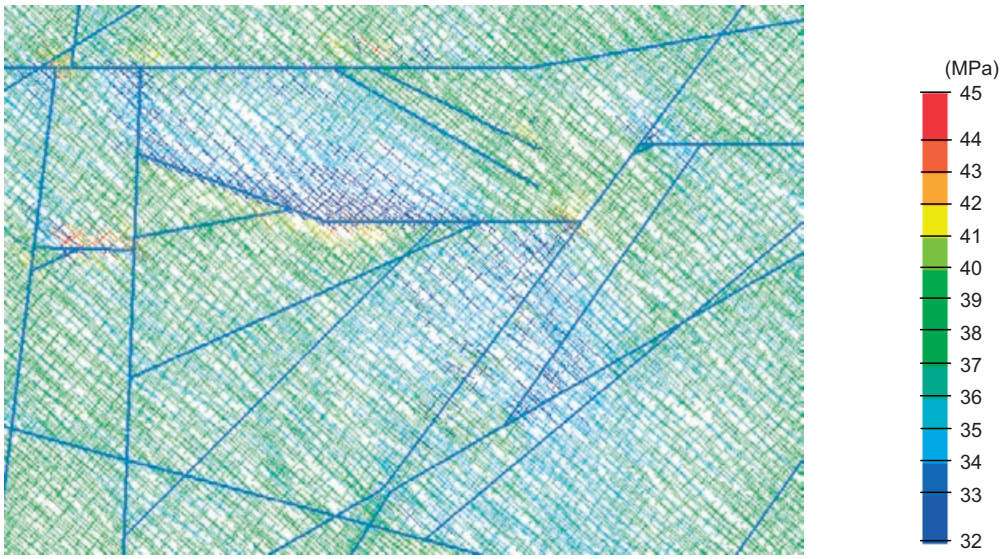

Model 9 a) Principal stress plot coloured by σ_1 – Elevation = -400 masl (Note: Different legend)

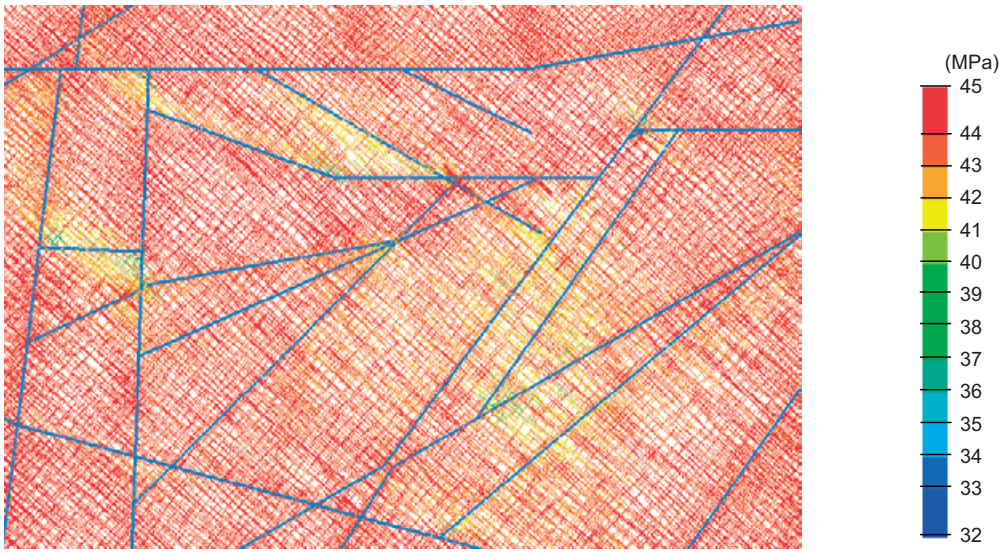

Model 9 b) Principal stress plot coloured by σ_1 – Elevation = -600 masl (Note: Different legend)

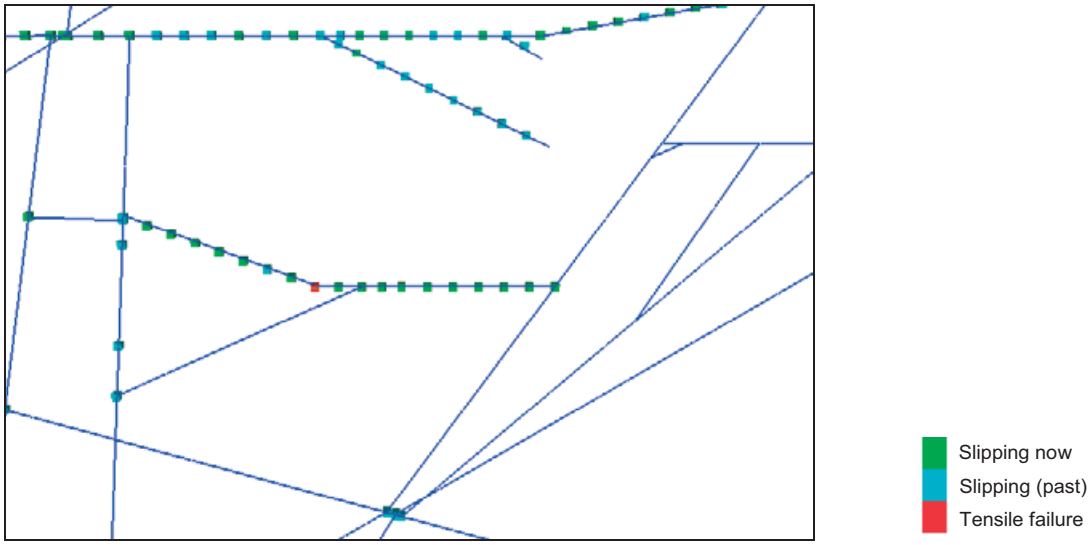

Model 9 c) Joint slip – Elevation = 0 masl

Model 9

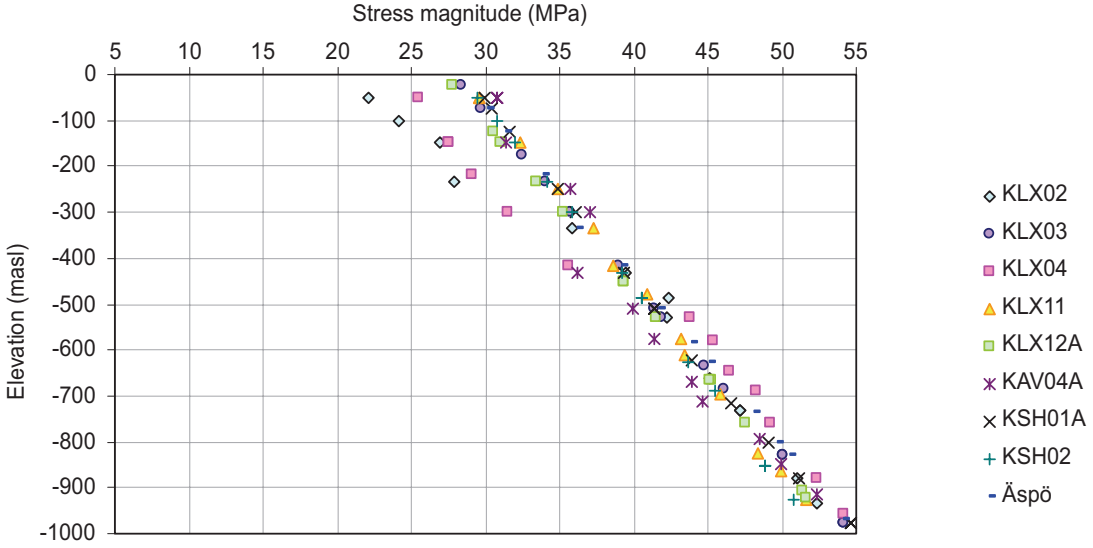

Model 9 d) Stress magnitude plot showing how σ_1 varies with elevation in different boreholes.

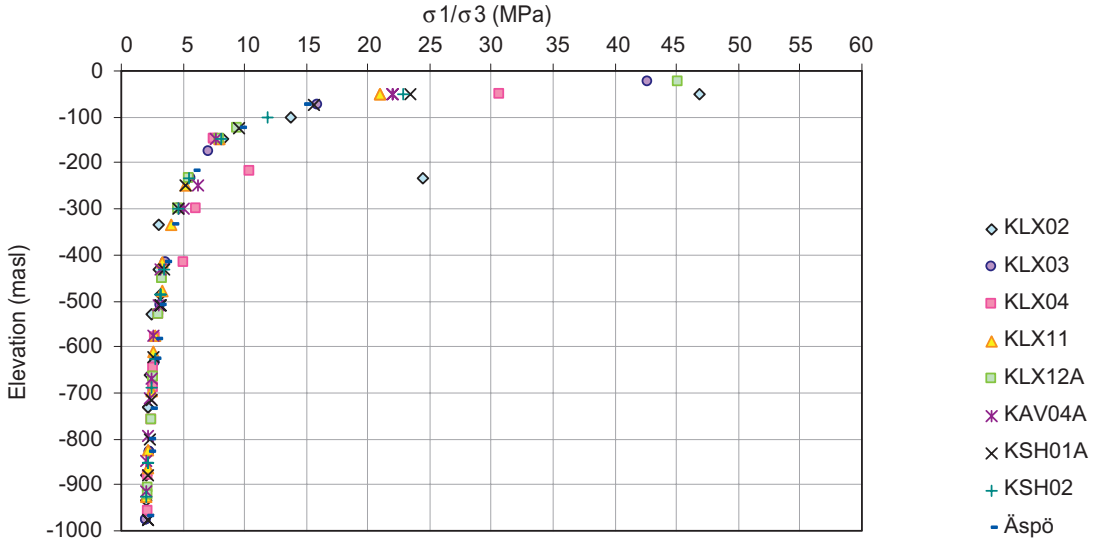

Model 9 e) Plot showing how the σ_1/σ_3 varies with elevation in different boreholes

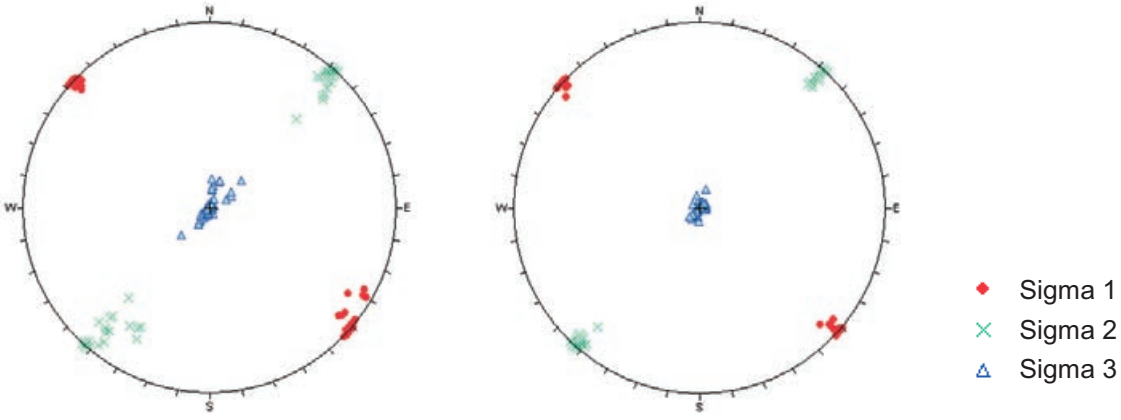

Laxemar *Simpevarp, Äspö, Ävrö*

Model 9 f) Pole plots showing the simulated principal stress orientations for Model 9. The left plot shows the results from the Laxemar boreholes; KLX02, KLX03, KLX04, KLX11 and KLX12A and the right plot shows the results for the boreholes in Simpevarp, Äspö and Ävrö; KSH01A, KSH02, "Äspö", KAV04A.

KLX02

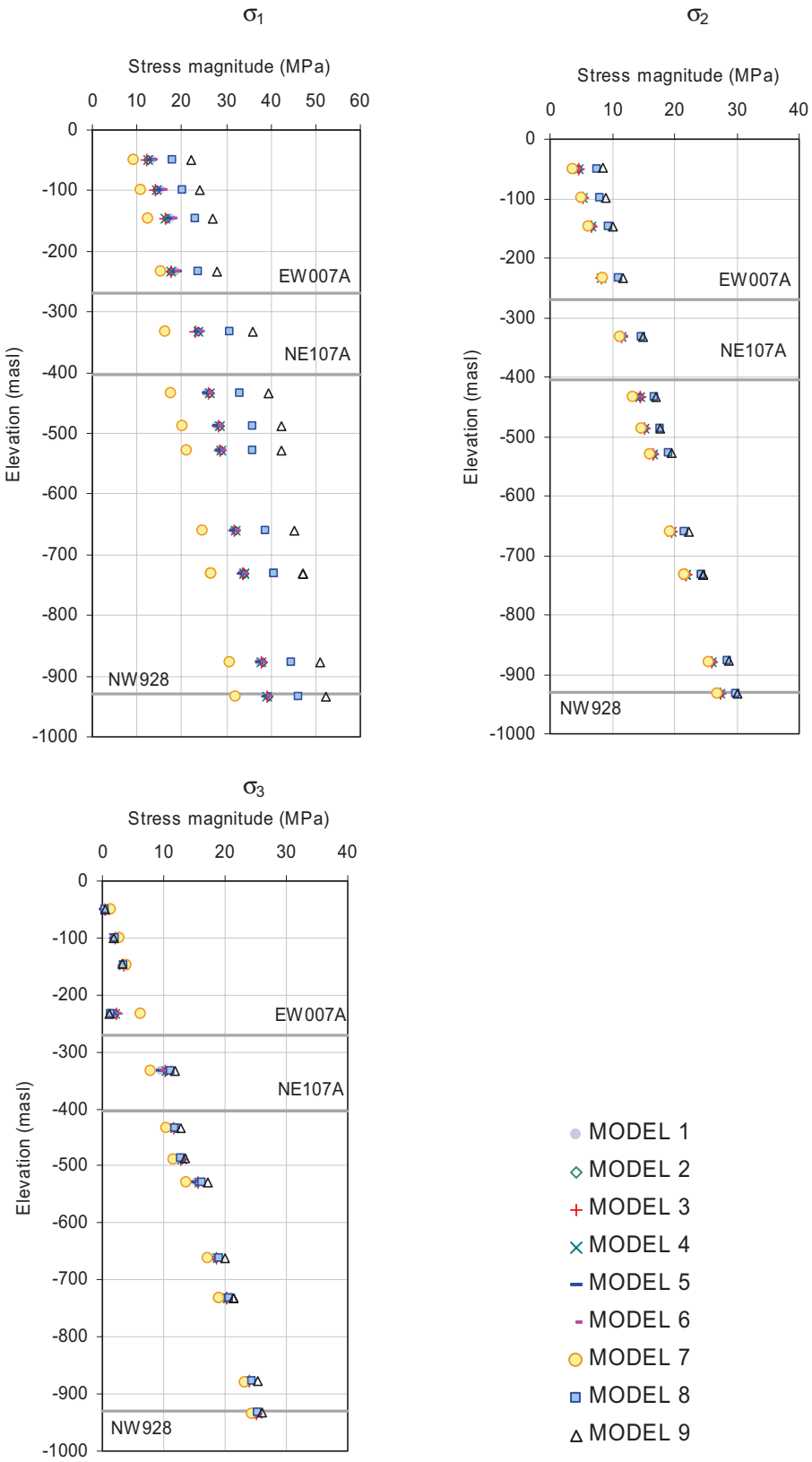

Depth-wise principal stress scanlines with the approximate location of borehole KLX02 in model cases 1–9 are compared. The approximate elevation of the modelled deformation zones crossing the scanline is also shown.

KLX03

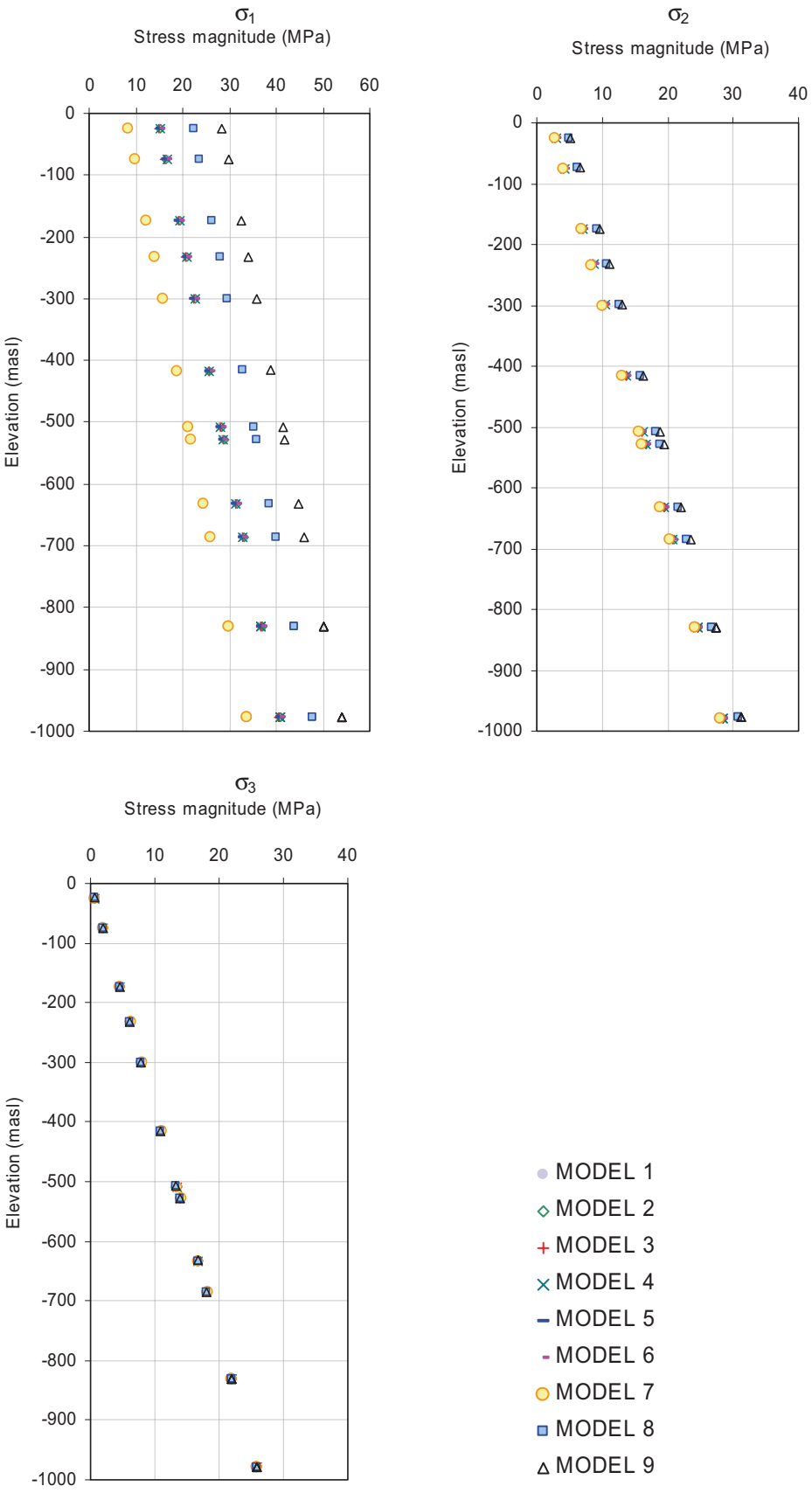

Depth-wise principal stress scanlines with the approximate location of borehole KLX03 in model cases 1–9 are compared.

KLX04

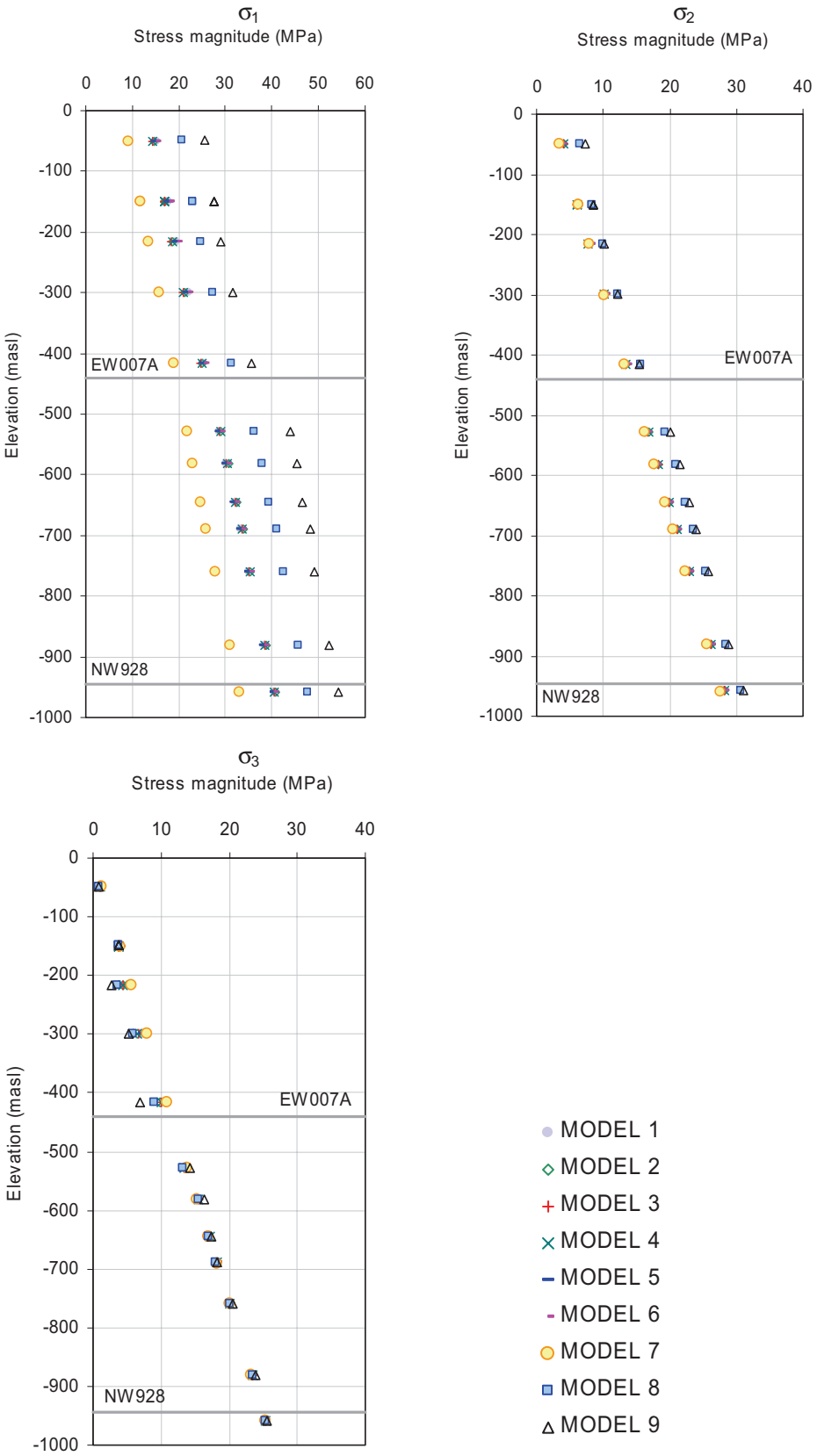

Depth-wise principal stress scanlines with the approximate location of borehole KLX04 in model cases 1–9 are compared. The approximate elevation of the modelled deformation zones crossing the scanline is also shown.

KLX11A

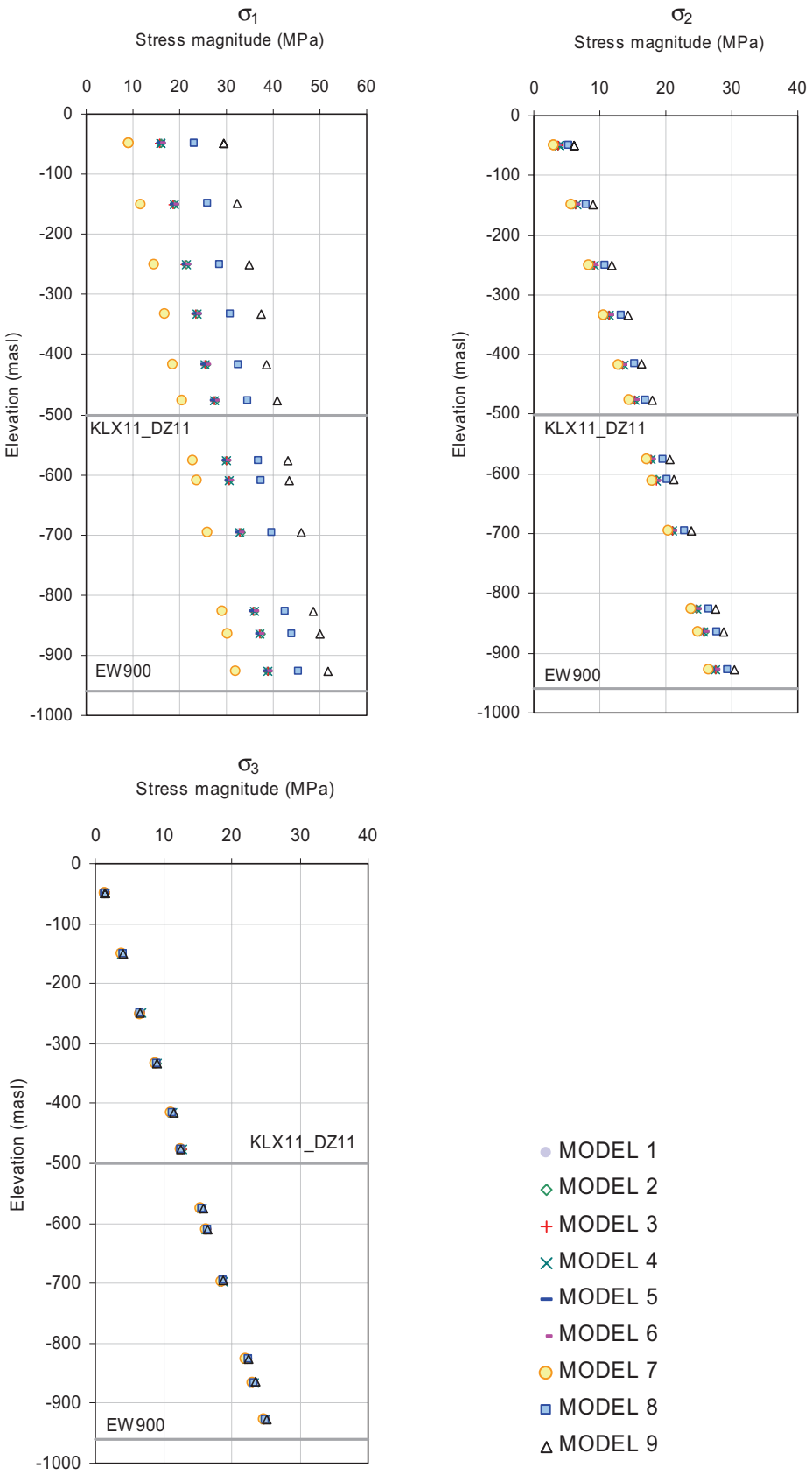

Depth-wise principal stress scanlines with the approximate location of borehole KLX11 in model cases 1–9 are compared. The approximate elevation of the modelled deformation zones crossing the scanline is also shown.

KLX12A

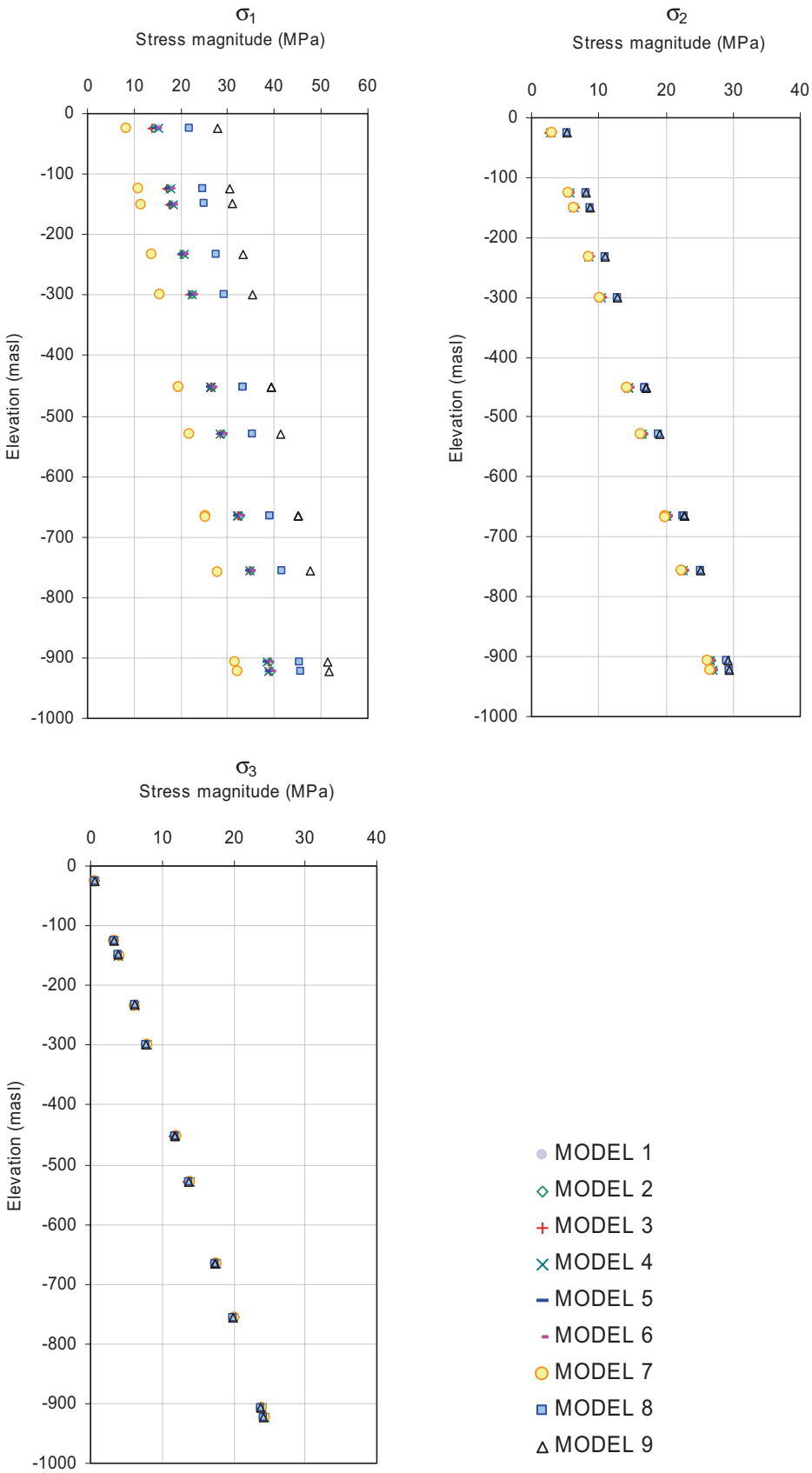

Depth-wise principal stress scanlines with the approximate location of borehole KLX12A in model cases 1–9 are compared.

KAV04A

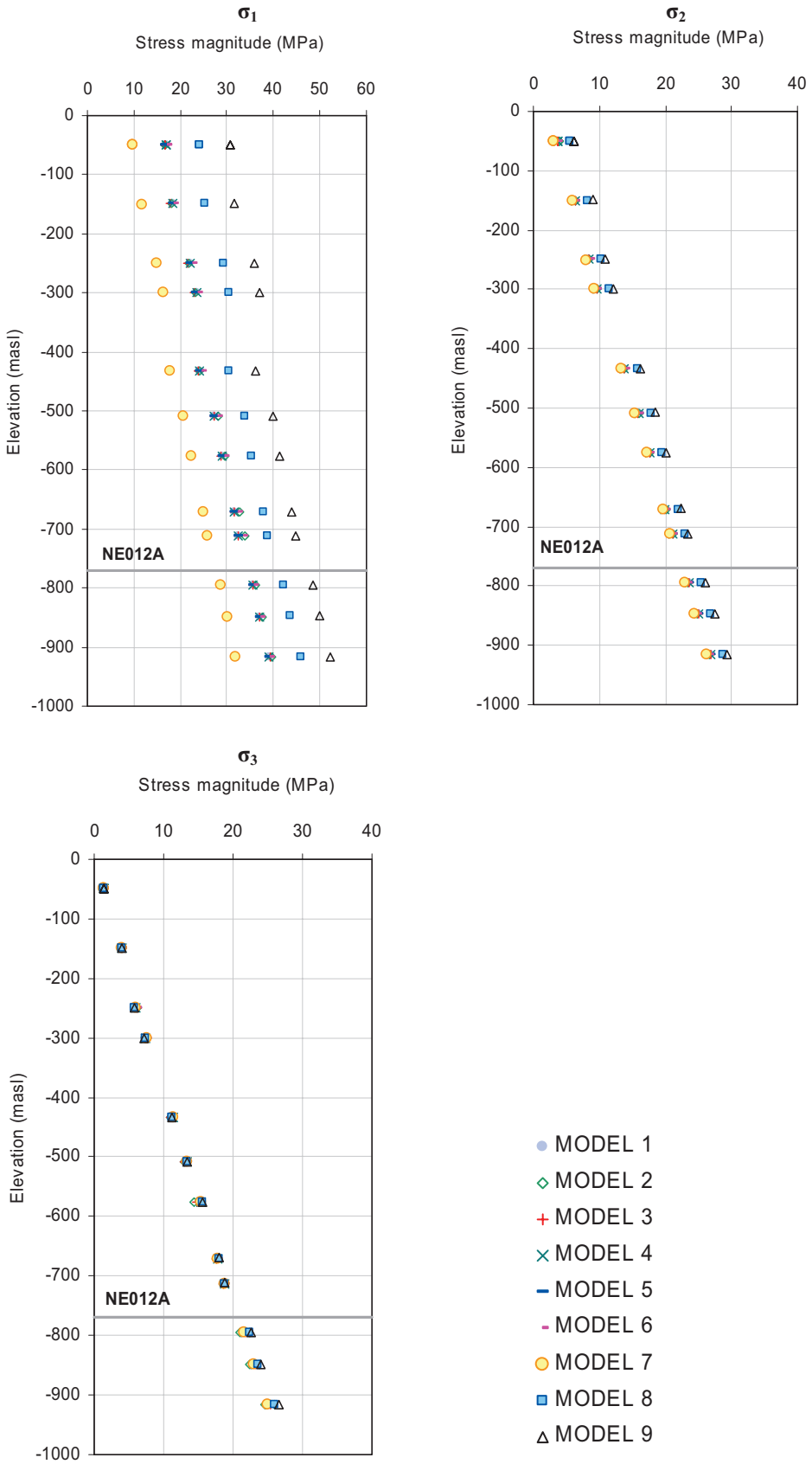

Depth-wise principal stress scanlines with the approximate location of borehole KAV04A in model cases 1–9 are compared. The approximate elevation of the modelled deformation zones crossing the scanline is also shown.

KSH01A

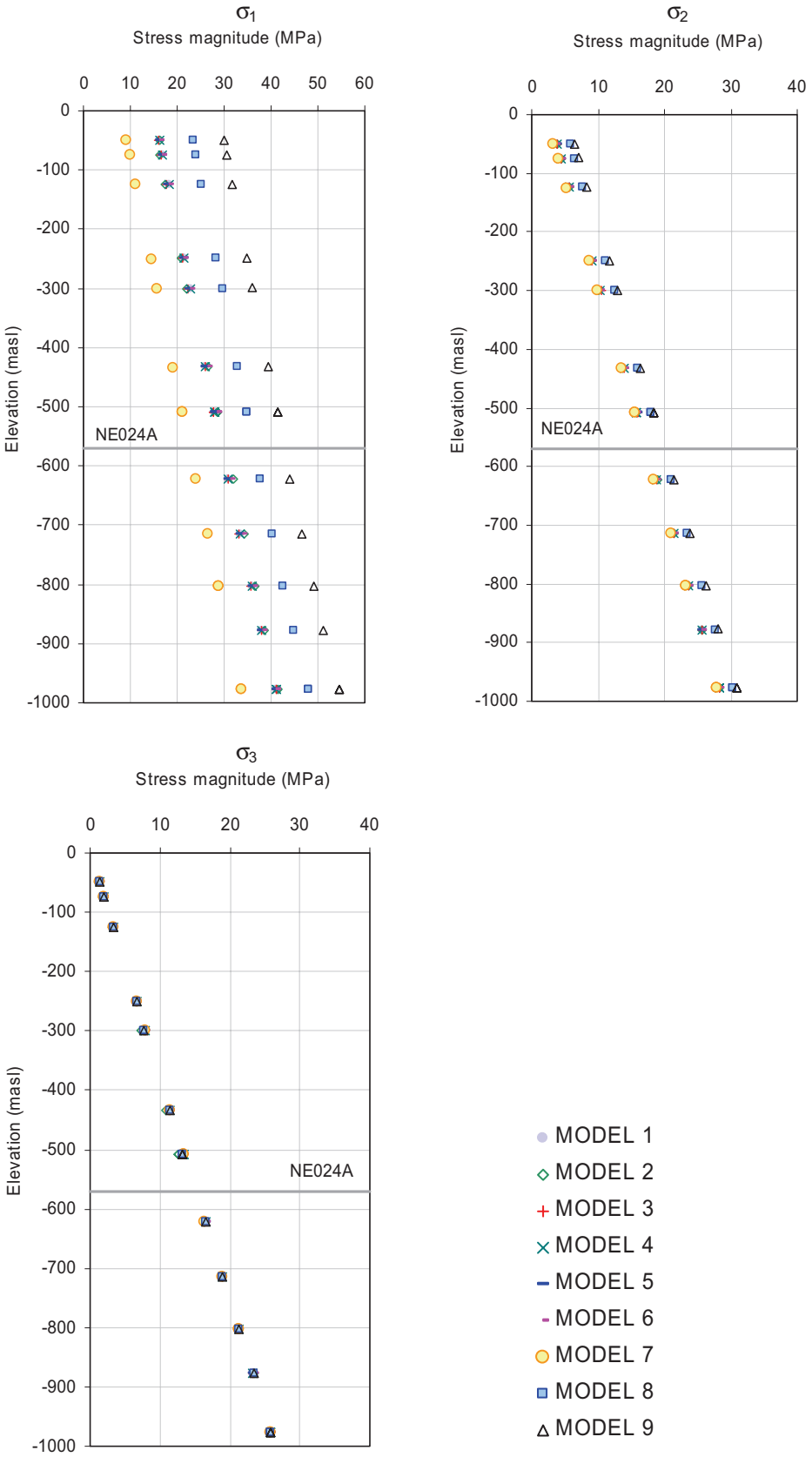

Depth-wise principal stress scanlines with the approximate location of borehole KSH01A in model cases 1–9 are compared. The approximate elevation of the modelled deformation zones crossing the scanline is also shown.

KSH02

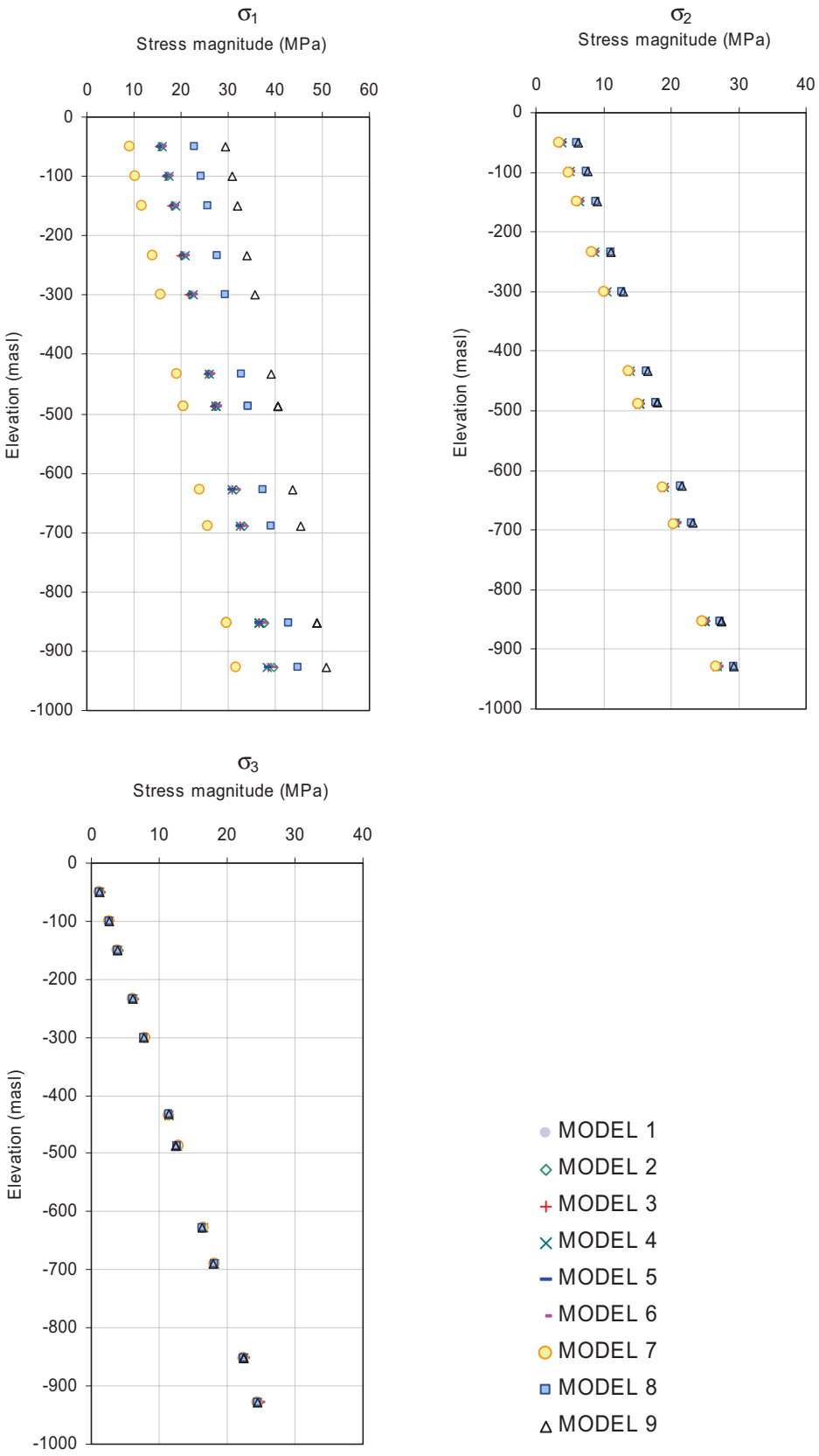

Depth-wise principal stress scanlines with the approximate location of borehole KSH02 in model cases 1–9 are compared.

“Äspö”

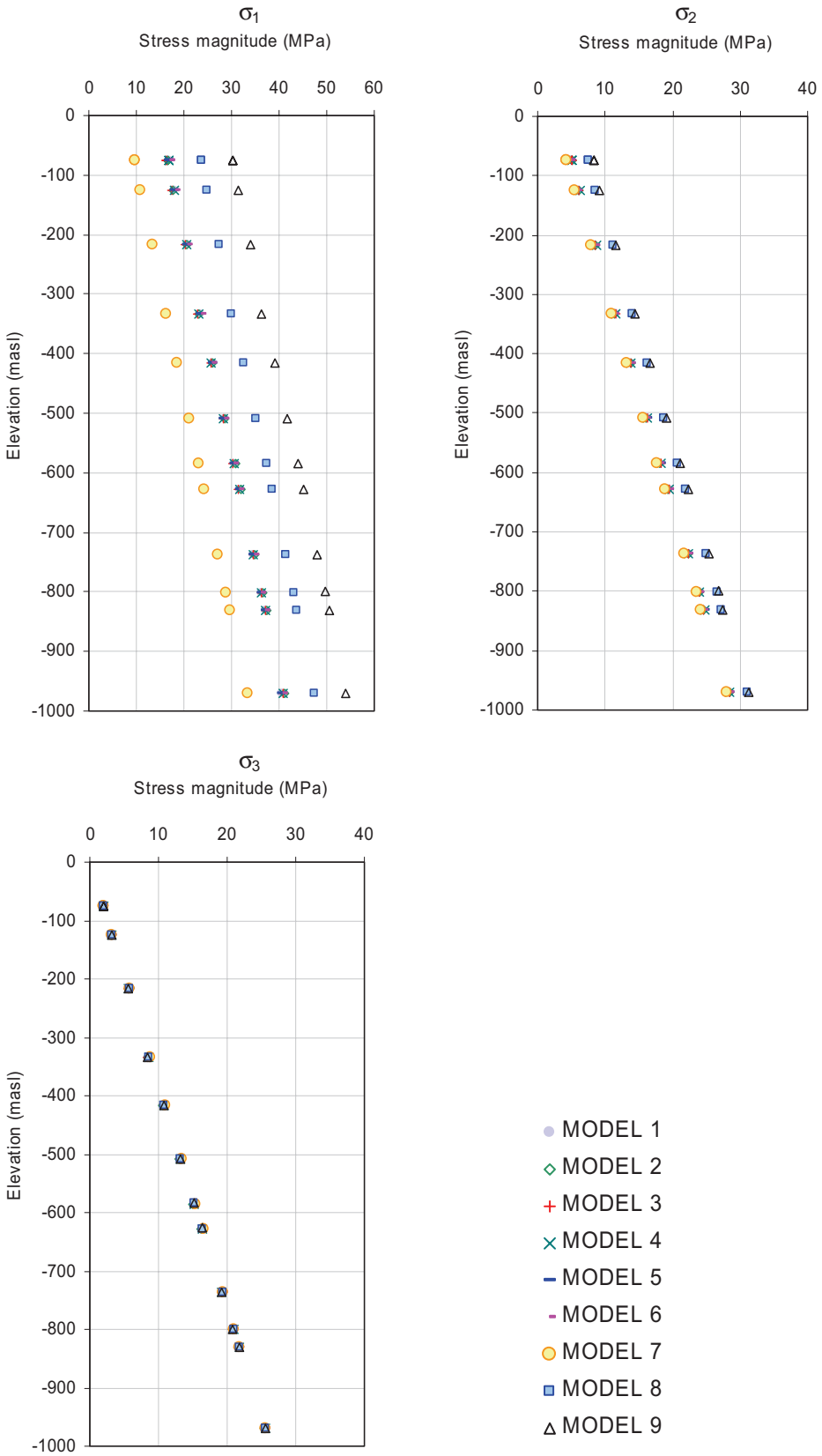

Depth-wise principal stress scanlines with the approximate location of Äspö Hard Rock Laboratory (results denoted “Äspö”) in model cases 1–9 are compared.

Appendix 8

Stochastic simulation of UCS

This appendix presents the results of stochastic simulation of UCS for rock domains RSMA01, RSMM01 and RSMD01 following the methodology described in Section 3.6.

Contents

A8.1 Stochastic simulation of lithologies

Stochastic simulations of lithologies or TRCs for rock domains RSMA01, RSMM01 and RSMD01 were performed as part of the thermal modelling, model version SDM-Site Laxemar /Sundberg et al. 2008/. Geological borehole data form the basis for these stochastic simulations. The output from these simulations is also used in the modelling of compressive strength.

A description of the eight TRCs defined is given in Table 3-11. The TRC proportions making up the three rock domains, RSMA01, RSMD01 and RSMM01 are presented in Table A8-1 – Table A8-3. The most noticeable difference between the proportions estimated from the simulations and the proportions estimated by the geological modelling team concerns TRC 58. The main reason for this is the exclusion from the lithological simulation data of fine-grained granite (511058) and pegmatite (501061) having borehole occurrences less than 1 m length.

Table A8-1. Proportions of TRCs in simulations of domain RSMA01 /Sundberg et al. 2008/. Proportions based on the geological model are from /Wahlgren et al. 2008/.

TRC	Rock name/code	Proportion of TRC in 1,000 realisations, 2 m scale	Proportions based on geological model *
56	Ävrö granodiorite (501056), Granite (501058)	64.6%	88.7%
46	Ävrö qtz monzodiorite (501046)	27.1%	
58	Fine-grained granite (511058) Pegmatite (501061)	1.8%	3.6%
30	Fine-grained dioritoid (501030) Quartz monzodiorite (501036)	4.8%	5.2%
102	Fine-grained diorite-gabbro (505102) Diorite-gabbro (501033)	1.7%	2.5%

* Boreholes located within domain RSMA01 in the central and southern part of Laxemar. In the geological model, proportions of Ävrö quartz monzodiorite and Ävrö granodiorite have not been estimated separately. Instead, both are included in Ävrö granite.

Table A8-2. Proportions of TRCs in simulations of domain RSMD01. Proportions based on the geological model are from /Wahlgren et al. 2008/.

TRC	Rock name/code	Proportion of TRC in 1,000 realisations, 2 m scale	Proportions based on geological model *
36	Quartz monzodiorite (501036)	82.9%	89.1%
136	Oxidised quartz monzodiorite (501036)	9.9%	
58	Fine-grained granite (511058) Pegmatite (501061)	3.5%	6.4%
102	Fine-grained diorite-gabbro (505102), Diorite-gabbro (501033), Ävrö quartz monzodiorite (501046), Dolerite (501027)	3.7%	c. 4%
			Other: < 1%

* In the geological model, the proportion of Quartz monzodiorite refers to both fresh and altered rock.

Table A8-3. Proportions of TRCs in simulations of domain RSMM01. Proportions based on the geological model are from /Wahlgren et al. 2008/.

TRC	Rock name/code	Proportion of TRC in 1,000 realisations, 2 m scale	Proportions based on geological model *
33	Diorite-gabbro (501033), Fine-grained diorite-gabbro (505102),	16.7	18.0%
56	Ävrö granodiorite (501056), Granite (501058)	24.7	77%
46	Ävrö qtz monzodiorite (501046)	56.4	
58	Fine-grained granite (511058) Pegmatite (501061)	2.2	5.2%
			Other: <1%

* In the geological model, proportions of Avrö quartz monzodiorite and Ävrö granodiorite have not been estimated separately. Instead, both are included in Ävrö granite.

Rock domains RSMA01 and RSMM01 are lithologically inhomogeneous. In order to capture the geological heterogeneity present within these rock domains in the stochastic simulations, these domains were divided into thermal subdomains, each of which was assumed to be statistically homogeneous. Each subdomain was then simulated separately. The basis for these subdivisions is described in /Sundberg et al. 2008/ and summarised in Table A8-4. In contrast to domains RSMA01 and RSMM01, domain RSMD01is lithologically quite homogenous, and subdivision into subdomains was judged unnecessary. However, fine-grained diorite-gabbro was modelled with anisotropy in RSMD01.

Stochastic unconditional simulations of the spatial distribution of TRCs at 2 m resolution were performed for each thermal subdomain or domain using the spatial properties derived from the analysis of the borehole data /Sundberg et al. 2008/. The model dimensions were 100×100×100 m, i.e. a total of 125 000 cells. One hundred realisations of geology for each rock domain were selected for the purpose of modelling UCS. These 100 realisations were divided among the subdomains in proportion to the borehole length characterising each subdomain (Table A8-4).

Visualisations of example geology realisations for all three rock domains are presented in Section A8.3. A full account of the simulation results are presented in /Sundberg et al. 2008/.

Table A8-4. Thermal subdomains defined in rock domains RSMA01 and RSMM01. A subdomain's proportion of the domain is based on the borehole length assigned to each subdomain.

Domain	Subdomain	Chatacteristic rock type(s)	Dominant TRC	Proportion of domain
RSMA01	A1	Ävrö granodiorite	56	74%
	A2	Ävrö quartz monzodiorite	46	18%
	A3	Very heterogenous	30	8%
RSMM01	M1	Ävrö quartz monzodiorite,	46	38%
	M2	Ävrö quartz monzodiorite + high proportion diorite-gabbro	46	35%
	M3	Ävrö granodiorite	56	11%
	M4	Ävrö granodiorite + high proportion diorite-gabbro	56	10%
	M5	Ävrö granodiorite + high proportion fine grained granite	56	6%

A8.2 Simulation of UCS for each TRC

A8.2.1 UCS variogram models for TRCs

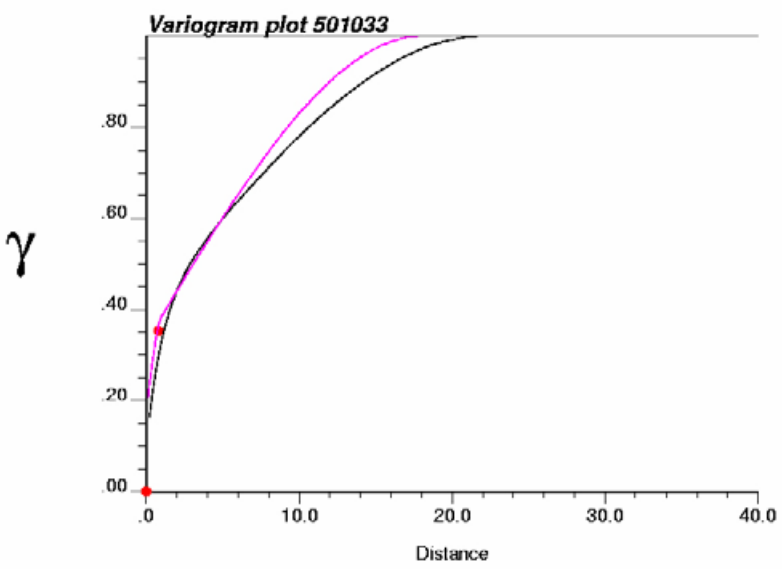

Figure A8-1. *Variogram model for TRC 33 (black) based on diorite-gabbro (type A). Variogram model based on type B (pink) shown for comparison. Standardised semi-variance of UCS at sample scale for diorite-gabbro at a lag distance of c. 1 m is indicated by the red dot (dot at origin excluded). Value based on only 4 data pairs.*

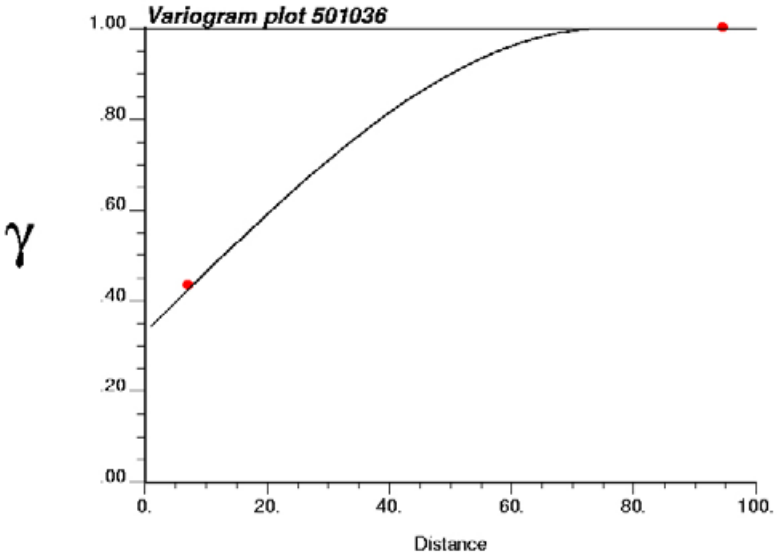

Figure A8-2. *Variogram model for TRC 36. Standardised semi-variance of UCS at sample scale for quartz monzodiorite at lag distances of c. 6 m and c. 100 is indicated by the red dots based on 47 and 17 data pairs respectively.*

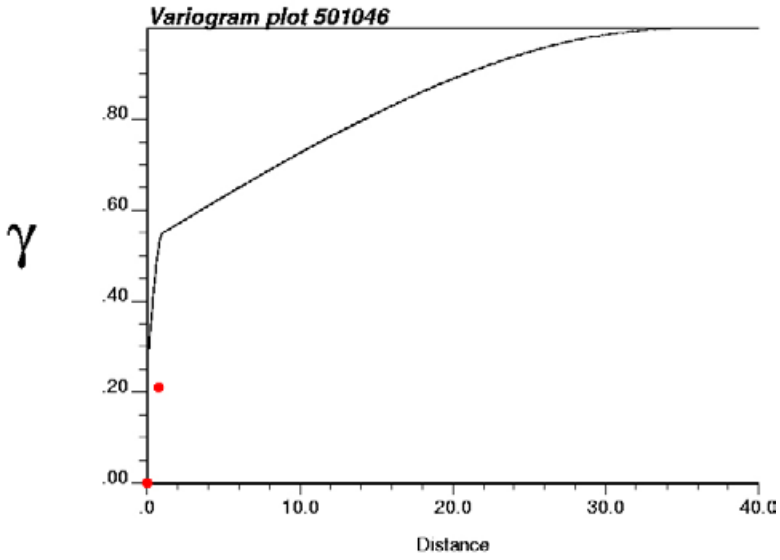

Figure A8-3. *Variogram model for TRC 46. Standardised semi-variance of UCS at sample scale for Ävrö quartz monzodiorite at a lag distance of c. 1 m is indicated by the red dot (dot at origin excluded) based on 26 data pairs respectively.*

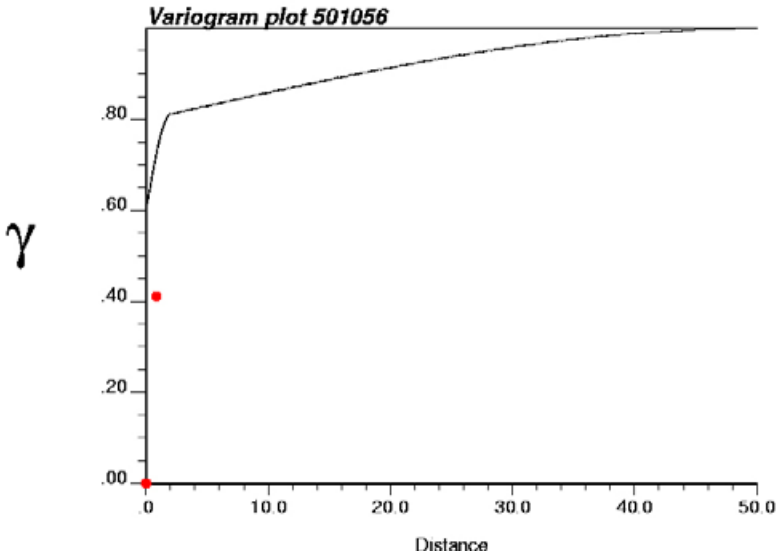

Figure A8-4. *Variogram model for TRC 56. Standardised semi-variance of UCS at sample scale for Ävrö granodiorite at a lag distance of c. 3 m is indicated by the red dot (dot at origin excluded) based on 44 data pairs respectively.*

A8.2.2 Histogram of simulated UCS values for each TRC

The histograms below are based on simulated UCS values from 100 realisations and apply to the scale of the UCS laboratory samples.

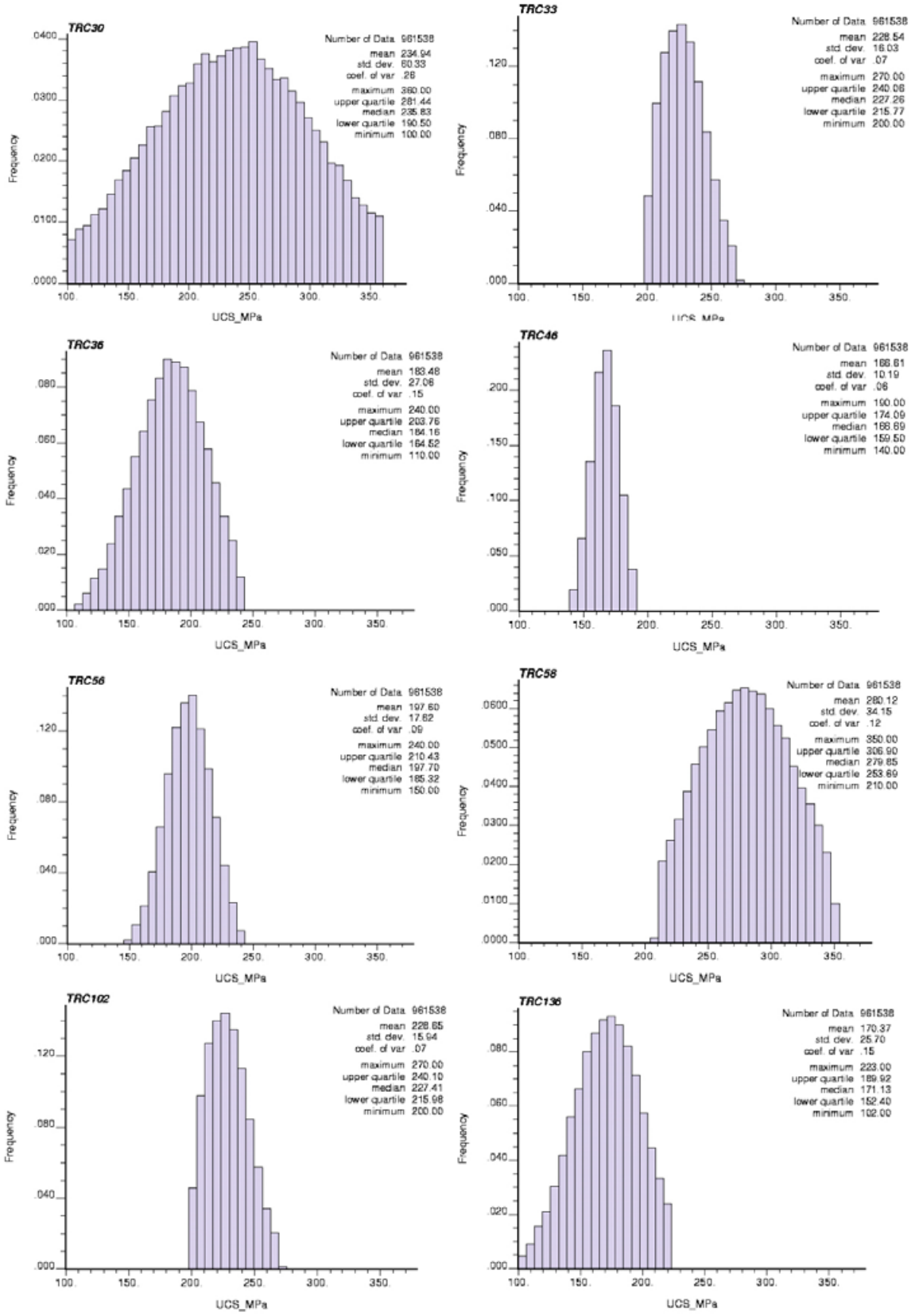

Figure A8-5. *Histogram of uniaxial compressive strength for TRCs based on stochastic simulation – 100 realisations.*

A8.2.3 Variogram model reproduction

The model variograms and the variograms calculated from realisations are compared below.

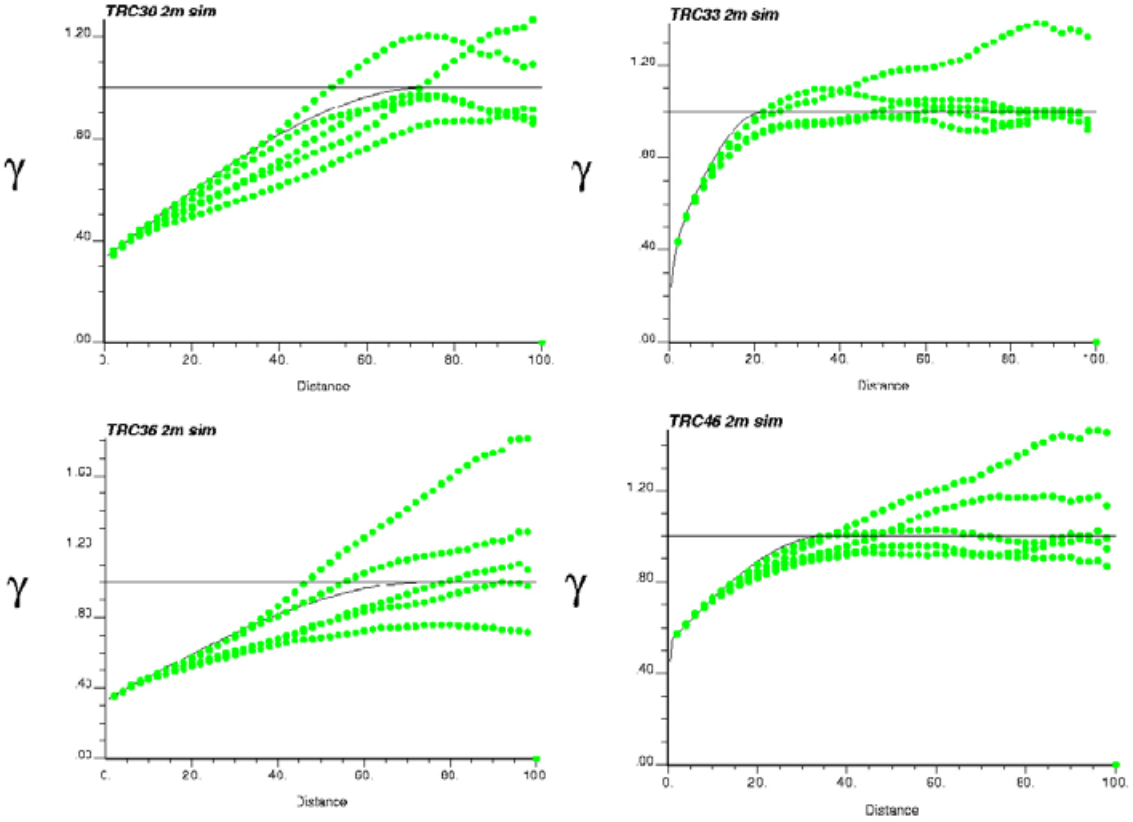

Figure A8-6. *Variogram model Comparison of the variogram model (black line) and variograms of 5 independent realisations for different TRCs. Lag distance (x axis) in meters (m). Variogram is standardised to the variance of the simulated data. Horizontal black lines correspond to the sills of the variogram models.*

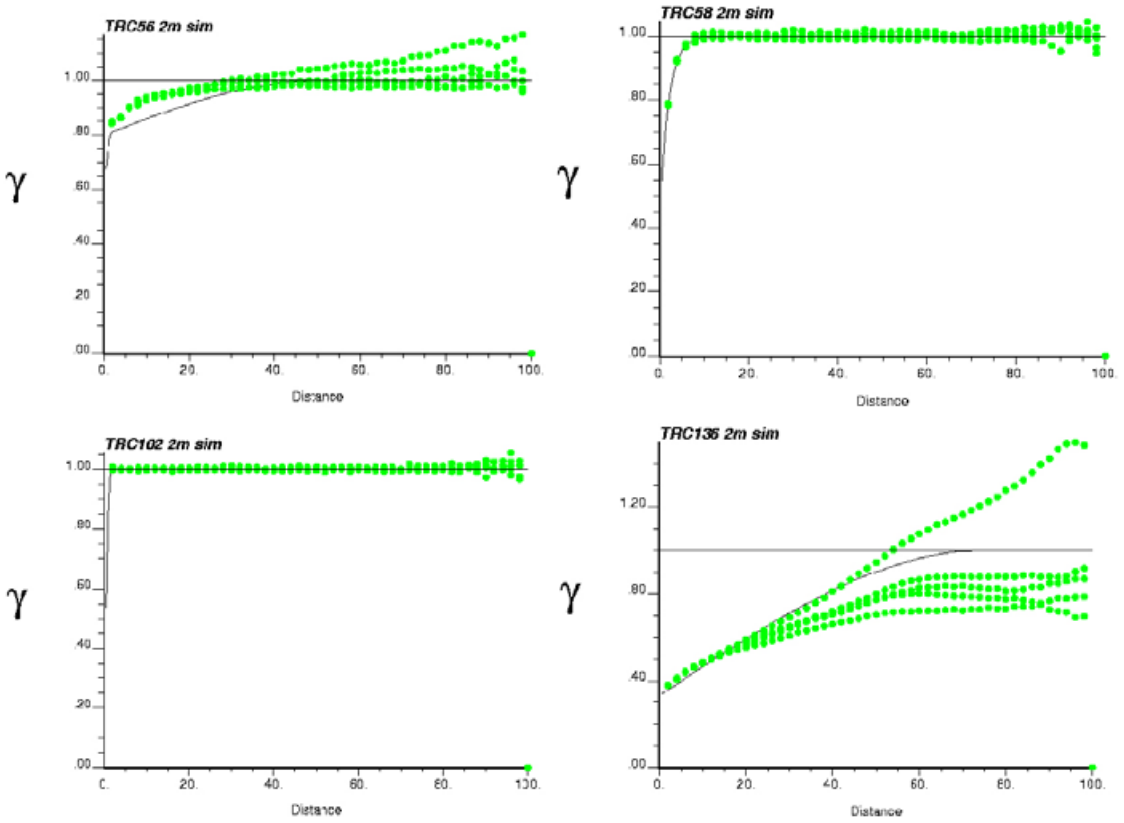

Figure A8-7. *Comparison of the variogram model (black line) and variograms of 5 independent realisations for different TRCs. Lag distance (x axis) in metres (m). Variogram is standardised to the variance of the simulated data. Horizontal black lines correspond to the sills of the variogram models.*

A8.2.4 Visualisations of UCS realisations for each TRC

Below, example realisations of compressive strength for each TRC are presented in 2D for simulations with a resolution of 2 m. All 2D-realisations represent a slice in the centre of a 3D cube. For example, the 25th slice of the xy-plane is the 25th slice that can be cut in the z-direction (there are 50 slices).

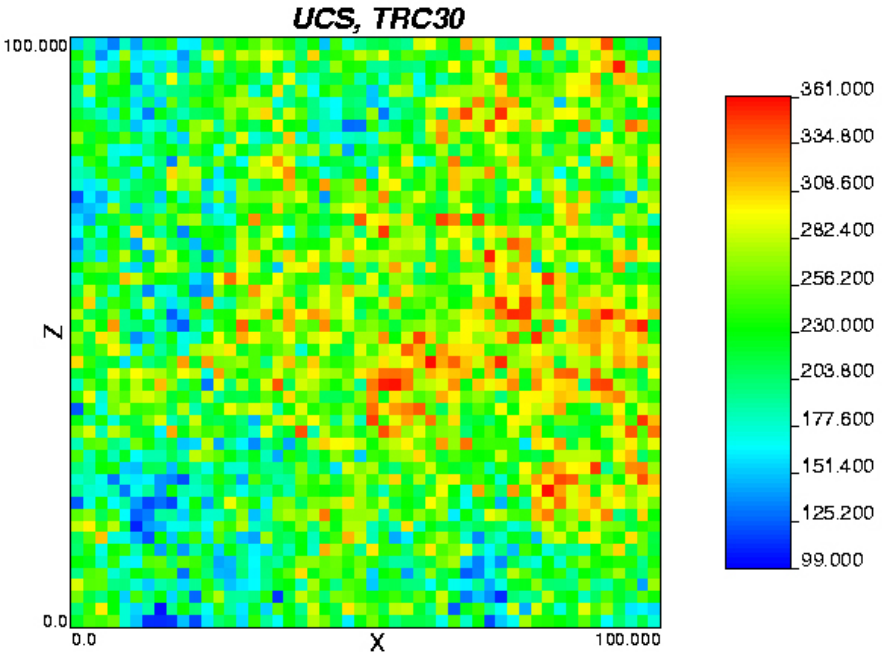

Figure A8-8. *2D slice from one 3D realisation (resolution = 2 m) illustrating the distribution of compressive strength values in TRC 30. Realisation 1, Slice = 25, xz-plane. Distance is in metres.*

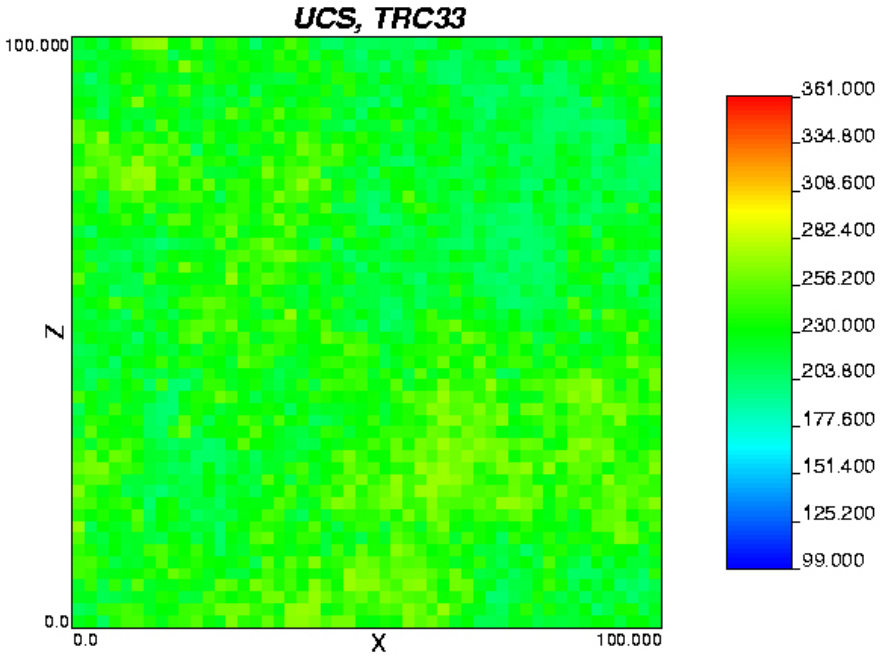

Figure A8-9. *2D slice from one 3D realisation (resolution = 2 m) illustrating the distribution of compressive strength values in TRC 33. Realisation 1, Slice = 25, xz-plane. Distance is in metres.*

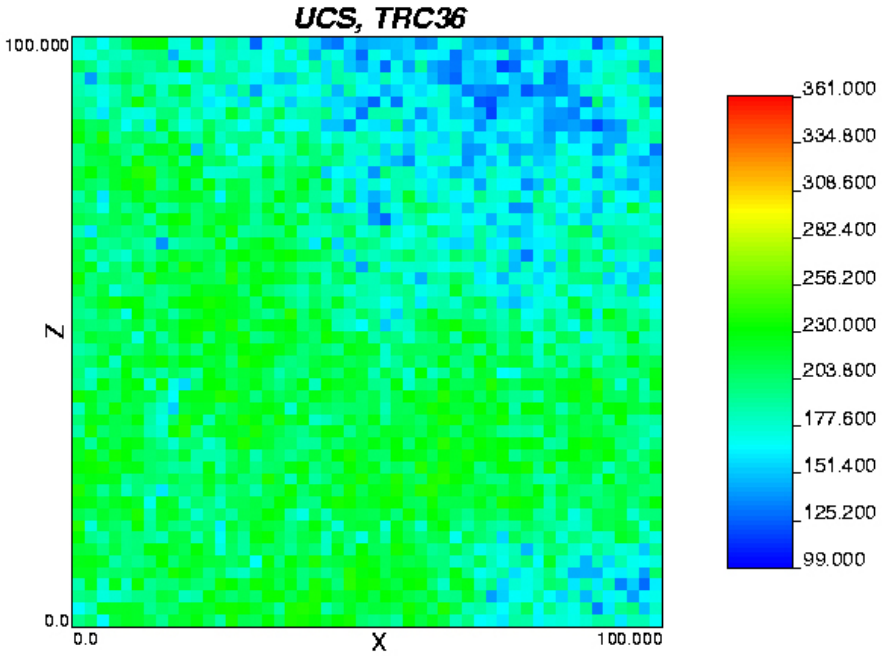

Figure A8-10. *2D slice from one 3D realisation (resolution = 2 m) illustrating the distribution of compressive strength values in TRC 36. Realisation 1, Slice = 25, xz-plane. Distance is in metres.*

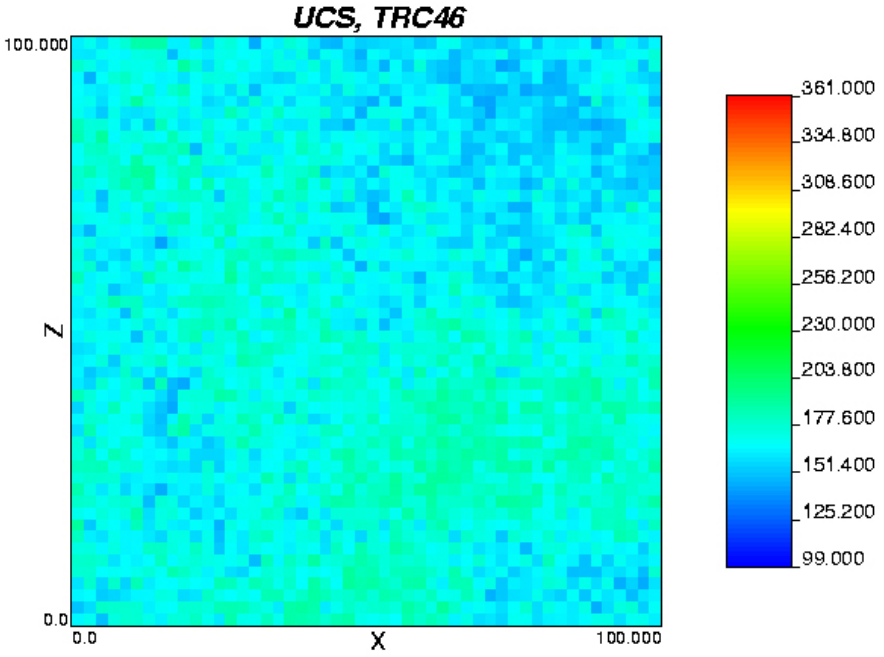

Figure A8-11. *2D slice from one 3D realisation (resolution = 2 m) illustrating the distribution of compressive strength values in TRC 46. Realisation 1, Slice = 25, xz-plane. Distance is in metres.*

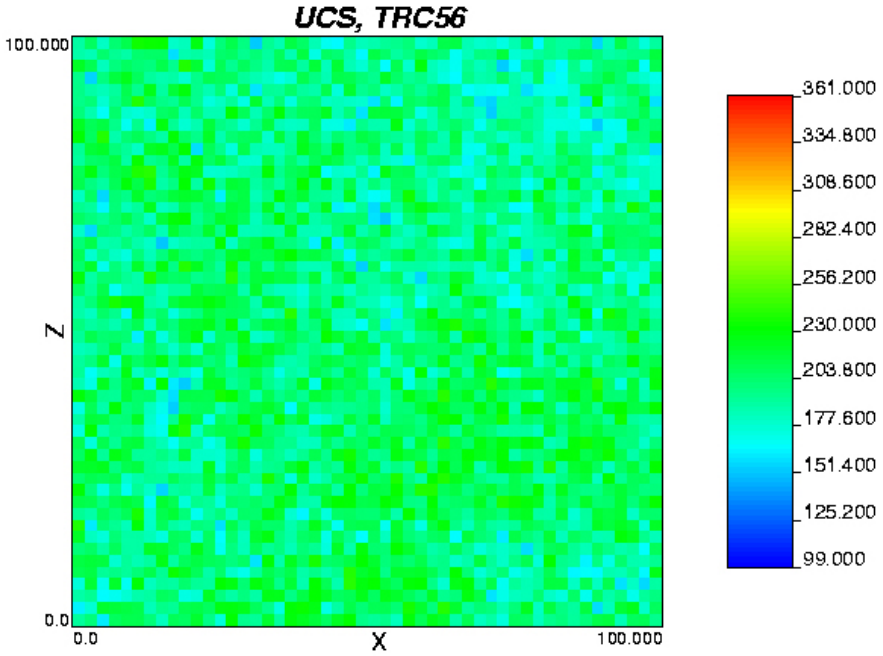

Figure A8-12. *2D slice from one 3D realisation (resolution = 2 m) illustrating the distribution of compressive strength values in TRC 56. Realisation 1, Slice = 25, xz-plane. Distance is in metres.*

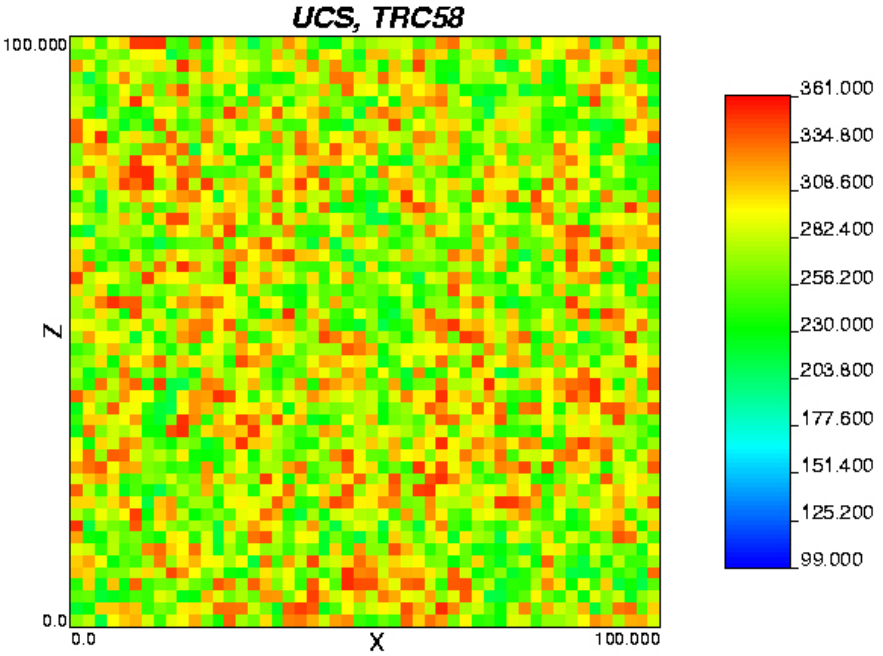

Figure A8-13. *2D slice from one 3D realisation (resolution = 2 m) illustrating the distribution of compressive strength values in TRC 58. Realisation 1, Slice = 25, xz-plane. Distance is in metres.*

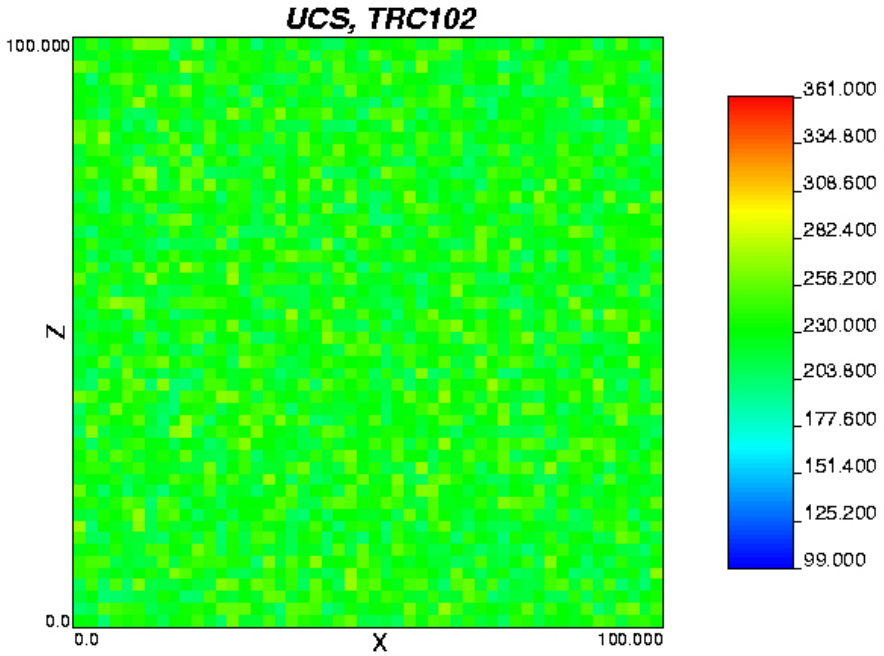

Figure A8-14. *2D slice from one 3D realisation (resolution = 2 m) illustrating the distribution of compressive strength values in TRC 102. Realisation 1, Slice = 25, xz-plane. Distance is in metres.*

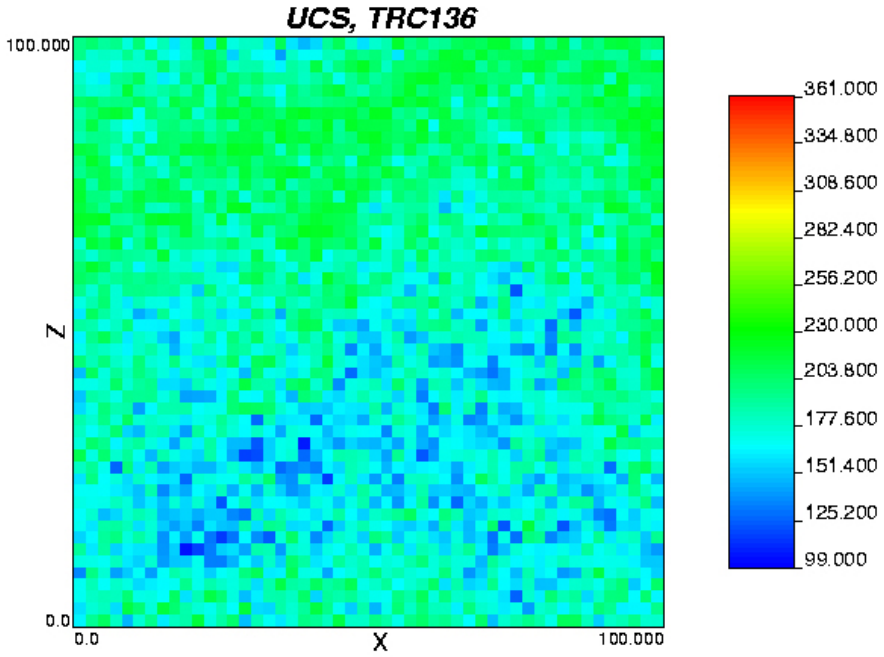

Figure A8-15. *2D slice from one 3D realisation (resolution = 2 m) illustrating the distribution of compressive strength values in TRC 136. Realisation 1, Slice = 25, xz-plane. Distance is in metres.*

A8.3 Simulation of UCS for each Rock domain

A8.3.1 Histogram of simulated UCS values for each Rock domain

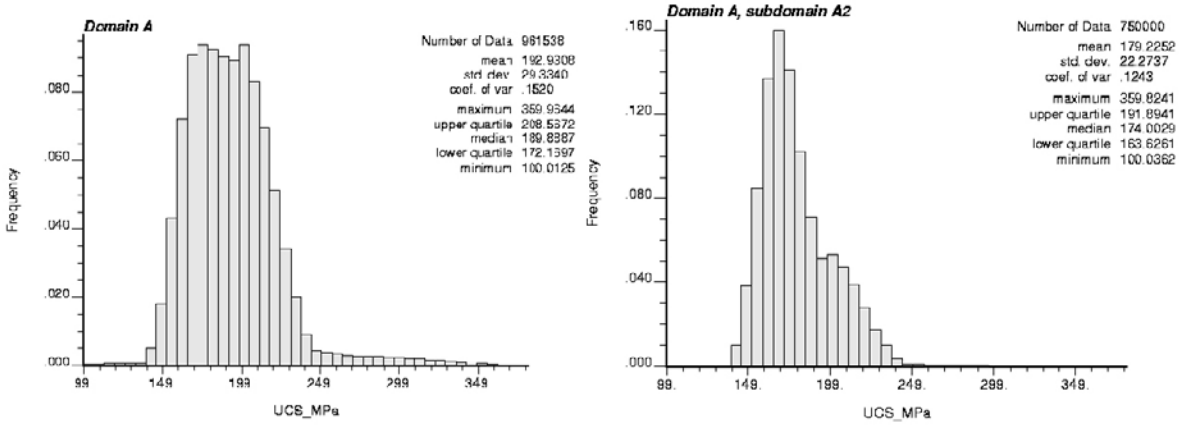

Figure A8-16. *Histogram of compressive strength at sample scale (dm) for rock domain RSMA01 (left) and subdomain A2 within domain RSMA01 based on simulations.*

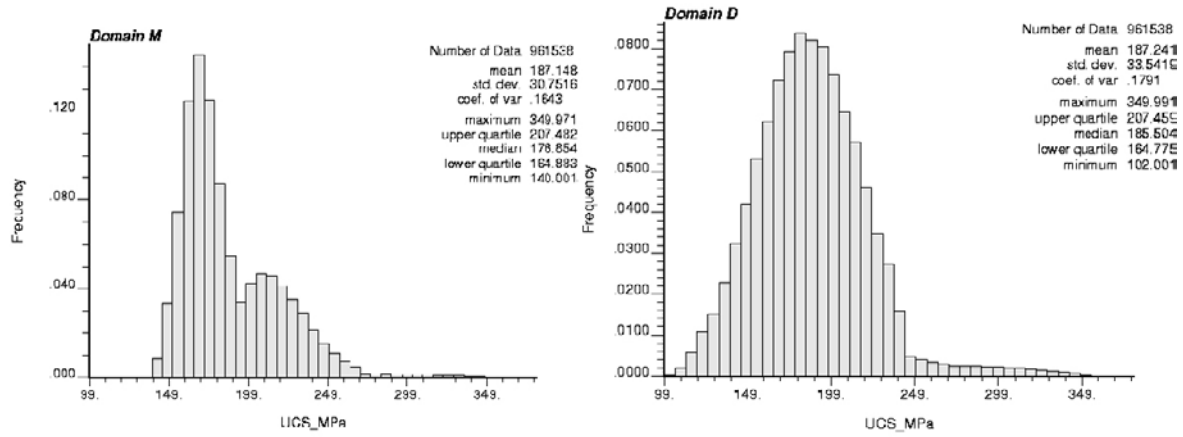

Figure A8-17. *Histogram of compressive strength at sample scale (dm) for rock domains RSMM01 and RSMD01 based on simulations.*

A8.3.2 Visualisations of UCS realisations for each Rock domain

In this appendix, example realisations of UCS and the corresponding realisations of TRCs are presented in 2D for simulations with a resolution of 2 m for rock domains RSMA01, RSMM01 and RSMD01. All 2D-realisations represent a slice in the centre of a 3D cube. For example, the 25th slice of the xz-plane is the 25th slice that can be cut in the z-direction (there are 50 slices). Distance is in metres.

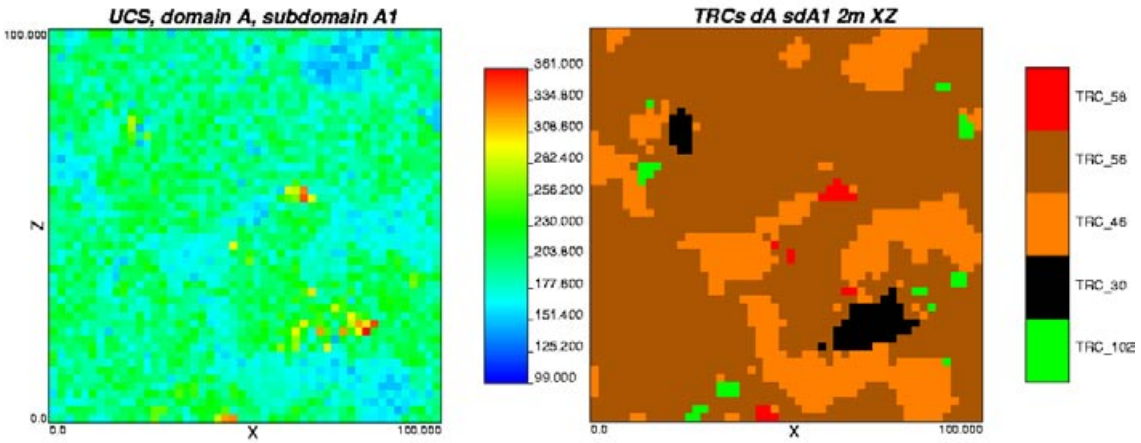

Figure A8-18. *2D slice from one 3D realisation for subdomain A1, domain RSMA01 (resolution = 2 m) illustrating the distribution of uniaxial compressive strength (left) and rock classes (right). Realisation = 1, Slice=25, xz-plane. Distance is in metres.*

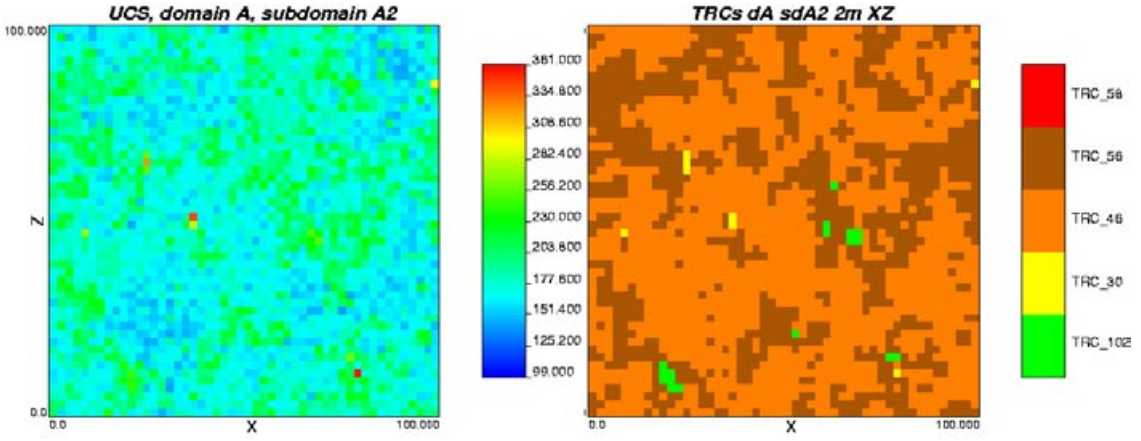

Figure A8-19. *2D slice from one 3D realisation for subdomain A2, domain RSMA01 (resolution = 2 m) illustrating the distribution of uniaxial compressive strength (left) and rock classes (right). Realisation = 1, Slice=25, xz-plane. Distance is in metres.*

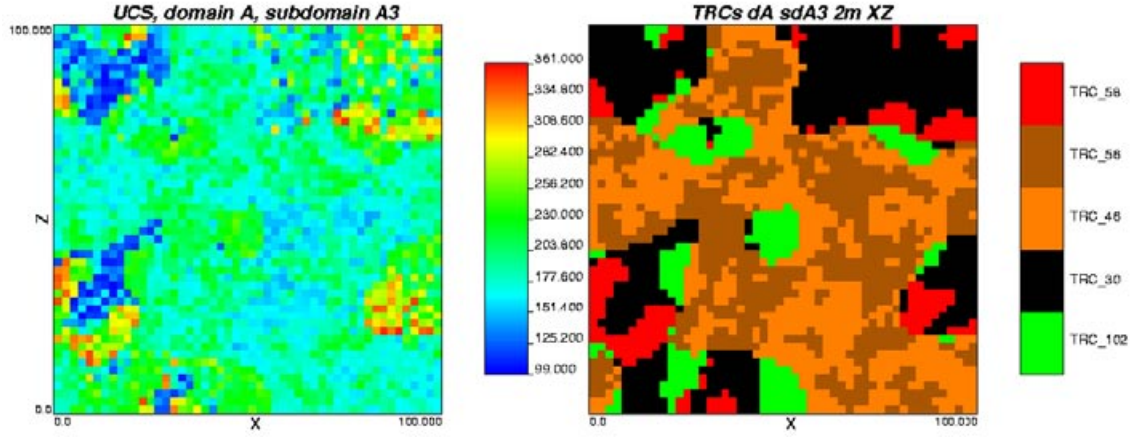

Figure A8-20. *2D slice from one 3D realisation for subdomain A3, domain RSMA01 (resolution = 2 m) illustrating the distribution of uniaxial compressive strength (left) and rock classes (right). Realisation = 1, Slice=25, xz-plane. Distance is in metres.*

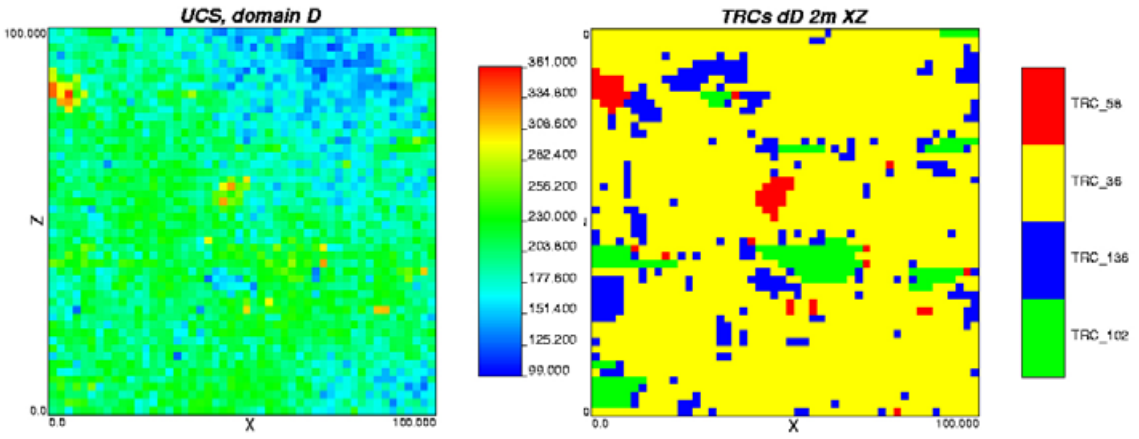

Figure A8-21. *2D slice from one 3D realisation for domain RSMD01 (resolution = 2 m) illustrating the distribution of uniaxial compressive strength (left) and rock classes (right). Realisation = 1, Slice=25, xz-plane. Distance is in metres.*

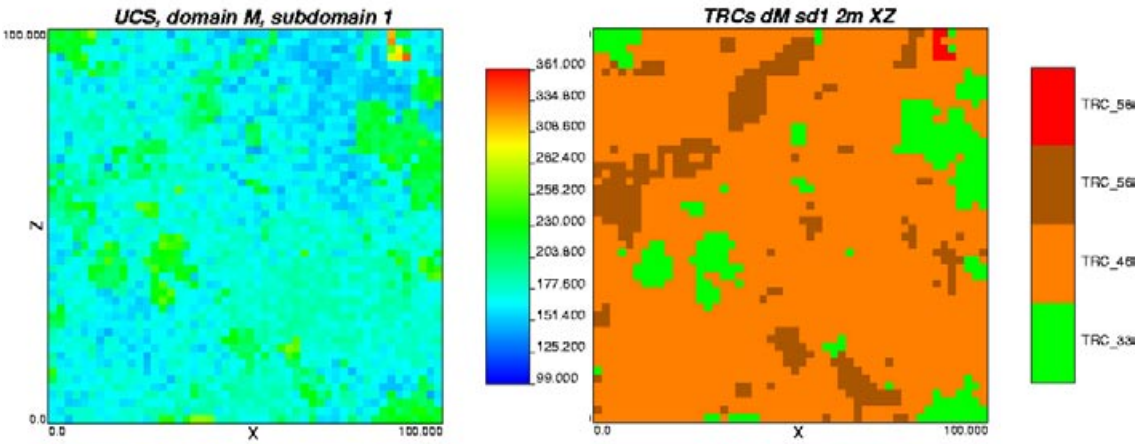

Figure A8-22. *2D slice from one 3D realisation for subdomain M1, domain RSMM01 (resolution = 2 m) illustrating the distribution of uniaxial compressive strength (left) and rock classes (right). Realisation = 1, Slice=25, xz-plane. Distance is in metres.*

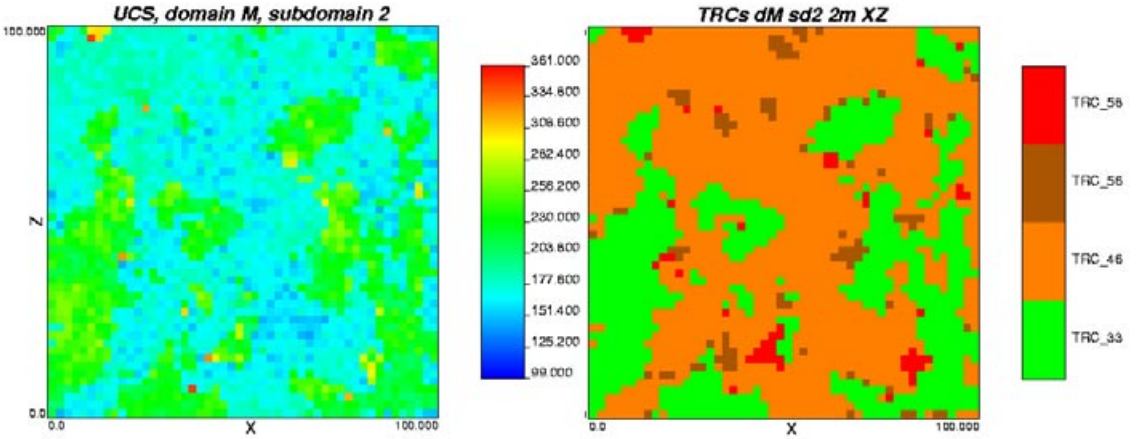

Figure A8-23. *2D slice from one 3D realisation for subdomain M2, domain RSMM01 (resolution = 2 m) illustrating the distribution of uniaxial compressive strength (left) and rock classes (right). Realisation = 1, Slice=25, xz-plane. Distance is in metres.*

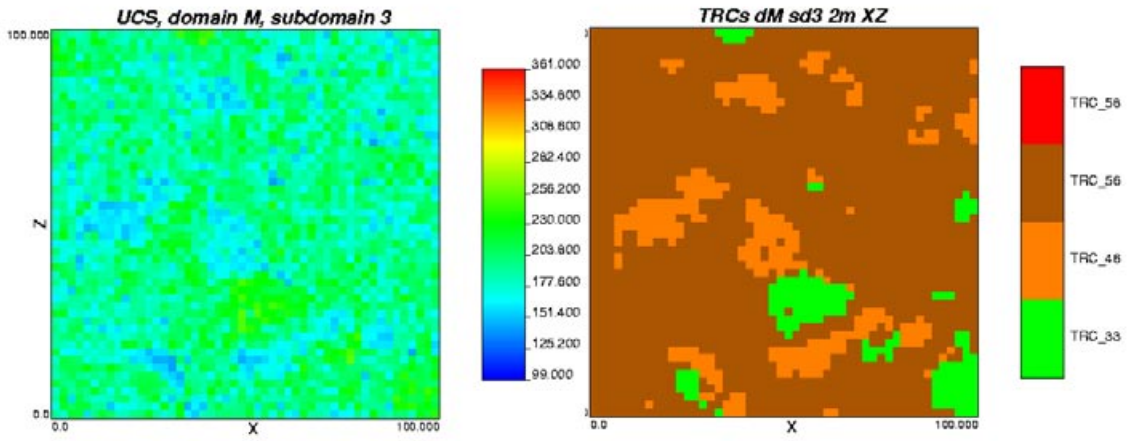

Figure A8-24. *2D slice from one 3D realisation for subdomain M3, domain RSMM01 (resolution = 2 m) illustrating the distribution of uniaxial compressive strength (left) and rock classes (right). Realisation = 1, Slice=25, xz-plane. Distance is in metres.*

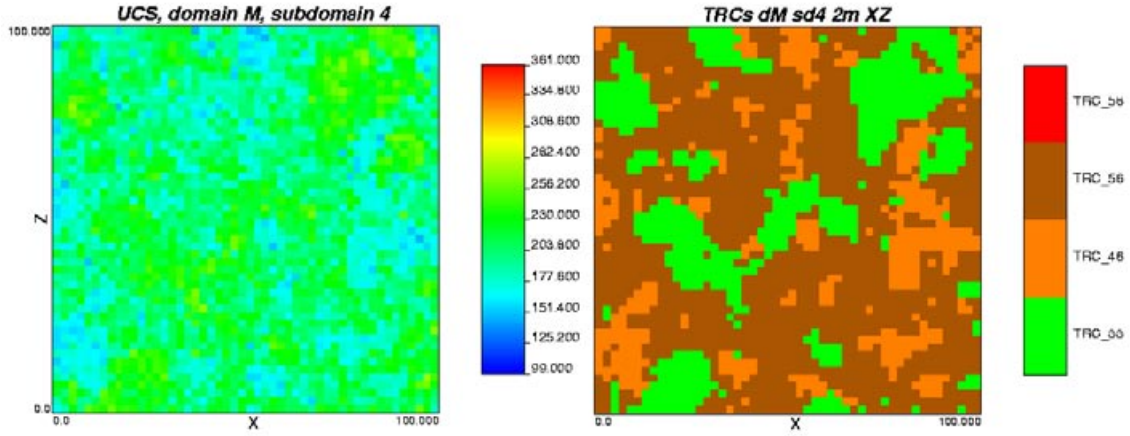

Figure A8-25. *2D slice from one 3D realisation for subdomain M4, domain RSMM01 (resolution = 2 m) illustrating the distribution of uniaxial compressive strength (left) and rock classes (right). Realisation = 1, Slice=25, xz-plane. Distance is in metres.*

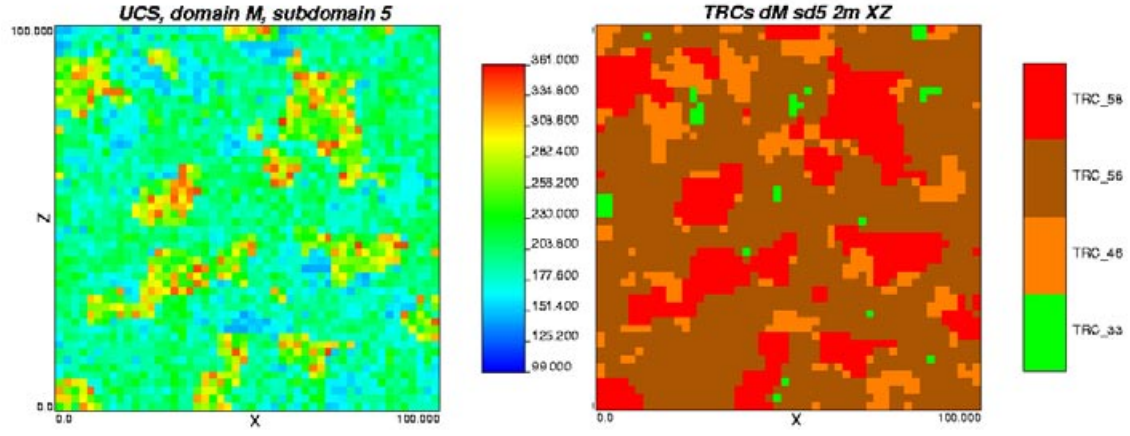

Figure A8-26. *2D slice from one 3D realisation for subdomain M5, domain RSMM01 (resolution = 2 m) illustrating the distribution of uniaxial compressive strength (left) and rock classes (right). Realisation = 1, Slice=25, xz-plane. Distance is in metres.*